Shock and Vibration

Underground Infrastructure under Explosion Loads

Lead Guest Editor: Jianwei Cheng
Guest Editors: Jerry Tien, Yi Luo, and Zongqing Tang

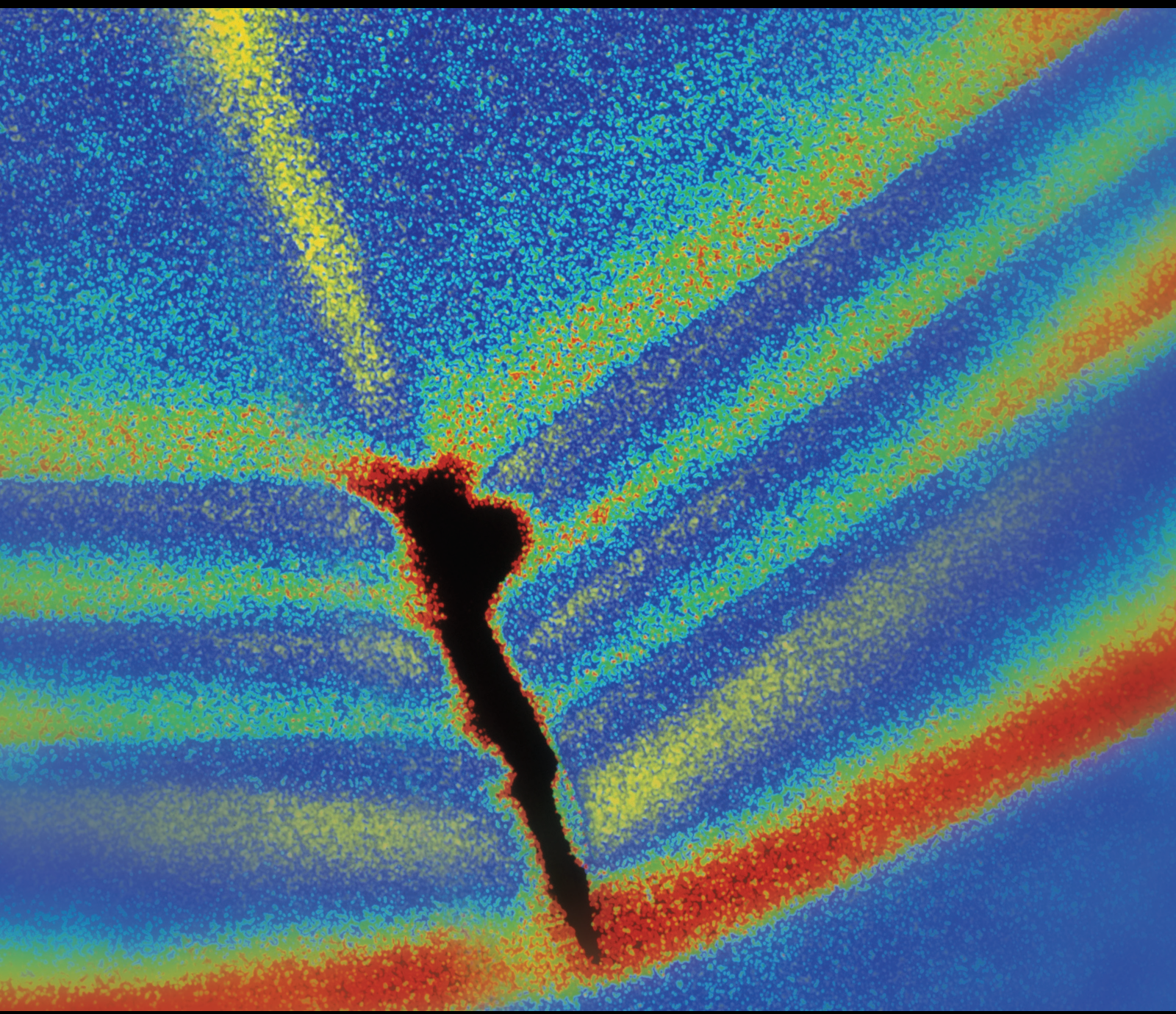

Underground Infrastructure under Explosion Loads

Shock and Vibration

Underground Infrastructure under Explosion Loads

Lead Guest Editor: Jianwei Cheng
Guest Editors: Jerry Tien, Yi Luo, and Zongqing Tang

Chief Editor

Associate Editors

Academic Editors

Contents

Hindawi
Shock and Vibration
Volume 2022, Article ID 8567416, 11 pages
https://doi.org/10.1155/2022/8567416

Research Article

Law of Countercurrent Energy Dissipation of Fresh Air by Coal and Gas Outburst Shock Waves

Haiteng Xue,[1,2,3] **Xijian Li**,[1,2,3] **Zhu Liu**,[1,2,3] **Fangrui Dai**,[1,2,3] **and Bei Hu**[1,2,3]

[1]*Mining College, Guizhou University, Guiyang 550025, China*
[2]*Institute of Gas Disaster Prevention and Coalbed Methane Development of Guizhou University, Guiyang 550025, China*
[3]*Engineering Center for Safe Mining Technology Under Complex Geologic Condition, Guiyang 550025, China*

Correspondence should be addressed to Xijian Li; xjli1@gzu.edu.cn

Received 20 August 2021; Revised 22 March 2022; Accepted 22 April 2022; Published 13 June 2022

Academic Editor: Zongqing Tang

Accidental coal and gas outbursts lead to major disasters in coal-producing countries and are difficult to mitigate. To elucidate the energy dissipation law for coal and gas outburst shock waves in a complex ventilation network of mines, a coal-and-gas-outburst-energy-propagation simulation and parameter determination test device were developed and used to perform physical simulation experiments under different outburst strength conditions. These experiments were combined with numerical simulations to obtain the propagation law of outburst shock waves in a roadway and analyze different outburst intensities according to the gas counterflow criterion, highlighting the hazard characteristics of shock waves in a fresh air tunnel. The results showed that when a shock wave passed through the turning roadway, its intensity and speed were greatly attenuated and that the overpressure value of a shock wave in a straight roadway was greater than that at a corner. Upon encountering a rigid wall, the superposition of the incident and reflected shock waves increased the peak overpressure of the shock wave per unit area. When a fresh air roadway is near the coal uncovering position in rock drift ("Shimen") a corresponding counter-backflow device should be installed at the location of the connecting road near the fresh air roadway, under the condition that normal ventilation is not affected. These numerical simulation results are consistent with general experimental trends, indicating that the analyses conducted in this study are reliable and can provide a theoretical basis for the prevention of secondary disasters due to coal and gas outbursts in mines.

1. Introduction

Coal is the dominant component in China's energy mix [1, 2]. However, with the depletion of shallow coal resources and increases in energy demand, coal mining in deep mines has become a research topic [3, 4]. According to recent surveys and statistics, the deepest mining depth of coal resources in China is 2000 m and it accounts for 70% of all coal resources. Rich deep coal reserves provide China's potential energy resource [5]. However, owing to the "high ground stress, high ground temperature, and high karst water pressure" environments of deep rock masses, many mining disasters have occurred. The increased probability of mining disasters has brought huge challenges to the development of deep coal resources [6].

Coal and gas outbursts are large-scale dynamic mine phenomena that are extremely destructive and have to be characterized by complex mechanisms [6]. There are two main forms of damage [7]: first, the instantaneous ejection of high-pressured gas and coal powder. In this case, the gas flow can directly injure nearby personnel and damage the on-site structure and equipment. Second, the shock wave generated by the outburst destroys the ventilation system and causes gas backflow, which not only suffocates personnel but also causes secondary disasters such as gas and coal dust explosions. Therefore, research on coal and gas, the mechanism of gas outbursts, and the effectiveness of ventilation facilities under catastrophic conditions are important issues that must be considered for improved coal mine safety. At present, three commonly used methods explore the mechanism of coal and gas outbursts: physical simulation experiments, numerical simulations, and mathematical models. For physical simulations, experiments are based on the results of the fluid mechanics similarity criterion. According to actual conditions,

certain similarity scales may be determined for the model; thus, the results of similar simulations are more in-line with actual processes. In China, the development of a large-scale truly three-dimensional coal and gas outburst quantitative physical simulation test system, which greatly improves the similarity between the field and the simulated test conditions, breaks the traditional qualitative interpretation of coal and gas outbursts, and provides a quantitative test platform for domestic and foreign scholars to explore the mechanism of coal and gas outbursts [8]. However, with respect to coal, the high-speed and high-pressure impulse airflow generated instantaneously with a gas outburst makes it difficult to perform on-site and indoor physical simulation experiments to visually reproduce the propagation process of impingement airflow.

Numerical simulation software is usually used to analyze the distribution of impinging airflow pressure and velocity in a tunnel at different times. Li et al. [9] derived a mathematical model of unsteady airflow and gas movement based on the theory of active ventilation network, which could calculate the airflow pressure of natural gas in the ventilation system of a mine. They also verified the accuracy of the model using prominent real-world cases. The scientific formulation of emergency plans for outburst disasters provides a theoretical basis for future research. Xue et al. [10] combined the discrete-element and Boltzmann methods to construct a numerical model for coal and gas outbursts and verified the feasibility of the model using a simple two-dimensional example simulating the protrusion process. Tao et al. [11] established a coupled model for coal thermophysical properties using the theory of elasticity, seepage mechanics, and heat transfer and compared the analytical and numerical solutions to verify the model, laying a theoretical foundation for the prevention of coal and gas outbursts. However, given the complexity of the actual roadway network of mines, the numerical simulation software could not address large and complex roadway networks. Therefore, when performing numerical simulations, the employed model must also be simplified, which may easily lead to a deviation of the results. In addition, in terms of mathematical models, mathematical analysis methods are mainly used to predict the risk of coal and gas outbursts [12–16] and do not employ a complete mechanical model. The above-mentioned research has provided an improved understanding of coal and gas outbursts. However, these different methods still present drawbacks due to insufficient understanding of the coal and gas outburst mechanism to be used in the field for forecasting, resulting in the continued occurrence of coal and gas outburst accidents. This indicates that in addition to studying the coal and gas outburst mechanism, coal and gas outbursts and the laws governing the movement of shock waves in complex roadways must also be further explored.

Elucidating the propagation of shock waves in mine tunnels after coal and gas outbursts is the key to reducing outbursts that cause secondary disaster accidents. Zhou et al. [17, 18] analyzed the formation and propagation process of the coal–gas two-phase flow in different types of tunnels and found that shock waves had the best attenuation effect in a T-shaped roadway. Wang et al. [19] combined numerical simulations and experiments to study prominent shock wave and gas flow characteristics and found that when the shock wave and airflow propagated toward the intersection, turbulence, reflection, and diffraction phenomena would occur. Furthermore, for most of them, the shock wave and airflow propagated to the roadway on the opposite side of the intersection. However, the aforementioned study did not involve interactions between the overpressure of shock waves and mine ventilation resistance after outbursts of coal and gas. Moreover, few studies have been conducted on the hazard characteristics of an outburst shock wave in a fresh air tunnel when the outburst of coal and gas occurs, and the outburst-prevention door is intact.

In view of this, this study describes a self-developed "coal and gas outburst energy propagation simulation and parameter determination test device," which was combined with numerical simulation methods to study both the propagation of outburst shock waves in a complex ventilation network and differences according to the gas counterflow criterion. Under the condition of outburst strength, the outburst shock wave presents the characteristics of gas counterflow in a fresh air tunnel. This study is expected to provide theoretical support for the prevention of secondary disasters related to coal and gas outbursts and emergency rescue.

2. Materials and Methods

2.1. Prominent Shock Wave Propagation Governing Equation. The continuity, momentum, energy, and composition equations of gases are used to describe the dynamic process of prominent shock wave propagation. The governing equation for prominent shockwave propagations are as follows:

$$\begin{cases} \dfrac{\partial \rho}{\partial t} + \dfrac{\partial (\rho \mu_i)}{\partial x_i} = 0, \\ \dfrac{\partial (\rho \mu_i)}{\partial t} + \dfrac{\partial \left(\rho \mu_j \mu_i\right)}{\partial x_j} = -\dfrac{\partial p}{\partial x_i} + \dfrac{\partial \tau_{ij}}{\partial c_j} + \rho g_i + F_i, \\ \dfrac{\partial (\rho E)}{\partial t} + \dfrac{\partial \left(\mu_i (\rho E + p)\right)}{\partial x_i} \\ = \dfrac{\partial}{\partial x_i}\left(k_{eff} \dfrac{\partial T}{\partial x_i} - \sum_{j'} h_{j'} J_{j'} + \mu_i \left(\tau_{ij}\right)_{eff} + S_h \right), \\ \dfrac{\partial (\rho \mu Y_i)}{\partial t} + \nabla \cdot \left(\rho \overrightarrow{v} Y_i\right) = -\nabla \cdot \overrightarrow{J}_i + R_i + S_i, \\ \overrightarrow{J}_i = -\rho D_{i,m} \nabla Y_i, \end{cases} \tag{1}$$

where τ_{ij} is the stress tensor, ρ is the gas density, S_i is the discrete term, F_i is the volumetric stress, ρ_{gi} is the gravitational volume force, $J_{j'}$ is the diffusion flux, and R_i is the netsource term for the chemical reaction.

The flow of coal and gas outburst shock waves is turbulent; therefore, the effect of turbulence needs to be considered in the simulation. The $k-\varepsilon$ turbulence model can be expressed as follows:

$$\begin{cases} \rho \dfrac{Dk}{Dt} = \dfrac{\partial}{\partial x_i}\left[\left(\mu + \dfrac{\mu_t}{\mu_k}\right)\dfrac{\partial k}{\partial x_i}\right] + G_k + G_b - \rho\varepsilon - Y_M, \\ \rho \dfrac{D\varepsilon}{Dt} = \dfrac{\partial}{\partial x_i}\left[\left(\mu + \dfrac{\mu_t}{\mu_k}\right)\dfrac{\partial \varepsilon}{\partial x_i}\right] + C_{1z}\dfrac{\varepsilon}{k}\left(G_k + C_{3z}G_b\right) - C_{2z}\rho\dfrac{\varepsilon^2}{k}, \end{cases} \quad (2)$$

where Y_M is the contribution of the compressible turbulent pulsation expansion, G_b is the turbulent energy produced by buoyancy, and G_k is the turbulent energy produced by the average velocity gradient. Here, $C_{1z} = 1.44$, $C_{2z} = 1.92$, and $C_\mu = 0.09$.

2.2. Numerical Model. Owing to the complexity of the physical test roadway network, the numerical simulation software could not achieve convergence. Therefore, according to the focus of the research, the test roadway was simplified, and a two-dimensional model for the prominent shock wave was subsequently established, as shown in Figure 1. This model mainly consists of the prominent cavity and ventilation network of the roadway in two parts. The size of the protruding cavity is 50 cm × 30 cm × 30 cm, and the size of the simulated roadway is 20 cm × 20 cm. The initial conditions used in this study are presented in Table 1.

2.3. Experimental Design of the Shock Wave Test System. To verify the results of the numerical simulations, a new coal and gas outburst energy propagation simulation and parameter determination test device is presented. The test system is based on a complex ventilation network and is designed to be scaled down. The system mainly consists of outburst cavities, simulated mine tunnels, pressure sensors, and ventilation power. A system and data acquisition terminal system are also included. A schematic of the test system is shown in Figure 2 with arrows indicating the flow direction of fresh airflow, and the straight roadway, where measurement points 4 and 5 are located, is the fresh air roadway. The size of the experimental roadway is 20 cm × 20 cm.

After vacuumizing the protruding chamber for 1 h, open the valve connected to the high-pressure tube of the gas cylinder to fill the protruding chamber with nitrogen. The charging pressure is 0.3, 0.4, 0.5, 0.7, 0.9, and 1 MPa, and the step charging is carried out with 0.1 MPa as a step until the pressure reaches the set value and becomes stable. Close the high pressure pipe valve connected to the gas cylinder, stand still for 30 s, and move the quick pressure relief device manually to simulate the start of protruding.

2.4. Gas Counterflow Model. Gas counterflow is the main factor behind a large number of underground worker deaths. There are two forms of counterflow: one in which an instantaneously high concentration of gas directly causes suffocation and death of on-site staff; the other in which a high concentration of gas reverses the ventilation airflow and causes a large amount of highly poisonous gases. Harmful gas enters the fresh air tunnel, causing workers outside the door and other workplace personnel to suffocate and die.

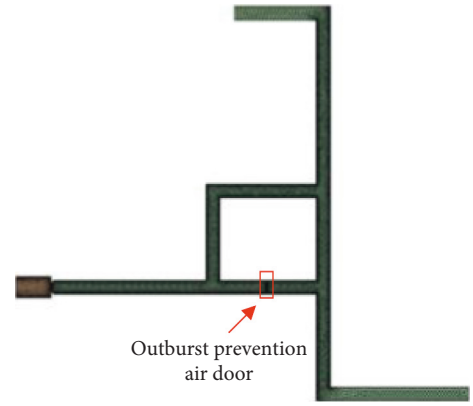

Figure 1: Meshing of the geometric model.

Table 1: Model initialization parameter settings.

	Parameter	Initial value	Unit
In the lane	Gas type	Air	
	Gas flow rate	0	m/s
	Proportion of gas volume	0	m^3/m^3
	Gas temperature	300	K
	Gas pressure	0.1	MPa
Inside the cavity	Gas type	CH_4	
	Proportion of gas volume	1	m^3/m^3
	Gas temperature	300	K
	Gas pressure	1, 0.9, 0.7, 0.5, 0.4	MPa

When the overpressure of the protruding shock wave is greater than the ventilation resistance of a certain section of the mine, it causes the airflow in that section of the tunnel to reverse, leading to gas reversal. In the calculations, the following assumptions are made:

(1) The simulated roadway in the physical test is a horizontal roadway with no height differences

(2) The gas flow after protrusion is comprised of an incompressible gas

(3) The changes in the temperature are ignored

The only possible situation in which the gas can reverse its direction after an outburst is when the total energy of the outburst shock wave is greater than the ventilation resistance of the tunnel. The theoretical condition for this is [20]as follows:

$$P_2 - P_0 + \left(\frac{\mu_2^2}{2} - \frac{\mu_0^2}{2}\right)\rho + g\rho\left(Z_1 - Z_0\right) > h_R, \quad (3)$$

where ρ is the air density (kg/m^3); g is the acceleration due to gravity (m/s^2); Z_1 and Z_2 are the elevations from the reference plane, m; h_R is the ventilation resistance, N/m^2–this is a pressure unit, not resistance; μ_2 is the shock wave front velocity, m/s; μ_0 is the airflow velocity under ventilation conditions, m/s; P_0 is the atmospheric pressure, which is 101.325 kPa; and P_2 is the shock wave pressure, kPa.

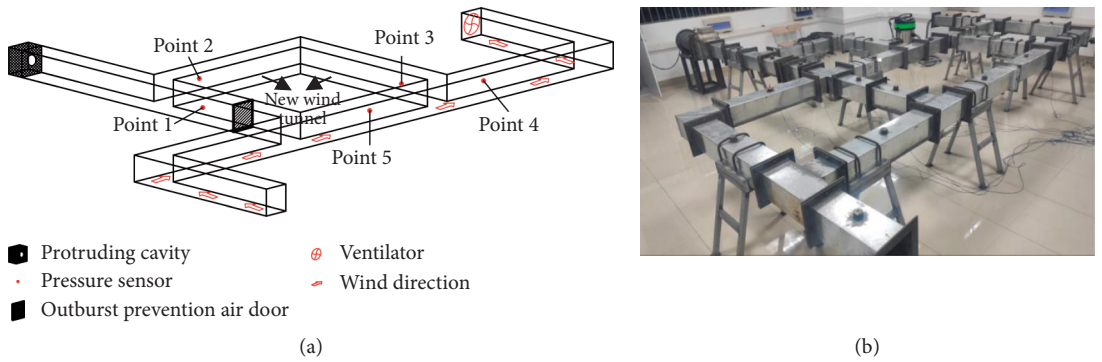

Figure 2: Physical experimental system. (a) Schematic of the physical experiment system. (b) Experimental system diagram.

The shock wave front velocity μ_2 may be expressed as [21] follows:

$$u_2 = c_1\sqrt{1+\frac{k+1}{2k}\frac{P_2}{P_0}}, \tag{4}$$

where c_1 is the speed of sound (340 m/s).

Ventilation resistance is the sum of the frictional and local resistances, which may be described as follows:

$$\begin{aligned} h_R &= h_f + h_P \\ &= \frac{\alpha LUQ^2}{S_1^3} + \xi\frac{\rho Q^2}{2S_1^2}, \end{aligned} \tag{5}$$

where h_f is the frictional resistance (N/m^2), h_P is the local resistance (N/m^2), α is the frictional resistance coefficient (kg/m^3); L is the length of the roadway (m), U is the perimeter of the roadway section (m), Q is the local section air volume (m^3/min), and ξ is the dimensionless local resistance coefficient.

After an outburst, a shock wave cannot continue to propagate in the roadway, and thus, there is no gas backflow, that is, the protruding shock wave does not generate frictional resistance against the wall of the roadway. Therefore, only local resistance in the roadway is considered, and equation (5) may be described as follows:

$$\begin{aligned} h_R &= h_p \\ &= \xi\frac{\rho Q^2}{2S_1^2}. \end{aligned} \tag{6}$$

The local resistance coefficient can be expressed as follows:

$$\xi == \left(1-\frac{S_0}{S_1}\right)^2. \tag{7}$$

Substituting equation (6) into equation (3), the results can be denoted as follows:

$$P_2 - P_0 + \left(\frac{\mu_2^2}{2}-\frac{\mu_0^2}{2}\right)\rho + g\rho(Z_1 - Z_0) > \xi\frac{\rho Q^2}{2S_1^2}. \tag{8}$$

Table 2: Model parameters.

Parameter	Value	Unit
A	0.0086	N s^2/m^4
U	0.80	m
Q	3.60	m^3/min
S_1	0.04	m^2
P	1.29	Kg/m^3
μ_0	1.50	m/s

The roadway is horizontal and straight, with no differences in height; thus, equation (8) may be expressed as follows:

$$P_2 - P_0 + \left(\frac{\mu_2^2}{2}-\frac{\mu_0^2}{2}\right)\rho > \xi\frac{\rho Q^2}{2S_1^2}. \tag{9}$$

Based on equation (9), the gas counterflow criterion may be obtained as follows:

$$P_2 > \xi\frac{\rho Q^2}{2S_1^2} + P_0 - \left(\frac{\mu_2^2}{2}-\frac{\mu_0^2}{2}\right)\rho. \tag{10}$$

Substituting equations (4) and (7) into equation (10), we obtain the following equation:

$$P_2 > \left(1-\frac{S_0}{S_1}\right)^2\frac{\rho Q^2}{2S_1^2} + P_0 - \left(c_1^2\frac{2kP_0 + P_2(k+1)}{4kP_0} - \frac{\mu_0^2}{2}\right)\rho. \tag{11}$$

Let $\Delta P = (1 - S_0/S_1)^2\rho Q^2/2S_1^2 + P_0 - (c_1^2 2kP_0 + P_2(k+1)/4kP_0 - \mu_0^2/2)\rho$. Equation (11) may then be expressed as follows:

$$P_2 > \Delta P. \tag{12}$$

By substituting the parameters and test data in Table 2 into (11), ΔP is obtained and compared to P_2. When $P_2 > \Delta P$, gas backflow occurs.

3. Results and Discussion

3.1. Simulation Result. Figure 3 shows simulation results for the cloud diagram of the pressure and velocity changes of the protruding shock wave when the protruding pressure is 1 MPa and t = 3–10 ms.

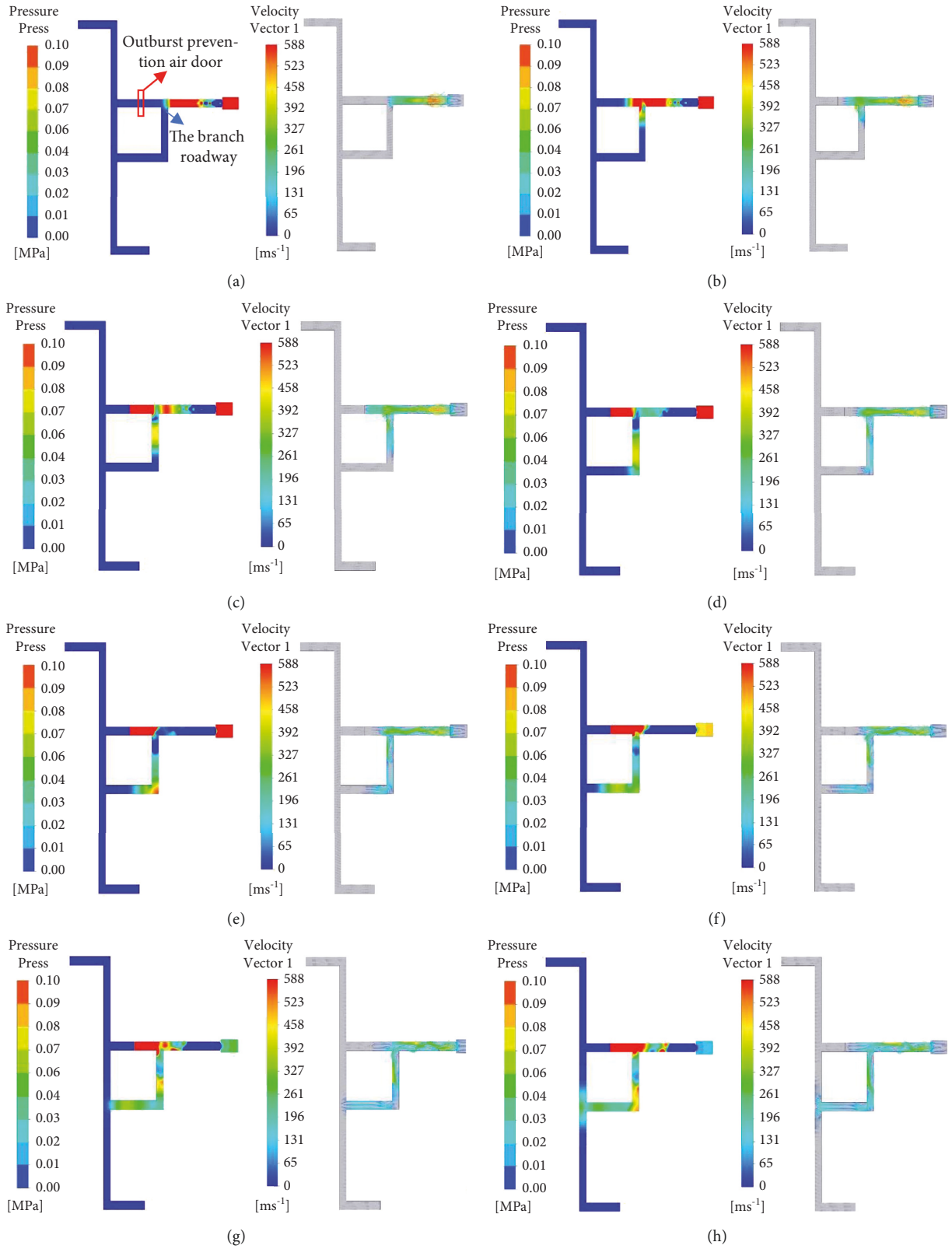

Figure 3: Cloud diagram of pressure and velocity changes in the prominent shock wave at different times. (a) $t = 3$ ms. (b) $t = 4$ ms. (c) $t = 5$ ms. (d) $t = 6$ ms. (e) $t = 7$ ms. (f) $t = 8$ ms. (g) $t = 9$ ms. (h) $t = 10$ ms.

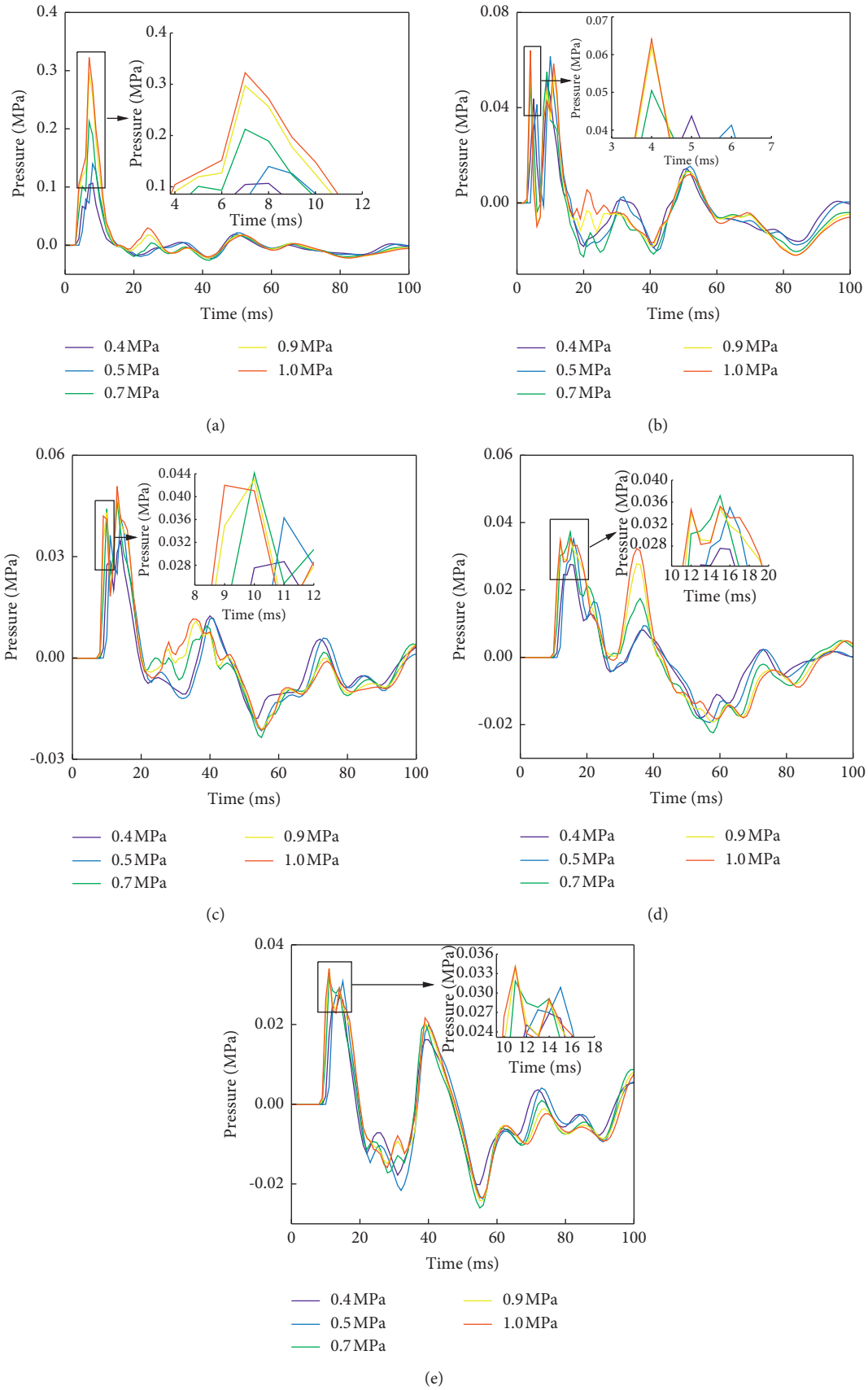

Figure 4: Variation of shock wave overpressure with time. (a) Point No. 1. (b) Point No. 2. (c) Point No. 3. (d) Point No. 4. (e) Point No. 5.

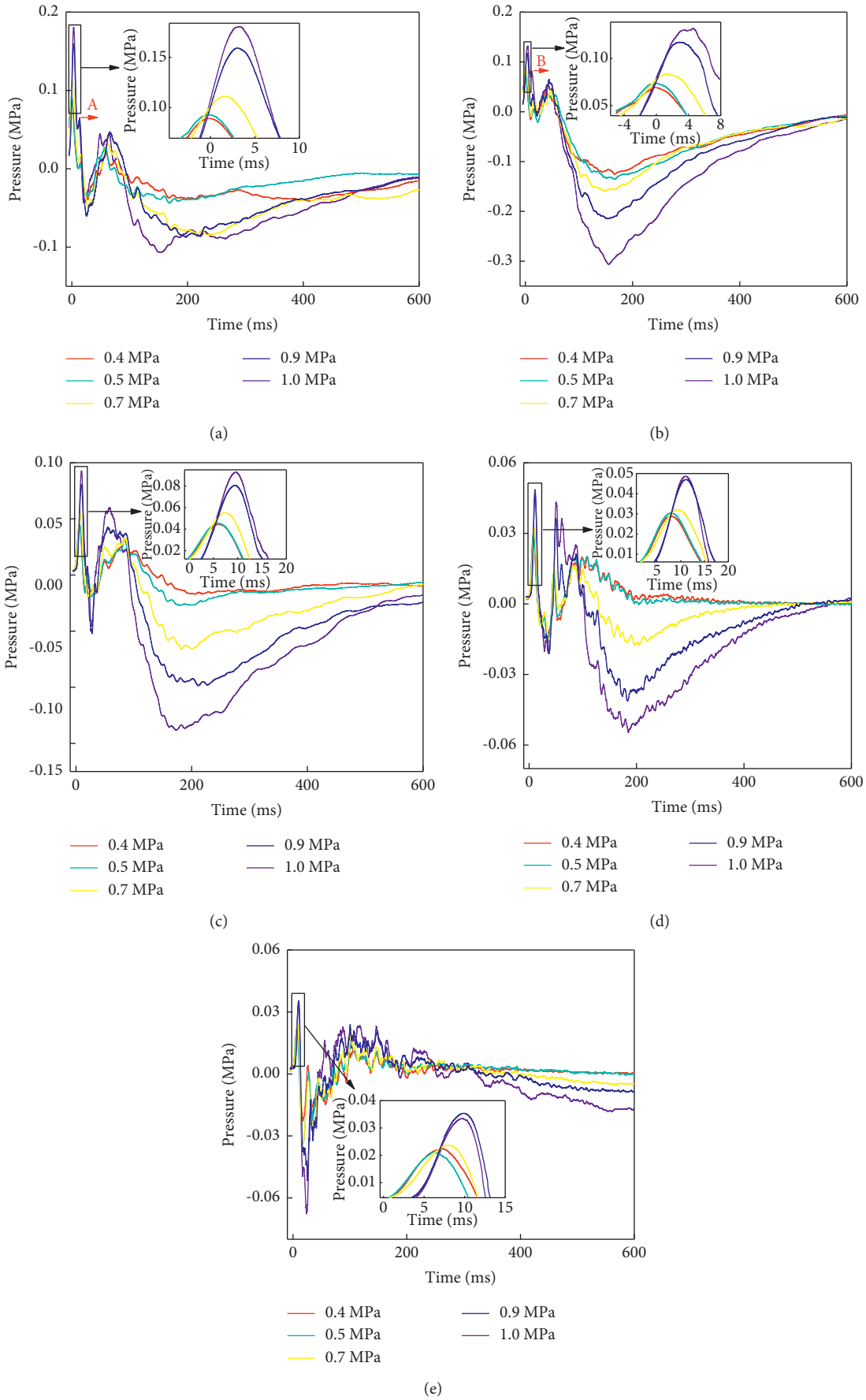

Figure 5: Shock wave overpressure change curve (a) Point No. 1. (b) Point No. 2. (c) Point No. 3. (d) Point No. 4. (e) Point No. 5.

Analysis of the simulation results are as follows:

(1) Figure 3(a) shows that at $t = 3$ ms, the shock wave arrives at a corner and diffracts; the shock wave front is spherical, and the maximum impact air velocity on the wave front is approximately 394 m/s. In terms of shock wave velocity, the vector diagram shows that the velocity direction of the shock wave is disordered. The maximum velocity of the disturbed airflow ahead was 56.70 m/s at the corner, and the maximum pressure was at the wall of the straight roadway, which was 0.015 MPa. The impact air pressure of the straight roadway is greater than the impact air pressure at the corner.

(2) Figure 3(b) shows that at $t = 4$ ms, the impact airflow is divided into two parts, and the front end of the impacting airflow propagating in the straight roadway is a positive shock wave; the shock wave propagating along the branch roadway is caused by the impact and reflection on the wall of the roadway. The direction of the impinging airflow is turbulent, and vortex flow is generated at the corner, forming an oblique shock wave. The front velocity of the impinging airflow is approximately 225 m/s in a straight tunnel, and the maximum pressure of the impinging airflow at the corner is approximately 385.17 m/s.

(3) Figure 3(c) shows that at $t = 5$ ms, the shock wave propagating in the straight roadway is reflected by the impact of the damper. Owing to the superposition of the reflected and incident shock waves, the pressure of the shock wave in front of the damper increases, and the maximum pressure is 0.25 MPa. The shock wave propagating in the branch roadway is converted from an oblique shock wave to a positive shock wave. The maximum pressure of the impinging airflow is approximately 146 m/s, and the impinging air velocity is greatly attenuated.

(4) Figure 3(d) shows that at $t = 6$ ms, the impinging airflow along the branch lane propagates to the next corner. Owing to the vortex area, the impinging airflow pressure is unevenly distributed, and the maximum pressure is 0.094 MPa, which is located in the roadway outside the corner. In the airflow disturbance zone in front of the corner, the maximum air velocity is 46.31 m/s. From the impact air velocity vector diagram, it can be found that the direction of the impact air velocity changes after hitting the air door. Owing to the blocking effect of the air door, the impinging air velocity of the airflow in the area near the air door decreases rapidly, and the maximum air velocity is 15 m/s, which is at the edge of the roadway wall.

(5) Figures 3(e) and 3(f) show that as the shock wave continues to propagate forward, the velocity of the impinging airflow decreases owing to the wall friction and the reflection and consumption of the impinging airflow at the corner. At $t = 7$ and 8 ms, the impact of the maximum velocities in the disturbance zone in front of the airflow are 41.31 and 38.11 m/s, respectively.

(6) Figures 3(g) and 3(h) show that owing to the expansion of the roadway, the shock wave suddenly expands. At this time, the wave front is converted from a plane wave to a spherical shape. Diffraction occurred because of the change in the airflow direction. The airflow pressure and speed are high, and at the corner wall airflow, the pressure and speed are low, resulting in the formation of low-pressure vortices at the corners on both sides. In addition to the shock wave that collides with the facing roadway wall, some shock waves propagate to both sides of the roadway. The maximum pressure of the shock wave propagating in the direction of the wind flow is 0.013 MPa. The maximum pressure of the impinging airflow propagating in the direction opposite to that of the wind flow is 0.011 MPa.

Figure 4 shows the curve of the shock wave overpressure with time. Under various pressure conditions, the following results may be observed from Figure 4:

(1) The maximum overpressure values of the shock waves at measuring points 1, 2, 3, 4, and 5 are 0.32, 0.064, 0.050, 0.035, and 0.034 MPa, respectively, and the maximum overpressure values of measuring points 1 and 3 are caused by the superposition of the reflected wave after the shock wave hits the rigid wall and incident shock wave. Before the impact airflow collides with the roadway wall, the maximum overpressures of the shock waves at measuring points 1 and 3 are 0.104 MPa and 0.042 MPa, respectively. The impact airflow bifurcates; thus, the reflection and wall friction at the corners of the roadway cause the shock wave overpressure to differ when the impinging airflow propagates to the measuring points at various positions. Under the same pressure conditions, the impulsive air pressure tends to attenuate continuously throughout the process, and the smaller the prominent pressure, the smaller the shock wave overpressure.

(2) Comparing the maximum overpressure values of measuring points 1 and 2, the impact of air pressure at measuring point 1 is much greater than that at measuring point 2. This is mainly due to the collision and reflection of the shunt and impact airflow with the corner wall surface, which consumes part of the shock wave. Does energy reduce the shock wave overpressure? Unclear what it means in the bifurcated roadway. Simultaneously, when the impact airflow encounters the bifurcation roadway, the shock wave is diffracted at the corner of the roadway, causing most of the impact airflow to propagate in the straight roadway.

(3) Comparing the maximum overpressure values of measurement at points 2 and 3, the maximum overpressure value of the shock wave at point 2 is greater than that at point 3; however, the pressure

drop is not large. This is due to the maximum overpressure at the two measurement points. The peak appearance time differs from that of the formation mechanism. The maximum pressure peak at point 2 is caused by the incident shock wave passing through the corner, and the appearance time is 4 ms, whereas the maximum pressure monitored by point 3 appears at the second extreme point, at a time of 13 ms. This pressure is caused by the collision of the incident shock wave with the rigid wall facing the T-shaped roadway, and the reflected shock wave generated is superimposed with the incident shock wave, increasing the intensity of the impact airflow in the area.

(4) Comparing the maximum overpressure values of points 4 and 5, the pressure peak at point 5 is slightly smaller than that at point 4. The propagation direction is opposite to the direction of the airflow; therefore, the resistance of the shock wave during the propagation increases, the intensity of the shock wave attenuates, and the shock wave overpressure at point 5 decreases.

(5) Under varying pressure conditions, the greater the outburst pressure, the greater the shock wave overpressure. Simultaneously, owing to the friction of the roadway wall and the obstructive effect of the corners, the shock wave overpressure exhibits a general attenuation trend.

Table 3: Model calculation results.

Test pressure/MPa	P_2/kPa	ΔP/kPa
1.0	49	8.5
0.9	47	7.8
0.7	32	6.6
0.5	30	−2.9
0.4	29	−4.1

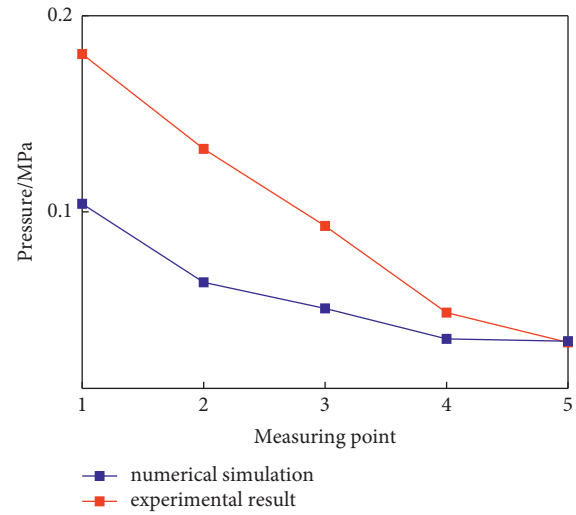

Figure 6: Comparison of experimental and simulated shock wave overpressures.

3.2. Analysis of the Experimental Results of the Shock Wave Test System. Figure 5 shows the change curve of the shock wave overpressure at different time periods. The following results are shown in Figure 5:

(1) The maximum peak overpressure of the shock wave at points 1 and 2 occur at 3.46 and 3.52 ms, respectively. The peak overpressures at the two measuring points are similar in time, indicating that the formation mechanisms most likely are the same and that these are all caused by the incident shock wave. After the maximum pressure peak is monitored at points 1 and 2, the pressure drops rapidly, and the second peak appears. Among these, peak A monitored at point 1, lasted for approximately 13.7 ms and the pressure is 0.064 MPa. Peak B is measured at point 2 and appears at 12.3 ms at 0.08 MPa. It can be seen that the impinging airflow at point 2 at the corner is relatively strong. This is because the impinging airflow collides and is reflected on the roadway wall at the corner. Thus, the reflected shock wave is formed and the subsequent continuous influx of impact leads to an increase in the intensity of the impact airflow at the corners, as shown in Figure 5(a). The peak overpressure of the shock wave monitored at point 1 is greater than that at point 2, which is consistent with the results of the numerical simulations.

(2) The shock wave continues to decay during propagation over a long distance. The maximum shock wave overpressure monitored at points 3, 4, and 5 are 0.092, 0.048, and 0.035 MPa, respectively. Reflecting shock waves collide with the incident shock waves, further weakening the shock wave energy and causing the shock wave pressure to attenuate; thus, the shock wave pressure at point 3 is reduced. At the same time, the diversion and reflection of the shock wave at the T-shaped roadway (points 4 and 5) causes the shock wave pressure monitored at measuring point 5 to greatly attenuate. Moreover, the shock wave passing through measuring point 5 is subject to frictional resistance and must overcome airflow resistance to propagate forward. This results in a shock wave overpressure at point 5 which is less than that at point 4; this is consistent with the numerical simulation results.

3.3. Analysis of Airflow Reversal in the Fresh Air Tunnel due to Outburst Shock Wave. The calculation results are listed in Table 3, which shows that, under various outburst pressure conditions, the measured experimental pressure P_2 value is greater than the value calculated using the model. This means that the ventilation resistance in the fresh air roadway is less than the overpressure value of the outburst shock wave, thereby causing the gas to flow backwards. However, the experimental results also revealed another phenomenon. In the near future, without affecting normal ventilation, the corresponding outburst-prevention facilities must be

installed at the connecting lane closest to the fresh air roadway. Similarly, the numerical simulation results are introduced in equation (11). Under all pressure conditions, P_2 is equal to or greater than ΔP, which causes the gas flow to reverse itself. The numerical simulation results are consistent with the calculation results, as shown in Table 3.

Figure 6 shows the comparison between the shock wave measured in the experiment and the shock wave overpressure obtained using numerical simulation. It can be seen that the changing trend of the shock wave overpressure curves obtained from experiment and numerical simulation are consistent, which proves that a reasonably simplified numerical simulation model is feasible.

4. Conclusions

A two-dimensional numerical simulation of propagation of outburst shock wave in the roadway was carried out, was performed in this study. The simulation results show that under identical pressure conditions, the pressure of impinging airflow tends to decay during the entire process, and the lower the protruding pressure, the lower the overpressure of the shock wave. After the shock wave hits the rigid wall, the superposition effect of the reflected wave and incident shock wave was significant. The shock wave was diffracted at the corner of the roadway, causing most of the impact airflow to propagate in the straight roadway.

An outburst shockwave physical simulation experiment was conducted using a new, self-developed coal and gas outburst energy propagation simulation package and parameter determination test device. The experimental results show that the shock wave continued to attenuate after long-distance (over how long?) propagation; it also diffracted at right angles, was weakened, and with its pressure was attenuated (by how much?). The superimposition of the reflected shock wave and the incident shock wave caused peak overpressure of the shock wave in the area to increase per unit area. The experimental results are consistent with the numerical simulation results.

Based on the results of both numerical simulation and physical experiment, combined with a consideration of the relationship between shock wave overpressure and roadway ventilation resistance, it was determined that under various pressure conditions, the measured pressure P_2 value of the experiment was greater than the ventilation resistance. This suggests that the overpressure generated by the prominent shock wave in the fresh air roadway pressure will cause gas backflow. At the same time, this also indicates that when the fresh air roadway is close to the coal uncovering? Position of Shimen, a corresponding antibackflow device should be installed at the location of the connecting road near the fresh air roadway without affecting normal ventilation. These results could be used to improve planning and safety in a variety of mines.

Data Availability

The data used to support the findings of this study have not been made available because they are confidential.

Conflicts of Interest

The authors declare that there are no conflicts of interest regarding the publication of this paper.

Authors' Contributions

In this paper, Xijian Li conceived and designed the experiments. Haiteng Xue and Zhu Liu performed the experiments. Fangrui Dai and Bei Hu processed the data. Haiteng Xue wrote the paper. All authors have read and approved the final manuscript.

Acknowledgments

This work was supported by the National Natural Science Foundation of China (Grant No. 51874107) and the Science and Technology Funding Projects of Guizhou Province (Grant No. 2018-5781).

References

[1] Y. Li and Z. Li, "Forecasting of coal demand in China based on support vector machine optimized by the improved gravitational search algorithm," *Energies*, vol. 12, no. 12, p. 2249, 2019.

[2] Y. Liu, H. Sun, B. Wang, L. Dai, and J. Cao, "Experimental accuracy and stability of gas outburst experimental system," *Geofluids*, vol. 2021, pp. 1–9, Article ID 6678608, 2021.

[3] H. Xie, C. Li, Z. He, C. Li, and F. Gao, "Experimental study on rock mechanical behavior retaining the in situ geological conditions at different depths," *International Journal of Rock Mechanics and Mining Sciences*, vol. 138, Article ID 104548, 2021.

[4] J. Li, H. Xie, L. Chen, C. Li, and Z. He, "Exploring deep-rock mechanics through mechanical analysis of hard-rock in situ coring system," *Advances in Civil Engineering*, vol. 2020, Article ID 8899156, 11 pages, 2020.

[5] H. Xie, M. Gao, R. Zhang, G. W. Peng, and A. Li, "Study on the mechanical properties and mechanical response of coal mining at 1000 m or deeper," *Rock Mechanics and Rock Engineering*, vol. 52, no. 5, pp. 1475–1490, 2019.

[6] F.-h. An, Y.-p. Cheng, L. Wang, and W. Li, "A numerical model for outburst including the effect of adsorbed gas on coal deformation and mechanical properties," *Computers and Geotechnics*, vol. 54, pp. 222–231, 2013.

[7] C. Zhang, E. Wang, J. Xu, and S. Peng, "Research on temperature variation during coal and gas outbursts: implications for outburst prediction in coal mines," *Sensors*, vol. 20, no. 19, p. 5526, 2020.

[8] L. I. Shucai, L. I. Qingchuan, and W. Hanpeng, "Research and development of large-scale true three-dimensional coal and gas outburst quantitative physical simulation test system," *Journal of China Coal Society*, vol. 43, no. S1, pp. 121–129, 2018.

[9] Z. Li, J. Yu, Y. Liu, and M. Zhang, "Numerical analysis of natural gas pressure during coal and gas outbursts," *Energy Science & Engineering*, vol. 9, no. 8, pp. 1068–1079, 2021.

[10] S. Xue, L. Yuan, J. Wang, Y. Wang, and J. Xie, "A coupled DEM and LBM model for simulation of outbursts of coal and gas," *International Journal of Coal Science & Technology*, vol. 2, no. 1, pp. 22–29, 2015.

[11] Y. Tao, J. Xu, D. Liu, and Y. Liang, "Development and validation of THM coupling model of methane-containing coal," *International Journal of Mining Science and Technology*, vol. 22, no. 6, pp. 879–883, 2012.

[12] X. Liu, G. Zhang, Z. Zhang, G. Zhang, and Z. Li, "Application of coupled LDA–KPCA and BO–mkrvm model to predict coal and gas outbursts," *Neural Processing Letters*, vol. 53, no. 4, pp. 2765–2794, 2021.

[13] C. Jianping, D. Jun, and L. Xiangwei, "Research on risk level of coal and gas outburst prediction based on PCA-Fisher discriminant analysis model," *Min Safety & Environmental Protection*, vol. 45, no. 3, pp. 61–71, 2018.

[14] N. Z. Long, A. M. Yi, and X. L. Zhang, "Prediction of coal and gas outburst intensity based on LLE-FOA-BP model," *Industry and Mine Automation*, vol. 45, no. 10, pp. 68–74, 2019.

[15] Y. Yingbiao, Z. Huijuan, and S. Jian, "Prediction of coal and gas outburst based on KPCA and T-S fuzzy neural network," *Measurement Science and Control Technology*, vol. 9, pp. 15–19, 2018.

[16] H. Fu, S. Feng, Z. Gao, and Y. Yang, "Study on double coupling algorithm based model for coal and gas outburst prediction," *China Safety Science Journal*, vol. 28, no. 3, pp. 84–90, 2018.

[17] A. Zhou, K. Wang, L. Fan, and B. Tao, "Propagation characteristics of pulverized coal and gas two-phase flow during an outburst," *PLoS One*, vol. 12, no. 7, Article ID 0180672, 2017.

[18] A. Zhou, K. Wang, and Z. Wu, "Propagation law of shock waves and gas flow in cross roadway caused by coal and gas outburst," *International Journal of Mining Science and Technology*, vol. 24, no. 1, pp. 23–29, 2014.

[19] K. Wang, A. Zhou, J. Zhang, and P. Zhang, "Real-time numerical simulations and experimental research for the propagation characteristics of shock waves and gas flow during coal and gas outburst," *Safety Science*, vol. 50, no. 4, pp. 835–841, 2012.

[20] G. Zhang, *Ventilation safety*, pp. 13–51, China University of Mining and Technology Press, Xuzhou, China, 2011.

[21] X. Li, H. Xue, L. Chen, Z. Liu, F. Dai, and M. Zhang, "Research on energy dissipation law and safety dimensions of protruding shock waves passing through door wall holes," *Journal of China Coal Society*, vol. 46, pp. 1–16, 2021.

Hindawi
Shock and Vibration
Volume 2022, Article ID 7842921, 19 pages
https://doi.org/10.1155/2022/7842921

Research Article

Study on Pressure Relief Technology of High-Pressure Water Jet of Residual Coal Pillar in Overlying Goaf in Close Seam Mining

Shang Yang,[1] Xuehui Li,[2] Jun Wang,[1,3] Shuhao Yang,[1] Zhen Shen,[1] and Guangzheng Xu[1]

[1]*College of Energy and Mining Engineering, Shandong University of Science and Technology, Qingdao 266590, China*
[2]*College of Transportation, Shandong University of Science and Technology, Qingdao 266590, China*
[3]*State Key Laboratory of Mining Disaster Prevention and Control, Shandong University of Science and Technology, Qingdao 266590, China*

Correspondence should be addressed to Xuehui Li; huizi6062@126.com and Jun Wang; wangjunsdkjd@126.com

Received 27 May 2021; Revised 11 November 2021; Accepted 3 December 2021; Published 13 January 2022

Academic Editor: Jianwei Cheng

To solve the problem of strong ground pressure behaviour under a residual coal pillar in the overlying goaf of a close-distance coal seam, this paper proposes the technology of weakening and relieving the residual coal pillar in the overlying goaf by a high-pressure water jet. Based on the geological occurrence of the No. 3 coal seam and mountain No. 4 coal seam in the Yanzishan coal mine, the high-pressure water jet pressure relief technology of residual coal pillars in the overlying goaf of close-distance coal seams was studied by theoretical analysis and field industrial tests. First, the elastic-plastic zone of the residual coal pillar and the stress distribution law of the floor are obtained by theoretical analysis, and the influence degree of the residual coal pillar on the support of the lower coal seam working face is revealed. Then, a high-pressure water jet combined with mine pressure is proposed to weaken the residual coal pillar. Finally, through the residual coal pillar hydraulic cutting mechanical model and "double-drilling double-slot" model, the high-pressure water jet drilling layout parameters are determined, and an industrial field test is carried out. The single knife cutting coal output and 38216 working face hydraulic support monitoring data show that high-pressure hydraulic slotting can weaken the strength of the coal body to a certain extent, destroy the integrity of the residual coal pillar, cut off the load transmission path of the overlying strata, and reduce the working resistance of the hydraulic support under the residual coal pillar to a certain extent, which is beneficial to the safe mining of the working face.

1. Introduction

In recent years, with the increase in coal mining intensity and mining depth, the occurrence conditions of coal seams have become more complex, the mining environment has worsened, and underground engineering disasters have become prominent [1–3]. For close-distance coal seam mining, the working face under the residual coal pillar in an overlying goaf is affected not only by the mining stress and tectonic stress but also by the residual coal pillar stress transmission, which makes the underground pressure behaviour of the lower coal seam working face more intense, and the support safety valve frequently opens, which seriously hinders the safe and efficient production by coal mines [4–8].

At present, the measures used to address the problem of strong mine pressure behaviour under the residual coal pillar in an overlying goaf mainly include coal seam directional blasting [9] and hydraulic fracturing [10]. Through the above treatment methods, the overall structure of the coal body can be destroyed, the strength of the coal body can be weakened, the connection form of the rock structure can be changed, the stress distribution form of the floor of the residual coal pillar can be improved, and the purpose of stress concentration can be alleviated. The above methods have been widely used in China because the geological conditions of different mining zones are different, the effect is also different, and there are some disadvantages. For example, coal seam directional blasting [11] not only involves a large amount of drilling

construction and low efficiency but is also likely to ignite harmful gas in the goaf, which poses a certain hidden danger to safe and efficient mining in coal mines. Conventional hydraulic fracturing technology [12, 13] easily controls fracture propagation by the original in situ stress, expands along the direction perpendicular to the minimum principal stress, and easily forms a cracking "blank zone" on both sides of the fracture. At the same time, there are many secondary fractures in the remaining coal pillar, and the high-pressure water loss is fast; thus, it is not easy to form the residual coal pillar damaged by pressure. With the continuous innovation of high-pressure water jet technology and the continuous improvement of high-pressure water generating devices, high-pressure water jet weakening technology has been applied to the prevention of dynamic disasters, control of hard roof stability in coal mines, and low-permeability coal seam gas extraction in underground coal mines. Relevant scholars [14–16] have used high-pressure hydraulic slotting to relieve the gas pressure inside the coal seam and increase the permeability of the coal mass, which thus improves the gas drainage efficiency and eliminates the outburst risk. Some scholars [17, 18] have used theoretical analysis, numerical simulation, and other research methods to study the pressure relief mechanism of high-pressure hydraulic slotting on coal and rock. After hydraulic cutting in the coal seam, a fully unloaded area, a transition pressure-relief area, and the original stress area are formed around the slot. After high-pressure hydraulic slotting in the roof, the strength of the roof is weakened, and the roof structure is changed, which can achieve the effect of unloading and releasing energy. Field practice has shown that high-pressure hydraulic slotting can reduce the stress load in the far and near fields and reduce the occurrence of dynamic disasters, such as rockburst and coal and gas outbursts.

In view of the mining conditions of carboniferous coal seams No. 3 and mountain No. 4 in the Yanzishan coal mine of the Datong Coal Mine Group, this paper adopts high-pressure water jet technology to weaken the residual coal pillar in the overlying goaf. First, the elastic-plastic zone of the residual coal pillar and the stress distribution law of floor are studied by theoretical analysis; the stress transfer mechanism of the overlying residual coal pillar floor in close proximity to coal seam downward mining is revealed; and then, based on theoretical analysis, numerical simulation, and field conditions, the drilling layout parameters of the high-pressure water jet destroying the residual coal pillar are determined. Finally, field industrial tests and effect inspections are carried out, and the research content of the paper can provide safety guarantees and theoretical guidance for the safe mining of close coal seams under similar conditions.

2. Engineering Geology

The 8216 working face of the No. 3 coal seam in the Yanzishan coal mine (hereinafter referred to as the 38216 working face) is located in the 302 panel of the No. 3 coal seam at the 910 level. The working face is 2540 m long and 180 m wide, with an average depth of 400 m, an average thickness of 5.0 m, and an average dip angle of 2°. In the east is the No. 3 layer panel roadway, in the south is the 8214 design working face of the No. 3 coal seam, in the west is the boundary of the No. 3 layer panel, and in the north is the 8218 design working face of the No. 3 coal seam. The upper part of the 38216 working face is the goaf of the 8216 working face and 8218 working face of the Mountain No. 4 coal seam (hereinafter referred to as the 48216 working face and 48218 working face), and the average spacing is 25 m. The residual coal pillar between the 48216 and 48218 working faces is located above the 38216 working face. The width of the coal pillar is 38 m. The coal pillar is 30 m from the 5216 roadway of the 38216 working face and 112 m from the 2216 roadway of the 38216 working face, as shown in Figure 1. The 5216 roadway is a tailgate with a size of 4.2 m × 3.4 m (width × height) and is supported by a "bolt-cable-mesh" framework, as shown in Figure 2(a). The 2216 roadway is a headgate with a size of 5.0 m × 3.3 m (width × height) and is supported by a "bolt-cable-mesh" framework, as shown in Figure 2(b). The distribution of roof and floor rocks is shown in Figure 3.

3. Elastic-Plastic Zone of the Residual Coal Pillar and the Stress Distribution Law of the Floor

Based on the mining conditions of working faces 38216, 48216, and 48218, theoretical analysis is used to study the failure characteristics and the stress distribution law of the residual coal pillar floor in the overlying goaf and reveal the influence degree of the residual coal pillar on the support of the lower coal seam working face.

3.1. Elastic-Plastic Zone of the Residual Coal Pillar in the Overlying Goaf. Analysis of mine pressure and strata control theory [19] showed that the residual coal pillar in the overlying goaf is deformed and damaged under the action of overlying strata pressure. Failure zone I, plastic zone II, and elastic zone III form from the outside to the inside, in which the elastic zone is the main bearing zone and the main medium for the downward transmission of the overlying load. In this part, combined with the mining conditions of the 48216 and 48218 working faces, and based on limit equilibrium theory [6], the elastic-plastic zone range of the residual coal pillar is analysed, and the elastic-plastic zone width of the residual coal pillar is obtained.

As shown in Figure 4, the structural model of the elastic-plastic zone of the residual coal pillar is presented. In the early stage of roadway excavation and the mining process of both sides of the working face, the section coal pillar is inevitably affected by mining, and the failure and plastic zones form at a certain width of the coal pillar edge. Based on limit equilibrium theory, the width of the elastic-plastic zone can be calculated:

$$B_0 = \frac{M}{2gf} \ln \frac{q_1 + c \cot \varphi}{g\left(p_1 + c \cot \varphi\right)}, \tag{1}$$

$$B_1 = B - 2B_0. \tag{2}$$

There B is the width of the residual coal pillar, m; B_0 is the sum of the widths of the failure zone and plastic zone, m; B_1 is the width of the elastic zone, m; M is the thickness of the coal seam, m; q_1 is the concentrated load above the residual

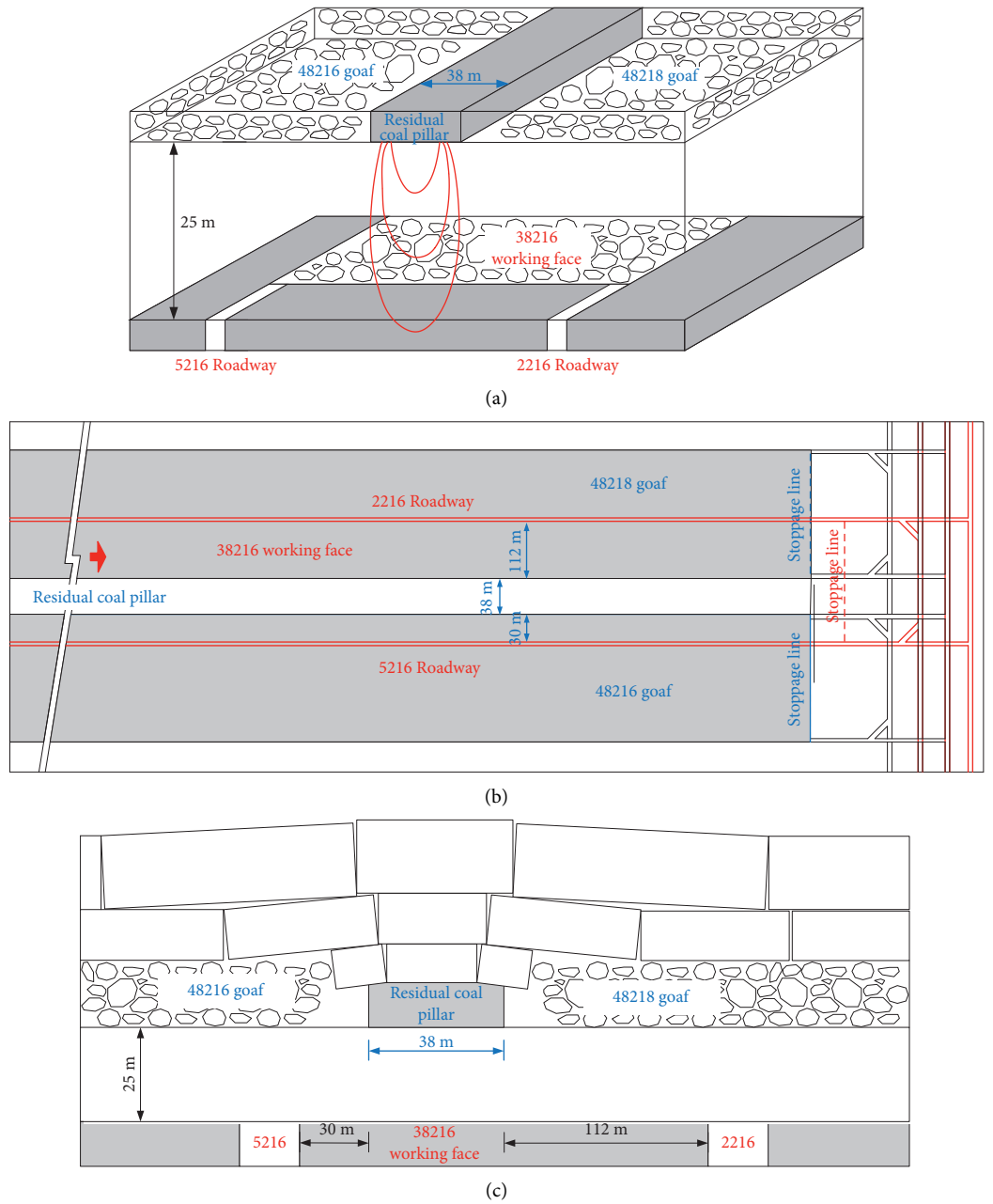

Figure 1: Spatial positional relationships between working faces. (a) Space location diagram. (b) Plane figure. (c) Section plan.

coal pillar, MPa; c is the cohesion of coal, MPa; φ is the angle of the internal friction of coal, °; g is the triaxial stress coefficient, $g = (1 + \sin\varphi)/(1 - \sin\varphi)$; f is the friction factor, $f = \tan\varphi$; and p_1 is the resistance of the support to the coal wall, MPa.

According to equation (1), the sum of the widths of the failure zone and plastic zone of the residual coal pillar B_0 calculated by limit equilibrium theory is related to the concentrated load above the coal pillar. According to mine pressure theory, the concentrated load above the overlying residual coal pillar q_1 is mainly caused by the weight of the overlying strata and the rotation of the cantilever beams on both sides of the pillar, as shown in Figure 5.

Due to the long mining time of the 48016 and 48218 working faces (mining completed in 2015-2016), the goaf on both sides of the residual coal pillar has been filled with overburden caving strata, and the overburden weight above the collapse line can be regarded as bearing by the gangue and residual coal pillar in the goaf, that is, the total load on the residual coal pillar P:

$$P = \left[BH + 2h(H - h)\tan\frac{\delta}{2} + h^2\tan\frac{\delta}{2}\right]\gamma. \quad (3)$$

There H is the burial depth of the residual coal pillar, m; h is the caving height of the strata in the goaf, m, where Yu [20]

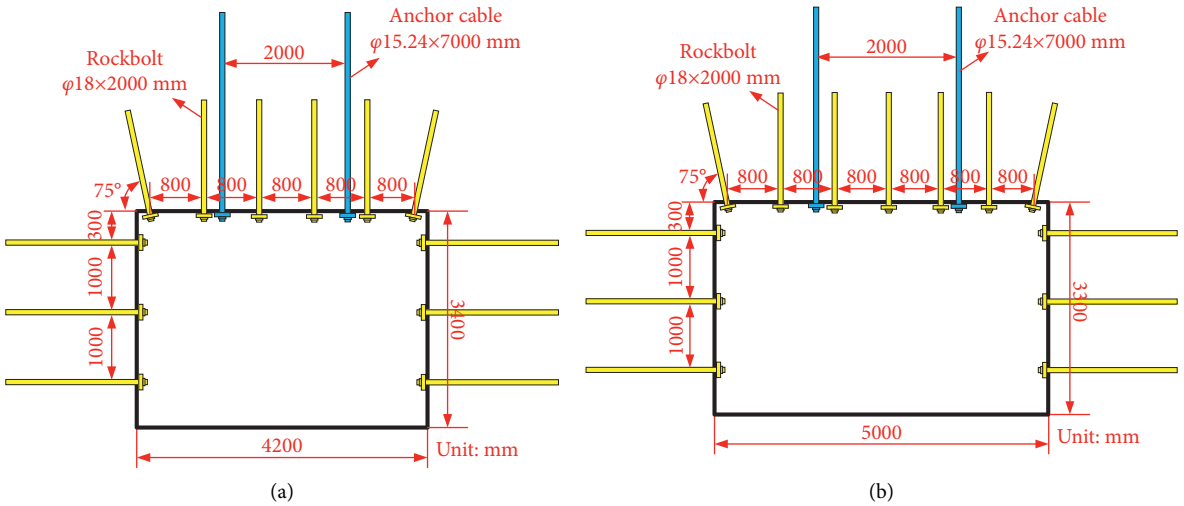

Figure 2: Support schemes of the roadway supports. (a) 5216 roadway. (b) 2216 roadway.

Stratigraphic Columnar	Lithological Characters	Thickness (m)	Depth (m)
	Fine medium sandstone	20	314
	Medium sandstone	15	329
	Kaolin mudstone	20	349
	Sandy mudstone	10	359
	Siltstone	10	369
	Mountain No.4 coal seam	6	375
	Siltstone	10	385
	Medium grained sandstone	10	395
	Lamprophyre	5	400
	No.3 coal seam	5	405
	Sand mud interbedding	9	414

Figure 3: Comprehensive drilling histogram.

found that the ratio of the caving height of the strata to the mining height is 10–12 in top-coal caving mining in the carboniferous system; δ is the caving angle of the overlying strata in the goaf, °, where according to the research of relevant scholars [21–23], the caving angle in the carboniferous system is generally 60°–63°; and γ is the average unit weight of the overlying strata, kN/m^3.

Concentrated load above the residual coal pillar q_1 is

$$q_1 = \frac{P}{B} = \frac{\left[BH + 2h(H-h)\tan(\delta/2) + h^2\tan(\delta/2)\right]\gamma}{B}. \quad (4)$$

According to the geological conditions of the 48216 and 48218 working faces in the Mountain No. 4 coal seam of the Yanzishan coal mine, the following parameters can be determined: B is 38 m, H is 375 m, h is 70 m, δ is 60°, and γ is 26 kN/m^3. By substituting the above parameters into

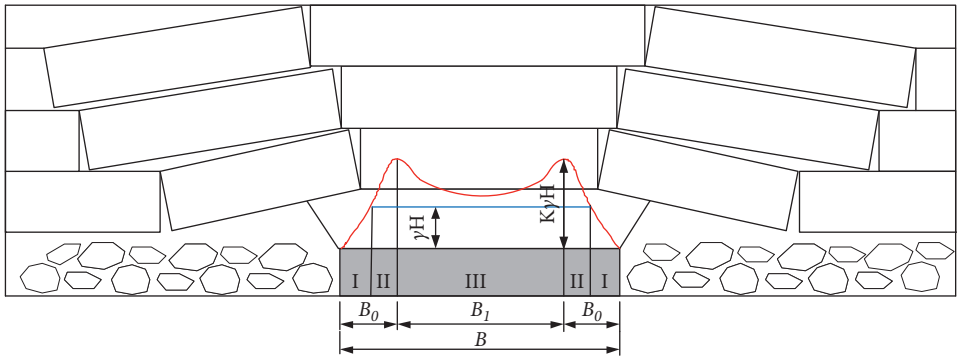

Figure 4: Structural model of the elastic-plastic zone of the residual coal pillar.

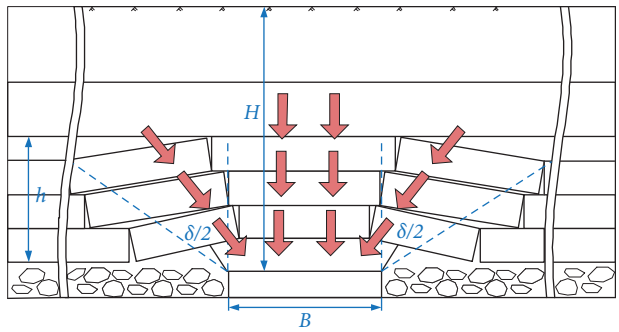

Figure 5: Calculation model of the concentrated load above the residual coal pillar.

equation (4), it can be concluded that the concentrated load above the residual coal pillar q_1 is 28.6 MPa.

According to the geological survey of the Mountain No. 4 coal seam, the coal seam thickness M is 6 m, the concentrated load above the coal pillar q_1 is 28.6 MPa, the cohesion of coal c is 1.76 MPa, the internal friction angle of coal φ is 22°, the friction coefficient of the contact surface between the coal seam and the roof and floor f is 0.4, and the resistance of the support to the coal wall p_1 is 0. By substituting the above parameters into equations (1) and (2), the sum of the width of the failure zone and plastic zone on one side of the residual coal pillar B_0 is approximately 4.2 m, and the elastic core zone B_1 is approximately 29.6 m.

3.2. Stress Distribution Law of the Residual Coal Pillar Floor in the Overlying Goaf. In close-distance coal seam mining, the lower coal seam working face is often located under the residual coal pillar in the overlying goaf. Because the overlying residual coal pillar plays a role in load transfer, it will form a complex stress environment around the working face of the lower coal seam, resulting in stress concentration, which seriously hinders safe and efficient production in coal mines. To understand the residual coal pillar floor stress size and distribution form in more detail, based on the theory of elasticity, the residual coal pillar and floor are simplified as an elastomer, and the residual coal pillar stress calculation model is established.

According to the analysis in Figure 6, the stress at any point M in the half-plane caused by the small concentrated load $\mathrm{d}F = \lambda q d\xi$ is as follows:

$$\begin{cases} \mathrm{d}\sigma_x = \dfrac{2\lambda q\, d\xi}{\pi} \dfrac{x^3}{\left[x^2 + (y-\xi)^2\right]^2}, \\ \mathrm{d}\sigma_y = \dfrac{2\lambda q\, d\xi}{\pi} \dfrac{x(y-\xi)^2}{\left[x^2 + (y-\xi)^2\right]^2}, \\ \mathrm{d}\tau_{xy} = \dfrac{2\lambda q\, d\xi}{\pi} \dfrac{x^2(y-\xi)}{\left[x^2 + (y-\xi)^2\right]^2}. \end{cases} \tag{5}$$

To determine the stress caused by the uniformly distributed load acting on the residual coal pillar, it is necessary to superimpose the stress caused by each small concentrated load, and the integral of equation (5) is obtained:

$$\begin{cases} \sigma_x = \dfrac{2}{\pi} \displaystyle\int_{-a}^{b} \dfrac{\lambda q x^3 \mathrm{d}\xi}{\left[x^2 + (y-\xi)^2\right]^2}, \\ \sigma_y = \dfrac{2}{\pi} \displaystyle\int_{-a}^{b} \dfrac{\lambda q x (y-\xi)^2 \mathrm{d}\xi}{\left[x^2 + (y-\xi)^2\right]^2}, \\ \tau_{xy} = \dfrac{2}{\pi} \displaystyle\int_{-a}^{b} \dfrac{\lambda q x^2 (y-\xi) \mathrm{d}\xi}{\left[x^2 + (y-\xi)^2\right]^2}. \end{cases} \tag{6}$$

For the uniformly distributed load above the residual coal pillar, λ_q is a constant, and the integral of equation (6) is obtained:

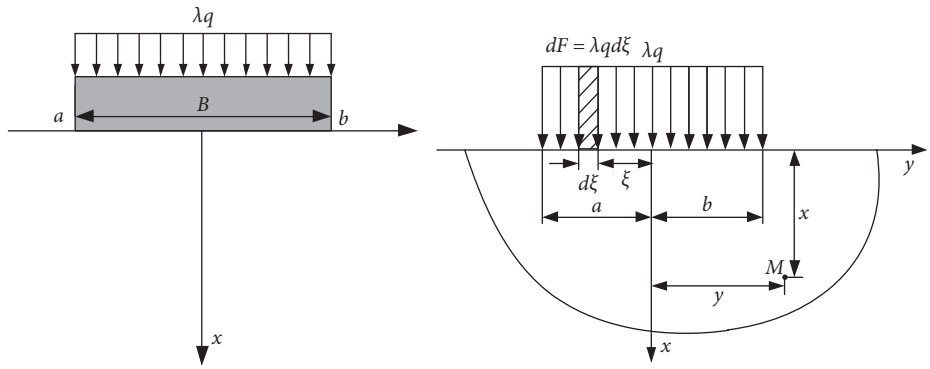

Figure 6: Stress calculation model of the residual coal pillar.

$$\begin{cases} \sigma_x = \dfrac{\lambda q}{\pi}\left[\arctan\dfrac{y+b}{x} - \arctan\dfrac{y-a}{x} + \dfrac{x(y+b)}{x^2+(y+b)^2} - \dfrac{x(y-a)}{x^2+(y-a)^2}\right], \\ \sigma_y = \dfrac{\lambda q}{\pi}\left[\arctan\dfrac{y+b}{x} - \arctan\dfrac{y-a}{x} - \dfrac{x(y+b)}{x^2+(y+b)^2} + \dfrac{x(y-a)}{x^2+(y-a)^2}\right], \\ \tau_{xy} = \dfrac{\lambda q}{\pi}\left[\dfrac{x^2}{x^2+(y+b)^2} - \dfrac{x^2}{x^2+(y-a)^2}\right]. \end{cases} \tag{7}$$

To better study the stress distribution law of the residual coal pillar floor in the overlying goaf, the mining conditions of the 48126 and 48128 working faces in the Yanzishan coal mine are taken as the research background, the stress of the residual coal pillar floor is analysed by equation (7), λq is a constant, and the distribution of horizontal stress, vertical stress, and shear stress at different depths of the residual coal pillar under uniform load are obtained by using Origin data processing software.

According to the analysis in Figure 7, the stress distribution law of the residual coal pillar floor is as follows:

(1) The vertical stress of the floor of the residual coal pillar is distributed as a whole in a "single-arch" pattern, which is distributed symmetrically in the centre of the coal pillar, and the peak values of the vertical stress occur at the central axis of the coal pillar. In the vertical direction, with increasing depth, the stress decreases; however, the range of stress influence expands, and the depth of the vertical stress concentration is approximately 60 m. In the horizontal direction, the stress decreases with increasing distance from the central axis of the coal pillar.

(2) The horizontal stress of the floor of the residual coal pillar is symmetrically distributed along the central axis of the coal pillar. In the vertical direction, as the depth increases, the whole stress changes from a single peak to a "double-arch" shape, the change trend of stress tends to ease, and the influence range of stress also expands. In the horizontal direction, the change trend is consistent with that in the vertical direction, and the stress decreases with the increase in the distance from the coal pillar central axis.

(3) The shear stress of the residual coal pillar floor has a "single peak" on one side. The shear stress value at the central axis of the coal pillar is 0. With increasing distance from the central axis of the coal pillar, the shear stress first increases and then decreases, and the stress peak is located at the edge of the coal pillar.

(4) According to the above analysis, the influence depth of the vertical stress of the residual coal pillar is 60 m, the influence depth of the horizontal stress is approximately 10 m, and the influence depth of the shear stress is small. Therefore, the vertical stress plays a leading role in the stress transfer process of the residual coal pillar floor.

According to the above analysis, the peak value of vertical stress in the floor of the residual coal pillar appears at the central axis of the coal pillar. According to the mining conditions of the 38216 working face, the 38216 working face is 25 m from the overlying residual coal pillar. According to Figure 7(a), at 25 m below the coal pillar, the stress concentration factor λ is approximately 2.33, and the stress transferred by the residual coal pillar is approximately 22.7 MPa.

3.3. Load-Bearing Capacity of the Working Face Support under the Residual Coal Pillar. In this part, theoretical calculations are used to analyse the influence of residual coal pillars on the working face from a quantitative point of view. According to the theory of mine pressure and strata control, as the 38126 working face supports advance and load is transferred by the overlying roof, it also bears the

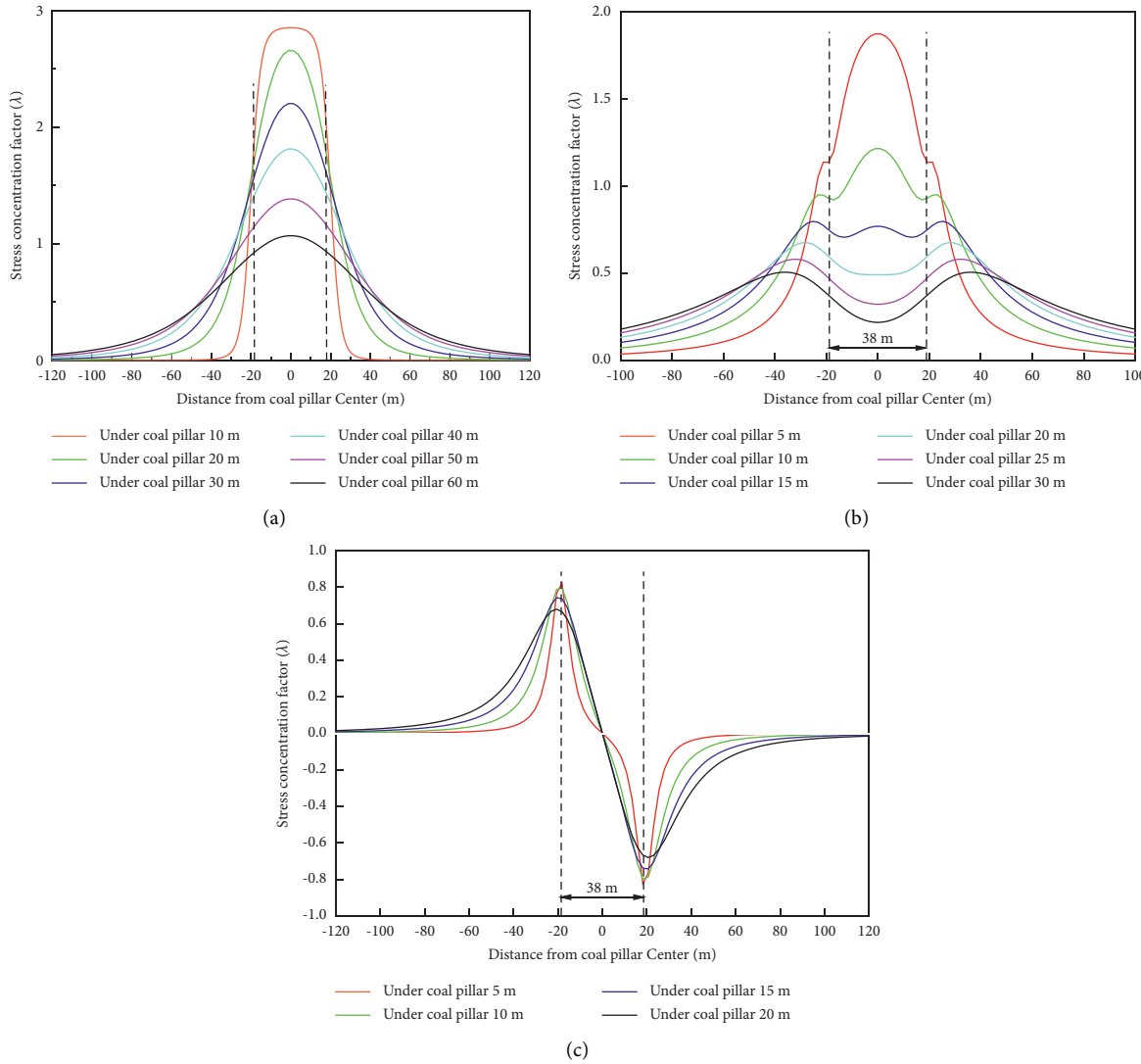

Figure 7: Stress distributions of the residual coal pillar floor at different depths. (a) Vertical stress. (b) Horizontal stress. (c) Shear stress.

concentrated load transferred by the overlying residual coal pillar. As shown in Figure 8, the working face under the residual coal pillar mainly bears the following loads:

$$P_m(n) = \frac{E_n H_n{}^3 (\gamma_n H_n + \gamma_{n+1} H_{n+1} + \gamma_{n+2} H_{n+2} + \cdots + \gamma_m H_m + \sigma_x)}{E_n H_n{}^3 + E_{n+1} H_{n+1}{}^3 + \cdots + E_m H_m{}^3}. \tag{8}$$

There E_i is the elastic modulus of layer $i (i = n, n+1, \ldots, m)$ above the lower coal seam, MPa; H_i is the thickness of the rock stratum of layer i $(i = n, n+1, \ldots, m)$ above the lower coal seam, m; γ_i is the volume force of the rock stratum of layer I $(i = n, n+1, \ldots, m)$ above lower coal seam, MN/m^3; and σ_x is the load transferred by the overlying residual coal pillar, MPa

According to the geological survey of the No. 3 coal seam and Mountain No. 4 coal seam, there are three rock strata between the 38216 working face and the 48216 and 48218 goafs: lamprophyre, medium-grained sandstone, and siltstone. The mechanical parameters of each rock stratum are shown in Table 1.

In addition, according to the previous theoretical analysis, the transfer load of the 38216 working face under the residual coal column is approximately 22.7. By substituting the above parameters into equation (8), the main load of the working face under the residual coal pillar is approximately 1.25 MPa, which is greater than the support strength of the hydraulic support (ZF12000/22/35). During the mining of the lower coal seam, it is easy to cause the working resistance of the hydraulic support under the residual coal pillar to be too large, and the safety valve is frequently opened, which may cause support crushing accidents.

According to the above research, after the upper coal seam is mined, the overlying strata break, rotate, and sink, and the generated load is transmitted downwards. A part of the load acts on the gangue in the goaf. Because the gangue in the goaf consumes and transfers part of the load in the compaction process, the load transferred from the gangue in the goaf to the floor is small. Part of the load is transmitted downward through the residual coal pillars and

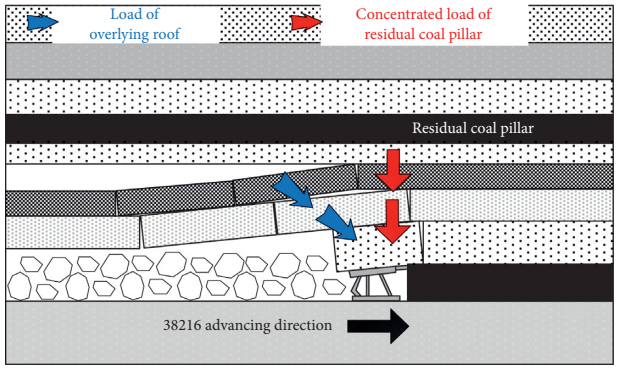

FIGURE 8: Structural model of the support bearing the load on the working face under a residual coal pillar.

distributes in the floor in the form of a "stress bubble," forming a stress concentration area, as shown in Figure 9. If the working face or roadway of the lower coal seam is located in the stress concentration zone, the pressure of the hydraulic support in the lower coal seam will increase, and the safety valve will be frequently opened. Roof subsidence, floor heave, and two sides moving close will occur in the roadway. This will seriously affect the safe mining of the lower coal seam.

4. Process Parameters of High-Pressure Water Jet Weakening the Residual Coal Pillar

4.1. Pressure Relief Method of Weakening the Residual Coal Pillar by a High-Pressure Water Jet. The width of the residual coal pillar in the goaf is a key factor affecting the size and distribution of the coal pillar floor stress. According to previous research results, the residual coal pillar deforms and is destroyed under the action of overlying pressure. From outside to inside, there are failure zone I, plastic zone II, and elastic core zone III. The elastic core zone is the main bearing area and the main medium for the downward transmission of the overlying load. Therefore, if the coal strength in the elastic core zone is artificially weakened, the integrity of the whole coal pillar will be reduced, the coal pillar will fail under the action of the overlying load, the load transmission path of the overlying strata will be cut off, and the lower close coal seam will be in the low-stress zone. Therefore, to improve the construction efficiency and reduce the construction cost, the idea of weakening residual coal pillars combined with applying a high-pressure water jet and mine pressure can be adopted. First, a high-pressure water jet is used to weaken the coal pillar and make the defect body in the elastic core to destroy the coal body around the defect body and reduce the integrity of the coal pillar; then, the whole coal pillar with defects is destroyed by using mine pressure. The load transfer form of the residual coal pillar before and after weakening is shown in Figure 10.

4.2. Determination of High-Pressure Water Jet Drilling Layout Parameters. The drilling layout parameters of high-pressure water jet mainly include the coal pillar width direction drilling layout parameters and coal pillar length direction drilling layout parameters. According to relevant research, when the spacing is too large, stress concentration easily occurs between the two boreholes, and the ideal failure effect cannot be achieved. When the spacing is too small, there will be a stress reduction zone between the two boreholes, which can achieve the ideal failure effect. However, with the increase in on-site construction quantities and construction time, considerable manpower and material resources are wasted [24]. Therefore, determining the reasonable drilling layout parameters of a high-pressure water jet can not only achieve the destruction effect of the residual coal pillar but also ensure construction progress.

4.2.1. Determination of Coal Pillar Width Direction Drilling Layout Parameters. According to the previous research results, the sum of the widths of the failure zone and plastic zone B_0 on one side of the residual coal pillar is approximately 4.2 m, and the elastic core zone B_1 is approximately 29.6 m, as shown in Figure 11(a). According to the above analysis, only when elastic core zone B_1 is damaged can the load transmitted by the floor be reduced. This is the scheme designed to destroy the elastic core zone of residual coal pillar B_1: elastic core zone B_1 is divided into four parts: high-pressure water jet destruction zones $B_{2\text{-}1}$ and $B_{2\text{-}2}$ and non-water jet destruction elastic core zones $B_{3\text{-}1}$ and $B_{3\text{-}2}$, as shown in Figure 11(b). First, a high-pressure water jet is used to destroy the coal body in zones $B_{2\text{-}1}$ and $B_{2\text{-}2}$, making it a plastic zone. The water jet damage zone loses its bearing capacity, and the overlying load is transferred to the non-water jet damage elastic core zones $B_{3\text{-}1}$ and $B_{3\text{-}2}$; if the remaining zones $B_{3\text{-}1}$ and $B_{3\text{-}2}$ reach a certain width (and can be regarded as a small coal pillar), plastic failure occurs under the action of mine pressure, the whole coal pillar is damaged, and the residual coal pillar loses its bearing capacity, as shown in Figure 11(c).

It is assumed that when the width of the coal pillar is B, the load above the residual coal pillar is q_1; when the width of the coal pillar is $B_{3\text{-}1} + B_{3\text{-}2}$, the load above the residual coal pillar is q' ($q' > q_1$), as shown in Figure 11(b). To ensure the complete failure of the elastic core zone of the residual coal pillar, the maximum width of $B_{3\text{-}1} + B_{3\text{-}2}$ in plastic failure under the action of load q' should be determined before the high-pressure water jet destroys $B_{2\text{-}1}$ and $B_{2\text{-}2}$. As shown in Figure 11(b), the widths of $B_{3\text{-}1}$ and $B_{3\text{-}2}$ are equal. Therefore, the maximum width of $B_{3\text{-}1} + B_{3\text{-}2}$ can be obtained only by determining the width of $B_{3\text{-}1}$ or $B_{3\text{-}2}$. Under the action of load q', the width of plastic zone q', $B_{3\text{-}1}$, or $B_{3\text{-}2}$ is as follows:

$$B_{3-1} \text{ or } B_{3-2} = \frac{M}{2gf} \ln \frac{q\prime + c \cot \varphi}{g(\tau + c \cot \varphi)}. \tag{9}$$

When $B_{2\text{-}1}$ and $B_{2\text{-}2}$ are destroyed, $B_{2\text{-}1}$ and $B_{2\text{-}2}$ coal become a plastic zone, the weight of overlying strata is shared by $B_{3\text{-}1}$, and $B_{3\text{-}2}$ the coal bodies, coal body after $B_{2\text{-}1}$ and $B_{2\text{-}2}$ failure and goaf gangue, and the concentrated load q' on the coal body in the $B_{3\text{-}1}$ and $B_{3\text{-}2}$ zone is as follows:

Table 1: Mechanical parameters of interlayer strata.

Rock stratum	Volumetric force γ_i (MN/m^3)	Thickness H_i (m)	Elastic modulus E_i (MPa)
Lamprophyre	0.0266	5	3.000×10^4
Medium-grained sandstone	0.0263	10	3.845×10^4
Siltstone	0.0262	10	2.800×10^4

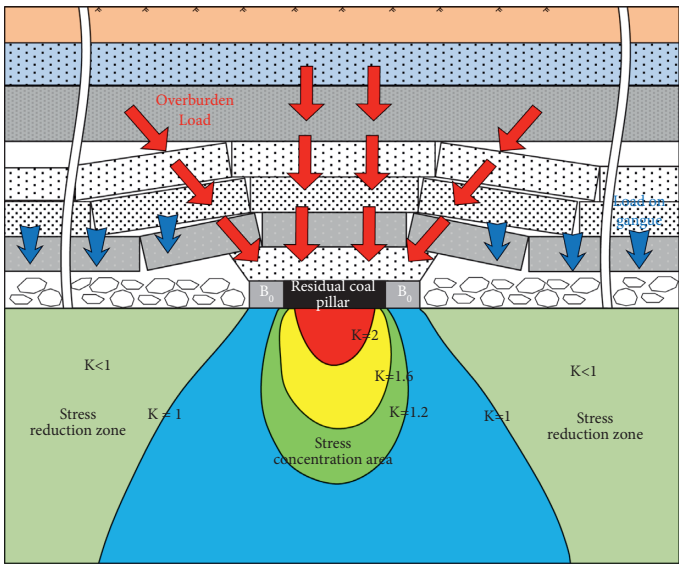

Figure 9: Transmission and distribution of the overlying load.

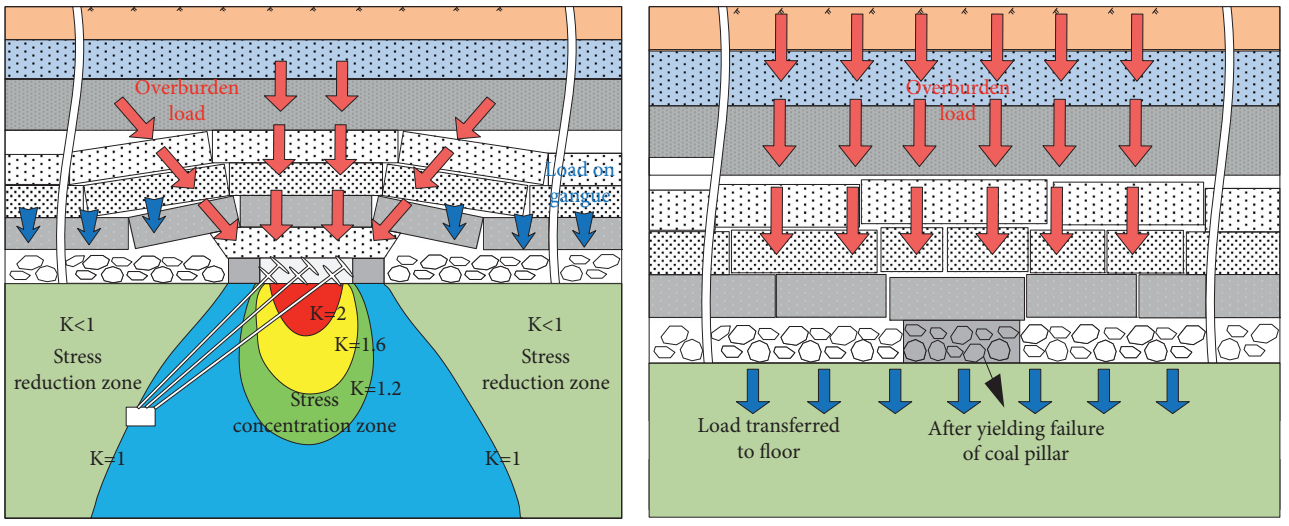

Figure 10: Load transfer before and after the weakening of the residual coal pillar. (a) Before weakening. (b) After weakening.

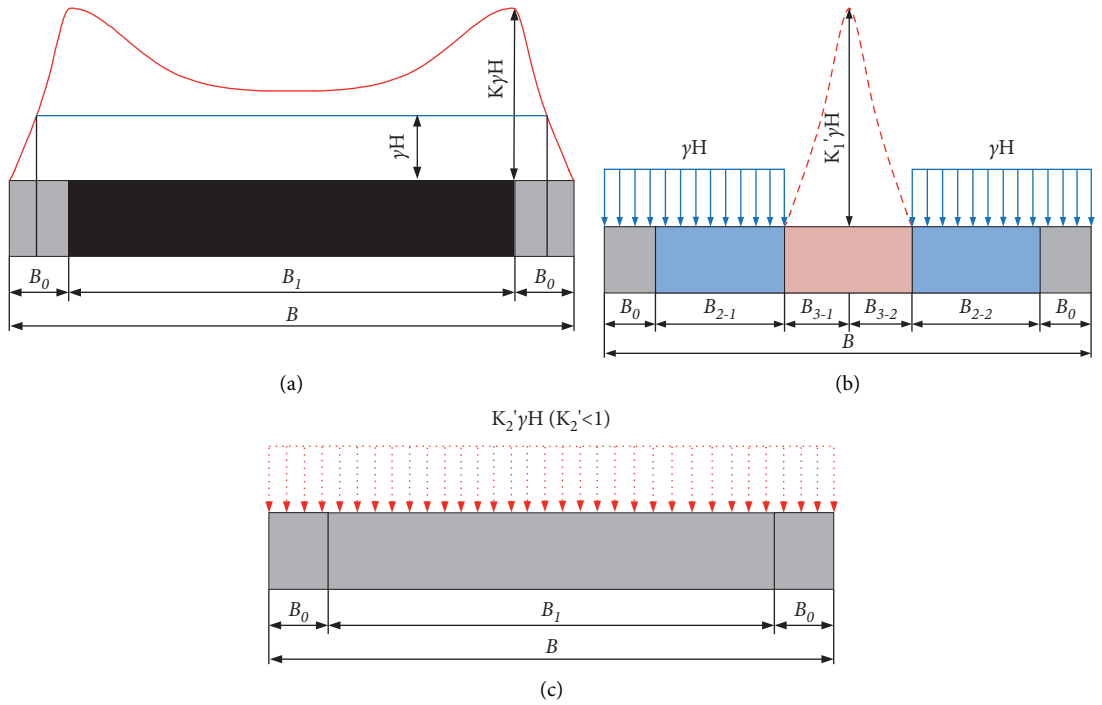

FIGURE 11: Mechanical model of the hydraulic cutting of the residual coal pillar. (a) Before coal pillar failure. (b) In the process of coal pillar failure. (c) After coal pillar failure.

$$q' = \frac{P'}{B_{3-1} + B_{3-2}} = \frac{\left[(B_{3-1} + B_{3-2})H + 2h(H-h)\tan(\delta/2) + h^2\tan(\delta/2)\right]\gamma}{B_{3-1} + B_{3-2}}. \tag{10}$$

When the overburden load acts on zones $B_{3\text{-}1}$ and $B_{3\text{-}2}$, zones $B_{3\text{-}1}$ and $B_{3\text{-}2}$ expand due to plastic failure. At this time, shear stress τ occurs on the interface of coal and rock in the $B_{2\text{-}1}$ and $B_{2\text{-}2}$ zones and acts on both sides of $B_{3\text{-}1}$ and $B_{3\text{-}2}$, as shown in Figure 11(b).

$$\tau = \gamma H \tan\varphi + c. \tag{11}$$

Substituting equations (10) and (11) into equation (9), we can obtain the following results:

$$B_{3-1} \text{ or } B_{3-2} = \frac{M}{2gf}\ln\frac{\left(\left[(B_{3-1} + B_{3-2})H + 2h(H-h)\tan(\delta/2) + h^2\tan(\delta/2)\right]\gamma/B_{3-1} + B_{3-2}\right) + c\cot\varphi}{g[\gamma H\tan\varphi + c(1+\cot\varphi)]}. \tag{12}$$

By substituting the above parameters (see Section 3.1 for details) into equation (12), $B_{3\text{-}1}$ can be obtained:

$$B_{3-1} = 3.378\ln\left(0.54 + \frac{13.8}{B_{3-1}}\right). \tag{13}$$

According to equation (13), $B_{3\text{-}1}$ is 4.4 m, and $B_{2\text{-}1}$ and $B_{2\text{-}2}$ are both 10.4 m. To ensure that the damage zone of the high-pressure water jet can be greater than 10.4 m, three boreholes are arranged in $B_{2\text{-}1}$ and $B_{2\text{-}2}$, and 2~3 slots are arranged in each borehole, with a slot spacing of 4 m, as shown in Figure 12. The borehole layout parameters are shown in Table 2.

4.2.2. Determination of Coal Pillar Length Direction Drilling Layout Parameters. In this part, FLAC 3D is used to study the influence of different drilling spacings in the length direction of the coal pillar on the stress field and plastic zone field of the coal body around the seam slot and determine the reasonable drilling spacing in the length direction of the coal pillar to provide a reference for on-site construction.

(1) Establishment of the Model. According to the research content of this part, the "double-drilling and double-slot" model is established, as shown in Figure 13. The model adopts the Mohr–Coulomb constitutive model. The model size is $X \times Y \times Z = (9\sim11)\text{ m} \times 15\text{ m} \times 10\text{ m}$, where the x-direction is the length direction of the coal pillar, the y-direction is the width direction of the coal pillar, and the z-direction is the vertical direction. The whole model is divided into three parts: drilling holes, slots, and surrounding coal bodies. The cylindrical shell grid is used for drilling holes and slots. To better study the damage, pressure relief effect, and

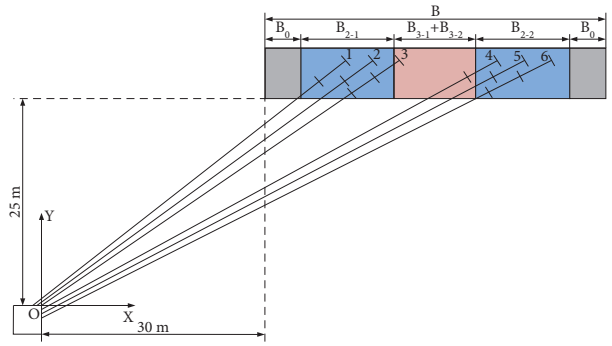

Figure 12: Coal pillar width direction drilling layout.

Table 2: Coal pillar width direction drilling layout parameters.

Borehole number	Starting point of drilling	Azimuth of drilling (°)	Elevation angle of drilling (°)	Length of drilling hole (m)	Number of slots	Gap between slots (m)
1	(−1.0, 0)	90	36	49.70	2	4
2	(−0.5, 0)	90	35	51.70	2	4
3	(0, 0)	90	33	53.80	3	4
4	(0, 0.5)	90	28	63.50	2	4
5	(0, 1.0)	90	27	66.40	2	4
6	(0, 1.5)	90	27	69.30	3	4

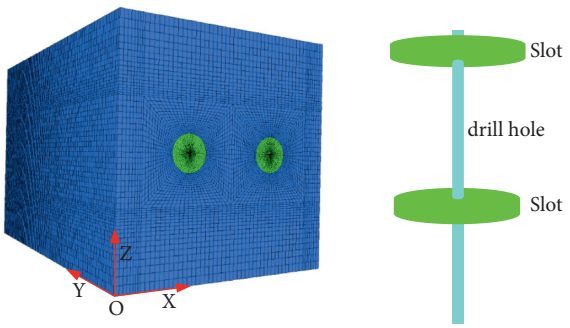

Figure 13: Double-drilling hole and double-slot model.

change law of coal bodies around drilling holes and slots, the division grid around drilling holes and slots is more dense. The surrounding coal body is a cylinder surrounded by a radial grid because it is far away from the borehole and fracture slot, and the division grid is relatively sparse. The model is divided into 945000~945600 units. According to Section 3.1, after the excavation of working faces 48216 and 48218 in the Mountain No. 4 coal seam, stress concentration occurs in the residual coal pillar, and the peak stress is 28.6 MPa. In this section, to ensure the accuracy and effectiveness of the simulation, a uniform load of 28.6 MPa is applied at the top of the model. The vertical displacement constraint is limited at the bottom of the model, and the horizontal displacement constraint is applied at the side. The physical and mechanical parameters of the model are shown in Table 3.

(2) Simulation Scheme. To better study the influence of different drilling spacings on the stress field and plastic zone field of coal around the slot, the drilling spacings in the length direction of the coal pillar are 3.0 m, 4.0 m, and 5.0 m, the slot radius is 0.75 m, the slot width is 0.2 m, and the slot spacing is 4 m.

To more intuitively understand the influence of different drilling spacings in the length direction of the coal pillar on the stress field and plastic zone field of the coal body around the slot, two observation sections are set: section 1 and section 2 (section 1 is parallel to the *xoz*-axis and passes through the slot section, as shown in Figure 14(a), while section 2 is parallel to the *xoy*-axis and passes through the borehole section, as shown in Figure 14(b)).

(3) Analysis of Simulation Results

(a) Vertical stress

(1) Section 1: as shown in Figure 15, a contour map of the vertical stress around the slot with different spacings in section 1 is shown. Figure 15 shows that with increasing drilling spacing, the stress value between drillings also increases, and a stress concentration area appears. When the distance between boreholes is 3 m, there is a stress overlap area between drillings, whose stress is less than the original rock stress, and it belongs to the stress reduction area. When the distance between drillings is 4 m, there is a stress concentration area between boreholes, the stress concentration value is 32 MPa, and the stress concentration degree is small. When the distance between drillings is 5 m, the stress concentration range between drillings increases, the stress concentration value also increases, reaching 42 MPa, and the stress concentration factor is 1.6.

(2) Section 2: as shown in Figure 16, a contour map of the vertical stress around the slot with

Table 3: Physical and mechanical parameters of the model.

Rock stratum	Density (kg/m^3)	Bulk modulus (GPa)	Shear modulus (GPa)	Tensile strength (MPa)	Cohesion (MPa)	Internal friction angle (°)	Thickness (m)
Coal	1410	2.1	1.3	1.50	1.76	22.00	6

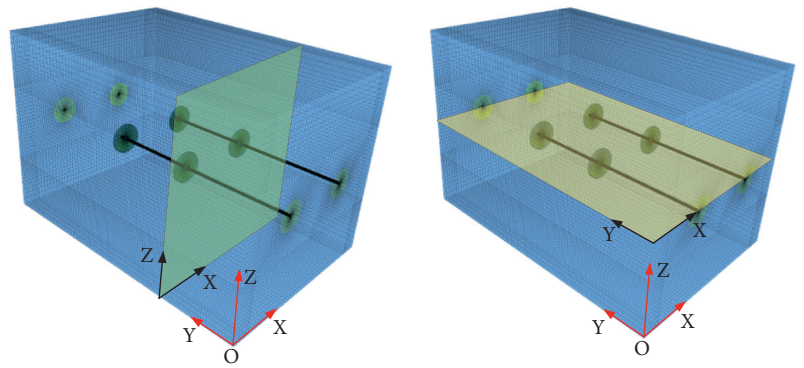

(a) (b)

Figure 14: Schematic diagram of the observation sections. (a) Section 1. (b) Section 2.

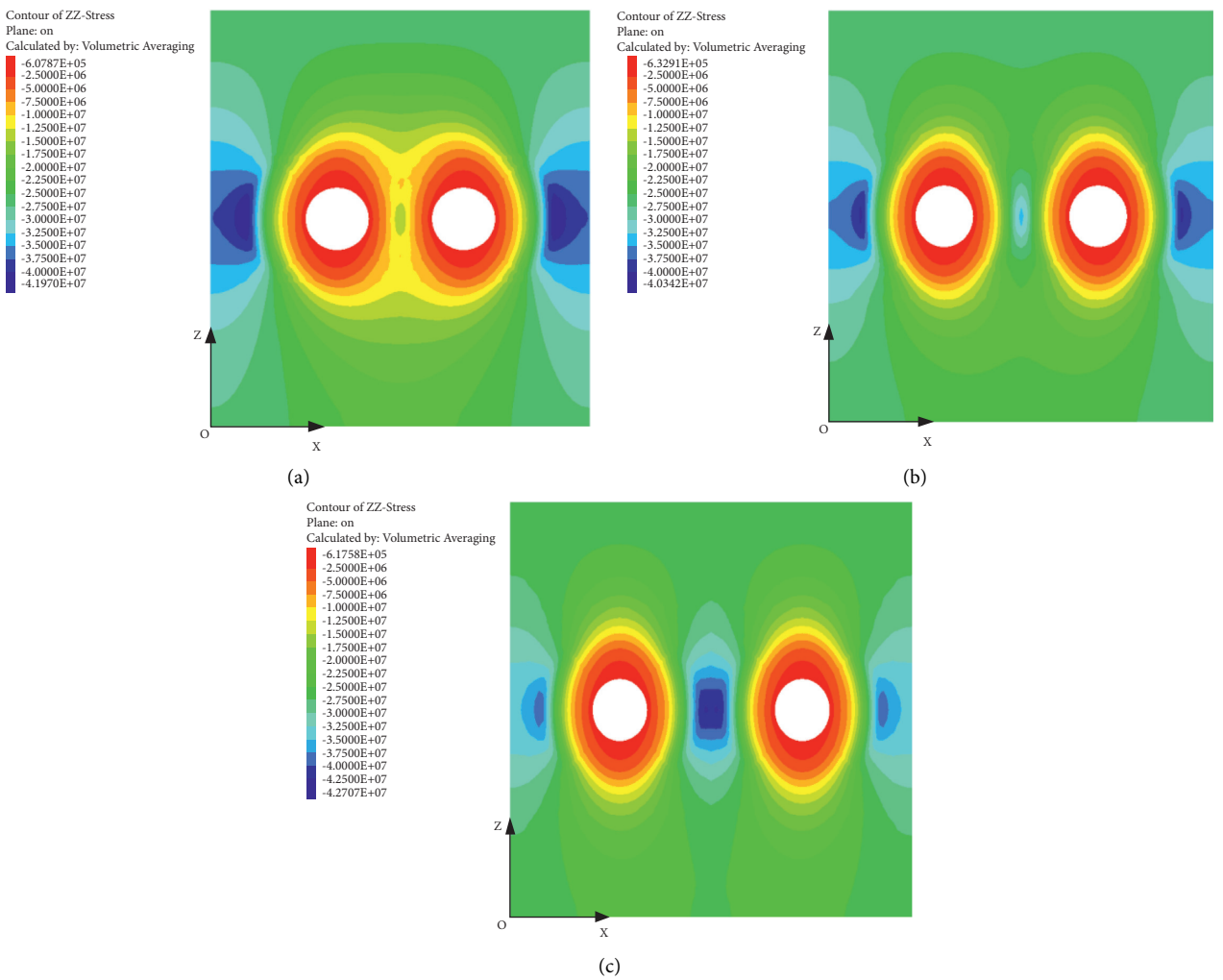

(a) (b)

(c)

Figure 15: Contour map of vertical stress around slots with different spacings in Section 1. (a) 3.0 m. (b) 4.0 m. (c) 5.0 m.

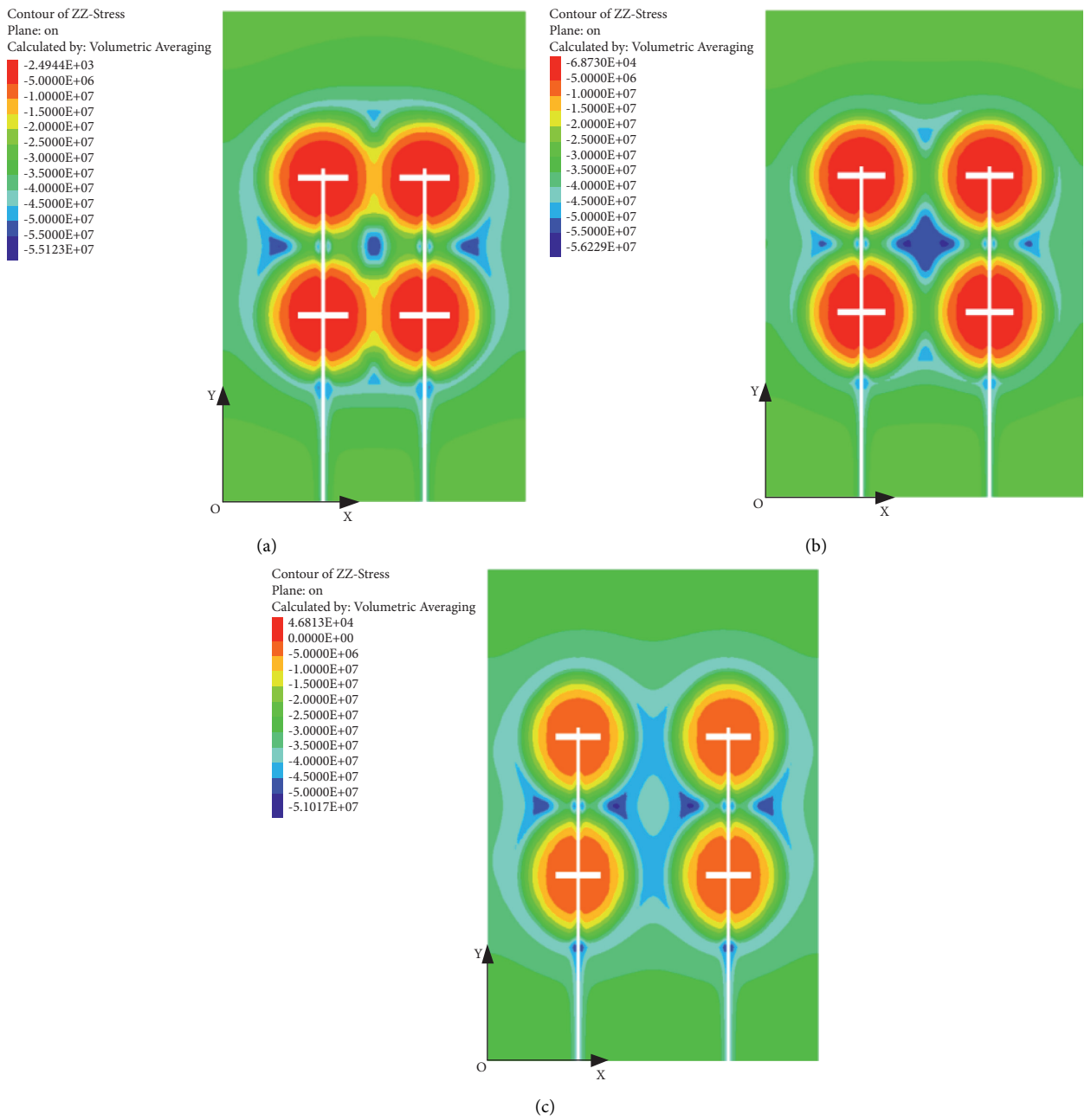

Figure 16: Vertical stress contour map around the slot with different spacings in Section 2. (a) 3.0 m. (b) 4.0 m. (c) 5.0 m.

different spacings in section 2 is shown. Figure 16 shows that the vertical stress of the "double-drilling and double-slot" model has the shape of a symmetrical "disc." According to the simulation results, when the drilling spacing is 3 m, there is only one stress concentration point with a stress of 53 MPa, between the four slots. When the drilling spacing is 4 m and 5 m, there are two stress concentration points between the four slots, with stresses of 56 MPa and 51 MPa, respectively. When the spacing is 4 m, the stress concentration degree is the highest, reaching 2.14. According to the above analysis, when the drilling spacing is 4 m or 5 m, there may be an area of original rock between the four slots, that is, the undamaged area.

(b) Plastic zone

As shown in Figures 17 and 18, the distribution of the plastic zone around the slot with different spacings in section 1 and section 2 is shown. As shown in the figures, when the spacing between drillings is 3 m, the plastic through zone is between drillings; that is, under the influence of both sides of the slot, the coal mass between boreholes is destroyed. When the spacing of drilling is 4 m,

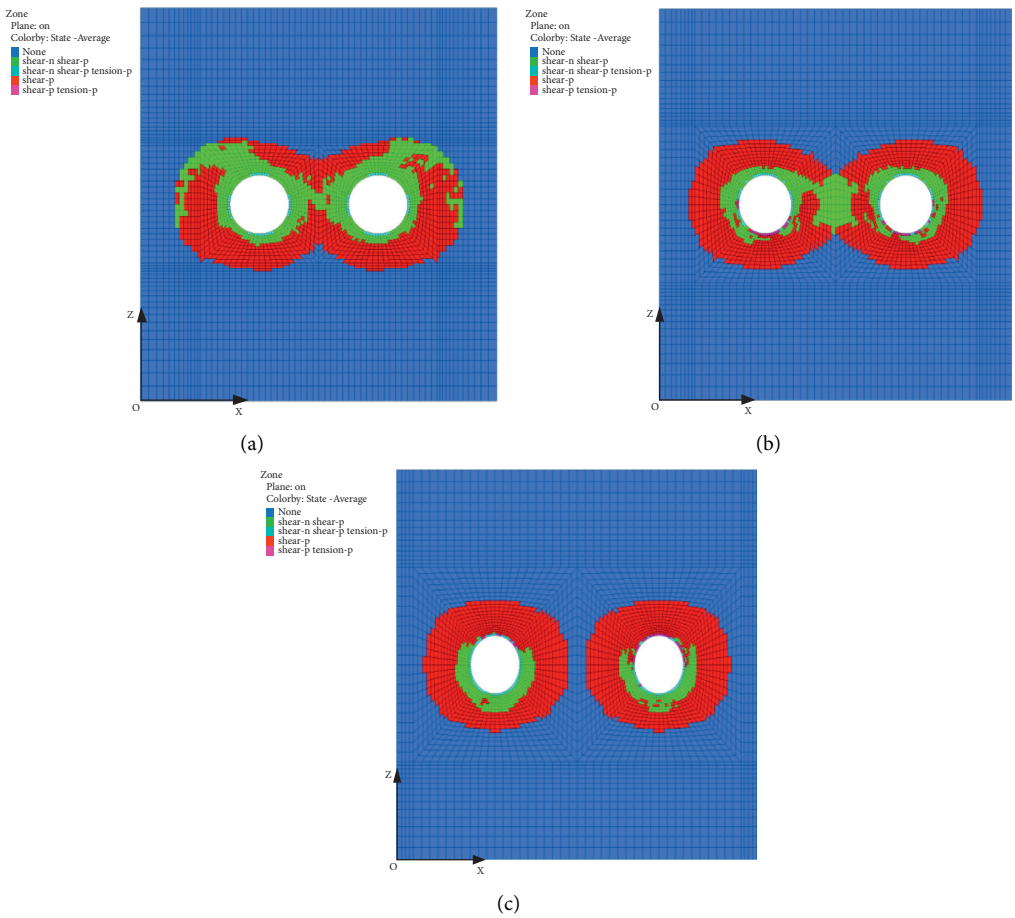

Figure 17: Distribution of the plastic zone around the slot with different spacings in Section 1. (a) 3.0 m. (b) 4.0 m. (c) 5.0 m.

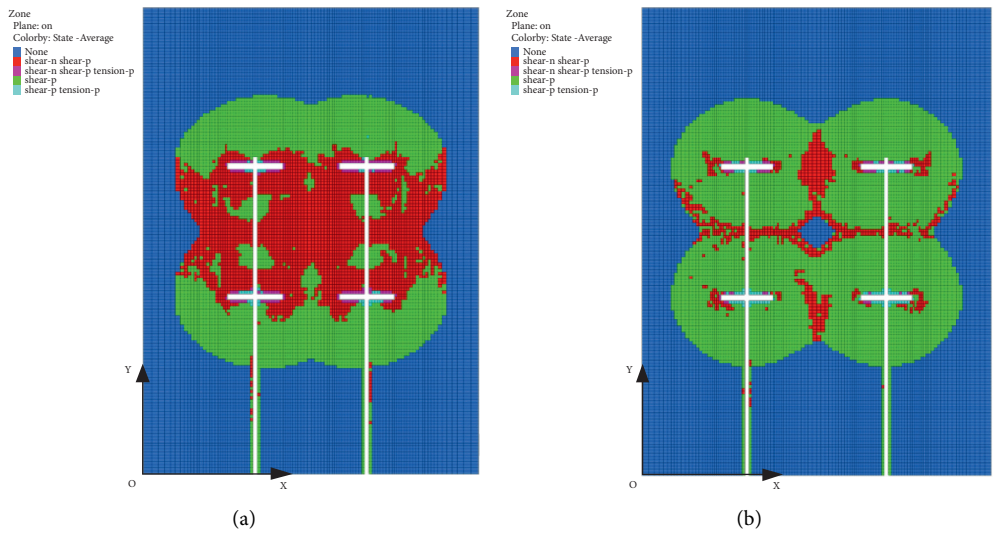

Figure 18: Continued.

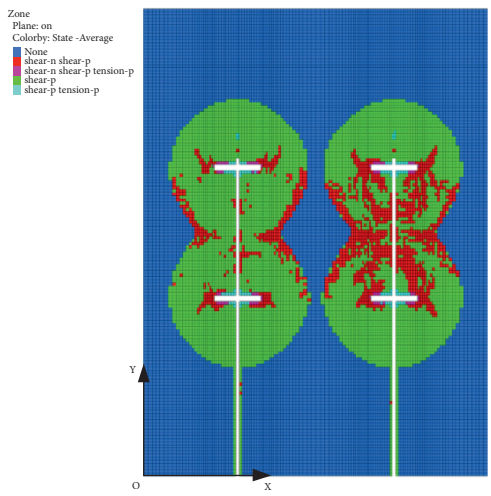

(c)

Figure 18: Distribution of the plastic zone around the slot with different spacings in Section 2. (a) 3.0 m. (b) 4.0 m. (c) 5.0 m.

there is still a plastic through zone between the drillings, but there is a certain range of original rock area between the four slots, which is smaller than that of the plastic through zone. When the distance between drillings is 5 m, the plastic through zone between drillings disappears. According to the above analysis results, the drilling spacing greatly influences the vertical stress and plastic zone between the boreholes, and with the increase in the drilling spacing, the range of the plastic zone between the drillings decreases in turn until it disappears. Therefore, considering the construction time, manpower, material resources, and other factors, it is suggested that the drilling spacing in the direction of the coal pillar length should be 3~4 m.

5. Field Implementation and Effect Test

5.1. Field Implementation

5.1.1. Field Implementation Equipment. The field equipment was mainly composed of a high-strength drill bit, a hydraulic slotting integral drill pipe, an ultrahigh-pressure rotating water tail, a high-pressure clean water pump, a high-low pressure conversion slot cutter, and an ultrahigh-pressure hydraulic hose (as shown in Figure 19). The equipment has good performance, a simple structure, and convenient operation.

5.1.2. Field Implementation Process. According to the research results in Section 4 and combined with the field conditions, a high-pressure water jet was used to destroy the residual coal pillar in the overlying goaf within 100 m of the middle section of the 38216 working face, and an ultrahigh-pressure hydraulic slotting device was placed in the design position of the 5216 roadway. According to the design scheme, workers on site drilled holes and cut seams, a total of 26 sections were arranged, and each section was set with 6 boreholes with different angles. The section spacing was 4 m. Implementation of the layout is shown in Figures 12 and 20.

The on-site construction process is as follows:

(1) The drilling rig is placed at the design position, the hydraulic slotting integral drill pipe, high-low-pressure conversion slot cutter, high-strength drill bit, and other devices are connected, the angle between the drill pipe and the roof (roadway side) is adjusted, and drilling with ordinary pressure water is performed until the design depth is reached.

(2) The ultrahigh-pressure rotating water tail is connected, the high-low pressure conversion slot cutter is placed in the set position, the water pump and the drilling rig are started, the water pressure is incrementally adjusted to 100 MPa for slotting, and the slotting time is 5 min.

(3) After cutting, the water pressure is adjusted to ordinary pressure, the 4 m drill pipe of the drilling rig is purged, and the water pressure is adjusted to 100 MPa again to continue cutting until the design scheme is completed. The field construction is shown in Figure 21.

5.2. Effect Test. To verify the effect of slotting, the amount of coal cinder discharged from each drilling hole and the pressure of the hydraulic support in the slotting zone are statistically analysed to verify the effectiveness and rationality of the slotting effect.

5.2.1. Amount of Coal Cinder Discharged from Each Drilling Hole. The hydraulic slotting pressure of each drilling hole is 100 MPa. During slotting, under the impact of a water jet and the rotation of the drill pipe, the coal blocks are discharged as small cinder particles with a diameter of 0.3~1.5 cm. As there are many boreholes on site, this part only gives the single-tool coal output of 12 boreholes on sections C and *M*, as shown in Table 4.

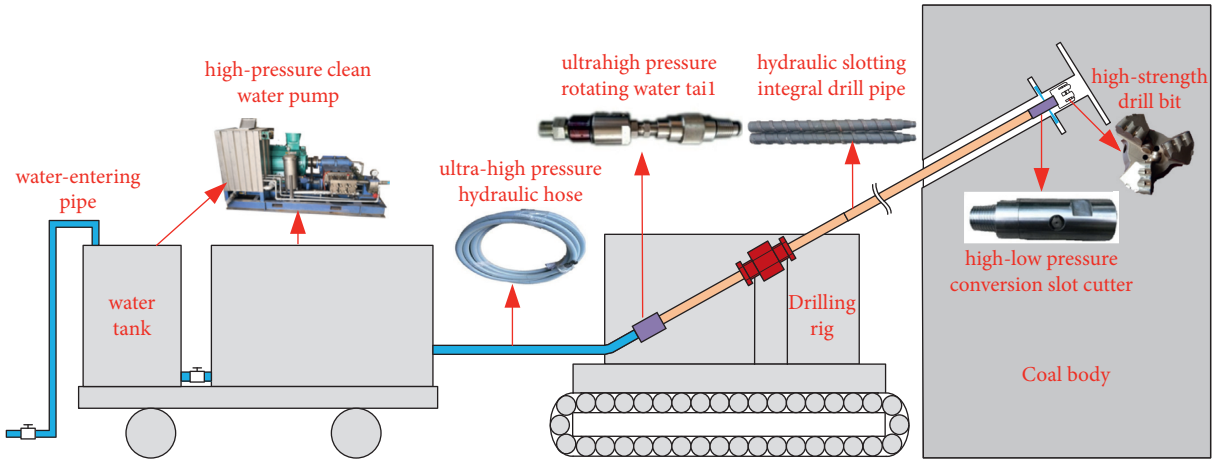

Figure 19: Ultrahigh-pressure hydraulic slotting device.

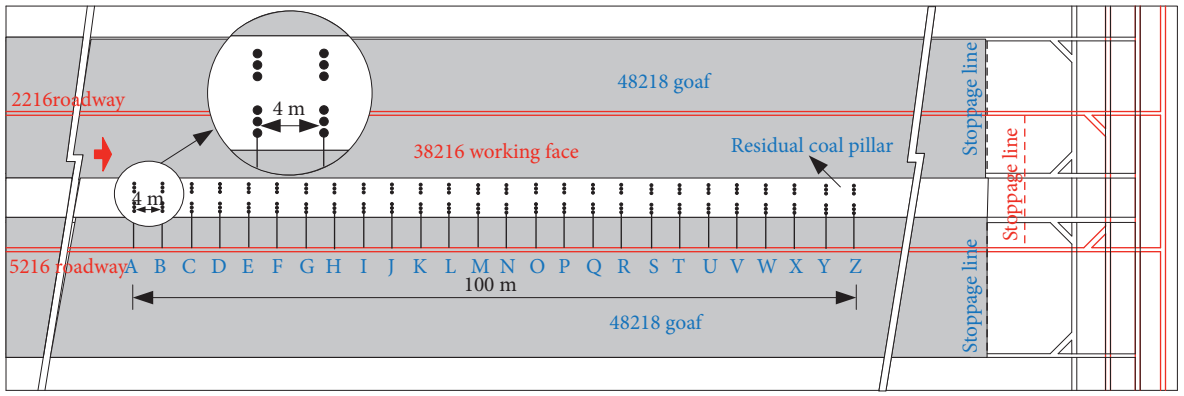

Figure 20: Layout of boreholes along the length of the residual coal pillar.

(a) (b)

Figure 21: Field construction. (a) Drilling stage. (b) Slotting stage.

Table 4: Statistics of single-drilling coal output.

Borehole name	Single cutting time (min)	Single coal output (t)	Number of slits (time)	Total slotting time (min)	Total coal output (t)
C-1	5	0.60	2	10	1.20
C-2	5	0.51	2	10	1.02
C-3	5	0.57	3	15	1.71
C-4	5	0.60	2	10	1.22
C-5	5	0.53	2	10	1.06
C-6	5	0.57	3	15	1.71
M-1	5	0.51	2	10	1.02
M-2	5	0.60	2	10	1.20
M-3	5	0.60	3	15	1.80
M-4	5	0.57	2	10	1.14
M-5	5	0.60	2	10	1.20
M-6	5	0.53	3	15	1.59

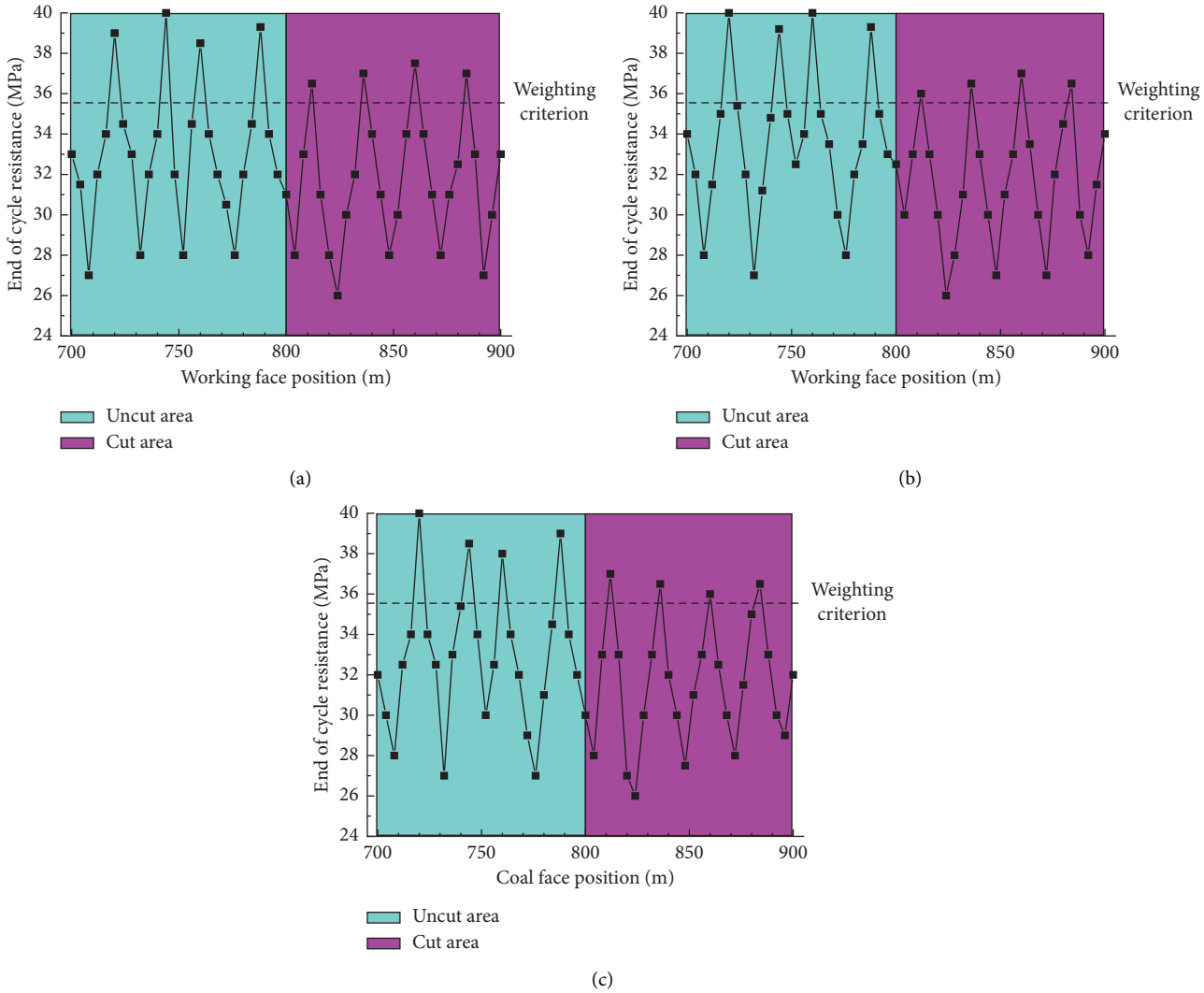

Figure 22: Data curve of typical hydraulic support under a residual coal pillar. (a) 25#. (b) 32#. (c) 39#.

$$r_c = \sqrt{\frac{M_c}{\pi h_c K_c \gamma_c}}, \tag{14}$$

Table 4 shows that at the same cutting time, the coal outputs of each drilling hole are different, approximately 0.51~0.60 t, and the average coal output of each drilling hole is 0.57 t. This may be due to the development of joints in the coal or the influence of mining, resulting in differences in the strength of coal in the same zone. Therefore, under the impact of a water jet, the single coal yield in the low-strength zone is higher, while the single coal yield in the high-strength

zone is lower.where r_c is the slot radius, m; M_c is the coal output of a single slot, t; h_c is the slot width, m; K_c is the crushing and rising coefficient of coal slag, 1.2; and γ_c is the density of coal, t/m^3.

To obtain the effective radius of the slot under high-pressure hydraulic cutting, the effective radius of the slot can be deduced by the average coal output of a single slot. By substituting $M_c = 0.57$ t, $h_c = 0.2$ m, $K_c = 1.2$, and $\gamma_c = 1.41$ t/m^3 into equation (14), the average slot radius is approximately 0.73 m.

5.2.2. Pressure Value of the Hydraulic Support in the Working Face. To understand the influence of a high-pressure water jet destroying a residual coal pillar on the 38216 working face, the mine pressure behaviour of the 38216 working face was monitored, and the load change of the hydraulic support in the slotted zone and uncut zone was understood. According to the layout of hydraulic supports in the working face, there are 25 hydraulic supports (#21–46) under the residual coal pillar. Due to the large amount of data, this part gives the data curves of three typical hydraulic supports (#25, #32, and #39) under the residual coal pillar, as shown in Figure 22.

According to Figure 22, the data change trends of the three hydraulic supports are the same. In the uncut zone, the average weighting interval is 22.6 m, the working resistance is 38~40 MPa, and the maximum value is 40 MPa; in the slotting zone, the average weighting interval is 20.6 m, the working resistance is 36~37 MPa, and the maximum value is 37 MPa. The above data show that slotting has little effect on the weighting intervals and has a great influence on the variation in the working resistance of the support, and the maximum working resistance of the hydraulic support in the slotted area is reduced by 3 MPa compared with that in the uncut area. Therefore, high-pressure hydraulic slotting can reduce the working resistance of the hydraulic support under the residual coal pillar to a certain extent, which is beneficial to the safe mining of the working face.

6. Conclusion

Based on the geological occurrence of the No. 3 coal seam and mountain No. 4 coal seam in the Yanzishan coal mine, application of high-pressure water jet pressure relief technology to residual coal pillars in the overlying goaf of close-distance coal seams was studied by theoretical analysis and field industrial tests to provide safety guarantees and theoretical guidance for safe mining of close-distance coal seams under similar conditions. The main conclusions are as follows:

(1) According to the mine pressure and strata control and limit equilibrium theories, the elastic-plastic zone range of the residual coal pillar and the stress distribution law of the floor are obtained by structural modelling of support bearing load on the working face under the residual coal pillar, and the influence degree of the residual coal pillar on the support in the lower coal seam is revealed.

(2) Weakening the pressure of the residual coal pillar by combining high-pressure water jet and rock pressure is proposed. First, the high-pressure water jet is used to weaken the coal pillar and make the defect body in the elastic core, to destroy the coal body around the defect body, and to reduce the integrity of the coal pillar; then, yield failure of the whole coal pillar with defects is induced with mine pressure, the load transmission path of the overlying strata is cut off, and the lower close coal seam is in the low-stress zone.

(3) By establishing a mechanical model of the hydraulic cutting of a residual coal pillar and the "double-hole and double-slot" model, the high-pressure water jet drilling layout parameters are determined. The single knife cutting coal output and the hydraulic support monitoring data show that high-pressure hydraulic slotting can weaken the strength of the coal body to a certain extent, destroy the integrity of the residual coal pillar, cut off the load transmission path of the overlying strata, and reduce the working resistance of the hydraulic support under the residual coal pillar to a certain extent, which is beneficial to the safe mining of the working face.

Data Availability

The data used to support the findings of this study are included within the article.

Conflicts of Interest

The authors declare that there are no conflicts of interest regarding the publication of this study.

References

[1] H. Xie, M. Gao, R. Zhang, G. Peng, W. Wang, and A. Li, "Study on the mechanical properties and mechanical response of coal mining at 1000 m or deeper," *Rock Mechanics and Rock Engineering*, vol. 52, no. 5, pp. 1475–1490, 2019.

[2] J. Lu, D. M. Zhang, G. Huang, and X. Li, "Effects of loading rate on the compound dynamic disaster in deep underground coal mine under true triaxial stress," *International Journal of Rock Mechanics and Mining Sciences*, vol. 134, no. 10, Article ID 104453, 2020.

[3] J. Ning, J. Wang, L. Jiang, N. Jiang, X. Liu, and J. Jiang, "Fracture analysis of double-layer hard and thick roof and the controlling effect on strata behavior: a case study," *Engineering Failure Analysis*, vol. 81, pp. 117–134, 2017.

[4] A. M. Suchowerska, R. S. Merifield, and J. P. Carter, "Vertical stress changes in multi-seam mining under supercritical longwall panels," *International Journal of Rock Mechanics and Mining Sciences*, vol. 61, pp. 306–320, 2013.

[5] H. Shang, J. Ning, S. Hu, S. Yang, and P. Qiu, "Field and numerical investigations of gateroad system failure under an irregular residual coal pillar in close-distance coal seams," *Energy Science & Engineering*, vol. 7, no. 6, pp. 2720–2740, 2019.

[6] J.-x. Yang, C.-y. Liu, B. Yu, and F.-f. Wu, "Calculation and analysis of stress in strata under gob pillars," *Journal of Central South University*, vol. 22, no. 3, pp. 1026–1036, 2015.

[7] C. L. Tian, X. L. Yang, H. T. Sun, Y. B. Liu, and Q. T. Hu, "Experimental study on the overburden movement and stress evolution in multi-seam mining with residual pillars," *Energy Science & Engineering*, vol. 7, no. 3, pp. 3095–3110, 2019.

[8] W. Ru, S. Hu, J. Ning et al., "Study on the rheological failure mechanism of weakly cemented soft rock roadway during the mining of close-distance coal seams: a case study," *Advances in Civil Engineering*, vol. 2020, Article ID 8885849, 20 pages, 2020.

[9] S. H. Tu, F. J. Dou, Z. J. Wang, and Y. Yuan, "Strata control technology of the fully mechanized face in shallow coal seam close to the above room-and-pillar gob," *Journal of China Coal Society*, vol. 36, no. 3, pp. 366–370, 2011.

[10] J. Z. Yang, K. G. Zheng, J. Z. Zhao, Y. J. Li, N. Dai, and H. Yang, "Research on fracturing treatment technology of concentrated stress disaster by the overlying coal pillar in close distance shallow seam," *Mining Safety & Environmental Protection*, vol. 47, no. 4, pp. 82–87, 2020, (in Chinese).

[11] B. Xia, X. Zhang, B. Yu, and J. Jia, "Weakening effects of hydraulic fracture in hard roof under the influence of stress arch," *International Journal of Mining Science and Technology*, vol. 28, no. 6, pp. 951–958, 2018.

[12] M. Behnia, K. Goshtasbi, M. F. Marji, and A. Golshani, "Numerical simulation of interaction between hydraulic and natural fractures in discontinuous media," *Acta Geotechnica*, vol. 10, no. 4, pp. 533–546, 2015.

[13] W. Y. Lu and C. C. He, "Numerical simulation of the fracture propagation of linear collaborative directional hydraulic fracturing controlled by pre-slotted guide and fracturing boreholes," *Engineering Fracture Mechanics*, vol. 235, no. 7, Article ID 107128, 2020.

[14] J. Xie, Y. P. Liang, Q. L. Zou, L. Li, and X. L. Li, "Elimination of coal and gas outburst risk of low-permeability coal seam using high-pressure water jet slotting technology: a case study in Shihuatian Coal Mine in Guizhou Province China," *Energy Science & Engineering*, vol. 7, no. 4, pp. 1394–1404, 2019.

[15] G. Si, S. Durucan, J.-Q. Shi, A. Korre, and W. Cao, "Parametric analysis of slotting operation induced failure zones to stimulate low permeability coal seams," *Rock Mechanics and Rock Engineering*, vol. 52, no. 1, pp. 163–182, 2019.

[16] Q. l. Zou, B. q. Lin, T. Liu, X. c. Hu, and C. s. Zheng, "Variations in coalbed gas content, initial gas desorption property and coal strength after drilling-slotting integration technique and gas drainage: insight into pore characteristics," *International Journal of Oil, Gas and Coal Technology*, vol. 15, no. 3, p. 235, 2017.

[17] F. Yan, B. Lin, C. Zhu et al., "A novel ECBM extraction technology based on the integration of hydraulic slotting and hydraulic fracturing," *Journal of Natural Gas Science and Engineering*, vol. 22, pp. 571–579, 2015.

[18] E. B. Yi and Y. J. Zhang, "Composite hazards prevention with breaking coal seam and roof by super high pressure water jet," *Journal of China Coal Society*, vol. 46, no. 4, pp. 1271–1279, 2021.

[19] R. Wang, J. B. Bai, S. Yan, and Z. G. Chang, "An innovative approach to theoretical analysis of partitioned width & stability of strip pillar in strip mining," *International Journal of Rock Mechanics and Mining Sciences*, vol. 129, no. 1, Article ID 104301, 2020.

[20] B. Yu, "Behaviors of overlying strata in extra-thick coal seams using top-coal caving method," *Journal of Rock Mechanics and Geotechnical Engineering*, vol. 8, no. 2, pp. 238–247, 2016.

[21] X. Zhang, C. B. Deng, and X. F. Wang, "Study on dynamic deformation of overlying strata and pressure behavior law for extraction of multiple coal seams," *Coal Science and Technology*, vol. 9, pp. 108–113, 2017.

[22] T. J. Kuang, "Study on overburden strata movement law at face end of high cutting fully–mechanized top coal caving face in ultra thick seam," *Coal Science and Technology*, vol. 6, pp. 191–196, 2016.

[23] B. Yu, R. Gao, X. B. Meng, and T. J. Kuang, "Near-far strata structure instability and associate strata behaviors in large space and corresponding control technology," *Chinese Journal of Rock Mechanics and Engineering*, vol. 37, no. 5, pp. 1134–1145, 2018.

[24] D. C. Ge, D. Li, F. X. Jiang et al., "Reasonable pressure-relief borehole spacing in coal of different strength," *Journal of Mining & Safety Engineering*, vol. 37, no. 3, pp. 578–593, 2020.

Hindawi
Shock and Vibration
Volume 2022, Article ID 5938950, 17 pages
https://doi.org/10.1155/2022/5938950

Research Article

The Study on the Shock Wave Propagation Rule of a Gas Explosion in a Gas Compartment

Shu-Chao Lin,[1,2,3] Qing-Zhao Hou,[1] Anna Derlatka,[4] Shan Gao,[5] Jin-Jun Kang,[3] and Xiao-Lei Dong[1]

[1]*Shaanxi Key Laboratory of Safety and Durability of Concrete Structures, Xijing University, Xi'an 710123, China*
[2]*Post-Doctoral Station of Civil Engineering, School of Civil Engineering, Tianjin University, Tianjin 300072, China*
[3]*College of Civil and Architectural Engineering, North China University of Science and Technology, Tangshan 063210, China*
[4]*Czestochowa University of Technology, 69 Dąbrowskiego St., Czestochowa 42-201, Poland*
[5]*School of Civil Engineering, Harbin Institute of Technology, Harbin 150090, China*

Correspondence should be addressed to Shan Gao; 13833185232@139.com

Received 7 October 2021; Accepted 21 December 2021; Published 6 January 2022

Academic Editor: Jianwei Cheng

Combined with the k-ε turbulence model of general application, a refined finite element model of a utility tunnel's gas compartment filled with the methane/air mixture is developed. A series of analyses are made by using the powerful industry-leading computational fluid dynamics (CFD) software flame acceleration simulator (FLACS) to study the shock wave propagation rule in the gas compartment. The longitudinal and transversal distribution laws of the explosion shock wave are gained taking into consideration the spatial characteristics of the gas compartment. The influences of a few parameters, such as initial conditions and section size of the gas compartment, on the shock wave propagation rule are further discussed. The basic procedure for predicting the peak pressure of the blast wave is provided by considering the initial conditions and the gas compartment, and the corresponding injury effect of the explosion wave on the living beings is assessed. The investigation demonstrates that the peak pressure by the coupled effect between the initial conditions is significantly influenced, especially at the upper and lower gas explosion limits. The peak pressure increases gradually as the width or height increases, and both basically meet the linear relation. The proposed method can forecast the peak pressure of the explosion shock wave in the gas compartment accurately. According to the peak pressure longitudinal and transversal distributions of the blast wave, the peak pressure is far greater than the killing pressure threshold in the underground and closed space; consequently, it is not safe for the living beings in the gas compartment.

1. Introduction

Nowadays, the process of the urbanization is accelerated constantly and the scale of the city is also enlarged substantially in the last few decades. The municipal pipeline system becomes more and more complicated and its corresponding management issue becomes increasingly apparent [1, 2]. Accordingly, the utility tunnel, namely, the underground pipe gallery, has emerged in this context [3]. It is an integrated underground pipe ditch or pipeline corridor, which is especially used to lay a variety of municipal pipelines, such as water supply, drainage, heating, gas, electricity, and telecom pipelines. The utility tunnel gradually becomes an important part of the lifeline engineering. It is favored by all walks of life for its easy maintenance, effective use of underground space, good city appearance, and protective effect. The utility tunnel is now extensively applied in major cities around the world [4]. Due to inevitable aging, corrosion, and other human factors, as soon as the leakage accident takes place, it very likely ends in an explosion in the gas compartment in the utility tunnel. Consequently, the research into the propagation law of a gas explosion in the gas compartment has been closely concerned [5, 6].

So far, a range of investigations has been carried out by some experts and scholars from home and abroad to

investigate the gas explosion propagation rule in the tunnel. Based on the three-dimensional CFD analysis software AutoReaGas, Pang et al. [7] implemented the numerical simulation analyses to explore the effect of the laneway support spacing on the blast wave properties of a methane/air mixture explosion in a direct laneway and concluded that the support spacing has a great influence on the blast wave distribution. Based on the numerical simulation results from the software AutoReaGas, Zhang et al. [8] put forward a new method to estimate the pressure drop of the explosion wave caused by a premixed methane/air mixture explosion in a closed-ended tunnel and confirm the reliability of this method by the test data. With the aid of the software FLACS, Zhu et al. [9] simulated the explosion process of the methane/air mixture in the direct full-scale tunnel and examined the pressure and its influencing factors, such as the methane gas volume concentration, tunnel blockage ratio, tunnel length, and tunnel cross section. With the application of the large eddy simulation method, Wang et al. [10] investigated the gas explosion shock wave propagation mechanism in the coal mine in consideration of the disaster-causing factors. Combining with the complicated structure characteristics of the goaf, Ke et al. [11] discussed the gas explosion shock wave and flame propagation mechanism in the goaf by using the open-source software OpenFOAM. Wang et al. [12, 13] performed a series of explosion tests to examine the combustion features and explosion characteristics of the methane/ethylene/air mixtures of different equivalence ratios and ethylene volume ratios in a sealed chamber at ambient temperature (20°C) and atmospheric pressure. In addition, they employed a theoretical method based on the adiabatic flame temperature to explore the flammability limits of the methane/air mixtures mixed with the gaseous fuels of different relative humidity. Based on the density functional theory and its detailed mechanism, Su et al. [14] probed intensively the chemical kinetic behavior of the methane/hydrogen mixture thoroughly at the explosion stage and acquired a better grasp and understanding of the methane/hydrogen mixture explosion initiation mechanism. However, the studies regarding the gas explosion propagation rule in the gas compartment are very few. Taking into account the role of the hydrogen, Zhang et al. [15] carried out the finite element analyses to examine the explosion of the methane/hydrogen mixture in the gas compartment of a utility tunnel by means of the commercial CFD analysis software FLACS. From the review of literature mentioned above, the previous works in this field are mostly set in the tunnel of the coal mine and involve its some specific structure characteristics, and lack of the potential risk assessment. In addition, there is an obvious size effect in gas explosion characteristics [16, 17].

Based on the above, and combined with the typical urban gas explosion incidents [18–21] over the latest years, a range of finite element analyses are performed on a typical and representative gas compartment in a utility tunnel to research the propagation rule of the gas blast. A new methodology is presented to forecast the blast wave properties in the gas compartment [22, 23].

2. Gas Compartment

2.1. Brief Introduction of Gas Compartment. A typical and representative gas compartment [24–27] of a real utility tunnel in China's Beijing City is introduced in this study, as shown in Figure 1, represented by the following parameters: section width, $w_c = 2.00$ m; section height, $h_c = 4.00$ m; length of gas compartment (distance between two adjacent firewalls), $L_c = 200.00$ m. The city gas is uniformly mixed together with the air at a specific ratio to create the gas mixture. The gas compartment is filled with the gas mixture at a certain length at one end of it. The gas mixture is ignited by the ignition source, whose temperature is up to about 2000°C. The initial temperature and initial gas volume concentration are 0°C and 9.50%, respectively. The atmospheric pressure is 1.01×10^5 Pa.

The incomplete and complete combustion reaction equations of the gas mixture can be expressed as follows:

$$\begin{aligned} 2CH_4 + 3O_2 &\longrightarrow 2CO + 4H_2O \,(\text{incomplete combustion}) \\ CH_4 + 2\,O_2 &\longrightarrow CO_2 + 2\,H_2O \,(\text{complete combustion}) \end{aligned} \tag{1}$$

2.2. Basic Theory. Computational fluid dynamics is now extensively employed in tackling all sorts of complex issues in fluid mechanics and becomes increasingly significant. It can accurately and reasonably predict a variety of physical phenomena of fluid, such as chemical reaction. After the experimental and theoretical fluid mechanics, the computational fluid dynamic has become a more and more important research tool in the past decades.

2.2.1. Governing Equations. The methane/air mixture explosion in a gas compartment in a utility tunnel can be deemed as a swift and violent combustion process [28, 29]. In the Cartesian (or rectangular) coordinate system, they are provided in partial differential form as follows.

Conservation equation of mass is given by

$$\frac{\partial}{\partial t}\left(\beta_v \rho\right) + \frac{\partial}{\partial x_j}\left(\beta_j \rho v_j\right) = \frac{\dot{m}}{V}, \tag{2}$$

where β_v is the volume porosity; β_j is the area porosity in the j direction; ρ is the mass density; $\dot{m}$ is the mass flow; V is the volume; v_j is the velocity in the j direction; x_j is the Cartesian coordinate; and t is the time.

Conservation equation of momentum is given by

$$\frac{\partial}{\partial t}\left(\beta_v \rho v_i\right) + \frac{\partial}{\partial x_j}\left(\beta_j \rho v_j v_i\right) = -\beta_v \frac{\partial p}{\partial x_i} + \frac{\partial}{\partial x_j}\left(\beta_j \sigma_{ij}\right) + R_i + R_W + (\rho - \rho_0) g_i, \tag{3}$$

where p is the hydrostatic pressure; σ_{ij} is the stress tensor; R_i is the distributed resistance in the x_i direction because of the subgrid obstruction; R_W is the flow resistance due to the interaction between the fluid and the vessel wall; ρ_0 is the

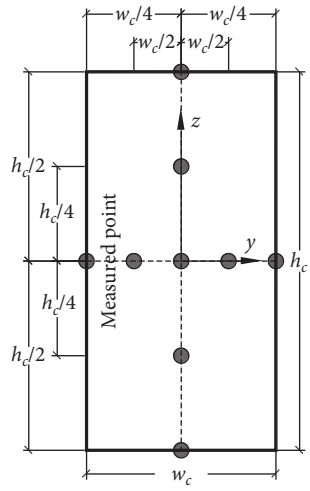

Figure 1: Gas compartment.

initial mass density; and g_i is the acceleration of gravity in the i direction.

$$R_i = -f_i A_i \rho |v_i| v_i, \tag{4}$$

where f_i is a constant associated with the obstruction type and the orientation and $A_i = (1 - \beta_i)/(\Delta x_i)$.

In equation (3), the stress tensor can be given by

$$\sigma_{ij} = \mu_{\text{eff}} \left(\frac{\partial v_i}{\partial x_j} + \frac{\partial v_j}{\partial x_i} \right) - \frac{2}{3} \delta_{ij} \left(\rho k + \mu_{\text{eff}} \frac{\partial v_k}{\partial x_k} \right), \tag{5}$$

where μ_{eff} is the effective viscosity; k is the turbulence kinetic energy; and δ_{ij} is the Kronecker Delta function.

Enthalpy is an important state parameter characterizing the material system energy in the thermodynamics. The change in the enthalpy is equal to all the energy released by the explosion in the detonation process. Conservation equation of enthalpy:

$$\frac{\partial}{\partial t} (\beta_v \rho h) + \frac{\partial}{\partial x_j} \left(\beta_j \rho v_j h \right) = \frac{\partial}{\partial x_j} \left(\beta_j \frac{\mu_{eff}}{\sigma_h} \frac{\partial h}{\partial x_j} \right) + \beta_v \frac{Dp}{Dt} + \dot{Q}, \tag{6}$$

where h is the enthalpy; σ_h is the turbulence constant for the variable $\beta_v Dp/Dt + Q$; D/Dt is the substantial derivative operator; and $\dot{Q}$ is the wall heat flux.

Conservation equation of chemical specie mass fraction is given by

$$\frac{\partial}{\partial t} (\beta_v \rho m) + \frac{\partial}{\partial x_j} \left(\beta_j \rho v_j m \right) = \frac{\partial}{\partial x_j} \left(\beta_j \frac{\mu_{\text{eff}}}{\sigma_m} \frac{\partial m}{\partial x_j} \right) + R_m, \tag{7}$$

where m is the mass of chemical specie; σ_m is the turbulence constant for the variable R_m; and R_m is the reaction rate of the gas.

Additionally, the conservation equations of turbulent kinetic energy and its dissipation rate [30] in the k-ε turbulence model can be described as follows:

$$\begin{aligned} \frac{\partial}{\partial t} (\beta_v \rho k) + \frac{\partial}{\partial x_j} \left(\beta_j \rho v_j k \right) &= \frac{\partial}{\partial x_j} \left(\beta_j \frac{\mu_{\text{eff}}}{\sigma_k} \frac{\partial k}{\partial x_j} \right) + P_k - \beta_v \rho \varepsilon \\ \frac{\partial}{\partial t} (\beta_v \rho \varepsilon) + \frac{\partial}{\partial x_j} \left(\beta_j \rho v_j \varepsilon \right) &= \frac{\partial}{\partial x_j} \left(\beta_j \frac{\mu_{\text{eff}}}{\sigma_\varepsilon} \frac{\partial \varepsilon}{\partial x_j} \right) + \frac{\varepsilon}{k} \left(C_1 P_k - C_2 \beta_v \rho \varepsilon \right). \end{aligned} \tag{8}$$

where k and ε are the turbulent kinetic energy and its dissipation rate, respectively; σ_k and σ_ε are the k-ε model constants for the variables (P_k - $\beta_v \rho \varepsilon$) and ($C_1 P_k$ - $C_2 \beta_v \rho \varepsilon$)$\varepsilon/k$, respectively; P_k is the turbulent kinetic energy production rate; and C_1 and C_2 are all the constants.

All the conservation equations can be rewritten into a unified compact form and given by

$$\frac{\partial}{\partial t} (\rho \phi) + \frac{\partial}{\partial x_j} \left(\rho v_j \varphi \right) = \frac{\partial}{\partial x_j} \left(\Gamma \frac{\partial \varphi}{\partial x_j} \right) + S, \tag{9}$$

where φ and ϕ are the general variables; Γ is the effective turbulent diffusion coefficient; and S is the source term.

The expressions for φ, ϕ, Γ, and S are summarized in Table 1.

2.2.2. Other Details. In FLACS, the algorithm to solve the fluid field is the proverbial semi-implicit method for pressure-linked equations (SIMPLE) algorithm in the computational fluid dynamics, which is proposed by Patankar and Spalding [31] in 1972. This algorithm determines the pressure field on the basis of the staggered grid by using the predictor-corrector method and its key issue is to construct the pressure and velocity correction equations.

The classical turbulence models (for instance, k-ε and RNG turbulence models) are not applicable to the fluid that is located near the wall. The main reason for this is that the viscous force predominates in the fluid. Hence, the introduction of the wall function can improve the modeling of the flow field adjacent to the wall [29]. It is very suitable for the physical field of the gas explosion in the software FLACS.

2.3. Finite Element Model. The grids define the spatial resolution as well as the extents of the simulation volume. The model of the methane/air mixture is illustrated in Figure 2. The grids do not have to be isotropic and equally spaced. Please note that this model is important to have fine enough

Table 1: Expressions for φ, ϕ, Γ, and S.

Conservation equation of	φ	ϕ	Γ	S
Mass	β_v	β_j	0	$\dot{m}/V$
Momentum	$\beta_v\ v_i$	$\beta_j\ v_i$	μ_{eff}	$\partial/\partial x_j\left[\beta_j\mu_{\text{eff}}\partial v_j/\partial x_i - 2/3\beta_j\delta_{ij}\left(\rho k + \mu_{\text{eff}}\partial v_k/\partial x_k\right)\right]$ $-\beta_v\partial p/\partial x_i + R_i + R_W + (\rho - \rho_0)g_i$
Energy	$\beta_v h$	$\beta_j h$	$\mu_{\text{eff}}/\sigma_h$	$\beta_v Dp/Dt + Q$
Mass fraction	$\beta_v m$	$\beta_j m$	$\mu_{\text{eff}}/\sigma_m$	R_m
k	$\beta_v k$	$\beta_j k$	$\mu_{\text{eff}}/\sigma_k$	$P_k - \beta_v\rho\varepsilon$
ε	$\beta_v\varepsilon$	$\beta_j\varepsilon$	$\mu_{\text{eff}}/\sigma_\varepsilon$	$\frac{\varepsilon}{k}\left(C_1P_k - C_2\beta_v\rho\varepsilon\right)$

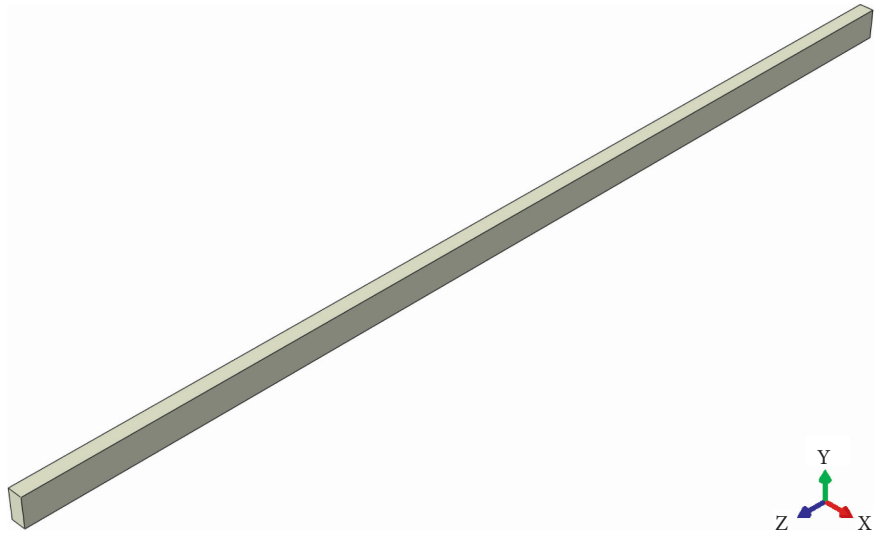

Figure 2: Finite element model.

grids to represent the detailed flow properties and the obstacles properly and the grids must extend quite a large distance from the area of interest to avoid too strong influence from the open boundaries.

The boundary conditions of the numerical simulation domain in Figure 2 are EULER by default. The mass and momentum conservation equations are imposed on the boundary conditions. The boundary conditions should be used with utmost care and attention; otherwise, they can influence the simulated results. The EULER boundary condition may give too high peak pressure in the confined situation.

There is a corresponding stable propagation detonation velocity for a certain gas mixture. The explosion is unstable if the detonation velocity is lower or higher than this stable propagation detonation velocity. The explosion eventually either becomes stable or is over.

3. Model Validation

The gas explosion propagation process in [32, 33] is simulated by using the software FLACS to validate the finite element model.

The parameters representing the square steel pipe in the gas explosion test are as follows: section height and width, hw_{p}; length, l_{p}; and wall thickness, t_{w}. There are two steel pipes made from the 16 Mn steel in this validation study: short pipe ($hw_{\text{p}} = 80$ mm; $l_p = 4{,}000$ mm; and $t_w = 12$ mm) and long pipe ($hw_{\text{p}} = 80$ mm; $l_p = 21{,}000$ mm; and $t_w = 12$ mm). They are filled with the premixed methane/air mixture, and the corresponding gas volume concentration is around 9.50%. The mechanical properties of the pipe material are as follows: yield strength, $f_y = 345$ MPa; Young's modulus, $E = 2.06 \times 10^{11}$ Pa; Poisson's ratio, $\nu = 0.30$; and mass density, $\rho = 7{,}850\ \text{kg/m}^3$. The inside of one of them is pasted with a layer of asbestos cloth of 0.80 mm in thickness by using the high temperature resistant adhesive. One end of the steel pipe is closed, while the other end is open. The ignition system is located at the closed end, and the energy of the ignition is around 2 J. The inside of the steel pipe needs to be rubbed down well with the sandpaper so that it can reduce the transition time and distance from deflagration to detonation, thus reducing or even avoiding the effect on the explosion test results. It should be noted that every test is repeated five times.

As listed in Tables 2 and 3, the discrepancies between them are a result of the following four primary reasons. First, the steel pipe is easily deformed slightly owing to the gas blast; thereby it can affect the pressure sensor measure precision. Second, the ignition source is difficult to be well modeled using an ignition temperature [34]. Third, there exists usually a very small amount of the inflammable and explosive gases of other types during the experiment [35]. And fourth, the heat insulation layer formed by the asbestos cloth in the experiment is not the ideal adiabatic boundary condition in the finite element model. But in general, the

Table 2: Blast wave peak pressures in short pipe (1.01×10^5 Pa).

Measured point no.		MP1	MP2	MP3	MP4
l/hw_p		9	22	34	47
Pipe without asbestos cloth	Test data	0.1838	0.1268	0.2538	0.1919
	Simulated results	0.1857	0.1246	0.2631	0.1866
Pipe with 4 m asbestos cloth	Test data	0.1905	0.1415	0.3123	0.3563
	Simulated results	0.1844	0.1420	0.3239	0.3697

Notes: the experimental data in the table above is the arithmetic mean of a given set of measured sample values from the repeated tests and l is the distance between the measured point and the ignition source.

Table 3: Explosion wave peak pressures in long pipe (1.01×10^5 Pa).

Measured point no.		MP1	MP2	MP3	MP4	MP5	MP6	MP7	MP8
l/hw_p		48	66	98	128	160	191	228	260
Pipe without asbestos cloth	Experimental data	—	—	—	0.3423	0.4257	0.3594	0.3320	0.3164
	Simulation results	—	—	—	0.3313	0.4182	0.3607	0.3442	0.3282
Pipe with 2 m asbestos cloth	Experimental data	0.2070	0.3969	0.7969	1.6583	2.1387	1.8876	1.4856	1.1621
	Simulation results	0.2013	0.4118	0.8260	1.6564	2.1901	1.8335	1.4763	1.2008

maximum relative deviations between test and simulation are all less than 5% and are insignificant, and the numerical simulation results coincide very well with the experimental data. Hence, they proved to be accurate and credible in the prediction of the blast wave peak pressures in the short and long pipes.

4. Blast Wave Space Distribution

To evaluate the injury effect on humans and animals and the damage effect on the gas compartment itself, the space distribution [36, 37] of the explosion shock wave in the gas compartment should be examined, which mainly includes the peak pressure longitudinal and transversal distributions. The propagation process of the gas explosion with different filled lengths in the gas compartment is simulated with the application of the reliable commercial CFD software FLACS. The specific research works are as follows.

4.1. Peak Pressure Longitudinal Distribution. On account of the related researches [8], and combined with the numerical results of this study, the blast wave peak pressure along the longitudinal direction can be expressed as follows:

$$p_L = p_{Lmax} \times \left(\frac{r_0}{r}\right)^{0.56} \quad r \geq r_0, \tag{10}$$

$$p_{Lmax} = 19.75 \times (r_0)^{0.84}, \tag{11}$$

where r_0 is the filled length of the gas and r is the distance from the measured point to one end of the gas compartment along the longitudinal direction.

The determination coefficients of equations (9) and (10) are 0.9865 and 0.9547, respectively. From equation (10), it can be concluded that the maximum pressure p_{Lmax} is $19.75 \times (r_0)^{0.84}$ at $r = r_0$. At $r_0 = 10$, 20, 30, 40, and 50 m, they are 138.52, 250.37, 341.83, 438.51, and 525.21 kPa, respectively, as depicted in Figure 3.

As Figure 4 describes, the peak pressure decreases along with the distance away from the gas zone, and the decreasing trend also decelerates. Furthermore, the larger the filled length of the gas is, the higher the peak pressure is. The maximum relative deviations between the simulated and fitting results are all less than 5%, indicating that the fitting and numerical simulation results coincide very well with each other, despite the filled length of the gas.

4.2. Peak Pressure Transversal Distribution. Based on the relevant studies [7], the blast wave peak pressure along the transversal direction can be given as follows:

$$p_T = \left(1 + \frac{|zy|}{hw_c}\right)^{r_0/2r} p_L, \tag{12}$$

where zy is the Cartesian coordinate of the measured point in the z or y direction and hw_c is the height or width of the gas compartment.

As Figure 5 illustrates, the peak pressure increases gradually with the increase in $|zy|$; the main reason for this is the reflection [38] of the blast wave that occurs in the internal wall of the gas compartment. Nevertheless, the increasing trend decelerates with the distance away from the gas zone [39]. The peak pressure on the wall of the gas compartment increases by about 22.47% compared with the peak pressure at the center of the section when $r = r_0$. The maximum relative deviations between the numerical simulation and fitting results are small enough so that the fitting results match well with the simulated results.

5. Parametric Studies

Unlike the explosive charge explosion, the gas explosion tends to be affected by environmental conditions. Consequently, there is an urgent need to get a comprehensive and systematic understanding of these interfering factors such as

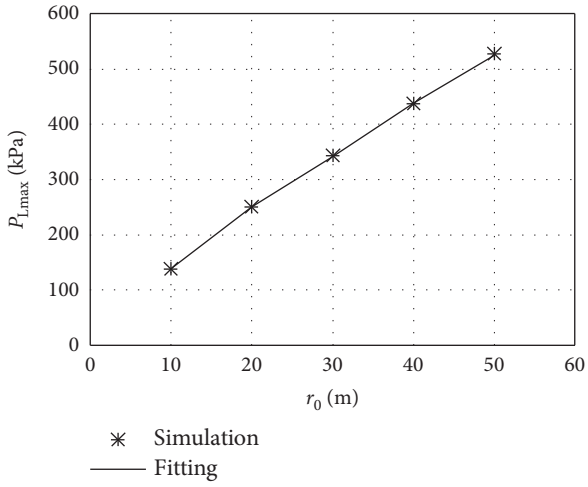

Figure 3: Relation between p_{Lmax} and r_0.

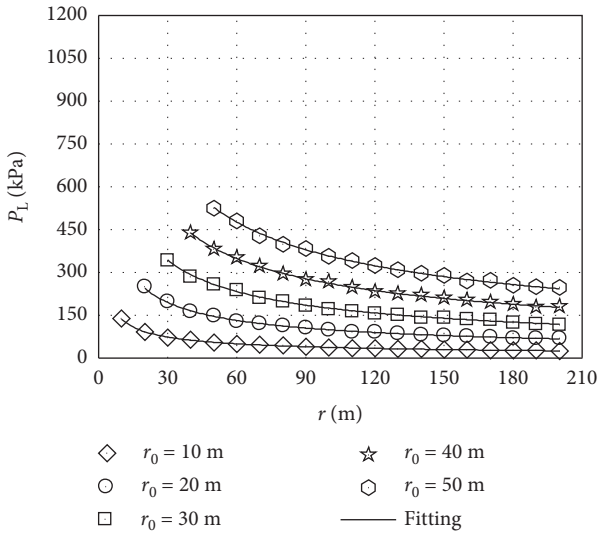

Figure 4: Peak pressure longitudinal distribution.

initial conditions [40–42] and gas compartment section size [43, 44]. The specific research works are as follows.

5.1. Initial Condition

5.1.1. Initial Temperature. As Figure 6 illustrates, the increase of the initial temperature would increase the gas combustion reaction rate, but decrease the corresponding total mass of the gas, since the gas would be expelled from the gas compartment. It indicates that the peak pressure primarily depends on the total mass of the gas.

5.1.2. Initial Gas Volume Concentration. As Figure 7 describes, the limited oxygen volume concentration determines the peak pressure. Therefore, as the initial gas volume concentration rises, the peak pressure rises to the maximum when the corresponding initial gas volume is nearly equal to the stoichiometric volume concentration [45] which is around 10%, and then reduces gradually.

The initial condition influence coefficient can be computed by dividing p_{ic} by p_{Lmax} from equation (10). Therefore, the difference in the filled length of the gas is eliminated as a matter of course. The corresponding suggested equation can be given by

$$\gamma_{ic} = \frac{p_{ic}}{p_{Lmax}} = \left(3.05 \times 10^{-5} - 0.0366\right)\left[10000C^2 - 1975C + 3.49 \times 10^{-2}T + 83.46\right] + 0.52. \quad (13)$$

As Figure 8 presents, the gas explosion parameters are greatly influenced by the initial temperature [46]. The upper gas explosion limit increases but the lower gas explosion limit decreases as the initial temperature increases. Consequently, the peak pressure by the coupled effect between the initial temperature and the initial gas volume concentration is significantly influenced, especially at the upper and lower gas explosion limits [47].

5.2. Gas Compartment Section Size. To examine the effect of the section size on the explosion wave peak pressure, a series of finite element analyses are performed on the gas compartments of different widths and heights, and their results are plotted in Figure 9.

As shown in Figure 9, the peak pressure increases gradually as the width or height increases, and both basically meet the linear relation. Additionally, both width and height enhance the blast wave peak pressure to varying degrees [48], and the height is slightly significant. The main reason for this is the gravity effect.

The section size influence coefficient can be calculated by dividing p_s by p_{Lmax} from equation (10). Therefore, the difference in the filled length of the gas is eliminated for granted. It can be expressed as follows:

$$\gamma_s = \frac{p_s}{p_{Lmax}} = 0.05\frac{w}{w_c} + 0.05\frac{h}{h_c} + 0.87. \quad (14)$$

An empirical relation among section size influence coefficient, width, and height can be gained using the linear regression analysis and described as equation (13). The determination coefficients of equation (13) are 0.9498. It can be found from Figure 9 that the fitting and finite element analysis results are nearly consistent with each other, despite the width or height of the gas compartment.

6. Suggested Methodology to Estimate the Blast Wave Properties

6.1. Proposed Method Basic Procedure. A new methodology is put forward to forecast the explosion wave peak pressure, whose basic procedures are given as follows:

(1) Give gas type, gas filled length, initial condition, gas compartment section size, etc. If not the methane

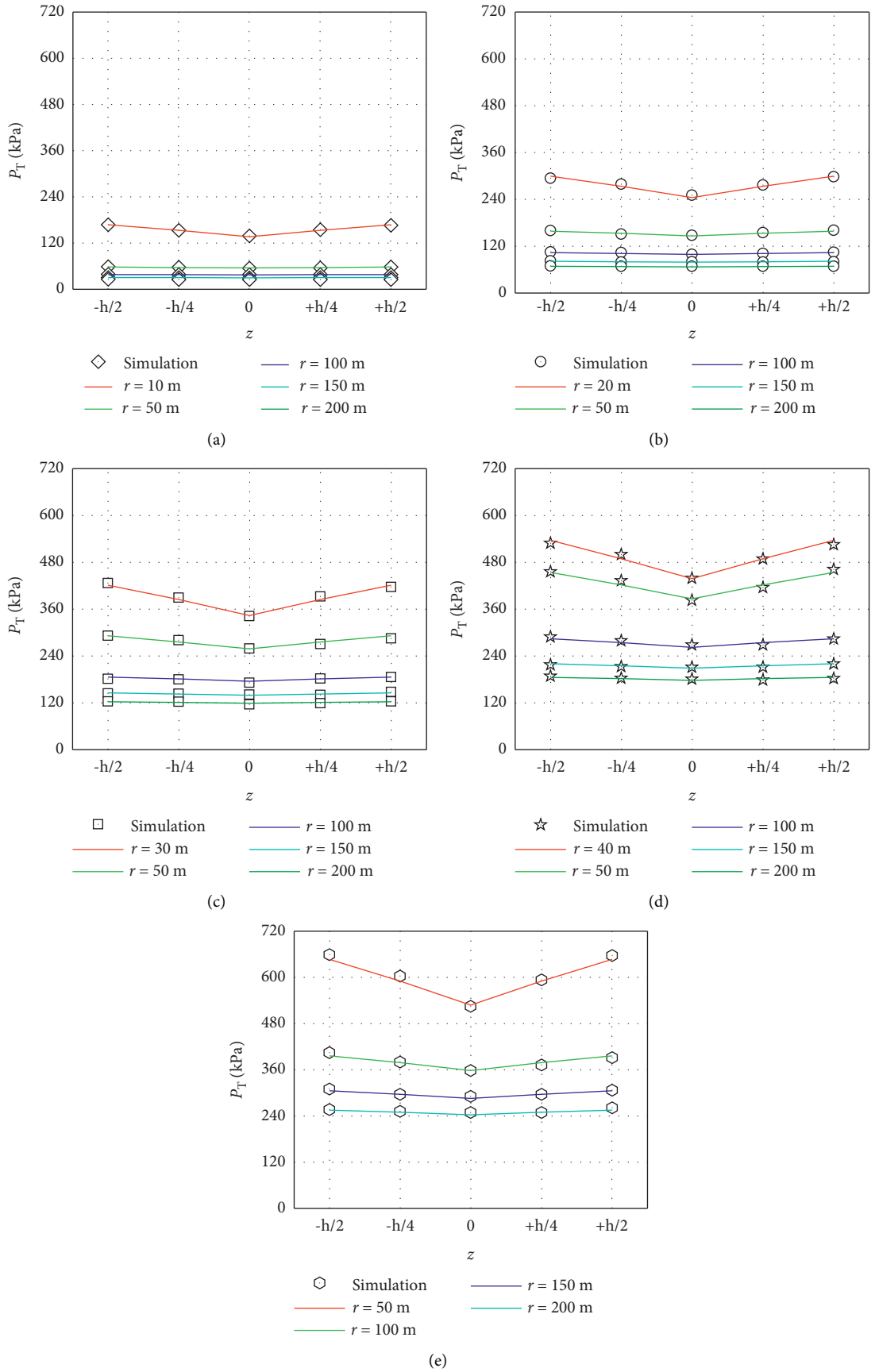

FIGURE 5: . Blast wave peak pressure transversal distribution. (a) $r_0 = 10$ m. (b) $r_0 = 20$ m. (c) $r_0 = 30$ m. (d) $r_0 = 40$ m. (e) $r_0 = 50$ m.

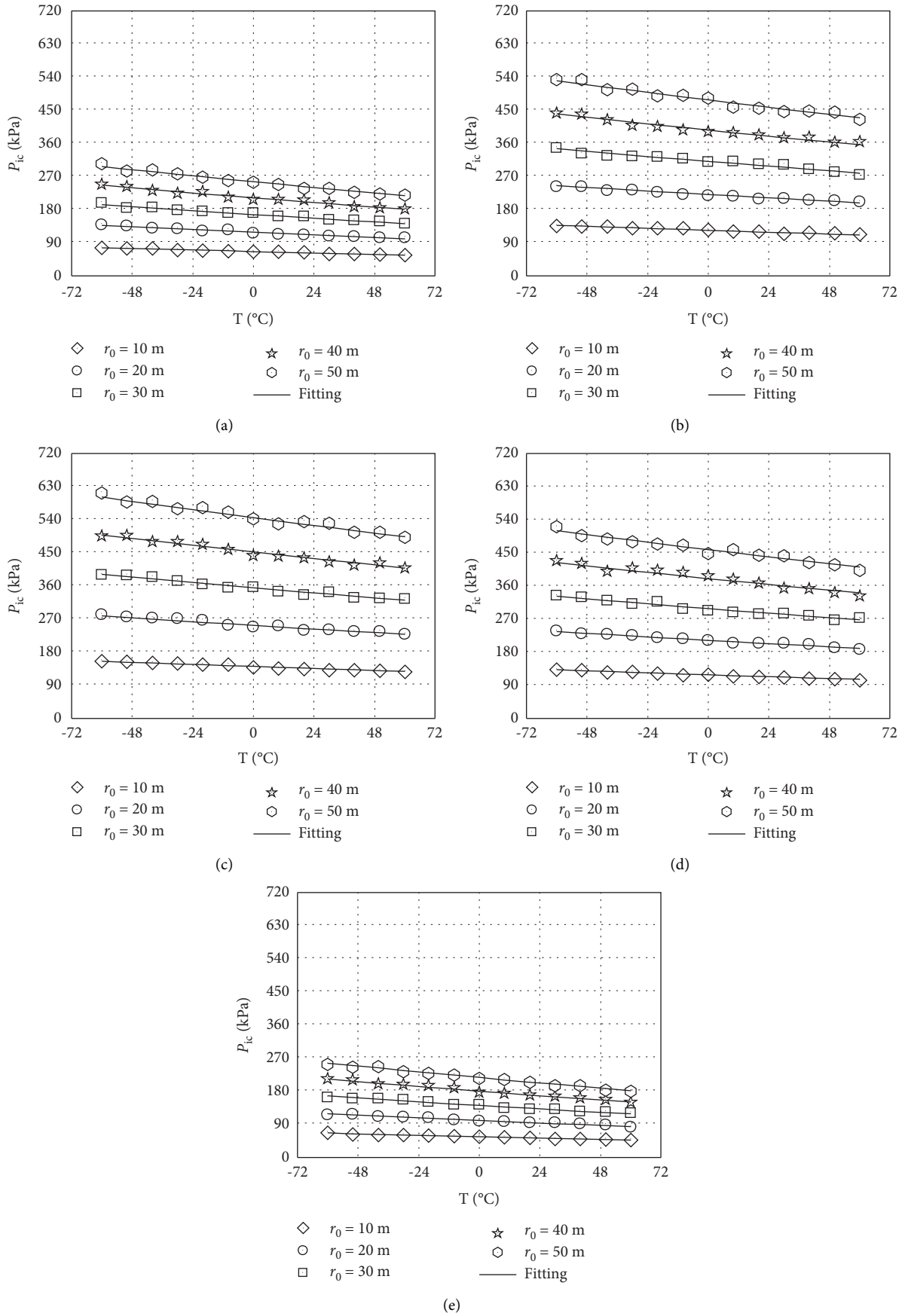

Figure 6: Relation between p_{ic} and T under different initial gas volume concentration environment conditions. (a) C = 6%. (b) C = 8%. (c) C = 10%. (d) C = 12%. (e) C = 14%.

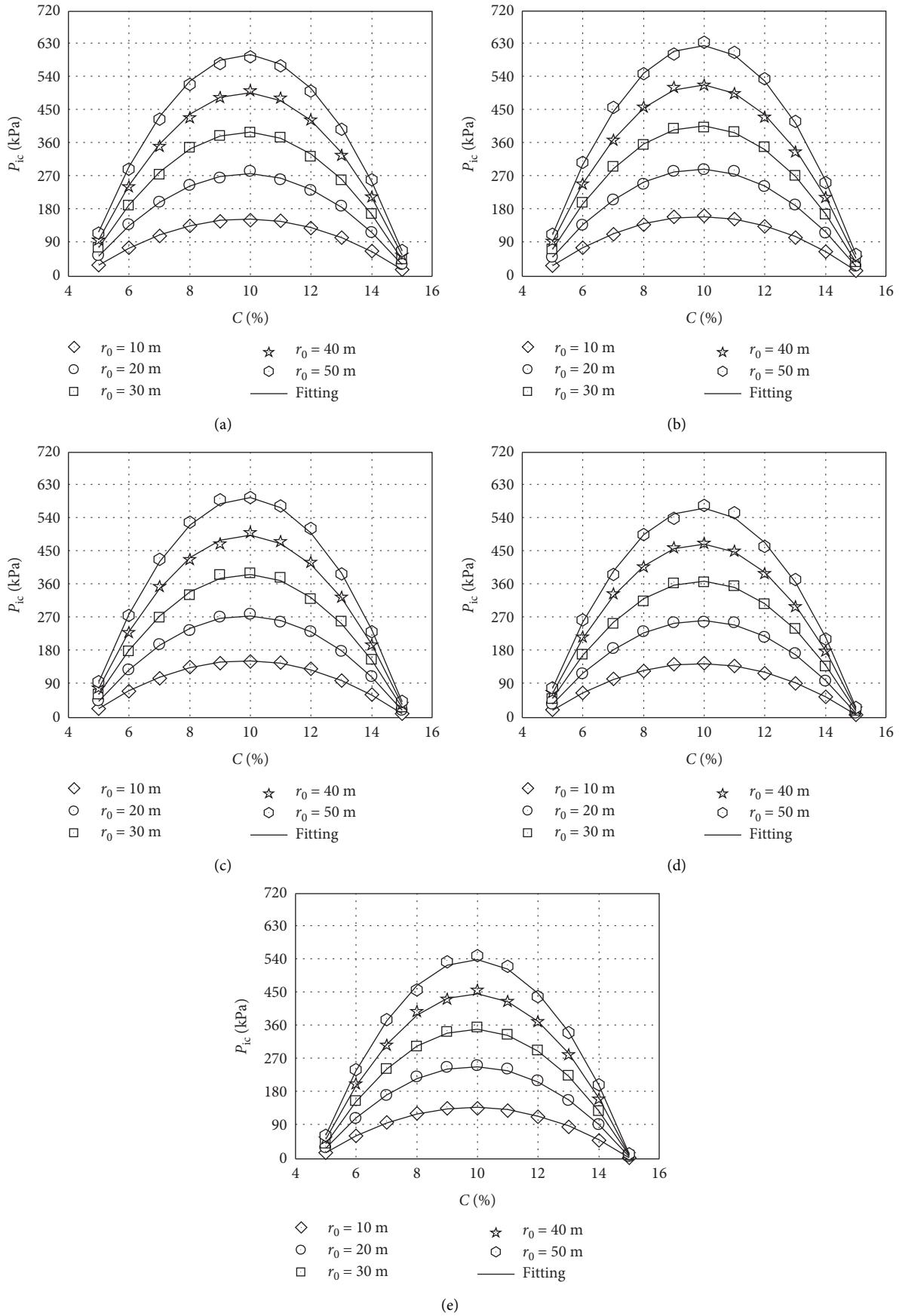

FIGURE 7: Relation between p_{ic} and C under different initial temperature environment conditions. (a) $T = -60$°C. (b) $T = -30$°C. (c) $T = +0$°C. (d) $T = +30$°C. (e) $T = +60$°C.

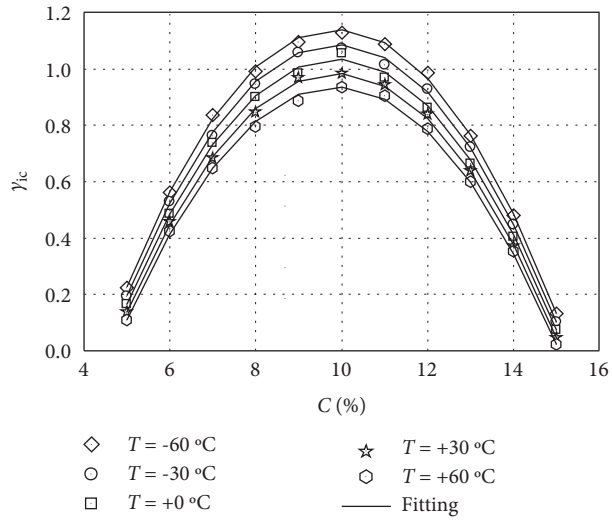

Figure 8: Relation among γ_{ic}, T, and C.

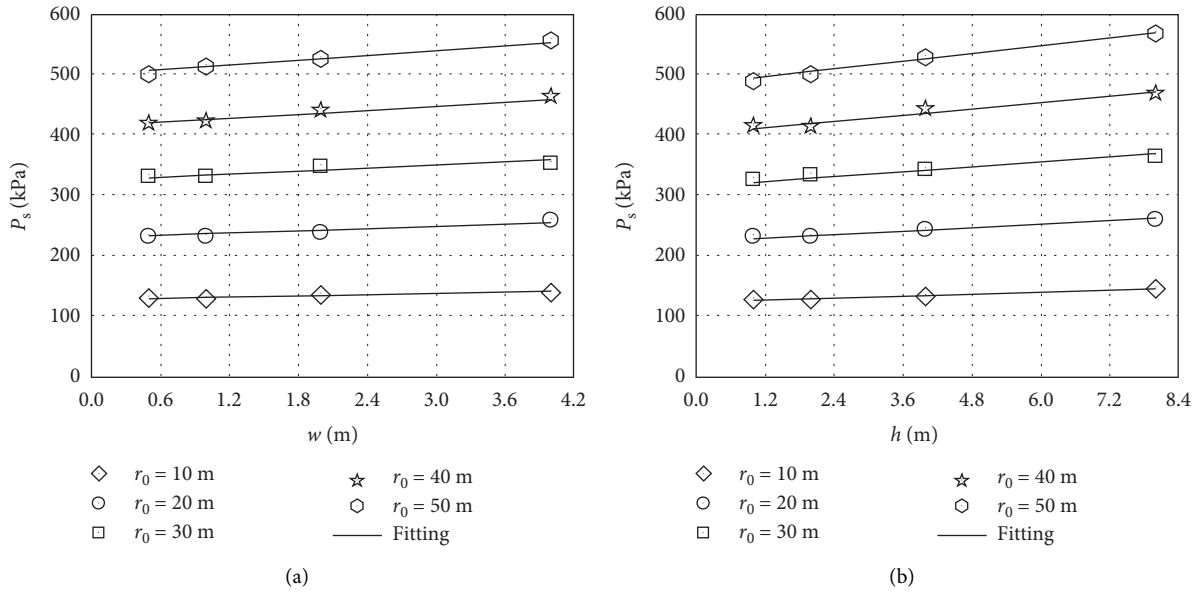

Figure 9: Relation between p_s and w (h). (a) Width. (b) Height.

gas, it is converted into the methane equivalent mass based on equation (14) widely employed to calculate the explosion wave peak pressure for different types of explosive charges. The corresponding initial gas volume concentration is also got. Repeat steps (2)–(3).

The other gas equivalent mass can be given by

$$m_{Eq} = \frac{E_{Other}}{E_{Methane}} m_{Other}. \quad (15)$$

where $E_{Methane}$ is the methane gas internal energy; E_{Other} is the other gas internal energy; and m_{Other} is the other gas total mass.

(2) The initial condition and section size influence coefficients γ_{ic} and γ_s can be gained on account of equations (12) and (13), respectively. Calculate the maximum pressure p_{Lmax} from equation (10). Thus, the maximum pressure considering the initial condition and the gas compartment section size is $\gamma_{ic}\gamma_s p_{Lmax}$.

(3) The blast wave peak pressure shows an uneven distribution in the gas compartment, and it is an urgent need to obtain the explosion wave peak pressure anywhere. It can be obtained by using equations (9) and (11).

(4) Draw the blast wave peak pressure nephogram.

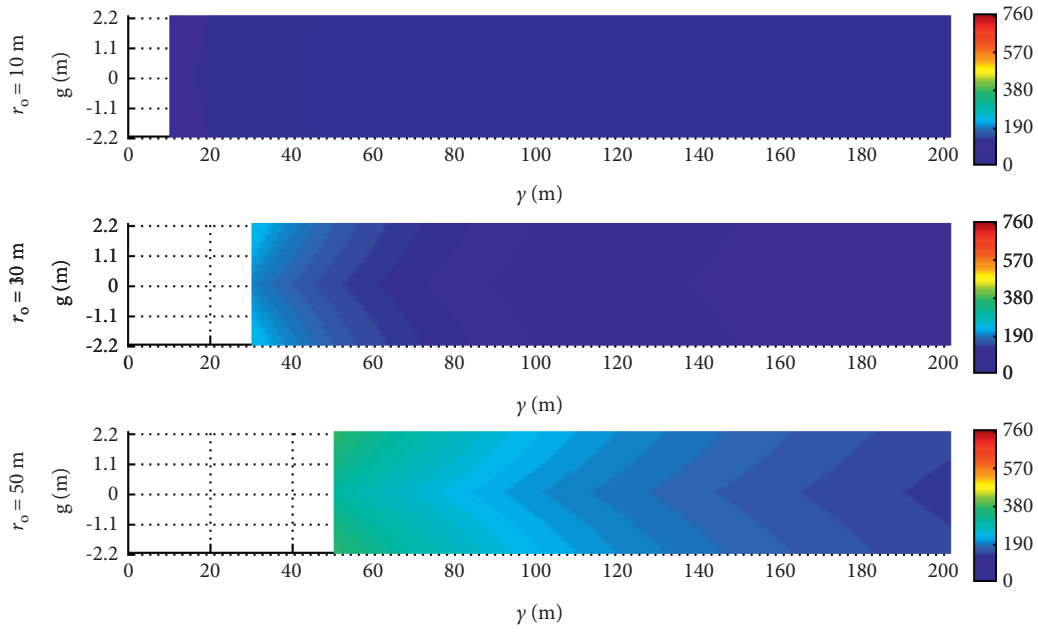

(a)

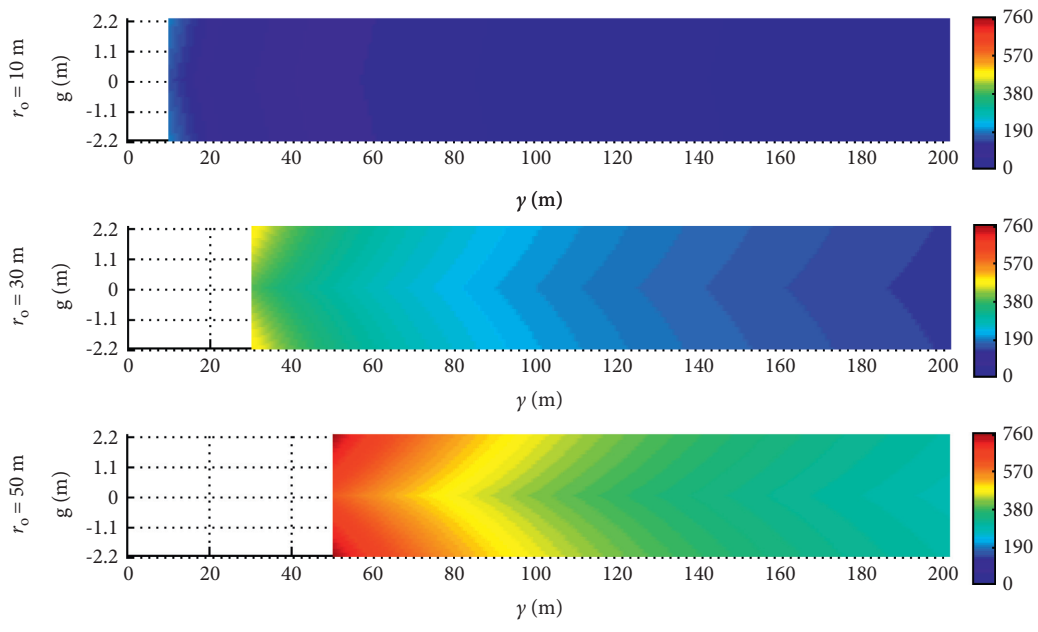

(b)

Figure 10: Continued.

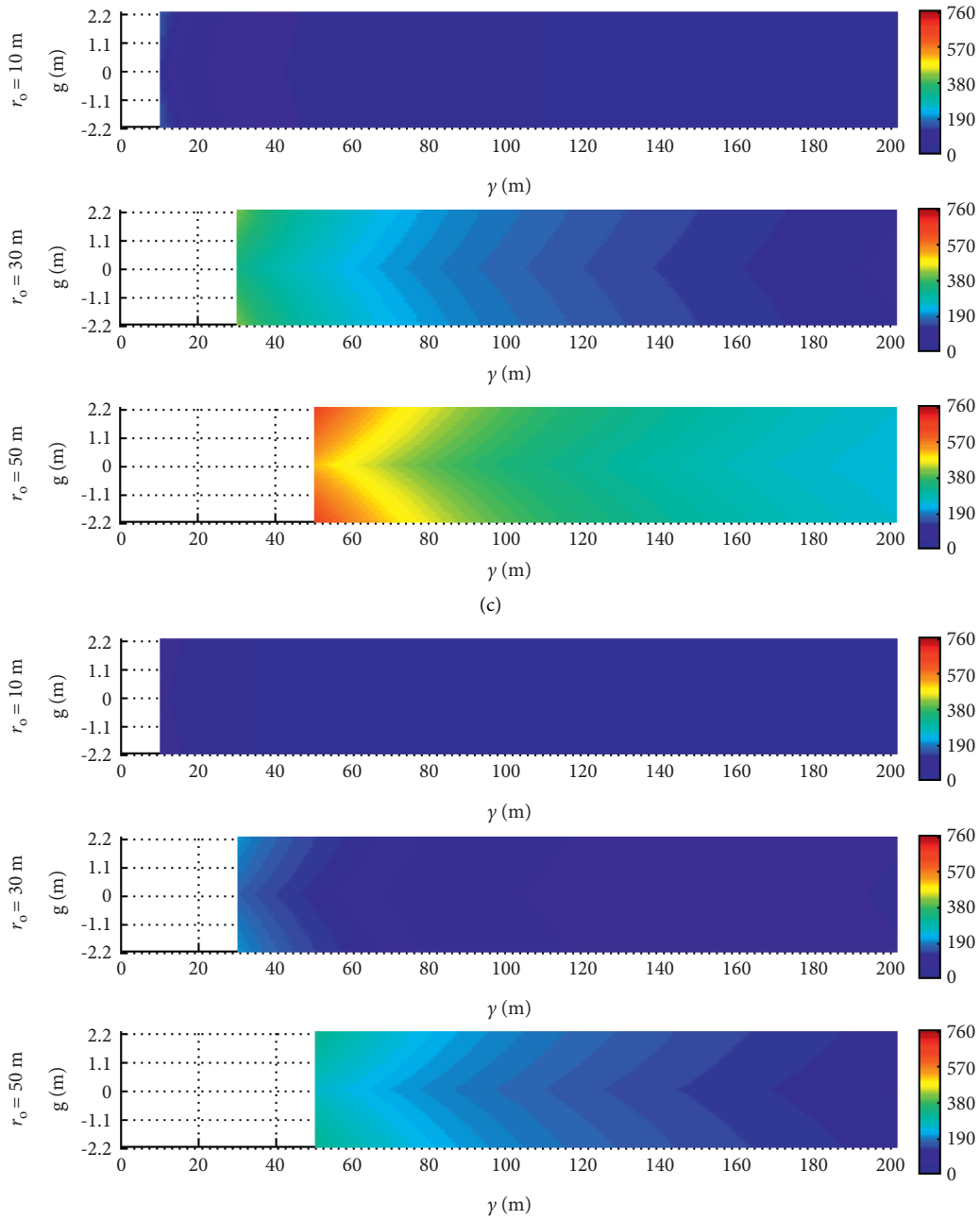

(c)

(d)

Figure 10: Continued.

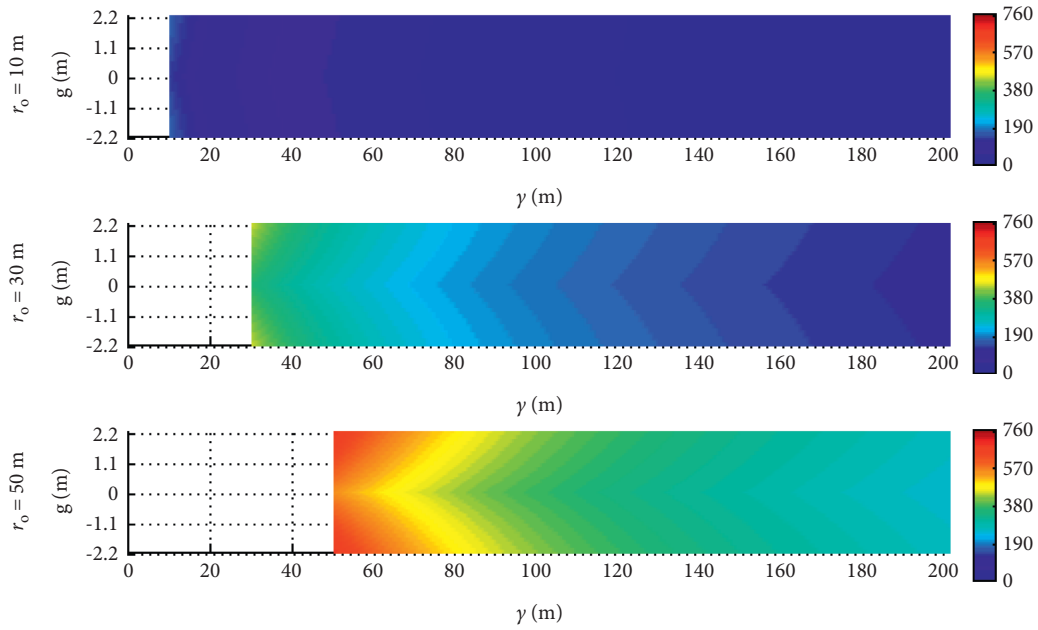

(e)

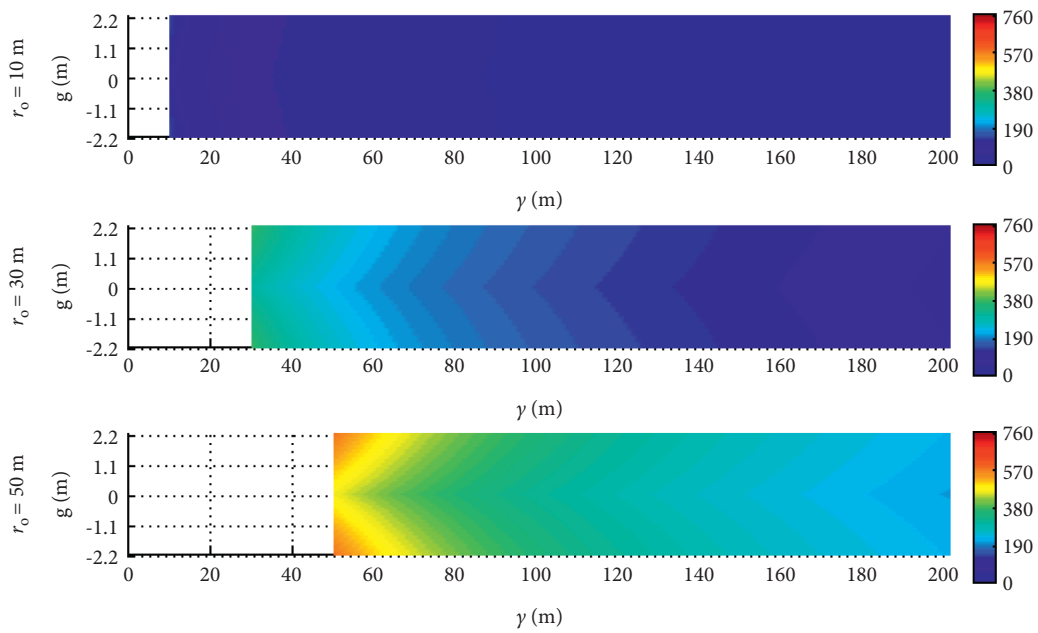

(f)

Figure 10: Continued.

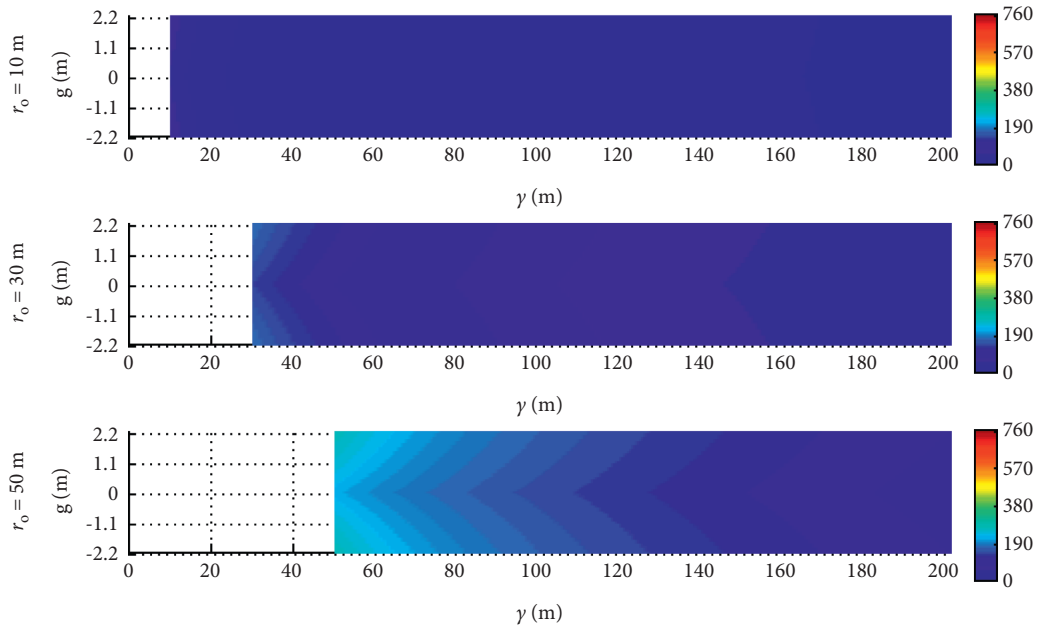

(g)

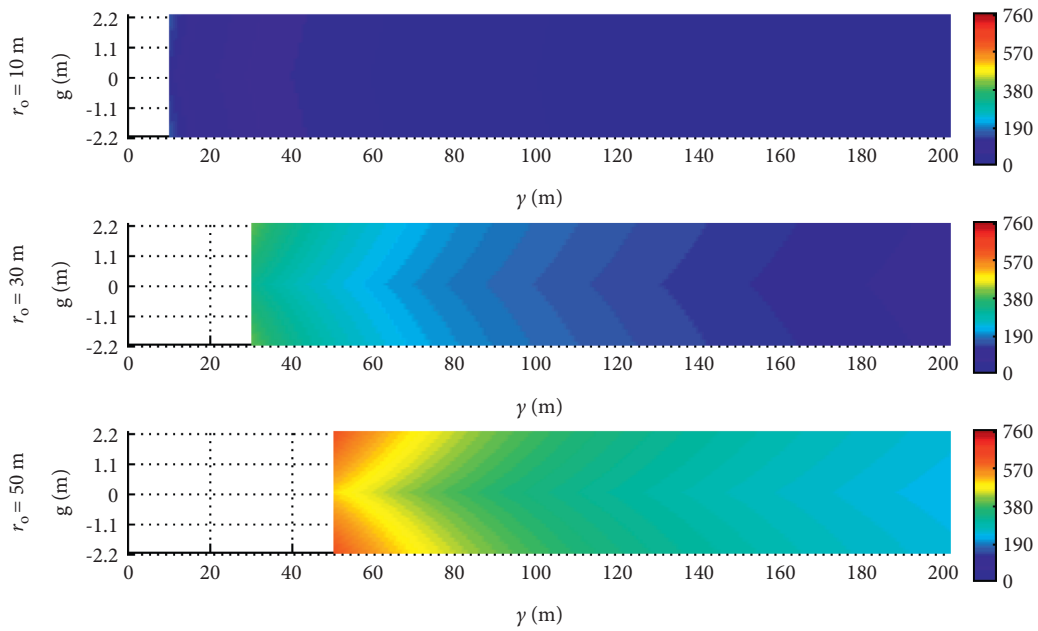

(h)

Figure 10: Continued.

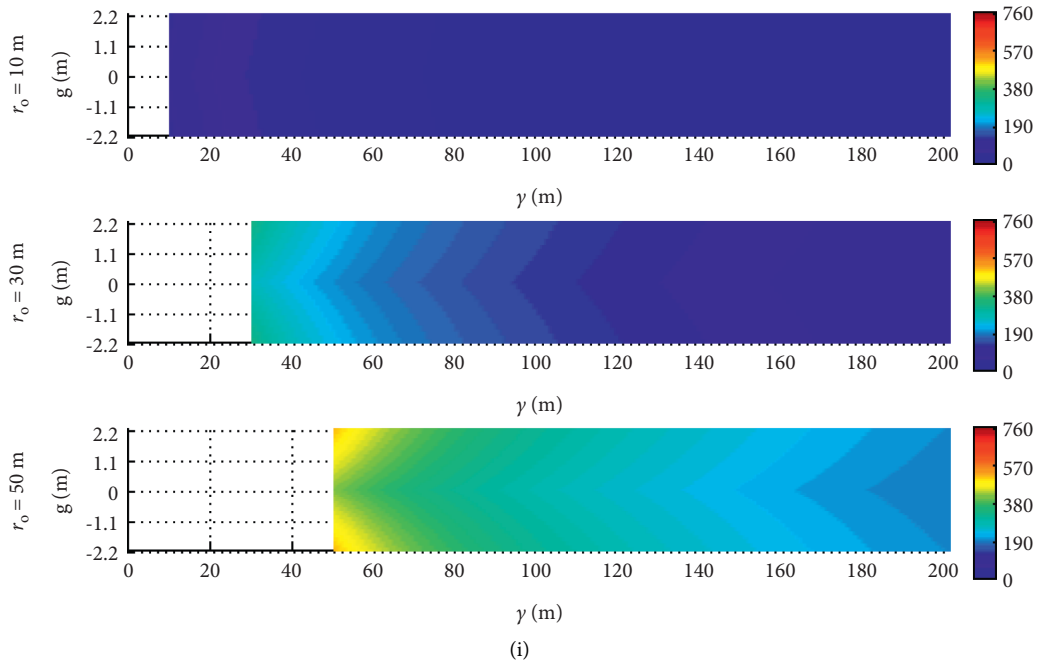

Figure 10: Explosion wave peak pressure nephograms (kPa). (a) $C = 6\%$ and $T = -2260^{\circ}$C. (b) $C = 10\%$ and $T = -60^{\circ}$C. (c) $C = 12\%$ and $T = -60^{\circ}$C. (d) $C = 6\%$ and $T = +0^{\circ}$C. (e) $C = 10\%$ and $T = +0^{\circ}$C. (f) $C = 12\%$ and $T = +0^{\circ}$C. (g) $C = 6\%$ and $T = +60^{\circ}$C. (h) $C = 10\%$ and $T = +60^{\circ}$C. (i) $C = 12\%$ and $T = +60^{\circ}$C.

The calculation formulae utilized in the suggested methodology are on account of the former studies and the simulation results. It demonstrates that the proposed methodology can give a good prediction of the blast wave peak pressure in the gas compartment.

6.2. Case Study. To evaluate the explosion shock wave killing power effectively, it is required to develop several quantitative killing criteria, for instance, pressure, impulse, and combination of the above two. Reference [23] provides 45.7 kPa for eardrum rupture with a failure probability of about 10% and 103.4 kPa in the duration of lung damage by 50 ms. In the meantime, the analogical killing criteria are to be found in other countries. In the research background of a gas compartment of a utility tunnel in China's Beijing City, the propagation process of the gas explosion is simulated by using the powerful industry-leading CFD software FLACS to analyze and discuss the blast wave space distribution.

As Figure 10 illustrates, the longer the filled length of the gas is and the lower the initial temperature is, the higher the blast wave peak pressure becomes. As the initial gas volume concentration increases, the peak pressure increases firstly and decreases afterward slowly.

According to the longitudinal and transversal distributions, the peak pressure is far greater than the killing pressure threshold in the underground and closed space; consequently, it is not safe for the living beings in the gas compartment.

7. Conclusion

In this work, a new methodology has been put forward to forecast the gas explosion shock wave peak pressure in the gas compartment. A range of analyses has been carried out on this issue. Some conclusions are deduced as follows:

(1) The peak pressure decreases along with the distance away from the gas zone, and the decreasing trend also decelerates; moreover, the longer the filled length of the gas is, the higher the peak pressure is.

(2) The peak pressure by the coupled effect between the initial temperature and the initial gas volume concentration is significantly influenced, especially at the upper and lower gas explosion limits. The peak pressure increases gradually as the width or height increases, and both basically meet the linear relation.

(3) The analysis procedure which is complete and rigorous demonstrates that the proposed methodology can effectively estimate the explosion wave peak pressure in the gas compartment.

(4) According to the longitudinal and transversal distributions, the peak pressure is far greater than the killing pressure threshold in the underground and closed space; consequently, it is not safe for the living beings in the gas compartment.

Data Availability

The simulation data used to support the findings of this study are included within the article.

Conflicts of Interest

The authors declare that they have no conflicts of interest.

Acknowledgments

The authors gratefully acknowledge the financial support provided by the Key Research and Development (R&D) Program of Tangshan (no. 19150232E), Xijing University's Innovation and Entrepreneurship Training Program for College Students in 2021 (X202112715007), and Postdoctoral Research Project of Chongqing (no. Xm2017189).

References

[1] W. Müller Christoph, "Piping analysis of large scale experiments with adina and dapsy," *Computers & Structures*, vol. 26, no. 1-2, pp. 111–121, 1987.

[2] H. Zhang, X. Zhang, S. Ji et al., "Recent development of fluid-structure interaction capabilities in the ADINA system," *Computers & Structures*, vol. 81, no. 8-11, pp. 1071–1085, 2003.

[3] J. V. Valdenebro and F. N. Gimena, "Urban utility tunnels as a long-term solution for the sustainable revitalization of historic centres: the case study of Pamplona-Spain," *Tunnelling and Underground Space Technology*, vol. 81, pp. 228–236, 2018.

[4] Y. Luo, A. Alaghbandrad, T. K. Genger, and A. Hammad, "History and recent development of multi-purpose utility tunnels," *Tunnelling and Underground Space Technology*, vol. 103, Article ID 103511, 2020.

[5] J. Weerheijm, J. Verreault, and M. M. van der Voort, "Quantitative risk analysis of gas explosions in tunnels," *Fire Safety Journal*, vol. 97, pp. 146–158, 2018.

[6] P. Ntzeremes, K. Kirytopoulos, and V. Leopoulos, "Development of a risk-based method for predicting the severity of potential fire accidents in road tunnels based on real-time data," *Environmental Research*, vol. 189, Article ID 109895, 2020.

[7] L. Pang, Q. Zhang, T. Wang, D. C. Lin, and L. Cheng, "Influence of laneway support spacing on methane/air explosion shock wave," *Safety Science*, vol. 50, no. 1, pp. 83–89, 2012.

[8] Q. Zhang, B. Qin, H. Yan, and D. C. Lin, "A methodology to predict shock overpressure decay in a tunnel produced by a premixed methane/air explosion," *Journal of Loss Prevention in the Process Industries*, vol. 44, pp. 275–281, 2016.

[9] Y. Zhu, D. Wang, Z. Shao, X. Zhu, C. Xu, and Y. Zhang, "Investigation on the overpressure of methane-air mixture gas explosions in straight large-scale tunnels," *Process Safety and Environmental Protection*, vol. 135, pp. 101–112, 2020.

[10] C. Wang, Y. Zhao, and E. K. Addai, "Investigation on propagation mechanism of large scale mine gas explosions," *Journal of Loss Prevention in the Process Industries*, vol. 49, pp. 342–347, 2017.

[11] G. Ke, S. N. Li, R. Han et al., "Study on the propagation law of gas explosion in the space based on the goaf characteristic of coal mine," *Safety Science*, vol. 127, Article ID 104693, 2020.

[12] T. Wang, Y. Zhou, Z. Luo et al., "Flammability limit behavior of methane with the addition of gaseous fuel at various relative humidities," *Process Safety and Environmental Protection*, vol. 140, pp. 178–189, 2020.

[13] T. Wang, Z. Luo, H. Wen et al., "The explosion enhancement of methane-air mixtures by ethylene in a confined chamber," *Energy*, vol. 214, Article ID 119042, 2021.

[14] B. Su, Z. Luo, T. Wang, C. Xie, and F. Cheng, "Chemical kinetic behaviors at the chain initiation stage of CH4/H2/air mixture," *Journal of Hazardous Materials*, vol. 403, Article ID 123680, 2021.

[15] S. Zhang, H. Ma, X. Huang, and S. Peng, "Numerical simulation on methane-hydrogen explosion in gas compartment in utility tunnel," *Process Safety and Environmental Protection*, vol. 140, pp. 100–110, 2020.

[16] Q. Zhang, L. Pang, and S. X. Zhang, "Effect of scale on flame speeds of methane-air," *Journal of Loss Prevention in the Process Industries*, vol. 24, no. 5, pp. 705–712, 2011.

[17] Q. Zhang, L. Pang, and H. M. Liang, "Effect of scale on the explosion of methane in air and its shockwave," *Journal of Loss Prevention in the Process Industries*, vol. 24, no. 1, pp. 43–48, 2011.

[18] P. J. Li, C. S. Chen, H. P. Chang, H. H. Ho, and B. Xie, "Explosion mechanism analysis during tunnel construction in the Zengwen Reservoir," *Tunnelling and Underground Space Technology*, vol. 97, Article ID 103279, 2020.

[19] T. Ji, X. Qian, M. Yuan et al., "Case study of a natural gas explosion in Beijing, China," *Journal of Loss Prevention in the Process Industries*, vol. 49, pp. 401–410, 2017.

[20] D. Wang, X. Qian, M. Yuan, T. Ji, W. Xu, and S. Liu, "Numerical simulation analysis of explosion process and destructive effect by gas explosion accident in buildings," *Journal of Loss Prevention in the Process Industries*, vol. 49, pp. 215–227, 2017.

[21] K. Wang, T. Shi, Y. He, M. Li, and X. Qian, "Case analysis and CFD numerical study on gas explosion and damage processing caused by aging urban subsurface pipeline failures," *Engineering Failure Analysis*, vol. 97, pp. 201–219, 2019.

[22] AASTP-1, *Manual of NATO Safety Principles for the Storage of Military Ammunition and Explosives*, North Atlantic Treaty Organization, Brussels, Belgium, 2006.

[23] DoD 6055.9-STD, *DoD Ammunition and Explosive Safety Standards*, Departments of Defense, Virginia, USA, 2008.

[24] X. Ding, L. Feng, C. Wang, Z. Chen, and L. Han, "Shaking table tests of the seismic response of a utility tunnel with a joint connection," *Soil Dynamics and Earthquake Engineering*, vol. 133, Article ID 106133, 2020.

[25] W. Zhang, L. Han, L. Feng et al., "Study on seismic behaviors of a double box utility tunnel with joint connections using shaking table model tests," *Soil Dynamics and Earthquake Engineering*, vol. 136, Article ID 106118, 2020.

[26] K. Ye, X. Zhou, Y. Zheng et al., "Estimating the longitudinal maximum gas temperature attenuation of ceiling jet flows generated by strong fire plumes in an urban utility tunnel," *International Journal of Thermal Sciences*, vol. 142, pp. 434–448, 2019.

[27] Q. Zhou, H. G. He, S. F. Liu et al., "Blast resistance evaluation of urban utility tunnel reinforced with BFRP bars," *Defence Technology*, vol. 1, pp. 1–19, 2020.

[28] ANSYS, *ANSYS Help*, ANSYS Corporation, Pennsylvania, 2019.

[29] FLACS, *FLACS User's Guide*, GexCon, Bergen, 2008.

[30] B. E. Launder and D. B. Spalding, "The numerical computation of turbulent flows," *Computer Methods in Applied Mechanics and Engineering*, vol. 3, no. 2, pp. 269–289, 1974.

[31] S. V. Patankar, *Numerical Heat Transfer and Fluid Flow*, Hemisphere publishing corporation, London, UK, 1980.
[32] B. Jiang, B. Lin, C. Zhu, C. Zhai, and Q. Liu, "Premixed methane-air deflagrations in a completely adiabatic pipe and the effect of the condition of the pipe wall," *Journal of Loss Prevention in the Process Industries*, vol. 26, no. 4, pp. 782–791, 2013.
[33] Q. Ye, G. G. X. Wang, Z. Jia, and C. Zheng, "Experimental study on the influence of wall heat effect on gas explosion and its propagation," *Applied Thermal Engineering*, vol. 118, pp. 392–397, 2017.
[34] E. Blanchard, P. Boulet, S. Desanghere et al., "Experimental and numerical study of fire in a midscale test tunnel," *Fire Safety Journal*, vol. 47, pp. 18–31, 2012.
[35] Y. Niu, B. Shi, and B. Jiang, "Experimental study of overpressure evolution laws and flame propagation characteristics after methane explosion in transversal pipe networks," *Applied Thermal Engineering*, vol. 154, pp. 18–23, 2019.
[36] L. Pang, T. Wang, Q. Zhang, Q. Ma, and L. Cheng, "Nonlinear distribution characteristics of flame regions from methane-air explosions in coal tunnels," *Process Safety and Environmental Protection*, vol. 92, no. 3, pp. 193–198, 2014.
[37] Y. Z. Li, "Study of fire and explosion hazards of alternative fuel vehicles in tunnels," *Fire Safety Journal*, vol. 110, Article ID 102871, 2019.
[38] A. M. Benselama, M. J.-P. William-Louis, F. Monnoyer, and C. Proust, "A numerical study of the evolution of the blast wave shape in tunnels," *Journal of Hazardous Materials*, vol. 181, no. 1-3, pp. 609–616, 2010.
[39] T. Forcier and R. Zalosh, "External pressures generated by vented gas and dust explosions," *Journal of Loss Prevention in the Process Industries*, vol. 13, no. 3-5, pp. 411–417, 2000.
[40] C. Bai, W. Liu, J. Yao, X. Zhao, and B. Sun, "Explosion characteristics of liquid fuels at low initial ambient pressures and temperatures," *Fuel*, vol. 265, Article ID 116951, 2020.
[41] Y. Z. Li, H. T. Su, H. J. Ji, and W. Y. Cheng, "Numerical simulation to determine the gas explosion risk in longwall goaf areas: a case study of Xutuan Colliery," *International Journal of Mining Science and Technology*, vol. 1, pp. 1–8, 2020.
[42] C. Guo, H. Shao, S. Jiang, Y. Wang, K. Wang, and Z. Wu, "Effect of low-concentration coal dust on gas explosion propagation law," *Powder Technology*, vol. 367, pp. 243–252, 2020.
[43] E. S. Oran, V. N. Gamezo, and R. K. Zipf Jr, "Large-scale experiments and absolute detonability of methane/air mixtures," *Combustion Science and Technology*, vol. 187, no. 1-2, pp. 324–341, 2015.
[44] S. Kundu, J. Zanganeh, and B. Moghtaderi, "A review on understanding explosions from methane-air mixture," *Journal of Loss Prevention in the Process Industries*, vol. 40, pp. 507–523, 2016.
[45] B. Vanderstraeten, D. Tuerlinckx, J. Berghmans, S. Vliegen, E. Van't Oost, and B. Smit, "Experimental study of the pressure and temperature dependence on the upper flammability limit of methane/air mixtures," *Journal of Hazardous Materials*, vol. 56, no. 3, pp. 237–246, 1997.
[46] M. Gieras, R. Klemens, G. Rarata, and P. Wolański, "Determination of explosion parameters of methane-air mixtures in the chamber of 40dm3 at normal and elevated temperature," *Journal of Loss Prevention in the Process Industries*, vol. 19, no. 2-3, pp. 263–270, 2006.
[47] F. Gharagheizi, "Quantitative Structure–Property relationship for prediction of the lower flammability limit of pure compounds," *Energy and Fuels*, vol. 22, no. 5, pp. 3037–3039, 2008.
[48] E. Salzano, F. S. Marra, G. Russo, and J. H. S. Lee, "Numerical simulation of turbulent gas flames in tubes," *Journal of Hazardous Materials*, vol. 95, no. 3, pp. 233–247, 2002.

Hindawi
Shock and Vibration
Volume 2021, Article ID 5893179, 12 pages
https://doi.org/10.1155/2021/5893179

Research Article

Influence of Roadway Cross-Section Shape on Gas Explosion Shock Wave Law in U-Type Ventilation Working Faces

Jiajia Liu,[1,2,3] **Mengqi Shen**,[1] **Shouqi Chen**,[1] **and Ming Yang**[1,2,3]

[1]*School of Safety Science and Engineering, Henan Polytechnic University, Jiaozuo 454000, China*
[2]*Collaborative Innovation Center of Coal Work Safety and Clean-Efficiency Utilization, Jiaozuo 454000, China*
[3]*State Key Laboratory Cultivation Base for Gas Geology and Gas Control, Henan Polytechnic University, Jiaozuo 454000, China*

Correspondence should be addressed to Jiajia Liu; liujiajia@hpu.edu.cn

Received 20 May 2021; Revised 10 November 2021; Accepted 29 November 2021; Published 18 December 2021

Academic Editor: Jianwei Cheng

In U-shaped ventilation working face, different tunnel section shapes are one of the important factors affecting the propagation of gas explosion shock wave. In order to study the propagation law of gas explosion shock wave in working face, the numerical simulation study was carried out by using Fluent simulation software combined with the actual situation of gas explosion in #415 working face of Chenjiashan Coal Mine in Shaanxi Province. By constructing a three-dimensional mathematical and physical model, a simulation study of the upper-corner gas explosion was carried out. The results are described as follows. (1) After the gas explosion shock wave propagates 40 m, the overpressure peak equidistant difference tends to be stable and attenuates and propagates in the form of a single shock wave. The study determines that the effective length of the U-shaped ventilation inlet/return tunnel is 40 m. (2) When the tunnel section is trapezoidal, the initial overpressure of the gas explosion shock wave propagating to the inlet/return airway is the highest, followed by rectangular and semicircular arches, but the internal overpressure attenuation trend of different cross-sectional shapes is the same. (3) The gas explosion shock wave propagates radially along the working face section during the working face propagation. The farther away the location is from the upper corner of the tunnel during a gas explosion with different cross-sectional shapes, the closer the cutoff overpressure peak is. The attenuation trend of overpressure with the propagation distance conforms to the power function law. The research results provide an important theoretical direction for the numerical simulation of gas explosions in coal mining faces.

1. Introduction

With the increase in coal mining depth, underground gas emission and gas accumulation are becoming more and more serious. The upper corner of a coal mining face is the hazardous area of gas accumulation in coal mine and is the hot spot for gas explosion accidents in coal mines. After the gas explosion accident in upper corner, the huge gas explosion shock wave will spread along the inlet and outlet tunnel, causing serious damage to underground facilities and miners.

The propagation process of explosion shock wave is a process of constant conversion between energy and the external environment. In this process, as the energy of explosion shock wave is gradually converted into gas energy, the propagation length of explosion shock wave is limited. Therefore, studying the effective length can determine the energy dissipation capacity of explosion shock wave propagation. In addition, the cross-section shape is also one of the factors affecting the propagation of the blast wave. Different cross-section shapes have an impact on the propagation speed of the blast wave and the external energy conversion capacity.

Scholars have conducted a significant amount of research on the propagation law of gas explosion shock waves. Both et al. adjusted and optimized the grid model parameters of turbulence and combustion by simulating gas explosions and significantly improved the prediction of the development model [1]. Jing et al. deduced the relationship between the peak value of overpressure and the gas velocity

and propagation distance in the process of a gas explosion [2]. Some scholars studied the influence of various conditions (initial temperature, ignition conditions, gas concentration, and barrier type) on gas explosion parameters [3–12]. Some scholars obtained the mechanism of suppressing a gas explosion by ultrasonic water mist and a vacuum chamber through experiments and numerical simulations [13, 14].

Some scholars studied the distribution and propagation law of gas explosion shock waves in different media of pipelines [15–18]. Some scholars studied the influences of pipe length, pipe diameter, and space distance on gas explosion overpressure [19–21]. Li and Hao simulated the ignition and propagation characteristics of gas explosions by introducing basic chemical reactions [22]. Some scholars studied the propagation law of gas explosion shock waves in roadways with different turning angles and on bifurcated roadways [23–27]. Some scholars simulated and studied the propagation law of gas explosion shock waves in the underground parallel roadway network [28, 29]. Some scholars simulated and analyzed the propagation law of gas explosion shock waves in coal mining face roadways [30, 31].

Many scholars have focused on the pipeline shock wave propagation law and its influencing factors in gas explosion studies, but the actual tunnel effective length and cross-section shape impacts of the gas explosion shock wave law have not been reported. The explosion energy generated by gas accumulation under different geological conditions and different gas pressures is different, so the effective length of blast wave propagation is also different. Studying the effective length of blast wave propagation is beneficial to determine the energy exchange ability of the energy generated by explosion with the outside world. Therefore, the author uses Fluent simulation software, combined with the actual situation of a gas explosion in the upper corner of the #415 working face in Chenjiashan coal mine, Shaanxi Province. To determine the effective length of the air inlet/return roadway, a numerical simulation of an upper-corner gas explosion of different cross-sectional shapes of a U-type ventilation roadway is carried out. The research results provide theoretical guidance for the prevention and control of gas explosion disasters in coal mining faces.

2. Construction and Verification of Mathematical Model

2.1. Basic Assumptions and Boundary Conditions of Numerical Simulation. Gas explosion is a very complex fluid elastic-plastic process, accompanied by chemical reaction, turbulence changes, and other phenomena, so it is difficult to simulate the law of mine gas explosion after considering all conditions. In order to simulate the law of mine gas explosion as much as possible and ensure the reliability of numerical simulation of gas explosion, some basic assumptions must be made:

(1) Both premixed gas and combustion products satisfy the ideal gas state equation

(2) The specific heat capacity of the mixed gas follows the mixing rule, and the specific heat capacity of each component is a function of temperature

(3) The wall of the physical model is a rigid adiabatic wall, and there is no relative displacement

(4) The gas explosion reaction is one-way and irreversible

(5) In the physical model, the gas filling area is a normal uniform mixture of gas and air, and it is an ideal state

The model parameters and boundary conditions of gas explosion numerical simulation are as follows. The boundary conditions: the pipe boundary is set as the adiabatic wall with the temperature of 300 K, and the outlet above the vertical pipe is set as the pressure outlet.

Basic model parameter: the initial conditions of the burned zone are $T = 1600$ K, H_2O volume fraction is 0.118, CO_2 volume fraction is 0.145, and initial pressure is 101325 Pa; the initial conditions of unburned zone are as follows: $T = 300$ K, CH_4 volume fraction is 0.053, O_2 volume fraction is 0.21, and H_2O and CO_2 volume fraction is 0; the initial conditions of the air zone are as follows: the volume fraction of CH_4, H_2O, and CO_2 is 0 and the volume fraction of O_2 is 0.233.

2.2. Construction of Gas Explosion Mathematical Model. A gas explosion is a combustion reaction process, and the reaction is rapid. Assuming that the mixture of methane and air is an ideal gas, the hydrodynamic mathematical model of methane gas is established without considering the unstable factors such as viscosity, heat conduction, diffusion, and detonation; the conservation equation of the process is described as follows.

Equation of state is as follows:

$$\begin{aligned} p &= p(\rho, T) \\ &= \rho RT. \end{aligned} \tag{1}$$

Continuity equation is as follows:

$$\frac{\partial \rho}{\partial t} + \frac{\partial (\rho u)}{\partial x} + \frac{\partial (\rho v)}{\partial y} + \frac{\partial (\rho w)}{\partial z} = 0. \tag{2}$$

Energy equation is as follows:

$$\frac{\partial}{\partial t}(\rho e) + u\frac{\partial (\rho e + p)}{\partial x} + v\frac{\partial (\rho e + p)}{\partial y} + w\frac{\partial (\rho e + p)}{\partial z} = 0. \tag{3}$$

Momentum equation is as follows:

$$\begin{cases} \dfrac{\partial u}{\partial t} + u\dfrac{\partial u}{\partial x} + v\dfrac{\partial u}{\partial y} + w\dfrac{\partial u}{\partial z} = -\dfrac{1}{p}\dfrac{\partial p}{\partial x}, \\ \dfrac{\partial v}{\partial t} + u\dfrac{\partial v}{\partial x} + v\dfrac{\partial v}{\partial y} + w\dfrac{\partial v}{\partial z} = -\dfrac{1}{p}\dfrac{\partial p}{\partial y}, \\ \dfrac{\partial w}{\partial t} + u\dfrac{\partial w}{\partial x} + v\dfrac{\partial w}{\partial y} + w\dfrac{\partial w}{\partial z} = -\dfrac{1}{p}\dfrac{\partial p}{\partial z}, \end{cases} \tag{4}$$

where P is the pressure; t is the time; x, y, and z are rectangular coordinate system parameters; u, V, and W are the velocities in three coordinate directions; ρ is the fluid density; T is the temperature; R is the gas constant; e is the specific energy; and $e = p/(\gamma - 1) + \rho(u^2 + v^2 + w^2)/2$ (γ is the gas index).

2.3. Turbulence Model and Combustion Model. Gas explosion will lead to turbulent combustion, so the turbulence model should be selected in numerical simulation, and the correlation terms and turbulence viscosity coefficients can be calculated by constructing differential equations. According to the number of differential equations required for solution, the turbulence model can be divided into zero equation model, single equation model, and two-side equation model [32]. The large eddy numerical model can better simulate the required results by referring to the literature and several times of practical calculation and debugging [33–35]. Therefore, the LES turbulence model is used in this paper to describe the characteristics of turbulent flow field in combustion process.

Chemical reaction rates can be calculated using four models: laminar finite rate model, laminar finite rate/vortex dissipation model, vortex diffusion model, and vortex diffusion conceptual model.

The laminar flow finite velocity model ignores the influence of turbulent pulsation and uses Arrhenius to calculate the combustion rate. The condition is laminar flame, which is not suitable for turbulent combustion. The laminar finite velocity/eddy current dissipation model is characterized by the fact that the reaction rate is smaller than Arrhenius and eddy current dissipation equation, which is suitable for single-stage and two-stage reaction mechanism but not for multistage reaction mechanism. The reaction rate of the eddy current dissipation model is controlled by turbulent mixing for non-premixed flames. Combining the advantages and disadvantages of the four models, the vortex dissipation vortex diffusion model suitable for the LES turbulence model is adopted in this paper.

2.4. Verification of Calculation Model. According to previous gas explosion experiments in pipelines [36], a full-scale simulation comparison of 1 : 1 was carried out using Fluent simulation software to verify the reliability of the large eddy simulation turbulence equation and eddy-dissipation vortex diffusion model. In the test, the width and height of the straight pipe are both 80 mm, the length is 19.2 m, and the length of the vertical pipe is 5 m. According to the setting of the experimental monitoring points, measuring point 1 is 19 m away from the leftmost end and is located on the central line of the horizontal pipeline, and measuring point 2 is located 0.5 m away from the central line of the horizontal pipeline. A section diagram of the physical model and the locations of the measuring points are shown in Figure 1. The left end of the pipeline is closed and filled with gas, and the pressure outlet is above the vertical pipeline.

The initial conditions and boundary conditions are consistent with those in the gas explosion experiment [37]; specifically, the gas concentration in the gas filling area is 0.053; O_2 concentration is 0.212; CO_2 concentration in the air area is 0.1456; and H_2O concentration is 0.11925. The pipeline boundary is set as an adiabatic wall, the temperature is 300 K, and the outlet above the vertical pipe is set as the pressure outlet.

The selected calculation model is as follows: the fluid flow is unsteady turbulent flow, the turbulence model adopts the large eddy simulation turbulence equation, the wall adopts a standard wall function, the chemical reaction of methane combustion adopts an eddy-dissipation vortex diffusion model that is suitable for turbulent combustion, and a simple algorithm is used for an iterative solution. The simple algorithm is a widely used numerical method to solve flow field in computational fluid mechanics. It can not only solve nonlinear problems but also complete the coupling of velocity and pressure. Therefore, the simple algorithm is used for iterative solution.

The experimental and simulation results are shown in Figure 2.

As can be seen from Figure 2, in measuring point 1, when the inflatable length is, respectively, 4 m, 5.5 m, and 7 m, the errors between the simulation results and the mean values of the four groups of experimental data are 2.9%, 7.5%, and 10.9%, respectively. In point 2, when the inflating length is 4 m, 5.5 m, and 7 m, respectively, the errors between the simulation results and the average values of the four groups of experimental data are 1.9%, 9.5%, and 5.4%, respectively. It can be concluded that the maximum error between the simulated results and the average values of the four groups of experimental data is 10.9% and the minimum error is only 1.9%. When comparing the numerical simulation data with the experimental data, due to the limitation of the numerical simulation conditions, there will be some error with the actual experimental data. Combined with Figure 2, when the inflatable lengths of pipes are 4 m, 5.5 m, and 7 m, respectively, the overpressure peak errors obtained by numerical simulation and experiment are all less than 15%, which are within the allowable range of international engineering error standards. The reliability of the LES + ED model used in gas explosion simulation is verified experimentally.

3. Determination of Effective Length of Intake/Return Air Roadway

The intake/return air roadway of the #415 working face in Chenjiashan coal mine of Shaanxi Province is arranged along the coal seam floor. The length of the r inlet roadway is 1192 m, and the length of the return air roadway is 1170 m.

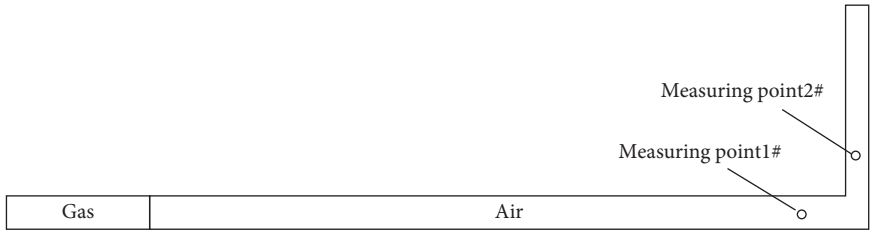

Figure 1: Section diagram of physical model.

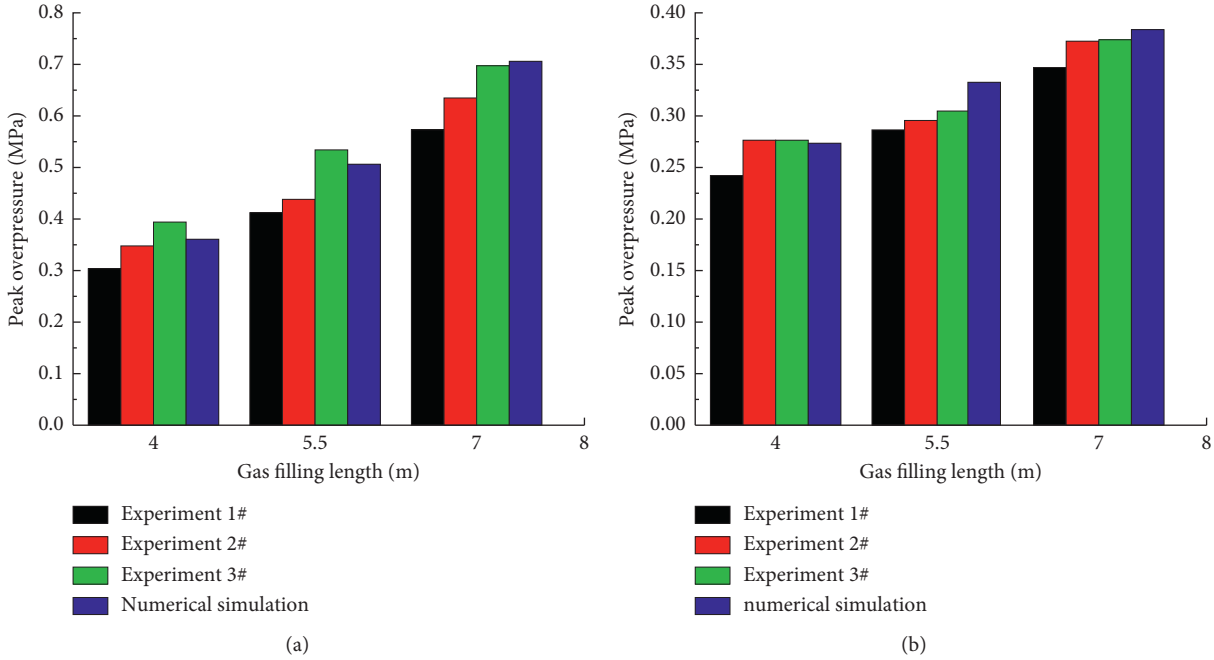

Figure 2: Comparison of CFD simulation and lab experiments results: (a) measuring point 1; (b) measuring point 2.

The cross-section of roadway is a semicircular arch with a parallel arrangement, and the inclined length of the working face is 175 m. In the numerical simulation study, the reasonable length of the intake/return air roadway not only makes the calculation results more accurate but also significantly reduces the workload of numerical calculation. Therefore, the author carried out a simulation study on the gas explosion with U-type ventilation to determine the reasonable effective length of the inlet/outlet roadway.

3.1. Establishing the 3D Model and Meshing. According to the specific parameters of the #415 working face in Chenjiashan coal mine of Shaanxi Province and the actual situation of the explosion, geometry and mesh modules in workbench are used to establish a three-dimensional physical model and grid division. As shown in Figure 3, the length of the inlet/return air roadways is 100 m, and the mesh size is 0.5 m. The mesh is refined by local mesh densification technology in the gas filling area and ignition point. As shown in Figure 3, the length of the return air roadway is 100 m, and 9 monitoring points are arranged in the return air roadway, each with a distance of 10 m.

3.2. Initial Conditions and Boundary Conditions. The explosion site of the November 28th major gas explosion accident in Chenjiashan coal mine was the upper corner of the #415 working face. The inlet and return air outlets are set as pressure outlets, and the others are standard wall surfaces. According to the accident analysis report of the government department of Chenjiashan coal mine gas explosion accident, the mass fractions of CH_4 and O_2 in the gas filling area of the upper corner are 0.095 and 0.212, respectively, and the burnt area is a ball with a radius of 0.5 m in the center of the upper corner. In this area, the mass fraction of CO_2 is 0.1456, the mass fraction of H_2O is 0.11925, the standard atmospheric pressure is 101325 Pa, and the temperature is 1600 K. A simple algorithm is used for an iterative solution; nine monitoring points are arranged in the return air roadway, each of which is 10 m apart.

3.3. Analysis of Numerical Simulation Results. The whole explosion can be regarded as a process that starts from the ignition zone, detonates the gas/air mixture in turn, and propagates from the combustion wave and shock wave to the unburned area. This can be divided into three stages: ignition

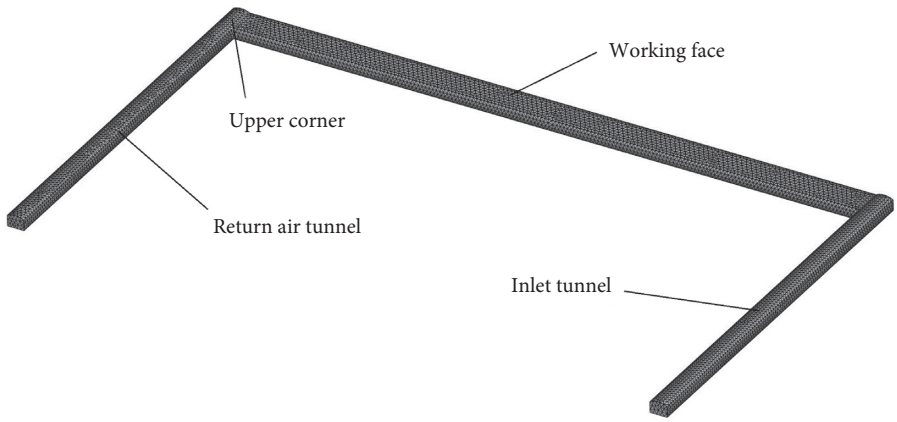

Figure 3: Three-dimensional physical model.

stage, compression combustion stage, and single shock wave propagation stage [37]. The propagation cloud diagrams of blast wave with different time scales shown in Figure 4 are given based on simple algorithms and simulation results, respectively, describing the propagation characteristics of blast wave at different moments. The propagation nephogram of the explosion shock wave and the pressure curve of each measuring point are shown in Figures 4 and 5.

The overpressure peak value, peak time, and variation of overpressure peak value between adjacent measuring points and equidistant attenuation coefficient are listed in Table 1.

According to the parameter data in Table 1, the variation of the overpressure peak value and arrival time with distance is shown in Figure 6. The variation of the overpressure peak's 10 m isometric difference between adjacent measuring points with distance is shown in Figure 7. With an increase in distance, the attenuation coefficient of the overpressure peak and data fitting prediction of each measuring point is shown in Figure 8.

(1) Figure 6 shows that the peak value of overpressure varies greatly within 40 m from the explosion area. The overpressure peak value of each measuring point basically attenuates linearly beyond 40 m from the explosion area. The time to reach the peak value increases linearly with an increase in distance.

(2) Figure 7 shows that the difference in the overpressure peak value of each measuring point at measuring points #1–4 is relatively large, and the difference in the overpressure peak value between adjacent measuring points at measuring points #4–9 basically fluctuates up and down with a very small amplitude. That is, starting from measuring point #4 (40 m away from the explosion area), the maximum overpressure attenuation is approximately 0.02 MPa for every 10 m propagation of the gas explosion shock wave.

(3) Figure 8 shows that the attenuation coefficient of the overpressure peak value of measuring point #4 (40 m away from the explosion area) to measuring point #9 (90 m away from the explosion area) presents an obvious linear increasing relationship, and its functional relationship is $y = 0.0066x + 0.1244$.

According to the results in Figures 6–8, the gas explosion shock wave starts to propagate stably in the form of a single shock wave from a distance of 40 m from the explosion area. Therefore, the length of intake/return air roadway for the gas explosion simulation with U-type ventilation is determined to be 40 m. When the length of U-shaped gas explosion simulation inlet and return air tunnel is determined to be 40 m, we can provide a certain reference for the specific location of explosion-proof door according to the effective length and choose different support modes to ensure the stability of roadway structure. In addition, it not only ensures the accuracy of the calculation results but also greatly reduces the workload of numerical simulation.

4. Study of Influence of Different Roadway Cross-Section Shapes on Shock Wave Law of Gas Explosion

According to different mine types, mining methods, geological conditions, hydrological conditions, and other factors, the roadway adopts different sectional shapes. The most commonly used cross-sectional shapes of roadways in China are rectangular, trapezoidal, and semicircular arch. Therefore, in the study of U-shaped ventilation gas explosion with different cross-section shapes, rectangle, trapezoid, and semicircle arch are adopted, respectively, as shown in Figure 9.

4.1. Physical Model and Initial/Boundary Conditions. Three-dimensional physical models of the intake/return air roadway and working face with rectangular, trapezoidal, and semicircular arch cross-sections are established as shown in Figure 10. The vertical height of the roadway is 0.3 m higher than that of the working face when the cross-sectional shape is a semicircular arch, and the roadway height is the same as that of the working face when the cross-sectional shape is rectangular or trapezoidal. The length of the inlet/return air roadway is 40 m. The initial and boundary conditions of the numerical simulation are the same as those in Section 3.2.

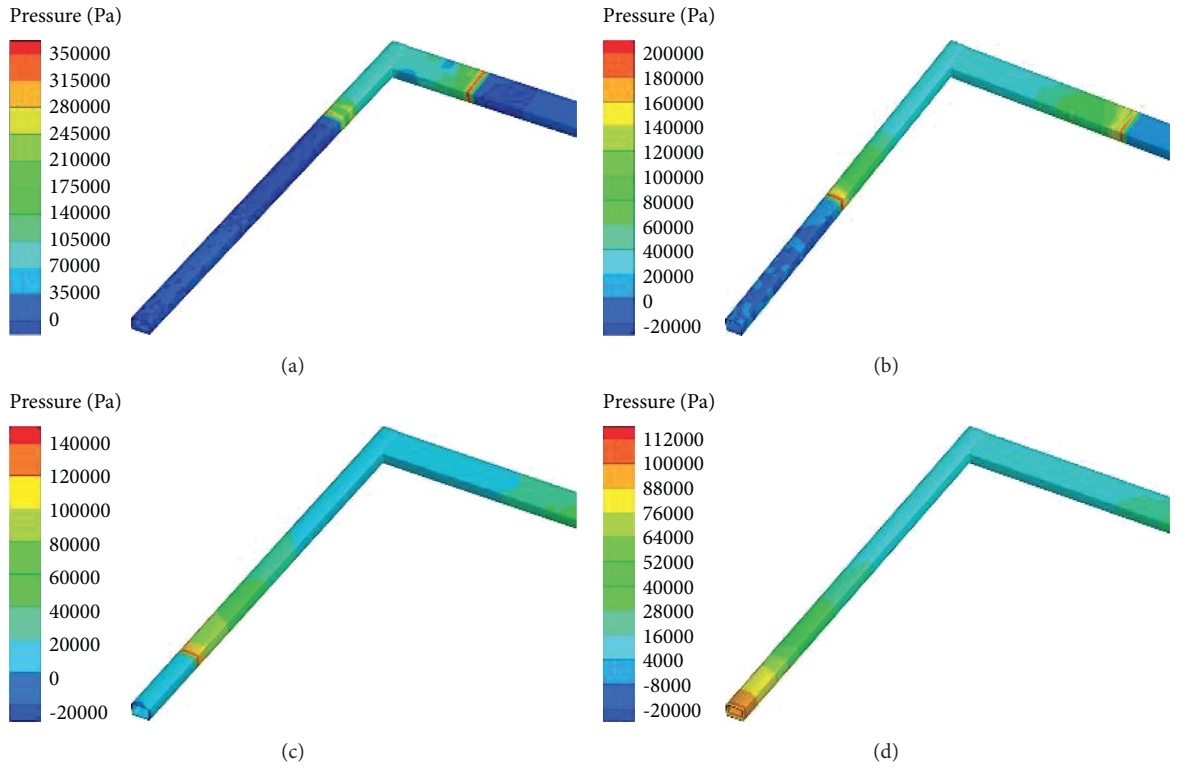

Figure 4: Cloud diagram of shock wave propagation at each moment: (a) $t = 33.5$ ms; (b) $t = 88$ ms; (c) $t = 140$ ms; (d) $t = 181$ ms.

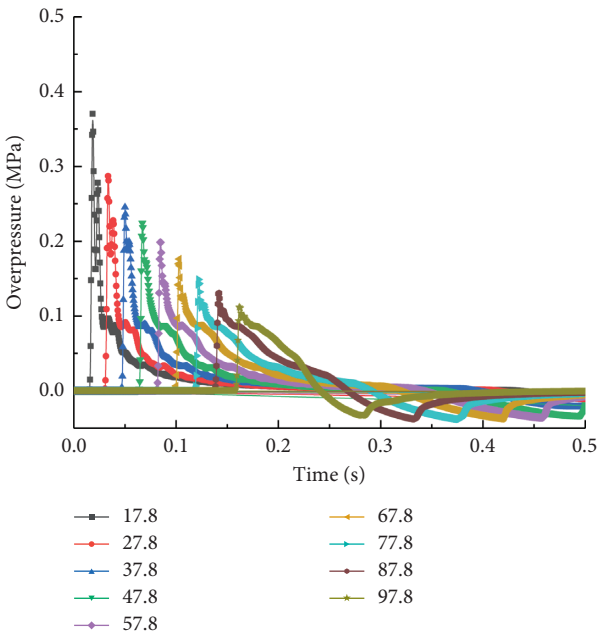

Figure 5: Overpressure change graph of each measuring point.

4.2. Analysis of Numerical Simulation Results. The numerical simulation of different cross-section shapes of roadway is carried out, the upper-corner gas is detonated by high temperature ignition point, the rectangular section is taken as an example, and the pressure nephogram of gas explosion shock wave is obtained at different times as shown in Figure 11. The pressure cloud image of gas explosion shock wave at typical time was selected to better explain the propagation characteristics of explosion shock wave in the upper corner of the U-shaped ventilation model.

According to the above pressure nephogram of gas explosion shock wave at different times, it can be seen that after the gas explosion occurs in the upper corner of U-type ventilation mode, the shock wave first propagates through the return air roadway and coal mining face, and the shock wave pressure gradually attenuates in the process of propagation. When the shock wave propagates to the corner where the working face is connected with the air inlet roadway, it can be seen that the shock wave is reflected and superimposed, which causes the overpressure of the shock wave to rise in a very short time.

The data of monitoring points are sorted out to get the change of overpressure at each point of 40 m inlet/return air roadway with different cross-section shapes, as shown in Figures 12 and 13.

Figures 12 and 13 show that when the upper-corner gas explosion occurs, the initial overpressure of the inlet/return air roadways with different cross-sectional shapes is different. When the cross-sectional shape is a trapezoid, the initial overpressure of the explosion shock wave propagating to the inlet/return air roadway is the largest, followed by the rectangular shape, and the minimum occurs with the semicircular arch. When the explosion shock wave propagates in roadways of different cross-sectional shapes, it is consistent with the initial overpressure at all positions in the roadway. The results show that the maximum overpressure

Table 1: Parameters of each monitoring point.

Monitoring point	Point 1#	Point 2#	Point 3#	Point 4#	Point 5#	Point 6#	Point 7#	Point 8#	Point 9#
Peak overpressure (MPa)	0.370	0.287	0.245	0.224	0.199	0.176	0.149	0.131	0.109
Peak time (s)	0.018	0.033	0.050	0.067	0.087	0.103	0.122	0.142	0.162
Peak value difference (MPa)		0.083	0.042	0.021	0.025	0.023	0.027	0.018	0.022
Attenuation coefficient K		0.224	0.338	0.395	0.462	0.524	0.597	0.646	0.705

Note: (1) the peak value difference is the overpressure peak value difference between adjacent measuring points and (2) attenuation coefficient K is the reduction rate of each measuring point relative to measuring point 1#.

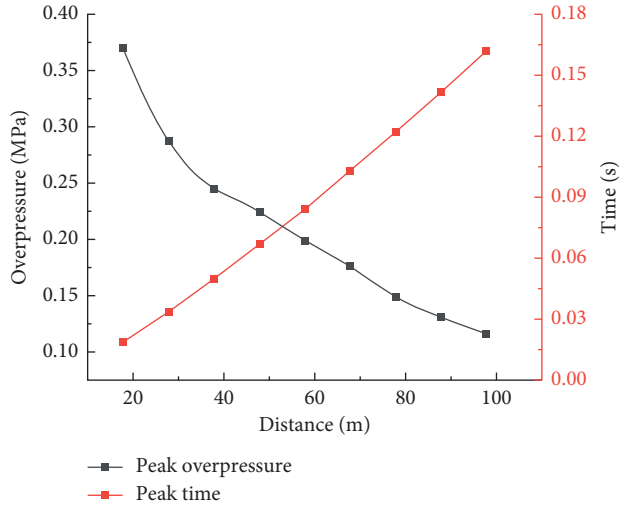

Figure 6: Peak overpressure and peak time change with distance.

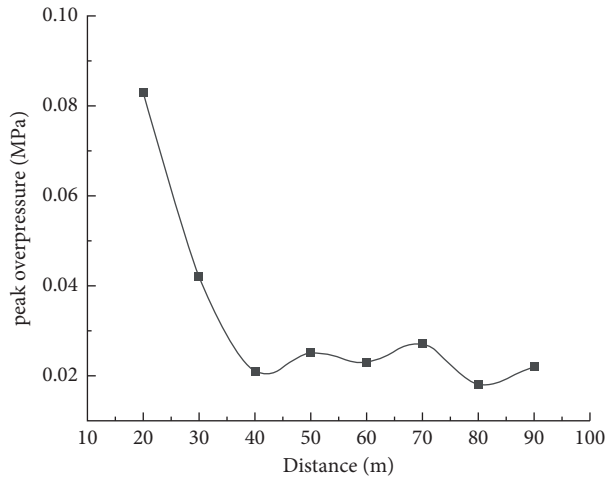

Figure 7: Overpressure difference between adjacent measuring points.

occurs with the trapezoidal shape, the second is rectangular, and the smallest is the semicircular arch. However, the attenuation trend of overpressure propagation is the same for all three cross-sectional shapes.

In the three-dimensional physical models of the above three roadway cross-sectional shapes, the size of the coal mining face is always consistent with the actual situation. Under the conditions of different cross-sectional shapes of the inlet/return air roadway, the overpressure changes at various working face position, which is shown in Figure 14.

Figure 14 shows that under the condition of different cross-sectional shapes of air inlet/return roadways, the initial overpressure of the working face cut is largest when the cross-sectional shape of the roadway is rectangular, followed by the semicircular arch and the trapezoid. With the propagation of the shock wave along the working face cut, the farther away from the upper corner of different cross-sectional shapes, the closer the overpressure at each point of the cut. The pressure attenuation trend is in line with the power function law. The overpressure attenuation model of

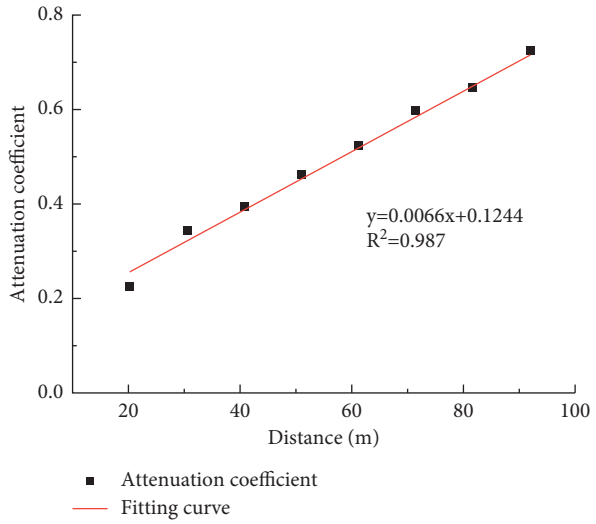

Figure 8: Attenuation coefficient varying with distance.

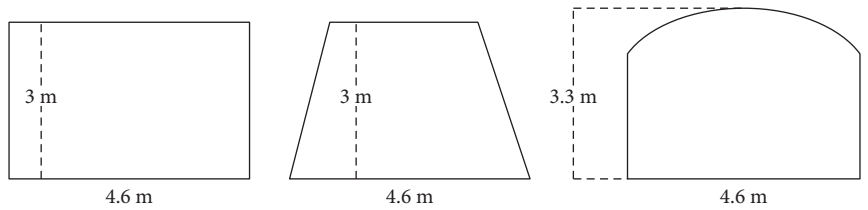

Figure 9: Different cross-sectional shapes.

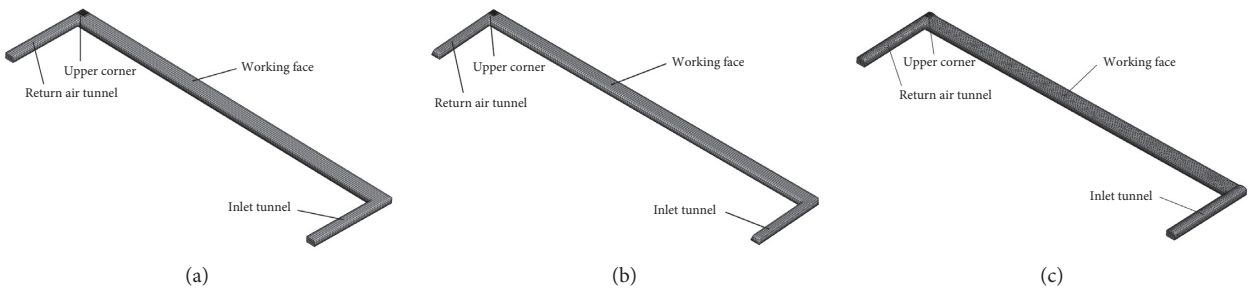

Figure 10: Physical models of different cross-sectional shapes: (a) rectangular section; (b) trapezoidal section; (c) semicircular arch section.

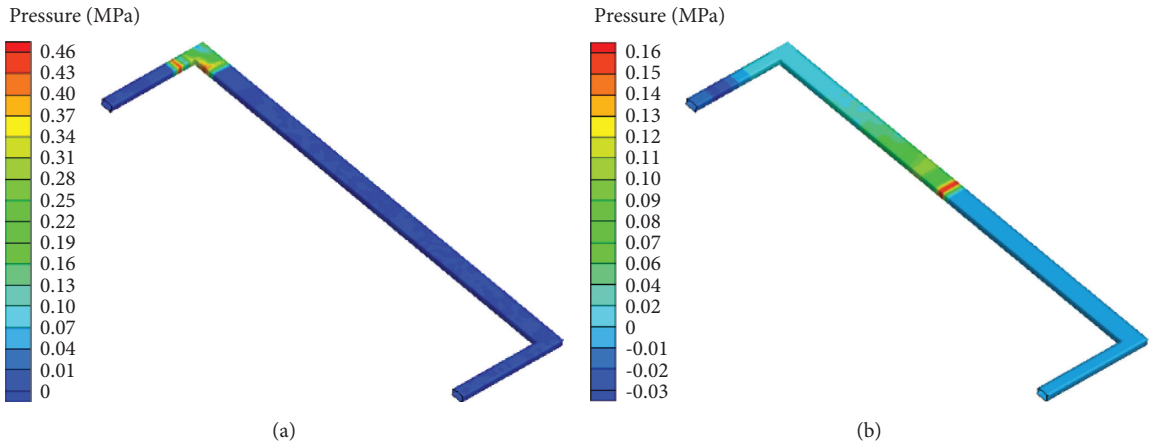

Figure 11: Continued.

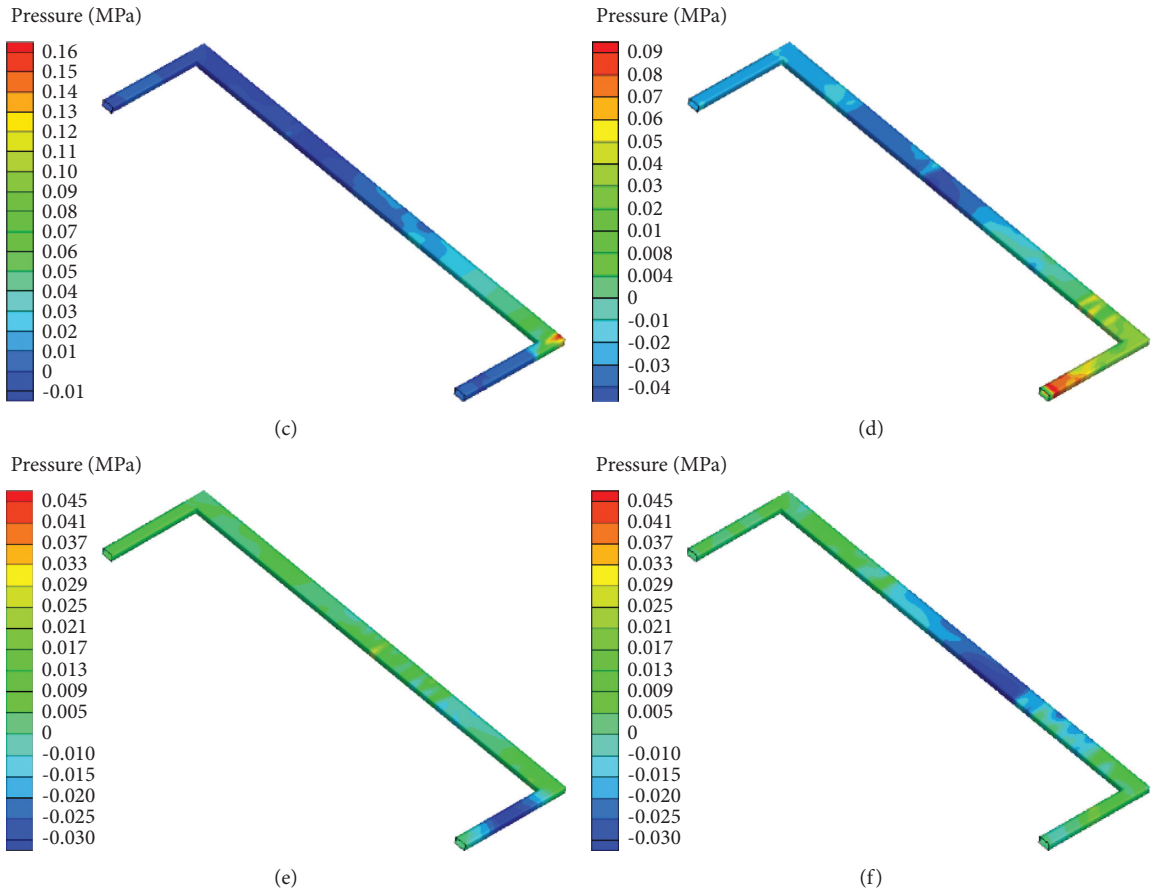

Figure 11: Pressure nephogram of shock wave at different times (rectangle): (a) $t = 0.02$ s; (b) $t = 0.15$ s; (c) $t = 0.36$ s; (d) $t = 0.44$ s; (e) $t = 0.6$ s; (f) $t = 0.94$ s.

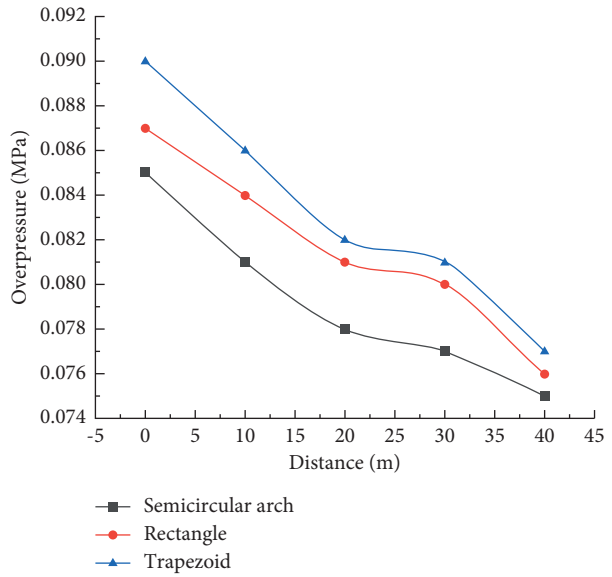

Figure 12: Pressure changes of air inlet tunnel with different cross-sectional shapes.

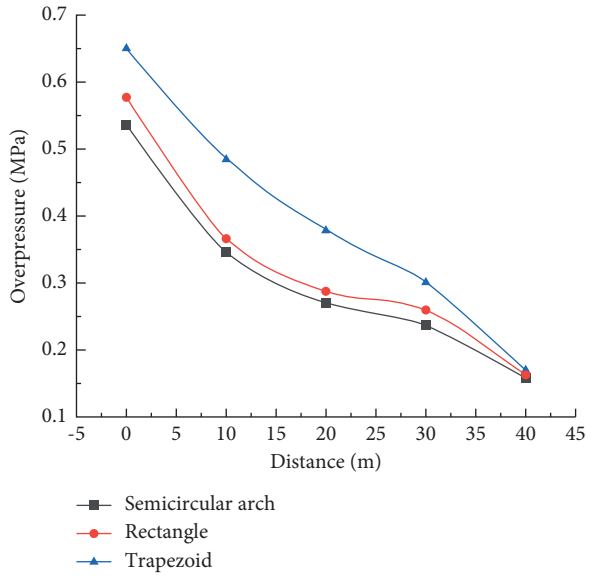

Figure 13: Pressure change of return air tunnel with different cross-sectional shapes.

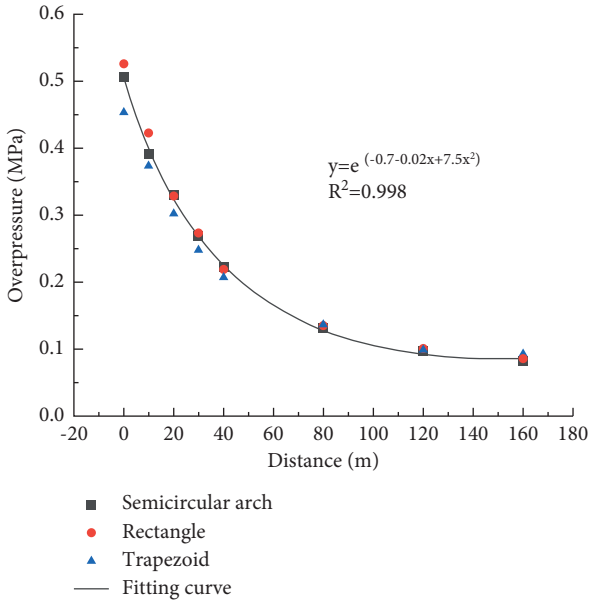

Figure 14: Changes of overpressure in the cut eye of the working face with different cross-sectional shapes.

the upper-corner gas explosion working face is obtained as follows: $y = e^{(-0.7-0.02x+7.5x2)}$.

5. Conclusions

(1) Through an analysis of the attenuation coefficient and overpressure difference of the adjacent measuring points, it is concluded that the blast wave of a gas explosion propagates stably in the form of a single shock wave at 40 m away from the explosion source, and the effective length of the inlet/return air roadway in the upper corner with U-type ventilation is determined to be 40 m.

(2) The simulation results of a gas explosion in the upper corner of three different cross-sectional shapes were analyzed. When the cross-sectional shape is a trapezoid, the initial overpressure of the explosion shock wave propagating to the inlet/return air roadway is the largest, followed by the rectangle and semicircle arch, but the attenuation trend of overpressure propagation in the three different cross-sectional shapes is the same.

(3) When the gas explosion shock wave propagates along the cut hole of the working face, the farther the distance from the upper-corner angle, the closer the overpressure at each point of the cut hole. The decay

trend of the overpressure conforms to the law of power function. The attenuation model is $y = e^{(-0.7-0.02x+7.5x\hat{2})}$.

Data Availability

The data used to support the findings of this study are included within the article.

Conflicts of Interest

The authors declare that they have no conflicts of interest.

Acknowledgments

This work was supported by National Natural Science Foundation of China (52074106 and 51734007). This project was also supported by Zhongyuan Postdoctoral Innovative Talent (ZYQR201810171), China Postdoctoral Science Foundation (2019M652536), and Henan Postdoctoral Foundation (001801016) and funded by the Doctoral Fund of Henan Polytechnic University (B2018-59).

References

[1] A. L. Both, G. Atanga, and H. Hisken, "CFD modelling of gas explosions: optimising sub-grid model parameters," *Journal of Loss Prevention in the Process Industries*, vol. 60, pp. 159–173, 2019.

[2] B. Y. Jing, B. Q. Lin, S. L. Shi, C. J. Zhu, and Z. W. Li, "Theoretical analysis on the attenuation characteristics of strong shock wave of gas explosion," *Procedia Engineering*, vol. 24, pp. 422–425, 2011.

[3] M. Gieras, R. Klemens, G. Rarata, and P. Wolański, "Determination of explosion parameters of methane-air mixtures in the chamber of 40dm3 at normal and elevated temperature," *Journal of Loss Prevention in the Process Industries*, vol. 19, no. 2-3, pp. 263–270, 2006.

[4] M. Scheid, A. Geiler, and U. Krause, "Experiments on the influence of pre-ignition turbulence on vented gas and dust explosions," *Journal of Loss Prevention in the Process Industries*, vol. 19, no. 2-3, pp. 194–199, 2006.

[5] H. T. Li, X. K. Chen, J. Deng et al., "CFD analysis and experimental study on the effect of oxygen level, particle size, and dust concentration on the flame evolution characteristics and explosion severity of cornstarch dust cloud deflagration in a spherical chamber," *Powder Technology*, vol. 372, 2020.

[6] S. Wang, Z. Shi, X. Peng et al., "Effect of the ignition delay time on explosion severity parameters of coal dust/air mixtures," *Powder Technology*, vol. 342, pp. 509–516, 2019.

[7] B. W. Lei, B. Wu, Y. T. Zhao, and M. A. Ashraf, "Numerical simulation and experimental study on formation of high concentration of h2 generated by gas explosion," *Polish Maritime Research*, vol. 23, 2016.

[8] Q. Liu, Y. Zhang, F. Niu, and L. Li, "Study on the flame propagation and gas explosion in propane/air mixtures," *Fuel*, vol. 140, pp. 677–684, 2015.

[9] Y. Xu, Y. M. Huang, and G. W. Ma, "A review on effects of different factors on gas explosions in underground structures," *Underground Space*, vol. 5, pp. 298–314, 2019.

[10] M. Yu, K. Zheng, and T. Chu, "Gas explosion flame propagation over various hollow-square obstacles," *Journal of Natural Gas Science and Engineering*, vol. 30, pp. 221–227, 2016.

[11] G. X. Jing, Y. L. Wu, S. S. Guo, H. Y. Shao, C. Liu, and S. Q. Zhang, "The influence of obstacles on the flame propagation law of gas and coal dust explosion," *Journal of Safety Science and Technology*, vol. 15, no. 9, pp. 99–104, 2019.

[12] P. F. Pan, Y. X. Tan, and Z. Q. Wang, "Study on the influence of strip obstacles on gas explosion characteristics," *Journal of Safety Science and Technology*, vol. 6, no. 5, pp. 71–76, 2010.

[13] F. H. Wang, W. Chen, X. P. Wen, W. L. Zhao, and Z. C. Liu, "Numerical simulation and mechanism analysis of gas explosion suppression by ultrasonic water mist," *Energy Sources Part A Recovery Utilization & Environmental Effects*, vol. 41, pp. 1–13, 2019.

[14] H. Shao, S. Jiang, X. Zhang, Z. Wu, K. Wang, and W. Zhang, "Influence of vacuum degree on the effect of gas explosion suppression by vacuum chamber," *Journal of Loss Prevention in the Process Industries*, vol. 38, pp. 214–223, 2015.

[15] K. Wang, S. Jiang, X. Ma, Z. Wu, W. Zhang, and H. Shao, "Study of the destruction of ventilation systems in coal mines due to gas explosions," *Powder Technology*, vol. 286, pp. 401–411, 2015.

[16] C. Wang, Y. Zhao, and E. K. Addai, "Investigation on propagation mechanism of large scale mine gas explosions," *Journal of Loss Prevention in the Process Industries*, vol. 49, pp. 342–347, 2017.

[17] A. H. Yan, B. S. Nie, L. C. Dai et al., "Numerical simulation on the gas explosion propagation related to roadway," *Procedia Engineering*, vol. 26, pp. 1563–1570, 2011.

[18] Z. A. Huang, Z. G. Liu, Y. S. Zhang, and Y. S. Zhang, "Numerical simulation and study on the transmission law of flame and pressure wave of pipeline gas explosion," *Safety Science*, vol. 50, no. 4, pp. 806–810, 2012.

[19] W. Cao, W. Gao, Y. Peng, J. Liang, F. Pan, and S. Xu, "Experimental and numerical study on flame propagation behaviors in coal dust explosions," *Powder Technology*, vol. 266, pp. 456–462, 2014.

[20] C. J. Zhu, B. Q. Lin, B. Y. Jiang, Q. Liu, and Y. D. Hong, "Numerical simulation of blast wave oscillation effects on a premixed methane/air explosion in closed-end ducts," *Journal of Loss Prevention in the Process Industries*, vol. 26, no. 4, pp. 851–861, 2013.

[21] Q. Zhang, L. Pang, and H. M. Liang, "Effect of scale on the explosion of methane in air and its shockwave," *Journal of Loss Prevention in the Process Industries*, vol. 24, no. 1, pp. 43–48, 2011.

[22] J. Li and H. Hao, "Numerical and analytical prediction of pressure and impulse from vented gas explosion in large cylindrical tanks," *Process Safety and Environmental Protection*, vol. 127, pp. 226–244, 2019.

[23] Q. Ye, B. Q. Lin, Z. Z. Jia, and C. J. Zhu, "Propagation law and analysis of gas explosion in bend duct," *Procedia Earth and Planetary Science*, vol. 1, no. 1, pp. 316–321, 2009.

[24] Q. Y. Yang, B. M. Shi, and L. L. Zhang, "Influence of turning angle on coal dust explosion induced by gas explosion," *China Safety Science Journal*, vol. 29, no. 7, pp. 58–63, 2019.

[25] B. J. Xie, Y. J. Du, and L. Wang, "Experiment and numerical simulation of flame propagation law of gas explosion in bifurcated pipe," *Journal of Chongqing University*, vol. 42, no. 6, pp. 69–77, 2019.

[26] W. B. Pang, Y. C. Li, and X. He, "Experimental study on arrival time of chemical explosion shock wave in T-channel," *Explosion and Shock Waves*, vol. 1, pp. 63–67, 2007.

[27] C. Zhai, B. Q. Lin, Q. Ye, Z. G. Lu, C. J. Zhu, and Z. Y. Zhang, "Influence of abnormal pipeline structure on gas explosion propagation characteristics," *Journal of Xi'an University of Science and Technology*, vol. 2, pp. 274–278, 2008.

[28] Y. Guo, C. Liu, D. Wang, and R. He, "Numerical study and safety spacing of buried parallel gas pipelines: a study based on TNT equivalent method," *International Journal of Pressure Vessels and Piping*, vol. 168, pp. 246–257, 2018.

[29] C. J. Zhu, B. Q. Lin, B. Y. Jiang, and C. Zhai, "Propagation characteristics of flame and shock wave of gas explosion in parallel roadway network," *Journal of China University of Mining & Technology*, vol. 40, no. 3, pp. 385–389, 2011.

[30] R. C. Liu and Y. F. Zhu, "Full scale simulation of gas explosion in long-wall face of coal mine," *China Safety Science Journal*, vol. 28, no. 12, pp. 58–64, 2018.

[31] B. Y. Jiang, B. Q. Lin, C. J. Zhu, C. M. Shen, and C. Zhai, "Numerical simulation of propagation characteristics of gas explosion shock wave in roadway network of coal mining face," *Journal of China Coal Society*, vol. 36, no. 06, pp. 968–972, 2011.

[32] Z. G. Liu, *Study on Detailed Chemical Reaction Mechanism Acceleration Algorithm for Large Eddy Simulation of Turbulent Combustion*, University of Chinese Academy of Sciences (Institute of Engineering Thermophysics), Beijing, China, 2019.

[33] X. Wen, M. Xie, M. Yu, and Z. Liu, "Dynamic characteristics of gas deflagration in small-scale confined space," *Combustion Science and Technology*, vol. 19, no. 4, pp. 347–351, 2013.

[34] X. Wen, M. Yu, H. Deng, and J. Chen, "Large eddy simulation of gas turbulence deflagration in small-scale confined space," *Ciesc journal*, vol. 67, no. 5, pp. 1837–1843, 2016.

[35] Z. Li, M. Yu, and W. Ji, "Numerical simulation of turbulent flame induced by obstacles in gas explosion," *Journal of henan polytechnic university (natural science edition)*, vol. 34, no. 2, pp. 167–170, 2015.

[36] G. X. Jing, Z. W. Jia, L. Cheng, Z. W. Duan, H. Li, and Z. Y. Gao, *Propagation Law and Damage Model of Gas Explosion under Complex Conditions*, Science Press, Beijing, China, 2017.

[37] J. D. Xu, S. L. Xu, and G. Y. Yang, "Experimental study on propagation of mine gas explosion," *Coal Science and Technology*, vol. 7, pp. 55–57, 2004.

Hindawi
Shock and Vibration
Volume 2021, Article ID 8775338, 14 pages
https://doi.org/10.1155/2021/8775338

Research Article

Energy Dissipation and Failure Characteristics of Layered Composite Rocks under Impact Load

Wenjie Liu[1,3,4], **Ke Yang**[1,2,3,4], **Wei Zhen**[1,3,4], **Xiaolou Chi**[1,3,4], **Rijie Xu**[1,3,4] and **Xin Lv**[1,3,4]

[1]*State Key Laboratory of Mining Response and Disaster Prevention and Control in Deep Coal Mines, Anhui University of Science and Technology, Huainan 232001, China*
[2]*Institute of Energy, Hefei Comprehensive National Science Center, Hefei 230031, Anhui, China*
[3]*National & Local Joint Engineering Research Center of Precision Coal Mining, Anhui University of Science and Technology, Huainan 232001, Anhui, China*
[4]*Key Laboratory of Mining Coal Safety and Efficiently Constructed by Anhui Province and Ministry of Education, Anhui University of Science and Technology, Huainan 232001, China*

Correspondence should be addressed to Ke Yang; keyang2003@163.com

Received 16 July 2021; Accepted 1 November 2021; Published 15 November 2021

Academic Editor: Jianwei Cheng

Horizontal layered composite rock samples composed of white and black sandstones with large differences in physical and mechanical properties were tested to explore the dynamic characteristics of layered composite rocks under impact load. Using the split Hopkinson pressure bar test system, the dynamic compression tests of two incident states of stress waves, that is, stress waves from white sandstone to black sandstone (W⟶B) and from black sandstone to white sandstone (B⟶W), were designed and carried out under different impact velocities. Combining the ultrahigh-speed photography system and digital photogrammetry for deformation measurement (DPDM), we obtained the stress wave propagation characteristics, failure characteristics, and particle size distribution characteristics of broken rocks of the composite rocks under the two conditions. The experimental results were compared and analyzed, while stresses and strength conditions at the interface of the composite rock samples were theoretically assessed, yielding the following main findings. The energy dissipation pattern of composite rock had an obvious strain rate effect. The reflected energy and fragmentation energy density of composite rock increased approximately as quadratic functions of the incident energy. Affected by the wave impedance matching relationship, the W⟶B and B⟶W samples were significantly different in terms of the stress wave shape, energy dissipation, average particle size, and fractal dimension of the broken rocks at low impact velocities. However, with an increase in the impact velocities, the two gradually shared the same behavior. When composite rock samples deformed and failed, the macrocracks mostly initiated from the white sandstone. When the crack tip stress of the white sandstone at the interface exceeded the strength of the weakened black sandstone, the crack continued to develop through the two-phase rock interface due to the difference in Poisson's ratios. The damage degrees and failure modes of the two parts of composite rocks were different: black sandstone was prone to tensile splitting with local shear failure, while white sandstone exhibited shear failure with local tensile splitting. The damage degree of white sandstone exceeded that of black sandstone.

1. Introduction

Layered composite rocks are mostly natural engineering geological bodies consisting of multiple layers of rocks with different lithologies and thicknesses deposited in a certain order and manner [1–3]. In underground coal mining, the excavation of layered composite rocks is inevitable. Affected by blasting excavation, activation of faults, and breaking of thick and hard roofs, roadways are often subjected to dynamic (impact) loads acting as stress waves of various velocities and frequencies. The structural complexity of layered composite rocks implies that their characteristics of stress wave propagation and attenuation are notably different from those of single rocks. Therefore, studying the dynamic

response characteristics of layered composite rocks is of great significance to the tunneling and support in roadways of layered composite rocks [4, 5].

Through theoretical analysis [6–9], numerical simulation [10–12], physical analog modeling [13–15], laboratory tests [16–23], and other methods, comprehensive and in-depth research on layered composite rocks and single rocks has been performed worldwide. Thus, in 1960, Jaeger [6] proposed the shear failure criterion for heterogeneous rocks, while in 2001, Tien and Kuo [7] proposed the shear failure criterion for transversely isotropic rocks. In 2014, the latter criterion was revised by Saeidi et al. [8] based on laboratory test results. In recent works on numerical simulation, Cao et al. [10] used compressive-shear tests and PFC2D numerical simulation methods to analyze the influence of bedding angle on the mechanical characteristics, crack propagation patterns, and acoustic emission response behaviors of transversely isotropic rock with cuts at both ends. In 2021, Xu et al. [11] used the particle flow discrete element numerical simulation method combined with the uniaxial compression tests on a transversely isotropic rock with prefabricated fractures. The influence of cracks and weak surfaces on the rock fracture shape was analyzed, six failure morphologies were determined, and the crack evolution process of each morphology was studied based on matrix tensor analysis. Maazallahi and Majdi [12] analyzed the deformation characteristics of a circular tunnel in a transversely isotropic rock under hydrostatic pressure and nonhydrostatic pressure. It was pointed out that the greater the stress anisotropy index, the greater the difference between the maximum and minimum displacements of the tunnel surface. In recent works on physical analog modeling, Shen et al. [15] prepared transversely isotropic similar material samples formed by the interbedding of two similar materials. Triaxial compression tests were carried out on five sets of transversely isotropic samples with different bedding angles, and the evolution of mechanical parameters, fracture types, and failure morphology of inclined interbedded similar rock material was analyzed. On laboratory tests research, Yang et al. [16] combined acoustic emission technology and DIC technology to carry out conventional triaxial compression tests, confining pressure reduction triaxial tests, and Brazil disc splitting tests on transversely isotropic shales with different bedding angles. They reported that the bending angle greatly influenced the elastic modulus, tensile strength, compressive strength, and failure morphology of the rock. When the confining pressure was reduced and the axial pressure was increased, the energy dissipation was larger and the damage was more severe, compared with the loading where the axial pressure was fixed while the confining pressure was reduced. Based on the uniaxial compression test of shale-coal layered composite sample combined with an acoustic emission monitoring device, Chen et al. [17] analyzed the stress-strain curve characteristics, the macroscopic initiation, failure pattern, and the progressive failure characteristics of the coal composite rocks. The drilling and blasting methods are often used when excavating the roadway in the rock mass. In engineering construction, more attention is paid to the failure characteristics of rocks under dynamic load. To this end, Li et al. [24] carried out a dynamic impact test study on single-joint red sandstone, which showed that the presence of joint weakened the dynamic compressive strength of sandstone. With an increase in the joint inclination angle, the degree of stress wave attenuation increased. The sandstone affected by the shock stress wave was mostly damaged by the tensile rib spalling. Han et al. [25] studied the dynamic characteristics of sandstone with different cement mortar thicknesses. As the thickness of the cementation increased, the failure morphology of the sandstone gradually changed from local tensile spalling to penetrating splitting.

Most of the above studies were focused on the mechanical characteristics, energy dissipation, failure criteria, and constitutive relations of layered composite rocks under static load, as well as dynamic characteristics of single rocks or jointed rocks under dynamic load. However, there are quite a few studies on the impact dynamics of layered composite rocks. This paper combined the SHPB test system with an ultrahigh-speed camera and digital photogrammetry for deformation measurement to carry out the impact compression tests on layered composite rock samples. The stress characteristics and strength conditions of composite rocks were analyzed theoretically. Also, the law of energy dissipation, deformation, and fracture characteristics of layered composite rocks under the two stress wave incident states, that is, stress waves passing from white sandstone to black sandstone (W⟶B) and from black sandstone to white sandstone (B⟶W), were revealed. The research results can provide a certain reference for rock-breaking and support of composite rock projects.

2. SHPB Test of Layered Composite Rocks

2.1. Sample Preparation. The sandstone samples required for the test were taken from the roof of the coal seam 4# in the Hujiahe Coal Mine, Binchang, Shaanxi Province of China. To control the discreteness of the rock samples, the unweathered rock samples with good integrity were wax-sealed on-site and transported to the laboratory. They were processed into cylindrical samples of $\Phi 50\,\text{mm} \times 25\,\text{mm}$ dimensions via cutting, drilling, and grinding procedures. Then, epoxy resin [24] was used to bond the sandstone single-body samples to form $\Phi 50\,\text{mm} \times \text{h}50\,\text{mm}$ "black sandstone-white sandstone" horizontal layered composite samples. During the sample bonding process, the amount of epoxy resin was strictly controlled to ensure that the two-phase rock components were fully and uniformly bonded while minimizing the binder thickness effect. When each sample was processed, the size and processing accuracy of the sandstone single-body sample and the composite rock sample were required to meet the standard requirements recommended by ISRM. At the same time, sandstone samples for the uniaxial compression test and Brazil splitting test were prepared. The main physical and mechanical parameters of black sandstone and white sandstone were measured, as shown in Table 1. To use the digital photogrammetry for deformation measurement for analyzing the deformation and failure pattern of the samples, uniformly

Table 1: Mechanical parameters of black sandstone and white sandstone samples.

Lithology	Compressive strength (MPa)	Elastic modulus (GPa)	Tensile strength (MPa)	Poisson's ratio	Longitudinal wave velocity ($m \cdot s^{-1}$)	Density ($kg \cdot m^{-3}$)
White sandstone	44.62	6.65	4.06	0.16	3946	2677
Black sandstone	65.29	7.12	5.02	0.13	3452	2718

distributed speckles with random size were made on the surface of each sample [26–28]. Figure 1 shows the composite rock samples after processing.

2.2. Test System and Plan. The impact compression tests of layered composite rocks were performed using the split Hopkinson pressure bar (SHPB) test system and an ultrahigh-speed camera system. As shown in Figure 2, the incident bar, transmitted bar, and spindle punch of the SHPB test system were made of high-strength alloy steel with a density of 7800 kg/m^3, an elastic modulus of 210 GPa, and a longitudinal wave velocity of 5190 m/s. The bar diameter was 50 mm, and the impact waveform was a sine. During the tests, the amplitude and impact velocities of the incident stress wave were controlled by adjusting the gas pressure inside the high-pressure air chamber or changing the spindle punch position. The strain signal generated during stress wave propagation in the incident and transmitted bars was collected by SG1, SG2 dynamic strain gauges, and SDY2107 A ultrahigh dynamic strainmeter, which was then displayed and stored by Yokowaga-DL850 E oscilloscope. The ultrahigh-speed camera system was composed of a FASTCAMSA-Z high-speed camera, flashlight, synchronous trigger control system, and so on. Before the test, the shooting speed of the high-speed camera was set to 120000 fps and the image resolution was set to 256×408 pixels to ensure that the camera could capture the entire deformation and failure process of the sample. When the stress wave propagated in the incident bar, the strain gauge transmitted the strain signal to the super dynamic strain gauge, which converted it into a voltage signal to synchronously trigger the high-speed camera and flashlight.

The image processing technology adopted in this paper is the digital photogrammetry for deformation measurement (DPDM) technology [29]. DPDM system is mainly composed of image acquisition hardware system and postprocessing software system. The hardware system of image acquisition mainly includes digital camera and lighting equipment. DPDM software includes PhotoInfor and PostViewer processing software. Image analysis software PhotoInfor is specially used for the processing and analysis of punctuation digital photos. Its main functions include image binarization, direct pick-up of punctuation recognition parameters, recognition of centroid coordinates, corresponding punctuation sorting, elimination of repeated points, image calibration, displacement calculation, quadrilateral mesh generation for strain calculation, and strain calculation. PostViewer, as a postprocessing program of image analysis result data, can generate and display contour lines, cloud maps, deformation grids, vector maps, and so on. Meanwhile, it also has query, statistical analysis, data extraction, batch processing, and output processing functions.

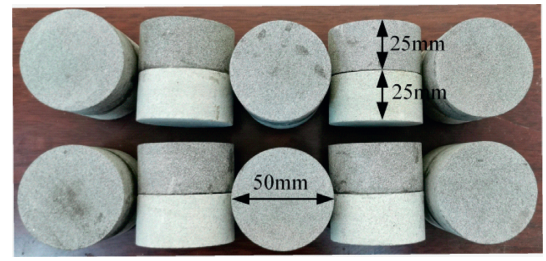

Figure 1: "Black sandstone-white sandstone" layered composite rock samples.

As shown in Figure 3, according to the incident direction of the stress wave, when the incident stress wave propagated from black sandstone to white sandstone, the respective test group was marked as B⟶W, and vice versa as W⟶B. A preliminary test was carried out on the layered composite rock before the main impact tests, which revealed that when the impact pressure exceeded 0.6 MPa, large-scale macrocracks appeared in the white sandstone samples. Based on the preliminary test results, the impact compression tests of the layered composite rocks were designed with five impact pressures of 0.40, 0.50, 0.60, 0.70, and 0.90 MPa. To reduce the contingency and improve the accuracy of the test results, at least three sets of parallel tests were performed for each impact pressure. After the test, valid test results were selected for analysis. Before impact loading, a small amount of petroleum jelly was applied to the bar-sample contact to reduce the friction effect on the test results.

2.3. Verification of Dynamic Stress Balance. The stress equilibrium state at both ends of the sample before its impact damage is the premise of the one-dimensional stress wave hypothesis and the stress (strain) uniformity hypothesis, which is necessary to obtain reliable test results. Figure 4 shows the stress at both ends of a typical impact compression test sample of layered composite rocks. It can be seen that, during the impact loading process of layered composite rocks, the sum of the incident and reflected stresses was approximately equal to the transmitted stress. Therefore, it can be considered that the sample was in a state of dynamic stress balance and satisfied the stress equilibrium condition.

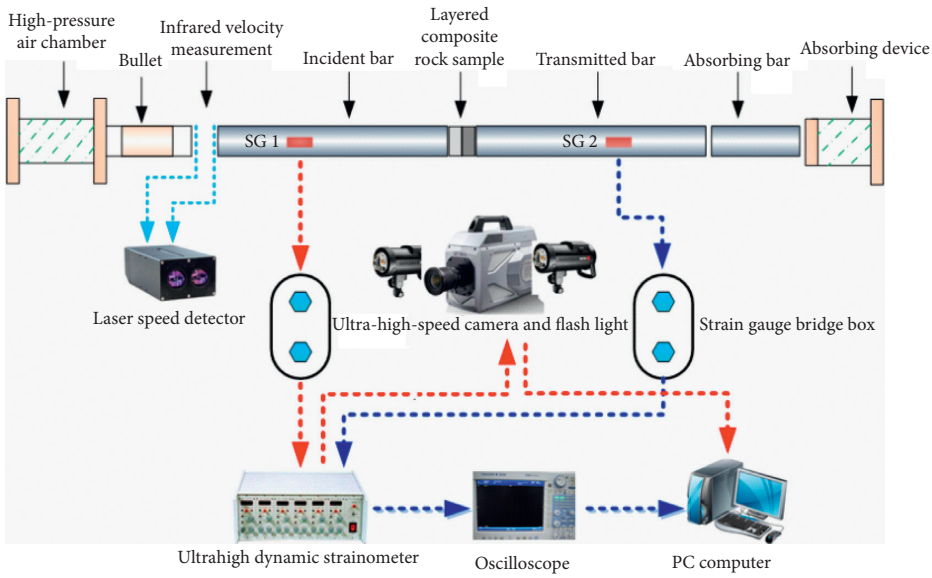

Figure 2: SHPB and high-speed photography system.

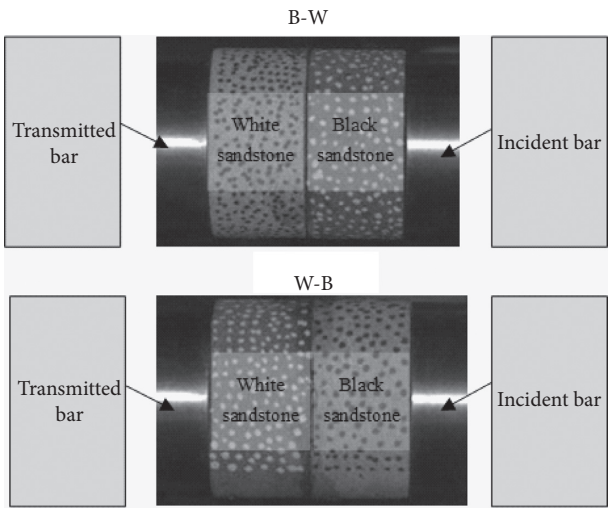

Figure 3: Schematic diagram of sample grouping.

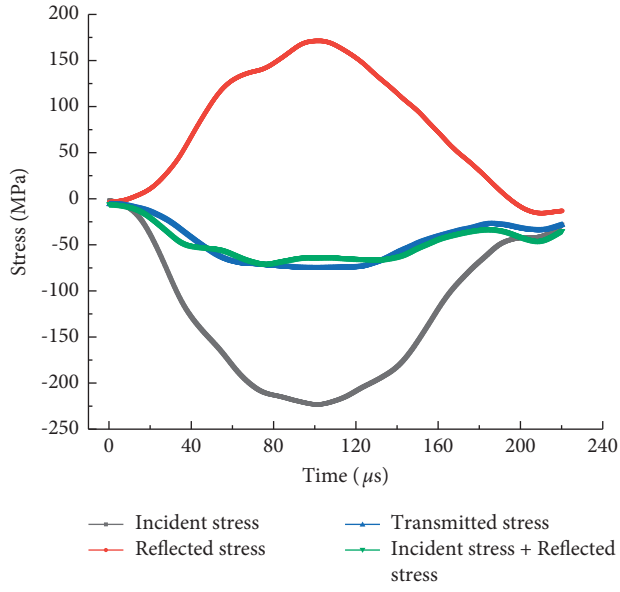

Figure 4: Verification of dynamic stress balance for a typical sample.

3. Test Results and Analysis

3.1. Analysis of Stress Wave Propagation Characteristics. Comparing and analyzing the stress waveforms of layered composite rocks under different impact velocities (Figure 5), one can see that, with an increase in impact velocity, the amplitudes of the incident, reflected, and transmitted waves of the layered composite rocks under study gradually increased. Under the same impact velocities, the incident waves of the W⟶B and B⟶W samples were the same, while the amplitudes of the reflected waves and the transmitted waves were quite different. This difference was obvious under low impact velocities (7~10 m/s) but less pronounced under high ones (10~13 m/s). From the analysis of stress wave propagation characteristics, it can be seen that the larger the wave impedance of the rock, the better the impedance matching effect between composite rocks and the incident bar. As a result, when the incident wave propagated to the interface between the composite rocks and the incident bar, more stress waves passed through the composite rocks to the transmitted bar. Therefore, under the same impact velocities, the amplitude of the transmitted wave of the B⟶W sample was larger than that of the W⟶B one. However, with increased impact velocity, the wave impedance matching effect between the sample and the incident bar on the stress wave propagation gradually decreased. Consequently, the shape and amplitude of the stress waves of the two samples became quite close.

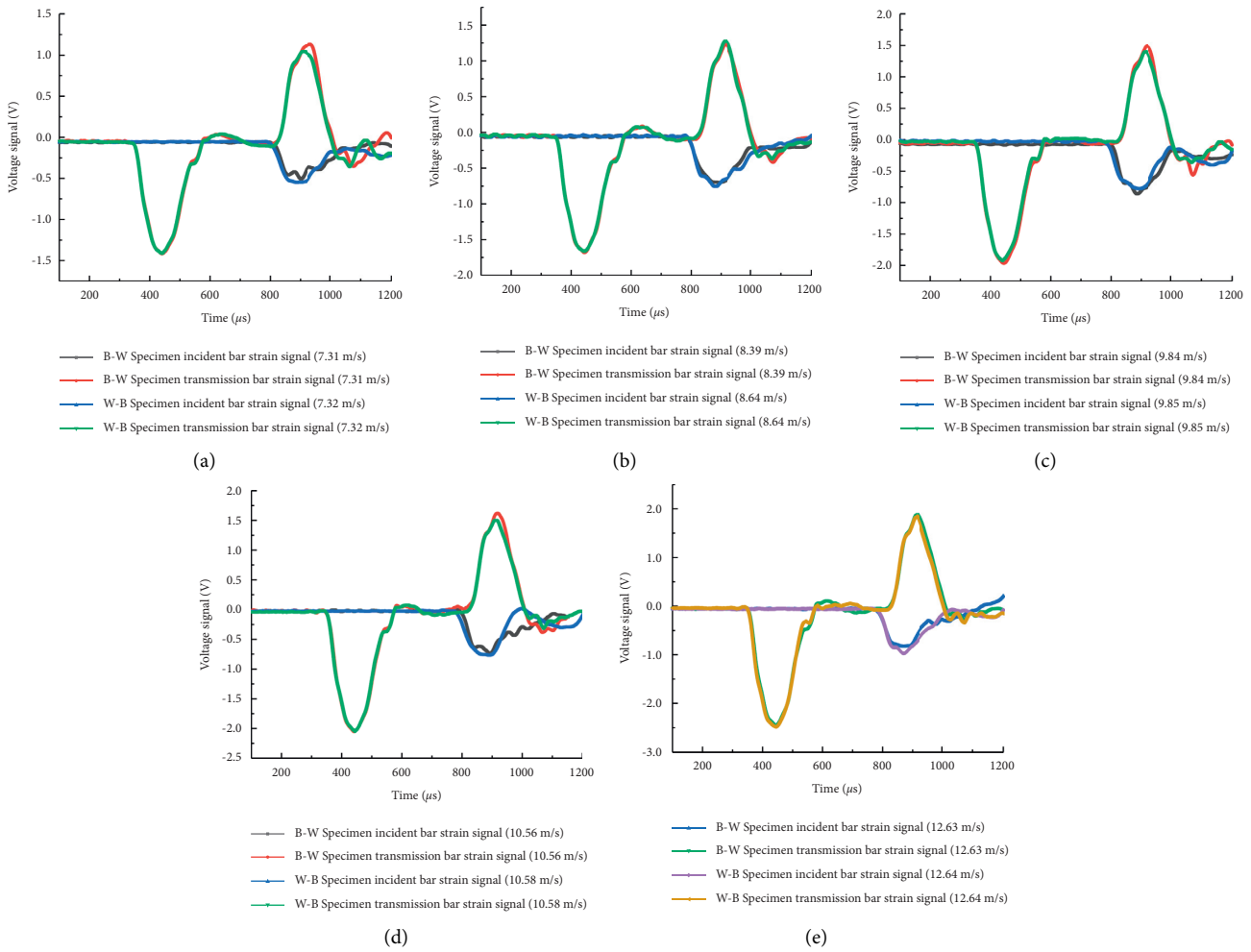

FIGURE 5: Waveforms of B⟶W and W⟶B composite rock samples at different impact velocities. (a) 7.2 m/s. (b) 8.6 m/s. (c) 9.8 m/s. (d) 10.4 m/s. (e) 12.6 m/s.

3.2. Analysis of Energy Dissipation. According to the thermodynamics theory, the material fracture is an energy-driven state instability phenomenon. The deformation and failure of layered composite rocks occur through the accumulation, migration, and dissipation of energy [30]. Therefore, the study of the energy dissipation under impact loading and the analysis of the damage characteristics of layered composite rocks from the energy standpoint is of great significance to better understand the energy absorption characteristics of layered composite rocks and to improve the anti-impact characteristics of the layered composite surrounding rock bearing structure of the roadway in a targeted manner. According to the one-dimensional elastic wave theory, the incident, reflected, and transmitted energies during the impact test can be calculated via the following equations [25]:

$$W_I = \mathrm{AEC}_B \int \varepsilon_I^2(t)dt\ , \tag{1}$$

$$W_R = \mathrm{AEC}_B \int \varepsilon_R^2(t)\mathrm{d}t, \tag{2}$$

$$W_T = \mathrm{AEC}_B \int \varepsilon_T^2(t)\mathrm{d}t, \tag{3}$$

where W_I, W_R, and W_T represent incident, reflected, and transmitted energies, respectively; $\varepsilon_I(t)$, $\varepsilon_R(t)$, and $\varepsilon_T(t)$ are the incident, reflected, and transmitted strains at time t, respectively; and A, E, and C_B are the cross-sectional area, the elastic modulus, and the propagation velocity of longitudinal waves of the pressure bar, respectively.

Formulas (1)–(3) were used to calculate the energy evolution curves of typical layered composite rocks under impact loading, as shown in Figure 6. It can be seen that the incident, reflected, transmitted, and absorption energies increased with time. To facilitate analysis, the energy evolution curves of layered composite rocks can be subdivided into the following three stages: slow growth stage, accelerated growth stage, and stable stage. In the slow growth stage (0~50 μs), the composite rocks were in the initial period of stress wave action, and each energy increment was low. Composite rocks mainly experienced elastic deformation with a few microcracks developed inside. Most of the absorbed energy was stored in composite rocks in the form

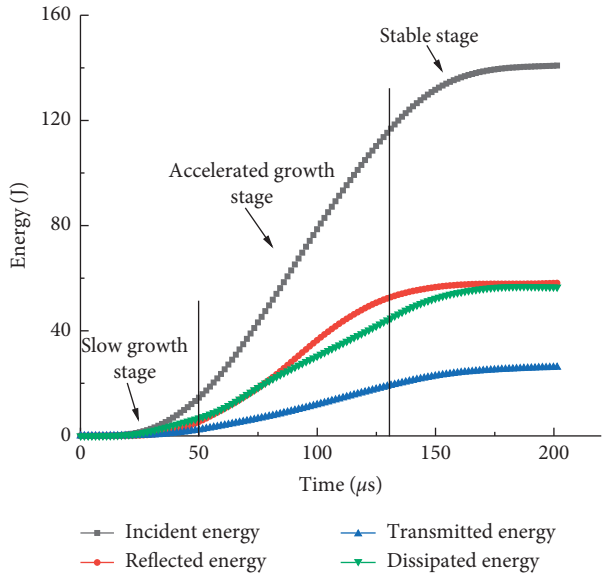

FIGURE 6: Energy evolution curve of typical layered composite rock mass.

of elastic energy. After entering the accelerated growth stage (50~150 μs), the sample energies grew approximately linearly with time. The growth rate of the incident energy was the largest, while that of the transmitted energy was the smallest. The performed analysis revealed that after the stress wave reached the incident bar-sample interface, it would be partly reflected and partly transmitted due to the difference in wave impedance between the two. The transmitted stress wave propagated back and forth in the incident bar, sample, and transmitted bar, continuously supplementing the reflected and transmitted energies. When the stress intensity exceeded the ultimate strength of the rock, the damage and failure in the composite rocks would change qualitatively. Numerous microcracks initiated in the composite rocks rapidly expanded and coalesced, forming macrocracks and continuously increasing the absorption energy. In the stable stage (150~200 μs), the composite rocks failed under the impact load, and the accumulated elastic energy was abruptly released. The energy transfer stopped, and eventually, the energy fluctuations stabilized.

According to the principle of energy conservation, with disregard of the energy loss caused by friction between the pressure bar and the sample during the stress wave propagation, the energy W_A absorbed by the layered composite rock sample under the action of impact load is [31]

$$W_A = W_I - W_R - W_T. \tag{4}$$

According to the energy dissipation characteristics, the energy W_A absorbed by the sample can be subdivided into the crack growth energy W_F, broken block projectile kinetic energy W_D, and other forms of energy consumption W_O. The latter mainly refers to the energy dissipated in other forms, such as heat energy, which usually can be ignored. The relationship between these energies is as follows:

$$W_A = W_F - W_D - W_O. \tag{5}$$

Previous studies have shown that, compared with the crack growth energy W_F, the projectile kinetic energy of the broken block W_D accounts for a small share. Therefore, the energy absorbed by the sample W_A is approximately equal to the energy consumption in crack propagation W_F [32]; that is, $W_A \approx W_F$.

Rock fragmentation is closely related to energy dissipation and rock volume. Compared with the energy dissipation per unit volume of rock, it can better reflect the energy absorption of rock fragmentation. Therefore, the fragmentation energy density is used to characterize the energy dissipation of rock fragmentation.

$$\varepsilon_d = \frac{W_A}{V} = \frac{W_F}{V}, \tag{6}$$

where ε_d is the fragmentation energy density and V is the sample volume.

Using equations (1)–(6), the distributions of respective energies in different samples were calculated and are plotted in Table 2. In the energy accumulation and dissipation processes occurring in composite rocks, the reflected energy W_R characterizes the propagation ability of the stress wave at the bar-sample interface. The fragmentation energy density ε_d reflects the sample's ability to absorb energy for crack propagation. Therefore, the following analysis mainly focuses on the variations of the reflected energy of the sample and ε_d with incident energy W_I.

According to the data in Table 2, the average values of each group were derived and are plotted in Figure 7. Figure 7(a) shows that the incident energy increased linearly with impact velocity, regardless of the sample type. Figure 5(b) shows that the reflected energy increased approximately as a quadratic function of the incident energy. When the latter was small, the reflected energy of B⟶W composite rocks significantly exceeded that of W⟶B ones. However, with increased incident energy, the difference in reflected energies of the two groups gradually decreased. At the incident energy of 230J, the reflected energies of the two were the same. Based on the analysis of the stress wave propagation characteristics in Section 3.1, when the stress waves reached the interface between the sample and the incident bar, more energy was transferred through the W⟶B composite rock samples because they had a better impedance matching effect with the incident bar than B⟶W samples. Therefore, the reflected energy of W⟶B composite rocks was relatively small. However, with increased impact velocity, the difference in impedance matching effects gradually weakened, and the reflected energy values in the two groups got closer to each other. It can be seen in Figure 7(c) that, given the difference in the impedance matching effects, the fragmentation energy density had the same trend with the incident energy: it behaves as a quadratic function of incident energy. When the incident energy was small, the fragmentation energy density of W⟶B composite rocks was significantly larger than that of B⟶W ones, but the two gradually became close as the incident energy increased. Due to a better impedance matching effect of W⟶B composite rocks, they

Table 2: Energy distribution of layered composite rock mass.

Sample type	Impact velocity (m/s)	Incident energy W_I (J)	Reflected energy W_R (J)	Absorbed energy W_A (J)	Fragmentation energy density ε_d (J·cm^{-3})
B⟶W	7.31	79.671	43.542	24.643	0.251
	7.35	78.732	41.806	24.957	0.254
	7.29	77.814	43.809	25.212	0.257
W⟶B	7.27	79.451	38.113	27.284	0.278
	7.32	79.135	37.508	28.566	0.291
	7.25	76.674	32.738	26.374	0.269
B⟶W	8.39	109.912	52.597	32.217	0.328
	8.38	111.217	51.165	35.033	0.357
	8.28	109.384	55.786	32.487	0.331
W⟶B	8.64	109.174	48.525	37.216	0.379
	8.54	108.317	50.743	39.211	0.446
	8.58	103.751	44.538	34.653	0.353
B⟶W	9.95	149.788	66.433	53.068	0.541
	9.84	145.979	65.691	50.947	0.519
	9.76	143.522	61.714	51.955	0.529
W⟶B	9.66	140.853	58.13	56.614	0.577
	9.85	145.947	61.46	59.984	0.611
	9.87	146.586	60.169	58.341	0.595
B⟶W	10.47	161.287	72.245	62.865	0.641
	10.56	164.523	70.745	64.328	0.656
	10.44	160.994	74.057	65.686	0.669
W⟶B	10.57	159.715	70.686	66.086	0.673
	10.64	166.827	70.067	67.899	0.692
	10.58	165.183	71.029	69.542	0.709
B⟶W	12.63	232.084	109.443	93.681	0.955
	12.62	229.321	105.488	90.352	0.921
	12.57	228.594	107.439	88.466	0.902
W⟶B	12.78	238.477	110.756	91.942	0.937
	12.64	232.635	104.686	91.193	0.929
	12.41	222.971	102.567	91.641	0.934

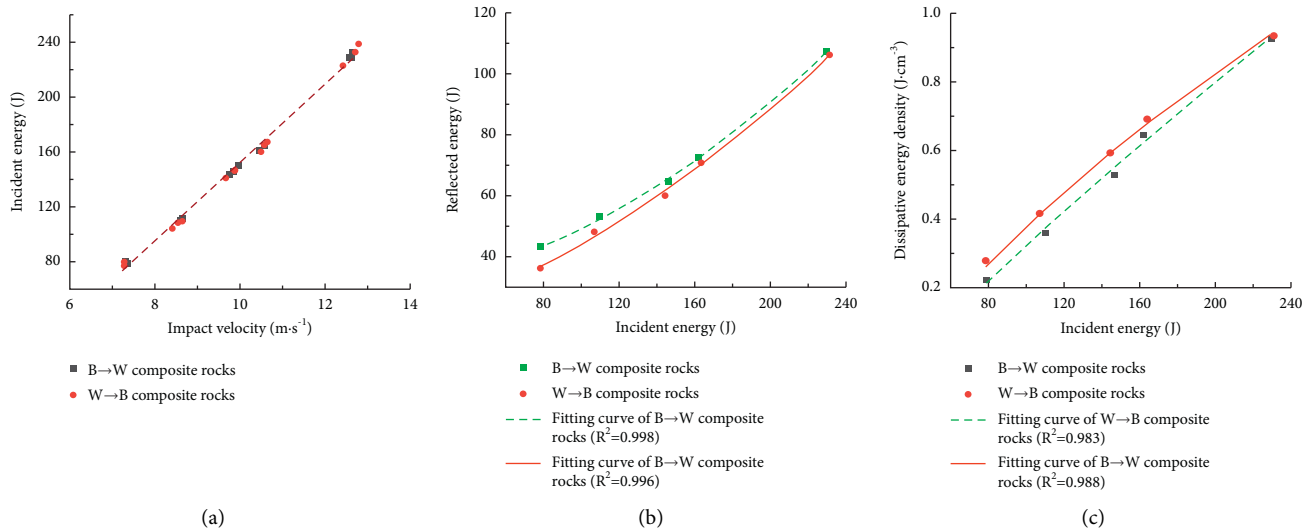

Figure 7: Energy evolution patterns of layered composite rock mass. (a) Impact velocity-incident energy. (b) Incident energy-reflected energy. (c) Incident energy and fragmentation energy density.

transmitted more energy than B⟶W ones at the same impact velocities. The crack propagation energy consumption W_F of W⟶B composite rocks was larger, so they were more prone to fragmentation. Therefore, the fragmentation energy density of W⟶B composite rocks was larger at low impact velocities. However, with increased incident energy, the energy input of W⟶B and W⟶B composite rocks tended to be the same, reducing the difference in their fragmentation energy densities.

3.3. Analysis of Failure Characteristics. To study the failure characteristics of layered composite rocks, it is necessary to analyze the stress characteristics and strength conditions at their interface. The development of cracks at the interface of layered composite rocks is closely related to the rocks' mechanical environment and mechanical properties at the interface. To facilitate analysis, it was assumed that when the composite rocks deformed and failed, the adjacent two phases of rock mass underwent no relative displacement, and the binder thickness binder at the interface could be ignored. According to the data in Table 1, the following inequalities hold: $E_R > E_C$ and $\mu_C > \mu_R$, where E_R and E_C are the elastic moduli of black and white sandstones, respectively, while μ_R and μ_C are their Poisson's ratios. When layered composite rocks deform and fail due to the difference in Poisson's ratios of their two phases, the radial stress will be restrained at the interface of black and white sandstones. The stresses acting in microunits at this interface are shown in Figure 8.

From the continuity condition of deformation and the static equilibrium equation, it can be obtained that [33]

$$\sigma_{iR} = \sigma_{iC} = \frac{E_R\mu_C - E_C\mu_R}{E_R(1+\mu_C) - E_C(1+\mu_R)}\sigma_1, \tag{7}$$

where $i = 2$, 3 and $\sigma_1 = \sigma_{1R} = \sigma_{1C}$.

This study adopted the Drucker–Prager failure criterion, which considers the effects of intermediate principal stress and hydrostatic pressure simultaneously, overcoming the main weakness of the Mohr–Coulomb criterion and making it suitable for rock materials. The criterion can be expressed as

$$f = \alpha I_1 + \sqrt{J_2} - K = 0, \tag{8}$$

where $I_1 = \sigma_1 + \sigma_2 + \sigma_3$ is the first invariant of stress and $J_2 = [(\sigma_1 - \sigma_2)^2 + (\sigma_2 - \sigma_3)^2 + (\sigma_3 - \sigma_1)^2]/6$ is the second invariant of stress deflection, while $U_f = \int_{\varepsilon_1}^{\varepsilon_2} \sigma_i + \sigma_{i+1}/2\mathrm{d}\varepsilon$ and $U_y = U_e - U_f = 1/2\sigma_c\varepsilon_e - \int_{\varepsilon_1}^{\varepsilon_2} \sigma_i + \sigma_{i+1}/2\mathrm{d}\varepsilon$ are experimentally determined constants related to the internal friction angle φ and cohesion force c of black and white sandstone rocks.

If $\sigma_2 = \sigma_3$, formula (2) can be simplified as

$$\sigma_1 = \frac{3 - 5\sin\phi}{3 + \sin\phi}\sigma_3 + \frac{6c\cos\phi}{3 + \sin\phi}. \tag{9}$$

If $\sigma_2 = \sigma_3 = 0$, the strength of the white sandstone far away from the black sandstone-white sandstone (BW) interface can be obtained as

$$\sigma_{UCS} = \frac{6c\cos\phi}{3 + \sin\phi}. \tag{10}$$

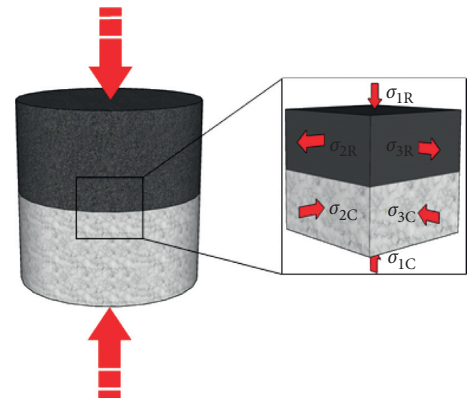

Figure 8: The triaxial stress state in a combined black sandstone-white sandstone sample and its interface.

According to equations (7)–(11), the strength of white sandstone at the interface can be obtained as

$$\sigma_{RC} = \frac{\sigma_{UCS}}{1 - \beta\lambda}, \qquad \beta = \frac{3 - 5\sin\varphi}{3 + 5\sin\varphi}, \tag{11}$$

for $0 < \alpha < 1$ and $0 < \lambda < 1$, where $\alpha = (3 - 5\sin\varphi)/(3 + 5\sin\varphi)$ and

$$\lambda = 1 - \frac{E_R - E_C}{(E_R\mu_C - E_C\mu_R) + (E_R - E_C)}. \tag{12}$$

It can be seen from equation (11) that, in layered composite rocks, the strength of the white sandstone at the interface is strengthened due to the difference in Poisson's ratios, and the strength of the white sandstone far away from the interface is less than the white sandstone strength at the interface. The strength of the black sandstone at the interface is weakened due to the same reason, and the strength of the black sandstone far away from the interface exceeds that of the black sandstone at the interface. Although the stress at both ends of the sample and the elastic modulus and Poisson's ratio of the rock samples change with time under the action of the stress wave, only the stress magnitude changes, but not its direction. That is to say, it only has a certain influence on the degree of weakening or strengthening of the rock mass at the interface. This effect may be less pronounced than the true stress concentration effect, but it does exist theoretically, directly affecting the initiation, expansion, and arrest of the cracks at the interface.

The high-speed camera was used to observe the deformation and failure process of layered composite rocks. Using the initial speckle image of layered composite rocks during impact loading as a reference and setting the time when the incident wave reached the interface between the incident bar and the sample to zero, the speckle images at typical times of impact loading were selected and analyzed using the PhotoInfor and PostViewer digital image processing software packages [34]. Figures 9 and 10 show the failure characteristics and maximum shear strain of B⟶W and W⟶B samples at the impact velocity of 9.8 m/s, respectively.

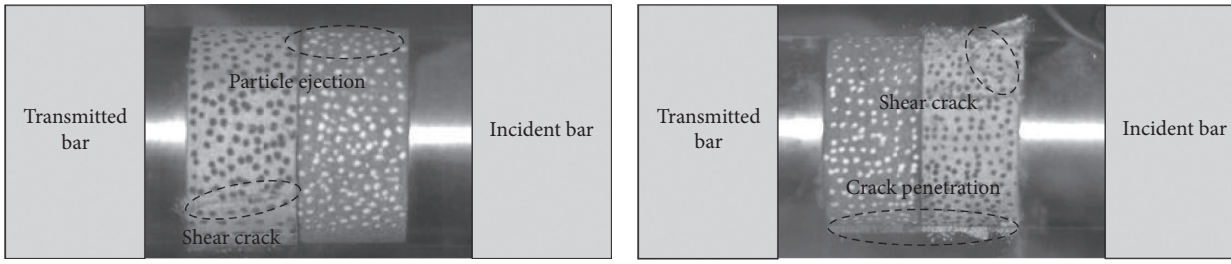

(a) (b)

Figure 9: Failure characteristics of the layered composite rock mass. (a) B⟶W sample. (b) W⟶B sample.

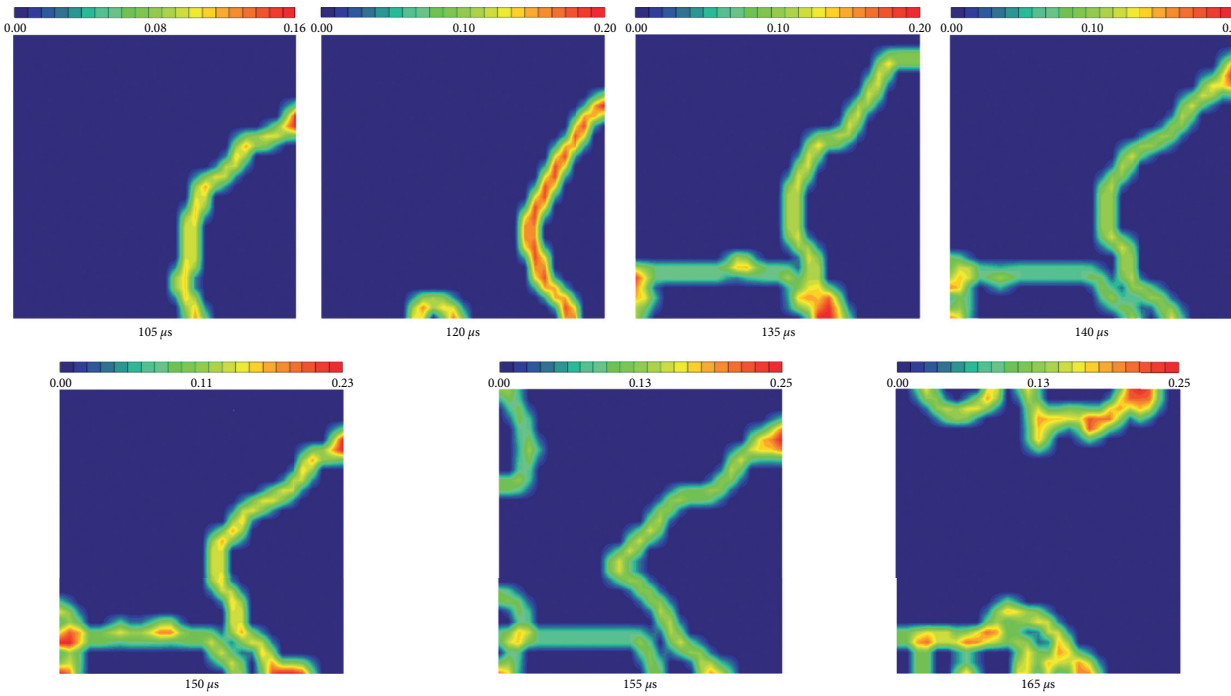

(a)

Figure 10: Continued.

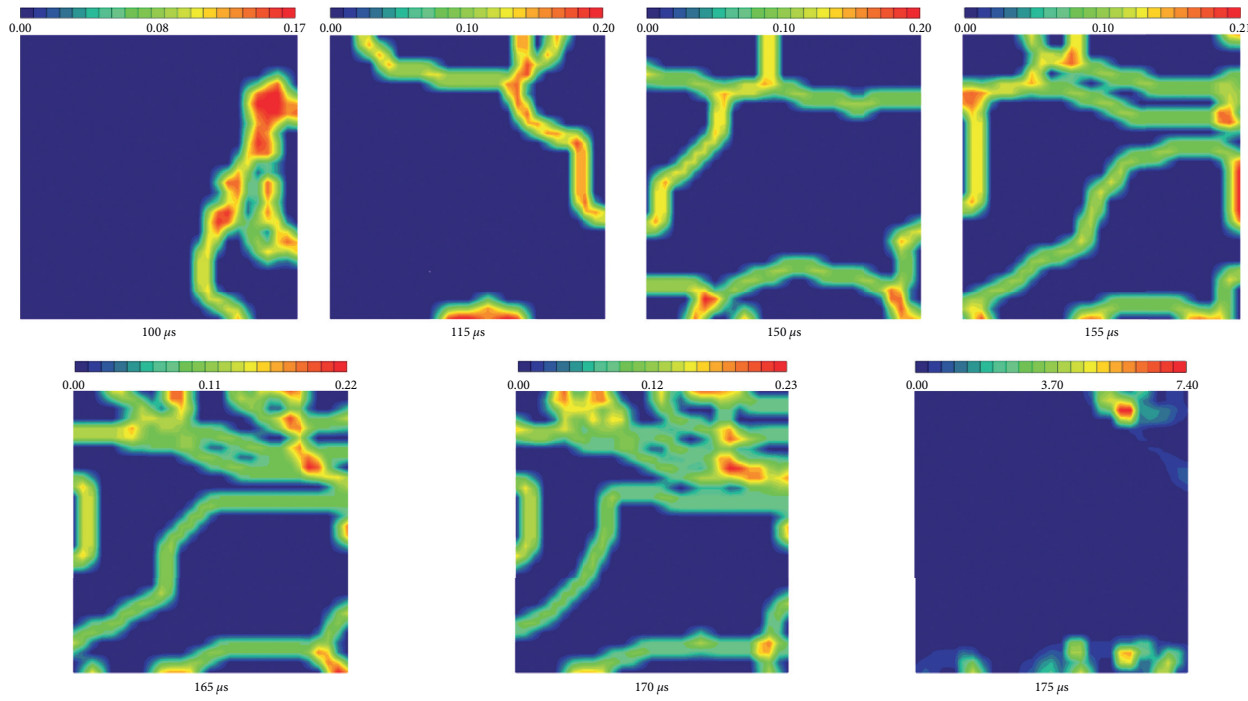

(b)

Figure 10: Maximum shear strain cloud diagram of layered composite rocks (9.8 m/s). (a) B⟶W sample. (b) W⟶B sample.

It can be seen in Figure 9 that, under the same stress wave, the macrocracks in layered composite rocks started to propagate from the white sandstone surface far away from the interface of the two-phase rock mass, gradually reaching the interface. When such cracks initiated from the white sandstone of the B⟶W sample and reached the interface, the stress at the crack tip was less than the strength of the weakened black sandstone [35]. As a result, the cracks were blocked when they developed into the interface. The black sandstone component experienced only the ejection of particles with no macrocracks and, thus, had good integrity. In contrast, more shear cracks developed in the W⟶B sample. The cracks developed from the white sandstone penetrated the interface of the two-phase rock mass, resulting in a higher degree of damage.

It can be seen from Figure 10 that, under the initial action of the stress wave, the maximum shear strain area in the B⟶W composite rocks exhibited an approximate V-shaped distribution. As the stress wave continued to act, the maximum shear strain concentration gradually increased. However, since the shear stress was less than the strength of the black sandstone, the latter underwent elastic deformation only. After the stress wave continued to act for 165 μs, the composite rocks were damaged, leading to the restoration of local elastic deformation. The maximum shear strain was mainly concentrated on the lower left and upper right sides of the observation area, corresponding to the propagation of shear cracks in the white sandstone of the B⟶W sample and the local particle ejection of the black sandstone. Compared with the B⟶W sample, the W⟶B sample had multiple areas of maximum shear strain concentration, most of which were located on the right side of the observation area, that is, in the white sandstone component. This implies that the deformation and failure of the W⟶B sample were more complicated than those of W⟶B one. After the stress wave acted for 175 μs, the composite rocks suffered severe compression and shear failure. The maximum shear strain value at the bottom and upper right side of the observation area was 7.4, corresponding to the development and propagation area of shear cracks in the W⟶B sample.

Based on the initiation and development of cracks on the surface of the composite rocks and the maximum shear strain zone evolution, the strength of each area of the composite rocks could be ranked as follows in the increasing order: white sandstone far away from the interface, white sandstone at the interface, black sandstone at the interface, and black sandstone far away from the interface. This ranking is consistent with theoretical analysis results. Other groups of tests showed similar damage characteristics.

3.4. Analysis of Failure Morphology and Fracture Characteristics. Broken parts of the tested samples were collected, and the failure morphologies of layered composite rocks under different impact velocities were analyzed and are summarized in Table 3.

It can be seen from Table 3 that, with increased impact velocity, the degree of sample fragmentation gradually intensified. The fragments of the rock sample transitioned from blocky to granular or even powdery forms. The degree of fragmentation of the white sandstone exceeded that of black sandstone, while the rock fragments at the interface

Table 3: Broken morphology of layered composite rock mass.

Impact velocity velocities ($m \cdot s^{-1}$)	B⟶W sample	W⟶B sample
7.2		
8.6		
9.8		
10.4		
12.6		

still existed in the form of combined bodies. When the impact velocity was small (7.2 ~ 8.6 m/s), the integrity of the composite rocks sample was good without the development of macrocracks and only had local granular tensile ejection. At the impact velocity of 9.8 m/s, the white sandstone reached the energy accumulation limit first. A single-slope shear failure occurred in the white sandstone component of the B⟶W sample, accompanied by local splitting failure. In contrast, the black sandstone component has good integrity without a macroscopic fracture surface. Different from the failure morphology of the B⟶W sample, the shear cracks in the white sandstone of the W⟶B sample crossed the interface of the two-phase rock mass and developed into the black sandstone, causing the layered composite rocks to undergo a shear failure. The splitting damage of composite rocks increased at high impact velocities (10 ~ 13 m/s). Under the staggered penetration of the cracks, the broken combined bodies at the interface were approximately cone-shaped. The larger the impact velocity, the smaller the size of the cone, indicating more severe damage to the sample.

To further analyze the crushing characteristics of layered composite rocks, standard sieves with sieve diameters of 31.5, 25, 20, 16, 10, 5, and 2.5 mm were selected according to the broken blocks' size characteristics, which were then screened and weighed. To intuitively reflect the crushing degree of the sample, the following formula was used to obtain the average particle size D_S of the broken rocks:

$$D_s = \frac{\sum \beta_i D_i}{\sum \beta_i}, \tag{13}$$

where D_i is the average size of broken rock fragments retained on screens of different apertures and β_i is the mass percentage of broken rocks with a screen aperture of D_i.

The crushed block's average crushing particle size can be used to compare the fragmentation degree of the layered composite rock samples in a simple and intuitive way, but it cannot directly reflect the distribution characteristics of crushed rock particles. In other words, the same Ds of broken rock mass does not mean that the mass of pieces on each screen is the same. However, the fractal dimension of rock specimens (D) can reflect the degree of rock fragmentation intuitively and quantitatively. Generally, the larger the fractal dimension is, the more and the smaller the volume of the broken block is, indicating that the specimen has a higher crushing degree. The distribution equation of the rock crushing degree can be obtained according to the mass-fragmentation relationship [36, 37]:

$$D = 3 - \alpha,$$

$$\alpha = \frac{\lg\left(M_{L_{eq}}/M\right)}{\lg L_{eq}}, \tag{14}$$

where M_{Leq} is the mass of broken rocks with the equivalent side length L_{eq}; M is the mass of broken rocks within the calculated size; D is the fractal dimension of the fragments; α is the slope value of M_{Leq}/M–L_{eq} in double logarithmic coordinates; M_{Leq}/M is the cumulative percentage of broken rocks with equivalent side length below L_{eq}. The performed calculation of the fractal dimension revealed that the fractal characteristics of composite rock fragments had phase-related patterns, which were not obvious in the entire size range. This phenomenon was also reported by other scholars [38, 39]. Therefore, to reduce the influence of discrete points on the slope and correlation coefficient of the lg (M_{Leq}/M) and lg (L_{eq}) fitting curves, we selected rock fragments within 2.5~31.5 mm to calculate the fractal dimension, as shown in Figure 11.

It can be seen in Figure 11 that, with increased incident energy, the fractal dimension of the composite rocks gradually increased, while the average particle size of the broken rocks gradually decreased. This indicates that the greater the incident energy, the more the broken rocks, the smaller the volume of broken rocks, and the higher the degree of fragmentation. When the incident energy was small, the average particle size of the broken rock of the W⟶B sample was small, and the fractal dimension was large. This implies that the W⟶B samples had a higher crushing degree under the same stress wave than B⟶W ones. But with an increase in incident energy, the two gradually became the same, which is not difficult to understand from an energy perspective. When the incident energy was low, the wave impedance matching effect on the stress wave propagation was stronger, resulting in more energy transmitted to the W⟶B sample with by the same incident wave. In addition, more stress waves were reflected

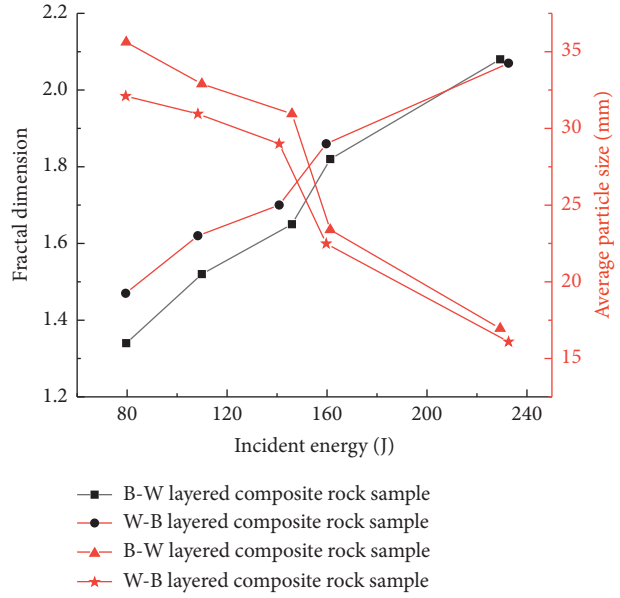

Figure 11: Relationship between the fractal dimension and average particle size with incident energy.

by the W⟶B sample when the stress wave propagated from the black sandstone to the transmitted bar. Microcracks in the composite rocks were fully developed under repeated actions of the stress wave, leading to a higher damage degree of the W⟶B sample. On the other hand, due to the low energy accumulation limit of the white sandstone, the white sandstone component of the composite rocks was damaged and failed first under the direct action of the stress wave. For the W⟶B sample, the stress wave directly acted on the white sandstone component through the incident bar, while the stress wave of the B⟶W sample was attenuated through the black sandstone before acting on the white sandstone. Therefore, under the same incident wave, the cracks in the white sandstone component of the W⟶B sample were more developed. At the interface of the two rock components, more cracks developed into the black sandstone rock, resulting in a higher degree of fragmentation of the composite rocks, increasing the fractal dimension and reducing the average particle size of the broken rocks. However, with an increase in incident energy, the black sandstone gradually reached its energy accumulation limit. The wave impedance matching effect was gradually weakened. Therefore, the degrees of fragmentation of the B⟶W and W⟶B samples gradually tended to be the same.

3.5. Study Limitations and Envisaged Follow-Up Steps. After the layered composite rocks were fractured, part of the broken bodies at the interface still existed in a combined form (Table 3), indicating that the fracture process of layered composite rocks was more complicated than that of a single body. When analyzing the deformation and failure of composite rocks, one should not analyze single rock masses separately but take account of their coupling and interface effects. In the follow-up study, the crack initiation,

propagation, and arrest at the interface will be explored and analyzed from the microstructure standpoint.

When the layered composite rocks deformed and failed, the two rock components affected each other's energy dissipation via the interface effect. The authors plan to determine the broken rock particle size distribution characteristics of single rocks and composite rocks under the same incident energy to further analyze the energy distribution patterns of composite rocks.

4. Conclusions

Using the SHPB test system and digital photogrammetry for deformation measurement, the stress wave propagation characteristics, energy evolution pattern, and failure characteristics of layered composite rocks were analyzed and studied. The main conclusions are as follows:

(1) Under the same impact velocity, affected by the wave impedance matching relationship, the stress wave propagation characteristics, energy dissipation pattern, deformation, and fracture characteristics of the W⟶B and B⟶W samples showed obvious differences. Compared with the B⟶W sample, the W⟶B sample had a smaller reflected wave and a larger transmitted wave. Also, the W⟶B sample had smaller reflected energy, a larger dissipated energy density, a larger fractal dimension, and a smaller average particle size of the broken rock. With an increase in impact velocity, the above differences gradually decreased and disappeared.

(2) Under the action of impact load, the energy evolution curve of layered composite rocks had obvious multistage behavior. The reflected energy and fragmentation energy density grew with incident energy approximately as quadratic functions. In the slow growth stage, composite rocks mainly experienced elastic deformation and stored a large amount of elastic energy. After entering the accelerated growth stage, the energy of composite rocks increased approximately linearly with time, and the deformation and failure of samples underwent qualitative changes. After the composite rocks failed, the value of each energy component tended to be stable.

(3) The deformation and failure of composite rocks was a gradual process. According to the initiation and development of surface cracks in the composite rocks and the evolution of the maximum shear strain area, the strength values of the composite rock areas could be ranked as follows in the increasing order: white sandstone far away from the interface, white sandstone at the interface, black sandstone at the interface, and black sandstone far away from the interface.

(4) The damage degrees and failure morphologies of the two-phase composite rocks were quite different. The white sandstone with lower strength and larger wave impedance was fractured more severely. Under high impact velocity, the black sandstone mainly underwent tensile splitting with local shear failure. In contrast, the white sandstone experienced shear failure with local tensile splitting.

Data Availability

The data used to support the findings of this study are available from the corresponding author upon request.

Conflicts of Interest

The authors declare that they have no conflicts of interest.

Acknowledgments

This work was financially supported by the National Key Research and Development Program of China (2016YFC0801402 and 2019YFC1904304) and the Institute of Energy, Hefei Comprehensive National Science Center, under Grant no. 19KZS203.

References

[1] N. Barton and E. Quadros, "Anisotropy is everywhere, to see, to measure, and to model," *Rock Mechanics and Rock Engineering*, vol. 48, no. 4, pp. 1323–1339, 2015.

[2] K. Winn, L. N. Y. Wong, and L. R. Alejano, "Multi-approach stability analyses of large caverns excavated in low-angled bedded sedimentary rock masses in Singapore," *Engineering Geology*, vol. 259, Article ID 105164, 2019.

[3] P.-T. Yeh, K. Z.-Z. Lee, and K.-T. Chang, "3D Effects of permeability and strength anisotropy on the stability of weakly cemented rock slopes subjected to rainfall infiltration," *Engineering Geology*, vol. 266, Article ID 105459, 2020.

[4] G.-R. Khanlari, M. Heidari, A.-A. Sepahigero, and D. Fereidooni, "Quantification of strength anisotropy of metamorphic rocks of the Hamedan province, Iran, as determined from cylindrical punch, point load and Brazilian tests," *Engineering Geology*, vol. 169, pp. 80–90, 2014.

[5] H. Kim, J.-W. Cho, I. Song, and K.-B. Min, "Anisotropy of elastic moduli, P-wave velocities, and thermal conductivities of asan gneiss, boryeong shale, and yeoncheon schist in korea," *Engineering Geology*, vol. 147-148, pp. 68–77, 2012.

[6] J. C. Jaeger, "Shear failure of anistropic rocks," *Geological Magazine*, vol. 97, no. 1, pp. 65–72, 1960.

[7] Y. M. Tien and M. C. Kuo, "A failure criterion for transversely isotropic rocks," *International Journal of Rock Mechanics and Mining Sciences*, vol. 38, no. 3, pp. 399–412, 2001.

[8] O. Saeidi, V. Rasouli, R. G. Vaneghi, R. Gholami, and S. R. Torabi, "A modified failure criterion for transversely isotropic rocks," *Geoscience Frontiers*, vol. 5, no. 2, pp. 215–225, 2014.

[9] S. L. Huang, X. L. Ding, A. Q. Wu, B. Lu, and Y. H. Zhang, "Study of multi-joint constitutive model of layered rock mass and experimental verification," *Chinese Journal of Rock Mechanics and Engineering*, vol. 31, no. 8, pp. 1627–1635, 2012.

[10] R. H. Cao, R. B. Yao, T. Hu, C. S. Wang, K. H. Li, and J. J. Meng, "Failure and mechanical behavior of transversely isotropic rock under compression-shear tests: laboratory testing and numerical simulation," *Engineering Fracture Mechanics*, vol. 241, Article ID 107389, 2021.

[11] G. Xu, X. Hu, R. Tang, and Z. Hou, "Fracture evolution of transversely isotropic rocks with a pre-existing flaw under

compression tests based on moment tensor analysis," *Acta Geotechnica*, 2021.

[12] V. Maazallahi and A. Majdi, "Numerical appraisal of rock mass anisotropy effect on elastic deformations of a circular tunnel," *Arabian Journal of Geosciences*, vol. 13, no. 13, p. 547, 2020.

[13] Y. M. Tien, M. C. Kuo, and C. H. Juang, "An experimental investigation of the failure mechanism of simulated transversely isotropic rocks," *International Journal of Rock Mechanics and Mining Sciences*, vol. 43, no. 8, pp. 1163–1181, 2006.

[14] B. W. Wang, Y. P. Li, C. H. Yang, W. Liu, and G. M. Zhang, "Influences of interface inclination on mechanical properties of composite bedded physical model material," *Rock and Soil Mechanics*, vol. 36, no. Supp.2, pp. 139–147, 2015.

[15] P. Shen, H. Tang, B. Zhang, Y. Ning, and C. He, "Investigation on the fracture and mechanical behaviors of simulated transversely isotropic rock made of two interbedded materials," *Engineering Geology*, vol. 286, Article ID 106058, 2021.

[16] S.-Q. Yang, P.-F. Yin, B. Li, and D.-S. Yang, "Behavior of transversely isotropic shale observed in triaxial tests and Brazilian disc tests," *International Journal of Rock Mechanics and Mining Sciences*, vol. 133, Article ID 104435, 2020.

[17] S. Chen, D. Yin, N. Jiang, F. Wang, and Z. Zhao, "Mechanical properties of oil shale-coal composite samples," *International Journal of Rock Mechanics and Mining Sciences*, vol. 123, Article ID 104120, 2019.

[18] Z. Yan, Y. Liu, F. Dai, and D. Hongbo, "Dynamic strength and cracking behaviors of single-flawed rock subjected to coupled static-dynamic compression," *Rock Mechanics and Rock Engineering*, vol. 53, no. 9, pp. 4289–4298, 2020.

[19] Z. Yan, Y. Liu, F. Dai, and D. Hongbo, "Experimental investigations of the dynamic mechanical properties and fracturing behaviors of racked rocks under dynamic loading," *Bulletin of Engineering Geology and the Environment*, vol. 79, pp. 5535–5552, 2020.

[20] Y. Liu, F. Dai, F. Dong, and N. Xu, "Experimental investigation on the fatigue mechanical properties of intermittently jointed rock models under cyclic uniaxial compression with different loading parameters," *Rock Mechanics and Rock Engineering*, vol. 51, pp. 47–68, 2018.

[21] X. Shang, Y. Wang, and R. Miao, "Acoustic emission source location from P-wave arrival time corrected data and virtual field optimization method," *Mechanical Systems and Signal Processing*, vol. 163, Article ID 108129, 2022.

[22] Y. Wang, X. Shang, and K. Peng, "Relocating mining microseismic earthquakes in a 3-D velocity model using a windowed cross-correlation technique," *IEEE Access*, vol. 8, pp. 37866–37878, 2020.

[23] P. Kang, H. Lv, Q. Zou, Z. Wen, and Y. Zhang, "Evolutionary characteristics of mode-I fracture toughness and fracture energy in granite from different burial depths under high-temperature effect," *Engineering Fracture Mechanics*, vol. 239, Article ID 107306, 2020.

[24] D. Li, Z. Han, Q. Zhu, Y. Zhang, and P. G. Ranjith, "Stress wave propagation and dynamic behavior of red sandstone with single bonded planar joint at various angles," *International Journal of Rock Mechanics and Mining Sciences*, vol. 117, pp. 162–170, 2019.

[25] Z. Han, D. Li, T. Zhou, Q. Zhu, and P. G. Ranjith, "Experimental study of stress wave propagation and energy characteristics across rock specimens containing cemented mortar joint with various thicknesses," *International Journal of Rock Mechanics and Mining Sciences*, vol. 131, Article ID 104352, 2020.

[26] F. Dai, S. Huang, K. Xia, and Z. Tan, "Some fundamental issues in dynamic compression and tension tests of rocks using split Hopkinson pressure bar," *Rock Mechanics and Rock Engineering*, vol. 43, no. 6, pp. 657–666, 2010.

[27] G. Gao, W. Yao, K. Xia, and Z. Li, "Investigation of the rate dependence of fracture propagation in rocks using digital image correlation (DIC) method," *Engineering Fracture Mechanics*, vol. 138, pp. 146–155, 2015.

[28] A. Mardoukhi, Y. Mardoukhi, M. Hokka, and V.-T. Kuokkala, "Effects of heat shock on the dynamic tensile behavior of granitic rocks," *Rock Mechanics and Rock Engineering*, vol. 50, no. 5, pp. 1171–1182, 2017.

[29] H. Li, H. W. Jing, and Q. Y. Zeng, "Development and application of digital photogrammetry software package for geotechnical engineering," *Chinese Journal of Rock Mechanics and Engineering*, vol. 25, no. 2, pp. 3859–3866, 2006.

[30] Q. Meng, M. Zhang, L. Han, H. Pu, and T. Nie, "Effects of acoustic emission and energy evolution of rock specimens under the uniaxial cyclic loading and unloading compression," *Rock Mechanics and Rock Engineering*, vol. 49, no. 10, pp. 3873–3886, 2016.

[31] C. J. Xia, H. P. Xie, Y. Ju, and H. W. Zhou, "Experimental study of energy dissipation of porous rock under impact loading," *Engineering Mechanics*, vol. 23, no. 9, pp. 1–5, 2006.

[32] Z. X. Zhang, S. Q. Kou, L. G. Jiang, and P.-A. Lindqvist, "Effects of loading rate on rock fracture: fracture characteristics and energy partitioning," *International Journal of Rock Mechanics and Mining Sciences*, vol. 37, no. 5, pp. 745–762, 2000.

[33] X. F. Xian and X. S. Tan, *Failure Mechanism of Layered Rock Mass*, Chongqing University Press, Chongqing, 1989.

[34] K. Yang, Z. Wei, L. T. Dou, X. L. Chi, W. J. Liu, and J. Q. Zhang, "Research on dynamic tensile energy evolution and fractal characteristics of water-bearing coal samples," *Journal of China Coal Society*, vol. 46, no. 2, pp. 398–411, 2021.

[35] K. Yang, W. J. Liu, L. T. Dou, X. L. Chi, Z. Wei, and Q. Fu, "Experimental investigation into interface effect and progressive instability of coal-rock combined specimen," *Journal of China Coal Society*, vol. 45, no. 5, pp. 1691–1700, 2020.

[36] H. P. Xie, J. N. Wang, and P. G. Qan, "Fractal characters of micropore evolution in marbles," *Physics Letters A*, vol. 218, no. 3-6, pp. 275–280, 1996.

[37] Y. Deng, M. Chen, Y. Jin, and D. Zou, "Theoretical analysis and experimental research on the energy dissipation of rock crushing based on fractal theory," *Journal of Natural Gas Science and Engineering*, vol. 33, pp. 231–239, 2016.

[38] T. Deng, L. D. Yang, and W. F. Han, "Influence of loading form on distribution of marble fragments," *Journal of Tong Ji University (Natural Science)*, vol. 35, no. 1, pp. 10–14, 2007.

[39] L. Shi, J. Y. Xu, E. L. Bai, and Z. G. Gao, "Research on impact fracture of rock based on fractal theory," *Journal of Vibration and Shock*, vol. 32, no. 5, pp. 163–166, 2013.

Hindawi
Shock and Vibration
Volume 2021, Article ID 4796500, 11 pages
https://doi.org/10.1155/2021/4796500

Research Article

Experimental Study of Gangue Layer Weakening with Deep-Hole Presplitting Blasting

Jianchi Hao,[1,2] **Lifeng Ren**,[1,2] **Hu Wen**,[1,2] **and Duo Zhang**[1,2]

[1]*College of Safety Science and Engineering, Xi'an University of Science and Technology, Xi'an 710054, Shaanxi, China*
[2]*Ministry of Education Key Laboratory of Western Mine Exploration and Hazard Prevention, Xi'an University of Science and Technology, Xi'an 710054, Shaanxi, China*

Correspondence should be addressed to Lifeng Ren; lifengrr@126.com and Hu Wen; wenh@xust.edu.cn

Received 21 July 2021; Accepted 16 October 2021; Published 10 November 2021

Academic Editor: Mickael Lallart

Advances in coal mining technology and an increase in coal output are resulting in increasingly challenging conditions being encountered at coal seams. This is particularly so at thin coal seams, where a large number of hard rock layers known as gangue are often present, which seriously affect the normal operation of the shearer and reduce coal output. Therefore, the effective weakening of hard gangue layers in a coal seam is crucial to ensure that the shearer operates effectively and that coal output is maximized. In this paper, the weakening effect of deep-hole presplitting blasting technology on the hard gangue layer in a coal seam is studied via a similar simulation. Four test schemes are designed: (1) A blasting hole spacing of 200 mm with the holes offset vertically. (2) A blast hole spacing of 300 mm with the holes offset vertically. (3) A blast hole spacing of 200 mm with the holes parallel to the gangue layer. (4) A blasting hole spacing of 200 mm with the holes offset vertically and initiation of interval blasting. The effect of the different blasting hole spacings and arrangements and different detonation methods on the weakening of coal seam clamping by gangue is studied, and the best configuration is identified. This improves the effect of weakening the coal gangue layer by deep-hole presplitting blasting.

1. Introduction

Intensive coal production is causing mining operations to move to coal seams under increasingly adverse environmental conditions, significantly increasing the difficulty of coal mining [1, 2]. For example, when mining thin coal seams with hard gangue layers, the hardness of the gangue layer impedes the shearer from cutting normally. Usually, this problem is addressed by weakening the gangue layer of the working surface using traditional blasting techniques. However, sometimes the blasting distance is short, the hole is shallow, and the workload is heavy. Ordinary blasting cannot effectively weaken the gangue layer, resulting in low recovery efficiency at the working face and potential safety risks [3–5]. Therefore, the key to ensuring smooth mining of hard coal seams with thin hard layers is finding a way to safely and efficiently weaken the gangue layer.

Deep-hole presplitting blasting technology, which can be used to enhance the permeability of a coal seam to promote gas extraction [6–12], can also be used to control hard interlayers in the coal seam [13, 14]. Carrying out this type of blasting in the working face can precrack the gangue in the coal body into small blocks, destroying its integrity and making it looser, and so reduce resistance to the shearer during coal cutting and ensure the smooth progress of mining [15, 16]. In this paper, deep-hole presplitting blasting is carried out in similar simulation tests that vary the spacing of the blasting holes and the mode of initiation and the blasting parameters are optimized to improve the weakening effect of deep-hole presplitting blasting on coal seam gangue layers.

2. Test Principles

Deep-hole presplitting blasting technology makes use of a detonation wave and the high-temperature, high-pressure gas produced by the explosion to cause deformation,

loosening, and crack formation in coal and rock around the blasting hole [17–20].

Immediately after the explosion, the wall of the blasting hole is instantaneously subjected to high pressure. The pressure then slowly drops. This process involves the following two effects of blasting [21]: the action of stress waves [22–25] and a quasi-static pressure process [26–29].

2.1. Principles of Simultaneous Blasting at Two Adjacent Holes

2.1.1. Stress-Enhancement Zone. When detonations are made in two adjacent blasting holes simultaneously, the stress waves released will meet and superimpose between the two holes and additional tensile stress will be generated in the vertical direction, as shown in Figure 1(a), thereby forming a tensile stress-enhancement zone, zone I in Figure 1(b).

When detonations are made in adjacent holes at the same time, the gas generated by the explosion can keep the two holes in a high-pressure, high-temperature, quasi-static pressure state for a long time. The stress superposition effect will occur everywhere along the line connecting the two holes, leading to the emergence of a stress-enhancement zone. Cracks are more likely to occur in the stress-enhanced area.

2.1.2. Stress-Reduction Zone. As shown in Figure 1(b), with simultaneous detonation at adjacent holes, a second zone between the two holes is affected by the detonation waves. A counteracting phenomenon of radial compressive stress and tangential compressive stress is generated, thus forming a pressure-reduction zone. It can be seen that large blasting products are more likely to be produced in this zone.

2.2. Principles of Interval Blasting between Two Adjacent Holes. In interval blasting, blasting hole B in Figure 1(b) acts as a control hole for blasting hole A, increasing the auxiliary-free surface of the blasting. When the stress wave reaches the free surface, it will be reflected to form a tensile stress wave. When the intensity of the tensile stress wave is greater than the tensile strength of the rock, the Hopkinson effect is produced. At the same time, the reflected waves in the coal body and the stress concentrations at the tip of the crack overlap one another, thereby expanding the range of the fracture zone. At detonation at blasting hole B, the explosion cavity formed by blasting hole A also functions as a control hole [30, 31]. The mechanical model for a control hole is shown in Figure 2.

In Figure 2,

$$\sigma_x = -a^2\frac{P_c}{L^2},$$
$$\sigma_{\theta c} = -a^2\frac{P_c}{L^2}. \tag{1}$$

Here, σ_x denotes the control hole radial stress, $\sigma_{\theta c}$ denotes the control hole tangential stress, a denotes the control hole radius, P_C denotes the explosive pressure, L denotes the hole spacing, r denotes the polar radius, and θ denotes the polar angle.

The tangential stress of the rock mass around the control hole can be expressed by the following formula:

$$\sigma_{\theta c} = S\left(1 + \frac{3a^4}{r^4}\right)\cos 2\theta, \tag{2}$$

where S is the explosive stress, MPa.

When $r = a$ and $\theta = 0, \pi$, the tensile stress value reaches its maximum value. This maximum value occurs at two points, A and B, as shown in Figure 2. The maximum value is

$$\sigma_{\theta c\max} = 4S. \tag{3}$$

From the above analysis, it can be seen that tensile stress is at its highest at points A and B on the borehole wall in Figure 2, resulting in the phenomenon of stress concentration. When the tensile strength of the rock mass is less than the tensile stress, initial cracks will occur at points A and B in the coal mass. When the tensile strength of the rock mass is always less than the tensile stress, the cracks will propagate until the tensile strength of the rock mass is greater than the tensile stress.

3. Similar Simulation Test System

A similar simulation uses an average coal seam thickness of 1.5 m on the working face and an average gangue layer thickness of 0.3 m as a reference. Variation in the stress and strain of the gangue layer during the entire deep-hole presplitting blasting process is analyzed, and the development law of blasting-induced cracks is explored.

A self-built three-dimensional similar simulation testing system, as shown in Figure 3, was used to measure the change in the explosion stress wave during blasting, the strain condition of the gangue layer, and the development of cracks after blasting.

The solid circle at the interface between the coal seam and the gangue layer in Figure 4 shows the position of the blasting hole in the test. The cubes in the gangue layer represent the specific positions where the strain bricks are buried.

The principal strain and principal stress can be calculated with the following formula [32]:

$$\varepsilon_{12} = \frac{\varepsilon_0 + \varepsilon_{90}}{2} \pm \sqrt{(\varepsilon_0 - \varepsilon_{90})^2 + (2\varepsilon_{45} - \varepsilon_0 - \varepsilon_{90})^2},$$
$$\sigma_{12} = \frac{E}{2}\left[\frac{\varepsilon_0 + \varepsilon_{90}}{1-\nu} \pm \frac{1}{1+\nu}\sqrt{(\varepsilon_0 - \varepsilon_{90})^2 + (2\varepsilon_{45} - \varepsilon_0 - \varepsilon_{90})^2}\right]. \tag{4}$$

Here, ε_0 is the 0° strain gauge strain; ε_{45} is the 45° strain gauge strain; ε_{90} is the 90° strain gauge strain; E is the elastic modulus of the material-the elastic modulus of the similar material used for the gangue layer = 600 MPa; and ν is Poisson's ratio of the material, $\nu = 0.2$.

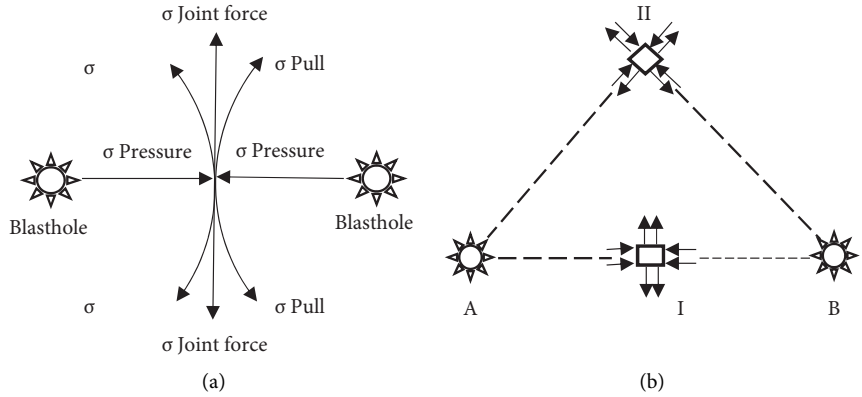

Figure 1: Stress analysis: (a) stress-enhancement zone and (b) stress-reduction zone.

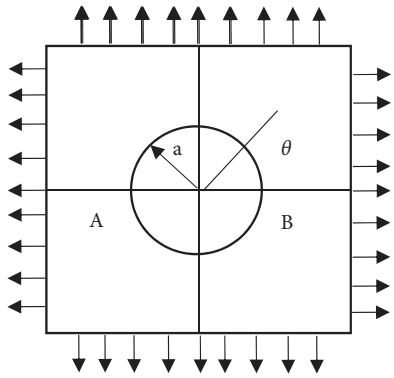

Figure 2: Model of control hole mechanics.

4. Similarity Criteria and Ratios of Similar Materials

4.1. Similar Criteria. The theoretical basis of similar simulation tests is the similarity principle. Generally, there are two conditions: (1) the existence of geometric similarity, similar motion, similar stress, similar boundary conditions, etc., and (2) a specific proportional relationship between the physical parameters of the similarity model and the simulated object [32–34]. The similarity criteria used in this experiment are as follows:

(1) Geometric similarity:

$$\alpha_L = \frac{L_p}{L_m}, \tag{5}$$

where α_L is the geometric similarity ratio between the prototype and the model; L_p is the generalized length of the prototype; and L_m is the generalized length of the model.

For this test, geometric similarity ratio between the prototype and the model α_L is 10.

(2) Volume-weight ratio:

$$\alpha_\gamma = \frac{\gamma_p}{\gamma_m}, \tag{6}$$

where α_γ is the volume-weight ratio of the prototype to the model; γ_p is the average density of the prototype rock formation, taken as 2.5 g/cm^3; and γ_m is the average density of the model material. Generally, γ_m is suitable for 1.5~1.8g/cm^3. $\gamma_m = 1.5 g/cm^3$ is taken in this model.

(3) Similar stress:

$$\alpha_\sigma = \frac{\gamma_p}{\gamma_m}\alpha_L = \alpha_\gamma \alpha_L, \tag{7}$$

where α_σ is the stress similarity ratio.

From (7), $\alpha_\gamma = 2.5/1.5 = 3/5$ and $\alpha_L = 10$. So, $\alpha_\sigma = 5/3 \times 10 = 16.67$.

Thus, the similarity ratio of the tensile strength σ_t, the compressive strength σ_c, the flexural strength σ_f, the shear strength σ_s, and the elastic modulus E of the material is 16.67.

4.2. Proportions of Similar Simulated Materials. The distribution of the coal seam, top floor, and lining layer at the on-site working face is used as the reference object of the test to simulate an actual coal-rock mass that is 5 m long, 5 m wide, and 6 m high. The similarity ratio is 1 : 10. In order to make the experiment more realistic, the distribution shown in Figure 5 was adopted for the experiment.

A large number of references were gathered that discuss similar simulated materials and the stress-strain-related parameters of coal and rock masses [35, 36]. Appropriate parameters relating to the coal seam, roof, and bottom plate were determined and are shown in Table 1. Of particular note is that the compressive strength of the sandwiched gangue layer is 6 MPa.

5. Results and Discussion

5.1. Test Design. In order to improve the gangue layer weakening effect, as well as utilize the stress wave generated by blasting and the expansion of the explosive gas, the blasting holes can be arranged in a vertically staggered manner. The advantage of this arrangement is that the shear stress generated by stress wave superposition is fully utilized and can break up the gangue layer more effectively. Four conditions were tested:

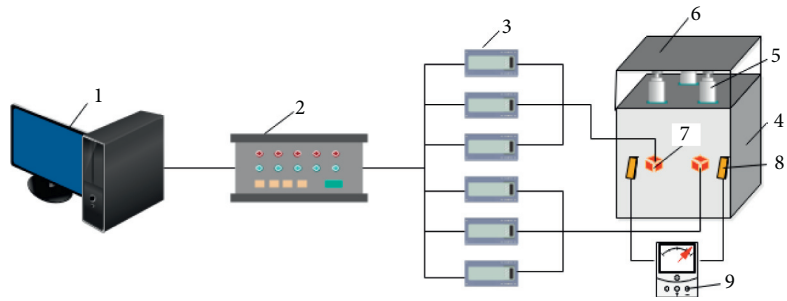

Figure 3: Ultradynamic test system. (1) Computer; (2) super-dynamic strain gauge; (3) sensor; (4) test box; (5) hydraulic jack; (6) steel return plate; (7) strain brick; (8) copper sheet; and (9) ohmmeter.

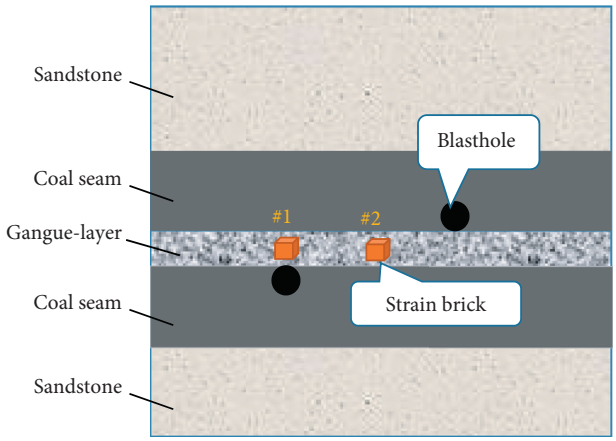

Figure 4: Positions of embedded strain bricks.

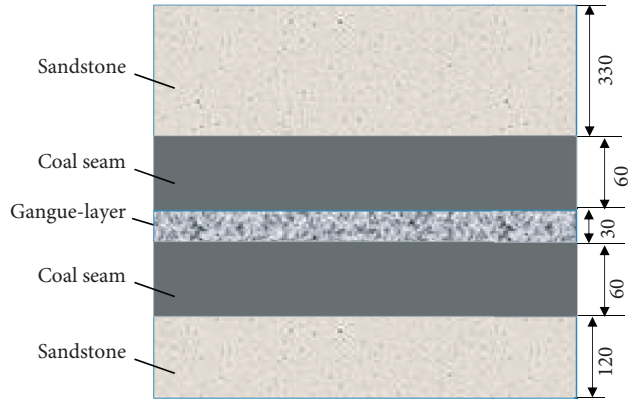

Figure 5: Distribution of rock layers in the model.

(1) A blasting hole spacing of 200 mm, staggered upper and lower holes, and simultaneous detonation at the two holes

(2) A blasting hole spacing of 300 mm, staggered upper and lower holes, and simultaneous detonation at the two holes

(3) A blasting hole spacing of 200 mm, the orientation of the line connecting the blasting holes parallel to that of the gangue layer, and simultaneous detonation at the two holes

(4) A blasting hole spacing of 200 mm, staggered upper and lower holes, and initiation of interval blasting at the two holes

5.2. Test Results

5.2.1. Test 1. Test 1 includes a hole spacing of 200 mm, vertically offset blasting holes, and simultaneous detonation.

(1) Stress and Strain Analysis. The principal stress and strain curves of the strain bricks were obtained by data processing and are shown in Figure 6.

It can be seen from Figure 6 that the maximum principal stress and strain at strain brick #1 both occur at around 40 μs; the maximum principal stress is 11.53 MPa, and the maximum principal strain is 0.032 m. These maxima both occur at around 110 μs at strain brick #2; the maximum principal stress is 30.66 MPa, and the maximum principal strain is 0.096 m.

Strain brick #1 is located in the gangue layer near the blast hole, for which observation and analysis indicate that it is mainly affected by the blast stress wave and the strain produced by fissures around the blasting hole. Strain brick #2 is located in the center of the line connecting the two adjacent blasting holes. More obvious stress concentration arises here due to the tangential stress caused by the superposition of the stress waves from the two blasting holes. The results show that the maximum principal stresses at both strain bricks are far greater than the 6 MPa compressive strength of the gangue layer and are thus able to play a role in weakening it; the maximum principal strain at strain brick #2 is about 3 times than that at strain brick #1.

(2) Resistivity Change Analysis. Changes in the resistance value can be taken as a reflection of the development of cracks through blasting. Before blasting, cracks have not yet developed and the cavity area has not been formed, so conductivity is good. After blasting, a large number of cracks and holes have been formed, so conductivity is poor. The resistance value measured using an ohmmeter was 2.3 MΩ before blasting and 8.1 MΩ after blasting. Thus, the resistance value was increased by a substantial amount, 252%, by blasting. This confirms that blasting generated a large number of cracks in the gangue layer.

Table 1: Proximate analyses of the sample.

Lithology	Thickness (mm)	Compressive strength (MPa)	Average density (g/cm^3)	Similar material ratio (cement: sand: coal powder: lime: gypsum: water)
Roof sandstone	330	3.2	1.52	0 : 7:0 : 0.5 : 0.5 : 0.8
Floor sandstone	120	3.2	1.52	0 : 7:0 : 0.5 : 0.5 : 0.8
Coal seam	120	0.6	0.83	0 : 5:2 : 0.7 : 0.3 : 0.8
Gangue layer	30	6.0	1.73	1.6 : 3.5 : 0:0 : 0.2 : 0.6

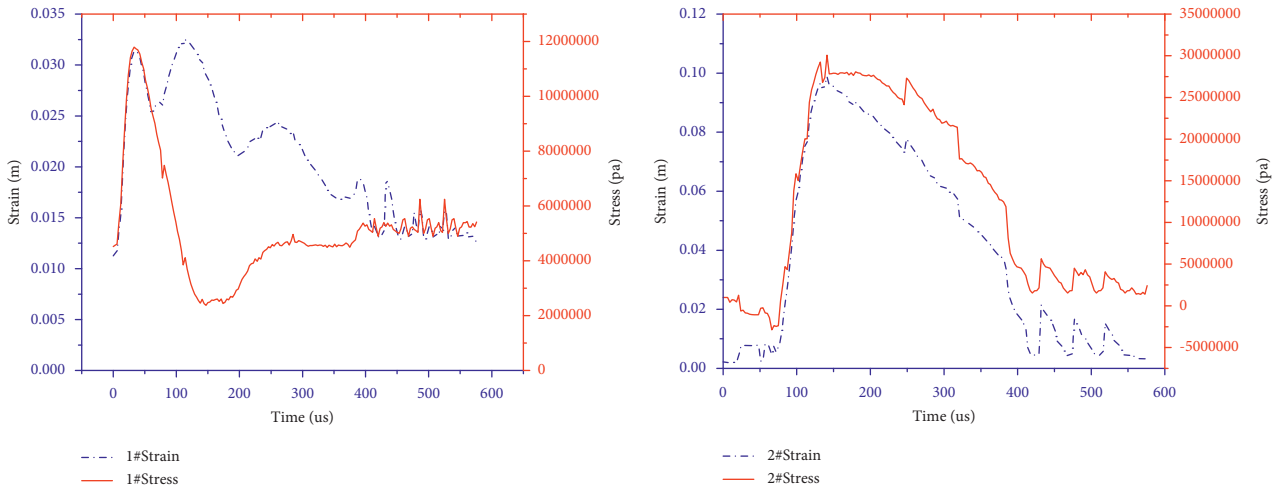

(a) (b)

Figure 6: Test 1 stress and strain curves of (a) strain brick #1 and (b) strain brick #2.

(3) Development of Cracks. The coal and rock mass are subjected to a blast shock wave during blasting, and there is clear displacement of the free surface. By removing the upper sandstone and the upper half of the coal seam, we can view the damage and the range of cracks produced during blasting directly. Figure 7 shows that a large number of cracks have formed and developed at the central point between the two blasting holes. In the coal seam within a certain range of the blasting holes, a cavity and a compressed comminution zone are also formed.

5.2.2. Test 2. Test 2 includes a hole spacing of 300 mm, vertically offset blasting holes, and simultaneous detonation.

(1) Stress and Strain Analysis. The principal stress and strain curves under these conditions are shown in Figure 8.

It can be seen from Figure 8 that the maximum principal stress and strain at strain brick #1 both occur at around 200 μs; the maximum principal stress is 11.23 MPa, and the maximum principal strain is 0.038 m. These maxima appear at around 240 μs at strain brick #2; the maximum principal stress is 27.66 MPa, and the maximum principal strain is 0.086 m.

As in test 1, the maximum principal stress at both strain bricks is far greater than the compressive strength of the gangue layer and so it is able to play a role in gangue layer weakening. In addition, there is a higher stress concentration in strain brick #2, as the maximum principal strain value is about 2 times that in strain brick #1.

(2) Resistivity Change Analysis. The resistance value was 2.9 MΩ before the experiment and 9.5 MΩ after blasting. This was again a large increase in resistance through blasting, 228%, and it shows that a large number of cracks were produced inside the gangue layer through blasting.

(3) Development of Cracks. It can be seen from Figure 9 that the locus of crack occurrence and development is the central point between the two blasting holes. The displacement of the free surface of blasting is obvious. A cavity and a compressive crushing zone are formed in the coal seam within a certain range of the blasting holes.

5.2.3. Test 3. Test 3 includes a hole spacing of 200 mm, blasting holes arranged parallel to the gangue layer, and simultaneous detonation.

The positions of the blasting holes and of the embedded strain bricks under these conditions are shown in Figure 10.

(1) Stress and Strain Analysis. The principal stress and strain curves of the two strain bricks were obtained through data processing and are shown in Figure 11.

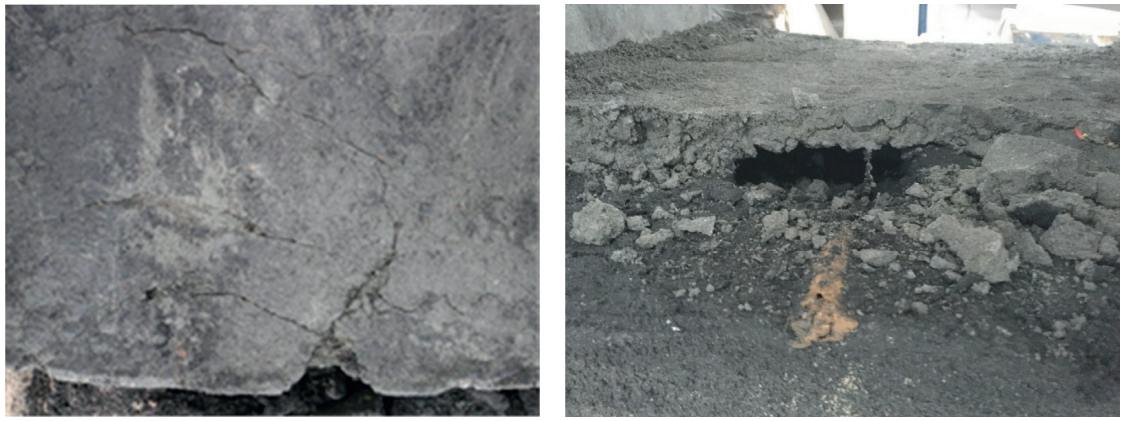

(a) (b)

Figure 7: Test 1 cracks after blasting. (a) Test 1 cracks formed after blasting. (b) Test 1 cavity zone formed after blasting.

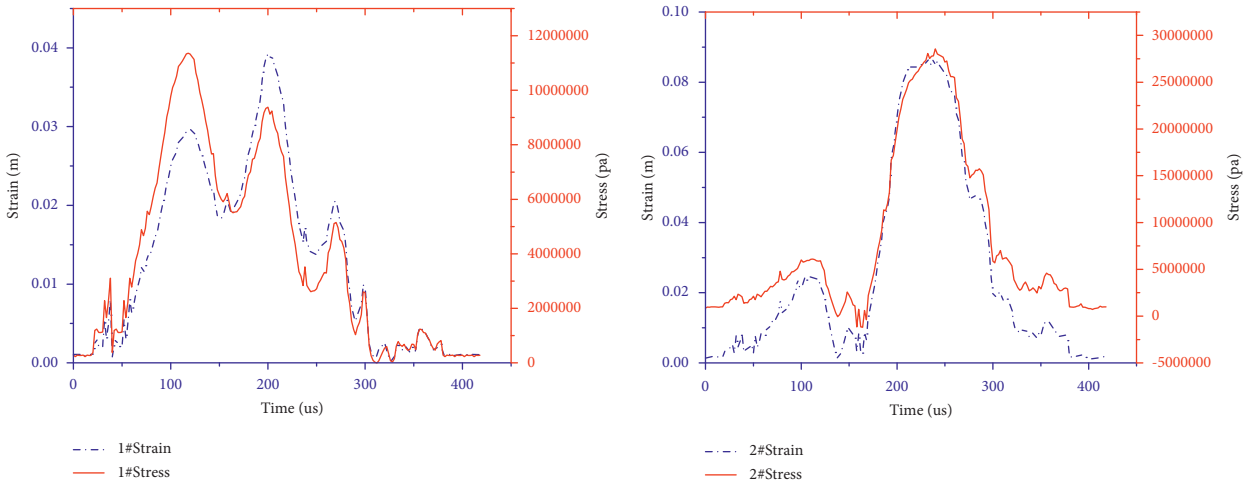

(a) (b)

Figure 8: Test 2 stress and strain curves for (a) strain brick #1 and (b) strain brick #2.

It can be seen from Figure 11 that the maximum principal stress and strain at strain brick #1 both occur at around 75 μs; the maximum principal stress is 7.93 MPa, and the maximum principal strain is 0.016 m. The maximum principal stress and strain occur at around 100 μs for strain brick #2; the maximum principal stress is 10.88 MPa, and the maximum principal strain is 0.031 m.

The maximum principal stress at both the strain bricks is only slightly higher than the compressive strength of the gangue layer (6 MPa), so little weakening of the gangue layer will be achieved. The maximum principal strain in strain brick #2 reaches about 2 times than that in strain brick #1, indicating that it is affected by tangential stress due to the superposition of the stress waves of the two blasting holes, leading to stress concentration.

(2) Resistivity Change Analysis. The resistance value was 3.2 MΩ before blasting and 7.1 MΩ after blasting, constituting an increase of 122% in resistivity with blasting. This shows that blasting caused a few cracks to form in the gangue layer.

(3) Development of Cracks. Figure 12 shows that cracks have occurred and developed at the central point between the two blasting holes, but that there are fewer of them than in tests 1 and 2. There is an obvious displacement of the free surface, and a cavity and a compressive crushing zone are formed in the coal seam within a certain range of the blasting holes.

5.2.4. Test 4. Test 4 includes a hole spacing of 200 mm, vertically offset blasting holes, and an interval between detonations.

(1) Stress and Strain Analysis. The principal stress and strain curves under these conditions are shown in Figure 13.

It can be seen from Figure 13 that the maximum principal stress and strain at strain brick #1 both occur at

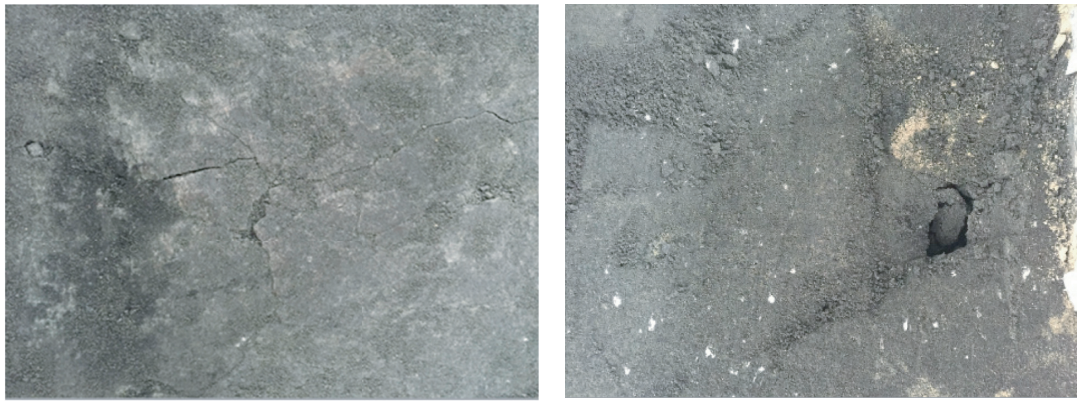

(a) (b)

Figure 9: Test 2 cracks after blasting. (a) Test 2 cracks formed after blasting. (b) Test 2 cavity zone formed after blasting.

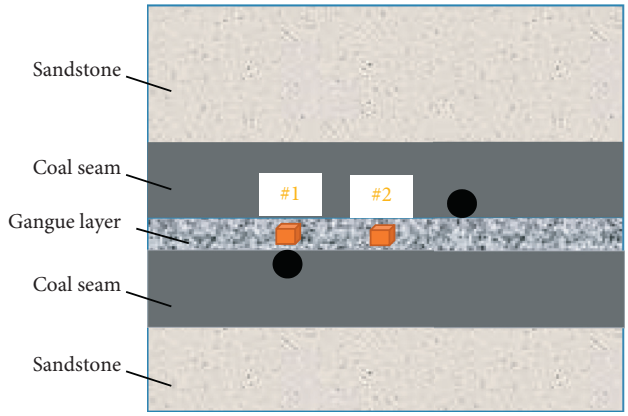

Figure 10: Arrangement of blasting holes and of embedded strain bricks for test 3.

around 220 μs; the maximum principal stress is 9.83 MPa, and the maximum principal strain is 0.037 m. These maxima occur at around 230 μs for strain brick #2; the maximum principal stress is 17.88 MPa, and the maximum principal strain is 0.022 m.

There is little evidence for stress concentration near strain brick #2. This is because when interval initiation is used, the gangue layer near strain brick #2 is not affected by the tangential stress caused by the superposition of the stress waves of the two blasting holes. The maximum principal stress at the two strain bricks is much higher than the 6 MPa compressive strength of the gangue layer, so gangue layer weakening can be achieved. Because there is no stress superposition, the strain value at strain brick #2 is slightly lower than at strain brick #1, which is adjacent to a blasting hole.

(2) Resistivity Change Analysis. The resistance value was 2.8 MΩ before blasting and 7.8 MΩ after blasting, an increase of 178%. This shows that a large number of cracks were produced inside the gangue layer through blasting.

(3) Development of Cracks. It can be clearly seen from Figure 14 that cracks were generated and developed along the line connecting the two blast holes and close to the second-detonation blast hole and that cracking is obvious. The blasting-free surface shows a large displacement. A cavity and compression crushing zone have also been formed in the coal seam within a certain range of the blasting hole.

5.3. Comparative Analysis of the Experimental Data. The following conclusions can be drawn from analysis of stress and strain, the change rate of resistance, and crack development in the various similar simulation tests:

(1) When comparing test 1 with test 2, the test variable is the spacing of the blast holes. The stress wave produced by blasting at two holes overlaps at the midpoint of the line connecting the holes, causing the maximum principal stress and maximum principal strain to be reached at that point and resulting in the formation of a large number of cracks. An increase in the blasting hole spacing results in lower maximum principal stress and maximum principal strain values. Moreover, little change is seen in the maximum principal stress and maximum principal strain generated near a blasting hole, indicating that the adjacent blasting hole has little influence on the effect of blasting near the hole.

(2) A comparison of test 1 and test 3 shows that the maximum principal stress and maximum principal strain are reached at the midpoint of the line connecting the two blasting holes, no matter which hole arrangement is adopted. This is because stress waves are superimposed at that point, resulting in stress concentration. However, because shear stress is generated in test 1, these maxima are significantly higher than they are in test 3. It can be seen staggering boreholes achieves a higher degree of weakening of gangue layers than does arranging them in parallel to the gangue bedding. Therefore, a staggered hole arrangement is recommended to achieve maximum weakening of gangue layers in a coal seam.

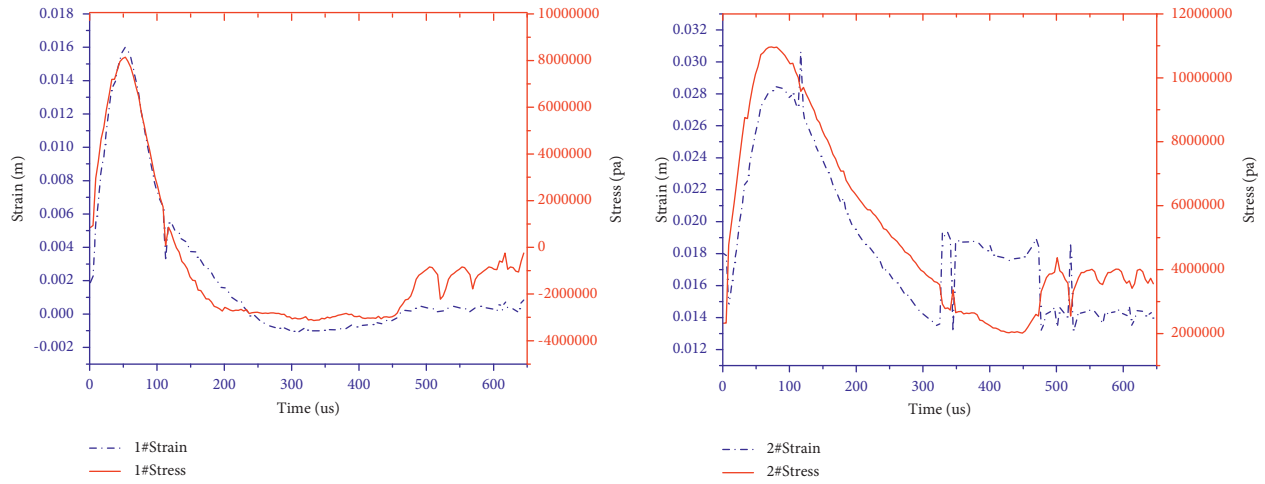

(a) (b)

Figure 11: Test 3 stress and strain curves of (a) strain brick #1 and (b) strain brick #2.

(a) (b)

Figure 12: Test 3 cracks after blasting. (a) Test 3 cracks formed after blasting. (b) Test 3 cavity zone formed after blasting.

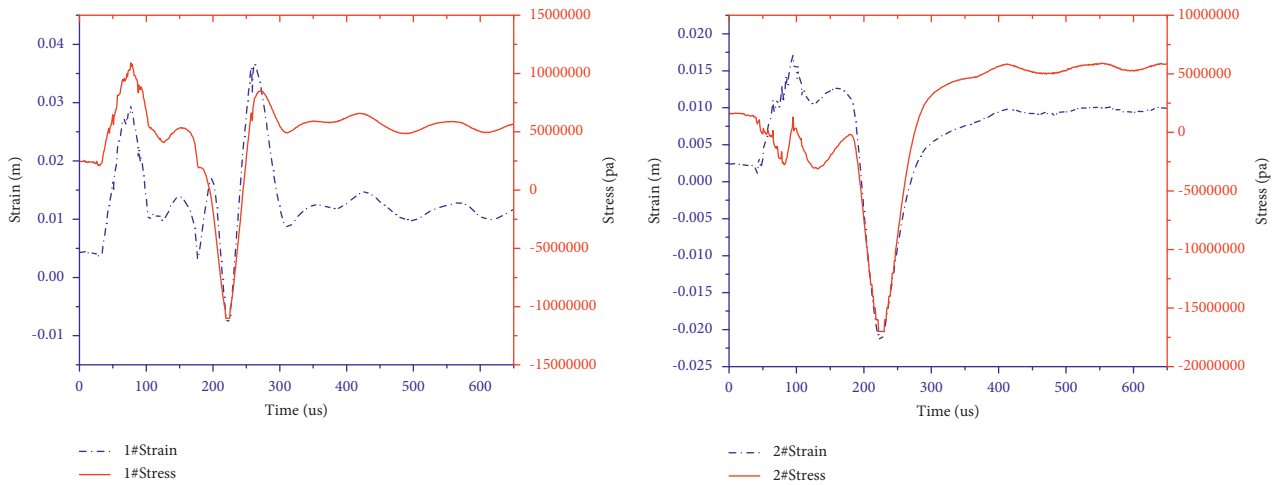

(a) (b)

Figure 13: Test 3 stress and strain curves of (a) strain brick #1 and (b) strain brick #2.

(a) (b)

Figure 14: Test 4 cracks after blasting. (a) Test 4 cracks formed after blasting. (b) Test 4 cavity zone formed after blasting.

(3) A comparison of test 1 and test 4 shows that maximum stress and strain are achieved at 130 μs with simultaneous initiation but slightly later at 220 μs with interval initiation. There is no stress concentration with interval initiation, and the maximum stress and strain values are lower than with simultaneous initiation, so simultaneous initiation is more effective for gangue weakening.

(4) In all of the tests, the maximum principal stress was greater than the compressive strength of the gangue-containing layer, indicating that all four approaches can achieve weakening of a gangue-containing layer.

6. Conclusion

Similar simulation tests in which deep-hole presplitting blasting was used to weaken coal gangue have allowed the following conclusions to be drawn:

(1) Maximum principal stress and maximum principal strain decrease with an increase in blasting hole spacing, and the time at which these values are reached increases. Little change, however, is seen in the maximum principal stress and maximum principal strain in the vicinity of the blast hole, which indicates that blasting at adjacent holes has little effect on the blasting hole wall.

(2) When detonation is simultaneous, the stress waves generated by the blasting of the two blasting holes are superimposed at the midpoint of the line connecting the two holes so that the maximum principal stress and maximum principal strain are reached at this point, resulting in the formation of a large number of cracks.

(3) When interval initiation is used, the postinitiation hole and the explosion cavity play a similar role as a control hole, but there is no obvious stress concentration between the two holes.

(4) Theoretical calculation was used to select appropriate parameters for similar simulation testing of deep-hole presplitting blasting. The effects of blasting under different parameter settings were compared using the method of controlling variables. This comparison shows that while arranging blasting holes in parallel with the gangue layer achieves the desired effect, it can lead to drilling difficulties in the process of weakening the gangue layer. Therefore, it is suggested that a staggered arrangement of boreholes be used as far as possible, as this allows shear stress to be utilized to break up the rocks more efficiently.

Data Availability

The figures, tables, and models data used to support the findings of this study are included within the article.

Conflicts of Interest

The authors declare that they have no conflicts of interest.

Acknowledgments

This work was supported by the National Natural Science Foundation of China (grant number: 51974240 and 52104217).

References

[1] P. N. Calder and J. N. Tuomi, "Control blasting at sherman mine," in *Proceedings of the 6th Annual Conference on "Explosives and Blasting Technique"*, pp. 312–330, Society of Explosives Engineers, Cleveland, OH, USA, 1980.

[2] F. Cai, Z. G. Liu, and C. Zhang, "Numerical simulation of improving permeability by deep-hole pre-splitting explosion in loose-soft and low permeability coal seam," *Journal of China Coal Society*, vol. 32, no. 5, pp. 499–503, 2007.

[3] S.-g. Cao, Y. Li, Y.-b. Liu, L.-q. Zhang, and A.-m. Xu, "Effectiveness analysis of methane-drainage by deep-hole controlled pre-splitting blasting for preventing coal and gas outburst," *Journal of Coal Science and Engineering*, vol. 15, no. 2, pp. 166–170, 2009.

[4] F. García Bastante, L. Alejano, and J. González-Cao, "Predicting the extent of blast-induced damage in rock masses," *International Journal of Rock Mechanics and Mining Sciences*, vol. 56, pp. 44–53, 2012.

[5] P. Gong, Y. Chen, Z. Ma, and S. Cheng, "Study on stress relief of hard roof based on presplitting and deep hole blasting," *Advances in Civil Engineering*, vol. 2020, Article ID 8842818, 12 pages, 2020.

[6] L. Ma, K. Li, D. Xiaohua, and S. Chinyanta, "Research on the effects of blasting vibration attenuation by pre-split crack with HT method," *Journal of Computer systems science and engineering*, vol. 31, no. 6, pp. 431–438, 2016.

[7] W. B. Guo, H. S. Wang, G. W. Dong, L. Li, and Y. G. Huang, "A case study of effective support working resistance and roof support technology in thick seam fully-mechanized face mining with hard roof conditions," *Sustainability*, vol. 9, pp. 29–35, 2017.

[8] G. Hu, X. B. Wang, and W. W. Wang, "Study on technology of increasing permeability of low gas permeability coal seam by long-drilling explosion," *Journal of Heilongjiang Institute of Science and Technology*, vol. 23, no. 2, pp. 159–162, 2013.

[9] P. Konicek, K. Soucek, L. Stas, and R. Singh, "Long-hole distress blasting for rock burst control during deep underground coal mining," *International Journal of Rock Mechanics and Mining*, vol. 61, pp. 141–153, 2013.

[10] C. J. Konya and A. Konya, "Effect of hole stemming practices on energy efficiency of comminution," *Journal of Energy Efficiency in the Minerals Industry*, pp. 31–53, 2018.

[11] J. X. Li, B. Q Lin, G. Q. Li, Q. Ye, and S. R. Xu, "The theory and application of loose blasting for increasing permeability and distress in long boreholes," *Journal of Coal Mine Safe*, vol. 433, pp. 52–54, 2010.

[12] W. Wang, Y. Z. Wei, M. G. Guo, and Y. Z. Li, "Coupling tenology of deep -HolePresplitting blasting and hydraulic fracturing enhance permeability technology in low -permeability and gas outburst coal seam: A case study in the no. 8 mine of Pingdingshan, China," *Advances in Civil Engineering*, vol. 2021, Article ID 5569678, 12 pages, 2021.

[13] Z. G. Liu, Y. H. Zhang, and Z. A. Huang, "Numerical simulating research on orifice pre-splitting blasting in coal seam," *Procedia Engineering*, vol. 45, pp. 322–328, 2012.

[14] J. C. Liu, H. T. Wang, Z. G. Yuan, and X. G. Fan, "Experimental study of pre-splitting blasting enhancing pre-drainage rate of low permeability heading face," *Procedia Engineering*, vol. 26, pp. 818–823, 2011.

[15] J. Liu, Z. G. Liu, J. H. Xu, K. Gao, and W. Zhou, "Application of deep borehole blasting on fully mechanized hard top-coal pre-splitting and gas extraction in the special thick seam," *International Journal of Mining Science and Technology*, vol. 25, pp. 755–760, 2015.

[16] J. S. Lee, S. K. Ahn, and M. Sagong, "Attenuation of blast vibration in tunneling using a pre-cut discontinuity," *Journal of Tunnelling and underground space technology*, vol. 52, pp. 30–37, 2016.

[17] Y. Lei, J. J. Liu, S. N. Zhang, W. Zhang, and H. D. Wang, "Contrast test of different permeability improvement technologies for gas-rich low-permeability coal seams," *Journal of Natural Gas Science and Engineering*, vol. 33, pp. 1282–1290, 2016.

[18] S. X. Cheng, Z. G. Ma, and P. Gong, "Controlling the deformation of a small coal pillar retaining roadway by non-penetrating directional pre -splitting blasting with a deep hole: a case study in Wangzhuang coal mine," *Energies*, vol. 13, no. 12, p. 3084, 2020.

[19] X. L. Li, Q. W. Hu, and X. B. Ma, "Experimental research on presplitting blasting of the final highwall of an opencast coal mine," *Journal of the Balkan Tribological Association,* vol. 22, no. 3, pp. 2857–2869, 2016.

[20] H. C. Sang, Y. Nakamura, and K. Kaneko, "Dynamic fracture process analysis of rock subjected to a stress wave and gas pressurization," *International Journal of Rock Mechanics and Mining Sciences*, vol. 41, pp. 433–440, 2004.

[21] P. K. Singh, M. P. Roy, and R. K. Paswan, "Controlled blasting for long term stability of pit-walls," *International International Journal of Rock Mechanics & Mining Sciences*, vol. 20, no. 70, pp. 388–399, 2014.

[22] Z. J. Sun, J. H. Li, and L. Ding, "Application of long-hole loose blasting in fully-mechanized mining," *Shanxi Coal*, vol. 12, pp. 55-56, 2011.

[23] Z. L. Wang, X. X. Chen, and S. R. Xing, "Study on stress field distribution characteristics under coal seam pre-splitting blasting," *Procedia Engineering*, vol. 84, pp. 913–919, 2014.

[24] Q. G. Sun, "Research on status quo and prevention counter measures of coal mine gas disaster in China," *Journal of China Coal*, vol. 40, no. 3, pp. 116–119, 2014, in Chinese.

[25] A. Thabet and D. Haldane, "Three-dimensional numerical simulation of the behavior of standard concrete test specimens when subjected to impact loading," *Journal of Computers and Structures*, vol. 79, no. 1, pp. 21–31, 2001.

[26] L. Wojtecki, M. J. Mendecki, W. M. Zuberek, and M. Knopik, "An attempt to determine the seismic moment tensor of tremors induced by distress blasting in a coal seam," *International Journal of Rock Mechanics and Mining Sciences*, vol. 83, pp. 162–169, 2016.

[27] X. G. Xie, T. Feng, and J. W. Yang, "Monitoring analysis of blasting shock effect motivating coal and gas outburst," *Journal of China Coal Society*, vol. 35, no. 2, pp. 255–259, 2010.

[28] X. L. Li, Q. W. Hu, X. B. Ma, K. G. Li, and J. Q. Xiao, "Experimental research on presplitting blasting of the final highwall of an opencast coal mine," *Journal of the Balkan Tribological Association,* vol. 22, no. 3, pp. 2857–2869, 2016.

[29] O. Yilmaz and T. Unlu, "Three-dimensional numerical rock damage analysis under blasting load," *Tunnelling and Underground Space Technology incorporating Trenchless Technology Research*, vol. 38, pp. 266–278, 2013.

[30] Y. Q. Zhang, H. Hao, and Y. Lu, "Anisotropic dynamic damage and fragmentation of rock materials under explosive loading," *International Journal of Engineering Science*, vol. 41, no. 9, pp. 917–929, 2003.

[31] P. S. Zhang and S. D. Liu, "Effect of explosive quake in working face on stability of laneway in coal mine," *Journal of Mining & Safety Engineering*, vol. 24, no. 2, pp. 208–211, 2007, in Chinese.

[32] J. X. Zhang, B. Y. Li, N. Zhou, and Q. Zhang, "Application of solid backfilling to reduce hard-roof caving and longwall coal face burst potential," *International Journal of Rock Mechanics and Mining Sciences*, vol. 88, pp. 197–205, 2016.

[33] Z. Y. Zhang, N. Zhang, and H. Shimada, "Optimization of hard roof structure over retained goaf-side gateroad by pre-split blasting technology," *International Journal of Rock Mechanics & Mining*, vol. 100, pp. 330–337, 2017.

[34] X. Y. Sun, G. G. Kou, and P. Q. Li, "Experimental study on similarity simulation of overburden movement under repeated mining," *Coal Technology*, vol. 37, no. 9, 2018.
[35] L. Ren, J. Deng, L. Ma, and J. C. Hao, "Effect of oxygen concentration on the oxidative thermodynamics and spontaneous combustion of pulverized coal," *ACS Omega*, vol. 6, no. 40, pp. 26170–26179, 2021.
[36] J. C. Hao, H. Wen, and L. Ma, "Theoretical derivation of a prediction model for CO_2 adsorption by coal," *ACS Omega*, vol. 6, no. 20, pp. 13275–13283, 2021.

Hindawi
Shock and Vibration
Volume 2021, Article ID 8451241, 11 pages
https://doi.org/10.1155/2021/8451241

Review Article

Damages of Underground Facilities in Coal Mines due to Gas Explosion Shock Waves: An Overview

Dezhi Ran, Jianwei Cheng, Rui Zhang, Yu Wang, and Yuhang Wu

School of Safety Engineering, China University of Mining and Technology, Xuzhou 221116, China

Correspondence should be addressed to Jianwei Cheng; cheng.jianwei@cumt.edu.cn

Received 19 July 2021; Accepted 18 October 2021; Published 30 October 2021

Academic Editor: Pengfei Wang

With coal mining depth increase, gas explosion accidents due to the high gas emission rates often occur which cause significant casualties and property damages. Among them, gas explosion shock waves not only can destroy the machines and equipment in mine roadways but also cause the failure of mine ventilation facilities resulting in secondary hazards. Thus, the mines' serious disasters could happen. For many years, researchers have already done a great lot of works to study damages caused by the impact of shock waves of the gas explosions in underground mines. Research results provide a baseline for judgments of hazard effects by explosions. In this paper, the formation mechanism of the gas explosion shock wave is introduced firstly. Then, the damages for underground facilities, such as mechanical equipment, roadway, and life-saving devices are summarized and reviewed. Finally, a brief discussion about the methods is given, and some preliminary suggestions are also listed for improvements in the future.

1. Introduction

Coal is one of the important natural resources in the world. With the increase of mining depth, both the gas pressure and content in the coal seam gradually increase, which lead to a surge of gas emission rate and result in frequent gas explosion accidents [1, 2]. In most cases, a gas explosion mainly causes high-temperature flames, high-pressure shock waves, and amounts of toxic gases. The gas explosion instantly produces a large number of high-temperature flames and disaster gases; these flames and gases could quickly spread in the underground confined space, which can cause miners' casualties. Moreover, the generated explosion shock wave overpressure can damage the mine ventilation facilities causing mine airflow disorder [3]. The destruction of the mine ventilation system could cause the secondary explosion generated by the propagation of high-temperature flames in underground mine tunnels. The greatest impact caused by high-pressure shock waves not only destroys the roadway but also brings difficulties for workers performing rescues. Therefore, it is particularly important to study the impact and consequence of gas explosion damage.

The study of the main kinetic damage of gas explosion shock waves and the propagation law of explosion shock waves in the tunnel with different characteristics and the influence of gas explosion on the network structure of mine ventilation system not only have important theoretical and practical values but also are crucial to the prevention and prediction of gas explosion disaster accidents. Given this point, it is very necessary to review the current stage of research on gas explosion shock waves in mines.

2. Gas Explosion Shock Waves

The harmful factors generated by gas explosions are mainly flame fronts, shock waves, and toxic and hazardous gases [4]. The explosive mixture formed in coal mines is essentially a mixture of air and coal gas, consisting primarily of methane and small amounts of ethane and other alkanes. Although most accidental gas explosions in coal mines are deflagrations, the worst-case scenario includes explosions that can be extremely destructive, generating explosion pressures of up to 10 MPa on reflection, which can destroy large amounts of equipment and facilities. And gas explosions can also cause secondary injuries, such as roof collapse accidents and

bracket smashing accidents. After the impact of high-temperature and high-pressure gas, the relatively confined space of the coal mine, gas density reduction, and water evaporation could again form a low-pressure area; after the conditions are ripe, the surrounding gas can fill this area causing secondary explosions to occur, resulting in the severity of the accident increased. Gas explosion shock airflow (also known as burst wind) can aggravate the casualties and equipment damage. Shock airflow, immediately after the shock wave, is generated by the rapid expansion of explosive gas products, and the impact of the shock wave on people and obstacles generated by the pressure is called the shock wave dynamic pressure.

2.1. Explosion Pressure. Underground coal mine gas explosion can produce a hugely destructive effect because the explosion occurs in the confined space of the coal mine and can form a larger explosion pressure than the free space. Gas explosion pressure can usually be divided into two parts, which are the explosion overpressure and dynamic pressure. Theoretical and experimental evidence is the fact that air shock wave damage to the target depends not only on the shock wave overpressure but also on the overpressure of the action time. Therefore, scholars mainly used to take into account the value of the overpressure and the positive pressure area of the action time of the specific impulse to measure the shock wave method.

2.1.1. Explosion Overpressure. The shock wave is a sharp change in the state parameters of the sudden jump surface; the shock wave propagates in the tunnel when the wave front surface reaches a certain point; the air pressure rises instantaneously and far exceeds the atmospheric pressure; at this time, the air pressure above the atmospheric pressure part is called overpressure. After reaching the peak, due to the propagation of the explosion, the explosion products sweep more and more air mass, and the expansion rate slows down, equivalent to a series of expansion waves followed by the shock wave so that the shock wave surges up and the pressure continues to decay. Thus, the overpressure is reduced to zero and then appears below the surrounding gas pressure, which leads to the occurrence of a secondary recoil phenomenon. Eventually, it backs up to the normal atmospheric pressure. With the increasing gas concentration in the mine tunnel, the peak pressure of the gas secondary explosion rises and then falls, and the maximum value is slightly greater than the equivalent concentration [5].

2.1.2. Explosive Dynamic Pressure. Explosive dynamic pressure is the shock wave behind the front of high-speed movement of the air medium flow formation of impact pressure, with obvious directionality. The gas explosion was generated by many gas products in the role of high-temperature rapid expansion, and shock waves together with the synergistic movement and the explosion shock waves continue to strengthen and speed up, resulting in shock waves, and waves after the explosion products break off and break off the shock wave with the energy obtained from the explosion products that continue to propagate along the roadway. After the propagation of the shock wave, the pressure rises, and the gas behind the wave flows under the action of inertia, forming a shock airflow, which is known as the burst wind [6]. Although the duration of the shock airflow is not long, the speed is generally up to 100 m/s or greater, and it can also make the formation of the impact on people and underground facilities and equipment to produce injury and damage.

2.2. Explosion Impulse. The specific impulse is directly determined by the overpressure versus time curve $P(t)$ of the air shock wave front and the positive pressure action time, where the magnitude of the positive specific impulse depends on the area enclosed by the positive pressure zone curve, and the magnitude of the negative specific impulse depends on the area enclosed by the negative pressure zone curve. The magnitude of the specific impulse can be obtained by the integral of the overpressure in time. We refer to the positive specific impulse by the specific impulse [7].

3. Gas Explosion Shock Wave Attenuation

Researchers' results are based on the gas explosion testing data conducted in the large size simulation tunnel. The decay model of the explosion shock wave overpressure is established. The relevant characterization parameters of the explosion shock wave are constantly corrected, researched to master the decay law of the shock wave overpressure in the experimental tunnel. Based on certain assumptions, the coupling equation of overpressure, air velocity, shock wave propagation velocity, and propagation distance after the decay of the strong shock wave of the gas explosion is established. It is found that the overpressure is inversely proportional to the propagation distance and roadway cross-sectional area, and the overpressure is proportional to the total energy released by a gas explosion. The air velocity and shock wave propagation velocity are inversely proportional to the square root of propagation distance and roadway cross-sectional area, and both of them are all proportional to the square root of the total energy of the gas explosion [8].

3.1. Mathematical Model of Gas Explosion Propagation. For gas explosion as a rapid combustion reaction, both mathematical models and experimental simulations need to satisfy the following equations.

The continuous equation is expressed in the following equation:

$$\frac{\partial \rho}{\partial t} + \frac{\partial (\rho u)}{\partial x} + \frac{\partial (\rho v)}{\partial y} + \frac{\partial (\rho w)}{\partial z} = 0. \quad (1)$$

The energy equation is expressed in the following equation:

$$\frac{\partial e}{\partial t} + u\frac{\partial e}{\partial x} + v\frac{\partial e}{\partial y} + w\frac{\partial e}{\partial z} = 0. \quad (2)$$

The momentum equation is expressed in the form of the following equation:

$$\frac{\partial u}{\partial t} + u\frac{\partial u}{\partial x} + v\frac{\partial u}{\partial y} + w\frac{\partial u}{\partial z} = -\frac{1}{p}\frac{\partial \rho}{\partial x},$$
$$\frac{\partial v}{\partial t} + u\frac{\partial v}{\partial x} + v\frac{\partial v}{\partial y} + w\frac{\partial v}{\partial z} = -\frac{1}{p}\frac{\partial \rho}{\partial y}, \quad (3)$$
$$\frac{\partial w}{\partial t} + u\frac{\partial w}{\partial x} + v\frac{\partial w}{\partial y} + w\frac{\partial w}{\partial z} = -\frac{1}{p}\frac{\partial \rho}{\partial z}.$$

The equation of state is expressed in the form of the following equation:

$$P = p(\rho, T) = \rho RT, \quad (4)$$

where, in equations (1)~(4), p is the pressure, MPa; t is the time, s; u, v, and w are the velocities in three coordinate directions, m/s; x, y, and z are right-angle coordinate system parameters, m; ρ is the fluid density, kg/m^3; T is the temperature, K; R is the gas constant; e is the specific energy, $e = p/(\gamma - 1) + \rho\ (u^2 + v^2 + w^2)/2$; and γ is the gas index.

3.2. Influencing Factors of Mine Gas Explosion Shock Wave. Gas explosion shock waves include overpressure and dynamic pressure; they can show regular decay with the propagation of the explosion in the shaft. When the gas explosion is in a mine tunnel, the shock wave just propagates along the direction of the tunnel. Coal mines have relatively confined space; then, there is the same distance of infinite space explosion when the shock wave is much larger. The main factors affecting the peak overpressure of the air shock wave are the total energy of the gas explosion, the cross-sectional area of the roadway, the initial state of the air, the roughness of the roadway, and the distance from the source of the explosion.

3.2.1. Total Energy of Gas Explosion E_0. The gas explosion energy comes from the heat of combustion reaction between gas and air; from the chemical equation of the reaction between CH_4 and O_2, 1 mol of CH_4 and 2 mol of O_2 reaction give off the energy of 882.6 kJ, according to the gas equation of state PV = nRT to get the molar volume of gas at room temperature and pressure of $V = \mathrm{nRT/P} = 24\mathrm{L} \times \mathrm{mol}^{-1}$. 1 m^3 of pure gas complete combustion (volume concentration of 9.5%) released heat is $Q\mathrm{e} = 1000/24 \times 882.6 = 3.68 \times 104$ kJ. Then, for the concentration of c and volume V of the gas-air explosive gas mixture, its complete combustion when the heat is released can be calculated according to the following formula:

$$E_0 = Q_e \times V \times c, \mathrm{kJ}. \quad (5)$$

3.2.2. Initial State Parameters of Air p_0, ρ_0. The shock wave is a strong compressional wave and is the result of the interaction and superposition of numerous weaker compressional waves. In the process of the shock wave along the roadway, the state parameters change abruptly, and the shock wave before and after the wave front surface of the state parameter changes has no continuity, accompanied by the generation of discontinuous between the new surface (shock wave front surface). To simplify the calculation, researchers often assume that the flow of gas explosion is a nonconstant flow (wave front surface state parameters change with time), and the atmospheric pressure of the underground air should be determined according to the actual situation in different coal mines.

3.2.3. The Cross-Sectional Area S and Hydraulic Diameter d_0 of the Roadway. The larger the initial overpressure of the shock wave, the faster the shock wave attenuation, and the greater the rate of change in the cross-sectional area of the roadway, the greater the shock wave attenuation coefficient [9], where the hydraulic diameter can be derived from

$$d_0 = \sqrt{\frac{4S}{\pi}}, m. \quad (6)$$

3.2.4. Roughness of the Roadway β. The roughness of the roadway is an important factor in the decay of the peak shock wave overpressure, which varies under different support measures. The Soviet scholar M.A. Sadovsky et al. demonstrated that, for the same diameter of the roadway, the pressure drop due to friction on the air shock wave front in the range from 10 to 500 kPa depended not only on the distance of the shock wave travels but also on the degree of roughness indicated by the roadway, and the equation for the pressure drop on the plane wave front taking into account the friction loss was given [10].

$$\frac{\Delta P}{\Delta P'} = e^{-\beta R/d_0}, \quad (7)$$

where ΔP is the overpressure of the air shock wave considering the friction of the roadway wall, kPa; $\Delta P'$ is the overpressure of the air shock wave without considering the friction of the wall of the roadway, kPa; and β is the coefficient of the roughness of the roadway surface.

The roughness coefficient of the wall can also be calculated according to the corresponding formula in gas dynamics, and according to the previous research, it is found that when the overpressure value is 10 kPa $\leq \Delta P \leq$ 300 kPa, the error is small and can be used.

$$\beta = \frac{2g\alpha}{v}, \quad (8)$$

where α is the frictional resistance coefficient of the tunnel, constant when Reynolds $Re \geq 10^5$ (fluid is in a completely turbulent state). v is the specific gravity of the air, N/m^3.

3.2.5. Distance from the Source of the Explosion L. For a certain amount of accumulation of explosive gas mixture generated by the shock wave overpressure value and the distance from the source has a direct relationship, the farther away from the source, the smaller the shock wave overpressure value.

3.3. Effect of Ignition Energy on the Characteristics of Gas Explosion. With the extraction of gas for industrial and domestic use, there is a great knowledge gap in the safety production of the coal mining industry by a gas explosion in the pipeline. Qiu established the RNGκ-ε turbulent flow field model based on the total energy equation and the step-by-step reaction explosion combustion model based on multiple control mechanisms, solved the explosion flow and reaction control equations by the finite volume method, and propagated the gas explosion under different ignition energy conditions. The conclusions showed that the greater the ignition energy, the greater the peak gas explosion pressure and flame propagation speed of the propagation law; the analysis of the positive feedback mechanism between the gas explosion pressure wave, explosion flame, and turbulence was an important factor to drive the development process of gas explosion [11].

3.4. Effect of Obstacles on the Characteristics of Gas Explosion. To study the propagation law of gas explosion in large size tunnels and the influence of obstacles on gas explosion, Jia established a two-dimensional model of mine tunnel using Fluent software to study the propagation law of gas explosion when the volume fraction of gas is 9.5%. The results showed that the reaction of the explosion started from 25 ms and finished after 6 ms, the flame propagation speed could reach 400 m/s, the maximum temperature could reach 3200 K, the maximum temperature at the center of the tunnel reached 2155.5 K, the maximum temperature of the tunnel was maintained at about 1,910 K after the reaction was completed, and the maximum value of the gas explosion shock wave was 1.08 MPa. When the obstacle existed, the shock wave at the obstacle shock wave rapidly increases. The closer the position of the obstacle to the explosion position, the greater the overpressure. The same position of different shapes of obstacles and round obstacle shock wave overpressure was the smallest [12]. Xu also found that when there was a square obstacle with a side length of 0.13 m in the pipe, the peak pressure during gas explosion reached 0.84 MPa; in the actual tunnel where there was a square obstacle, it especially should strengthen the arrangement of explosion isolation facilities; for different shapes of obstacles, with the increase of obstacle size, the peak explosion overpressure also increased [13]. Gao explored the effect of flexible obstacles in the flexible duct system and piping system of the auxiliary ventilation system on the gas explosion propagation law and established a gas explosion simulation model using the open-source CFD source generation OpenFOAM. The process variables in the XiFoam tool were used for deflagration, and the maximum pressure was increased by 29% and 77.8%, respectively, and the maximum flame propagation speed was increased by 6.8% and 20%, respectively, over the empty pipe flame propagation speed in the duct system and piping system models [14].

3.5. Effect of Different Section Shapes of Roadway on the Characteristics of Gas Explosion. Different section shapes have different stability degrees. Wu selected three different shapes of roadway sections according to the size and direction of ground stress at the site, used the same support method and construction method, and analyzed several sections for stability examples with parameters such as convergence displacement, displacement rate, and loosening range, thus obtaining that the influence of section shape on roadway support was huge, and the addition of bottom arch could not only prevent the bottom arch and prevent the bottom bulge but also suppress the displacement of the two gangs and the top [15]. Jia used circular, square, rectangular, and trapezoidal section test tubes to monitor the temperature and pressure changes to explore the propagation of gas explosions in the roadway. The results showed that the flame took the longest time to fill the alleyway with trapezoidal sections; however, the square section had the highest temperature. The maximum explosion pressure in the lane was about 0.6 MPa, but the lane with a trapezoidal section took the longest time period to reach the maximum explosion pressure, with the lowest gas explosion temperature [16].

3.6. Effect of Roadway Wall Conditions on the Characteristics of Gas Explosion. Ma estimated the effect of tunnel roadway conditions on gas-air explosions by numerical calculations and theoretical analysis. During the methane-air explosion, rough tunnel walls caused stronger turbulence. In the methane-air premixing zone, the effect of turbulence was manifested by a significant increase in explosion pressure. In the far zone of air shock wave propagation, turbulence reduced the shock wave intensity, but the effect was not significant. In the original methane-air premixing zone, the explosion pressure of the methane-air mixture in the rough-walled tunnel was higher than that in the smooth-walled tunnel. However, the air shock waves outside the premixed zone in the rough-walled tunnel were weaker than those in the smooth-walled tunnel [17].

4. Impact of Explosion Shock Wave on Mine Ventilation Facilities

4.1. Mine Fans. The fan is the heart of the mine, providing fresh air for the mine, excluding contaminated air, reducing the occurrence of gas explosions, coal dust explosions, and other disasters, and playing a pivotal role in the safe construction of the mine [18, 19]. At present, many experts in related fields have conducted much research in the process of gas explosion shock wave propagation and already have a lot of theoretical knowledge; for example, Li et al. studied the explosion pressure and impact generated by large explosions through numerical simulation [20]; Ye et al. conducted theoretical and experimental research on the propagation law of flame and shock wave in the bend [21]; Song revealed the invented new dynamic response characteristics and laws of the explosion door of the vertical wind shaft during the explosion impact [22].

However, scholars have ignored the effect of explosion shock waves on the fan. Liu used Fluent simulation software to construct a three-dimensional model of the vertical shaft-fan-explosion door to simulate the effect of different gas

concentrations and explosion distances on the fan when the explosion door could not be opened normally [23]. The peak overpressure at the fan and explosion door increased with the increase of gas accumulation, and both showed a linear relationship. Analyzing the effect of different explosion distances on the fan and explosion door, the simulation results showed that the peak overpressure at the fan and explosion door decreased with the increase of explosion distance, both in a power function relationship , as shown in Figure 1.

4.2. Ventilation Network. The ventilation network is a topology consisting of hundreds of intricate tunnels and nodes; the main role is to convey the airflow, separating the new and dirty air, if the network chaos will lead to serious safety accidents [24]. The powerful pressure of the explosion shock wave exceeds the air supply pressure, which will cause the wind flow reversal and stagnation phenomenon, leading to the original network chaos, and thus make the scope of the disaster expand [25]. Underground gas explosion shock wave damage by the overpressure and positive pressure zone impulse jointly determine that when the shock wave propagation process will encounter obstacles, it will occur reflection, around the projection phenomenon.

Li and Cao constructed a three-dimensional network model of the mine ventilation system by studying the spreading law of smoke flow from underground fires and used visual implementation of a smoke flow spreading to simulate the dynamic spreading process of smoke flow in three-dimensional shafts, revealing the development of smoke temperature and concentration in space and time [26]. Yang studied dynamic characteristics of high-pressure shock airflow propagation in ventilation networks and the key nodes and flutter structure characteristics of ventilation networks and established the flutter structure characteristics analysis model of ventilation networks [27]. Qiu studied the propagation characteristics and attenuation law of explosion shock waves in flat, bend, bifurcation, A-type networks, and parallel networks and explored the overpressure at the bend or bifurcation of pipe attenuation coefficient and the bend or bifurcation angle and the initial pressure of the coupling relationship and explored the sudden change in its section overpressure attenuation coefficient, increase coefficient and reflection coefficient, respectively, with the section change rate, and the initial pressure of the coupling relationship [28]. At this stage, scholars mainly carry out the effect of the explosion on common types of networks given the actual situation that coal mine gas explosion may cause a large number of casualties, analyze the factors where gas explosion damages the ventilation system the most, and establish the gas explosion damage model.

An H-shaped ventilation system means that the working face has 4 ventilation roadways (2 inlets and 2 return or 3 inlets and 1 return). The advantage of this ventilation system is that the working face has a large ventilation capacity and the gas does not gush to the working face. The disadvantage is that there is a large amount of roadway construction and maintenance. The maintenance of the roadway in the open area must prevent air leakage. Therefore, this type of ventilation system is also often used in the top coal comprehensive mining workings with a high gas release. With the improvement of coal mining mechanization, an H-shaped ventilation system is mainly used at this stage, but then there is a great potential danger of gas explosion. Therefore, the H-shaped ventilation system has become the object of research by many scholars. Ma used Fluent to simulate the process of gas explosion shock wave disrupting the normal ventilation of the tunnel to investigate the changes of pressure and airflow pattern during the process of gas explosion and venting in the H-type tunnel; the molar fraction of CO_2, temperature, and fluid movement in the tunnel before and after the explosion were compared and analyzed to obtain the propagation characteristics of the explosion shock wave in the tunnel. The results showed that the explosion shock wave was reflected by the wall of the tunnel and superimposed with the forward shock wave, increasing the pressure value in the superimposed area; the explosion shock wave changed the flow state of the airflow in the contact tunnel so that the airflow in the contact tunnel changed from double vortex mode to single vortex mode; the gas detonation process had a larger capacity of the tunnel on the side of the gas detonation area; and many shock waves generated by the explosion were discharged along the tunnel with a larger capacity. After the explosion, the tunnel could resume normal ventilation [29].

The common ventilation system is mainly U type and $U+L$ type, coal mining working face mostly uses U type ventilation, and high gas mine U type ventilation working face of the upper corner gas has been a difficult problem of coal mine gas management. With the development of research, the high-production and high-efficiency mining process has been realized, the unit production of workings has been increasing, and the amount of gas gushing out has been increasing, so that mines with little gas in the original workings and low gas mines also have the upper corner gas accumulation over the limits. $U+L$ shaped ventilation system is evolved based on of U shaped backward type. It adds a flat lane to the outer side of the working face or the backwind flat lane as a special gas discharge lane, commonly called "tail lane," forming a form of 1-in-2-back. The advantage of this ventilation system is that the air volume of the two backwind flat lanes can be controlled by adjusting the resistance, to control the amount of gas gushing to the working face from the mining area so that the upper corner does not exceed the limit. The disadvantage is that it increases the construction volume of 1 tailing lane and the maintenance volume of the lane is large. When the amount of gas gushing from the coal mining working face is very large, a special gas discharge lane can be used, but it must conform to the relevant provisions of the "Coal Mine Safety Regulations." At present, China's coal mining working face gas outflow is very large by the extraction of gas and increases; the amount of air still does not meet the requirements and often uses $U+L$ shaped ventilation system. For the above two ventilation systems on the destruction of a gas explosion, research is less.

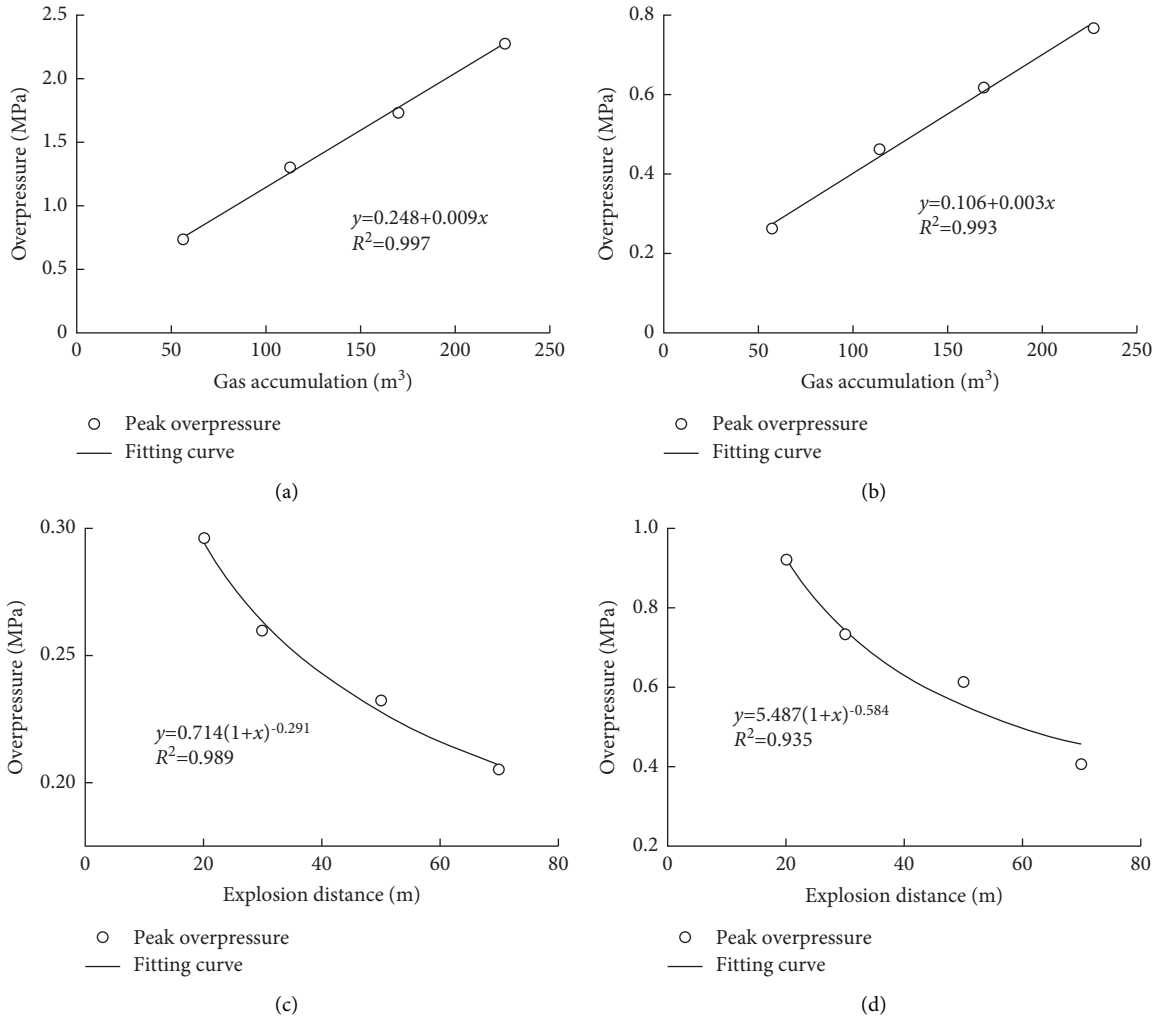

Figure 1: Fitting of influence law of overpressure peak value [23]. (a) Effect of gas accumulation on the peak overpressure at the explosion door. (b) Effect of gas accumulation on the peak overpressure at the fan. (c) Explosion distance on the peak overpressure at the fan. (d) Explosion distance on the peak overpressure at the explosion door.

4.3. Fireproof Mine Seal. Seals are used to control and direct ventilation airflow through underground coal mines, diluting and allowing harmless methane, carried coal dust, and other contaminants to enter the workings and other areas of the mine. They should be constructed using traditionally accepted methods and materials that have been proven to work adequately or methods and materials that have been tested and proven to have a minimum strength equal to or greater than traditionally accepted mine control.

A fundamental research direction at the National Institute for Occupational Safety and Health (NIOSH) was eliminating the occurrence or mitigating the effects of coal mine explosions. The researcher conducted a collaborative effort to develop and evaluate new innovative seal designs to assess the strength characteristics and resistance to air leakage of numerous innovative seal designs and ventilation control structures used in underground coal mines to provide enhanced explosion protection for mining personnel. To address the prevalent geologic mining conditions and loose and friable coal, encountered in establishing seals, Eric S. Weis evaluated the effectiveness of using pressurized grout bags (packer bags) along the mine roof and veins instead of bottom and vein couplings for standard types of solid concrete block seals. The results showed that the use of these fast-setting grout-filled packer bags, internally pressurized to 300 kPa, not only provided a seal that could withstand a 138 kPa static pressure explosion but also provided a better seal than the joint ribs.

Zhang used numerical simulation to investigate the mechanical properties of brick seals under impact loading [30]. The characteristics of gas explosion in the confined area and the propagation characteristics of the shock wave were analyzed, and the pressure variation of the shock wave on the seal caused by the gas explosion was predicted. A series of numerical simulations of the brick seal under different pressure variations were carried out to obtain the safety variations of the brick seal under different conditions, as shown in Figure 2.

The analysis of the explosion process showed that when the gas explosion occurred, the maximum shock pressure of

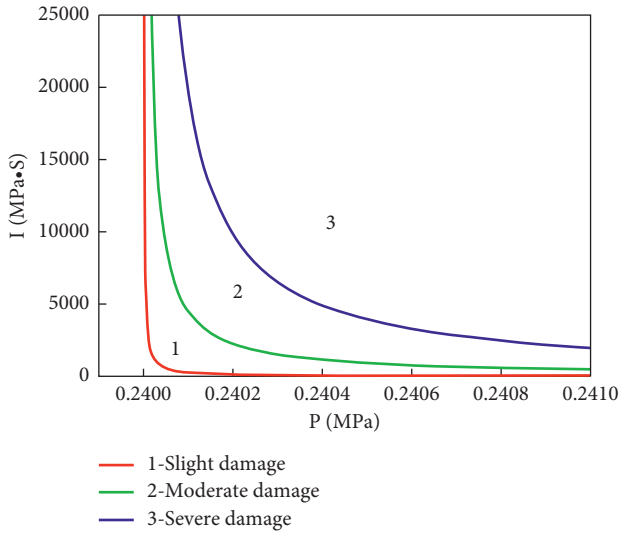

Figure 2: Damage curve of 1.5 m thick brick seal [30].

the quasi-static structure reached 0.83 MPa; when the dust explosion occurred, the possible explosion pressure was between 0.79 and 0.89 MPa. However, due to the different spatial structure, when there was sufficient propagation distance, there would be a dynamic increase in the quasi-static basis; when the explosion pressure might rise to 1.75 MPa, this shock wave would be reflected when propagating to the seal; the shock wave and the reflected wave superimposed on the impact pressure were larger, 4.50 MPa, and the use of the impact load under the action of the brick seal damage variable D, respectively, was defined as 1/5 (minor damage of brick seal layer), 1/3 (moderate damage), and 1/2 (serious damage) state judgment method; by analyzing the degree of damage of brick seal layer under the action of different impact loads, fitting the curve, the damage curve of single brick seal layer was derived.

5. Impact of Explosion Shock Wave on Mechanical Equipment

Mine machinery and equipment mainly include brackets, coal mining machines, and transporters, where the role of the bracket is to support the stability of the overlying rock layer. However, scholars at home and abroad have less research on the damage to mechanical equipment caused by explosion shock waves; if the shock waves damage the bracket, they not only block the passage of people in the tunnel but also easily cause smashing accidents caused by the collapse of the roof. We can use the form of accident tree analysis and give a certain weight to mechanical equipment and a comprehensive assessment of the risk of explosive accidents, only through a variety of preventive measures to achieve a significant reduction in the risk of explosion. The use of numerical and experimental simulations can only be a general design of the appearance of mechanical equipment, ignoring the details. Although most of the mechanical equipment is intrinsically safe or explosion-proof, at this stage, there are still great problems, especially with electrically charged equipment; shock wave destruction of equipment may also lead to the explosion-proof performance of electrical equipment failure, resulting in greater accidents, so shock wave damages and explosion-proof performance of electromechanical equipment failure chain research have great prospects for development.

6. Impact of Explosion Shock Wave on the Underground Moveable Rescue Chamber

The life-saving cabin is a kind of underground rescue equipment, as shown in Figure 3. The life-saving cabin can isolate toxic and harmful gases in case of the mine disaster, provide necessary conditions for human survival such as oxygen and food, and prolong the survival time of risk-averse personnel; in the event of an explosion accident, we mainly need to resist the huge gas shock wave pressure and need to have strong antidetonation performance, but there are still great problems about the rescue chamber mechanism design.

6.1. Overall Research. In response to the current problem of the quantitative relationship between the factors affecting the explosion resistance of the rescue chamber and the increase in mass, Wang studied the improvement of the explosion resistance of different sections of the rescue chamber under the factors of structural form change, outer skin thickening, reinforcement thickening, and flange thickening using finite element calculation method based on an actual type of cabin, calculated the value of the increase in mass of the cabin under different factors, and analyzed the explosion resistance. The quantitative relationship between the increase of explosion strength and weight was analyzed. Research findings showed that when increasing the same quality, the thickness of the reinforcement on the cabin explosion resistance of the most obvious effect is more than the skin thickening which is 5.3 times higher than the flange thickening which is 2.7 times higher. Thickening the

Figure 3: Moveable rescue chamber [31].

reinforcement was to enhance the cabin explosion resistance of the most economical and reasonable method. The design of the rescue chamber not only requires compliance with the current national standards but also requires convenience and high safety, as shown in Table 1 [31].

The coal mine rescue chamber becomes important equipment for miners to escape from underground, and its structural strength directly determines the life safety of miners. To improve the strength of the rescue chamber, Yang established a finite element model of the rescue chamber in the ABAQUS environment and used the explicit integration method to obtain the effect of the pressure on the rescue chamber during the coal mine gas explosion. The maximum stresses in the rescue chamber were found in the corner stress concentrations and the middle part of the ribs and reached the yield strength, but the overall stresses in the rescue chamber were within the allowable range [32].

Bai used the explicit kinetic analysis software LS-DYNA to study the TNT equivalent of gas explosion in the underground tunnel of the rescue chamber, the propagation characteristics of the shock wave, and the impact load on the cabin, and the propagation process of the explosion shock wave was obtained by simulation with the ALE fluid-solid coupling algorithm. When the shock wave was transmitted from the front end to the rear end of the rescue chamber and decays to 10% of its peak load, the TNT equivalent of gas when the load on the cabin reached the specification was determined, and the actual load curve of each part of the cabin was obtained, which provided a basis for calculating the dynamic response of the rescue chamber to impact when the load was applied and for optimizing the design [33].

Jing used the finite element software AUTODYN, using the principle of fluid-solid coupling, to simulate the explosion of rectangular section, circular section, and an arch section rescue chamber, respectively, to obtain the surface impact load distribution of these three different sections of the rescue chamber in the explosion flow field. It could be concluded that, under the same conditions, the surface impact load of the arch-shaped rescue chamber was the smallest among these three types of rescue chambers [34].

6.2. Refuge Door Research. In the event of an accident, emergency underground refuge chambers play an important role in ensuring the safety of trapped personnel. In the structural dynamic response of a refuge door under explosion, the load was investigated in a finite element model based on the FEM platform. Before entering the physical prototype pit explosion test, it provides a theoretical basis and data reference for further performance improvement of the product [35].

In the structural dynamic response of a coal mine refuge door under explosion, the load was investigated by building a finite element model based on the FEM platform. The results show, that under the action of 0.6 MPa shock wave, the stress and deformation of the protective door meet the requirements, and the airtightness was good, which provides a theoretical basis and data reference for further improvement of the performance of the physical prototype before entering the explosion test in the pit [36], as shown in Figure 4.

The main design parameters of the explosion-resistant structure of the refuge door were determined by theoretical calculations, and the ANSYS/LS-DYNA software was used to perform dynamic finite element numerical simulations of the explosion-resistant structure of the refuge door. The results of the simulations and the explosion tunnel tests showed that the explosion-resistant structure of the protective door could resist the explosion impact pressure of not less than 0.5 MPa and ensure its safety and reliability in the underground refuge protection [37], as shown in Figure 5.

Under the action of the triangular shock wave pressure of 0.5 MPa, the maximum displacement of the overall structure appears at $t = 0.111$ s, and the maximum value of the displacement of the overall structure appears in the middle position of the door body, reaching 0.528 mm, the displacement value gradually decreases from the middle to all around, and the displacement value of the overall structure is within 0–0.528 mm.

7. Impact of Explosion Shock Wave on the Roadway

Coal mine gas explosion is extremely dangerous and can cause mass death and injury in a relatively short time. And once the accident occurs, the explosion wave will also damage the roadway surrounding rock materials and structure, so that the roadway failure damages, and even collapses, resulting in trapped personnel, and then directly impedes the rescue work that should be carried out, bringing great difficulties to rescue [38].

Lu found that the deep coal rock body under the coupling effect of gas explosion load and high stress and the stress time curve in the surrounding rock was characterized by multiple wave peaks, and the tunnel surrounding rock was successively subjected to shock waves, compression waves, and elastic waves, corresponding to the generation of multiple stress wave peaks, negative pressure zones, and obvious stress oscillations. In the corner of the roadway stress curve, there was a certain lag period, and with the increase of ground stress, the lag period would be reduced or even disappear. Under the coupling effect of explosion load and initial stress, stress concentration would appear at the corner of the tunnel top and bottom plates, showing obvious expansion and deformation in both horizontal and vertical directions, resulting in macroscopic damage at the corner of

Table 1: Mass and explosion resistance increase table under different factors [31].

No.	Factors (%)	Mass increase (%)	Increase in explosion resistance (%)	The ratio of increase in explosion resistance to increase in mass	Ratio mean
1	Skin thickness increased 50	18.6–18.8	9.0–17.7	0.48–0.94	0.71
2	Stiffener increased 100	3.6–4.6	10.2–21.7	2.83–4.72	3.80
3	Flange thickness increased 100	26.5–26.8	34.0–39.8	1.28–1.48	1.40

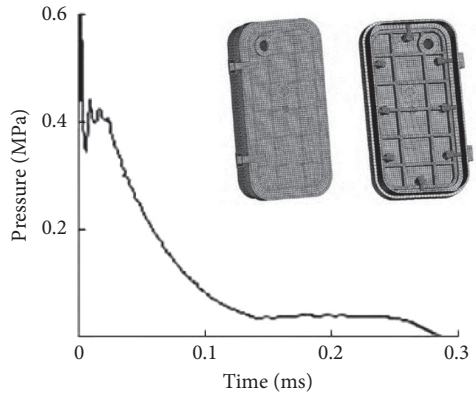

Figure 4: Shock wave pressure curve of the protective closed door [36].

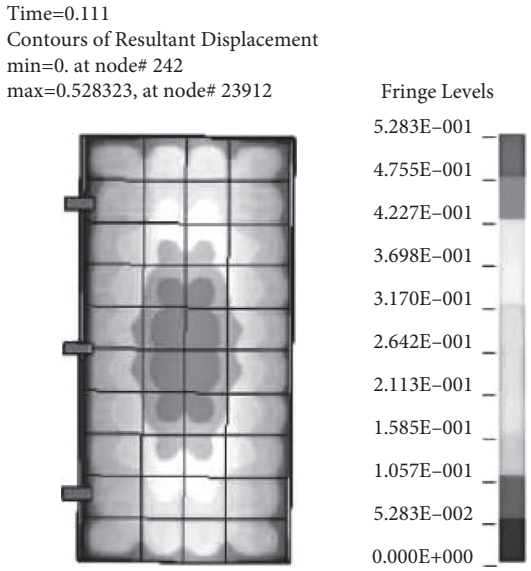

Figure 5: Maximum displacement [37].

the tunnel, but no obvious macroscopic damage at the two walls and roof and floor. The transient unloading caused by gas explosion mainly occurs in a small part of the area around the two gangs and the top and bottom of the roadway, and with the increase of the lateral pressure coefficient, the range of plastic damage to the surrounding rock of the two gangs of the roadway decreases [39].

Wang used numerical analysis to study the explosion resistance of underground chambers under different directional explosion loads. Through comparative analysis of the time course of the explosion compressive stress curve and dynamic crack distribution pattern of the underground chamber and the anchored chamber under the same equivalent explosion load, the top explosion produced the smallest displacement, followed by the arch side explosion, the largest in the straight wall side explosion, and the straight wall side explosion produced the largest displacement position which is the bottom of the sidewall, rather than the location of the closest explosion source cavity wall. During the explosion load, due to the reinforcement of the anchor

rods, tensile "split" occurs between the anchor rods, and at the same time, the phenomenon of "spalling" occurs in the anchoring area and the end of the anchoring area. Under the same equivalent top explosion, arch side explosion, and straight wall side explosion, the displacement and dynamic crack distribution of the anchored chamber are similar, and the explosion resistance of the anchor reinforced chamber is improved [40].

8. Safety Distance Study to Avoid Explosion Shock Wave

The safety distance in a general term refers to the minimum straight-line distance from the center of the explosion to the operator not being injured by the explosion wave in the event of a gas explosion underground [41]. Safety distance is a relative concept and can be understood from both safety and injury-causing perspectives. In the former case, the personnel can be protected from the explosion shock wave outside the distance; in the latter case, the personnel within the distance will be injured.

After the underground gas explosion, the explosion shock wave and shock airflow will be propagated along the underground roadway; under the influence of friction and other heat losses in the wall of the roadway, its intensity decays. In the process of explosion propagation, to prevent the explosion shock wave on the underground operators that caused injury and ensure safety, we must determine the human body and underground ventilation structures to cause certain destruction of the critical shock wave parameters and to ensure that the operator is located in the location of the shock wave parameters less than the critical value, to ensure a certain safety factor. Polish scholars based on a statistical analysis of gas explosion accidents stated that mine gas explosion 500 m away from the source has two 90° bend locations, which can be used as a safe distance for rescue and relief personnel [42].

9. Discussion

At this stage, scholars mainly use numerical simulation, but the gas explosion is in various forms, and the pattern is still complex. The energy release coming from an explosion is huge. The energy source location is random, considering the influence of many aspects, so the model construction, initial conditions, boundary conditions set, and monitoring point location selection are very problematic. The possibility of gas explosion in the underground mining face is large, but the mathematical model is too large to solve; to solve the mine full-scale gas explosion is difficult to simulate the problem; the main summer at this stage uses the explosion shock wave propagation segmental relay simulation method; the return wind alley pressure is the initial pressure of the winding shaft that converted to the bottom of the shaft gas explosion that occurred in the explosion equivalent.

In the form of experiments, simulating the mine environment in proportion to its complexity and pipe wall reduction is still only in the theoretical stage, there is a large deviation, and the study of the impact of gas explosion is simply considered a single variable and the experimental design to strive for simplicity, which led to the study of gas explosion mechanism stagnation. A gas explosion is a huge energy, for the relevant control and rescue devices to put forward a great demand for explosion resistance. On the research of pressure-resistant materials and device design, there is a good prospect. The gas explosion caused by the danger not only requires the use of safety system engineering means to consider multiple factors, but the most important thing is also to achieve a real strengthening of personnel management.

10. Conclusions

This paper summarizes the latest research results of gas explosion shock wave damage to ventilation facilities, mechanical devices, roadways, and rescue chambers, with the primary goal of pointing the way to future research and design for explosion resistance in coal mines. Rather than considering the explosion resistance of a single mine facility, this overview takes a systematic approach to the overall mine facility, including not only experimental and numerical simulation findings but also an overview of the use of new technologies.

In short, there is still a lot of room for development for gas explosion damage research, at this stage, mainly using a combination of experimental and simulation methods, of which numerical simulation is the development trend, but for the boundary conditions and the initial conditions, we still need a lot of experimental data. Regarding gas extraction and its complex construction process, there may be many safety risks of the gas explosion, but there is less research on the impact of gas shock waves on the gas extraction damage of gas extraction devices.

Data Availability

The data used to support the findings of this study are included within the article.

Conflicts of Interest

The authors declare that there are no conflicts of interest regarding the publication of this paper.

References

[1] L. Qi, "Analysis of the hazards of coal mine gas and integrated control measures," *Energy and Energy Conservation*, vol. 4, pp. 126–128, 2013.

[2] W. Song, J. Cheng, W. Wang et al., "Underground mine gas explosion accidents and prevention techniques- an overview," *Archives of Mining Sciences*, vol. 66, no. 2, pp. 297–312, 2021.

[3] H. Yu and J. G. Wu, "Study on control technology for mine gas explosion," *Coal Technology*, vol. 29, no. 10, pp. 85–87, 2010.

[4] I. Ivanov, A. M. Baranov, S. Akbari, S. Mironov, and E. Karpova, "Methodology for estimating potential explosion hazard of hydrocarbon with hydrogen mixtures without identifying gas composition," *Sensors and Actuators B: Chemical*, vol. 293, 2019.

[5] L. Wen, "Research on secondary explosion process and its law in confined space," Master thesis, Liaoning University of Engineering and Technology, Liaoning, China, 2018.
[6] S. Yang, G. Jing, and Z. Jia, "Injury study on impact current of gas explosion in coal mine," *Journal of China Coal Society*, vol. 34, no. 10, pp. 1354–1358, 2009.
[7] W. Zhou, "Numerical analysis of explosive blast shock wave spread and dynamic instability of spherical shell," Master thesis, Taiyuan University of Technology, Taiyuan, China, 2010.
[8] B. Jiang, "Multiparameter temporal and spatial evolution of gas explosion and its suppression using gas-olid jet curtain," PhD thesis, China University of Mining and Technology, Beijing, China, 2014.
[9] K. Wang, A. Zhou, W. Gaoju, and Z. Pin, "Influences of roadway cross-section variation on outburst shock wave propagation," *Journal of China Coal Society*, vol. 37, no. 6, pp. 989–993, 2012.
[10] H. Tan, "Discussion on the effect of air blasting wave of blasting operation on the stability of the tunnel's country rock," *Gold*, vol. 4, pp. 24-25, 1998.
[11] R. Qiu, "Numerical simulation study of gas explosion dissemination in ingnition energy," *Safety In Coal Mines*, vol. 42, no. 1, pp. 5–8, 2011.
[12] J. Jia and J. Su, "Study on the influence of obstacles on gas explosion in driving face," *Shanxi Science Technology*, vol. 35, no. 6, pp. 21–23+27, 2020.
[13] A.-M. Xu, X. X. Chen, and J. Jia, "Effects of obstacles on gas explosion shock wave propagation," *China Safety Science Journal*, vol. 29, no. 9, pp. 96–101, 2019.
[14] G. Ke, S. Li, Y. Liu, J. Jia, and X. Wang, "Effect of flexible obstacles on gas explosion characteristic in underground coal mine," *Process Safety and Environmental Protection*, vol. 149, 2021.
[15] Z. Wu, Y. Luo, and B. Qin, "Study on the influence of section shape on the stability of roadway," *Mine pressure and roof management*, vol. 4, pp. 41–43+40, 2004.
[16] J. Jia and F. Wang, "Propagation of gas explosions in roadways with different cross-sectional shapes," *Energy Sources, Part A: Recovery, Utilization, and Environmental Effects*, vol. 43, p. 4, 2021.
[17] Q. J. Ma, Q. Zhang, and L. Pang, "Influence of the tunnel wall surface condition on the methane-air explosion," *Combustion, Explosion and Shock Waves*, vol. 50, p. 2, 2014.
[18] J. Cheng, X. Zheng, W. Luo et al., "A compound binder of coal dust wetting and suppression for coal pile," *Process Safety and Environmental Protection*, vol. 147, pp. 92–10, 2020.
[19] J. Cheng, Y. Wang, Y. Lei et al., "Study on coal dust crusting for coal pile based on a compound binder," *Powder Technology*, vol. 376, pp. 149–166, 2020.
[20] J. Li and H. Hong, "Numerical and analytical prediction of pressure and impulse from vented gas explosion in large cylindrical tanks," *Process Safety and Environmental Protection*, vol. 127, 2019.
[21] Y. Qing, L. Bai-quan, Z.-z. Jia, and C.-j. Zhu, "Propagation law and analysis of gas explosion in bend duct," *Procedia Earth and Planetary Science*, vol. 1, p. 1, 2009.
[22] W. Song, "Study on the safety protection theory and technology of explosion doors for vertical shafts in coal mines," PhD thesis, Henan University of Technology, Zhengzhou, China, 2018.
[23] J. Liu, S. Chen, J. Ren, and J. Hu, "Research on influence of gas accumulation amount and explosion distance on fan and explosion-proof door," *Journal of Safety Science and Technology16*, vol. 9, pp. 57–63, 2020.
[24] J. Cheng, W. Luo, Z. Zhao et al., "Controlling coal spontaneous combustion fire in longwall gob using comprehensive methods-a case study," *Mining, Metallurgy & Exploration*, vol. 38, no. 4, pp. 1801–1816, 2021.
[25] R. Zhang, J. Cheng, Z. Wang, and Z. Shao, "Recapitulation and prospect of research on flow field in coal mine gob," *Shock and Vibration*, vol. 2021, Article ID 3730606, 24 pages, 2021.
[26] C. Li, Z.-G. Cao, Z.-X. Li, L. Hu, and D. Hou, "3D simulation modeling techniques of fire fume spread process for underground mines," *Journal of China Coal Society*, vol. 38, no. 2, pp. 257–263, 2013.
[27] Y. Yang, "Study on the dynamics effect of gas explosion in the mine ventlitation network," PhD thesis, Anhui University of Technology, Ma'anshan, China, 2011.
[28] J. Qiu, "Study on propagation characteristics of shock wave in pipe network and simulation of catastrophic process for gas explosion," PhD thesis, Anhui University of Technology, Ma'anshan, China, 2018.
[29] H. Ma, X. Chen, and D. Jing, "Simulation study on gas explosion and discharge process in H-type ventilation roadway," *China Safety Science Journal*, vol. 31, no. 1, pp. 45–51, 2021.
[30] X. Zhang, J. Cheng, and C. Shi, "Damage assessment for underground brick seal under explosion impact load," *Arabian Journal of Geosciences*, vol. 14, p. 5, 2021.
[31] L. Wang, "Relationship between factors affecting anti-explosion strength and weight increase of mine refuge chamber," *Safety In Coal Mines*, vol. 51, no. 12, pp. 163–166, 2020.
[32] X. Yang, L. Jin, and J. Li, "Explosion simulation and analysis of coal mine rescue capsule," *Coal Mine Machinery*, vol. 33, no. 2, pp. 113-114, 2012.
[33] B. Bai, Z. Li, Z. Wang, and L. Zhao, "Research on the tnt equivalent and impact load in anti-explosion of mine rescue capsule," *Science Technology and Engineering*, vol. 14, no. 17, pp. 1–5+20, 2014.
[34] J. Cheng, F. Liu, Y. Shi et al., "Model tests of effects on fire smoke control in highway tunnels," *Journal Gradevinar (Civil Engineer)*, vol. 72, no. 9, pp. 781–792, 2020.
[35] Z. Jing, A. Zhang, B. Zhang, and Y. Gu, "Simulation analysis of explosion impact load on different cross-section rescue capsule," *Coal Mine Machinery*, vol. 34, no. 5, pp. 103–105, 2013.
[36] W. Wang, Y. Ni, L. Dan, and W. Lei, "Structural dynamic analysis of coal mine refuge chamber protective closure doors based on finite element method," *Hoisting and Conveying Machinery*, vol. 06, pp. 45–48, 2017.
[37] Z. Liu, "Dynamic analysis on finite element structure of protective sealing door applied to underground mine refuge chamber," *Mine Construction Technology*, vol. 37, no. 3, pp. 41–43, 2016.
[38] B. Zhige, "Research on anti-explosion performance of mine refuge chamber airtight blast door," *Mining Safety & Environmental Protection*, vol. 39, no. 6, pp. 18–22+101, 2012.
[39] X. Lu, "Research on roadway damage mechanism under coupling of gas explosion load and the high ground stress," Master thesis, China University of Mining and Technology, Beijing, China, 2019.
[40] G. Wang, C. Wang, Y. Yu, and X. Chang, "Research on anchored effect of tunnels under explosion load in different directions," *Chinese Journal of Underground Space and Engineering*, vol. 13, no. 6, pp. 1645–1653, 2017.
[41] X. Lang, "Study on the aettenuation law and safe distance of gas explosion shock wave," Master thesis, China University of Mining and Technology, Beijing, China, 2015.
[42] S. Wang and Z. Xie, "Exploration on the safety distance of methane explosion in mines," *Journal of China University of Mining & Teehnology*, vol. 4, pp. 4–11, 1989.

Hindawi
Shock and Vibration
Volume 2021, Article ID 4361712, 10 pages
https://doi.org/10.1155/2021/4361712

Research Article

Mathematical Model of Maximum Commutation Half Cycle for Thermal Countercurrent Oxidation of Low-Concentration Gas in Coal Mine Ventilation

Kuan Wu,[1,2] **Shiliang Shi**,[1,2] **and Yong Chen**[1,2,3]

[1]*School of Resources, Environment and Safety Engineering, Hunan University of Science and Technology, Xiangtan, China*
[2]*Hunan University of Science and Technology Southern Coal Mine Gas and Roof Disaster Prevention and Control and Safety Production Key Experiment, Xiangtan, China*
[3]*China Coal Technology Engineering Group Chongqing Research Institute, Chongqing, China*

Correspondence should be addressed to Kuan Wu; 170101020001@mail.hnust.edu.cn

Received 23 July 2021; Revised 12 September 2021; Accepted 14 September 2021; Published 13 October 2021

Academic Editor: Jianwei Cheng

The Fluent computational fluid dynamics software was used to study the relevant factors affecting the maximum commutation half cycle for thermal countercurrent oxidation of low-concentration gas in coal mine ventilation. Based on orthogonal experiments, the maximum commutation half cycle for thermal countercurrent oxidation of the exhaust gas in the coal mine ventilation under 25 working conditions with the combination of different methane concentrations, inlet speeds, porosities, and oxidation bed filling lengths is investigated. SPSS data processing software was used to perform regression analysis on the numerical simulation data, and a mathematical model for predicting the maximum commutation half cycle under the influence of four factors was obtained. Through experiments, the mathematical model of the maximum commutation half cycle by the numerical simulation was verified. After introducing the wall heat loss correction coefficient, the complete prediction model of the maximum commutation half cycle was obtained. Comparing the experimental test value with the calculated value using the corrected model, the relative error was not more than 3%. The complete mathematical model corrected can be applied to the design calculation of the maximum commutation half cycle for thermal countercurrent oxidation of low-concentration gas in actual coal mine ventilation.

1. Introduction

Coal is a fossil energy source which provides about 30% of the total energy consumption in the world [1–3]. Plenty of environmental problems and natural disasters may occur during coal mining, i.e., roof fall, gas, fire, and dust pollution [4–6]. Coal mine ventilation gas is the second most important greenhouse gas after carbon dioxide, and the effect of a unit mass of gas on the atmospheric greenhouse effect is 21 times that of the same mass of carbon dioxide. Coal mine ventilation is one of the main sources of industrial gas emissions. Reducing coal mine ventilation gas can reduce the greenhouse gas emissions. At the same time, the main component of the ventilation gas is methane, which is a high-quality and clean gas energy. Therefore, reasonable recovery and utilization of coal mine ventilation gas have the dual significance of energy saving and environmental protection. The coal mine ventilation has the characteristics of large discharge amount, low gas concentration, and unstable concentration, making it difficult for coal mine ventilation gas to be burned directly without auxiliary fuel using traditional burners. At present, thermal countercurrent oxidation is one of the main technologies to achieve the reduction in low-concentration gas emission and rational utilization of coal mine ventilation. The key of this technology is to continuously change the flow direction of the gas fed into the reactor so that the ventilation gas can absorb heat and warm up in the heat accumulator to ensure the self-sustainability of the methane oxidation process [7–9].

So far, most studies on the thermal countercurrent oxidation of low-concentration gas in coal mine ventilation have focused on the temperature field of thermal countercurrent oxidation, methane conversion rate, and oxidation bed resistance and its influencing factors, while few studies on the maximum commutation half cycle for thermal counterflow oxidation of low-concentration gas in coal mine ventilation have been reported [10–15]. The authors of [16] reported the theoretical calculation formula of maximum half cycle of the reciprocating inert porous medium burner, which comprehensively considered the relationship of mutual restriction between the length of the burner, the gas supply parameters, the heating value of the gas, and the physical properties of the porous medium. However, the formula involved too many parameters. In addition to the burner length, methane concentration, inlet velocity, and porosity, the calculation also required adiabatic combustion temperature, the highest temperature of the combustion zone, effective thermal conductivity, etc. Thus, practical application has certain limitations, and the calculation formula did not consider the influence of wall heat loss. In this study, the orthogonal design and numerical simulation were combined to analyze the four influencing factors for the maximum commutation half cycle, and the mathematical model of the maximum commutation half cycle was obtained through regression analysis. Then, the obtained mathematical model was verified by the experiment of thermal countercurrent oxidation of low-concentration gas in coal mine ventilation, and the wall heat loss coefficient was introduced to correct the model. Finally, a complete prediction model of the maximum commutation half cycle was obtained, which can provide theoretical guidance for the design and operation of thermal countercurrent oxidation units for low-concentration gas in coal mine ventilation.

2. Principle of Thermal Countercurrent Oxidation of Coal Mine Ventilation Gas

As shown in Figure 1, when the device is started, the oxidation bed is preheated by the electric heating element, so that the central temperature reaches the ignition temperature (800°C). Coal mine ventilation gas flows into and through the oxidation bed in one direction, and the gas is heated by the heat exchange medium (honeycomb ceramic heat storage body). The temperature is continuously increased until the methane is oxidized. Then, the hot oxidized gas continues to move to the other end of the oxidation bed, transferring heat to the heat exchange medium and gradually cooling down. With the continuous entry of gas, the temperature on the inlet side of the oxidation bed gradually decreases and the temperature on the outlet side gradually increases. Before there is enough heat on the inlet side to heat the gas to the oxidation temperature, the commutation begins and the gas flow reverses. The key of the oxidation device is to continuously change the flow direction of the gas fed into the oxidation bed, so that the gas absorbs heat and warms up in the heat storage body, so as to ensure the self-sustainment of the oxidation process. At the same time, a heat exchanger is installed in the middle of the device to recover part of the heat of the reaction, which is used to produce hot water or to generate power.

3. Numerical Simulation Scheme of Maximum Commutation Half Cycle

3.1. Influencing Factors of Maximum Commutation Half Cycle. The thermal countercurrent oxidation of low-concentration gas in coal mine ventilation needs to choose a suitable commutation half cycle. If the commutation half cycle is too small, it will cause a large amount of exhaust gas to be blown away without having time to oxidize during the commutation. In addition, the switching process causes instability of the air flow inside the device, which will inevitably cause adverse effects on the oxidation of methane. Therefore, the reversing time should be appropriately extended within the allowable range of the device to reduce the impact of the reversing process of the gas flow on the oxidation of methane. Moreover, extending the reversing time can increase the service life of the solenoid valve. However, an excessively large commutation half cycle will result in an excessively high outlet temperature, which is not conducive to heat accumulation. When the commutation half cycle is higher than the critical value, the highest temperature area of the oxidation bed is close to the outlet, the width of the high-temperature platform is too small, the exhaust gas cannot be completely oxidized, and the thermal countercurrent oxidation cannot be self-sustained. This critical commutation half cycle is regarded as the maximum commutation half cycle of thermal countercurrent oxidation.

The influencing factors of the maximum commutation half cycle for thermal countercurrent oxidation of low-concentration gas in coal mine ventilation include methane concentration, air inlet velocity, oxidation bed porosity, filling length, filling materials and physical properties of ventilation gas, and heat loss on the oxidation bed wall. The thermal countercurrent oxidation bed is usually filled with honeycomb ceramics and mostly made of cordierite and mullite. The physical properties of these two materials are relatively close. The methane concentration of coal mine ventilation gas is low, and the influence of methane concentration changes on its physical properties can be ignored, so the exhaust gas can be approximated as air. Therefore, the physical parameters of the filling material and the ventilation gas are fixed and can be considered as known quantities in the calculation. The wall heat loss is related to the thermal insulation performance of the oxidation bed device and the ambient temperature, and its influence on the maximum half cycle of the commutation is more complicated, so it is temporarily ignored in the numerical simulation analysis. Therefore, the factors affecting the maximum commutation half cycle of thermal countercurrent oxidation are simplified to four factors, i.e., methane concentration, inlet velocity, oxidation bed porosity, and filling length. This study first summarizes the mathematical model for the maximum commutation half cycle of thermal countercurrent oxidation under the action of 4 factors, then makes reasonable corrections to the mathematical model by considering the thermal insulation performance of the thermal

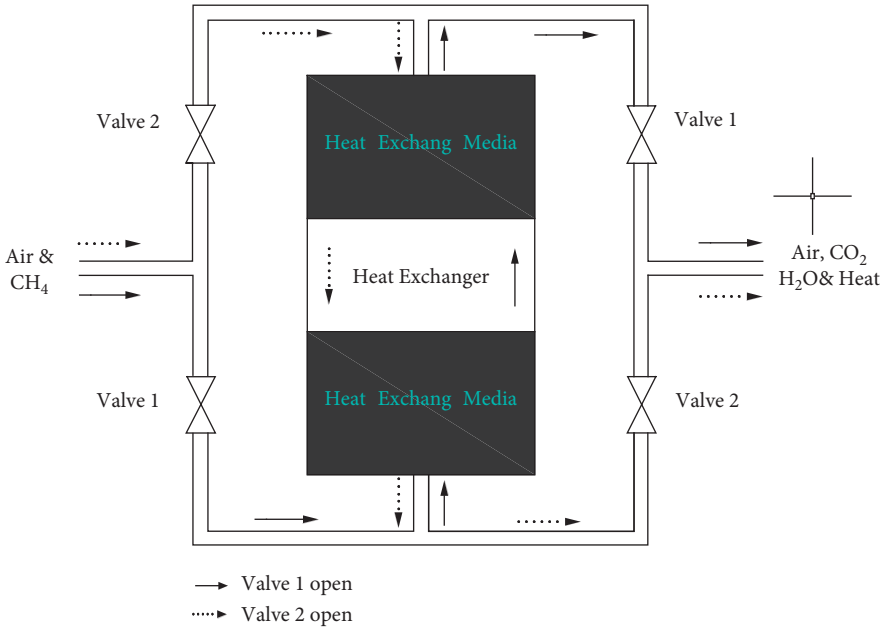

Figure 1: Schematic diagram of the thermal countercurrent oxidation device.

countercurrent oxidation system, and finally obtains a complete prediction mathematical model for the maximum commutation half cycle.

3.2. Calculation Model. In this paper, we simulated a self-designed thermal countercurrent oxidation device for coal mine ventilation, with the ventilation gas processing capability of 500 m^3h. The thermal oxidation bed was a horizontal structure, and the air flowed left and right in the oxidation bed. The oxidation bed had a length of 2.0 m, a width of 0.8 m, and a height of 0.8 m, filling with several square honeycomb ceramics with the same specifications. Since the gas flow channels in the oxidation bed were evenly distributed and the equivalent diameter of the gas flow channels was much smaller than the size of the oxidation bed, the thermal oxidation bed can be considered as a uniform porous medium, and the equivalent continuous method can be used for simulation.

The simulation of the thermal countercurrent oxidation reaction of ventilation gas involves many aspects, including heat conduction, convection, radiation, and chemical reaction. The detailed simulation of the process is computationally intensive. For simplicity, the following assumptions were made in the study [17–20]:

(1) Honeycomb ceramics have good thermal conductivity and radiation ability, and the entire oxidation bed has a good thermal insulation performance. The temperature distribution in the oxidation bed is uniform. Thus, the simulation can be simplified to a one-dimensional problem.

(2) Honeycomb ceramics have a large specific surface area, and the convective heat transfer coefficient between gas and solid is large enough. Therefore, there is a local thermal equilibrium between the gas and the solid, that is, their temperatures are equal at any point (single temperature model).

(3) The porous medium is an optically thick medium.

(4) The chemical reaction is simplified into a single-step overall reaction:

$$\text{state equation: } \rho_g = \frac{p}{RT}, \tag{1}$$

$$\text{continuity equation: } \varepsilon\frac{\partial \rho_g}{\partial t} + \frac{\partial}{\partial x}\left(\rho_g u\right) = 0, \tag{2}$$

$$\text{momentum equation: } \varepsilon\frac{\partial}{\partial t}\left(\rho_g u\right) + \frac{\partial}{\partial x}\left(\rho_g uu\right) = -\frac{\partial p}{\partial x} + \mu\frac{\partial^2 u}{\partial x^2} - C_x\frac{1}{2}\rho|u|u, \tag{3}$$

$$\text{energy equation: } (1-\varepsilon)\frac{\partial}{\partial t}(\rho_s C_s T) + \varepsilon\frac{\partial}{\partial t}(\rho_g C_g T) + \frac{\partial}{\partial x}(\rho_g C_g \mathrm{Tu}) = \frac{\partial^2}{\partial x^2}(k_{\mathrm{eff}} T) - \frac{\partial}{\partial x}\left(\sum_{i=1}^{5} h_i J_i\right) + \varepsilon \Delta H \omega_{\mathrm{CH_4}}, \quad (4)$$

$$\text{composition equation: } \varepsilon\frac{\partial}{\partial t}(\rho_g Y_i) + \frac{\partial}{\partial x}(\rho_g u Y_i) = -\frac{\partial}{\partial x} J_i + \varepsilon\omega_i. \quad (5)$$

The radiative transfer heat of porous media can be approximately described by the Rosseland model:

$$q_x(x) = -\frac{16}{3}\frac{\sigma T^3}{\alpha}\frac{dT}{dx}. \quad (6)$$

In the formulas, the subscript s represents the solid scalar and the subscript g represents the gas scalar. In the momentum equation (3), C_x is the internal resistance coefficient of porous media. In the energy equation (4), the effective thermal conductivity $k_{\mathrm{eff}} = k_e + k_r$ is used as the thermal conductivity, where $k_r = (16/3)(\sigma T^3/\alpha)$, in which α is the attenuation coefficient (m^{-1}) and σ is the Stefan–Boltzmann constant, 5.672×10^{-8} W/(m·K); k_e is the equivalent thermal conductivity of gas and solid, and its calculation method can be found in the literature [11]. ω_i is the mass generation rate of the ith substance, h_i is the specific enthalpy of the ith substance, H is the heat of reaction, Y_i is the mass fraction of the ith substance, and J_i is the diffusion flux of component i, $J_i = \rho_g D_i \nabla Y_i$.

3.3. Single Value Condition

3.3.1. Boundary Conditions. Considering the ventilation gas mixture as an ideal gas, the inlet boundary condition uses the velocity inlet boundary condition to describe the ventilation gas flow at the inlet of the oxidation bed and the mass fraction of each component in the ventilation gas. The flow direction is perpendicular to the inlet plane, and the air temperature is set to 300 K. The outlet of the oxidation bed uses the pressure outlet boundary. Assuming that the flow is fully developed, the first derivative of the outlet boundary in the normal direction is zero. It is also necessary to define the "reflux" condition on the pressure outlet boundary, which is a practical boundary condition when fluid enters the calculation domain from the outside and a backflow occurs on the pressure outlet boundary. The strong oxidation reaction in the thermal oxidation bed may cause the backflow phenomenon at the outlet. The composition of the backflow gas is air, so the mass fraction of methane is 0 and the mass fraction of oxygen is 0.23.

3.3.2. Commutation Conditions. The time that the ventilation gas continuously flows in one direction in the oxidation bed is called a half commutation cycle, and the commutation action is completed instantaneously without time. The flow state, temperature, and physical property parameters of the gas as well as the physical property parameters of the ceramic honeycomb body did not change before and after the commutation moment.

The ventilation gas enters the oxidation bed from one end of the oxidation bed and changes direction after lasting for a half cycle. The original pressure outlet becomes a velocity inlet. The inlet velocity and direction and gas composition are the same as the previous half cycle. The original velocity inlet becomes pressure outlet, the export parameter setting is the same as the first half cycle. In this way, a forward-reverse continuous flow time of the mixed gas in the oxidation bed constitutes a commutation cycle, and this cycle is carried out until it enters a stable state. In Fluent, the periodic switching of boundary conditions was realized by running the journal file, and the cyclic calculation was completed.

3.3.3. Initial Conditions. Prior to system operation, the oxidation bed needs to be preheated to reach the temperature required for the ventilation gas oxidation, so as to enable the device to operate self-sustainably. Studies have shown that, after the oxidation bed enters stable operation, the operating state has nothing to do with the start-up process. Therefore, in the numerical simulation in this study, the influence of the start-up process of the oxidation bed was not considered, and only the influence of physical parameters and operating parameters on the performance of the oxidation bed during the operation was investigated. Meanwhile, the initial temperature of the porous medium was set to the temperature distribution function of the oxidation bed at the end of the start-up process, and the UDF program was imported into Fluent to realize the initialization of the temperature field of the oxidation bed. The initial concentration and temperature were the same as the parameters of the inlet ventilation gas.

3.4. Numerical Simulation Solutions. This study combined orthogonal design and numerical simulation to investigate the maximum commutation half cycle. Orthogonal experimental design is an experimental design method that studies multiple factors and multiple levels. It can achieve results equivalent to a large number of comprehensive experiments with the minimal number of tests. Before the orthogonal test, the test plan was first determined through the orthogonal table. The influencing factors of the maximum commutation half cycle for the thermal countercurrent oxidation of low-concentration gas in coal mine ventilation include methane concentration, air inlet velocity, oxidation bed porosity, filling length, filling materials, physical properties of ventilation gas, and heat loss on the oxidation bed wall. The thermal countercurrent oxidation bed is usually filled with honeycomb ceramics, mostly made of cordierite and mullite. These two materials have relatively

close physical properties. The methane concentration of coal mine ventilation gas is low, and the influence of methane concentration changes on its physical properties can be ignored, so the exhaust gas can be approximated as air. The physical parameters of the filling material and the ventilation gas were fixed; thus, they were considered as quantities in the calculation. The wall heat loss is related to the thermal insulation performance of the oxidation bed device and the ambient temperature, and its influence on the maximum half cycle of the commutation is more complicated. Therefore, the wall heat loss was temporarily ignored in the numerical simulation analysis.

Therefore, the four influencing factors of the maximum commutation half cycle (T), i.e., methane concentration (c), inlet velocity (v), oxidation bed porosity (ε), and filling length (L), were used as independent variables for orthogonal design. According to the preliminary site inspection and actual measurement, comprehensively considering the oxidation effect and application conditions of the exhaust gas, we determined the level range corresponding to the four factors and designed the orthogonal test table. Meanwhile, in order to highlight the uniformity of the selected values and the disparity of results, the experimental program was designed in an equally spaced manner, with 5 levels for each factor. Thus, the "4 factors, 5 levels" orthogonal experimental design method was adopted in the study. Based on the above parameters and spatial location determination principles, the orthogonal test table was designed. The factors and levels are shown in Table 1.

Table 1: Influencing factors and levels of the orthogonal test.

Group number	c (%)	v (m/s)	L (m)	ε
1	0.25	0.10	0.6	0.65
2	0.50	0.15	0.8	0.70
3	0.75	0.20	1.0	0.75
4	1.00	0.25	1.2	0.80
5	1.25	0.30	1.4	0.85

Table 2: Numerical simulation results.

Test number	c (%)	v (m/s)	L (m)	ε	T (min)
1	0.25	0.10	0.6	0.65	20.63
2	0.25	0.15	0.8	0.70	14.32
3	0.25	0.20	1.0	0.75	10.28
4	0.25	0.25	1.2	0.80	7.23
5	0.25	0.30	1.4	0.85	4.73
6	0.50	0.10	0.8	0.75	28.51
7	0.50	0.15	1.0	0.80	17.09
8	0.50	0.20	1.2	0.85	10.36
9	0.50	0.25	1.4	0.65	25.98
10	0.50	0.30	0.6	0.70	7.20
11	0.75	0.10	1.0	0.85	25.05
12	0.75	0.15	1.2	0.65	51.54
13	0.75	0.20	1.4	0.70	36.02
14	0.75	0.25	0.6	0.75	9.30
15	0.75	0.30	0.8	0.80	7.68
16	1.00	0.10	1.2	0.70	81.71
17	1.00	0.15	1.4	0.75	48.31
18	1.00	0.20	0.6	0.80	11.11
19	1.00	0.25	0.8	0.85	8.07
20	1.00	0.30	1.0	0.65	22.95
21	1.25	0.10	1.4	0.80	67.89
22	1.25	0.15	0.6	0.85	12.68
23	1.25	0.20	0.8	0.65	33.63
24	1.25	0.25	1.0	0.70	27.12
25	1.25	0.30	1.2	0.75	21.25

4. Simulation Results and Analysis

In order to investigate the influencing factors of the maximum commutation half cycle for the thermal countercurrent oxidation of low-concentration gas in coal mine ventilation, a total of 25 working conditions with the combination of different methane concentrations, inlet velocities, porosities, and oxidation bed filling lengths through orthogonal tables were used to perform numerical simulation. The simulation results are shown in Table 2.

According to the theory of orthogonal test, each factor was averaged at the same level to obtain the comprehensive average value of each factor at the same level. Then, the difference between the maximum value and the minimum value among the average values of different levels of each factor was calculated to obtain the range (r) of each influencing factor. The range value can reflect the significance of the influence of the factor on the result. The larger the range value, the greater the difference in the level of the factor and the more important the factor. Through the range analysis, the influences of each factor on the different maximum commutation half cycle of thermal countercurrent oxidation can be derived. Figure 2 shows the fitting curves and ranges of the comprehensive average of the 4 factors.

It can be found from Figure 2 that the range between the maximum and minimum values of the inlet velocity is the largest among the four factors, indicating that the inlet velocity is the most important factor affecting the maximum commutation half cycle for the thermal countercurrent oxidation of low-concentration gas in coal mine ventilation. The influence of the 4 factors on the maximum commutation half cycle of thermal countercurrent oxidation can be ordered from high to low as $v > L > c > \varepsilon$. From Figure 2(a), as methane concentration increases, the maximum commutation half cycle gradually increases, which is mainly because the increase of the methane concentration in the exhaust gas leads to the increase of the heat entering the oxidation bed. Figure 2(b) shows that, as the inlet velocity increases, the maximum commutation half cycle gradually decreases. This is mainly because the increased inlet velocity causes the increase in the outlet heat loss, thereby reducing the commutation time. Figures 2(c) and 2(d) show that the maximum commutation half cycle increases with the increase of the oxidation bed filling length and decreases with the increase of the porosity of the oxidation bed. The reason is that when the porosity of the oxidation bed is larger, the solid area is smaller and the heat storage capacity of the oxidation bed is worse; thus, the fresh exhaust gas cools the inlet end more vigorously and the reversing time is shortened. As the filling length of the oxidation bed increases, the length of the oxidation bed preheating section is also correspondingly increased, and the heat stored in the oxidation bed increases, thereby prolonging the reversing time.

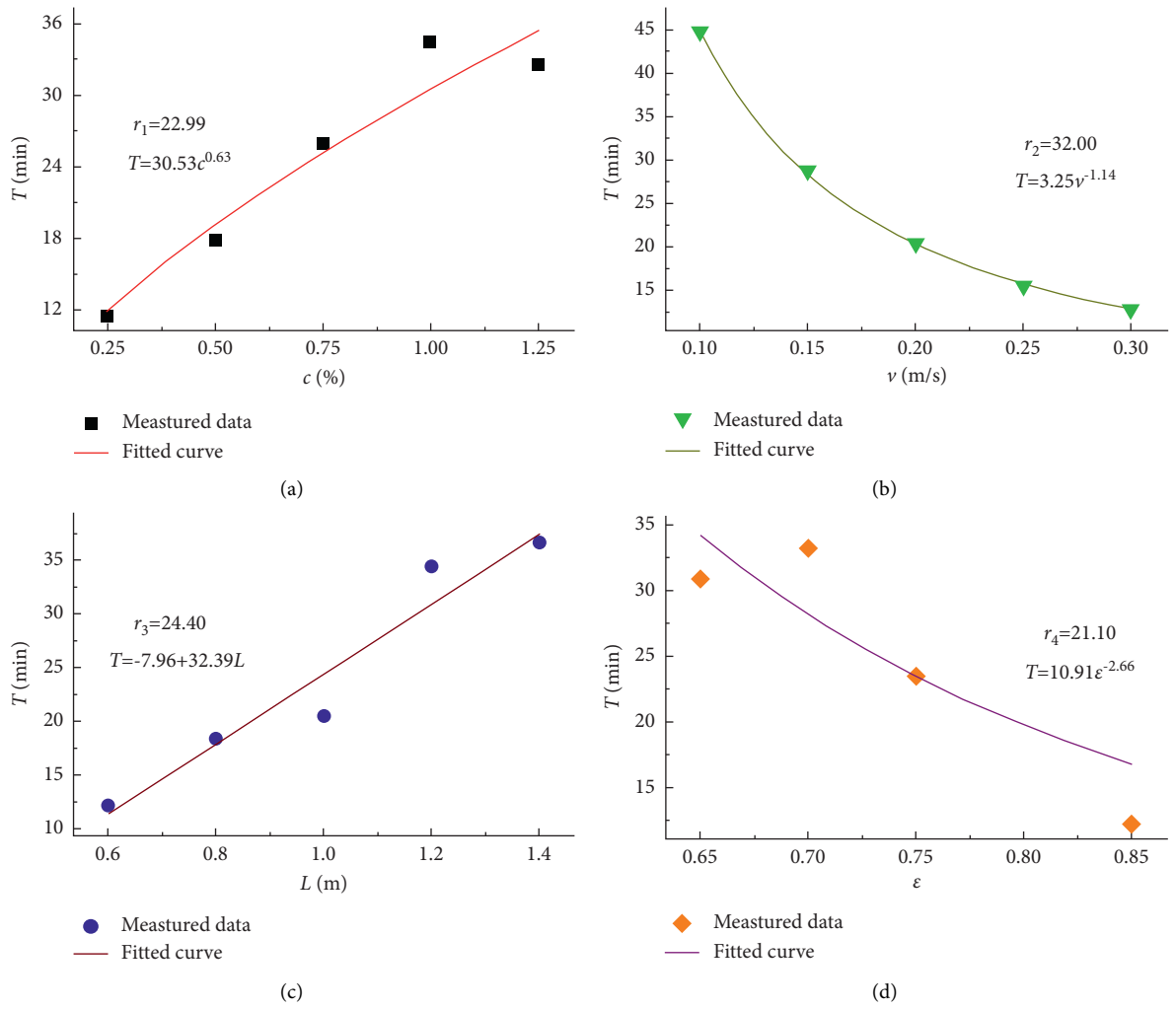

Figure 2: Comprehensive average values and ranges of 4 factors.

5. Establishment and Correction of Mathematical Model

5.1. Multiple Nonlinear Regression Equation. According to the fitting curve of the comprehensive average of the four factors, the influence of the filling length of the oxidation bed on the maximum commutation half cycle is linear, while the influence of the exhaust gas inlet velocity, methane concentration, and porosity on the maximum commutation half cycle is nonlinear, which can be more suitably described by the power function. On the basis of the above numerical simulation analysis, combined with the theoretical calculation formula of the maximum half cycle of the reciprocating inert porous medium burner in the literature [9], the relationship between the maximum half cycle and the influencing factors can be determined by the following objective function:

$$T = a_1 L(1-\varepsilon)^{a_2} v^{a_3} c^{a_4}, \quad (7)$$

where a_1 is the coefficient to be solved; a_2, a_3, and a_4 are the indexes to be solved; T is the maximum commutation half cycle, min; L is the length of the oxidation bed, m; ε is the porosity of the oxidation bed; c is the methane concentration of the ventilation gas, %; and v is the air inlet velocity, m/s.

According to the 25 sets of sample data in Table 2, we selected nonlinear regression in SPSS, input the regression model into the model expression, and set the initial value and constraints. Then, the coefficient to be solved, a_1, and the indexes to be solved, a_2, a_3, and a_4, were calculated, and the calculation equation of the maximum commutation half cycle was obtained as follows:

$$T = 23.433L(1-\varepsilon)^{1.189} v^{-1.088} c^{0.654}. \quad (8)$$

From the calculated statistical report, it can be found that the relative deviation between the numerical simulation data and the formula calculation data did not exceed 10%, and R^2 was 0.997. It can also be seen from the comparison result in Figure 3 that there is a good agreement between the formula calculation results and the numerical simulation results.

5.2. Verification and Revision of Mathematical Model. In order to experimentally verify the prediction mathematical model of the maximum commutation half cycle obtained by

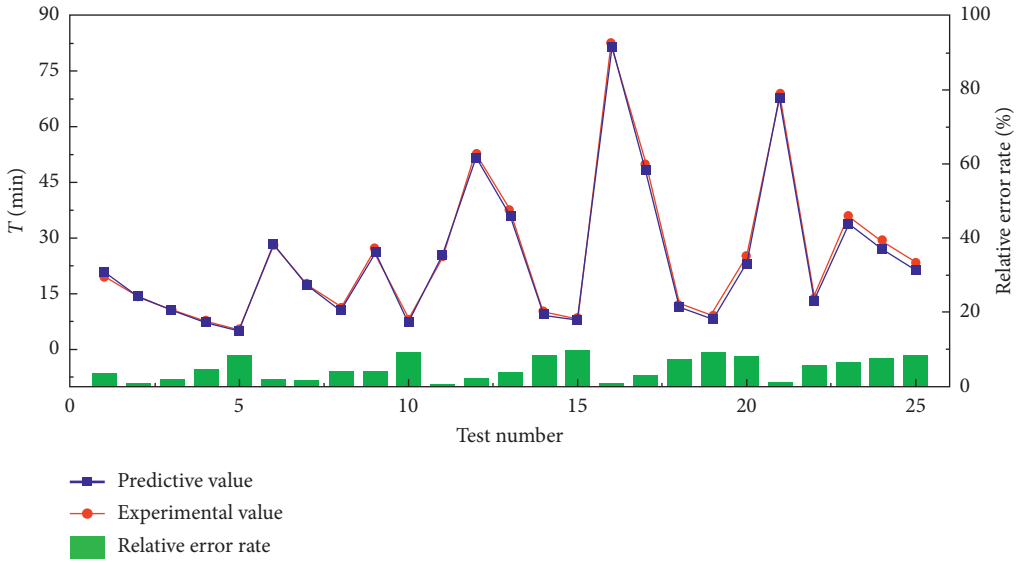

Figure 3: Comparison of numerical simulation values and formula calculation values.

numerical simulation regression analysis, an experimental system for thermal countercurrent oxidation of low-concentration gas in coal mine ventilation was established. The experimental system consisted of five parts: gas supply system, temperature acquisition system, water cooling system, gas composition analysis system, and the device body. The entire experimental system is shown in Figure 4. The compressed air from the air compressor was mixed with the methane gas from the methane cylinder at a certain volume ratio through the regulator valve and pressure reducing valve to obtain the simulated ventilation gas. The time relay and the solenoid valve cooperated with each other to make the simulated gas enter and discharge alternately from both ends of the oxidation bed of the device body. Fifteen thermocouples were evenly arranged in the direction of the central axis of the oxidation bed in the device body to monitor the temperature of the oxidation bed along the axis and at the inlet and outlet. The temperature data was collected through the acquisition card and displayed and stored in the computer in real time. The preheating temperature and heating power of the electric heater were controlled by using the temperature controller. In order to protect the solenoid valve, water coolers were provided at both ends of the device body to cool the outlet high-temperature exhaust gas. The gas chromatograph was used to detect the methane concentration in the intake and exhaust gas online.

After connecting the experimental system and ensuring the air tightness of the experimental instruments, equipment, and connecting parts, the experiment can begin. The experimental steps are as follows:

(1) Turn on the main power switch of the device and power up the system. Then, start the air compressor to make the gas enter the air tank for storage first, and the air compressor is kept in an open position.

(2) Turn on the time relay, set the commutation time, and the commutation control system will start to work. Turn on the computer connected to the data acquisition card and open the data acquisition operating system on the computer. Set the channels and parameters that need to be collectedm and display the indicated values of each parameter in real time.

(3) Open the methane cylinder container and adjust the outlet pressure to 0.2 MPa through the pressure reducing valve.

(4) Subsequently, open the valves for air and methane and adjust them to their preset flow rates, and then make corresponding fine adjustments to make the displayed value consistent with the preset value.

(5) Run the system under a fixed commutation cycle. When the temperature difference between the current circle and the next cycle does not exceed 0.1°C, the system can be considered in the stable operation. After the measured parameters have reached the required values, the system is considered to be successfully started. Then, we can start the formal experiments.

(6) Adjust the parameters of each operating condition according to the experimental conditions. After the adjustment, the system is allowed to run for a certain period of time. Then, determine whether the system is in a stable state or not by observing the difference in temperature between the measured points of the oxidation bed in two consecutive cycles. After the condition stabilizes, the data can be collected and recorded. In the next working condition, repeat the above process to obtain the corresponding experimental results.

(7) At the end of the experiment, first turn off the methane gas source, close the methane pressure reducing valve, stop data collection, save the experimental data, and then turn off the computer.

(8) Turn off the flow meter, and then turn off the air source and the periodic commutation control

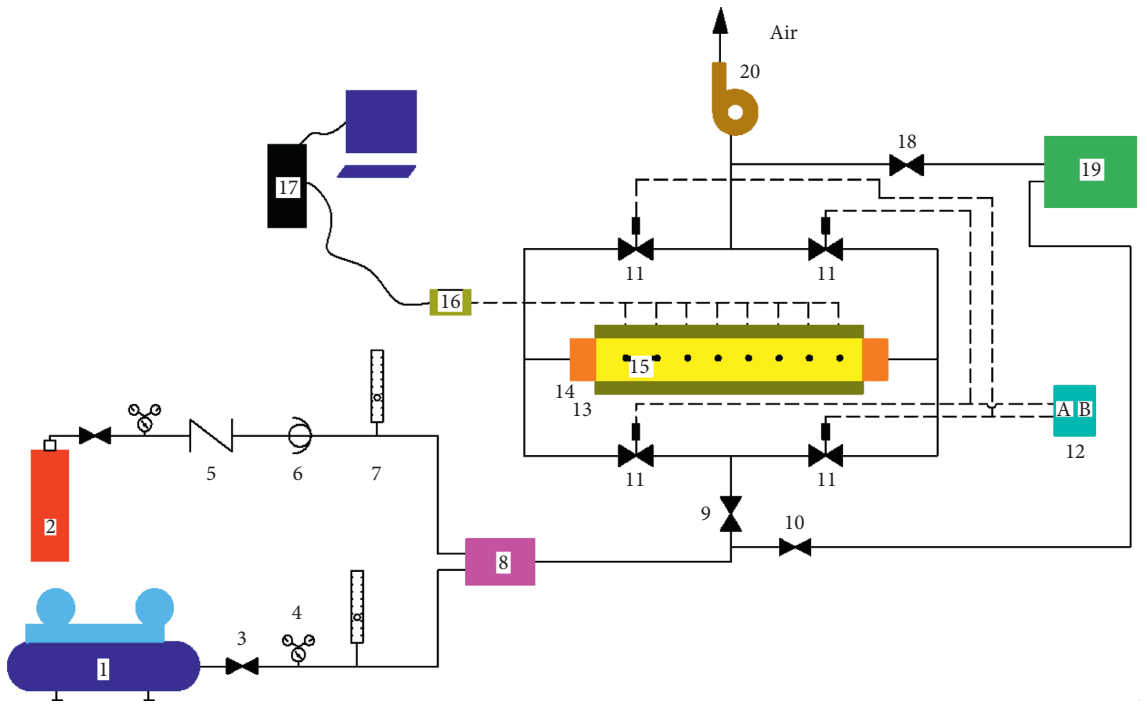

Figure 4: Experimental system for thermal countercurrent oxidation of low-concentration gas in coal mine ventilation (1: air compressor; 2: methane cylinder; 3: regulating valve; 4: pressure reducing valve; 5: one-way valve; 6: flame arrester; 7: rotor flow meter; 8: mixer; 9: intake main valve; 10: intake sampling valve (usually closed); 11: solenoid valve; 12: time relay; 13: device main body; 14: cooler; 15: thermocouple; 16: collection card; 17: computer; 18: exhaust gas sampling valve (usually closed); 19: gas chromatograph; 20: draft fan).

system. Turn off the power of the console, properly store the experimental instruments, and end the experiment.

(9) For the next experiment, repeat the above operation.

Four specifications of honeycomb ceramics were used in the experiment, two of which had the porosities of 0.56 and 0.70, with a square channel shape; and the other two had the porosities of 0.36 and 0.4, with a circular channel shape. The channel was square. The filling length of the oxidation bed was determined by the filling quantity of the honeycomb ceramics. The experiment only investigated the two cases with filling lengths of 0.8 m and 1.2 m. The methane concentration of the simulated gas was adjusted by controlling the two gas flow rates, and the inlet velocity was controlled by the intake valve. The commutation half cycle of the thermal countercurrent oxidation was manually set by the time relay. By changing the methane concentration, inlet velocity, porosity, and filling length, the measured values of the maximum commutation half cycle under the five combined working conditions were obtained. The measured values were compared with the calculated values, as shown in Table 3.

From the test results in Table 3, it can be found that the experimental results of the maximum commutation half cycle under the five working conditions measured were smaller than the calculated values by the uncorrected formula, and the relative error exceeded 15%. The reason is that the empirical calculation formula summarized from by numerical simulation is based on the assumption that there is no heat loss on the wall. In practice, because of the temperature difference between the device wall and the environment, there will be a part of heat loss, resulting in a shorter maximum commutation half cycle. Therefore, the empirical formula based on the numerical simulation needs to be further corrected to be suitable for the practical situation. The wall heat loss correction coefficient k was introduced to obtain the following complete mathematical model of the maximum commutation half cycle of thermal countercurrent oxidation:

$$T = 23.433kL(1-\varepsilon)^{1.189}v^{-1.088}c^{0.654}, \tag{9}$$

where k is the wall heat loss correction coefficient, which is related to the thermal insulation performance of the device, generally set to 0.8-0.9. The thermal insulation performance of the device body of this experimental system is poor. Thus, the wall heat loss coefficient was set to $k = 0.82$ for correction. As shown in Table 3, after correction, the relative error between the calculated value and the measured value does not exceed 3.0%, indicating that the maximum commutation half cycle calculated by the complete mathematical model is consistent with the measured data. Therefore, the obtained formula can be applied to the design calculation of the maximum commutation half cycle for thermal countercurrent oxidation system of low-concentration gas in the actual coal mine ventilation.

Table 3: Comparison of experimental and calculated values of the maximum commutation half cycle.

Working condition number	Methane concentration (%)	Inlet velocity (m/s)	Porosity	Filling length (m)	Measured value (min)	Calculated value before correction (min)	Error before correction (%)	Calculated value after correction (min)	Error after correction (%)
1	0.30	0.20	0.56	1.20	23.17	27.77	16.58	22.77	1.73
2	0.60	0.30	0.70	1.20	14.33	17.83	19.60	14.62	1.96
3	0.40	0.30	0.56	0.80	11.50	14.38	20.00	11.79	2.44
4	0.50	0.25	0.70	0.80	10.33	12.86	19.67	10.55	2.04
5	0.70	0.35	0.70	1.20	13.33	16.67	20.04	13.67	2.49
6	0.30	0.20	0.36	1.2	36.51	43.36	15.79	35.55	2.69
7	0.60	0.30	0.4	1.2	34.27	40.65	15.69	33.33	2.82
8	0.40	0.30	0.36	0.8	18.51	22.44	17.53	18.40	0.57
9	0.50	0.25	0.4	0.8	23.73	29.33	19.09	24.05	1.33
10	0.70	0.35	0.4	1.2	31.82	38.02	16.30	31.17	2.07

6. Conclusions

In this study, the orthogonal experiment design method was used to obtain the maximum commutation half cycle for thermal countercurrent oxidation of coal mine ventilation gas under 25 working conditions using the Fluent computational fluid dynamics software. In addition, the relationship between the maximum commutation half cycle and various factors was analysed. From the results of the numerical simulation analysis, it can be seen that the maximum commutation half cycle was closely related to the methane concentration of ventilation gas, the inlet velocity, the porosity of the honeycomb ceramic, and the filling length of the oxidation bed. When other conditions were constant, the maximum commutation half cycle of thermal countercurrent oxidation increased with the increase of intake methane concentration of ventilation gas and filling length, while decreased with the increase of air inlet velocity and porosity of oxidation bed. On this basis, the SPSS data processing software was used to perform regression analysis on the numerical simulation data, and the multiple regression equations with four influencing factors including methane concentration, inlet velocity, porosity, and filling length of oxidation bed were obtained. The deviation between the predicted values and the data simulation values was small, and the degree of fit was high. In addition, the maximum commutation half cycle obtained by the numerical simulation was verified by experiments. After introducing the wall heat loss correction coefficient, the complete mathematical model for the calculation of the maximum commutation half cycle was obtained. The experimental results and the calculated results after correction were compared, and the relative error was not more than 3%. The complete mathematical model after correction can be applied to the design calculation of the maximum commutation half cycle for thermal countercurrent oxidation of low-concentration gas in the actual coal mine ventilation. Because of the limitation of experimental parameters, the prediction model has certain limitations. Therefore, to improve the accuracy of the maximum commutation half cycle prediction, it is necessary to supplement a larger amount of numerical simulations and experiments, as well as more accurate data fitting methods.

Data Availability

Data sharing is not applicable to this article as no datasets were generated or analysed during the current study.

Conflicts of Interest

The authors declare that they have no conflicts of interest.

Acknowledgments

This research was financially supported by the National Natural Science Foundation of China (51774135 and 51974120), Hunan Postgraduate Research and Innovation Funding Project (CX2018B657), and Southern Coal Mine Gas and Roof Disaster Prevention and Control Work Safety Key Laboratory Open Fund Project (E21825).

References

[1] J. F. Zhang, S. L. Shi, Y. Lu, and Y. Bo, "Symbiotic disasters of mine gas and coal spontaneous combustion: coupling relationship, disaster mechanism, prevention and control technology," *China Safety Science Journal*, vol. 30, no. 10, pp. 149–155, 2020.

[2] Y. J. Li, P. F. Wang, R. H. Liu, Y. Jiang, and H. Han, "Determination of the optimal axial-to-radial flow ratio of the wall-mounted swirling ventilation in fully mechanized excavation face," *Powder Technology*, vol. 360, pp. 890–910, 2020.

[3] Y. J. Li, P. F. Wang, R. H. Liu, and R. Gao, "Optimization of structural parameters and installation position of the wall-mounted air cylinder in the fully mechanized excavation face based on CFD and orthogonal design," *Process Safety and Environmental Protection*, vol. 130, pp. 344–358, 2019.

[4] S. L. Shi, A. Y. Wu, R. Q. Li et al., "Numerical simulation and scheme optimization on gas drainage through high level borehole in working face," *Journal of Safety Science and Technology*, vol. 12, no. 7, pp. 71–76, 2016.

[5] S. Y. Hu, Y. Gao, G. R. Feng, F. Hu, C. Liu, and J. Li, "Experimental study of the dust-removal performance of a wet scrubber," *International Journal of Coal Science & Technology*, vol. 8, no. 2, pp. 228–239, 2021.

[6] P. F. Wang, X. H. Tan, L. Y. Zhang, Y. Li, and R. Liu, "Influence of particle diameter on the wettability of coal dust and

the dust suppression efficiency via spraying," *Process Safety and Environmental Protection*, vol. 132, pp. 189–199, 2019.

[7] Y. H. Niu, "Prospect and utilization status of Low concentration gas in vitiated air at mines," *Industrial Safety and Environmental Protection*, vol. 28, no. 3, pp. 3–5, 2002.

[8] X. Y. Wang and J. Du, "Present situation and prospect of oxidation technology about mine methane with concentration less than 1%," *Coal Technology*, vol. 27, no. 9, pp. 1–3, 2008.

[9] F. K. Zhang and L. J. Xu, "Effect of methane on global warming and mitigating measure," *Mining Safety & Environmental Protection*, vol. 31, no. 5, pp. 6–9, 2004.

[10] B. Zhang, Y. Q. Liu, R. X. Liu et al., "Oxidation of coal mine ventilation air methane in thermal reverse-flow reactor," *Journal of China Coal Society*, vol. 34, no. 11, pp. 1475–1478, 2009.

[11] Y. Lu, F. Jiang, and Y. H. Xiao, "Experimental study of coal mine ventilation air methane oxidization," *Journal of China Coal Society*, vol. 36, no. 6, pp. 973–977, 2011.

[12] S. Su, A. Beath, H. Guo, and C. Mallett, "An assessment of mine methane mitigation and utilisation technologies," *Journal of China Coal Society*, vol. 30, no. 23, pp. 123–170, 2005.

[13] W. Krzysztof, "Harnessing methane emissions from coal mining," *Process Safety and Environmental Protection*, vol. 86, no. 5, pp. 315–320, 2008.

[14] P. F. Wang, T. Feng, S. L. Li, and P. Ma, "Resistance characteristics of thermal reverse-flow oxidation bed for coal mine ventilation air methane," *Natural Gas Industry*, vol. 32, no. 6, pp. 73–77, 2012.

[15] J. R. Shi, M. Z. Xie, and L. Zhou, "Flammable limits and maximum half cycle for inert porous medium burner with reciprocating flow," *CIE Journal*, vol. 58, no. 2, pp. 1983–1988, 2007.

[16] P. F. Wang, T. Feng, and X. L. Hao, "One-dimensional numerical simulation of thermal reverse-flow oxidation of ventilation air methane in coal mine," *Journal of Mining & Safety Engineering*, vol. 29, no. 3, pp. 434–439, 2012.

[17] E. B. Liu, D. C. Tian, W. S. Li, J. Chen, and Q. Chen, "Study on erosion behavior and separation efficiency of a shale gas vertical separator," *Energy & Fuels*, vol. 35, pp. 3878–3886, 2021.

[18] E. B. Liu, X. J. Wang, and W. W. Zhao, "Analysis and research on pipeline vibration of a natural gas compressor station and vibration reduction measures," *Energy & Fuels*, vol. 35, pp. 479–492, 2021.

[19] E. B. Liu, D. J. Li, W. S. Li et al., ""Erosion simulation and improvement scheme of separator blowdown system —a case study of Changning national shale gas demonstration area," *Journal of Natural Gas Science and Engineering*, vol. 88, Article ID 103856, 2021.

[20] Z. H. Lu, "Calculation of effective thermal conductivity of foam porous media," *Journal of Nanjing University of Science and Technology*, vol. 25, no. 3, pp. 257–261, 2001.

Hindawi
Shock and Vibration
Volume 2021, Article ID 2115767, 10 pages
https://doi.org/10.1155/2021/2115767

Research Article

Research on the Decompression Effects of Shaft Explosion-Proof Door at Different Lifting Heights

Xue-Bo Zhang,[1,2,3,4] **Shuai-Shuai Shen**,[1] **Zhi-Yang Gao**,[1] **Ming Yang**,[1,2,3] **and Jing-Zhang Ren**[1]

[1]*College of Safety Science and Engineering, Henan Polytechnic University, Jiaozuo, China*
[2]*State Key Laboratory Cultivation Base for Gas Geology and Gas Control, Henan Polytechnic University, Jiaozuo, China*
[3]*State Collaborative Innovation Center of Coal Work Safety and Clean-Efficiency Utilization, College of Safety Science and Engineering, Henan Polytechnic University, Jiaozuo, China*
[4]*Henan Shenhuo Group Co. Ltd., Yongcheng 476600, China*

Correspondence should be addressed to Zhi-Yang Gao; gzy@hpu.edu.cn

Received 12 May 2021; Revised 25 June 2021; Accepted 19 July 2021; Published 27 September 2021

Academic Editor: Jianwei Cheng

To study the decompression effects of shaft explosion-proof door at different lifting heights, this paper designed the gas explosion testing system. Based on the test results, this paper made a numeric analysis of the change regularities of the shock wave overpressure when the shaft explosion-proof door was lifted at different heights. Finally, this paper determined the proper lifting height of the shaft explosion-proof door and put forward the active decompression concept. The research showed that (1) the shock wave overpressure at the explosion-proof door decreased in a power exponential relationship as the lifting height increased. When the lifting height increased from 0 cm to 5 cm, the peak overpressure at the explosion-proof door decreased from 36.06 kPa to 22.47 kPa, dropping by 37.7%. When it was lifted at a height of 40 cm, the overpressure dropped to 11.20 kPa and the decompression reached 68.9%. (2) The overpressure at the ventilator decreased in a power exponential relationship as the lifting height increased. When the lifting height of the explosion-proof door increased from 0 cm to 5 cm, the decompression ratio reached the maximum 18.4%. After that, the decompression effect became worse and worse. (3) The explosion-proof door could depressurize and protect the ventilator at gas explosion but with limited effects. To protect the ventilator and the explosion-proof door to the maximum, it was suggested that the pressure sensor was set up somewhere in the mine where the gas explosion is likely to occur. In this way, the explosion was sensed in time and the explosion-proof door could be actively lifted for decompression. This paper was of great guiding significance in optimizing the design of the explosion-proof door equipment, reducing the loss of gas explosion accidents as well as carrying out the emergency rescue.

1. Introduction

The gas explosion of the underground coal mine is one of the major disasters in coal mines, which poses a great threat to the life safety of underground workers. The prevention and suppression of explosion are a major research topic in the field of underground coal mining [1–3]. Explosion-proof door is an important part of the coal mine ventilation system. In the case of underground gas explosion, the explosion-proof door can be lifted quickly to release pressure and reduce the damage to the ventilator. Also, the door can be closed quickly after the shock wave to create conditions for postdisaster rescue [4]. Therefore, it is very important to ensure the stable operation of the ventilation system and remove the harmful and poisonous gas after the explosion accident.

At present, the cover-type explosion-proof door is still mainly used in the return air shaft of the coal mine. Gas explosions have happened in mines with different gas grades, and they have caused damage to the cover-type shaft explosion-proof doors [5]. For example, at Xinhua No. 4 mine (low gas level) in Pingdingshan City, the explosion-proof door was lifted and dislocated after falling. At Taiyuan Tunlan coal mine (high gas level), the

explosion-proof door was driven hundreds of meters away, and the deviation was over 20 meters. Explosions continuously occurred at Chenjiashan coal mine (outburst mine) in Tongchuan City, Shanxi Province. In the explosions, the explosion door was driven hundreds of meters away and the ventilator got damaged. Therefore, it is of great practical significance for the explosion-proof door to timely release pressure and reset after explosion accidents because it not only reduces the casualties and losses of the accidents but also facilitates the emergency rescue.

Many scholars have carried out considerable detailed studies on the law of underground shock wave motion. According to the experiment, Savinko put forward the attenuation formula of shock motion intensity in straight roadways and pointed out that the speed of shock wave pressure attenuation mainly depended on the size, structure, and support pattern of the fractured surface [6]. Baiquan et al. systematically studied the effects of different roadway conditions on gas explosion through experimental methods. Their research showed that obstacles could aggravate the turbulence effect in the flame transmission process, thus causing the positive feedback mechanism in the explosion process [7–10]. Bin et al. studied the influence of C_2H_4 and H_2 on premixed gas explosion through experiments, and the research results play a guiding role in chemical industry explosion prevention [11–13]. In the design of a gate-type explosion-proof door, Hu determined its counterweight through force analysis and sealed it with plate-type rubber strips [14]. Xuebo et al. designed a shaft explosion-proof door of return air with buffering and resetting functions. Through hydraulic devices, the device could effectively reduce the damage of the shock wave to the ventilation door and increase its reliability [15]. Qiusheng et al. established an overturning model of the explosion-proof door body by analyzing the stress relationship of the door body in the mine [16]. Through numerical simulation, Jiajia et al. proposed that a linear relationship existed between the gas accumulation amount and the peak overpressure at the fan and the explosion-proof door and that the peak overpressure would increase along with the increase of the gas accumulation amount [17]. Tian et al. first established the MFBL explosion-proof door model, and then they simulated and analyzed the relationship between the lifting height of the explosion-proof door and the explosion equivalent through the Fluent software [18].

Scholars have carried out a lot of studies on the law of the shock motion in the gas explosion, and some scholars have studied the new explosion-proof doors. At present, the widely used cover-type shaft explosion-proof doors are overall relatively low in the protection efficiency. However, few scholars have carried out research on how the explosion-proof door is actively lifted to release pressure. This paper analyzed the decompression effects of the explosion-proof door at the door itself and the ventilators at its different lifting heights and put forward the concept about the active opening of the explosion-proof door. The research results provided theoretical support for improving the decompression effects of the explosion-proof door and optimizing the design of the explosion-proof door equipment.

2. Gas Explosion Experiment System Design and Experiment Result Analysis

The team independently developed the gas explosion experiment system, which is composed of return air roadway, return air shaft, ventilator, explosion-proof door, ignition device, high-frequency dynamic pressure transmitter, high-speed camera, etc., as shown in Figure 1. The return air shaft and air drift are round pipes with a diameter of 40 cm, and the return air roadway is semicircular pipes with a radius of 20 cm.

Experimental procedures: (1) a methane-air mixture with a certain concentration was prepared by using the flow meter and the pressure gauge. The gas mixture was filled in the first section of the pipeline with preinstalled film through exhausting air, length 1 m (as shown in Figure 1). The methane concentration of mixed gas was 9.5% filled with the exhaust air method. Also, the aeration time was 4.46 min. (2) The power of the ignition device is switched on, and the spark ignition device was controlled with computers. The high-frequency dynamic pressure transmitter on the pipe wall started to collect data. The ignition point time was recorded as 0 s. In the coordinate system shown in Figure 1, the coordinates of each monitoring point are $P1$ (70, 20), $P2$ (0, 110), SZ (310, 20), and BZ (460, 15). In order to protect the experimental equipment, the opening height of the explosion-proof door is 100 cm. (3) Data collected by using the high-frequency dynamic pressure transmitter were extracted and summarized for analysis.

In the experimental process, the flame transmission of the shock wave in the gas explosion is shown in Figure 2, and the shock wave overpressure changes in the blast zone (BZ) and the spread zone (SZ) are shown in Figure 1.

As can be seen from Figure 2, the flame plane first expanded in a spherical shape after the premixed gas was ignited. Limited by the pipeline, the flame plane would then transform into a rugby shape and propagate forward. It can be seen from Figure 2 that the shock wave had the obvious reflection effect when it transmitted to the return air roadway and the turning point of the return air shaft. This indicated that part of the shock wave energy was transferred to the return air shaft and some energy was reflected to the return air shaft in the form of reflection, and the remaining energy was transmitted to the air in the form of sound wave, thermal radiation, and heat transfer.

As shown in Figure 3, (1) after the gas explosion, the overpressure reached the peak value at an approximate time in the explosion zone and the transmission zone. This was the interaction result of a small experimental model and high transmission speed of shock wave. (2) It can be seen from the development of the shock wave that the shock wave overpressure in the explosion transmission zone was greater than that in the explosion area. This was because the shock wave in the blast zone had not yet developed to the maximum. When the reaction of all the

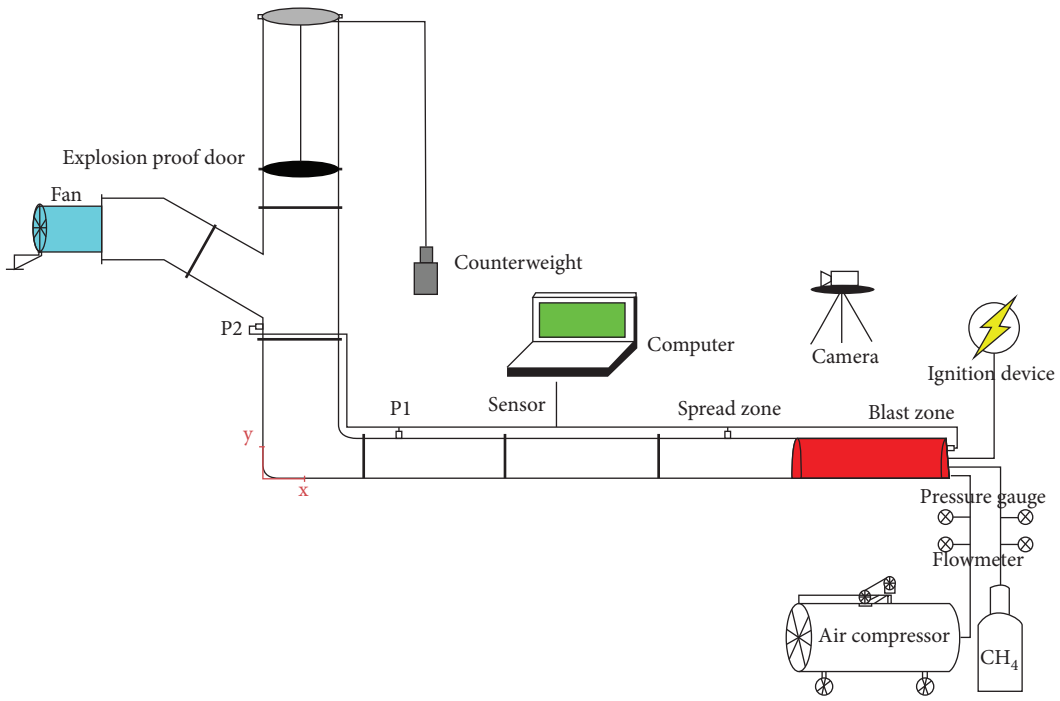

Figure 1: Gas explosion experiment system.

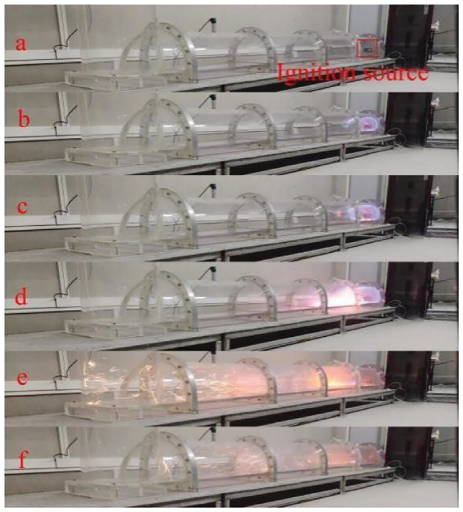

Figure 2: The flame transmission of the shock wave.

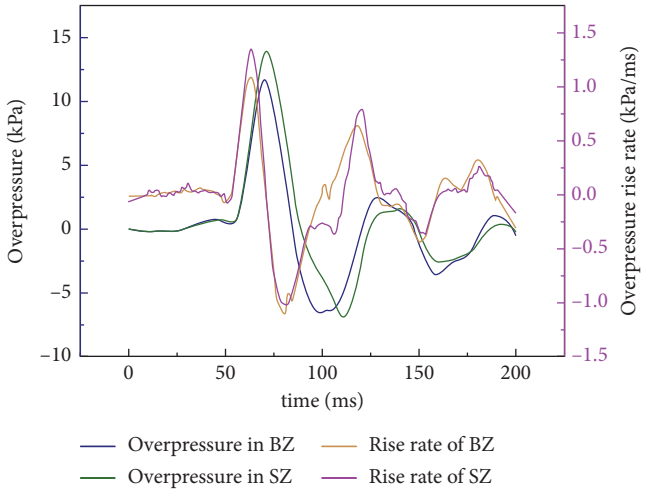

Figure 3: Overpressure change diagram in the experimental process.

accumulative gas finished, the shock wave overpressure reached the peak value, so the peak value in the transmission area was relatively great. Because of the shock motion, the overpressure became negative in the blast zone and the transmission zone, and the maximum negative pressure in the transmission zone was smaller than that in the blast zone. This was because it took some time for the shock wave to transmit from the blast zone to the transmission zone. As can be seen from Figure 3, the rising speed curve of the overpressure in the blast zone rose became negative, which was slightly before the curve in the transmission area. (3) The rising speed of the overpressure in both zones fluctuated at 100 ms because the size of the gas explosion experiment system was small. The monitoring points of both zones were within the coverage of the shock wave reflection, and the distance between the transmission zone and the corners was shorter, so the fluctuation got more obvious.

3. Decompression Effect Analysis of Explosion-Proof Door at Different Lifting Heights

3.1. Mathematical Model Building and Verification

3.1.1. Mathematical Model Building. Gas explosion can be assumed to be an ideal gas heated accelerated expansion process, which can be described by a mathematical model composed of kinetic process control equation (mass

conservation equation, momentum conservation equation, energy conservation equation, and component balance equation), turbulence model, and gas chemical reaction model (combustion model and turbulence flame velocity model).

The turbulence model includes $k-\varepsilon$ model, LES model, and DES model. Gas chemical reaction models include laminar flow finite rate model, eddy-dissipation model, laminar flow finite rate/eddy-dissipation model, and EDC model. The laminar finite rate model uses the Arrhenius formula to calculate the chemical source terms but ignores the influence of turbulence fluctuation, so it is suitable for simulating laminar flame propagation. The eddy-dissipation model (EDM) can simulate the rapid combustion of most fuels, and the overall reaction rate is controlled by turbulent mixing. When the LES turbulence model is used (LES + eddy-dissipation model), turbulent mixing rate is replaced by subgrid-scale mixing rate, which can better simulate the propagation process of gas explosion shock wave. The eddy-dissipation concept (EDC) model is an extension of eddy-dissipation model, which can simulate the turbulent reaction flows with chemical reaction mechanisms. However, typical mechanisms have different rigidity, their numerical integration calculation is very expensive, and the model can only be used when the fast chemical reaction is assumed to be invalid. Therefore, the LES turbulence model and eddy-dissipation model (EDM) are finally adopted to simulate the propagation law of gas explosion shock wave.

Combustion model and turbulent flame velocity model:

$$
\begin{aligned}
R_{\mathrm{fu}} &= -\min\left(|R|, \left|R_{j,\mathrm{fu}}\right|\right),\\
R_{i,\mathrm{fu}} &= \nu'_{i,\mathrm{fu}} M_{\omega,i} A \rho \tau^{-1} \mathrm{sgs} \min\left(\frac{Y_{i.\mathrm{fu}}}{\nu_{i,\mathrm{fu}} M_{\omega,\mathrm{fu}}}\right),\\
R_{j,\mathrm{fu}} &= \nu'_{j,\mathrm{fu}} M_{\omega,j} AB \rho \tau^{-1} \mathrm{sgs} \frac{\sum_j Y_{j,\mathrm{fu}}}{\sum_j^N \nu''_{j,\mathrm{fu}} M_{\omega,j}},\\
\tau^{-1}\mathrm{sgs} &= \sqrt{2 S_{ij} S_{ij}},
\end{aligned}
\tag{1}
$$

where $Y_{i,\mathrm{fu}}$ is the mass fraction of any production species, $Y_{j,\mathrm{fu}}$ is the mass fraction of a particular reactant, A and B are empirical constants equal to 4.0 and 0.5, respectively, $\tau^{-1}sgs$ is the subgrid-scale mixing rate, and S_{ij} is the strain rate tensor.

The gas explosion is an unsteady process, and there was no slip on the model wall. A simple algorithm was adopted for iterative solution, and the iteration step size was 0.0005 s.

3.1.2. Physical Model. According to the gas explosion experiment system, a geometric model with a size of 1 : 1 was established, as shown in Figure 4. Different lifting heights of explosion-proof doors were selected based on the diameters of the roadways. The experiment established the geometric models of explosion-proof doors at lifting heights of 0 cm (nonlifting), 5 cm, 10 cm, 20 cm, 30 cm, 40 cm, and ∞ cm (no explosion-proof door).

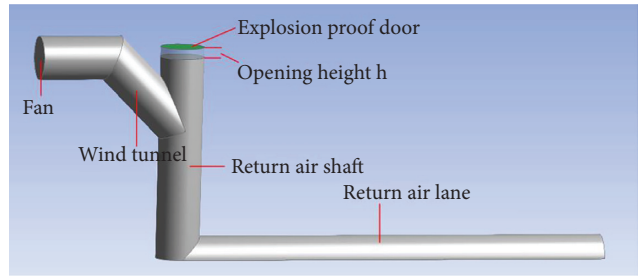

Figure 4: Physical model diagram.

The initial conditions are as follows:

(1) The initial pressure of the whole region is 0 Pa relative to the atmospheric pressure

(2) The initial temperature is 300 K

(3) The initial velocity of the whole area is 0 m/s

(4) The whole area is full of air

The boundary conditions are as follows:

(1) The outlet of the fan is set as pressure outlet, and the outlet pressure is 0 Pa relative to atmospheric pressure

(2) The standard wall function is adopted for the near wall surface, and the explosion-proof door is set to be nonsliding wall surface

The gas explosion processes of these seven geometric models were simulated, respectively, and the influence of explosion-proof doors' lifting heights on the decompression effect of shock waves was analyzed.

3.1.3. Mathematical Model Verification. In Section 2, the propagation characteristics of shock wave in the blast zone and spread zone are revealed. In order to verify the applicability of the mathematical model, numerical simulation was carried out based on the experiment. The experimental results at $P1$ and $P2$ in Figure 1 are compared with the simulation results to verify the correctness of the established model. The experimental results and the numerical simulation results are compared as shown in Figure 5.

In Figure 5, the position of $P1$ and $P2$ is shown in Figure 1; it could be known from the numerical simulation results and the experimental results that the shock wave attenuation laws were basically identical, but the peak value of the overpressure was relatively greater in the numerical simulation. This was mainly because the walls of the roadways were set up as no slipping and no heat transfer. However, the energy produced from the gas explosion was transmitted to the environment through heat transfer or vibration in the experiment. Therefore, the simulated result was relatively greater. This proved the reliability of the established mathematical model for gas explosion.

3.2. Research on the Decompression Effects of the Explosion-Proof Door at Different Lifting Heights. At different lifting heights, the cloud chart about the overpressure in the

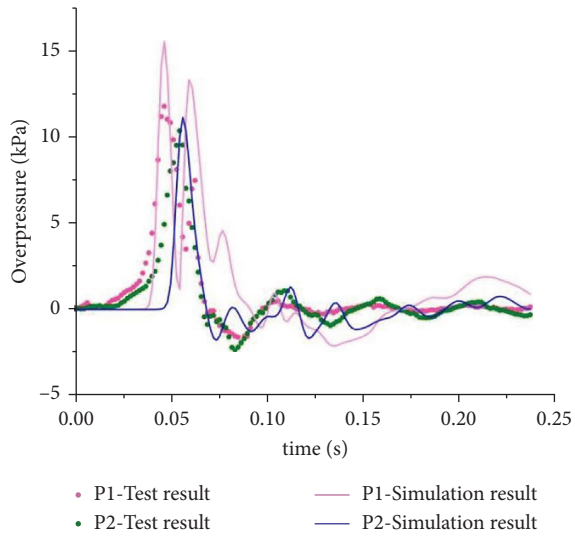

Figure 5: Comparison diagram of experimental results and simulation results.

cross section of the roller and the overpressure changes at the monitoring points are shown in Figures 6 and 7 when the overpressure reached the maximum at the explosion-proof door.

It can be seen from Figures 6 and 7 that (1) as the lifting height of the explosion-proof door increased, the area where the overpressure reached the maximum at the explosion-proof door became smaller and smaller, namely, the decompression area got larger near the explosion-proof door. (2) As the lifting height of the explosion-proof door increased, the peak value of the overpressure near the explosion-proof door decreased gradually at an increasingly low speed; when the lifting height of the explosion-proof door increased from 0 cm to 5 cm, the peak value of the explosion-proof door decreased from 36.06 kPa to 22.47 kPa, and the overpressure peak value decreased by 38%. When the lifting height of the explosion-proof door increased from 30 cm to 40 cm, the overpressure decreased from 12.64 kPa to 11.20 kPa, and the overpressure decreased by 11.4%. A power exponential relationship existed between the peak overpressure at the explosion-proof door and the lifting height, and the equation was $y = 37.69 \times x^{-0.032}$. (3) As the lifting height of the explosion-proof door increased, the second peak of the overpressure change curve would also decrease, and the decline rate decreased with the increase of the lifting height. It showed that as the lifting height of the explosion-proof door increased, the reflection peak value between the explosion-proof door and the shock wave gradually weakened. A power exponential relationship existed between the reflection overpressure peak value and the lifting height, and the equation was $y = 14.14 \times (x + 2.25)^{-0.55}$. In conclusion, with the increase of the opening height of the explosion-proof door, the decompression effect near the explosion-proof door is more obvious. Also, the pressure relief efficiency decreases with the increase of opening height and approaches to 0.

3.3. Analysis on the Decompression Effects of the Ventilator at Different Lifting Heights. At different lifting heights, the cloud chart of the overpressure and the overpressure changes at the monitoring points are shown in Figures 8 and 9 when the overpressure reached the maximum at the ventilator.

By comparing the changes of the explosion-proof door at different lifting heights, it can be seen from Figures 8 and 9 that (1) as the lifting height of the explosion-proof door increased, the area that reached the maximum overpressure near the ventilator decreased slightly. The peak overpressure was 11.17 kPa at the ventilator when the explosion-proof door was not opened, but it was 8.60 kPa at the ventilator without the explosion-proof door. This indicated that the opening height of the explosion-proof door had little effect on the overpressure distribution near the ventilator. (2) The peak overpressure decreased at low speed along with the increase of the lifting heights. When the lifting height increased from 0 cm to 5 cm, the overpressure distribution diagram showed the most obvious changes near the ventilator, and the overpressure decreases most at the ventilator. The peak overpressure decreased from 11.17 kPa to 9.11 kPa at the ventilator, which decreased by 18.4%. The subsequent increase in the lifting height of the explosion-proof door had little influence on the overpressure at the ventilator. When the lifting height increased from 30 cm to 40 cm, the peak overpressure decreased from 8.70 kPa to 8.60 kPa at the ventilator, dropping by 1%. A power exponential relationship existed between the peak overpressure at the ventilator and the lifting height, and the fitting equation was $y = 9.48 \times (x + 0.002)^{-0.03}$. (3) In Figure 9(b), y' is the derivative of the overpressure fitted curve at the ventilator. It can be seen from the curve that the peak overpressure satisfied the following condition: $y' < 0$. $|y'|$ is the absolute value of y'. $|y'|$ was relatively great in value when the lifting height of the explosion-proof door was relatively small in value. Along with the increase of the lifting height, the overpressure rapidly reduced and was approximated to 0. As a result, the overpressure reduction rate at the ventilator gradually decreased and was approximated to 0.

4. Proposal of the Active Opening Concept of the Explosion-Proof Door

4.1. The Reasonable Lifting Height Computation of the Explosion-Proof Door. The reasonable lifting height of the explosion-proof door is mainly determined by the maximum overpressure borne by the explosion-proof door and the ventilator. Suppose that the return air shaft is a circular shaft with the diameter of $2R$ and the shorn cross-sectional area of the joint part is A, then the explosion-proof door bears local resisting shear stress [19]:

$$\Delta P_r \leq \frac{A\tau_s}{\left(\pi R^2\right)}. \tag{2}$$

In the equation, τ_s is the shear strength of the explosion-proof door, $\tau_s \approx \sigma_s/\sqrt{3}$, and σ_s is the yield limit of the explosion-proof door.

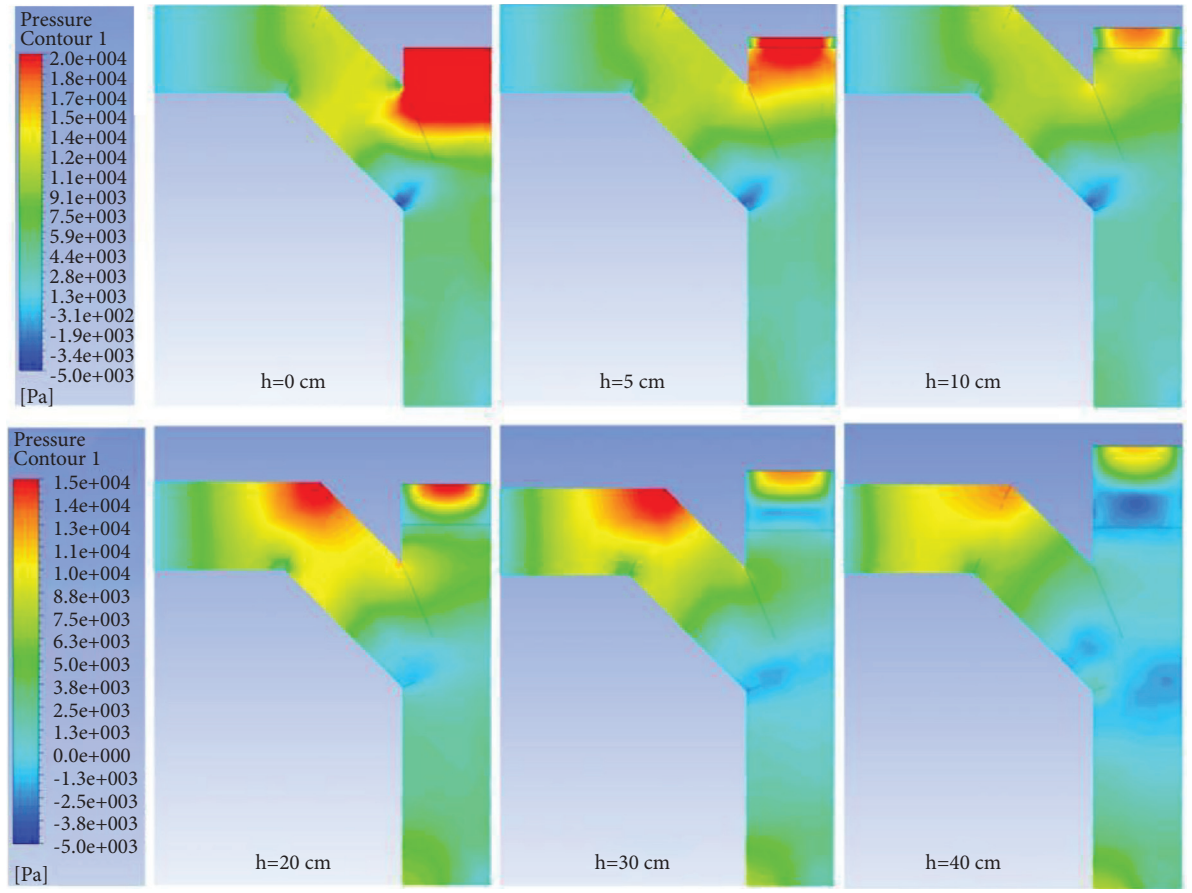

Figure 6: Cloud chart about the overpressure distribution of the explosion-proof door at different lifting heights.

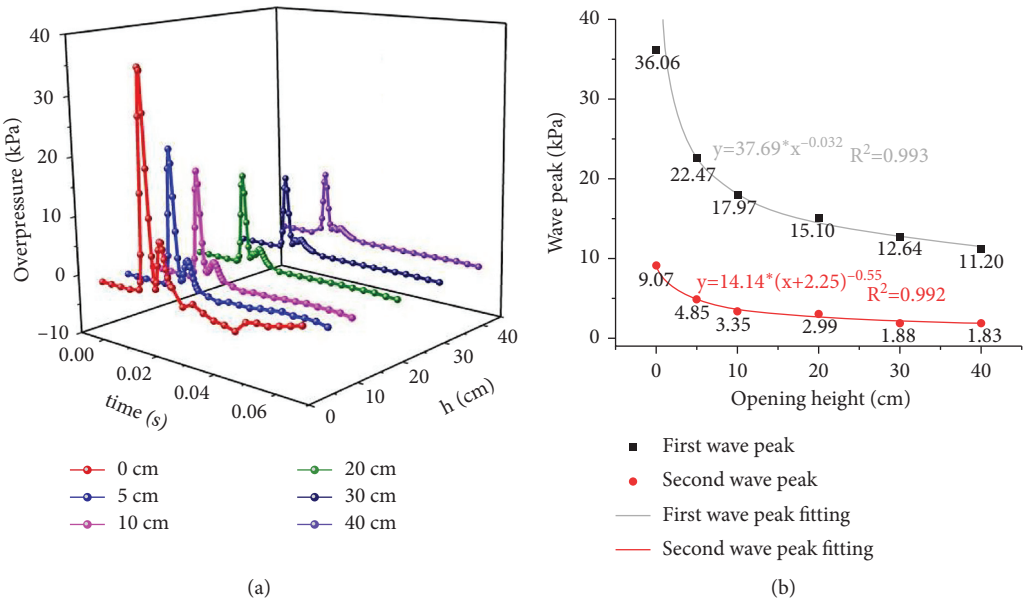

Figure 7: (a) Overpressure change curve and (b) peak value fitting diagram.

When the shock wave reached the lower side of the explosion-proof door, the stress borne by the door body included the upward impact force produced by the overpressure and the downward gravity produced by the weight of the door itself. To simplify the computation, the model was simplified as a circular plate with a radius of R and simple support around it. The following can be obtained according to the force balance:

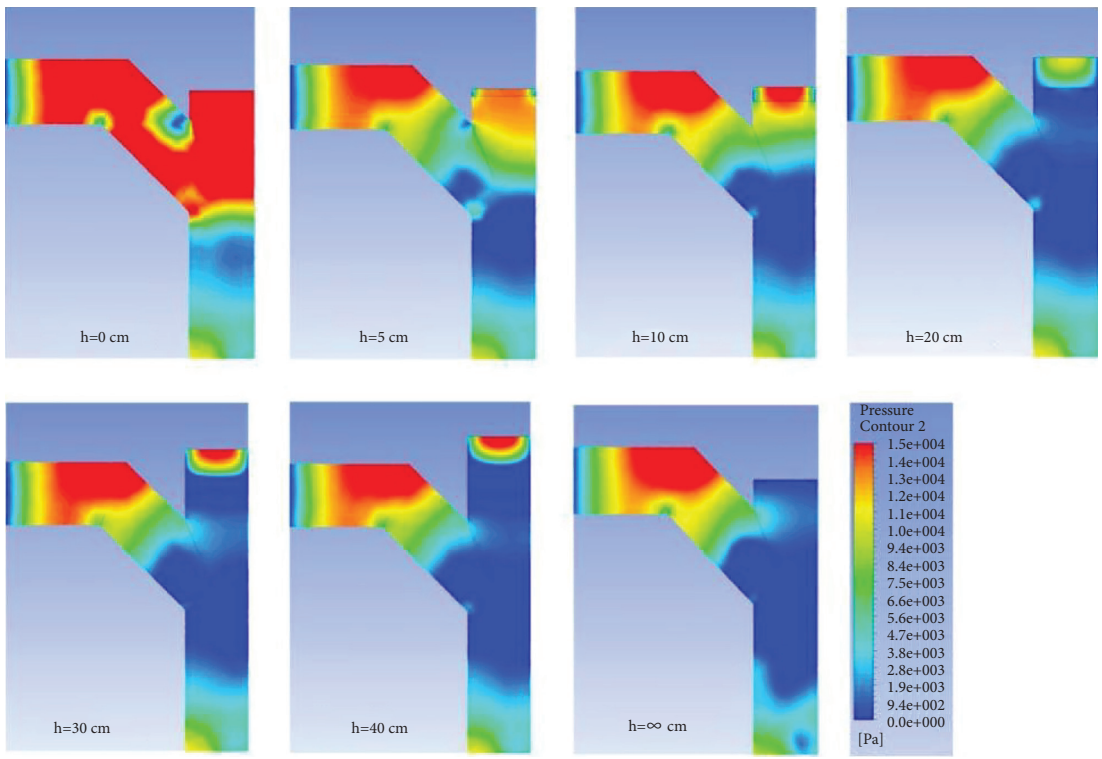

Figure 8: Cloud chart about the overpressure distribution of the ventilator at different lifting heights.

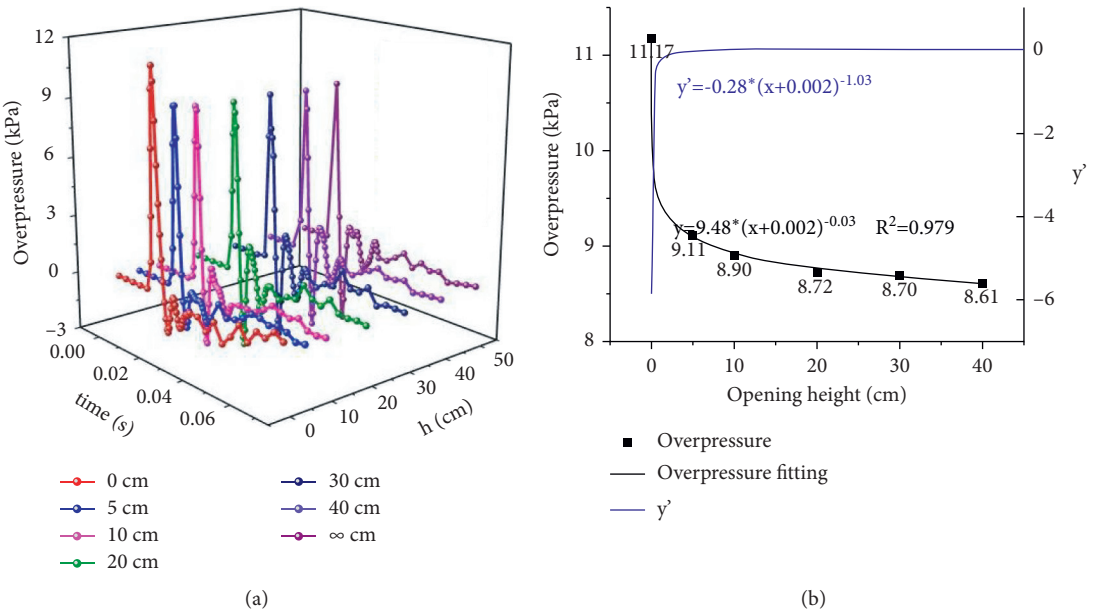

Figure 9: (a) Overpressure change curve and (b) peak value fitting diagram.

$$p - \delta\rho_x g = \Delta P_x. \tag{3}$$

In the equation, δ is the thickness of the door plate, ρ_x is the steel plate density of the explosion-proof door, and g is the acceleration of gravity. Thus, the maximum overpressure borne by the door plate was as follows:

$$p \le \frac{\delta\rho_x g + A\sigma_s}{\left(\sqrt{3}\,\pi R^2\right)}. \tag{4}$$

The explosion-proof doors are mainly made of low carbon steel, with σ_s = 225 MPa, density ρ_x = 7800 kg/m^3, and g = 9.8 m/s^2. The radius of the return air shaft R is 0.2 m,

Table 1: $|y'|$ values of different opening heights.

Opening heights (cm)	$\lvert y' \rvert$ (%)
1.01	27.7
5	5.3
10	2.6
20	1.3

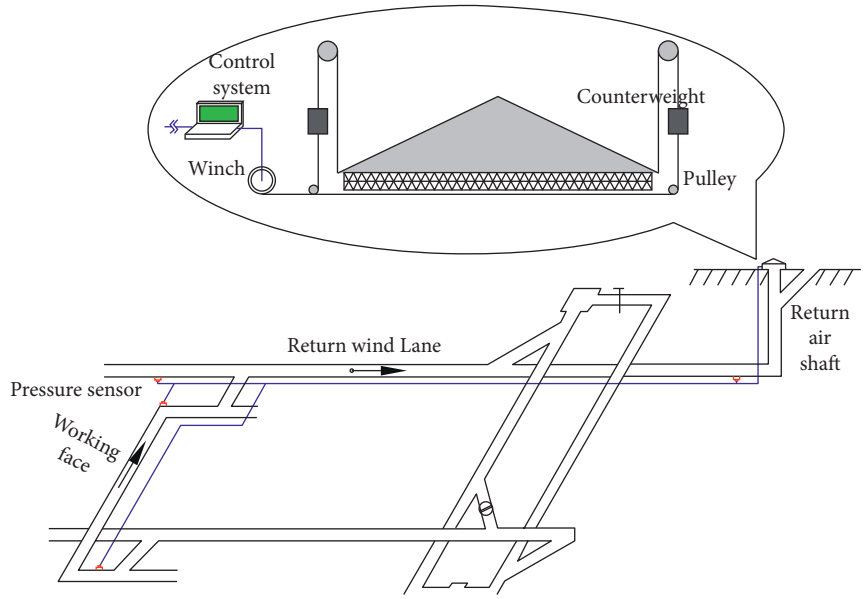

Figure 10: Active opening schematic diagram of the explosion door.

the thickness of the explosion-proof door is 0.15 cm, and the shorn part is basically a rectangle with a dimension of 0.15 cm × 1.5 cm, so we can calculate that the overpressure by the door plate was 23.37 kPa.

When the overpressure 23.37 kPa was substituted into the fitted equation $y = 37.69 \times x^{-0.032}$ of the maximum overpressure borne by the explosion-proof door and the lifting height, $h \geq 1.01$ cm was obtained. Namely, when the lifting height of the explosion-proof door exceeded 1.01 cm, it could effectively prevent the damage caused by the shock wave to the explosion-proof door. When the lifting height of the explosion-proof door (1.01 cm) was substituted into the fitted equation $y = 9.48 \times (x + 0.002)^{-0.03}$ of the overpressure value at the ventilator and the lifting height changes of the explosion-proof door, the overpressure at the ventilator (9.47 kPa) was obtained. The image of y' is shown in Figure 9(b). The values of $|y'|$ in different opening heights are shown in Table 1.

From Table 1, we can know that when the opening height is greater than 5 cm, the $|y'|$ value is less than 5%, namely, the increase of subsequent open height on the fan pressure effect is not obvious. In order to protect the fan and the explosion-proof door at the same time, the opening height of the explosion-proof door should not be less than 5 cm.

4.2. The Active Opening Concept of the Explosion-Proof Door. Based on the research results, the opening of the explosion-proof door could better relieve the pressure in the area near the explosion-proof door, but the decompression effect at the main ventilator is poor. When the lifting height of the explosion-proof door increased from 0 m to 40 cm, the overpressure at the explosion-proof door decreased by 68.9%, but the overpressure at the ventilator only dropped by 22.9%. The cover-type shaft explosion-proof door cannot effectively protect the ventilator. However, the cover-type shaft explosion-proof doors are still widely used in China. To maximize the decompression effect and protect the ventilator to the maximum, it is suggested that the pressure sensors are installed in places (stope face, coal face, etc.) where gas explosions easily happen underground, and they are connected with the mine monitoring system. Meanwhile, the explosion-proof door should also have the automatic quick-opening function. The automatic opening of the explosion-proof door and the monitoring data of the sensor are coordinately controlled. Once the monitoring system senses the gas explosion and the explosion strength reaches a certain value, the explosion-proof door could open actively and rapidly to release the pressure before the shock wave arrives. Moreover, the explosion-proof door is lifted to a reasonable height to achieve the best decompression effect so that the main ventilator and the explosion-proof door are well protected, reducing the losses caused by explosion accidents. The implementation method is shown in Figure 10.

As shown in Figure 10, the pressure sensor is installed at the position where gas accumulation is easy to occur, and the winch and pulley block are installed at the wellhead. When

the gas explosion occurs, the pressure sensor detects the sudden change of pressure and transmits it to the ground control system through the optical fiber signal cable. The control system converts the photoelectric signal into power through the winch. The winch realizes the horizontal lifting of the explosion-proof door through the cable and pulley block connected under the counterweight of the explosion-proof door, so as to achieve the purpose of protecting the explosion-proof door.

5. Conclusions

(1) The gas explosion experiment system was independently developed to study the law of shock wave overpressure changes in the blast zone and transmission zone during the gas explosion. By comparing the experimental results with the simulation results, this experiment also verified the applicability of establishing the mathematical model for gas explosion.

(2) This paper also analyzed the decompression effects of both the explosion-proof door and the ventilator at different lifting heights. The opening of the explosion-proof door could better release the pressure borne by the door, but the decompression effect at the main ventilator was poor. When the lifting height of the explosion-proof door increased from 0 m to 40 cm, the overpressure at the explosion-proof door decreased by 68.9%, but the overpressure at the ventilator only decreased by 22.9%. The shock wave overpressure at the explosion-proof door and the ventilator decreased in a power exponential relationship as the lifting height of the explosion-proof door increased. With the increase of the lifting height, the overpressure decrease rate gradually became smaller.

(3) This paper put forward the active opening concept of the explosion-proof door and calculated its reasonable lifting height. To maximize the decompression effect of the explosion-proof door and protect the ventilator to the maximum, it is suggested that the pressure sensors are installed in places (stope face, coal face, etc.) where gas explosions easily happen underground. Meanwhile, the explosion-proof door automatically and quickly opens and achieves the coordinated control together with the sensor data. The explosion-proof door could open actively and rapidly at the reasonable lifting heights to release the pressure before the shock wave arrives, reducing the losses caused by explosion accidents. The research results can provide theoretical support for improving the decompression effect of explosion-proof doors and optimizing the design of explosion-proof door equipment.

Data Availability

All the data used to support the findings of this study are available from the corresponding author upon request.

Conflicts of Interest

The authors declare that there are no conflicts of interest regarding the publication of this paper.

Acknowledgments

This study was supported by the National Key Research and Development Program of China (grant no. 2018YFC0808103), the National Natural Science Foundation of China (grant nos. 51734007, 51704099, and 52074106), the Program for Innovative Research Team in University of Ministry of Education of China (grant no. IRT_16R22), the Key R&D and Promotion Projects in Henan Province (grant no. 212102310105), and the Doctoral Fund of Henan Polytechnic University (grant no. B2019-56).

References

[1] X. Jingde, *Study on Propagation Law and Influencing Factors of Shock Wave of Mine Gas Explosion*, China University of mining and Technology, Beijing, China, 2003.

[2] H. Tiezhu, *Numerical Simulation of Gas Explosion Propagation Law*, China University of mining and Technology, Beijing, China, 2008.

[3] L. Weixin, L. Bao, and W. Lei, "Study on overpressure and temperature distribution in Roadway after gas explosion in coal mine," *Coal Science and Technology*, vol. 40, no. 452, pp. 41–43, 2012.

[4] S. Weibin and S. Yuning, "Analysis on development status of explosion-proof door in vertical air shaft of coal mine," *China Science and technology of work safety*, vol. 11, no. 6, pp. 108–114, 2015.

[5] S. Weibin, *Research on Safety protection Theory and Technology of Mine Shaft Explosion Proofdoor*, Henan University of technology, Zhengzhou, China, 2018.

[6] C. Savinko, *Underground Air Shock Wave*, Metallurgical Industry Press, Beijing, China, 1979.

[7] L. Baiquan, Z. shining, and Z. Rengui, "The fluence of barriers on flame and explosion wave ingas explosion," *Journal of Coal Science and Engineering*, vol. 2, pp. 53–57, 1998.

[8] L. Baiquan, "Determination and analysis of dynamic characteristic parameters of gas explosion," *Journal of coal industry*, vol. 2, pp. 164–167, 2002.

[9] L. Baiquan, Z. shining, and Z. Rengui, "Induction condition and analysis of shock wave during gas explosion," *Experimental Mechanics*, vol. 24, pp. 36–41, 1998.

[10] L. Baiquan, Z. Shining, and Z. Rengui, "Influence of obstacles on flame and explosion wave during gas explosion," *Journal of China University of mining and technology*, vol. 2, pp. 3–5, 1999.

[11] S. Bin, L. Zhenmin, W. Tao, C. Xie, and F. Cheng, "Chemical kinetic behaviors at the chain initiation stage of Ch4/h2/air mixture," *Journal of Hazardous Materials*, vol. 403, 2021.

[12] W. Tao, L. Zhenmin, W. Hu et al., "The explosion enhancement of methane-air mixtures by ethylene in a confined chamber," *Energy*, vol. 214, 2021.

[13] W. Tao, Z. You, L. Zhenmin et al., "Flammability limit behavior of methane with the addition of gaseous fuel at various relative humidities," *Process Safety and Environmental Protection*, vol. 140, 2020.

[14] H. Hao, W. Kezhi, and B. Hongfeng, "Design of new explosion proof door for return air shaft in coal mine," *Coal*, vol. 23, no. 11, pp. 43-44, 2014.
[15] Z. Xuebo, S. Shuaishuai, and Y. Ming, "Return air shaft explosion-proof door with buffer and reset function," 2020.
[16] L. Qiusheng, L. Kai, and Y. Guiying, "Analysis of explosion impact force on explosion proof cover," *Coal mine safety*, vol. 46, no. 4, pp. 213-214, 2015.
[17] L. Jiajia, C. Shouqi, and R. Jingzhang, "Study on the influence of gas accumulation and explosion distance on fan and explosion door," *China Science and technology of work safety*, vol. 16, no. 9, pp. 57–63, 2020.
[18] Q. Tian, P. Rongkun, and G. Qiuyue, "Simulation study on pressure relief of MFBL explosion door under different explosion conditions," *Journal of Nanjing University of Technology (Natural Science Edition)*, vol. 43, no. 2, pp. 177–183, 2021.
[19] F. Xisheng, "Research on mine automatic reset air shaft explosion proof door," *Coal Science and Technology*, vol. 40, no. 6, pp. 58–61, 2012.

Hindawi
Shock and Vibration
Volume 2021, Article ID 8552247, 28 pages
https://doi.org/10.1155/2021/8552247

Research Article

Application of BigML in the Classification Evaluation of Top Coal Caving

Meng Wang, Caiwang Tai, Qiaofeng Zhang, Zongwei Yang, Jiazheng Li, Kejun Shen, and Kang Wang

College of Mining Engineering, Liaoning Technical University, Fuxin 123000, China

Correspondence should be addressed to Caiwang Tai; 471920665@stu.lntu.edu.cn

Received 14 June 2021; Revised 5 August 2021; Accepted 17 August 2021; Published 2 September 2021

Academic Editor: Jianwei Cheng

Longwall top coal caving mining is one of the main methods of mining thick coal seams in China. Therefore, carrying out the classification evaluation of top coal caving is of great significance to ensure mining success and reduce the risk of mining technology. In order to realize the classification evaluation of top coal caving, this article introduces the method of using BigML to establish the classification evaluation model of top coal caving. Furthermore, using the data from the CNKI database as sample data, a classification evaluation model of top coal caving is established on BigML. After training, testing, and optimization, the model is used to evaluate the top coal caving in No. 3 coal seam of Gucheng Coal Mine, and the evaluation result is grade 1, which is consistent with the engineering practice. The final research results show that the application of BigML in the classification evaluation of top coal caving is successful; the evaluation of top coal caving through BigML is reliable; BigML provides another scientific reliability way for the classification evaluation of top coal caving.

1. Introduction

According to the *World Energy Statistics Review* published in 2020, global coal consumption decreased by 0.6% in 2019, and the proportion of coal in primary energy reached the lowest level in 16 years, but the proportion of coal in primary energy is still up to 27% [1]. Therefore, in the continuous development of other energy sources, coal is still one of the most critical energy sources [2], especially for a country such as China that is "rich in coal, poor in oil, and less in gas" and whose economy is developing rapidly, the status of coal is vital. In 2015, China's coal production and consumption had reached 47% and 50.01% of the world's coal production and consumption [3], respectively. By 2019, when global coal consumption is declining, China's coal consumption will still account for 51.7% of the world's coal consumption [1]. It shows that a large amount of coal needs to be consumed to support China's rapid economic development. Among the proven recoverable coal reserves in China, thick coal seams account for 44% of the total recoverable coal reserves [4], and coal seams with a thickness of more than 5 m are as much as 10 billion tons [5], so nearly half of the coal consumed comes from the mining of thick coal seams [6]. As the longwall top coal caving mining technology has the advantages of high output, high efficiency, low energy consumption, low cost, and strong adaptability [7], it is estimated that the use of longwall top coal caving mining in thick seams can double the production efficiency and reduce the production cost by 30% to 40% [8]. Therefore, since China introduced it from abroad in the 1980s, it has become the primary technology for mining thick coal seam in China, Australia, Turkey, Russia, and Vietnam through continuous development and improvement [9–16]. The top coal caving (that is, the difficulty of top coal mining under the action of in situ stress and gravity [17]) is one of the critical factors determining the success of longwall top coal caving mining, and it is also an essential reference for designing longwall top coal caving mining technology and improving the recovery rate of top coal [18]. In addition, if the top coal caving can be understood from the feasibility study to the formal design stage, the relevant technical risks will be significantly reduced [19]. Therefore, the evaluation of top coal caving has

always been a hot spot in the research of longwall top coal caving mining at home and abroad.

At present, the evaluation of top coal caving at home and abroad is mainly based on observation and empirical methods [7, 19], established mathematical evaluation models [20], and numerical simulations [21–23]. However, there are some shortcomings in these methods. For example, based on observation and experience, there are strict requirements on the experience level of the evaluator, and at the same time, they also need to bear the massive risk of mistakes due to lack of experience. The establishment of mathematical models and numerical models to evaluate top coal caving requires that the model builder has a very high level of professional knowledge. At the same time, as the simulation size of the current numerical simulation is getting larger and larger, the requirements for the computer are getting higher and higher, which makes the technical cost and time cost of the evaluation very high, and the evaluation efficiency is not high. In recent years, with the continuous development of science and technology, advanced artificial intelligence and machine learning algorithms such as ant colony clustering algorithms, expert systems, and artificial neural networks have been gradually used in coal production [24–26]. Therefore, experts and scholars are also trying to use artificial intelligence algorithms. Moreover, machine learning algorithms are used to evaluate top coal caving and have achieved certain results. For example, Mohammadi et al. [27] used fuzzy multicriteria decision-making methods to establish a classification system for evaluating the caving of the direct roof of coal seams; Yongkui et al. [28] used Bayesian theory and rough set theory to establish a Bayesian classifier model used for the evaluation and prediction of roof caving properties of coal seams, which can accurately classify; Oraee and Rostami [29] used fuzzy logic algorithms to establish a fuzzy system for quantitative analysis of roof caving in longwall top coal caving mining face and applied the model to Tabas·Palward Mine's longwall top coal caving mining face which located in Palward District, Yazd Province, and the model prediction results in application are consistent with the on-site measured results; Shi et al. [17] established a top coal caving prediction model based on vector support vector machines, and the test results showed that the model has a certain feasibility and generalization; Yu and Mao [30] used SPSS statistical software to establish a top coal caving prediction model based on an artificial neural network. The training and test results show that the model has good top coal caving prediction capabilities. However, most of the prediction models of the above experts and scholars are built by computer programming, which requires higher computer language and professional level of users, especially when users want to optimize and modify the model to make it conform to the actual situation. Therefore, it leads to the poor portability of the model and the difficulty of popularization and application.

Therefore, in order to make the model have better portability, at the same time, without programming, it is easy to use the established model to evaluate the caving ability of top coal, and even easy to modify and optimize the established model to make it more in line with their practical application. In this article, BigML is applied to establish the classification evaluation model of top coal caving. It is hoped that through this, it is possible to easily use the established model to evaluate the top coal caving without programming, and even easily modify and optimize the established model to make it more in line with their actual application situation.

2. Introduction to BigML

BigML (https://bigml.com) is a cloud-based machine learning platform dedicated to enabling all people who understand computer language and do not understand computer language to build their machine learning prediction model without writing a line of code and to make it automatic, remote callable, programmable, and extensible. It can perfectly and easily solve modeling tasks such as classification, regression, time series forecasting, cluster analysis, anomaly detection, correlation analysis, and realize model visualization. Because BigML has powerful functions and advanced algorithms and it is easy to use, it can realize a one-stop service from data loading, data cleaning, model building, and model evaluation to the final model prediction. So, BigML has been widely used in agriculture [31], medicine [32], finance [33], and other scientific research fields and has successfully helped thousands of analysts, software developers, and scientists all over the world solve machine learning tasks from "end-to-end" and seamlessly transform data into operational models for remote services, or embed them locally into applications for prediction. In addition, BigML has more than 147000 global users, and more than 600 universities and research institutions have cooperated with it. The global user distribution of BigML is shown in Figure 1.

3. Influencing Factors of Top Coal Caving and Its Evaluation Grade Division

3.1. Influencing Factors of Top Coal Caving. Two main factors are affecting top coal caving: geological and mining technology factors. In the longwall top coal caving mining, the mining technology is generally determined by geological factors [34], so this article mainly studies the top coal caving under the influence of geological factors. The practical experience [30] and research [9] show that the buried depth (H), thickness of coal seam (M), thickness of gangue (MG), uniaxial compressive strength of coal (Rc), fracture development degree (DN, that is, the product of the number of through cracks N_{1m} on the surface of $1\,m^2$ coal and the fractal dimension D_1 of the number of cracks counted by the coal sample), and filling coefficient of direct roof (K, $K = \sum hk_p/M$) are essential geological factors affecting top coal caving [35]. Therefore, this article considers the factors above influencing factors for the classification evaluation of top coal caving.

3.2. Top Coal Caving Evaluation Grade Division. The top coal caving is generally divided into five grades, namely, "(1) excellent caving," "(2) good caving," "(3) fair caving," "(4) poor caving," and "(5) extremely poor caving" [18].

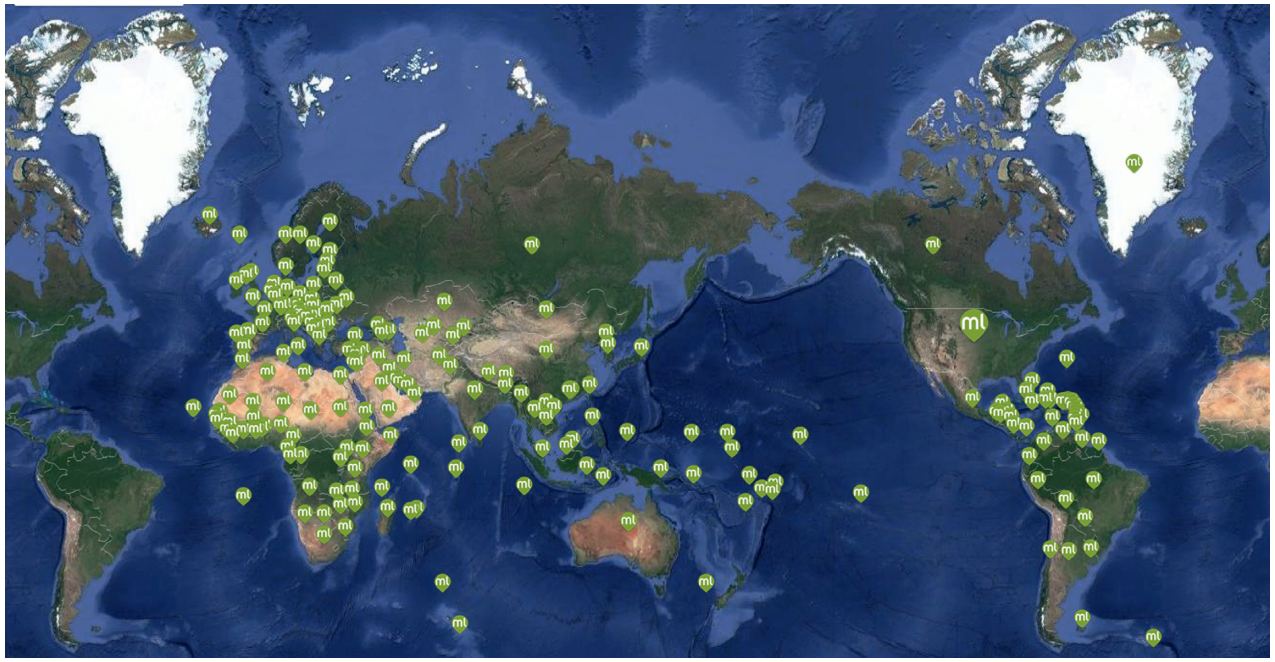

Figure 1: Global user distribution map of BigML.

However, the engineering practice shows little difference between grades "4" and "5." Both are difficult to cave. Therefore, in this article, the top coal caving is only divided into four grades, which are "(1) excellent caving," "(2) good caving," "(3) fair caving," and "(4) poor caving." The specific situation of each grade is shown in Table 1.

4. Sample Data and Data Preprocessing

4.1. Source of Sample Data. There are a large number of research studies on top coal caving in the CNKI publicly published paper database. Therefore, to meet the needs of model training and testing, this article obtained 68 sets of sample data from the CNKI publicly published paper database. The specific conditions of the sample data are shown in Table 2, and the data distribution is shown in Figure 2. Through the shape and volume of the violin in the data distribution diagram (Figure 2), it can be seen that the "grade" of the obtained sample data is unbalanced. Therefore, to ensure that the established model has good stability and strong prediction ability, the sample imbalance is a problem worthy of attention, and it is necessary to reasonably select model performance evaluation indicators to evaluate the model.

4.2. Data Cleaning and Segmentation. Although all the sample data are from CNKI's publicly published paper database, outliers are inevitable in these sample data. The quality of the data sample generally has an essential impact on establishing the model and the predictive ability of the established model. Therefore, cleaning the data sample and eliminating outliers make the established model better predictive. BigML's data anomaly detection function is based on the most advanced isolated forest algorithm [36], which has a powerful ability of outlier detection. Therefore, this article uses BigML's data anomaly detection function to do outlier detection on the data samples in this article. Before BigML performs data anomaly detection, it is set to find at least three sets of relatively abnormal sample data. After testing, only the sample with the coal seam name "No. 8-1 coal seam of Baode Mine" is an outlier (in BigML, it is usually considered that the score is more than 60%, which is the actual abnormality [37]). The BigML anomaly detection result is shown in Figure 3. Therefore, "No. 8-1 coal seam of Baode Mine" is removed from the sample data set to obtain clean sample data. The sample data distribution after cleaning is shown in Figure 4.

In order to train the model and test the model's performance, using the data segmentation function of BigML, the sample data are randomly divided according to 7 : 3, 70% of which is the training set and 30% is the test set. The sample data distribution of the training set and test set after segmentation is shown in Figure 5.

5. Selection of Model Performance Evaluation Indicators

Top coal caving classification evaluation is a problem of classification and prediction. In classification prediction model training and testing, model performance evaluation indicators play a vital role in obtaining the optimal classifier. Therefore, choosing appropriate model performance evaluation indicators is essential to identifying and obtaining the optimal classifier [38]. Most of the performance indicators of the current evaluation and classification prediction model are based on the confusion matrix similar to Table 3, and these performance indicators can be divided into three categories.

Table 1: Caving grade of top coal.

Grade	Top coal caving	Description
1	Excellent	The top coal can cave very well. As long as the appropriate caving support is selected, the coal can be discharged, and no extra measures need to be taken.
2	Good	The top coal can also cave well. Similarly, the coal can be discharged after selecting the appropriate caving support, but there are large blocks in the discharged coal, which is easy to cause the phenomenon of the bayonet, so corresponding measures need to be taken.
3	Fair	The top coal can cave, but not well. At the same time, the discharged coal is large and often has a bayonet phenomenon. Corresponding measures must be taken to discharge the coal.
4	Poor	The top coal is very difficult to cave, and more measures are needed to release the coal.

Table 2: Sample data.

Number	Coal seam name	H (m)	Rc (MPa)	MG (m)	M (m)	DN	K	Grade
1	No. 3 coal seam of Yaoqiao Mine	193	25.00	0.30	6.70	7.50	0.71	4
2	No. 13-1 coal seam of Xieqiao Mine	357	10.00	0.12	12.00	14.00	2.44	2
3	No. 3 coal seam of Dayan No. 2 Mine	435	16.60	0.00	8.80	9.23	0.52	2
4	No. 3 coal seam of Qishan Mine	300	14.00	0.00	8.00	10.10	1.00	2
5	No. 2 coal seam of Taoer Mine	290	6.50	0.20	7.20	16.77	1.44	1
6	No. 2 coal seam of Xuecun Mine	300	16.00	0.40	14.50	16.20	0.36	3
7	No. 4-2 coal seam of Cuijiagou Mine	262	17.50	0.05	6.85	9.50	1.78	2
8	No. 5 coal seam of Xuangangjiaojiazhai	140	2.80	0.00	6.50	14.71	1.20	2
9	No. 15 coal seam of Yangquan No. 1 Mine	250	20.00	0.30	6.00	8.01	1.91	3
10	No. 7-8 coal seam of Pingdingshan No. 1 Mine	300	14.00	0.00	7.90	12.09	1.16	2
11	No. 3 coal seam of Lu'anwangzhuang Mine	200	16.00	0.00	7.00	7.43	0.56	2
12	No. 4-2 coal seam of Xiashijie Mine	177	17.50	0.00	12.00	9.10	0.17	3
13	No. 18 coal seam of Hegang Nanshan Mine	150	10.00	0.40	12.20	11.20	1.34	3
14	No. 15 coal seam of Yinying Mine	220	8.50	0.00	6.30	10.65	0.82	2
15	No. 2-4 coal seam of Gujiaojialequan	127.5	10.00	0.52	8.20	9.11	0.56	4
16	No. 3 coal seam of Xinzhuang Mine	175	10.00	0.00	7.00	13.02	0.78	2
17	No. 3 coal seam of Tang'an Mine	200	15.00	0.30	6.50	13.82	0.81	2
18	No. 5 coal seam of Xiangshan Mine	230	8.50	0.00	6.50	16.08	0.72	2
19	No. 2-4 coal seam of Dongliang Mine	300	16.00	0.30	12.50	14.80	1.14	3
20	No. 2-14 coal seam of Wulong Mine	300	16.00	0.40	14.50	16.20	0.36	3
21	No. 11 coal seam of Yaodatong Mine	300	30.00	0.40	8.60	9.85	0.25	4
22	No. 3 coal seam of Fenghuangshan Mine	140	35.00	0.10	6.50	8.01	0.62	4
23	No. 10 coal seam of Shuiyu Mine	190	6.50	0.00	7.20	16.77	1.44	1
24	No. 5 coal seam of Liujialiang Mine	140	2.80	0.00	6.00	19.40	1.20	2
25	Shenyang Puhe Mine lignite	357	10.00	0.12	12.00	14.00	2.44	2
26	No. 8-9 coal seam of Wangfeng Mine	90	14.00	0.70	8.00	10.10	0.00	4
27	No. 3 coal seam of Baodian Mine	435	16.60	0.00	8.80	9.23	0.52	2
28	No. 3 coal seam of Xinglongzhuang Mine	412.5	13.74	0.30	7.80	12.88	0.58	2
29	No. 2 coal seam of Chaohua Mine	160	5.00	0.00	8.40	16.00	0.73	2
30	No. 5 coal seam of Dalong Mine	200	6.70	0.20	6.50	17.00	0.60	2
31	No. 3 coal seam of Yong'an Mine	193	25.00	0.10	6.70	7.50	0.71	4
32	No. 15 coal seam of Yangquan No. 4 Mine	240	20.00	0.20	6.50	8.60	0.40	3
33	No. 6-17 coal seam of Gaozhuang Mine	300	14.00	0.00	8.00	10.05	1.00	2
34	No. 2-1 coal seam of Micun Mine	130	5.00	0.00	8.50	17.60	1.14	2
35	No. 2 coal seam of Xingtai Mine	360	20.00	0.40	6.20	8.30	0.41	3
36	No. 8-1 coal seam of Baode Mine	263.5	8.00	0.15	7.46	9.50	0.52	3
37	No. 4-2 coal seam of Buertai Mine	424.5	15.00	0.12	6.71	15.00	2.04	2
38	No. 3 coal seam of Wangpo Mine	380	25.00	0.00	6.97	12.00	0.39	2
39	No. 12 coal seam of Huojitu Mine	106	33.00	0.14	6.45	14.20	1.20	2
40	X coal seam of No.3 Hebi Mine	750	6.50	0.30	8.00	16.00	0.33	2
41	No. 8 coal seam of Wobei Mine	600	8.91	0.88	2.75	26.16	1.04	1
42	No. 8301-5 coal seam of X Mine	484	24.00	0.26	6.39	9.00	1.40	4
43	No. 8101-5 coal seam of X Mine	240	13.80	0.45	7.43	12.40	0.61	3
44	No. 8101-8 + 10 coal seam of X Mine	273	13.80	0.30	9.00	12.00	2.30	3
45	No. 2-1304 coal seam of Zhaozhuang Mine	440	14.03	0.19	6.36	11.98	0.44	2
46	No. 28071-2 coal seam of Anlin Mine	365	13.58	0.00	5.06	3.00	2.60	3

Table 2: Continued.

Number	Coal seam name	H (m)	Rc (MPa)	MG (m)	M (m)	DN	K	Grade
47	Coal seam of Zhangshuanglou Mine	600	14.60	0.30	4.50	18.00	1.25	2
48	Coal seam of Changcun Mine	350	20.00	0.30	6.70	2.00	1.23	2
49	Coal seam of Wangcun Mine	250	25.00	0.20	6.50	2.00	1.28	2
50	Coal seam of Zhangcun Mine	230	20.00	0.20	7.00	2.00	0.68	2
51	No. 16 coal seam of Lutian Coal Mine	150	9.55	0.30	8.07	30.25	0.90	2
52	No. X coal seam of Datong No. 2 Mine	325	30.00	0.35	7.75	6.00	0.25	4
53	No. X coal seam of Tiefa Daming Mine	200	22.50	0.25	8.25	10.00	0.95	3
54	No. X coal seam of Nantun Mine	500	7.00	0.15	7.00	12.00	0.25	1
55	No. X coal seam of Xinji Mine	325	17.50	0.25	8.00	8.00	0.80	3
56	Mine big coal of No. 6 Hebi Mine	325	12.50	0.25	6.50	10.00	1.50	2
57	No. 7 coal seam of Sanhejian Mine	200	17.50	0.05	7.50	12.00	0.60	2
58	No. X coal seam of Guzhuang Mine	200	17.50	0.15	7.00	12.00	0.95	2
59	No. X coal seam of Yangchangwan Mine	350	14.50	0.25	10.00	12.50	1.50	2
60	No. X coal seam of Baicaoyu Mine	500	7.00	0.25	9.75	14.00	0.95	2
61	No. X coal seam of Yuhua Mine	500	12.50	0.15	7.75	14.00	0.80	2
62	No. X coal seam of Jiahe Mine	405	17.5	0	2.4	13.5	1.45	1
63	No. 3 coal seam of Bofang Mine	390	12	0	4.5	13	1.5	1
64	No. 13 coal seam of Jinshan Mine	235	6.4	0.5	13.53	14.5	2	1
65	No. 4 coal seam of Majialiang Mine	540	25	0	7	15	1	1
66	No. X coal seam of Wajinwan Mine	310	11	0	4.22	15	1.5	1
67	No. X coal seam of Shigejie Mine	424	16.5	0.3	6.64	13.5	1.65	1
68	No. X coal seam of Wuyang Mine	350	10	0.1	6.59	14	0.77	1

*Data come from the database of publicly published papers on CNKI.

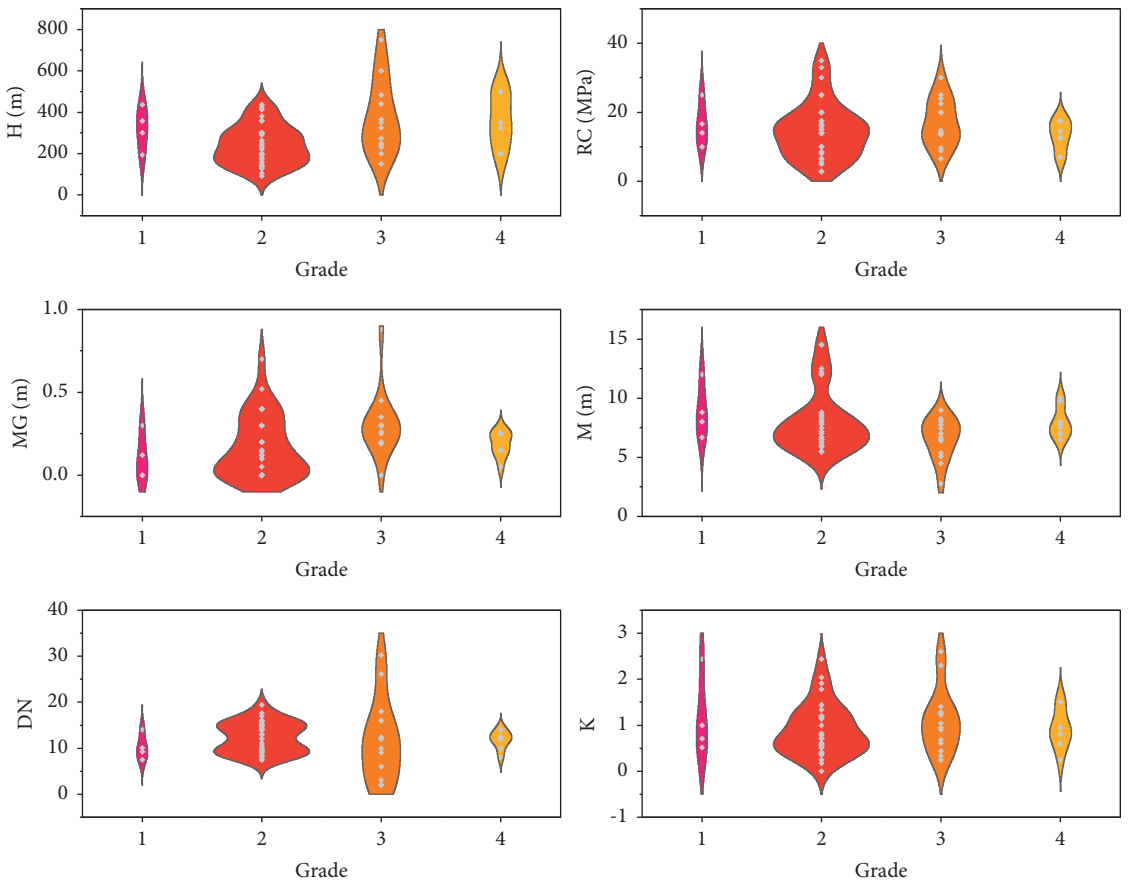

Figure 2: Distribution of sample data.

5.1. Paired Indicators. The paired indicators mainly include the evaluation indicators of the binary prediction model, such as accuracy and error rate (Acc&Err), precision and recall (P&R), and true positive rate and true false rate (TPR&TFR), and the evaluation indicators of the multiclassification prediction model, such as macro-accuracy and macro-error rate and macro-precision and macro-recall, which are expanded from binary classification to multiclassification.

Accuracy and error rate (Acc&Err) is used to calculate the proportion of the samples with correct prediction classification and the samples with wrong prediction classification to the total samples. The calculation formula of accuracy and error rate is shown in equations (1) and (2). The range of accuracy and error rate (Acc&Err) is both [0, 1]. Generally, the closer the accuracy is to 1, the better the performance of the model. On the contrary, the closer the error rate is to 0, the better the model's performance:

$$accuracy = 1 - \frac{\mathrm{FP} + \mathrm{FN}}{N_{\mathrm{sample}}} = \frac{\mathrm{TP} + \mathrm{TN}}{N_{\mathrm{sample}}}, \tag{1}$$

$$\mathrm{error}\, rate = \frac{\mathrm{FP} + \mathrm{FN}}{N_{\mathrm{sample}}}, \tag{2}$$

where FP is the number of samples predicted to be false positives, FN is the number of samples predicted to be false negatives, TP is the number of samples predicted to be true positives, TN is the number of samples predicted to be true negatives, and N_{sample} is the total number of samples.

Precision rate and recall rate, respectively, calculated the proportion of the predicted positive samples to the predicted positive samples and the actual positive samples. The calculation formula of precision and recall is shown in equations (3) and (4). The range of precision and recall is both [0, 1]. Ideally, the closer the precision and recall are to 1, the better the model's performance. However, in practice, the relationship between FP and FN is the relationship between type I error and type II error, so precision and recall (P&R) is a contradictory relationship. Therefore, it is generally necessary to find a balance between the precision and recall:

$$precision = \frac{\mathrm{TP}}{\mathrm{TP} + \mathrm{FP}}, \tag{3}$$

$$recall = \frac{\mathrm{TP}}{\mathrm{TP} + \mathrm{TN}}, \tag{4}$$

where TP is the number of samples predicted to be true positives, TN is the number of samples predicted to be true negatives, and FP is the number of samples predicted to be false positives.

True positive rate and true false rate (also called sensitivity and specificity, TPR&TFR), respectively, calculate the proportion of samples correctly predicted as positive cases to the total positive samples, and the proportion of samples correctly predicted as negative cases to the total negative samples. The calculation formula of true positive rate and true false rate is shown in equations (5) and (6). The range of true positive rate and true false rate is both [0, 1]. Ideally, the closer the true positive rate is to 1 and the closer the true false rate is to 0, the better the model performance:

$$TPR = sensitivity = \frac{\mathrm{TP}}{\mathrm{TP} + \mathrm{FN}}, \tag{5}$$

$$TFR = specificity = \frac{\mathrm{TN}}{\mathrm{TN} + \mathrm{FP}}, \tag{6}$$

where FP is the number of samples predicted to be false positives, FN is the number of samples predicted to be false negatives, TP is the number of samples predicted to be true positives, and TN is the number of samples predicted to be true negatives.

Macro-accuracy and macro-error rate and macro-precision and macro-recall are also called averaged-accuracy and averaged-error rate and averaged-precision and averaged-recall, which extended from the problem of dichotomy for requirements of multiclassification problems. They all treat each category equally, add up the same indicators of different categories, and then calculate the average to realize the evaluation of the multiclassification prediction model. Therefore, their value range and significance are the same as evaluating the two-classification prediction models. Their calculation formula is shown in the following equations:

$$macro - accuracy = \frac{1}{n} \times \sum_{i=1}^{n} \frac{\mathrm{TP}_i + \mathrm{TN}_i}{N_{i\mathrm{sample}}}, \tag{7}$$

$$\mathrm{macro} - \mathrm{error}\, rate = \frac{1}{n} \times \sum_{i=1}^{n} \frac{\mathrm{FP}_i + \mathrm{FN}_i}{N_{i\mathrm{sample}}}, \tag{8}$$

$$\mathrm{macro} - \mathrm{precision} = \frac{1}{n} \times \sum_{i=1}^{n} \frac{\mathrm{TP}_i}{\mathrm{TP}_i + \mathrm{FP}_i}, \tag{9}$$

$$\mathrm{macro} - \mathrm{recall} = \frac{1}{n} \times \sum_{i=1}^{n} \frac{\mathrm{TP}_i}{\mathrm{TP}_i + \mathrm{TN}_i}, \tag{10}$$

where FP_i is the number of samples predicted to be false positive in class i, FN_i is the number of samples predicted to be false negative in class i, TP_i is the number of samples predicted to be true positive in class i, TN_i is the number of samples predicted to be true negative in class i, $N_{i\mathrm{sample}}$ is the total number of samples of class i, and n is the number of categories.

5.2. Comprehensive Indicators. The comprehensive indicators mainly include F-measure (also known as F-score, $F1$) [40], Matthews correlation coefficient (Phi coefficient) [41], Kendall's tau, and Spearman's rho, used for binary classification. Furthermore, as well as for evaluating the multiclassification prediction model, the macro-F-measure and macro-Matthews correlation coefficient (macro-Phi coefficient) of the evaluation indicators of the multiclassification prediction model are expanded from the evaluation indicators of the two-classification prediction model.

F-measure is proposed to solve the contradictory model performance measurement value of precision and recall.

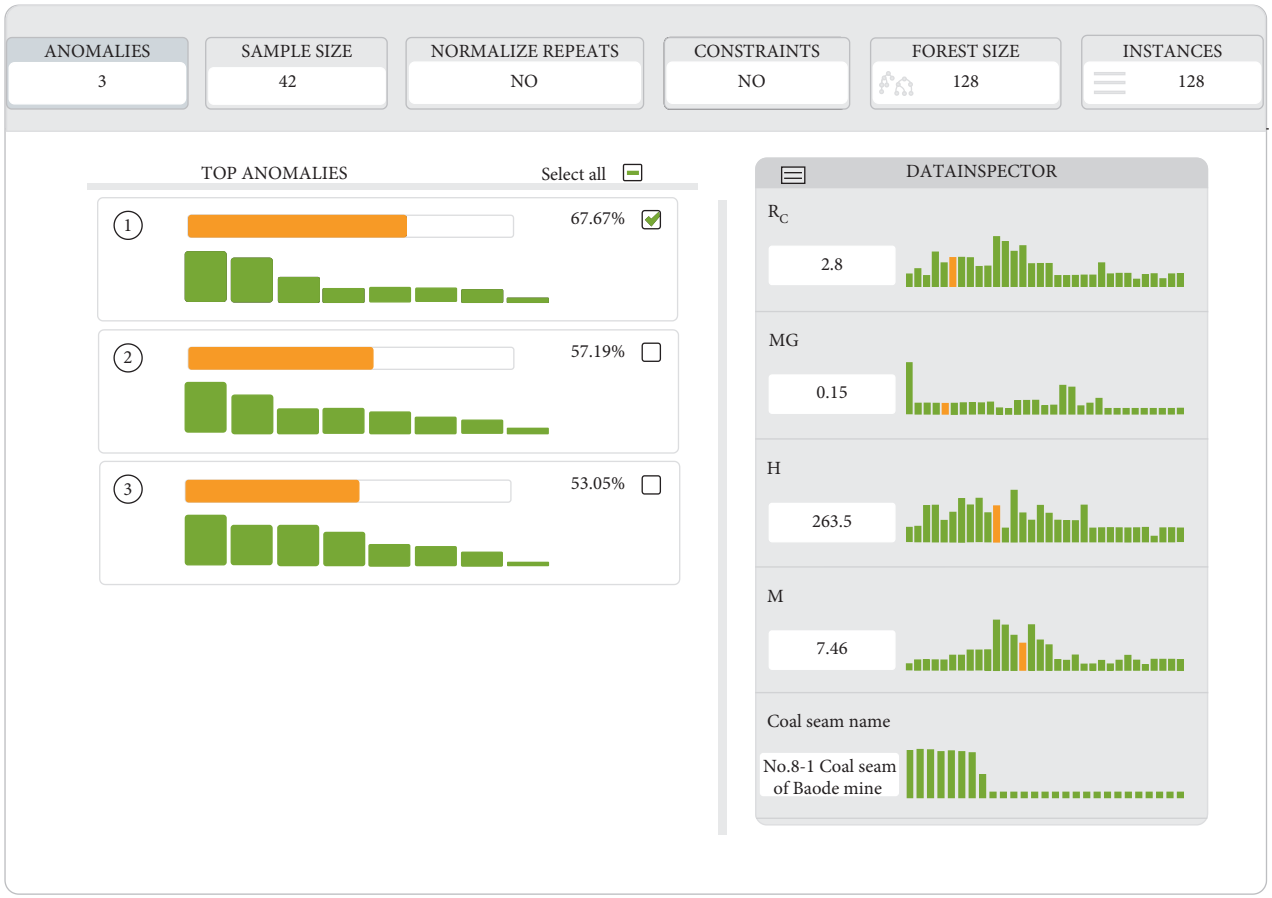

Figure 3: Anomaly detection results of sample data.

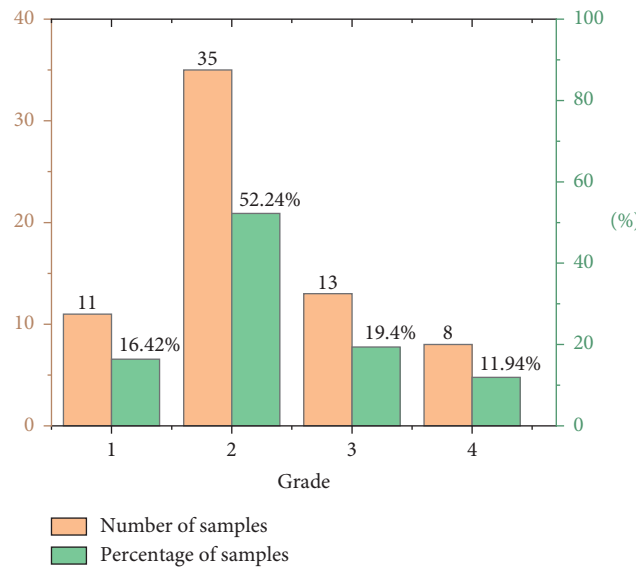

Figure 4: Sample data distribution after cleaning.

Therefore, *F*-measure is a balance point between precision and recall (that is, the harmonic average of precision and recall), which can take into account the precision and recall of the classification model at the same time. Its formula is shown in equation (11). The value range of *F*-measure is [0, 1]. Ideally, the closer the *F*-measure value is to 1, the better the model performance, and vice versa, the worse the model performance:

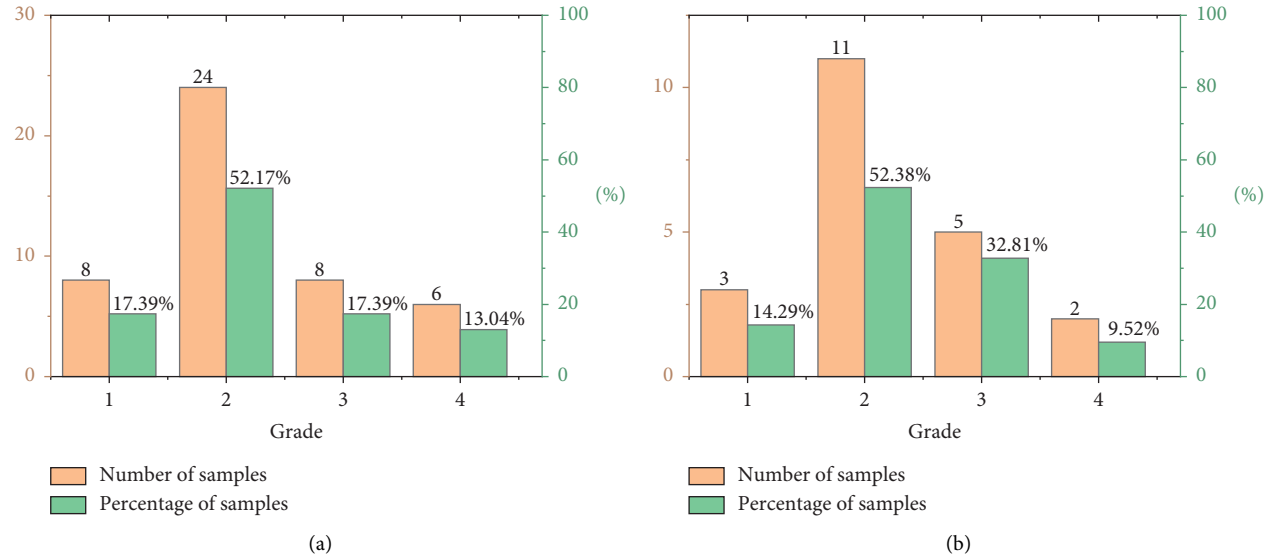

Figure 5: Sample data distribution of training set and test set. (a) Distribution of training sample data. (b) Distribution of test sample data.

$$\begin{cases} \dfrac{1}{F_1} = \dfrac{1}{2} \cdot \left(\dfrac{1}{P} + \dfrac{1}{R} \right), \\ F_1 = \dfrac{2 \times P \times R}{P + R} = \dfrac{2\mathrm{TP}}{2\mathrm{TP} + \mathrm{FP} + \mathrm{FN}}, \end{cases} \tag{11}$$

where P is precision, R is recall, FP is the number of samples predicted to be false positives, FN is the number of samples predicted to be false negatives, and TP is the number of samples predicted to be true positives.

The Matthews correlation coefficient (Phi coefficient), which is mainly used to measure the two classification problems, is a relatively balanced indicator. It comprehensively considers TP, TN, FP, and FN, and it can also be used in the case of unbalanced sample data categories. The value range of Phi coefficient is [−1, 1], a value of 1 indicates that the prediction is entirely consistent with the actual, a value of 0 indicates that the predicted result is not as good as the random predicted result, and −1 indicates that the predicted result is utterly inconsistent with the actual result [42]. Its calculation formula is shown in the following equation:

$$\text{Phi}\,coefficient = \frac{\mathrm{TP} \times \mathrm{TN} - \mathrm{TP} \times \mathrm{FN}}{\sqrt{(\mathrm{TP} + \mathrm{FP}) \times (\mathrm{TP} + \mathrm{FN}) \times (\mathrm{TN} + \mathrm{FP}) \times (\mathrm{TN} + \mathrm{FN})}}, \tag{12}$$

where FP is the number of samples predicted to be false positives, FN is the number of samples predicted to be false negatives, TP is the number of samples predicted to be true positives, and TN is the number of samples predicted to be true negatives.

Macro-F-measure and macro-Matthews correlation coefficient (macro-Phi coefficient) are also called averaged F-measure and averaged-Matthews correlation coefficient, respectively. It is also based on the needs of the multiclassification problem and extended from the two classification problems. They all treat each category equally, add up the same indicators of different categories, and then calculate the average to realize the evaluation of the multiclassification prediction model. Their value range and significance are the same as the evaluation of the two-classification prediction models. Their calculation formula is shown in the following equations:

$$\text{macro} - F_1 = \frac{1}{n} \times \sum_{i=1}^{n} \frac{2 \times P_i \times R_i}{P_i + R_i} = \frac{1}{n} \times \sum_{i=1}^{n} \frac{2\mathrm{TP}_i}{2\mathrm{TP}_i + \mathrm{FP}_i + \mathrm{FN}_i}, \tag{13}$$

$$\text{macro} - \text{Phi}\,coefficient = \frac{1}{n} \times \sum_{i=1}^{n} \frac{\mathrm{TP}_i \times \mathrm{TN}_i - \mathrm{TP}_i \times \mathrm{FN}_i}{\sqrt{(\mathrm{TP}_i + \mathrm{FP}_i) \times (\mathrm{TP}_i + \mathrm{FN}_i) \times (\mathrm{TN}_i + \mathrm{FP}_i) \times (\mathrm{TN}_i + \mathrm{FN}_i)}}, \tag{14}$$

Table 3: Confusion matrix of two-classification problems [39].

	Actual positive class	Actual negative class
Predicted positive class	True positive (TP)	False negative (FN)
Predicted negative class	False positive (FP)	True negative (TN)

where FP_i is the number of samples predicted to be false positive in class i, FN_i is the number of samples predicted to be false negative in class i, TP_i is the number of samples predicted to be true positive in class i, TN_i is the number of samples predicted to be true negative in class i, and n is the number of categories.

5.3. Visual Indicators. Visual indicators mainly include ROC curve [43] and AUC [44], precision-recall curve (also known as PR curve) [45], gain curve [46], K-S curve and K-S statistical value [47], and lift curve [48] and lift value.

ROC curve, also known as receiver operating characteristic curve, is a comprehensive indicator that reflects TPR and FPR with the decision threshold [49]. It is a curve composed of points (TPR and FPR), the abscissa is FPR, and the ordinate is TPR. ROC curve is mainly used to compare the relative performance of different classification models. However, when the ROC curves of different classification models intersect, it is not easy to reasonably evaluate the models' relative performance.

AUC, also known as the area under the ROC curve, is often used in conjunction with the ROC curve. The value range of AUC is [0, 1]. According to experience, when the AUC value is less than 0.5, the predictive ability of the model is worse than random guessing, but if the prediction is reversed, it is better than random guessing; when the AUC value is equal to 0.5, the model has no predictive value, just as a random guess; when AUC value is more than 0.7, the model's predictive ability can be considered acceptable; when the AUC value is equal to 1, the model's predictive ability is perfect, and using this model, no matter what threshold is set, a perfect prediction can be obtained (most of the time does not exist). The specific AUC value range and its empirical evaluation of the model are shown in Table 4.

PR curve is a curve that reacts to the relationship between precision and recall. It is also used to evaluate the relative performance of different classification models and can be used with the AUC value. The PR curve is an essential supplement to the ROC curve, especially in unbalanced sample categories; the PR curve can reflect the classifier's quality more effectively than the ROC curve.

The gain curve (or cumulative gain curve) is an indicator to describe the global accuracy. It represents the relationship between the percentage of correct predictions for positive cases and the effort required to achieve them, measured by the percentage of prediction cases. The Y-axis in the gain curve is equal to recall and sensitivity (TPR), and the X-axis is the percentage of positive instances. The formulas of these indicators are shown in the following equations:

$$gain = recall = TPR = \frac{\mathrm{TP}}{\mathrm{TP} + \mathrm{FN}}, \tag{15}$$

$$\%\ \text{of positive}\ instances = \frac{\mathrm{TP} + \mathrm{FP}}{\mathrm{TP} + \mathrm{FP} + \mathrm{TN} + \mathrm{FN}}, \tag{16}$$

where FP is the number of samples predicted to be false positives, FN is the number of samples predicted to be false negatives, TP is the number of samples predicted to be true positives, and TN is the number of samples predicted to be true negatives.

K-S curve (Kolmogorov–Smirnov curve), also called Lorentz curve, is used to describe the quality of the classification model. The K-S curve draws two curves with TPR and FPR as the vertical axis and the threshold as the horizontal axis. Thus, it reflects the difference between TPR and FPR at the same threshold. In general, the farther the two broken lines are, the better the classification model distinguishes between positive and negative samples. The K-S statistical value measures the maximum difference between TPR and FPR within the range of all possible thresholds, that is, the upper limit of the classification model for the discrimination between positive and negative samples. The calculation formula of the K-S statistic is shown in equation (17). The value range of the K-S statistic is [0, 1]. Ideally, the closer the K-S statistic is to 1, the stronger the classification model's ability to distinguish between positive and negative samples. According to experience, when the K-S statistic is less than 0.2, the model cannot distinguish between positive and negative samples, and when the K-S statistic is more significant than 0.4, the model can distinguish between positive and negative samples [51]. The specific range of K-S statistics and its empirical evaluation of the model are shown in Table 5:

$$\mathrm{K-S\ statistic} = \max(\mathrm{TPR} - \mathrm{FPR}), \tag{17}$$

where FPR is the negative cumulative response, FPR = FP/TR + FP, and TPR is sensitivity.

Lift curve, which measures the increase in the accuracy of the model's prediction results under a certain threshold compared to the accuracy of the random prediction results without the model. In short, it is how much the prediction effect has been improved by using this model and not using this model for prediction. The larger the lift, the better the prediction effect of the model. The calculation of lift is shown in the following equation:

$$\begin{aligned} \mathrm{lift} &= \frac{\mathrm{TP}/\mathrm{TP} + \mathrm{FP}}{\mathrm{TP} + \mathrm{FN}/\mathrm{TP} + \mathrm{TN} + \mathrm{FP} + \mathrm{FN}} \\ &= \frac{TP \times (\mathrm{TP} + \mathrm{TN} + \mathrm{FP} + \mathrm{FN})}{(\mathrm{TP} + \mathrm{FP}) \times (\mathrm{TP} + \mathrm{FN})}, \end{aligned} \tag{18}$$

where FP is the number of samples predicted to be false positives, FN is the number of samples predicted to be false negatives, TP is the number of samples predicted to be true positives, and TN is the number of samples predicted to be true negatives.

The above parameters and indicators for evaluating model performance are provided in BigML. Through the

Table 4: AUC value range and its empirical evaluation of the model [50].

Range of AUC values	Model performance evaluation
0.50~0.60	Fail
0.60~0.70	Poor
0.70~0.80	Fair
0.80~0.90	Good
1.00	Excellent

brief introduction of the above indicators, it is not difficult to find that these indicators evaluate the performance of the classification prediction model from different evaluation angles to realize the multidirectional and multiangle analysis and measurement of the prediction model performance [52]. In addition, it can also be seen that there is no single indicator that can evaluate the performance of the classification prediction model in an all-around way, and more is the collaborative evaluation of multiple parameter indicators. It can be seen from Figure 4 that the sample data of top coal caving have severe category imbalance (i.e., grade imbalance), and the classification evaluation of top coal caving is a multiclass prediction problem. So, it is necessary to select multiple parameters and indicators from the above indicators to evaluate the prediction model's performance to ensure that the prediction model is robust.

Accuracy/error rate is the most commonly used indicator for researchers to evaluate the performance of classification prediction models, because they calculated the ratio of the number of correctly classified predictions to the total number of predictions and the number of incorrectly classified predictions accounted for the total number of predictions, and they can objectively reflect the global quality of the model. However, accuracy/error rate is not a good indicator when the sample data categories are unbalanced, because when the sample data categories are unbalanced, the prediction will favor the category that accounts for the majority of the total sample and ignore the category that accounts for the minority of the total sample, resulting in the category that accounts for the minority of the total sample does not have the classification prediction ability or the classification prediction ability is weak. In addition, because the top coal caving classification evaluation is a multiclassification prediction problem, this article will not take the accuracy/error rate and precision and recall rate as the indicators of model performance evaluation. So, only take the macro-accuracy/macro-error rate and macro-precision and the macro-recall rate as the auxiliary indicators. Moreover, taking the macro-Matthews correlation coefficient, ROC curve, PR curve, K-S curve, gain curve, lift curve K-S statistics, AUC value, and lift value are the leading indicators to evaluate the model's performance.

6. Predictive Model Establishment and Its Performance Evaluation

It is often not easy to get a more robust and stable classification prediction model, and therefore, it is also challenging to achieve overnight. Therefore, more needs to continue exploring and optimizing the model to obtain a more robust and stable classification prediction model. In BigML, the methods of establishing classification prediction models include models (decision trees), ensemble (bagging, random decision forests, and boosted trees), deep nets, logistic regression, and other methods. However, it is not easy to know in advance the specific ways and methods to obtain. So, it is necessary to use the modeling method provided by BigML to establish one or more exploratory models and continuously evaluate and optimize the models to obtain a robust and stable classification evaluation model of top coal caving.

BigML is not only a very friendly machine learning platform, which can build models (decision tree), ensemble (bagging, random decision forests, and boosted trees), deep nets, and logical regression models with one click. Nevertheless, it also considers that noncomputer professional users may have model parameter adjustment and optimization problems, so the "automatic optimization" function is also specially set up. The user can efficiently complete the modeling task through this function by simply specifying training samples and training objectives. The model parameters will be automatically adjusted to the theoretical optimal by BigML. In order to evaluate the performance of model establishment, BigML has set up modules such as single model evaluation, multimodel evaluation, and cross-validation evaluation. These modules only need the user to specify the model to be evaluated and the test set sample used to evaluate the model, and then the model performance evaluation can be easily completed.

6.1. Establishment of the Classification Evaluation Model of Top Coal Caving. The decision tree is the most commonly used method to establish a classification prediction model, so this article uses the decision tree in BigML to establish the top coal caving exploratory classification evaluation model. In addition, when the model (decision tree) in BigML is used to establish the classification evaluation model of top coal caving exploratory, the "automatic optimization" function in BigML is used to build the model, and the prepared training set samples are taken as the model training samples, and the "Grade" in the samples is taken as the training target. Finally, BigML obtains the classification evaluation model of top coal caving based on the training set samples, as shown in Figures 6–9. In order to evaluate the performance of the top coal caving grading evaluation model established by BigML, the "single model evaluation" module of BigML is used to test the model and evaluate the model's performance. The test sample is the test set sample because the sample is small, with only 21 groups, so the sampling method is set to be replaceable. The evaluation results are shown in Figures 10– 13 and Tables 6 and 7.

According to Tables 6 and 7 and Figures 10–13, it can be seen that the established classification evaluation model of top coal caving can be barely accepted when the probability threshold is 50% (the default probability threshold of the classification prediction model is 50%, which is also a commonly used threshold for establishing classification

Table 5: K-S statistical range and its empirical assessment of model differentiation ability.

Range of K-S statistics	Model differentiation ability
0.00~0.20	Fail
0.20~0.40	Poor
0.40~0.50	Fair
0.50~0.60	Good
0.60~0.750	Very good
0.75~1.00	Excellent

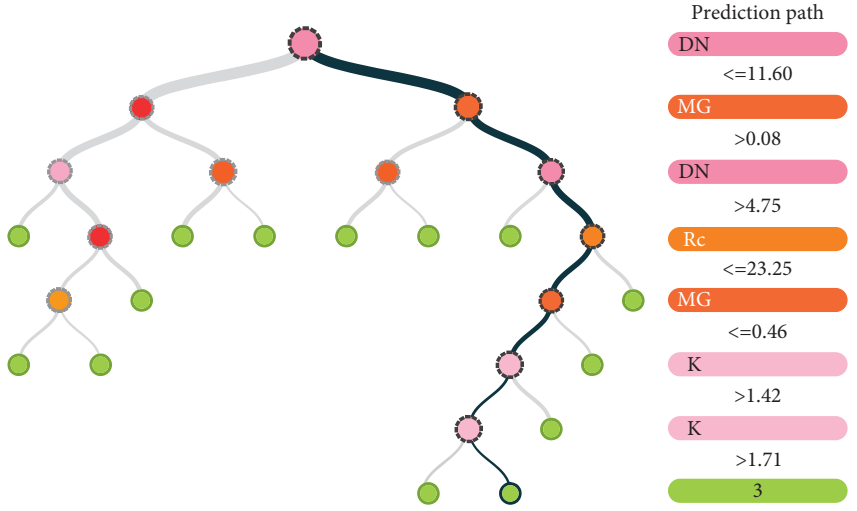

Figure 6: The established decision tree model.

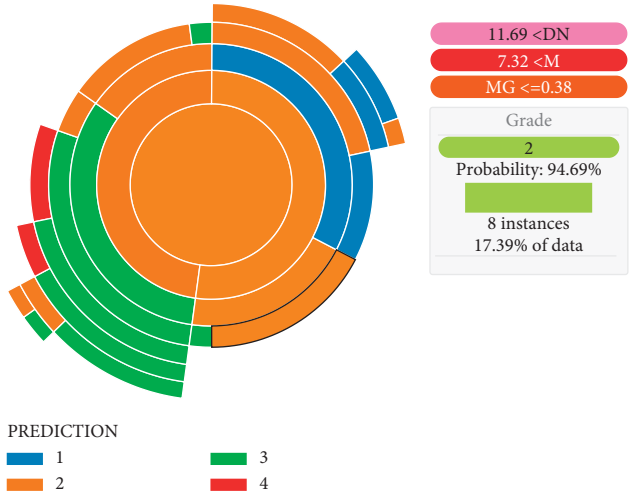

Figure 7: Prediction distribution of the decision tree model from the perspective of the sunburst chart.

prediction models [53]). The global prediction accuracy rate (ACCURACY) of the model is 80.95%, the average recall rate (AVG.RECALL) and precision rate (AVG. PRECISION) are 79.17% and 85.42%, respectively, and the average Matthews correlation coefficient (AVG. Phi) and average *F*-measure (AVG. *F*) of the model reach 0.7436 and 0.8087, respectively. However, from the model's graphical performance evaluation indicators, lift curve (Figure 13), the lift value of each grade is greater than 100% (that is, the model's prediction ability for top coal caving of each grade is stronger than the random model). However, from the values of ROC AUC, PR AUC, and K-S in the ROC curve (Figure 10), PR curve (Figure 11), and K-S curve (Figure 12), the model has a certain prediction ability for top coal caving of grade 2 and grade 4, while it has low prediction ability for top coal caving of grade 1 and grade 2. The ROC AUC and PR AUC of grades 2 and 4 are greater than 0.7, and the K-S values are 100%, while the ROC AUC and PR AUC of grades 1 and 3

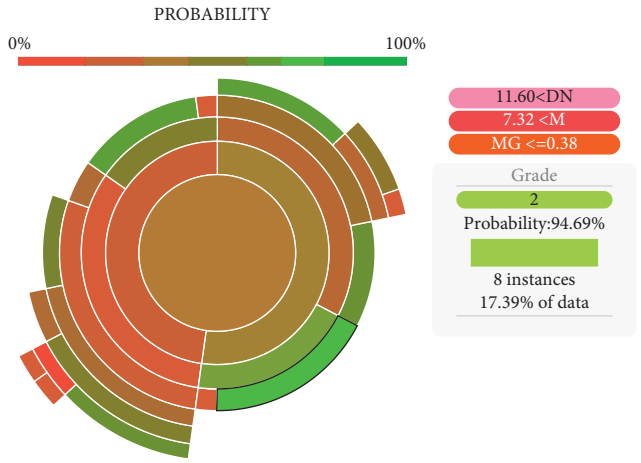

Figure 8: Prediction probability distribution of the decision tree model from the perspective of the sunburst chart.

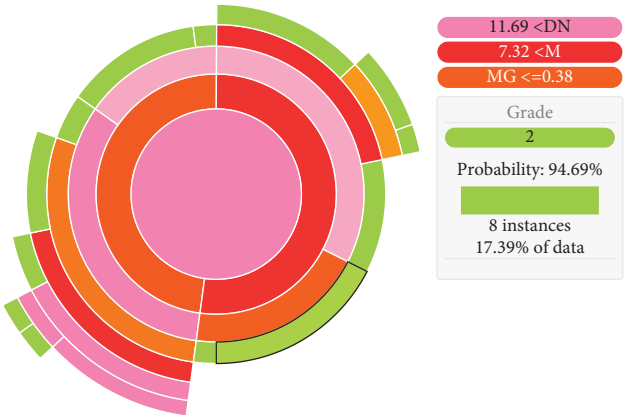

Figure 9: Variable distribution of the decision tree model from the perspective of the sunburst chart.

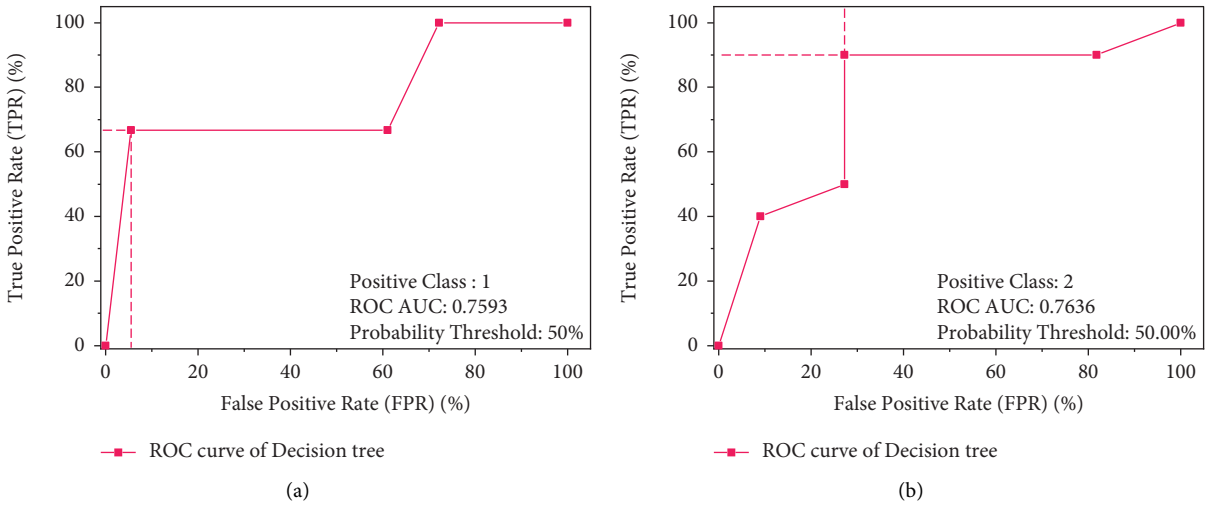

Figure 10: Continued.

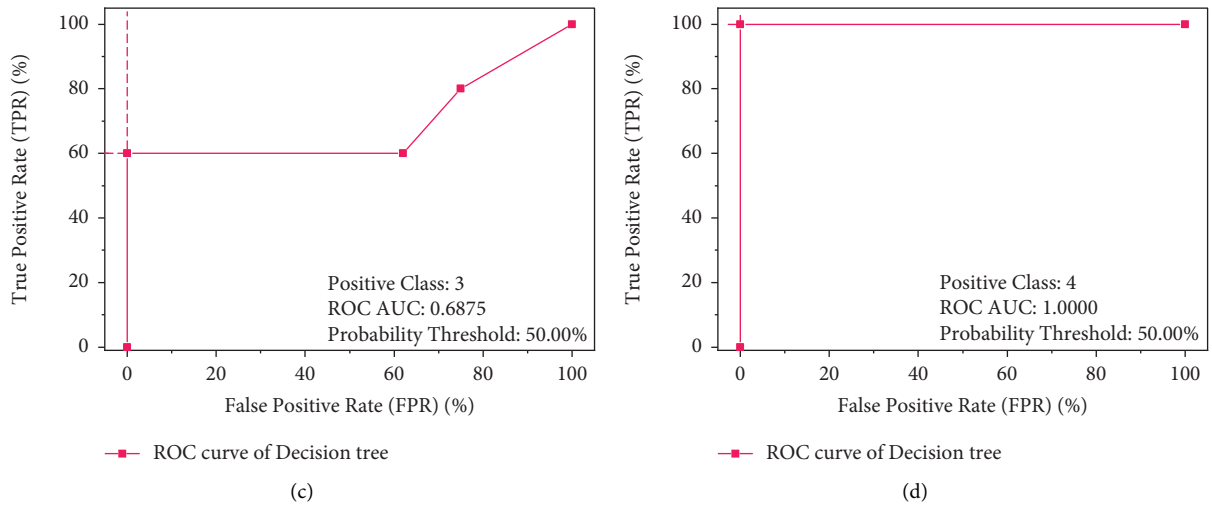

Figure 10: ROC curve of each classification test of the decision tree model.

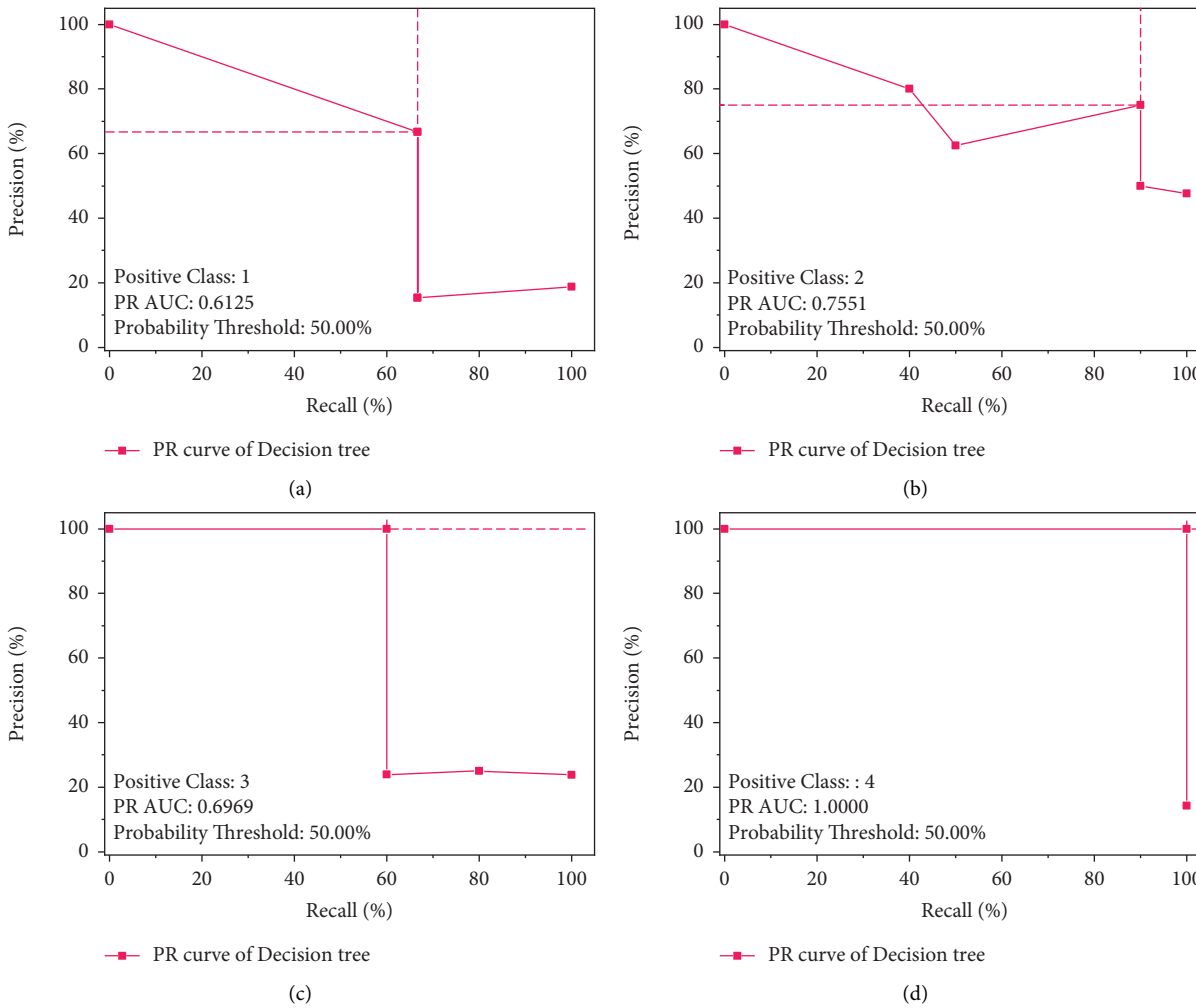

Figure 11: PR curve of each classification test of the decision tree model.

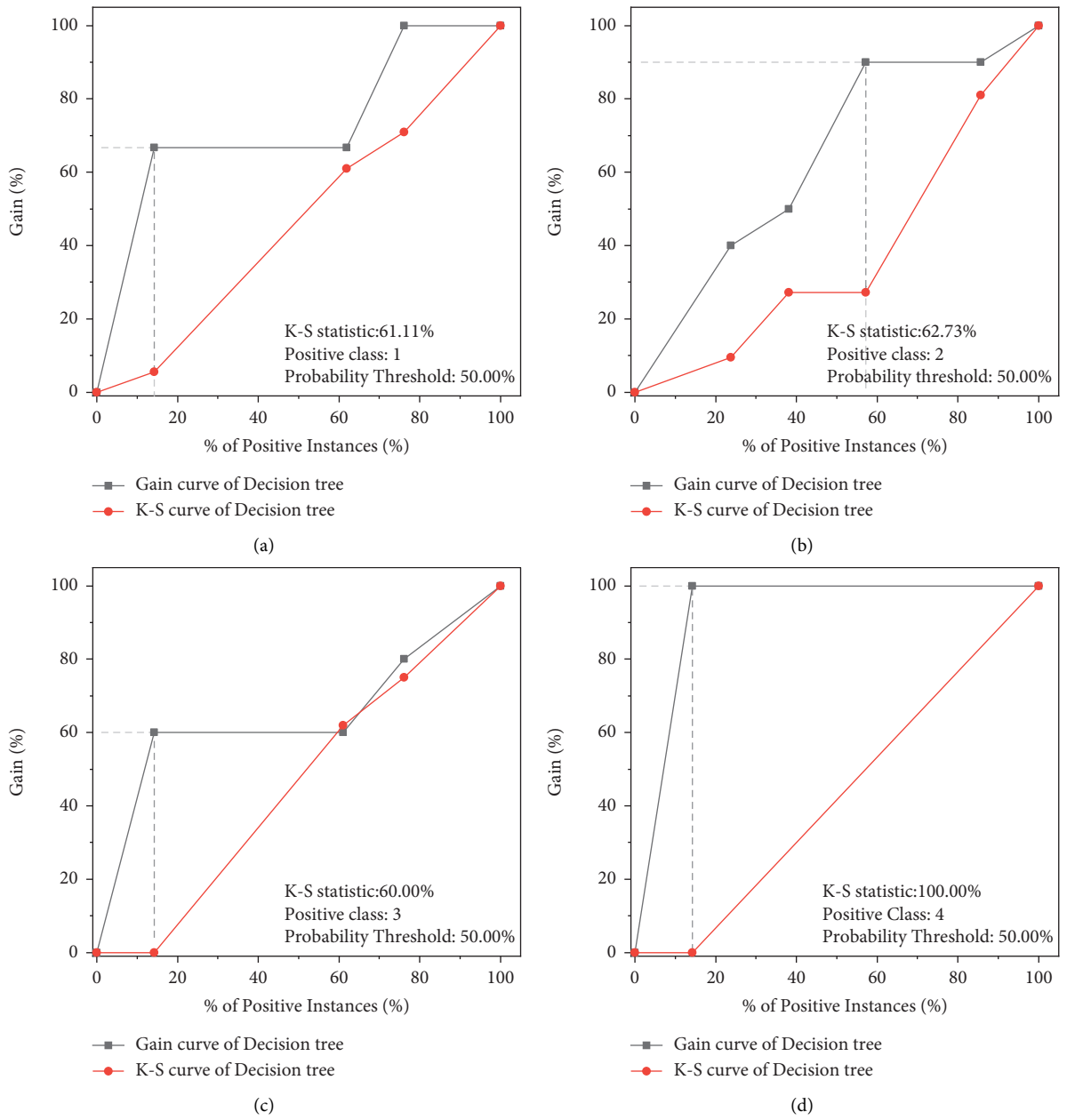

Figure 12: K-S and gain curve of each classification test of the decision tree model.

are less than 0.7, and the K-S values are about 60%. Optimization or a better modeling method can be considered to establish a classification evaluation model of top coal caving to achieve a perfect prediction of each grade top coal caving.

The deep network is also a method to establish a classification prediction model, so try to use the deep network in BigML to establish a better top coal classification and caving classification evaluation model. When using the deep network in BigML to establish the top coal classification and caving classification evaluation model, the "automatic optimization" function is also used for modeling, and the automatic method is selected as "Network search." The model training sample is the training set sample, and the training target is the "Grade" in the sample. After the model is trained, use the test set sample data to test and evaluate the model's performance, and the test sampling method is still set to replaceable sampling. The test results are shown in Figures 14 –17 and Tables 8 and 9.

According to Tables 8 and 9, when the probability threshold is 50%, the global performance of the classification evaluation model of top coal caving established by the deep network is not much better than that established by the decision tree. The global prediction ACCURACY of the classification evaluation model of top coal caving established by the deep network is 80.95%, the same as that established by the decision tree; the AVG.RECALL and AVG.PRECISION are 82.26% and 83.04%, respectively, and the AVG. Phi and AVG. F are 0.7571 and 0.8084, respectively, which

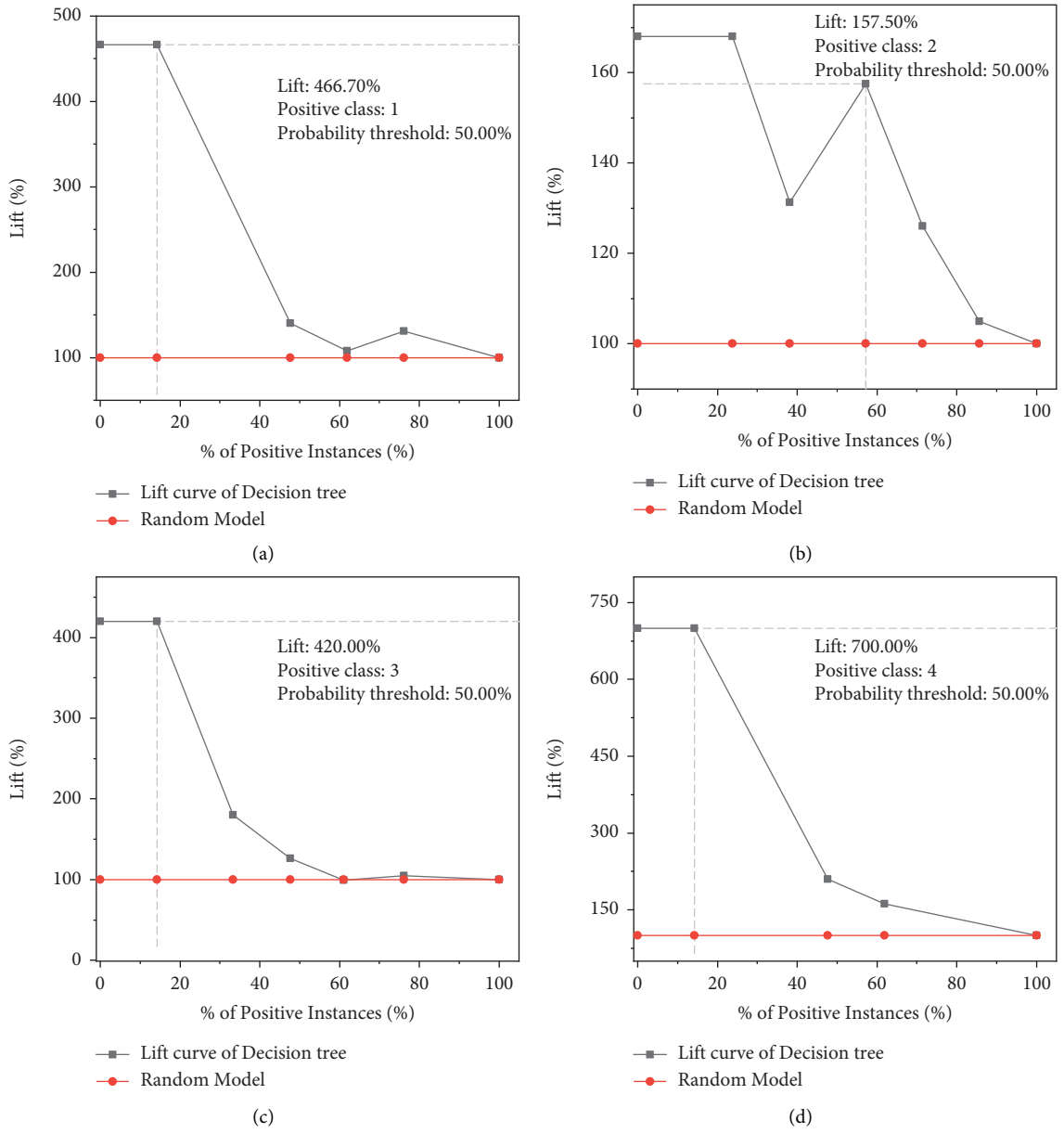

Figure 13: Lift curve of each classification test of the decision tree model.

are little different from the AVG.RECALL, AVG.PRECISION, AVG. Phi, and AVG. *F* of the classification evaluation model of top coal caving established by a decision tree. The global performance parameters of these models show that the global performance of the classification evaluation model of top coal caving established by the deep network is not much better than that established by the decision tree.

However, according to Figures 14–17, among the local evaluation parameters of the model, the model established by the deep network is better than the decision tree. From the model's graphical performance evaluation indicators, lift curve (Figure 17), the lift value of each evaluation grade is greater than 100%, which means that the prediction ability of the model established by the deep network for top coal caving of each grade is stronger than the random model. From the ROC AUC, PR AUC, and K-S values of each grade in ROC curve (Figure 14), PR curve (Figure 15) and K-S curve (Figure 16), the ROC AUC, PR AUC, and K-S values of each grade in the classification evaluation model of top coal caving established by the deep network are greater than or equal to that established by the decision tree. In addition, from the ROC AUC, PR AUC, and K-S values of each grade of the classification evaluation model top coal caving established by the deep network, it can be seen that the model has good prediction ability for the top coal caving of each grade. The ROC AUC of each grade in model is greater than 0.7, the PR AUC is basically greater than or equal to 0.7, and the K-S value is greater than 80%. The above analysis shows that under the probability threshold of 50%, although the

Table 6: Confusion matrix of decision tree model test results and model evaluation related indicators.

Actual vs. predicted	1	2	3	4	Actual	Recall (%)
1	2	1	0	0	3	66.67
2	1	9	0	0	10	90.00
3	0	2	3	0	5	60.00
4	0	0	0	4	3	100.00
Predicted	3	12	3	3	21	79.17 AVG.RECALL
Precision (%)	66.67	75.00	100.00	100.00	86.42 AVG.PRECISION	80.95 ACCURACY

Table 7: Performance evaluation results of the decision tree model.

Grade	*F*-measure	Phi coefficient
1	0.67	0.61
2	0.82	0.63
3	0.75	0.73
4	1.00	1.00
	0.8087 AVG. *F*	0.7436 AVG. Phi

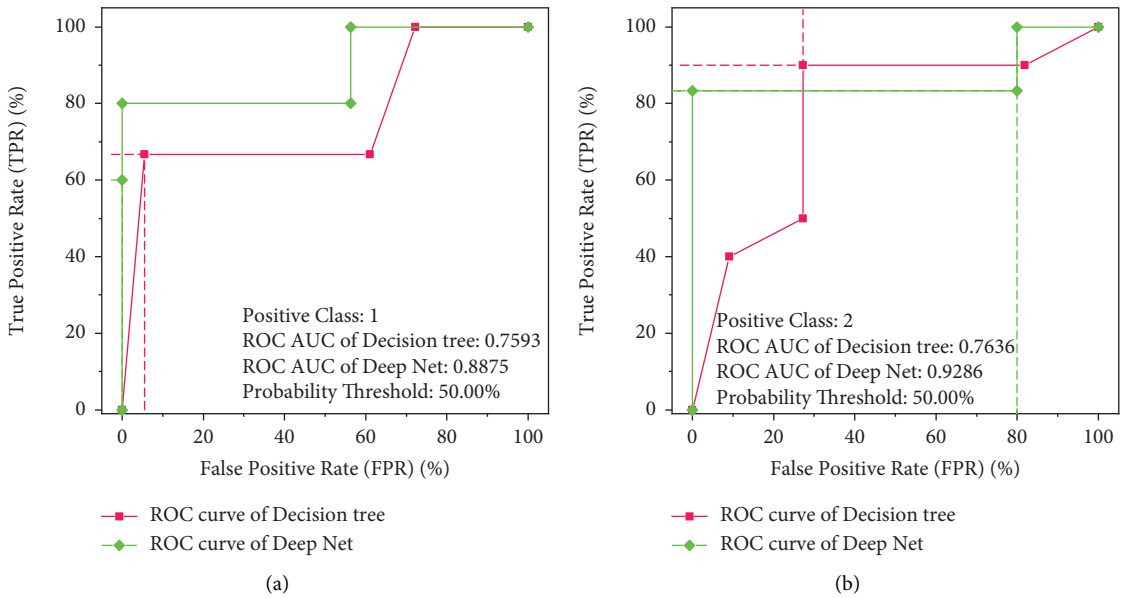

Figure 14: Continued.

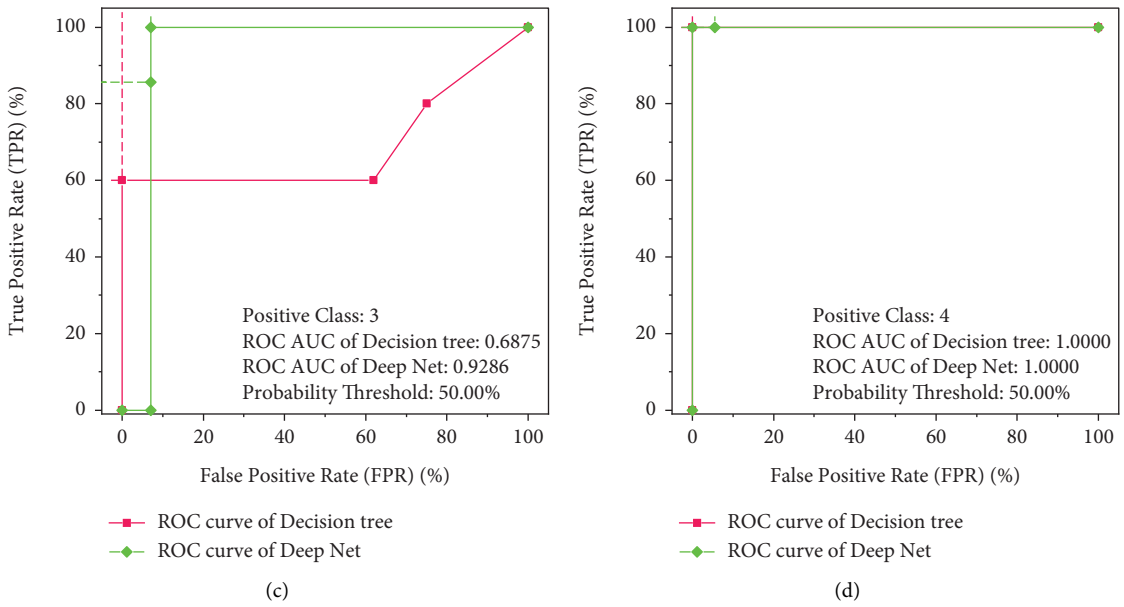

Figure 14: ROC curve of each classification test of the deep network model.

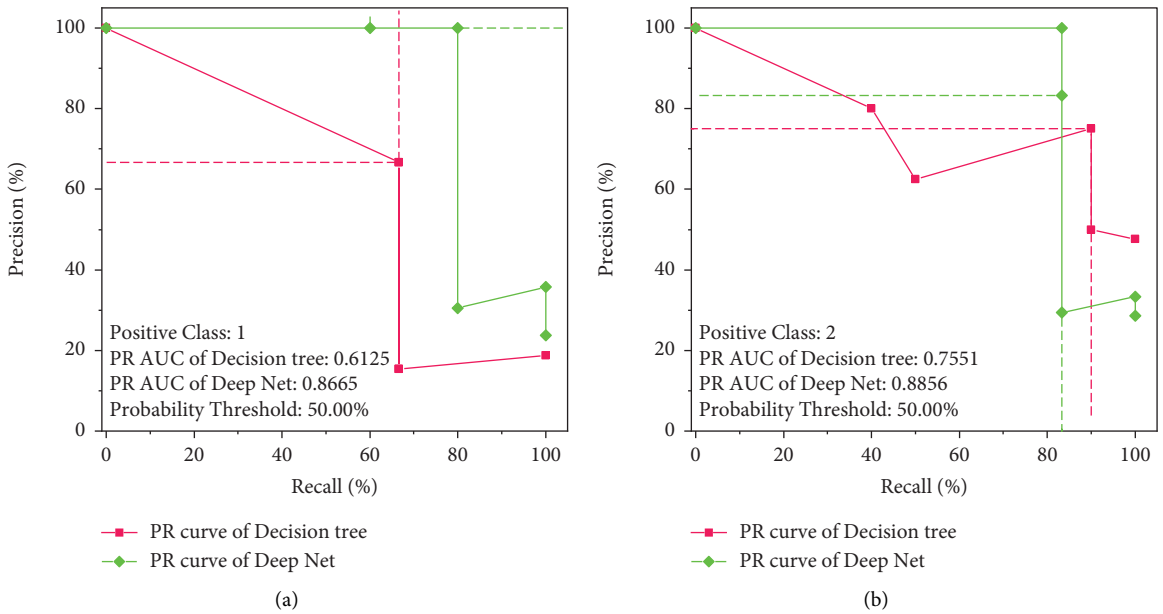

Figure 15: Continued.

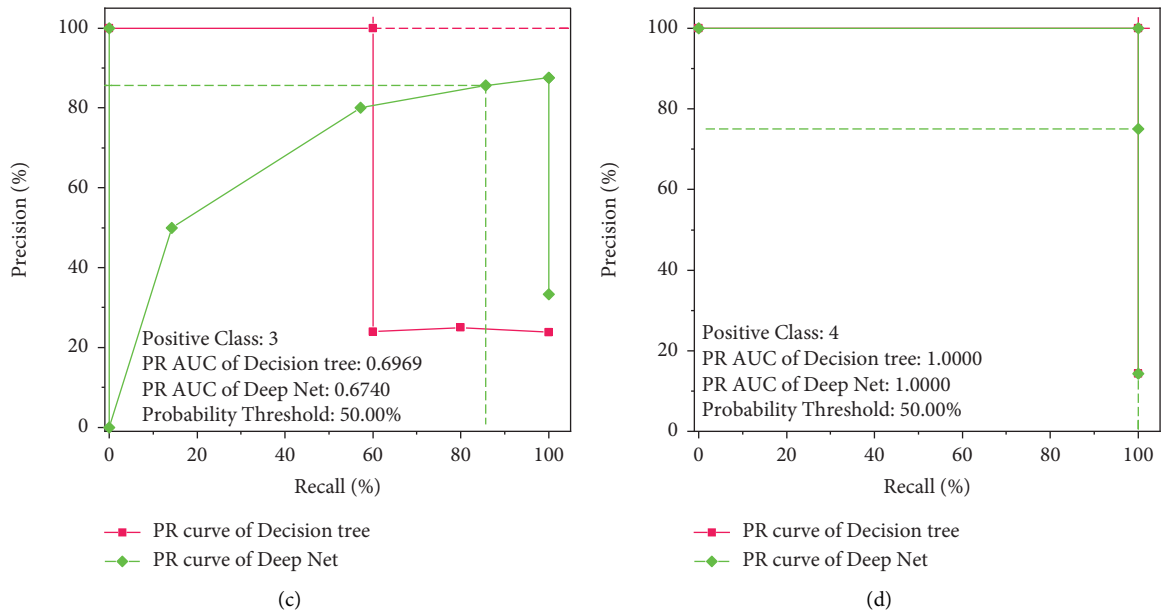

Figure 15: PR curve of each classification test of the deep network model.

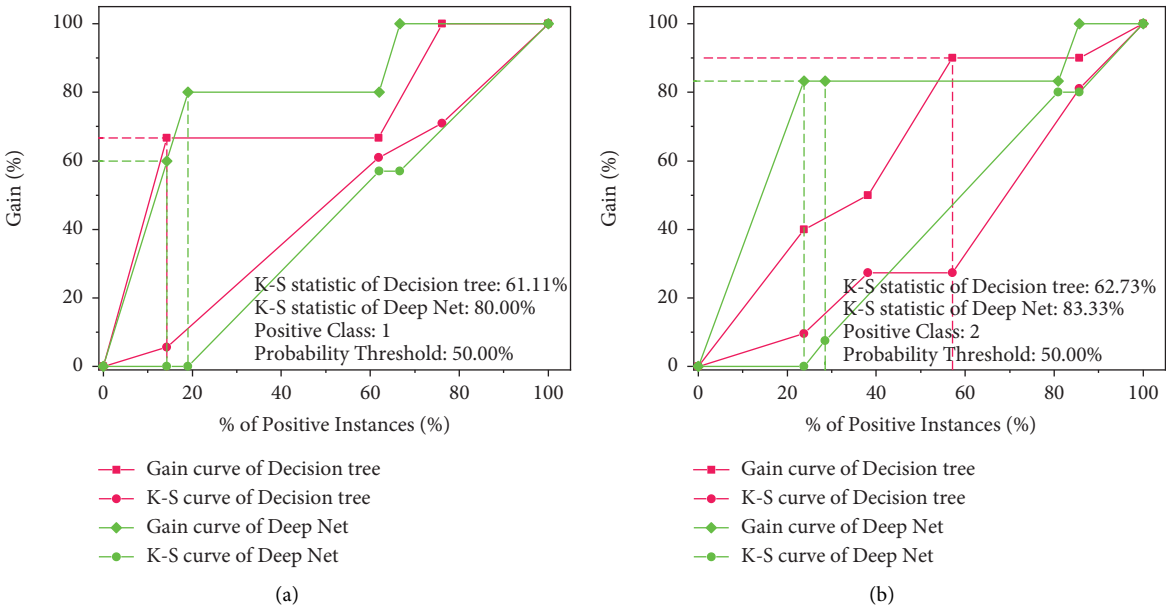

Figure 16: Continued.

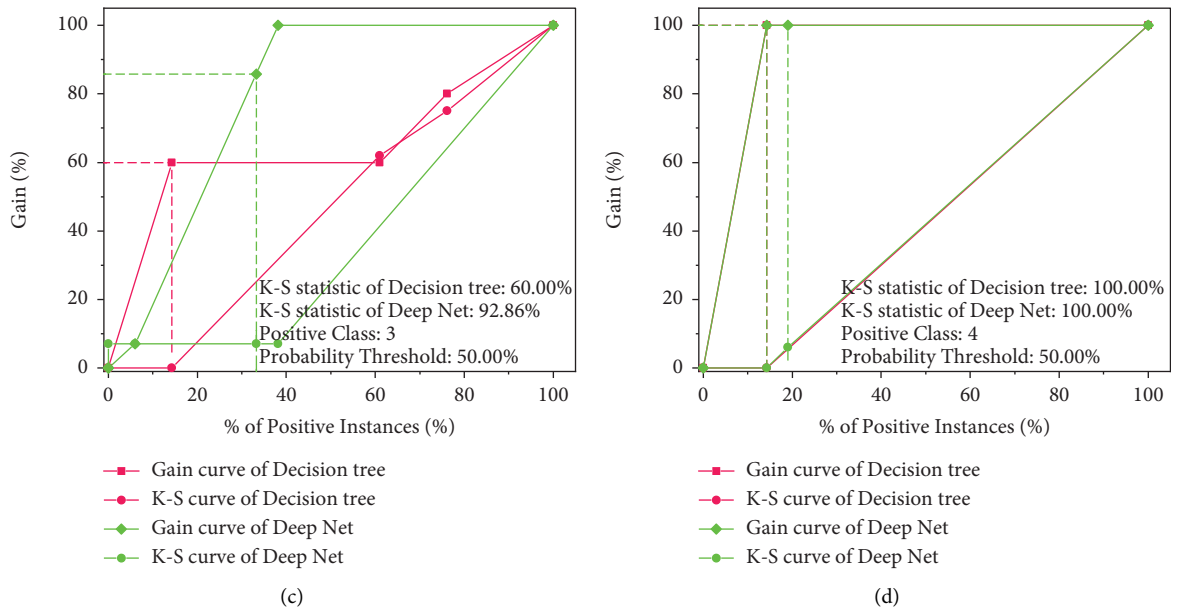

Figure 16: K-S curve and gain curve of each classification test of the deep network model.

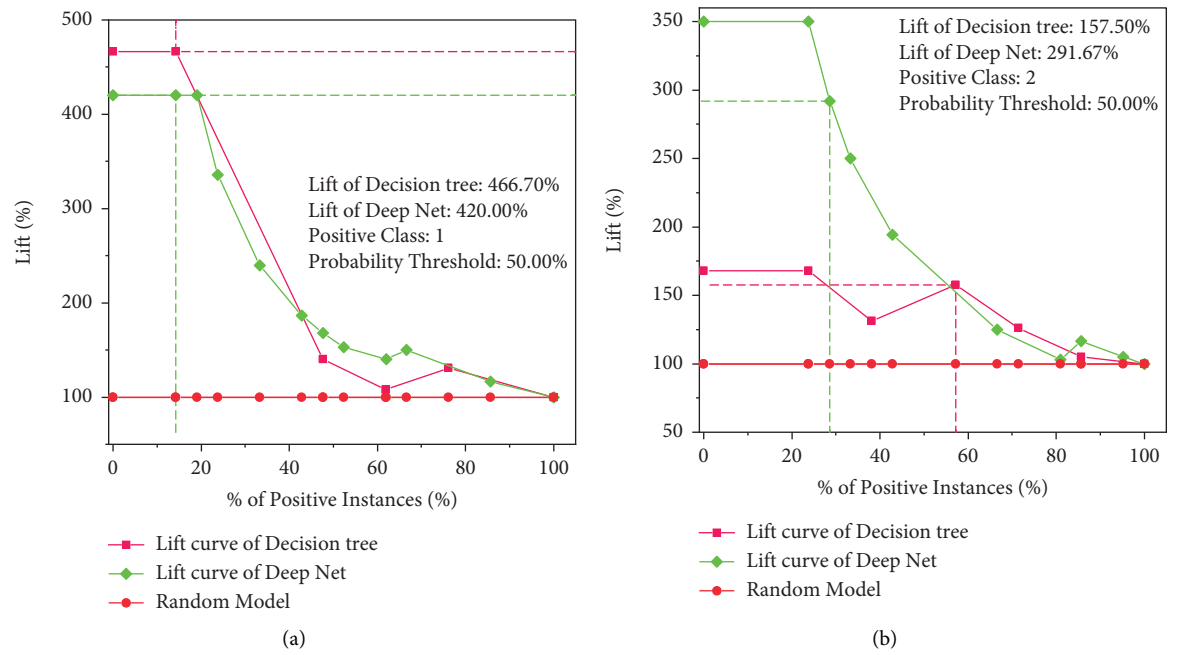

Figure 17: Continued.

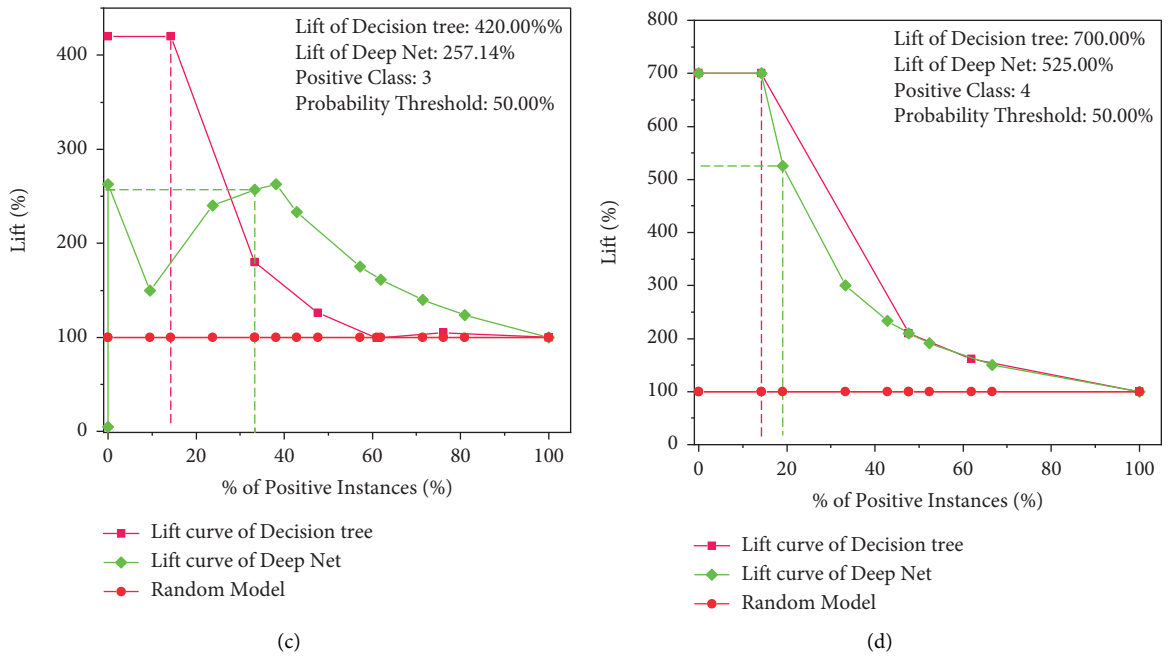

Figure 17: Lift curve of each classification test of the deep network model.

classification evaluation model of top coal caving established by deep network and the classification evaluation model of top coal caving established by decision tree have little difference in global performance, the classification evaluation model of top coal caving established by deep network is better than that established by decision tree model in local. In order to get a more robust classification evaluation model of top coal caving, the combination and average of the two models can be considered.

6.2. Optimization of Top Coal Caving Classification Evaluation Model. In the modeling process, it is not difficult to find that, in general, if several different models can be combined and their prediction results are averaged, the ideal prediction results can be obtained. At the same time, if the combined average model can balance the shortcomings of a single participating combined model, then the final model generally obtained is robust and stable. However, it is based on this idea to develop a fusion modeling method in BigML. The fusion modeling method combines different models and averages their predictions to balance the weaknesses of each model so that the model can produce better performance. The principle is similar to model integration, except that the fusion modeling method can combine and average a single decision tree and combine and average models such as logistic regression and deep network.

In order to optimize the model and get a more robust and stable classification evaluation model of top coal caving, the classification evaluation model of top coal caving established by decision tree and depth network is fused. According to the model performance evaluation parameters, although the global performance of the classification evaluation model of top coal caving established by decision tree and deep network is similar, the local performance of the model established by the deep network is better than that of the model established by a decision tree. Therefore, the weight of the prediction result of the model established by the decision tree and depth network is 1 : 3. After the model fusion, the model's performance is tested and evaluated with the sample data of the test set, and the test sampling mode is set to replaceable sampling. The test results are shown in Figures 18– 21 and Tables 10 and 11.

According to Tables 10 and 11 and Figures 18–21, it can be seen that under the probability threshold value of 50%, the classification evaluation model of top coal caving established by fusion is perfect and robust no matter from the global or local view, which has fully met the demand of prediction. The global prediction ACCURACY, AVG. RECALL, and AVG. PRECISION of the classification evaluation model of top coal caving established by fusion reached 90.45%, 95.45%, and 88.75%, respectively. In addition, the AVG. Phi and AVG. F of the classification evaluation model of top coal caving established by fusion reached 0.8838 and 0.9115, respectively. From the ROC AUC, PR AUC, and K-S values of each grade in the ROC curve (Figure 18), PR curve (Figure 19), and K-S curve (Figure 20) in model local performance evaluation parameters, the ROC AUC, PR AUC and K-S values of each grade of the classification evaluation model of top coal caving established by fusion are greater than or equal to that established by decision tree and depth network, respectively. At the same time, from the model's lift curve (Figure 21), the lift value of each evaluation grade is greater than 100%, which also shows that the model's prediction ability established by fusion is stronger than the random model. In addition, through the ROC AUC, PR AUC, and K-S values of each grade of the classification evaluation model of top coal caving established by fusion, it

Table 8: Confusion matrix of deep network model test results and model evaluation related indicators.

Actual vs. predicted	1	2	3	4	Actual	Recall (%)
1	3	1	1	0	5	60.00
2	0	5	0	1	6	83.33
3	0	1	6	0	7	86.71
4	0	0	0	3	3	100.00
Predicted	3	7	7	4	21	82.26 AVG.RECALL
Precision (%)	100.00	71.43	86.71	75.00	83.04 AVG.PRECISION	80.95 ACCURACY

Table 9: Performance evaluation results of the deep network model.

Grade	*F*-measure	Phi coefficient
1	0.75	0.73
2	0.77	0.67
3	0.86	0.79
4	0.86	0.84
	0.81	0.7436
	AVG. F	AVG. Phi

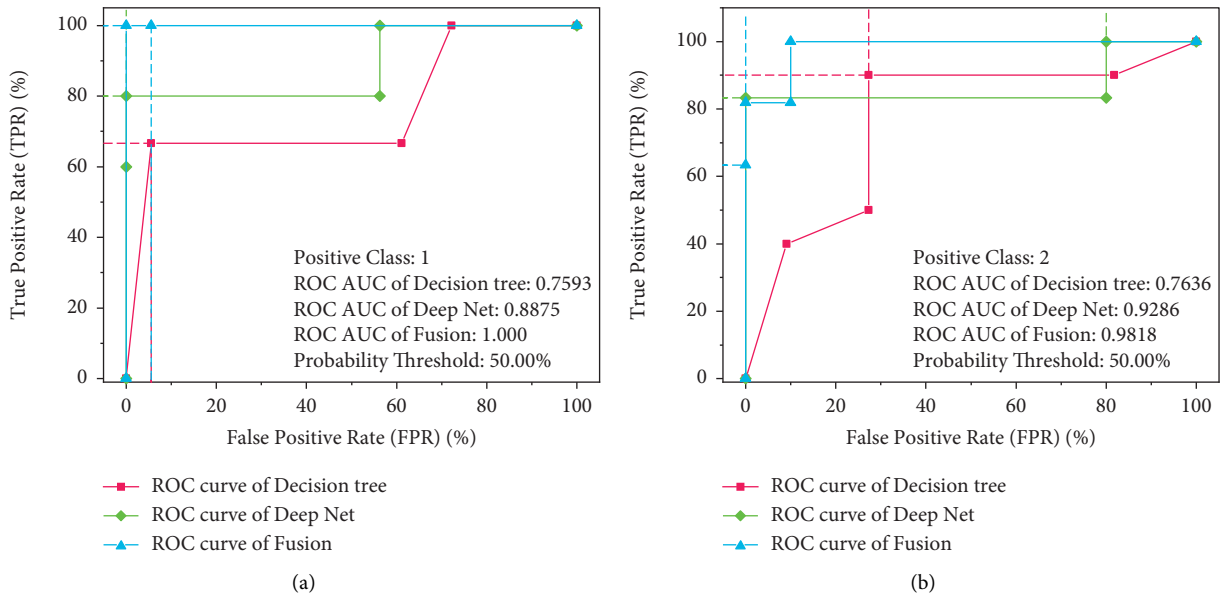

Figure 18: Continued.

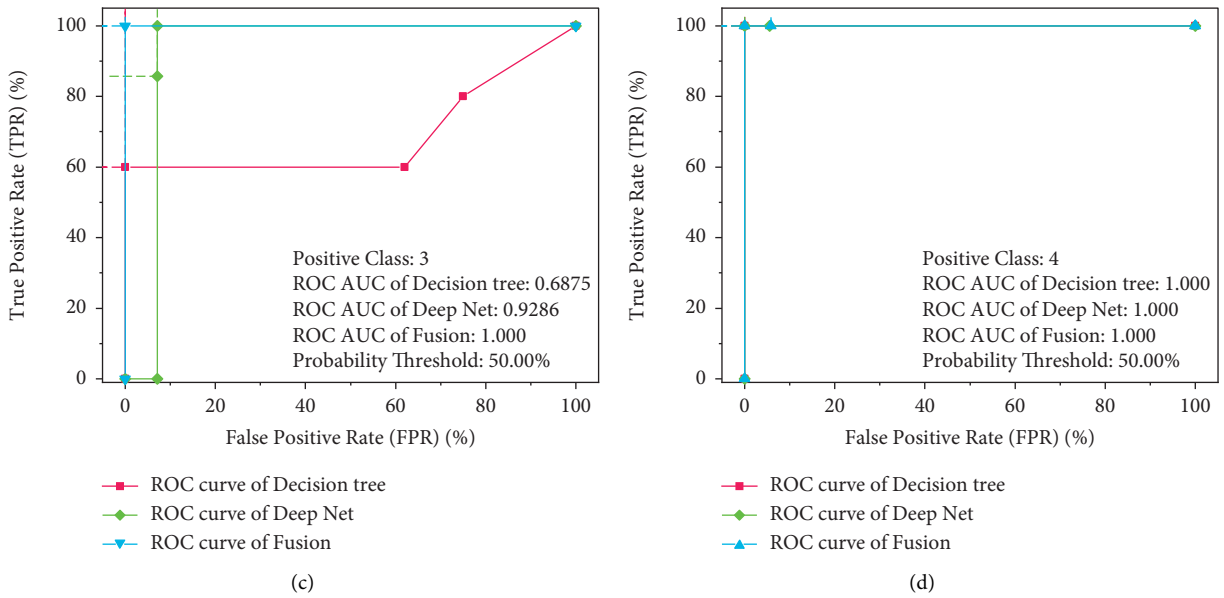

Figure 18: ROC curve of each classification test of the fusion model.

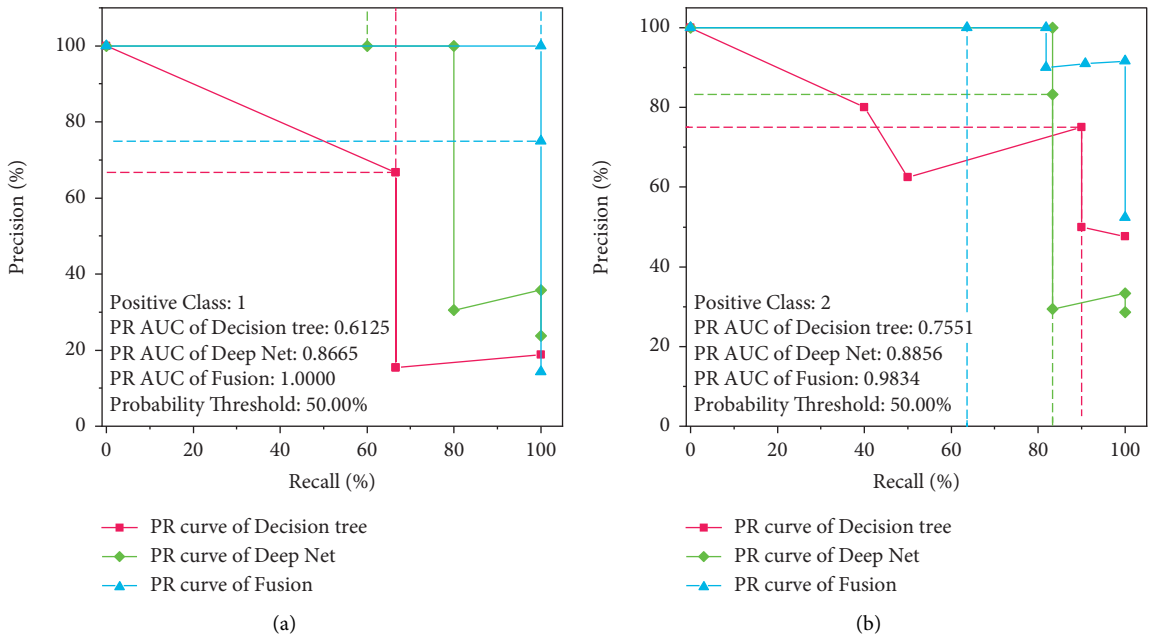

Figure 19: Continued.

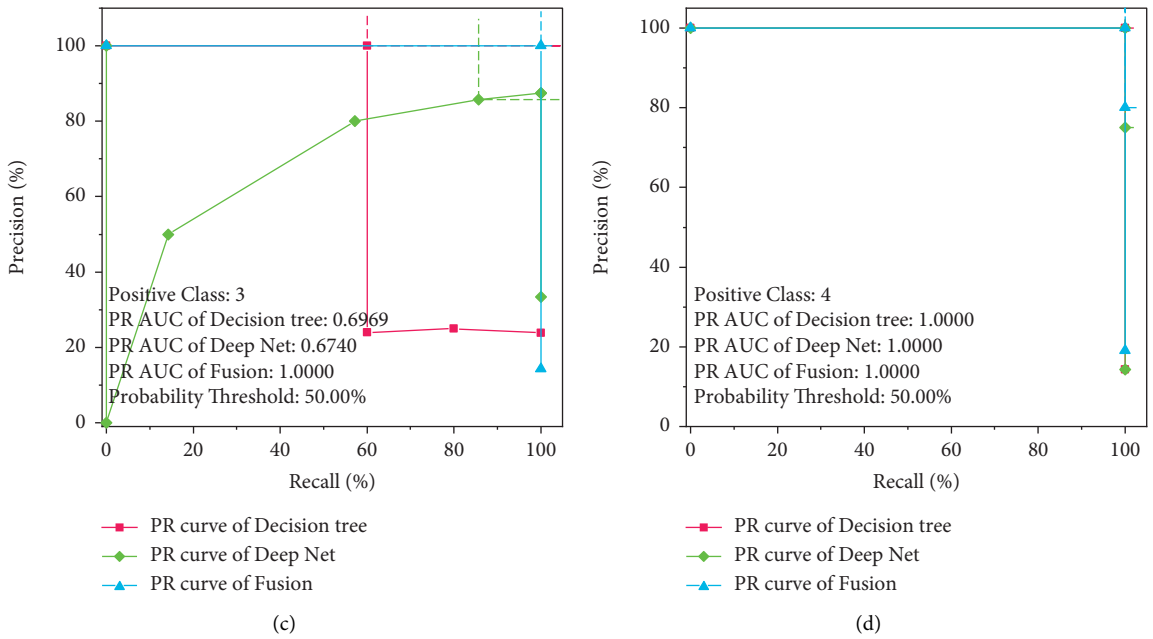

Figure 19: PR curve of each classification test of the fusion model.

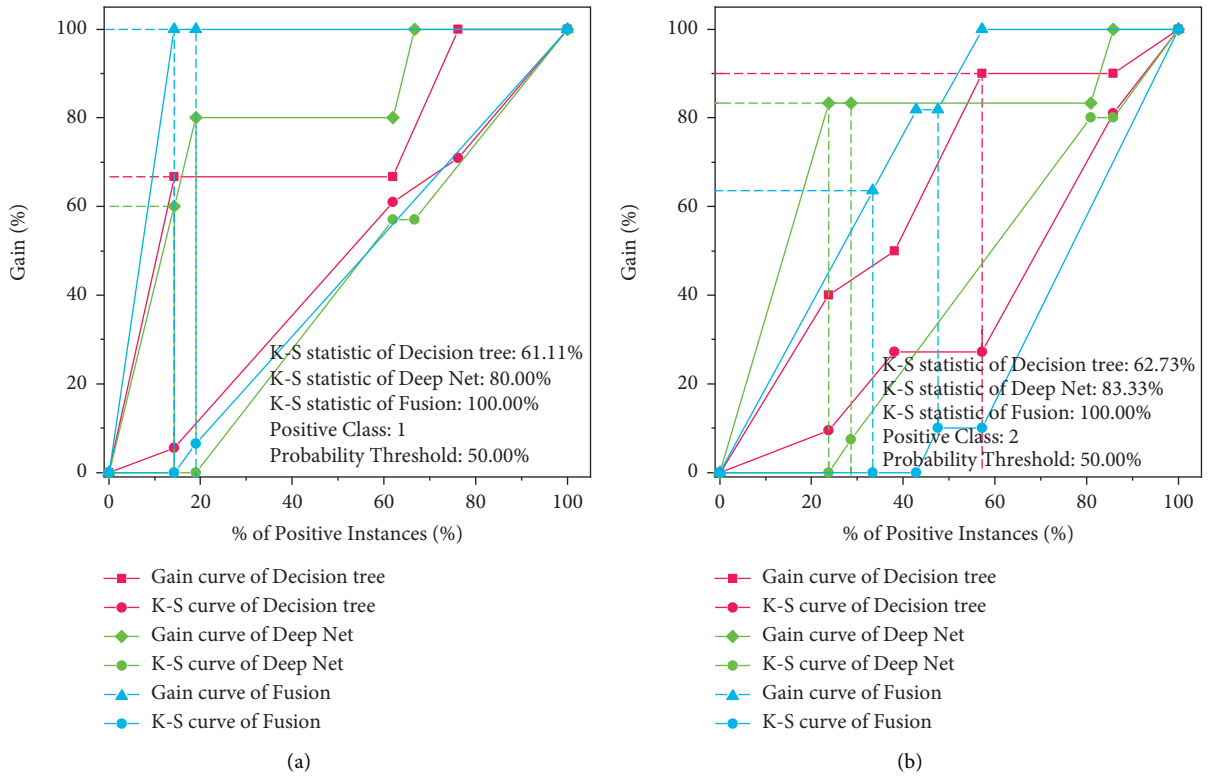

Figure 20: Continued.

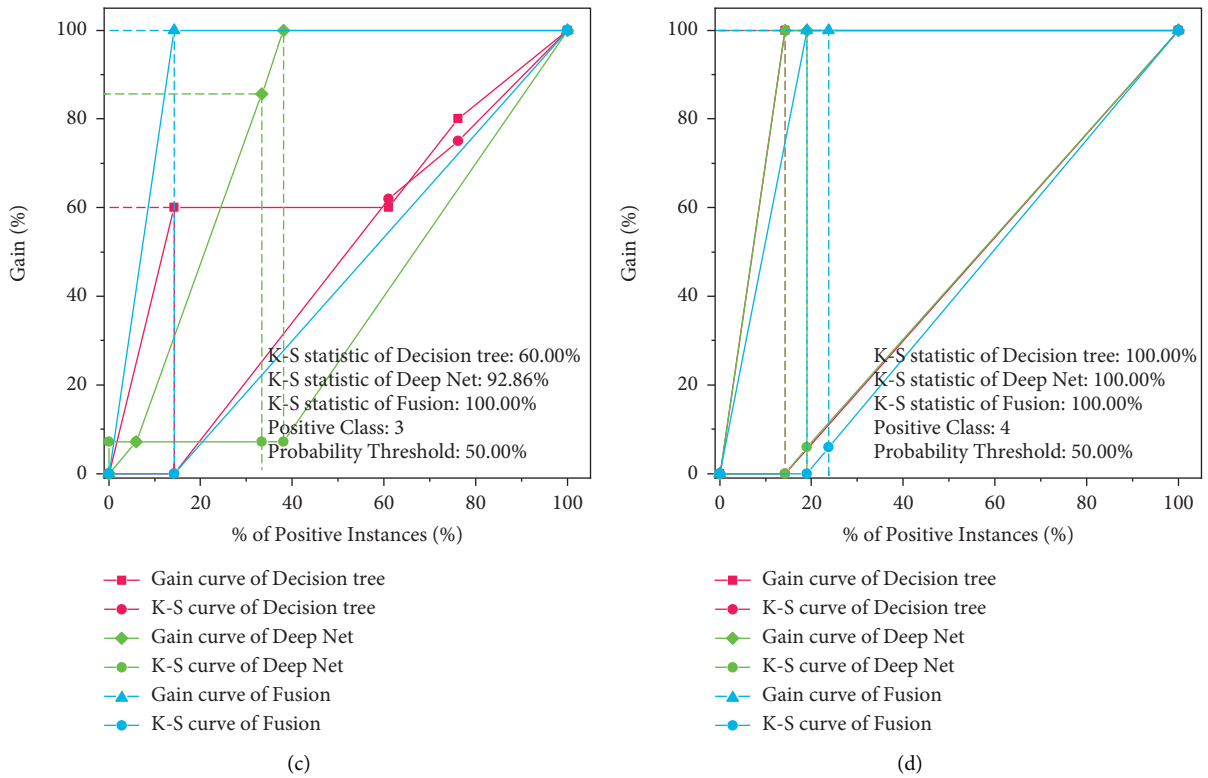

Figure 20: K-S curve and gain curve of each classification test of the fusion model.

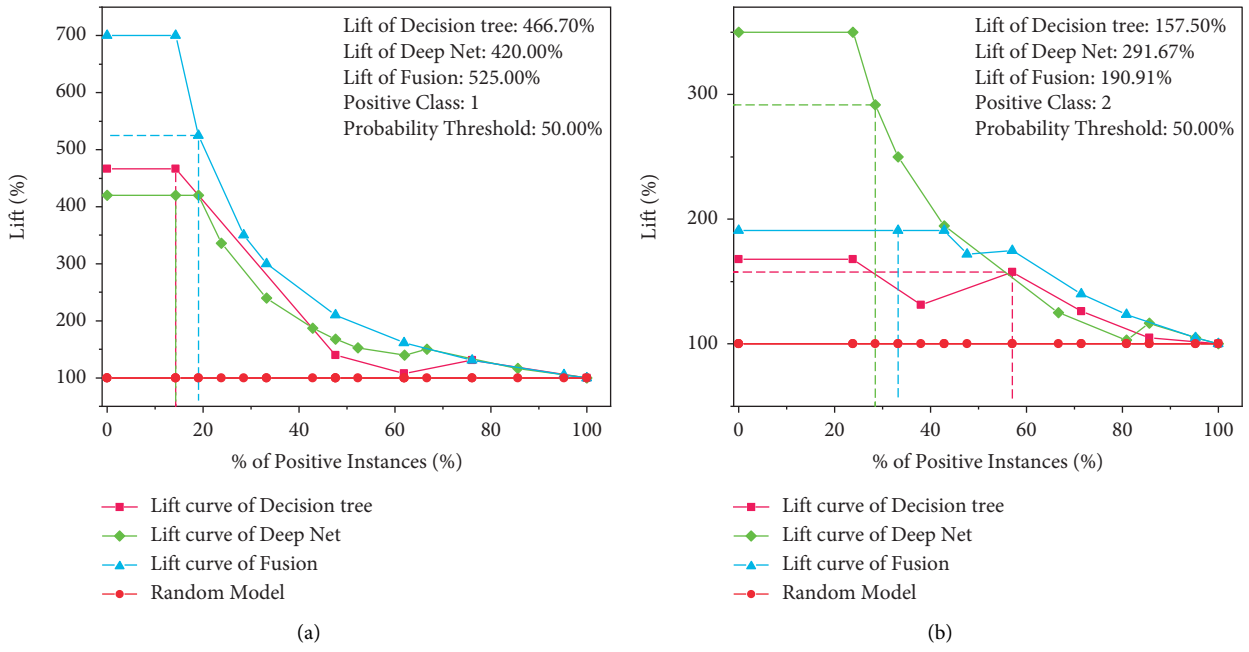

Figure 21: Continued.

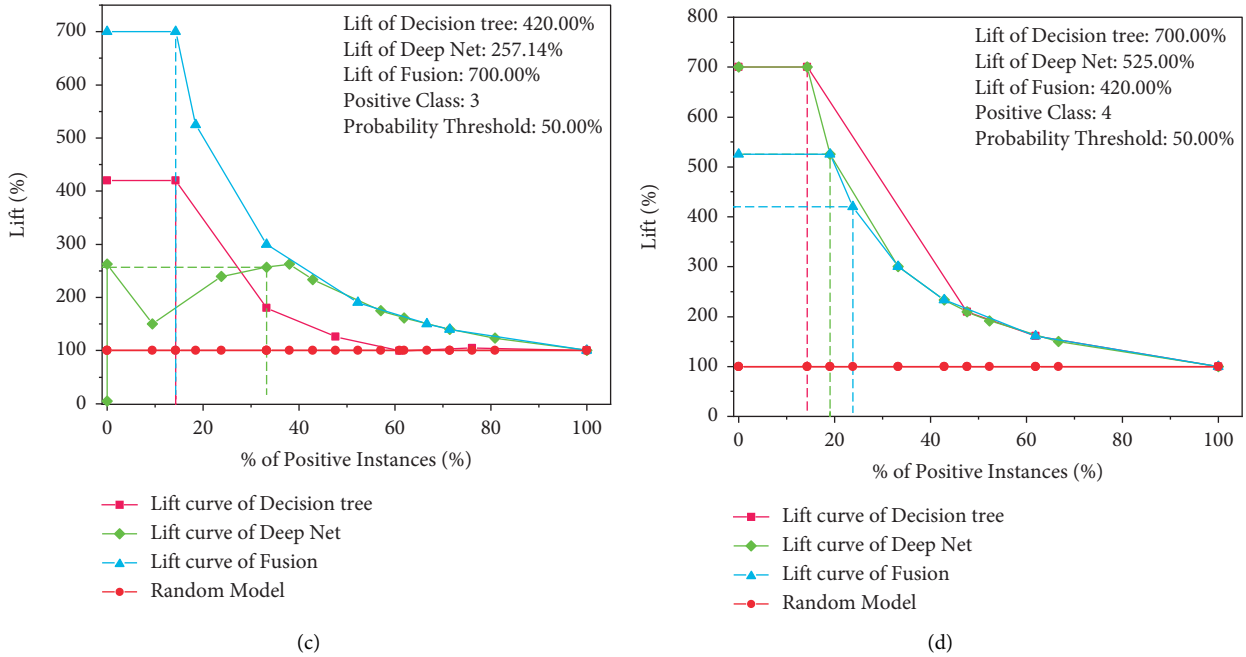

Figure 21: Lift curve of each classification test of the fusion model.

Table 10: Confusion matrix of fusion model test results and model evaluation related indicators.

Actual vs. predicted	1	2	3	4	Actual	Recall (%)
1	3	0	0	0	3	100.00
2	1	9	0	1	11	81.82
3	0	0	3	0	3	100.00
4	0	0	0	4	4	100.00
Predicted	3	7	7	4	21	96.45 AVG.RECALL
Precision (%)	75.00	100.00	100.00	80.00	88.75 AVG.PRECISION	90.45 ACCURACY

Table 11: Performance evaluation results of the fusion model.

Grade	*F*-measure	Phi coefficient
1	0.86	0.84
2	0.90	0.83
3	1.00	1.00
4	0.89	0.87
	0.9115 AVG. *F*	0.8838 AVG. Phi

can be seen that the model has good prediction ability for the top coal caving of each grade. The ROC AUC of each model grade is greater than 0.9, the PR AUC is basically greater than or equal to 0.9, and the K-S value is 100%. The above analysis shows that under the probability threshold of 50%, the classification evaluation model of top coal caving established by fusion is perfect and robust and has fully met the prediction needs, whether from the global or local point of view.

7. Practical Application of Prediction Model in Engineering

Because the evaluation model of top coal caving classification is optimized by the fusion method, the model is perfect and robust no matter from the global or local view and has fully met the demand of prediction, so the model is applied to the evaluation of top coal caving of No. 3 coal seam in Gucheng Coal Mine. Gucheng Coal Mine belongs to Lu'an

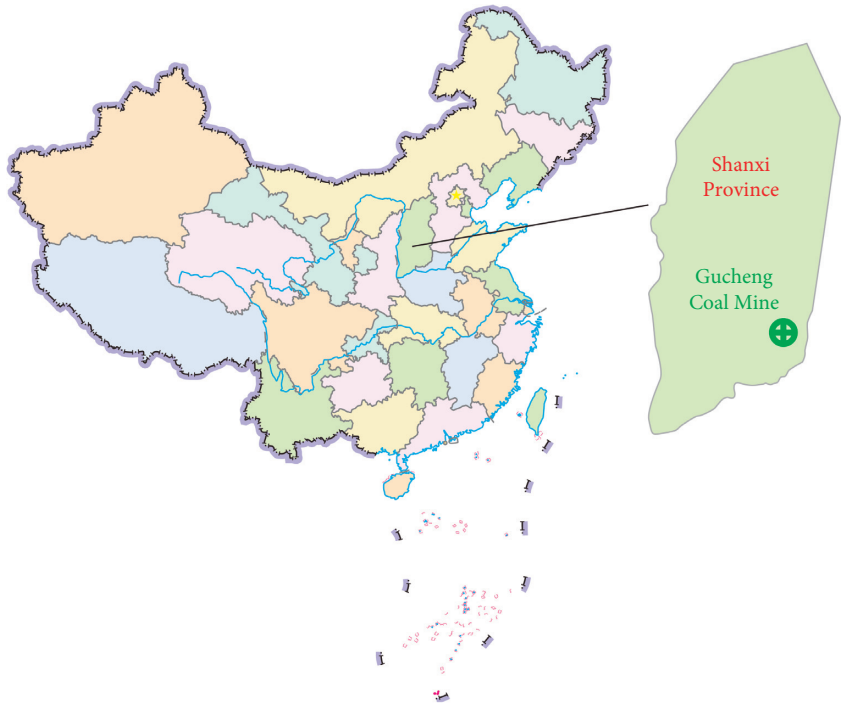

Figure 22: Geographical location of Gucheng Mine.

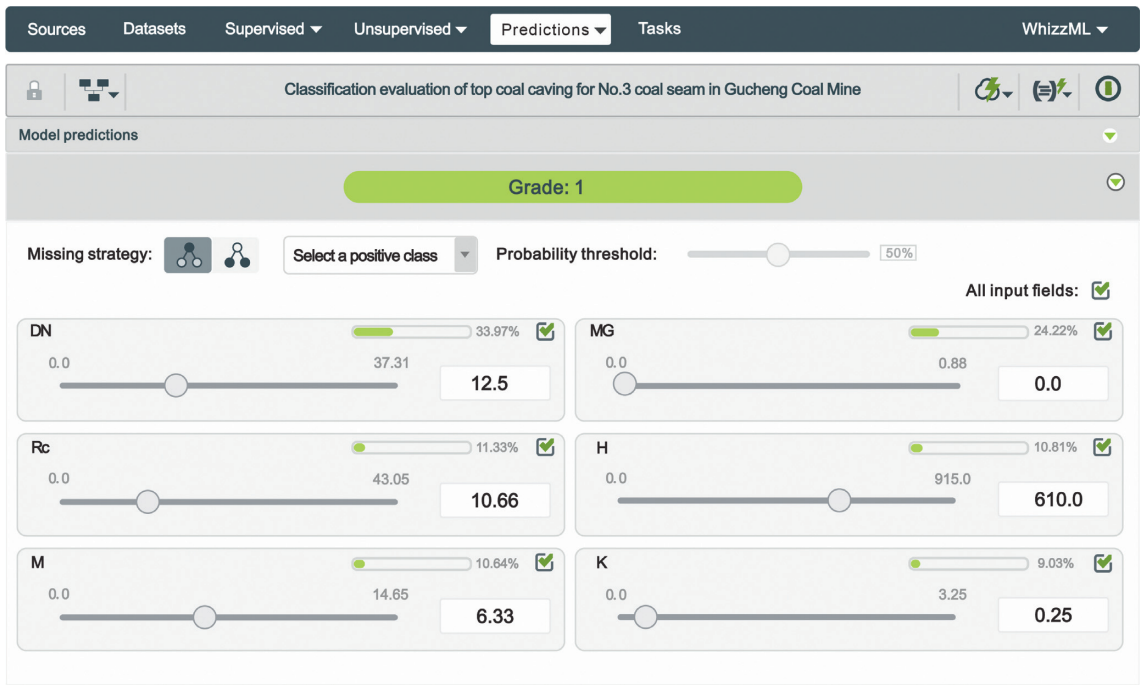

Figure 23: Top coal caving prediction results of No. 3 coal seam in Gucheng Coal Mine.

(Group) Co., Ltd., located west of Changzhi City, Shanxi Province, China. Its geographical location is shown in Figure 22. The average thickness of No.3 Coal Seam in Gucheng Coal Mine is 6.33 m, without gangue; The buried depth of coal seam is 583–637 m, with an average of 610 m; the average uniaxial compressive strength of coal is 10.66 MPa, which belongs to medium-hard coal. The top coal can be mined with caving, and the filling coefficient of the direct roof is 0.25; the development degree of coal seam joints is good ($DN = 12.5$). The prediction result shows that the top coal caving grade of No.3 Coal Seam in Gucheng Coal Mine is grade 1, as shown in Figure 23. From the

engineering side, the predicted results are consistent with the actual situation. In the mining of No. 3 coal seam in Gucheng Coal Mine, the top coal can cave well without extra measures.

8. Conclusion

Because of the current, most of the evaluation and prediction models of top coal caving established by experts and scholars are established by computer programming, which makes it difficult for people who do not understand the calculation language to use or modify the models and makes it difficult for these models to be widely applied in the actual application process. This article introduces a method to establish the evaluation and prediction model of top coal caving without programming. At the same time, the model can be used to predict and evaluate top coal caving and modify the model according to its own needs without programming. This method establishes the prediction model of top coal caving by using the machine learning platform BigML based on the cloud. At the same time, this paper establishes the prediction model of top coal caving evaluation by using BigML and applies it to evaluating top coal caving of No. 3 coal seam in Gucheng Coal Mine. The evaluation result is grade 1, which is consistent with the engineering practice. It fully proves that the application of BigML in evaluating top coal caving is successful and feasible and provides another more convenient method for the classification evaluation and prediction of top coal caving. In addition, it provides another way to realize the classification evaluation of top coal caving properties and the establishment of other evaluation predictions using machine learning without programming.

Data Availability

The data used to support the findings of this study are included within the article.

Conflicts of Interest

The authors declare that they have no conflicts of interest.

Acknowledgments

This work was supported by the discipline innovation team of Liaoning Technical University (LNTU20TD-01).

References

[1] By Fuel Type-Exajoules, Consumption Emissions and C. Dioxide, "BP statistical review of world energy 2020," 2020.

[2] M. D. Leonard, E. E. Michaelides, and D. N. Michaelides, "Substitution of coal power plants with renewable energy sources - shift of the power demand and energy storage," *Energy Conversion and Management*, vol. 164, pp. 27–35, 2018.

[3] B. Dudley, "BP statistical review of world energy 2016," 2016.

[4] J. Wang, B. Yu, H. Kang et al., "Key technologies and equipment for a fully mechanized top-coal caving operation with a large mining height at ultra-thick coal seams," *International Journal of Coal Science & Technology*, vol. 2, no. 2, pp. 97–161, 2015.

[5] N. Zhang, C. Liu, and M. Pei, "Effects of caving-mining ratio on the coal and waste rocks gangue flows and the amount of cyclically caved coal in fully mechanized mining of super-thick coal seams," *International Journal of Mining Science and Technology*, vol. 25, no. 1, pp. 145–150, 2015.

[6] M. Bhattacharya, S. Rafiq, and S. Bhattacharya, "The role of technology on the dynamics of coal consumption-economic growth: new evidence from China," *Applied Energy*, vol. 154, pp. 686–695, 2015.

[7] Z. Wang, G. Zhang, and L. Zhao, "Recognition of rock-coal interface in top coal caving through tail beam vibrations by using stacked sparse autoencoders," *Journal of Vibroengineering*, vol. 18, no. 7, pp. 4261–4275, 2016.

[8] J. Wu, Y. Qin, and M. Zhai, "Mining safety of longwall top-coal caving in China," in *Proceedings of the 8th U.S. Mine Ventilation Symposium*, Rolla, Missouri, June 1999.

[9] T. D. Le, R. Mitra, J. Oh, and B. Hebblewhite, "A review of cavability evaluation in longwall top coal caving," *International Journal of Mining Science and Technology*, vol. 27, no. 6, pp. 907–915, 2017.

[10] N. E. Yasitli and B. Unver, "3D numerical modeling of longwall mining with top-coal caving," *International Journal of Rock Mechanics and Mining Sciences*, vol. 42, no. 2, pp. 219–235, 2005.

[11] H. Alehossein and B. A. Poulsen, "Stress analysis of longwall top coal caving," *International Journal of Rock Mechanics and Mining Sciences*, vol. 47, no. 1, pp. 30–41, 2010.

[12] G. Si, S. Jamnikar, J. Lazar et al., "Monitoring and modelling of gas dynamics in multi-level longwall top coal caving of ultra-thick coal seams, part I: borehole measurements and a conceptual model for gas emission zones," *International Journal of Coal Geology*, vol. 144-145, pp. 98–110, 2015.

[13] G. Si, J.-Q. Shi, S. Durucan et al., "Monitoring and modelling of gas dynamics in multi-level longwall top coal caving of ultra-thick coal seams, Part II: numerical modelling," *International Journal of Coal Geology*, vol. 144-145, pp. 58–70, 2015.

[14] V. Klishin, S. Nikitenko, and G. Opruk, "Longwall top coal caving (LTCC) mining technologies with roof softening by hydraulic fracturing method," *IOP Conference Series: Materials Science and Engineering*, vol. 354, Article ID 012015, 2018.

[15] V. I. Klishin, V. N. Fryanov, L. D. Pavlova, and G. Y. Opruk, "Modeling top coal disintegration in thick seams in longwall top coal caving," *Journal of Mining Science*, vol. 55, no. 2, pp. 247–256, 2019.

[16] Z. Ti, J. Li, M. Wang, K. Wang, Z. Jin, and C. Tai, "Fracture mechanism in overlying strata during longwall mining," *Shock and Vibration*, vol. 2021, Article ID 4764732, 15 pages, 2021.

[17] Y. K. Shi, T. T. Sun, J. Hao, and S. Hao, "Prediction of top coal caving ability based on support vector machine," *Applied Mechanics and Materials*, vol. 217-219, pp. 2702–2705, 2012.

[18] A. Vakili and B. K. Hebblewhite, "A new cavability assessment criterion for longwall top coal caving," *International Journal of Rock Mechanics and Mining Sciences*, vol. 47, no. 8, pp. 1317–1329, 2010.

[19] P. Humphries, B. Poulsen, and T. Ren, "Longwall top coal caving application assessment in Australia," *ACARP Report for project C*, vol. 130187, 2007.

[20] B. Singh and R. Goel, *Engineering Rock Mass Classification*, Elsevier, Amsterdam, Netherlands, 2011.

[21] Y.-S. Xie and Y.-S. Zhao, "Numerical simulation of the top coal caving process using the discrete element method," *International Journal of Rock Mechanics and Mining Sciences*, vol. 46, no. 6, pp. 983–991, 2009.

[22] J. Wang, S. Yang, Y. Li, L. Wei, and H. Liu, "Caving mechanisms of loose top-coal in longwall top-coal caving mining method," *International Journal of Rock Mechanics and Mining Sciences*, vol. 71, pp. 160–170, 2014.

[23] Y. Xin, P. Gou, and F. Ge, "Analysis of stability of support and surrounding rock in mining top coal of inclined coal seam," *International Journal of Mining Science and Technology*, vol. 24, no. 1, pp. 63–68, 2014.

[24] K. Yu, W. Qiang, M. Elhoseny, and X. Yuan, "Application of ant colony clustering algorithm in coal mine gas accident analysis under the background of big data research," *Journal of Intelligent and Fuzzy Systems*, vol. 38, no. 2, pp. 1381–1390, 2020.

[25] Z. Ruilin and I. S. Lowndes, "The application of a coupled artificial neural network and fault tree analysis model to predict coal and gas outbursts," *International Journal of Coal Geology*, vol. 84, no. 2, pp. 141–152, 2010.

[26] H. Jiang, Q. Song, K. Gao, Q. Song, and X. Zhao, "Rule-based expert system to assess caving output ratio in top coal caving," *PloS One*, vol. 15, no. 9, Article ID e0238138, 2020.

[27] S. Mohammadi, M. Ataei, R. Kakaie, A. Mirzaghorbanali, Z. F. Rad, and N. Aziz, "A roof cavability classification system and its use for estimation of main caving interval in longwall mining," in *Proceedings of the 2020 Coal Operators' Conference*, pp. 104–115, Wollongong, Australia, February 2020.

[28] S. Yongkui, L. Pengrui, W. Ying, Z. Jingyu, and L. Meijie, "The prediction of the caving degree of coal seam roof based on the naive bayes classifier," *Electronic Journal of Geotechnical Engineering*, vol. 19, no. Z2, p. 201, 2014.

[29] K. Oraee and M. Rostami, "Qualitative and quantitative analysis of hangingwall caving in longwall mining method using a fuzzy system," in *Proceedings of the 21st world mining congress & expo*, Poland, Krakóów-Katowice-Sosnowiec, September 2008.

[30] J. H. Yu and D. B. Mao, "Prediction of top-coal caving and drawing characteristics using artificial neural networks in extremely thick coal seam," *Applied Mechanics and Materials*, vol. 743, pp. 612–616, 2015.

[31] G. A. Rao, R. Nagaswetha, and D. N. Singh, "Voice based virtual agri farming analyzer with BigML algorithms," in *Proceedings of the 2019 8th International Conference System Modeling and Advancement in Research Trends (SMART)*, Moradabad, India, November 2019.

[32] Y. Abdul Ghffar, M. Osman, S. Shrestha et al., "Usefulness of semisupervised machine-learning-based phenogrouping to improve risk assessment for patients undergoing transcatheter aortic valve implantation," *The American Journal of Cardiology*, vol. 136, pp. 122–130, 2020.

[33] X. Tian and L. Liu, "Does big data mean big knowledge? integration of big data analysis and conceptual model for social commerce research," *Electronic Commerce Research*, vol. 17, no. 1, pp. 169–183, 2017.

[34] M. Khanal, D. Adhikary, and R. Balusu, "Prefeasibility study-geotechnical studies for introducing longwall top coal caving in Indian mines," *Journal of Mining Science*, vol. 50, no. 4, pp. 719–732, 2014.

[35] P. Humphries and B. Poulsen, "Geological and geotechnical influences on the caveability and drawability of top coal in longwalls," *Sociological Research Online*, pp. 56–66, 2008.

[36] F. T. Liu, K. M. Ting, and Z.-H. Zhou, "Isolation forest," *2008 Eighth IEEE International Conference on Data Mining*, in *Proceedings of the 2008 Eighth IEEE International Conference on Data Mining*, Washington, DC, USA, December 2008.

[37] T. B. Team, *Anomaly Detection with the BigML Dashboard*, BigML, Inc, Corvallis, OR, USA, 2021.

[38] H. Mohammad and M. N. Sulaiman, "A review on evaluation metrics for data classification evaluations," *International Journal of Data Mining & Knowledge Management Process*, vol. 5, no. 2, pp. 1–11, 2015.

[39] K. Stąpor, "Evaluating and comparing classifiers: review, some recommendations and limitations," in *Proceedings of the 10th International Conference on Computer Recognition Systems CORES 2017*, pp. 12–21, Polanica Zdroj, Poland, May 2017.

[40] Y. Sasaki, "The truth of the F-measure," *Teach Tutor Mater*, pp. 1–5, 2007.

[41] S. Boughorbel, F. Jarray, and M. El-Anbari, "Optimal classifier for imbalanced data using matthews correlation coefficient metric," *PloS One*, vol. 12, no. 6, Article ID e0177678, 2017.

[42] J. Lever, M. Krzywinski, and N. Altman, "Classification evaluation," *Nature Methods*, vol. 13, no. 8, pp. 603-604, 2016.

[43] T. Fawcett, "An introduction to ROC analysis," *Pattern Recognition Letters*, vol. 27, no. 8, pp. 861–874, 2006.

[44] C. X. Ling, J. Huang, and H. Zhang, "AUC: a better measure than accuracy in comparing learning algorithms," *Advances in Artificial Intelligence*, in *Proceedings of the Conference of the canadian society for computational studies of intelligence*, pp. 329–341, Calgary, AB, Canada, May 2003.

[45] J. Davis and M. Goadrich, "The relationship between precision-recall and ROC curves," in *Proceedings of the 23rd international conference on Machine learning*, Pittsburgh, Pennsylvania, June 2006.

[46] T. Brandenburger and A. Furth, "Cumulative gains model quality metric," *Journal of Applied Mathematics and Decision Sciences*, vol. 2009, Article ID 868215, 14 pages, 2009.

[47] T. M. Khoshgoftaar, M. Golawala, and J. V. Hulse, "An empirical study of learning from imbalanced data using random forest," in *Proceedings of the 19th IEEE International Conference on Tools with Artificial Intelligence(ICTAI 2007)*, vol. 2, Patras, Greece, October 2007.

[48] M. Kuhn and K. Johnson, "Measuring performance in classification models," *Applied Predictive Modeling*, Springer, New York, NY, pp. 247–273, 2013.

[49] M.-H. Horng, "Performance evaluation of multiple classification of the ultrasonic supraspinatus images by using ML, RBFNN and SVM classifiers," *Expert Systems with Applications*, vol. 37, no. 6, pp. 4146–4155, 2010.

[50] T. Srivastava, *11 Important Model Evaluation Metrics for Machine Learning Everyone Should Know*, https://www.analyticsvidhya.com/blog/2019/08/11-important-model-evaluation-error-metrics/, 2019.

[51] N. Seliya, T. M. Khoshgoftaar, and J. Van Hulse, "A study on the relationships of classifier performance metrics," in *Proceedings of the 2009 21st IEEE International Conference on Tools with Artificial Intelligence*, Washington, DC, USA, November 2009.

[52] R. C. Prati, G. E. A. P. A. Batista, and M. C. Monard, "A survey on graphical methods for classification predictive performance evaluation," *IEEE Transactions on Knowledge and Data Engineering*, vol. 23, no. 11, pp. 1601–1618, 2011.

[53] Q. Zou, S. Xie, Z. Lin, M. Wu, and Y. Ju, "Finding the best classification threshold in imbalanced classification," *Big Data Research*, vol. 5, pp. 2–8, 2016.

Hindawi
Shock and Vibration
Volume 2021, Article ID 3730606, 24 pages
https://doi.org/10.1155/2021/3730606

Review Article

Recapitulation and Prospect of Research on Flow Field in Coal Mine Gob

Rui Zhang[1], **Jianwei Cheng**[1], **Zui Wang**[1] and **Zhenlu Shao**[1,2]

[1]*School of Safety Engineering, China University of Mining and Technology, Jiangsu, Xuzhou, China*
[2]*Xinjiang Coalfield Fire-Extinguishing Engineering Bureau, Urumqi, Xinjiang, China*

Correspondence should be addressed to Jianwei Cheng; cheng.jianwei@cumt.edu.cn

Received 10 June 2021; Accepted 27 July 2021; Published 17 August 2021

Academic Editor: Pengfei Wang

Coal mine gob, mined-out areas in underground coal mines, often accumulates explosive methane-air mixtures that pose a deadly hazard to miners. A good understanding of the flow field in a sealed coal mine area is crucial in preventing and minimizing accidents associated with mine combustible gases and also for planning and implementing a mine rescue strategy. In recent years, the research on the flow field in the gob has changed from qualitative research in the past to quantitative research. This paper synthesizes the research results of flow field in gob in recent 40 years, covering the permeability of quarried areas, the airflow simulation in quarried areas, and the influence of ventilation parameters and geohydrological conditions on the flow field. Firstly, the overburden failure mechanism and fracture development characteristics of the mine gob, the distribution of porosity and permeability in the gob, and the relationship between them are introduced. Secondly, the development of research methods and numerical models used to study the flow field in mine gob is discussed. The distribution of the flow field in the gob under different conditions is expounded. Thirdly, the research on the prevention and control of fire and explosion risks in the gob is discussed. Finally, the problems to be solved in such research direction are addressed and suggestions are put forward.

1. Introduction

For a long time, the problem of gob disaster has been the focus of most researchers. The gob is the abandoned space after coal mining, and its internal medium is the falling gangue and residual coal, which is rich in pores and cracks. Gas and air are distributed in various areas of gob in the form of mixed gas with different concentrations. Due to the wind pressure of air leakage flow in working face, the impact of roof failure, the power of gas emission, the fire pressure of spontaneous combustion of residual coal and other external forces, the mixed gas flows in the gob, and the concentration of components also change, so the flow field distribution is very complex [1]. In addition, the gob is prone to spontaneous combustion of residual coal, which provides a long-term fire source for gas explosion and causes secondary gas explosion, resulting in serious consequences of accident disasters. In-depth study of the flow field distribution in the gob is not only conducive to mastering the flow of mixed gas but also reveals the mutual transformation law of gas combustion and explosion in the gob, which is of great significance for the prevention and control of coal spontaneous combustion and gas explosion disasters.

The viewpoint of flow field in gob was first proposed in 1978 [2], which was formed with the development of computational fluid dynamics and computer technology. Based on rock mechanics, porous media seepage dynamics, and numerical simulation, the research object is the space outside the underground roadway or the coal and rock area, which is aimed at directly revealing the nature and mechanism of disasters. Practice has proved that it is an effective analysis method to explore the gob gas distribution law and prevent disaster accidents of the gob.

This paper will start from three aspects: the permeability of the gob, the theory of quarry flow field simulation, and the influence of environmental factors on the flow field distribution. It will explain the methods of setting the porosity and permeability of the gob in numerical simulation, compare different analysis methods of the quarry flow field problem,

combine the quarry simulation experiments with relevant materials and the simulation results, and sort out the influence of different environmental factors on the gas flow situation in the gob. The research on the prevention and control of fire and explosion risks in the mined area is also analyzed, and finally, suggestions are made for future research directions of the mined area flow field.

2. Permeability of the Gob

2.1. Theory of Stope Fracture Formation. From the process of mineral pressure during mining when the rocks on the roof are risen and fallen, to the compaction of the back of the gob, the medium inside the gob is a porous medium with the nonuniform medium. The pore size distribution is related to the working face height, the size and arrangement of the rock, the lithology of the coal bed and adjacent layers, the original stress and the mining stress, etc. There are two different characteristics of voids in the gob, i.e., mined voids and original voids, which differ significantly in their characteristics, and generally speaking, the size and permeability of mined voids are much larger than those of original voids [3]. In general, the size and permeability of the active pore space are much larger than those of the primary pore space. The active pore space is interconnected throughout the entire area of the extraction space and is not only spatially unevenly distributed but is also influenced by the extraction pressure during the extraction process.

2.1.1. The Mine Pressure Hypothesis. The formation of mining overburden fractures is associated with various mine pressures and deformation damage to the surrounding rock within the quarry. From the beginning, mine pressure phenomena have been observed and different explanations have been proposed based on the complex nature of the rock mass. These explanations, which reveal the intrinsic connection between mine pressure phenomena, are called mine pressure hypotheses. The pressure arch hypothesis was proposed by the Germans Haacke and Gulitzel in 1928. In the same vein as the pressure arch hypothesis, the cantilever beam hypothesis was proposed by the German Sledke and later supported by the British Ferriday and the former Soviet Germain, among others [4]. By the 1950s, the articulated block hypothesis and the prefracture hypothesis emerged. The preformed fissure hypothesis was first proposed by a Belgian geologist. In the late 1970s and early 1980s, scholars represented by academician Qian based on the articulated block hypothesis and the rock performed fissure hypothesis, and through on-site observation of the internal movement of rock formations and extensive production practice, the masonry beam theory of rock structure was proposed and developed into a hypothesis. In recent years, as the scientific study of rock formations continued to deepen and to understand the broader issues in rock formation activities, Academician Qian et al. [5] further proposed the key layer theory of rock control based on the masonry beam.

2.1.2. The "O" Circle Theory and the Critical Layer Theory [6–10]. Multiple layers of rock of varying thickness and strength exist above the direct top. It has been proven that one to several of these thick hard rock layers play a major controlling role in the overlying rock activity of the quarry. The rock layers that control the activity of the overlying rock layers in the quarry, either locally or up to the surface, are referred to as key layers. The former is referred to as the subcritical layer and the latter as the main critical layer. The key layer is generally a relatively thick and hard rock layer with the following characteristics: geometric features, with thicker single layers relative to other similar rock formations.

Lithological characteristics, relatively hard compared to other rock formations, i.e., higher modulus of elasticity and higher strength; deformation characteristics, where the subsidence deformation of the key layer is synchronized with the amount of subsidence of all or part of the overlying rock layers; fracture features, where the fracture of a key layer will result in the simultaneous fracture of all or 1ocal overlying rock layers, causing movement of the rock over a 1arger area; the bearing characteristics, in the form of a slab structure before the key layer breaks as the bearing body for all or part of the rock, become a masonry beam structure after the break if the S-R stability conditions for rock block structures are met, succeeding as the bearing body.

The practice has shown that seam activity leads to the creation of a large number of mining fissures, and for coal seams with low permeability, the formation of mining fissures can lead to an increase in permeability of tens to hundreds of times, which creates conditions for the extraction and transport of gas from the coal seam. Two types of fissures are formed in the overlying rock after coal mining: one is the off-bed fissures, which are along-bed fissures that appear between the bed and the seam as the seam sinks, and which cause the coal seam to expand and deform and unload the gas and cause the unloaded gas to gush out along the off-bed fissures; the other is the vertical fracture fissures, which are through-bed fissures that form as the seam sinks and breaks, and these fissures enable the gas to rise and float continuously, forming a rising float.

Along the direction of workface advancement, the dynamic distribution of deviations under the key layer shows a two-stage development pattern. Before the initial breakage of the key layer, the amount of deviations increases continuously as the workface advances, and the maximum amount of deviations is located in the middle of the extraction zone. After the initial breakage of the key layer, the key layer tends to be compacted in the middle of the extraction zone, while a delamination zone is still maintained on each side of the extraction zone. The interlayer zones in the upper and lower chutes are connected through the cuttings and the interlayer zone on the working face side, forming an interconnected ring of interlocking interlayer fracture development around the mining void. Generally speaking, the geometry of the open-cut eye, the upper and lower chute, and the working face side are rectangular; that is, the mining void area forms the shape of the moving rock layer as shown in Figure 1, which is called the "O" shaped circle of the mining fissure, the porosity of this area is large,

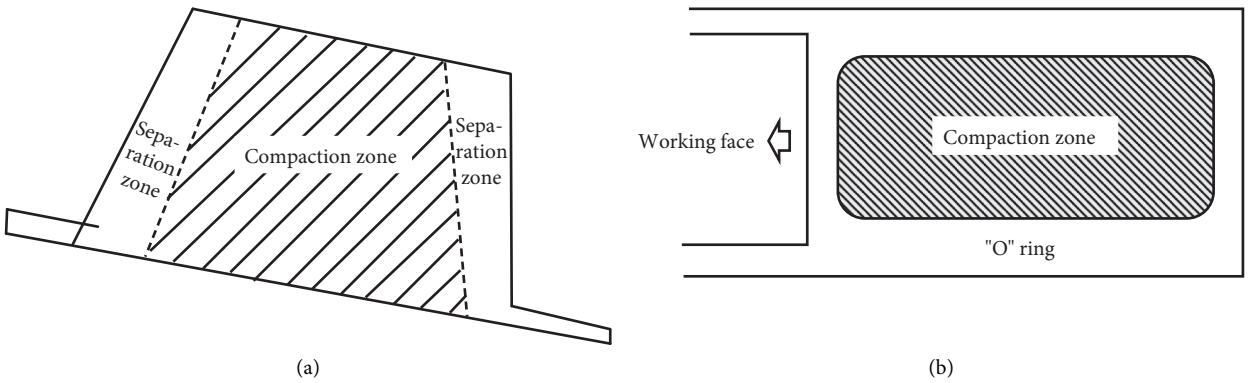

Figure 1: Diagram of the "O" ring. (a) Tendency profile. (b) Plan view.

easy for the wind flow, and is the main wind leakage channel at the early stage of the mining of the back mining face. With the back mining workface gradually far away from the position of the cutting eye, cutting eye position of the loose triangle by the back mining workface at both ends of the role of wind pressure gradually reduced, when the workface advance to a certain distance, if there are no other sources of wind leakage in the gob and the role of wind leakage sink, the location is no longer the main wind leakage channel in the gob.

2.1.3. The Zoning of Overburden Movement Failure in Gob. When the coal is fully extracted, the overlying rock layer loses its supporting role and gradually breaks up, collapses, delaminates, fractures, and deforms, showing a process of sinking of the overlying rock layer from static to dynamic to static.

The theory of "three horizontal zones and three vertical belts" was proposed by our academician Qian [11]. The overburden fractures formed by mine pressure and complex stresses are divided in different directions, forming "three zones" in the vertical direction, i.e., the caving band, the fracture band, and the bending subsidence belt, which are similar to the "three zones" in the longwall working face as suggested by Karmis et al. [12]. The basic structure and zoning of the overburden in the gob is shown in Figure 2.

(i) Caving Band. The overburdened rock in the extraction area has been affected by complex mining, and the rock body at the direct top is completely fractured, resulting in a random rock block shape size and arrangement. The medium in the free-fall zone is loose, isotropic, and porous, and it is the main medium in the flow field of the extraction zone. It is generally considered that the coefficient of fragmentation and expansion in this area is around 1.5. As the workings continue to advance, the first blocks to fall are compacted by the subsequent collapse and the coefficient of fragmentation is reduced by approximately 31%.

(ii) Fracture Band. When the underground workings are mined under certain conditions in time and space, the overlying rock layer emerges in a regular arrangement after fracturing, which is the main characteristic of the fissure zone. The fissures are mainly divided into two types

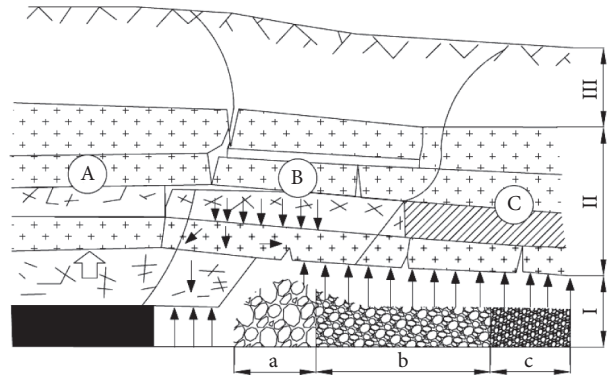

Figure 2: Zoning of the overlying rock layers of the quarry and delineation of the mining void. (A) Zone of influence of coal wall support. (B) Zone of rock departure. (C) Zone of recompaction. (a) Zone of natural accumulation. (b) Zone of load influence. (c) Zone of compaction and stability. (I) Caving band. (II) Fracture band. (III) Bending subsidence belt.

according to the different forces: one is subject to bending and tensile stress, which is approximated as a fissure in the direction of the vertical rock layer; the other is a fissure in which the rock layer and the rock layer are subject to staggered displacement by mineral pressure, which is approximated as a fissure parallel to the rock layer. As mining continues, the gob gradually increases and the fissure zone is extended in the upper part of the overburden. After a certain depth has been reached in the mining space, the extension stops at the maximum height.

(iii) Bending Subsidence Belt. The extent of the area is defined by the top of the rift zone as the lower boundary and the ground surface as its upper boundary. The pressure on the rock within the curved subsidence zone is less than that described by the riser zone, and the rock movement appears not as fragmentation or randomness, but as displacement of the entire area. Perpendicular to the surface, there is a small amount of subsidence displacement. However, in harder rock formations, dislocation fractures are very likely to occur due to misalignment movements between rock layers.

Gao [13] established a "four-zone" model of rock movement and divides the overlying rock into four zones

according to the mechanical structure characteristics after its destruction, namely, fracture zone, separation zone, bending zone, and loose alluvial zone. Singh and Kendorski [14] found that the area of the collapse zone and the fracture zone depends on the thickness of the coal seam, the strength of the roof, and the characteristics of the rock combination.

2.2. Study of Porosity Distribution Characteristics in the Gob. In the process of coal mining, due to the influence of mining, the overlying rock layer is damaged, which will not only produce new fissures but also lead to the enlargement of the primary fissures, which will in turn change the porosity of the rock body, and the result leads to changes in the permeability of the rock body. Mastering the characteristics of the porosity distribution in the gob is the key to studying the flow field in the gob. It is impossible to accurately simulate the flow field in the gob by simple porosity analysis alone; therefore, it is important to improve the accuracy of the measurement of the pore distribution in the gob for the study of the flow field in the gob.

2.2.1. Fractional Expansion Coefficients and Distribution Functions in the Gob. As time passes, the overlying rock layer gradually sinks under its own weight, the force on the free-fall zone gradually increases, the rock layer is gradually compacted, the porosity of the free-fall zone gradually decreases, and the initial fragmentation and expansion coefficient is larger compared with that after the fall, resulting in a lower height of the flow field in the gob. The height of the zone can be calculated by the following formula [15]:

$$M = \frac{H - S}{K - 1}, \tag{1}$$

where M is the height of the fall zone (m); S is the actual settlement value of the lower rock beam (old top) in the fissure zone (m); H is the mining height (m); and K is the coefficient of fragmentation and swelling of the fallen rock body.

As can be seen from the above equation, if the fragmentation effect of the rock fall is not taken into account, i.e., $K1$, the value of M will tend to infinity, indicating that the overburden of the quarry will fall all the way to the surface, resulting in a wide range of estimates of the fall zone. Therefore, the fragmentation and swelling effect of the rock fall has an important influence on the development pattern of deformation and damage of the overlying rock in the quarry, and the fragmentation and swelling characteristics of the rock fall should be fully considered in numerical calculations to make the numerical results more realistic [16].

The volume of the rock after crushing should be increased compared with the whole state, and this property is called the crushing and swelling of the rock. The crushing and swelling coefficient is the ratio between the volume of the rock in the loose state after crushing and the volume of the rock in the whole state before crushing [17]. Practice and research have shown that after the collapse of the roof, broken rocks form a haphazard pile of loose bodies in the gob, and depending on the mechanical properties of the rocks, the size and arrangement of the broken rocks vary, and so does their coefficient of fragmentation and expansion, which is generally 1.10–1.40. Fragmentation coefficient and residual expansion coefficient of common coal measures rock are shown in Table 1. In general, hard rocks are broken in large pieces and arranged neatly, and their coefficient of fragmentation and expansion is small, generally 1.10–1.20. The coefficient of fragmentation and swelling of the soft rock layer is large, generally 1.30–1.40, and the coefficient of fragmentation and swelling of the medium-hard rock layer is between the hard and soft rock layers, generally 1.20–1.30 [18].

Palchik [19] used vertical boreholes to probe the height of the fallout zone of the medium-weathered, strongly weathered, and deeply buried hard overburden rocks in the shallow buried gob, and the theoretical calculation and observation results showed that the fragmentation and swelling coefficients of the strongly weathered rocks ranged from 1.06 to 1.165, and the fallout ratios ranged from 6.07 to 15.6, while the fragmentation and swelling coefficients of the medium-weathered rocks ranged from 1.09 to 1.24, and the fallout ratios ranged from 4.1 to 11.25. The coefficient of fragmentation and swelling of hard overburden rocks can be 1.38 times of that of strongly weathered rocks, while the riser ratio is only 0.26 times of that of strongly weathered rocks, which leads to the conclusion that the higher the strength of rocks, the higher the coefficient of fragmentation and swelling, and the smaller the height of riser zone.

In order to study the compaction characteristics of fractured rocks in the coal bed roof, Su et al. [20] sieved sandstone, sandy mudstone, and mudstone in the roof of the Xin'an coal bed in Yima into 5 block sizes (0~5, 5~10, 10~15, 15~20, and 20~25 mm) and then took 20% of each of the above 5 block sizes and mixed them as mixed block sizes (0~25 mm), and in order the compaction tests were carried out on a hybrid electrohydraulic servo rock mechanic test system using a home-made device. The stress-strain relationships for the three types of crushed rock compaction tests were obtained, and the effects of rock strength, block size, and compaction stress on the compaction characteristics of the crushed rock were analyzed.

It can be seen from Figure 3 that the breaking expansion coefficient of each rock increases as the block diameter increases. The relationship between the crushing coefficient and the block diameter of the sandy mudstone crushed rock in Figure 5 can be described by a logarithmic relationship, which is different from the linear function between the crushing coefficient and the block diameter of the coal rock in the study of Miao et al. [21], and may be related to the range of the block diameter of the crushed rock; analyzing Figure 4, the residual crushing coefficient of the crushed rock after experiencing compaction is not much related to the rock strength and the block diameter. The reduction of the crushing and swelling coefficient is related to the block diameter, and the larger the block diameter, the greater the reduction.

Using similar material simulation tests, Zhang [22] developed two different models to study the dynamic 1aw of

Table 1: Coefficient of fragmentation and residual fragmentation of common coal rocks.

Lithology	Crushing and swelling factor K_P	Residual swelling factor K_P'
Crushed coal	<1.2	1.05
Muddy shale	1.4	1.1
Sandy mudstone	1.6~1.8	1.1~1.15
Sandstone	1.5~1.8	1.03~1.1
Medium-hard sandstone	1.3~1.5	1.03~1.08

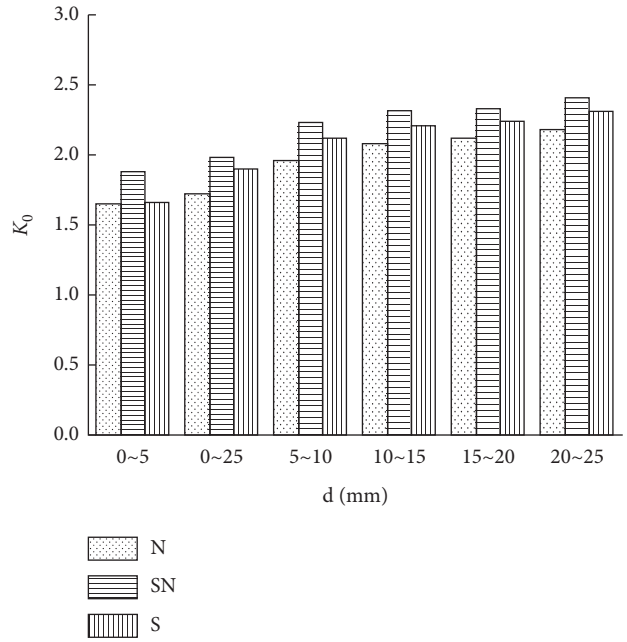

Figure 3: Coefficient of fragmentation and swelling of rock as a function of block diameter.

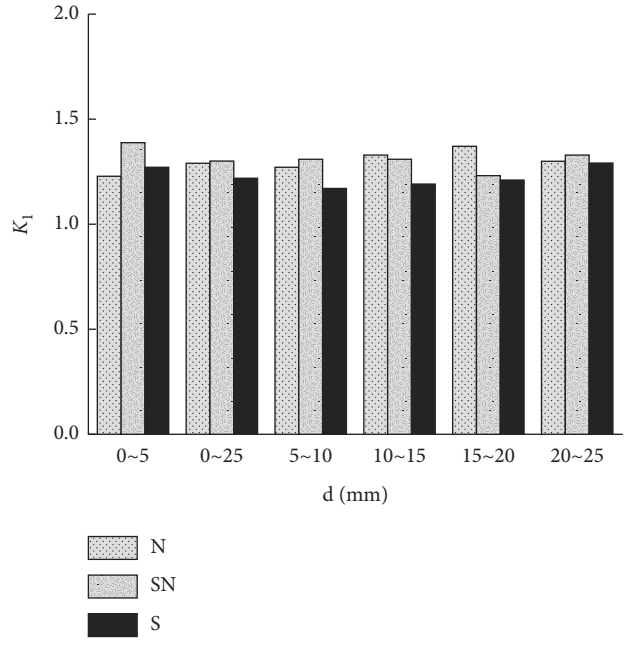

Figure 4: Residual coefficient of fragmentation and swelling of crushed rock as a function of block diameter.

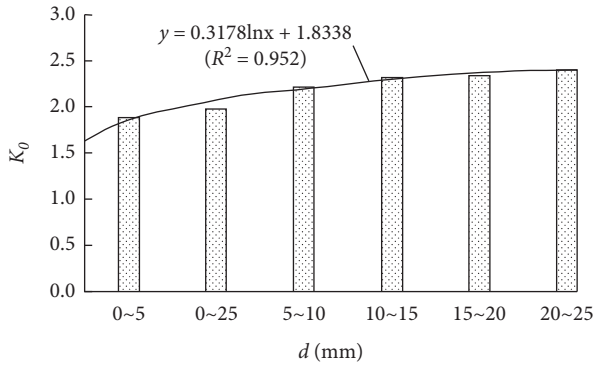

Figure 5: Crushing and swelling coefficient of sandy mudstone rubble as a function of block size.

fracture and swelling of the mined rock mass during longwall mining and partial mining of small strips, respectively. The vertical fracture expansion of the modeled rock mass was approximated to replace the volumetric fracture expansion to analyze the dynamic fracture expansion and compressibility of the mined rock mass. The vertical fragmentation coefficient is defined as the ratio of the distance between two adjacent model points in the vertical direction before and after deformation, i.e.,

$$K = \frac{h'_{n-n+1}}{h_{n-n+1}}, \tag{2}$$

where h'_{n-n+1} and h_{n-n+1} are the vertical distances between two adjacent measurement points n and n+1 before and after mining, respectively, m.

The rock fragmentation coefficient of different areas under full and partial mining conditions was obtained in relation to the distance from the coal seam and the observation time; that is, the rock fragmentation coefficient of the observation line located near the boundary of the gob was the largest during full mining of the longwall; the rock fragmentation coefficient of each observation line varied greatly during the mining process and then leveled off soon after the end of mining; the rock fragmentation coefficient of partial mining of the strip was much smaller than that of full mining of the longwall. The coefficient of rock fragmentation and swelling of partial mining is much smaller than that of longwall mining, the coefficient of rock fragmentation and swelling of partial mining varies with the height of waves, and the compressible amount of coal seam area is larger during loading. These understandings

are important to explain the residual settlement of the surface in the gob.

The porosity of a fractured rock mass is a function of its coefficient of fracture and expansion, and the study of the coefficient of fracture and expansion is the basis for calculating porosity. The porosity of a fractured rock mass can be expressed by the ratio of the pore volume to the total volume of the rock mass in the fractured state, and according to the definition of the porosity of a fractured rock mass and the coefficient of fracture and swelling, the following relationship exists between the two:

$$n = 1 - \frac{1}{K_\rho}, \tag{3}$$

where n is the porosity of the crushed rock and K_ρ is the crushing and swelling coefficient of the crushed rock.

Considering the original porosity of the coal seam roof rock S_0, then the total porosity of the rock in the free stacking state is

$$n_{m0} = 1 - \frac{1}{K_\rho} + S_0, \tag{4}$$

where n_{m0} is the total porosity of the emergent rock in the free-stacked state and S_0 is the original porosity of the top slab.

When the workings are finished, as time passes, the rock in the fall zone tends to compact under its own weight and the overlying load, the coefficient of fragmentation becomes smaller, and the final remaining coefficient of fragmentation is called the residual coefficient of fragmentation.

The coefficient of fragmentation and swelling is spatially distributed and follows a certain pattern from the start of the fall to the final compaction of the mined area. Li [23], based on the negative exponential decay law, ignored the influence of the shape of the extraction zone, specifically with respect to the distance of a boundary L, and considered that along the direction perpendicular to L, there is

$$K_{p,l} = K'_\rho + \left(K_P^{(0)} - K'_\rho\right)e^{-a_l d}, \tag{5}$$

where $K_P^{(0)}$ is the initial crushing and swelling factor and K'_ρ is the central compaction fragmentation and swelling coefficient; a_l is the decay rate; according to the law of mineral pressure, point d is the distance from L.

The geometry of the extraction zone does not affect the distribution of the crushing and swelling coefficient, and the distribution pattern of the rock fall in the extraction zone is complex, so the extraction zone is a nonuniform medium. For the whole three-dimensional space, the rock fall fragmentation coefficient is a function of the location of the extraction zone, i.e., the distribution of the fall fragmentation coefficient is

$$K_p(x, y) = \max\left\{K_{p,l}\right\}. \tag{6}$$

In Li's study [24], based on equations (5) and (6), the distance of the points within the gob from the working face and the boundary is reflected in the spatial distribution function of the fragmentation and swelling coefficient of the gob as

$$K_p(x, y) = K_{p,\min} + \left(K_{p,\max} - K_{p,\min}\right)e^{-a_1 d_1\left(1-e^{-\delta a_0 d_0}\right)} (\delta < 1), \tag{7}$$

where δ is the adjustment function that controls the distribution shape of the model. $K_{p,\max}$ is the initial crushing and swelling coefficient, i.e., the maximum value. $K_{p,\min}$ is the compaction coefficient of fragmentation and swelling, i.e., the minimum value. $a_0.a_1$ is the decay rate, and $d_0.d_1$ is the distance between any point and the boundary and the working surface, m.

2.2.2. Porosity Distribution Model. The voids within the fractured rock scatter of a fall zone are usually irregular and disordered [25, 26]. These voids cannot be described and studied using conventional Euclidean geometry. Numerous studies have shown that the shapes of the various sizes of rock masses produced by rock fragmentation have a fractal structure: i.e., individuals of different sizes have statistically significant self-similar characteristics. Further studies have shown that the voids between these broken rock masses and the piles of broken rock masses are also fractal in structure [27].

Xia and Huang [28] used the Menger sponge fractal model to study the void distribution characteristics of the rock scatter in the fall zone. The void distribution model of the adventitious scatter within the adventitious zone based on the Menger sponge fractal model is shown in Figure 6, with the similarity ratio of

$$\begin{aligned} t &= \frac{y}{x} \\ &= \frac{1}{k}, \end{aligned} \tag{8}$$

where y is the volume of the first level transformed small cubic.

y can be considered as the generating element of a Koch curve of dimension:

$$D = \frac{\ln N}{\ln(1/t)}. \tag{9}$$

Bringing equation (9) into equation (8), we can obtain the void volume fraction dimension of the rock scatter in the bubble fall zone D_k:

$$D_k = \frac{\ln\left(k^3 - n\right)}{\ln k}. \tag{10}$$

Based on this model, the total fractal void ratio P of the rock bulk in the fall zone was obtained as

$$\begin{aligned} P &= \frac{V - M/\rho}{V} \\ &= 1 - \frac{\rho r_{\max}^{3-D}}{\rho_0\left(r_{\max}^{3-D} - r_{\min}^{3-D}\right)}, \end{aligned} \tag{11}$$

where ρ_0 is the density of the rock fall, kg/m^3; V is the total fractal volume of rock bulk within the fall zone, m^3; M is the mass of the fallen rock bulk, kg; ρ is the density of the

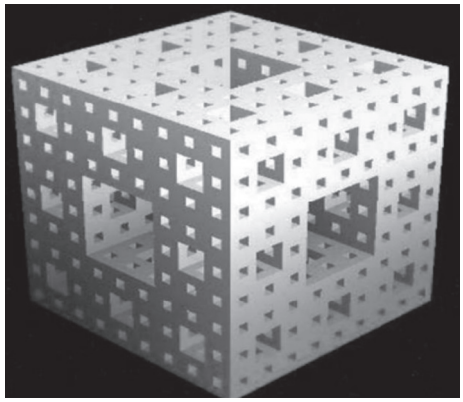

Figure 6: Menger sponge model.

crushed rock bulk, kg/m^3; and R is the diameter of individual rock mass, m.

Wang et al. [29] divided the extraction zone into free accumulation zone and pressure accumulation zone along the working face advance direction, as shown in Figure 7.

Derived from the theory of surrounding rock movement in the stope,

$$\begin{aligned} h(x) &= m' - S_m\left[1 - e^{-a\left(L_f/L\right)^b}\right] + \left(1 - K_f\right)\sum h', \\ s_m &= m' + \left(1 - K_R\right)\sum h', \\ &\frac{3(b-1) + \sqrt{(5b-1)(b-1)}}{2ab} \\ &= 1, \end{aligned} \tag{12}$$

where x is the strike distance of a point in the gob from the working face, m; $h(x)$ is the gap between the rock fall and the roof at x, m. L_f is the length of the free accumulation zone, m; $\sum h'$ is the equivalent direct roof thickness, m; m' is the equivalent mining height, m. s_m is the displacement of the rock seam after it has moved and stabilized, m; L is the distance of the basic stabilization point of the rock seam from the working face, usually about 50~60m; a and b are coefficients that vary with the distance of the rock seam from the coal seam and the lithological characteristics. K_f is the coefficient of fragmentation of rock in the free stacking zone, and K_R is the coefficient of residual fragmentation of rock after compaction.

The above equation forms a closed system of equations with a, b, and s_m as unknowns. For a given seam, the equivalent direct roof thickness h' and the equivalent mining height m' can be considered known, so the length of the free stacking zone L_f, the coefficient of fragmentation of the rock in the free stacking state x, and the coefficient of residual fragmentation of the rock in the compacted state K_R can be measured to find a, b, and s_m, which in turn allows the sinking displacement of the roof at any x to be determined $s(x)$ at any x.

The coefficient of rock fragmentation and swelling in the pressure-bearing accumulation zone can be derived from the following equation based on the top slab subsidence displacement:

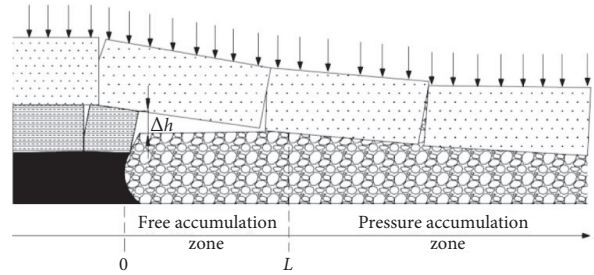

Figure 7: Schematic diagram of the state of rock accumulation in the extraction area.

$$K_p(x) = \frac{m' - s(x) + \sum h'}{\sum h'}, \tag{13}$$

where $Kp(x)$ is the coefficient of fragmentation of the rock fall at x in the pressure zone.

When $x = L_f$, we have

$$K_p\left(L_f\right) = K_f. \tag{14}$$

When $x \longrightarrow +\infty$, there is

$$K_p(+\infty) = K_R. \tag{15}$$

This means that the coefficient of fragmentation is continuous from the free zone to the compressive zone. Knowing the coefficient of fragmentation, the void ratio of the fallen rock can be calculated using the following formula:

$$n = 1 - \frac{1}{K}, \tag{16}$$

where n is the void ratio of the rock fall and K is the coefficient of fragmentation and swelling of the rock fall.

The derived continuous model of the porosity distribution in the extraction zone is not only continuously derivable within each partition but also continuous at the partition boundary. This property helps to ensure the stability of the solution for seepage in the extraction zone.

Other literature sets the porosity of the gob as a constant, or by analyzing the lithology of the roof slab of the comprehensive gob and the crushing and swelling characteristics of the fallen gangue, the overburden of the gob is divided into three zones, namely, the natural accumulation zone, the mining influence zone, and the compaction stability zone, and the porosity is set as a constant in each zone, and then the physical model and boundary conditions are solved according to the set permeability.

Gao and Wang [30] used FLUENT, based on the porous media seepage theory, to set the permeability of the gob to be uniformly distributed. The results showed that the flow field of the air leakage in the gob can only be simulated by using FLUENT. There results show that the wind flow pattern in the gob is more realistic only if the permeability distribution that more faithfully reflects the rock emergence and compaction pattern in the gob is used. However, these studies are basically flat studies of the porosity of the extraction zone, in

the vertical direction are assumed to have no change in the porosity of the extraction zone, and do not comprehensively consider the influence of pressure, time, and media particles on it; to address the problem, Zhang et al. [31] conducted a spatial three-dimensional analysis of the porosity of the extraction zone, the porosity in the extraction zone as a second-order tensor was studied, and the calculation method of the porosity in each direction was derived. The porosity in the vertical direction of the gob was also analyzed, and the relationship between porosity and rock grain size was obtained through simulation tests, and the whole relationship curve was drawn. At the same time, the correctness of this relationship was proved by using field observations and theoretical analysis. Deng et al. [32] determined that the distribution of porosity in the gob in the strike direction varies nearly negatively exponentially by studying the distribution of mineral pressure and roof lithology in the gob.

2.3. Study on the Distribution Characteristics of Permeability in the Gob. In order to further study the specific situation of permeability in each location of the extraction zone after the end of surface recovery, Tu et al. [33] approximated the contour plot of permeability distribution in the extraction zone by using the difference algorithm that comes with Suffer software in order to combine the magnitude of permeability in each drilling stabilization stage. As can be seen from the graph, except for the part just after recovery, the permeability rate is obviously larger than the permeability rate on the cut hole side of the fully compacted workings because the recovery zone is not completely compacted. Within 1000 m of the workface strike length, the permeability is lowest in the middle of the extraction zone and gradually increases toward the edge, with a transverse "O" distribution from the inside to the outside, which is symmetrical from top to bottom and from left to right.

Wang et al. [34] considered the characteristics of different porosity in each zone and belt of the extraction zone, combined with the Kozeny–Carman equation, and obtained a three-dimensional inhomogeneous permeability model for the extraction zone, which assumes that the porosity variation obeys the sigmoid function from the working face, both ends to the compaction zone and within the fracture zone. The paper firstly studied the porosity models $n(x)$ and $n(y)$ in the strike direction of the working face, as well as in the tendency direction in the one-dimensional case, and then extended to the two-dimensional model on this basis by replacing the one-dimensional model $n(x)$ as the porosity of the compaction zone on the tendency and the porosity of the fractured rock in $n(y)$ after full compaction with $n(x)$ to obtain the two-dimensional porosity distribution model $n(x, y)$, for the porosity three-dimensional model, the variable n_z is introduced to represent the difference between the maximum and minimum porosity values parallel to the xoy coordinate plane, and $n(x, y, z) = n(x, y)$ within the collapse zone and the bottom slab fracture zone, and within the fracture zone, the maximum porosity at the working face in the two-dimensional model $n(x, y)$ is replaced by $n_{\min} + (n_{\max} - n_{\min}/1 + e^{a_3(z-z_c)-b_3})$, indicating that within the fracture zone, the maximum porosity above the working face gradually decreases with increasing height, thus obtaining the three-dimensional inhomogeneous distribution model of porosity in the gob as

$$n(x, y, z) = n_{\min} + \frac{n_z}{1 + e^{a_1 x - b_1}} + \frac{n_z e^{a_1 x - b_1}}{\left(1 + e^{a_2 y - b_2}\right)\left(1 + e^{a_1 x - b_1}\right)},$$

$$y < \frac{l_y}{2},$$

$$\text{when} \quad n_z = \begin{cases} n_{\max} - n_{\min}, & z_d \ll z < z_c, \\ \dfrac{n_{\max} - n_{\min}}{1 + e^{a_3(z-z_c)-b_3}}, & z_c \ll z < z_f. \end{cases} \tag{17}$$

In the formula, a_3 related to the height of the vertical three bands, $a_3 = 2b_3/(Z_f - Z_c)$, b_3 takes the value of 5.

Substituting the above equation into the Kozeny–Carman equation, the expression for the inhomogeneous permeability of the extraction zone is

$$k = \frac{d_0^2 n^3}{180(1 - n)^2}, \tag{18}$$

where k is the permeability, m^3; d_0 is the effective particle diameter, taken as 0.014 m; and n is the porosity.

Ren and Edwards [35] established a three-dimensional geotechnical model of the mining void area of the longwall working face based on finite difference or finite element software, determined the three-dimensional stress or strain distribution in the mining void area, and derived the three-dimensional spatial continuous distribution of permeability in the mining void area through the relationship between stress or strain and permeability. Wang [36] constructed a three-dimensional spatial dynamic distribution model of porosity and permeability in the gob based on Usher's mathematical function.

2.4. Relationship between Permeability and Porosity. Both porosity and permeability are basic parameters of porous media. A large number of experiments have proved that there is a certain relationship between porosity and permeability for a particular porous medium.

Kong [37] introduced the permeability of a porous medium that is a single bead filling case made of a single spherical particle filling. According to the Carman–Kozeny empirical formula, the following equation is available:

$$K_P = \frac{C\varphi^3}{\tau\Omega^2}, \tag{19}$$

where C is the Kozeny constant, a dimensionless constant related only to the geometry of the capillary interface; τ is the tortuosity; φ is the porosity; and Ω is the specific surface.

By the above, it can be seen that the permeability is inversely proportional to the tortuosity and specific surface and proportional to the third power of porosity.

For narrowly screened granular media, many scholars regard Darcy's law as a laminar flow law for fluids within porous media, while macroscopic hydrodynamic theories and methods are used to study the relationship between porosity, permeability, and interparticle relationships in granular media stacked beds. The relational equations of porosity and permeability are usually written as a function of the squared geometric scale of the particles. Taking spherical granular media as an example, they have the same form of the equation as follows:

$$K_P = \frac{d^2\varphi^3}{C(1-\varphi)^2}, \tag{20}$$

where d is the particle diameter.

For the coefficient C, Ergun gave $C = 150$, Bear gave $C = 180$, and Kozeny–Carmen gave $C = 172.8$.

Lei et al. [38] conducted tests for five different narrow sieved sands with particle size range from 100 to 450 μm and particle size ratio of 1.25 : 1 to analyze the law of permeability and porosity of granular media with particle size, and the results showed that under the same porosity condition, the smaller the particle size, the more curved and narrow the flow channel is, and the smaller the permeability is. The permeability of this sand can be expressed by the following equation:

$$K_{\mu m} = 1.718 \times 10^4 d_{\mathrm{mm}}^{1.465} \varphi^{4.69}. \tag{21}$$

For the porous media in the extraction area, the porosity and permeability of the extracted pores in the extraction area are much larger than the porosity and permeability of the original pores. Therefore, the main consideration for the porous media in the gob is the mining pore. Influenced by the mining pressure, the porosity and permeability of the porous media in the extraction area are functions of the location of the extraction area. For specific conditions, the relationship between permeability and porosity is not fixed, but a general trend is that permeability increases with increasing porosity.

3. Current Status of Theoretical Research on Flow Field in Gob

3.1. Methodology for Studying Flow Field in Gob

3.1.1. Graphical Method and Filtered Flow Field Model. Early studies on the gas flow law in the gob usually analyzed the air leakage in the gob by considering the gob and the retreating working face as two parallel wind paths, and the model was applicable to the study of the U-type ventilation method without leakage sources and sinks after the retreating face, but the theory was not applicable to the situation where the number of leakage sources was too many or the geometry of the gob was complicated, which had obvious limitations. In 1978, Chinese scholars Huang and Wang [39], etc., set the quarry with the long-walled backward coal mining method as a standard rectangular body, set the air-gob as a homogeneous porous medium, considered that the air flow conditions on each plane parallel to the quarry floor are similar, and cited the theory of fluid mechanics about the vortex-free steady motion in the plane, in the case of one source and one sink, one-source and one-sink quarry means that the air is fed from the inlet down-slot. In the case of one-source and one-sink quarry, the air is fed from the inlet down-slot and discharged from the return down-slot, and there is no air leakage. The graphical method is used to describe the gas flow law in the rectangular gob, and the mine ventilation system is adjusted according to the graphical results. However, once the number of air leakage sources is too large or the geometry of the quarry is complicated, the graphical method is difficult to apply and even technically infeasible.

In the same period, Polish and Soviet scholars put forward the filter flow field theory, which regarded the medium in the gob as a longitudinal and horizontal pipe network and believed that the flow of gas in the gob was similar to the flow in the pipe network. Shi et al. [40] used a computer to divide the fallout zone in the gob into a number of square grids, and each square grid was replaced by a filter flow branch network. The filter flow velocity and air leakage volume of the fallen strip in the gob were determined, and the computer simulation of the technical measures to reduce the air leakage volume in the gob was carried out according to the theory of filter flow field, and the results showed that the air leakage reduction ranged from 17.08% to 24.26%. Ding et al. [41] gridded the bubble fall zone in the gob, as shown in Figure 8, and established the mathematical model of the filter flow field in the gob, calculated the wind resistance of each branch of the filter flow field in the gob, and programmed a C language program to solve the filter flow field according to the law of wind volume balance and the law of wind pressure balance, as well as the iterative method of Scott-Hensley, to obtain the wind speed of each branch of the filter flow in the gob:

$$h = R'Q + R''Q^2, \tag{22}$$

where h is the resistance of the filtered flow field branches, Pa; R' is the filtration flow field laminar wind resistance, kg/(m^4•s); R'' is the filtration flow turbulent wind resistance, kg/m^7; and Q is the air volume of filter flow branch, m^3/s.

3.1.2. Similarity Simulation Method. Similarity simulation (including physical similarity simulation and electrical simulation) is based on similarity theory and plays an important role in the early research stage of flow field in the gob. The so-called similarity principle means that when the mathematical models of two physical fields, the same or different, are isomorphic, the distribution laws of the two field quantities are the same, but with different signs such as functions or coefficients, and when the solution of one field has been solved or is easy to solve, the other unknown and relatively difficult field can be solved based on it. The similarity simulation method is relatively simple to use, and

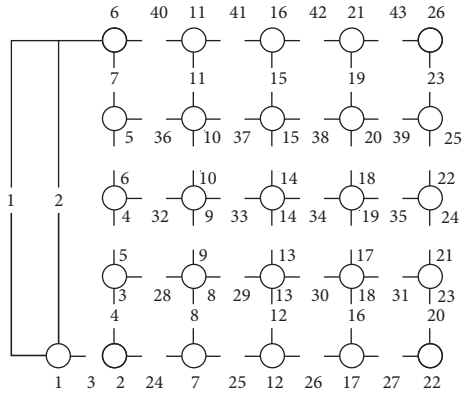

Figure 8: Air leakage branches and node numbers in the extraction area.

researchers can study different physical fields under various conditions by creating similar simulations in the laboratory.

Electrical simulation is one of the simulation methods with more advantages. Zhu and Hui [42] introduced the electric simulation method into the study of mine ventilation, comparing the wind field with the electric field, and proved by practice that the introduction of the electric simulation method into coal mines is useful for the study of problems such as ventilation, but there are some problems with the electric simulation, such as the unsatisfactory treatment of the junction conditions in places where the field changes drastically, the poor mastery of the model dissection technique, the poor orthogonality in some parts of the flow network, and the existence of some errors.

Xu et al. [43] used the physical similarity simulation method to realize the qualitative study of wind flow state by analyzing the smoke flow state. Yang et al. [44] established a model of coal seam permeability coefficient based on similar material experiments simulating coal mining with fractal dimension of mining fractures.

3.1.3. CFD Numerical Simulation Method. Numerical simulation, also known as computer simulation, is the study of engineering and physical problems by means of numerical computation and image display using an electronic computer as a carrier. CFD is a branch of computational fluid dynamics, where the mathematical description of the overall flow field of interest is obtained by numerically solving a system of equations to reflect the fluid flow, heat and mass transfer laws and related phenomena.

With the continuous progress of computer science and technology, a lot of CFD commercial software has been created, such as PHOENICS and FLUENT. PHOENICS is the world's first set of commercial software for computational fluids and computational heat transfer, which was developed by the main founder of international computational fluids and computational heat transfer, Professor D. B. Spalding, a member of the Royal Academy of Engineering, and more than 40 Ph. Although PHOENICS was introduced into the field of coal mine flow field earlier, the software is completely applied to the calculation of the flow field of rock fall media in the gob, there are still many problems, such as the adaptation and debugging of specific problems, with large differences and limitations, and there are still some problems to overcome in the integration of analysis and calculation with this professional problem. FLUENT is currently international more popular commercial CFD software package, with a high market share. It has rich physical models, advanced numerical methods, and powerful pre- and postprocessing functions and has a wide range of applications. It uses the finite volume method based on a completely unstructured grid and has a gradient algorithm based on grid nodes and grid cells.

In recent years, CFD numerical simulation of wind flow motion and gas transport and its distribution pattern in mining sites has been carried out in China. Zhou et al. [45] used PHOENICS software to simulate the distribution law of the wind flow and temperature field at the back mining workings and concluded that the wind flow temperature at the back mining workings decreases with the increase of wind speed in a negative power function, increases linearly with the increase of incoming wind flow temperature, and varies with the length of the workings and the location of the coal miner. The numerical simulation program (G3) of the field flow in the gob prepared by Li [23] has the following characteristics: (1) it can adapt to various complex boundary conditions and treat the gob as a bubbling nonhomogeneous medium; (2) it takes into account the natural coupling effect when gas gushes out and can reflect the relationship between the influence of factors such as working face advancement and ventilation volume; (3) it is operable and can make arbitrary simulation test faces for various situations, which is convenient. Theoretically, it can depict the flow state of air leakage in the gob, dynamically depict the distribution state of gas, oxygen, carbon monoxide concentration and temperature, and their change process, and give the graphical distribution solution of each phase of gas and temperature change in the gob under the mining conditions of the working face; (4) it realizes the integration of the joint solution of "a multiphase problem" in the gob, which can meet the needs of the study of the problem. G3 can assist in analyzing many safety problems such as gas emission from the gob, spontaneous combustion and fire, nitrogen injection and fire extinguishing, and large area pressure equalization and pressure regulation. It is powerful and comprehensive and represents the development direction of domestic application software in the field of numerical simulation of field flow in the gob.

3.2. Numerical Model Equation Study

3.2.1. Linear Gas Seepage Theory. The numerical model equations were initially simplified according to Darcy's law, which is a typical representative of linear gas seepage theory, and it is believed that the gas flow law in coal seams is basically in line with the linear percolation law. In the international aspect, the former Soviet Union scholars used Darcy's law for the first time to analyze and study the problem of linear gas seepage in coal seams by using the

nature of gas adsorption, which opened a new chapter for the study of linear gas seepage theory. In China, experts such as Zhou and Sun [46] agreed with the linear gas seepage theory, and on this basis, they analyzed and studied the flow of gas in coal seams for the first time, and regarded coal seams as continuous and uniformly distributed porous media, which laid the theoretical foundation for the analysis and study of gas flow theory by domestic experts and scholars. The linear seepage theory believes that the flow rate of gas in coal and the pressure difference obey a linear mathematical relationship; that is, the flow rate is proportional to the pressure difference of gas. Since the 1980s, scholars in China have carried out research on the numerical equations of linear flow theory and have modified and improved them on this basis.

In 1986, Tan and Yuan [47] combined the theory of seepage mechanics and thermodynamics, treated coal seam gas as real gas, proposed the seepage equation of real gas in the coal seam of the mine, and simplified the equation. In 1989, Yu et al. [48] proposed the idea that the amount of gas involved in seepage in coal seam is the partial amount of gas content in coal body, and under the assumption that the process of gas adsorption and desorption in coal body is completely reversible, the controlling equation of gas seepage in the coal seam was established; in 2010, Yang and Li [49] established a mathematical model of gas flow in the coal body around the borehole based on Darcy's law and the assumptions of coal seam gas flow theory and applied the law of mass conservation to obtain the equation of gas flow around the borehole and its fixed solution conditions.

3.2.2. Nonlinear Gas Seepage Theory. Darcy's law has a good fit for laminar flow motion that conforms to the linear drag relationship, but in practice the flow of wind flow in the gob is often very complex, with a large portion of the area being transitional seepage or turbulent flow. In these regions, fluid motion does not conform to Darcy's law. Therefore, many scholars have proposed nonlinear seepage laws based on this problem and conducted research based on nonlinear seepage theory.

In 1984, Higuchi Sumitoshi, a professor at Hokkaido University, Japan, determined the methane permeability of coal samples by varying the pressure difference and found that Darcy's law was not quite consistent with the coal seam gas flow law. Based on a large number of experimental studies, he proposed the basic law of coal seam gas flow that is more consistent with the power law:

$$V_N = -A\left(\frac{\mathrm{d}p}{\mathrm{d}x}\right)^m, \tag{23}$$

where V_N is the uncaused gas flow rate in the corresponding standard state; A is the uncaused gas permeability coefficient; m is the state constant; and $\mathrm{d}p/\mathrm{d}x$ is the uncaused gas pressure gradient along the X-axis.

Sun [50] considered that the mathematical model of gas flow proposed by Professor Higuchi was not rigorous and concluded that the gas flow in coal seams is actually a mixed unsteady flow of compressible fluid by permeation-diffusion in an anisotropic and nonhomogeneous pore-fissure twofold medium. He established the first partial differential equation for compressible gas flow in coal seams under the conditions of homogeneous and nonhomogeneous coal seams according to the generalized form of power law and made practical calculations to verify the flow of gas flow field in homogeneous coal seams based on the actual measured gas flow parameters in 23051 working face of the Jiaozuo Zhongmacun Mine, and the results showed that it was closer to the actual situation than Darcy's law. In 1994, Liu [51] concluded that the coal seam gas flow model derived in the literature [41] on the basis of the power law and the application of the invariant had errors in the process, and the numerical results obtained by it were unreliable, and derived the correct flow model when the gas flow followed the power law in the paper.

Deng et al. [52] analyzed a large amount of experimental data, on this basis generalized the universal characteristic equation of motion for seepage curves, and proposed a nonlinear equation of motion for gas seepage in low-permeability pore-fracture media. However, this type of model mainly adopts the method of phenomenology, which is only a generalization and distillation of the experimental phenomena and does not have the function of in-depth explanation, which is manifested in this study mainly by scholars fitting mathematical equations according to the physical phenomena of nonlinear seepage, and it is difficult to reflect the intrinsic causes and influencing factors that cause the nonlinear flow of gas in coal.

To fill this research gap, Zhang and Cheng [53] took nonlinear seepage mechanism as the theoretical basis, combined with actual experimental research results, and established a nonlinear seepage equation describing the characteristics of gas seepage based on mechanical equilibrium equation; the physical meaning of which is as follows: the seepage resistance consists of two parts, the first part is viscous resistance, which is proportional to the primary side of the seepage velocity, and the second part is the additional seepage resistance caused by adsorption, which is proportional to the adsorbed gas content in the coal. It is precisely because of the existence of the intermolecular adsorption between coal and gas, which reduces the flow rate of gas in the coal body. The equation is the Darcy flow equation when the adsorbed gas content in the coal is zero. While most scholars currently use heat shrink tubing to seal the coal sample, using oil pressure to offset the air pressure to implement an annular seal on the sample so that the specimen is partially subjected to the oil pressure, this literature utilizes a sealing cylinder sleeve combined with a sealing reagent to implement a coal sample seal under constrained annular strain, fundamentally eliminating the influence of this factor on the experimental results.

3.2.3. Ground-Field Effect Flow-Solid Coupling Gas Flow Theory. With the in-depth research on the flow of gas in porous media, domestic and foreign experts and scholars also gradually realize that the effect of ground-field effect on gas flow cannot be ignored, and based on Darcy's law, a large

number of analytical studies are conducted in gas percolation, and a mathematical model of gas percolation under the conditions of gas-solid coupling action is established.

By varying the pressure difference, scholars determined the permeability of gas-bearing coal under different conditions, integrated a large amount of experimental data, and found that the permeability of the coal body gradually increased with the decrease of gas pressure under low-pressure conditions, and they defined this physical phenomenon as the Klinkenberg effect. It is also suggested that the mechanism underlying this effect is that the gas slips on the solid surface under low-pressure conditions, leading to an accelerated flow of gas in the coal body, which is macroscopically manifested as an increase in the permeability of the coal body. However, the literature [54] argues that this effect does not actually exist, and it is not the slip of gas molecules on the solid surface, but the adsorption between coal and gas molecules that leads to the change of permeability. Liu et al. [55] considered the Klinkenberg effect, the effective stress, and desorption shrinkage on gas seepage and coal deformation, established a fluid-solid coupling model describing gas seepage and coal skeleton deformability, and applied it to practical engineering. The results show that the Klinkenberg effect is more rapid in the vicinity of the extraction borehole than in the absence of the Klinkenberg effect, and the farther away from the extraction borehole, the less effect of the Klinkenberg effect.

Experts and scholars at home and abroad have also conducted a lot of systematic analyses and studies on the deformation laws, mechanical properties, and their rheological characteristics of coal body samples containing gas. Wang et al. [56] studied the effect of electric field on the seepage properties of gas in coal using a triaxial seepage experiment device and an electric field implementation device, refined Darcy's seepage law under the original conditions, proposed the basic law of gas seepage under the condition of ground electric field action, and established the corresponding mathematical model of gas seepage. Based on the research results of other scholars, Sun [57] and others created a gas-solid coupling theory of gas transmissive flow in the multicoal seam system.

4. The Influence of Environmental Factors on the Distribution of Flow Field in the Gob

4.1. Ventilation Method. According to the actual mining situation and considering the geological characteristics, the selection of working face ventilation method varies. At present, U-type ventilation is most commonly used in coal mines. With the increasing maturity of coal mining theory and to meet the demand for safe mining under different geological conditions, various ventilation methods have been developed based on U-type ventilation. In recent years, scholars have made specific studies on the distribution of flow field in the gob under different ventilation methods.

4.1.1. U-Type Ventilation. The U-type ventilation system is mainly used in coal mining workings of low gas mines, where there is only one air inlet and one air return lane, and it can be divided into U-back and U-forward according to the direction of workings. U-type backward ventilation is shown in Figure 9. In China's coal mines, the U-back type is commonly used in the working face. The gas in the upper corner of U-ventilated working face of high gas mine has been a difficult problem for coal mine gas management. With the development of coal science and technology, coal mining working face has realized high-production and high-efficiency comprehensive mechanized production, and the unit production of working face has been improved continuously, and the gas gushing out has been increased, so that the mines with little gas in the original working face and low gas mines also have the upper corner gas accumulation over limit [58]. Many scholars have analyzed the wind flow and gas flow law of U-type ventilation working face through on-site observation and research.

In order to obtain the flow field distribution in the mining void area of U-type comprehensive mining working face, Tao [59] established a two-dimensional physical model of the mining void area according to the actual situation of 11124 working face and conducted numerical simulation studies on the constructed model using FLUENT software and adaptive grid encryption technology. The study showed that the air leakage in the gob mainly occurred in the range of 0~20 m, and some of the air leakage into the gob returned to the working face in this area, while most of the air leakage returned to the working face in the inclination of 140~160 m; the wind velocity contours in the gob were not symmetrical in the inclination direction; in the direction of the gob, the wind velocity of air leakage showed a gradually decreasing trend.

Tian et al. [60] arranged one release point and five sampling points in the working face, used the instantaneous release method to continuously release SF_6 gas at the wind source location, conducted gas sampling at the sampling points at regular intervals to analyze the SF_6 gas concentration in the gas, estimated the air leakage volume and minimum air leakage velocity in the gob according to the time and concentration of SF_6 in the gas sample, and analyzed the measured data to make a general inference about the location of air leakage in the working face. Through the analysis of the measured data, the location of the air leakage channel in the working face can be roughly deduced, as shown in Figure 10. After that, the numerical simulation software FLUENT was used to verify the air leakage in the U-type ventilation gob. The actual measurement results of the corresponding wind speed and air leakage velocity of each monitoring point are compared with the numerical simulation results as shown in Figure 11. The numerical simulation results are consistent with the actual measurement results on-site. The air leakage in the gob is distributed in a U-type, which flows into the gob from the inlet side of the working face and deflects to the return side after a certain depth and flows out; the air leakage in the gob of the U-type ventilation system is mainly in the lower corner area of the working face, which is more prone to spontaneous combustion.

With the increase of coal mining at the working face, the single U-type ventilation system cannot meet the safety production of coal mining enterprises, and in order to keep

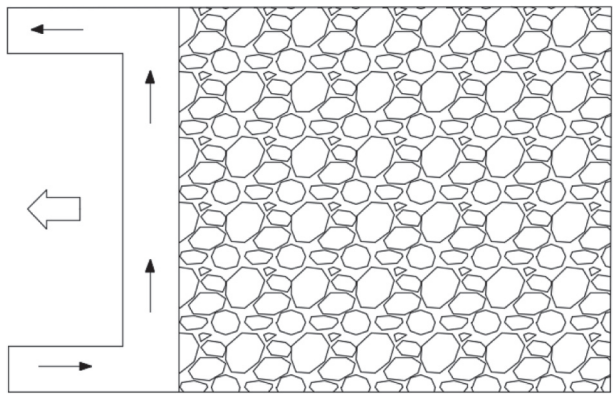

Figure 9: U-type backward ventilation.

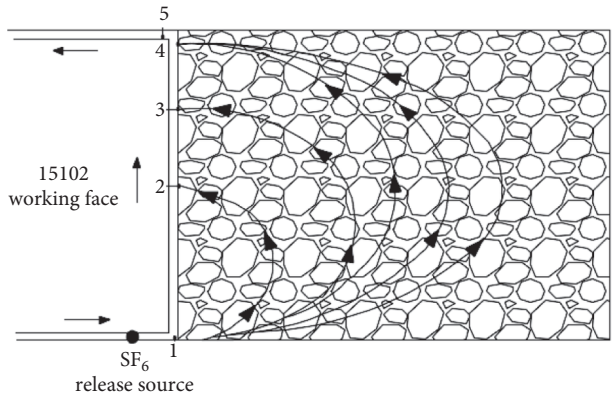

Figure 10: Schematic diagram of air leakage channel in gob of 15102 working face.

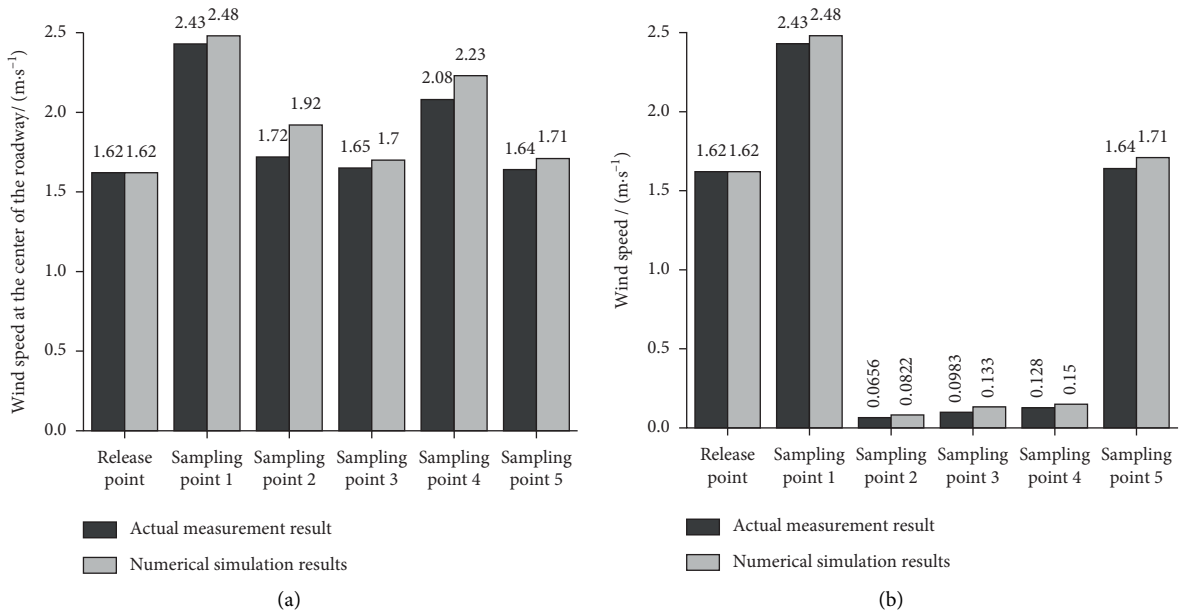

Figure 11: Comparison of field measurement and numerical simulation results. (a) Monitor the corresponding location. (b) Monitor the corresponding location.

the gas concentration at the working face from exceeding the limit, new ventilation methods have emerged based on the U-type ventilation system, among which U + I-type and U + L-type are more widely used at the comprehensive working face. In U + I-type ventilation, the gas tail lane is arranged on the inner side of the return air lane, and the gas

carried by the leakage is discharged through the gas tail lane; while in U + L-type ventilation, the gas tail lane is arranged on the outer side of the return air lane. Although these two ventilation methods are good for controlling the gas concentration in the corner of the working face, both of them change the air leakage in the gob compared with the U-type ventilation method, causing the flow field in the gob to change.

Ma et al. [61] used the UDF interface to establish the calculation models of coal gas seepage in the mined area based on the moving coordinates of the working face and the gas dispersion and transport in the retracement tunnel and quantitatively compared the U-type and U + I-type ventilation methods under different working face advance speed and working face air distribution conditions. The paper concluded that the location of air leakage in U-type ventilation was mainly concentrated in the lower corner of the working face, while in U + I-type ventilation, there were air leakage channels in the whole working face; the size of gas concentration in the return air lane under U-type ventilation is about twice that of U + I-type ventilation, and with the increase of wind speed in the inlet air lane, U + I-type ventilation and U-type ventilation have more gas concentration. With the increase of wind speed in the inlet lane, the gas concentration in the return lane of both U + I-type and U-type ventilation methods shows a decrease in the form of decrease, and with the increase of working face advancement speed, the gas concentration in the return lane of U-type ventilation method shows a decrease in the form of increase, while the gas concentration in the return lane of U + I-type ventilation method shows a decrease in the form of decrease. Compared with the U-type ventilation method, the gas concentration in the upper corner can be reduced by 25% to 50% under the U + I-type ventilation method.

Wu et al. [62] conducted numerical simulation of the flow field in the gob under U-type and U + L-type ventilation using FLUENT software and compared and analyzed the distribution of gas concentration in the gob and the distribution of spontaneous combustion hazard zone in the gob under the two ventilation methods, as shown in Figure 12, and the results showed that the gas concentration in the gob of U + L-type ventilation was lower than that of U-type ventilation and the gas explosion range in the gob was lower than that of U-type ventilation. The range of gas explosion moves to the deep part of the gob, but the width of gas explosion area becomes smaller. The gas concentration in the middle of the gob increases faster along the direction of the gob, and the spontaneous combustion hazard area in the gob moves deeper in the gob with U + L-type ventilation than U-type ventilation, and the width of the spontaneous combustion hazard area in the gob also increases significantly.

4.1.2. Y-Type Ventilation. The Y-type ventilation method is a ventilation system that adds fresh air flow on the return side and flows out from the side of the gob after converging with the lacking air from the working face. The use of Y-type ventilation method in the coal face increases the air volume in the return air tunnel, which can effectively solve the problem of gas overrun in the upper corner and is conducive to gas extraction, so it has good promotion value, as shown in Figure 13.

Yu et al. [63] established a two-dimensional solution model for the flow field in the gob under Y-type ventilation, applied the computational fluid dynamics software FLUENT to numerically simulate the distribution of the air leakage field and gas concentration field in the gob, conducted a comprehensive comparison of the air distribution ratios of different main and subinlet lanes, and concluded that the gas management effect was best when the air distribution ratio was 5 : 1.

Yang et al. [64] established the physical model of U-type and Y-type ventilation air-gob and used FLUENT software to numerically simulate the air leakage flow field, air leakage volume, and gas distribution in the air-gob under these two ventilation methods, and the simulation results are shown in Figure 14. Most of the air flow in U-type ventilation flows into the working face through the inlet alley and finally discharges through the return alley, and a small part of the air flow leaks into the air-gob from the lower corner of the working face, and in Y-type ventilation, most of the air from the machine tunnel flows through the working face, then converges with the air from the wind tunnel, and enters the air-retention lane, finally discharges through the return air lane, and some of the air leaks into the air-gob from the lower corner of the working face to the middle of the working face, and the closer the air leaks into the air-gob, the more it blows to the bottom of the air-gob, and then it flows from the air-gob to the interface between the air-gob and the air-retention lane. The more the air leaks into the air-gob from the side of the machine tunnel, the more it can be blown to the bottom of the air-gob and then flow into the air-gob from the interface between the air-gob and the alley. After analyzing the air leakage data of the two types of ventilation, it is concluded that the air leakage at the end of the working face from 0 to 30m accounts for 50% of the air leakage at the working face with Y-type ventilation, and the air leakage at the working face to the air-gob from 30 to 90m accounts for 46% of the total air leakage, and the total air leakage is more than that of U-type ventilation, which is not suitable for the coal mining face with coal spontaneous combustion. In addition, under Y-type ventilation, most of the gas in the gob is carried by the air leakage from the working face to the gob to be discharged along the air-retention lane, and very little of the low volume fraction gas ($\leq$0.5%) is gushed to the corner of the working face, so the volume fraction of gas in the gob is lower than that in U-type ventilation, which can avoid the accumulation of high concentration gas in the gob. The use of two-in-one Y-type ventilation can fundamentally solve the problem of gas accumulation in the upper corner and gas overload in the return airway.

Zhao et al. [65] took 5301 working face of the Sihe Mine of the Jin Coal Group as the research object and studied the gas gushing law in the gob under partial Y-type ventilation according to the measured parameters of gas gushing, and two gas gushing were considered in the literature, which

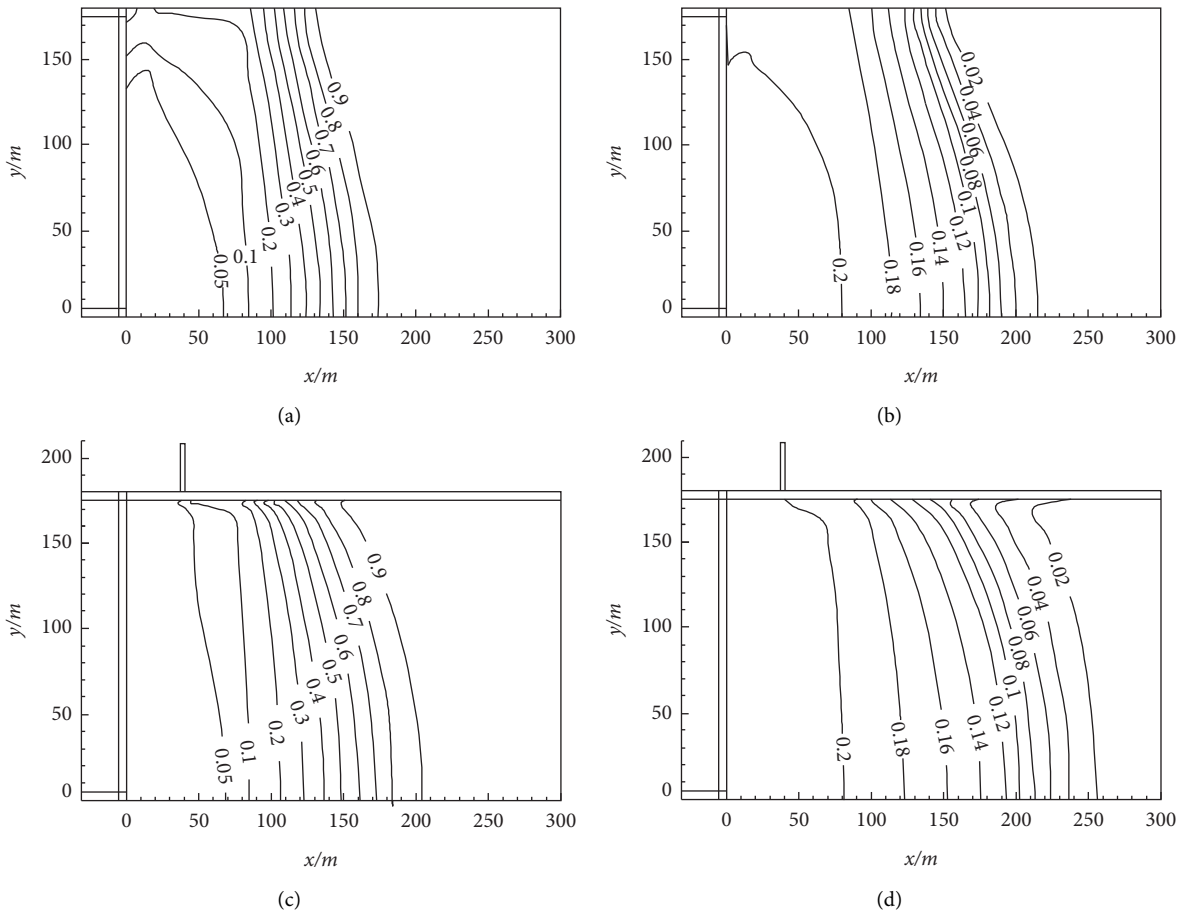

Figure 12: Simulation results of flow field in U-type and U + L-type ventilation gob. (a) Gas concentration distribution in U-type ventilation gob. (b) Oxygen concentration distribution in U-type ventilation gob. (c) Gas concentration distribution in U + L-type ventilation gob. (d) Oxygen concentration distribution in U + L-type ventilation gob.

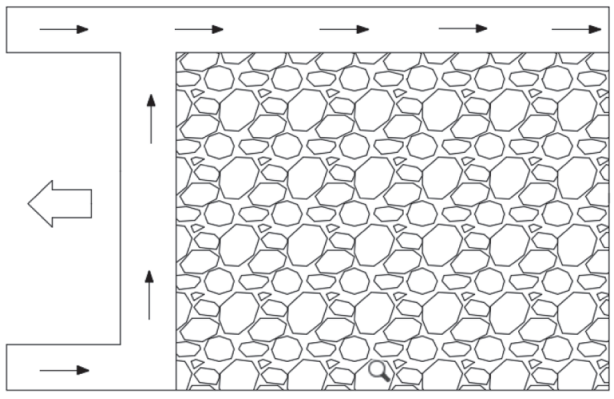

Figure 13: Y-type backward ventilation.

were coal left in the gob and gas gushing from the adjacent layer on the gob, set at 0.3 m from the bottom plate of the gob and the adjacent layer area of the gob (19.28 to 19.80 m from the bottom plate of the gob). Bottom plate was 19.28~19.80 m height range, and different locations in the gob defined different gas outflow rate; according to the O-ring theory, we set the gob void rate and permeability.

4.1.3. W-Type Ventilation. W-type ventilation is mainly used in long working face with high gas, where both the inlet and return airway are in the coal body. In order to solve the problem of gas overrun in the upper corner in U-type ventilation, two-in-one W-type ventilation is often used with the upper and lower flat as the inlet airway and the middle roadway as the return airway. Because of the maintenance difficulties of W-type forward ventilation tunnel, the air leakage is relatively large, and the gas gushing from the gob is also large, W-type backward ventilation is generally used, as shown in Figure 15.

Li and Li [66] established a finite element numerical model of the flow pattern of wind leakage in the bubble fall gob based on the equation of wind leakage and seepage in nonhomogeneous porous media, combined with field examples, and the calculation was based on MATLAB to develop a calculation program to display the results graphically. The sparse and dense transition is carried out by using the frontier generation method for the sectioning of the gob and the accuracy of the boundary sectioning of the wind leakage condition in the quarry as the basis of the regional grid density function; the spatial shape of the area is reflected by the change of the flow field height. Theoretically, the wind pressure distribution contours and flow function

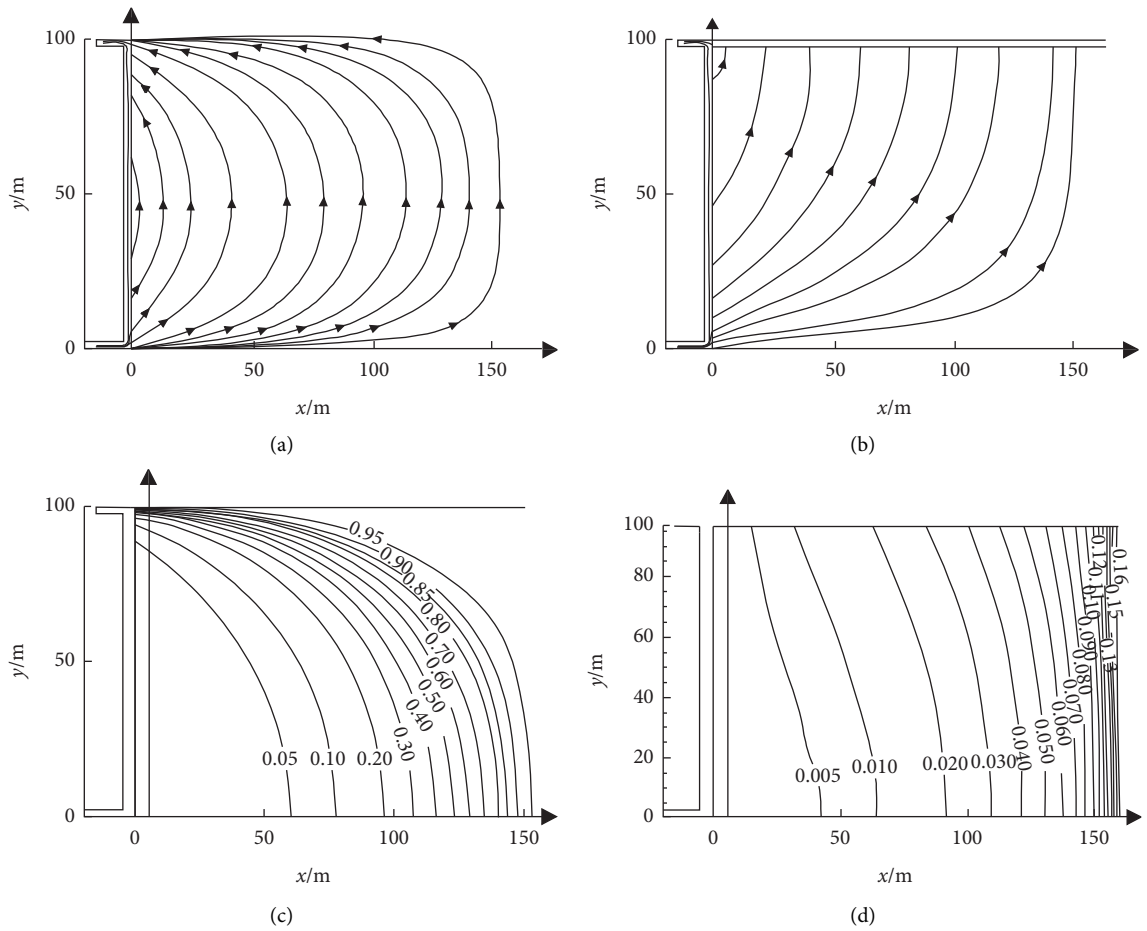

Figure 14: Simulation results of flow field in U-ventilated and Y-ventilated gob. (a) Flow diagram of the U-type ventilation and recovery workings in the mining void area. (b) Flow diagram of gob of Y-type ventilation and retrieval working face. (c) Gas distribution map of U-type ventilation gob. (d) Y-type ventilation gob gas distribution map.

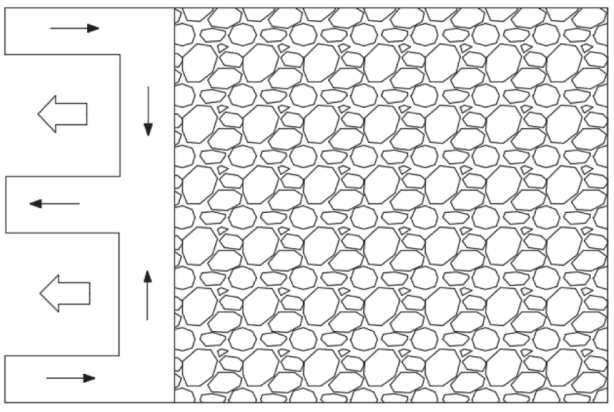

Figure 15: W-type backward ventilation.

lines (distribution solutions) of the W-type ventilation gob are depicted, and it is pointed out that the W-type ventilation gob obviously reduces the wind pressure difference between the two ends of the working face and the effect of reducing the range of wind leakage.

Cheng and Xin [67] compared the W-type ventilation method with U-type ventilation, and the simulation results showed that the leakage wind flow fields of the two are obviously different, and under U-type ventilation conditions, most of the leakage wind in the gob penetrates into the deep part of the gob, while W-type ventilation reduces the pressure difference between the two ends of the working face by about 35% compared with that of U-type due to the effect of equal pressure at both ends of the working face, causing the leakage wind in the gob to be closer to the working face under W-type ventilation. At the same time, because the air leakage will carry a lot of gas from the gob into the working face, W-type ventilation reduces the air leakage from the working face to the gob, thus suppressing the gas leakage from the gob to the working face, and fundamentally solving the problem of frequent overlimit gas accumulation in the upper corner of U-type ventilation and the return airway.

4.1.4. J-Type Ventilation. This type of ventilation is a new type of ventilation system proposed only in recent years. It has a stronger and more controllable gas discharge capacity than the U-type ventilation commonly used in coal mines and is mainly suitable for high gas discharge workings in coal seams that are not prone to spontaneous combustion, which

can well solve the corner gas problem on the workings, as shown in Figure 16.

According to the actual situation of 5201 header working face of the Wangzhuang Coal Mine in Lu'an, Wang and Wu [68] compared and analyzed the flow field and gas transport characteristics of J-type ventilation and U-type ventilation by using PHOENICS software. The simulation results of U-type ventilation and J-ventilation extraction zone are shown in Figures 17 and 18, respectively. The flow field and gas transport law of J-type ventilation gob were studied systematically under different conditions of gob size, gas discharge capacity of special alley, and extraction fan installation position. The results show that the J-type ventilation system can eliminate the concentrated air leakage in the upper corner of the gob and effectively solve the problem of gas accumulation in the upper corner of U-type ventilation.

Gao and Sun [69] investigated the air leakage pattern in the gob, the distribution pattern of gas in the gob and the upper corner under different air volume conditions in the J-type ventilation system by means of numerical simulation. With the increase of inlet air volume, the area of low concentration of gas in the gob gradually deepens to the upper right of the gob, and the distribution range increases significantly. The magnitude of gas concentration reduction in the deep gob is larger than that in the shallow gob. The gas concentration in the upper corner also decreases gradually with the increase of the inlet air volume, and the gas concentration in the upper corner is lower than the 1% upper limit standard stipulated in the safety regulations when the air volume increases to 2350 m^3/min.

4.2. Coal Seam Dip Angle. The geological conditions of China's coal mines are complex and variable, and the coal seam inclination is not the same even for the same well field. The coal seam inclination is the main factor affecting the changing damage form of the overlying rock layer in the mining field. With the development of coal seam inclination from gentle to sharp inclination, the deformation and damage characteristics of the roof after coal seam mining will change, and the porous media parameters in the gob are closely related to it, which in turn affects the leakage flow field and the distribution of gas and pressure in the gob.

Lu and Zhang [70] used UDEC numerical simulation to study the law of overlying rock strata spanning fall in the mining void zone of inclined extrathick coal seam and obtained the distribution of porosity in the mining void zone by the amount of overlying rock subsidence in the mining void zone. The results show that the porosity in the fallout zone is maximum along the strike at the edge of the gob and minimum at the deep part; it is maximum at the upper corner and lower corner along the tendency and minimum at the middle and upper part; in the vertical direction, the porosity in the gob decreases with increasing height from the bottom plate, and the difference between the edge and the deep part also decreases gradually.

Yang and Zhang [71] studied the effect of coal seam inclination on the flow field and gas distribution in the mining void area of U + L-type ventilation face in a more systematic way, which divided the mining void area into bubble zone and fracture zone, where the bubble zone was subdivided into free accumulation zone, load-influenced zone, and compaction stability zone, set the porosity of the bubble zone to be uniformly distributed in segments, and investigated the effect of the coal seam inclination of 5.75°, 35.75°, with the increase of the coal seam inclination, the pressure difference between the two ends of the working face and the pressure difference between the working face and the tailing lane increase gradually, and the increase increases first and then decreases; the increase of the pressure difference between the two ends of the working face is greater than the pressure difference between the working face and the tailing lane; under the condition of keeping the air volume in the inlet lane, the return lane and the tailing lane unchanged, and the air volume in the working face decreases with the increase of the coal seam inclination. The air volume decreases, but the proportion of decrease is small and the trend is decreasing, and the distribution law of air leakage shows that the air leakage at the upper and lower ends is large, and the air leakage at the middle of the working face is small. As the coal seam inclination increases, the gas in the gob is affected by the uplift effect and the leakage flow, and the gas concentration gradually decreases. The gas concentration gradually decreases due to the uplift effect and leakage flow.

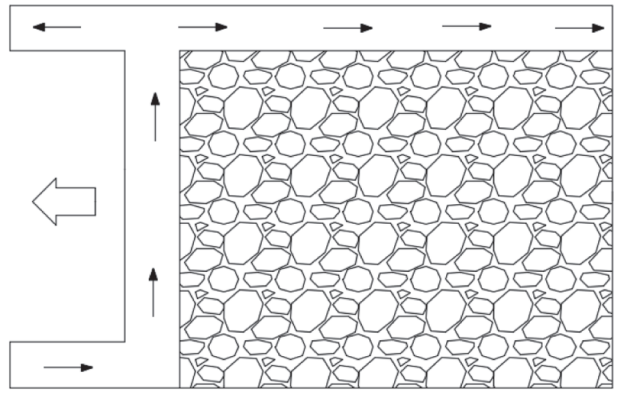

Figure 16: J-type backward ventilation.

5. Study on the Prevention and Control of Fire and Explosion Risks in Gobs

5.1. Study on the Prevention and Control of Fire in the Gob. The development of mechanization and automation of coal mining technology has greatly improved the production efficiency of mines, but accordingly, it has also caused an increase in coal left in the gob and increased air leakage, resulting in spontaneous combustion accidents in the gob. According to statistics, more than 50% of natural fires occur in mines in the gob, and it is important to study the flow field in the gob to prevent coal spontaneous combustion from causing mine fires [72].

The study of the flow field of the gob on the prevention and control of fire risk is mainly from the perspective of the flow field of the gob to analyze and predict the natural fire in

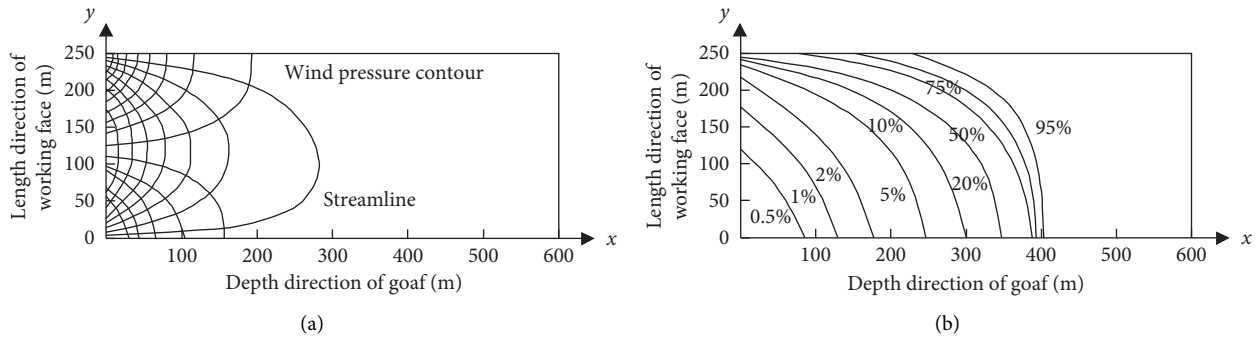

Figure 17: Simulation results of flow field and φ (CH4) in U-type ventilation gob. (a) Flow line and pressure distribution. (b) φ (CH4) distribution.

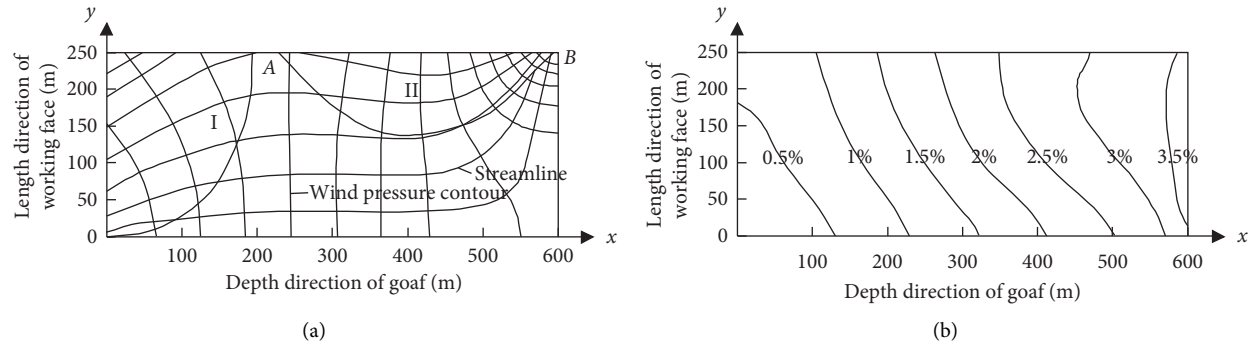

Figure 18: Simulation results of flow field and φ (CH4) in J-type ventilation gob. (a) Flow line and pressure distribution. (b) φ (CH4) distribution.

the gob, and also to study whether the injection of inert gas, grouting, fracture filling, or pressure balancing measures in the gob are beneficial to the prevention and control of spontaneous combustion fires, and the research means are mainly numerical simulation software, fire beam monitoring system arranged on-site, etc. Combined with a series of existing theoretical theories of coal spontaneous combustion, the analysis is carried out.

In order to analyze and predict the natural fire in the gob, the method of dividing the spontaneous combustion "three zones" (i.e., dispersal zone, spontaneous combustion zone, and choking zone) in the gob has been adopted, and many scholars and research institutions at home and abroad have determined the indexes of dividing the three zones in the gob after doing a lot of in-depth research on this, including the temperature rise rate of the coal left in the gob, the wind speed of the coal leakage in the gob, and the wind speed of the coal leakage in the gob. The indicators of air leakage are often the air velocity and the oxygen concentration in mine gobs [73–77]. In addition, a large number of researchers have studied the prediction and analysis of the flow field in the gob for natural fires and other conditions. For example, Zhou [72] obtained the change pattern of the temperature field in the gob during the advancement of the working face through a four-dimensional dynamic simulation study. The migration rate of the high-temperature zone is affected by factors such as porosity. At the same time, there is a dynamic change between the high-temperature zone and the high oxygen zone in the gob. Zhang et al. [78] used the discrete element modeling software Particle Flow Code (PFC) to simulate the pore evolution and porosity distribution of the overlying rock in the mined-out area and established a dynamic porosity model for the mined-out area. The flow field in the area was simulated, and the regular gas flow distribution in the mined-out area was obtained. Compared with the actual mine measurement results, it was verified that the flow field distribution in the mined-out area considering the porosity dynamics can accurately and reliably identify residual coal spontaneous combustion prone area. Zheng et al. [79] studied the competitive adsorption characteristics of multicomponent gas and its influence on coal oxidation and found that the gas adsorption selectivity order on the coal surface is $CO_2 > CH_4 > O_2 > N_2$. Under ambient conditions, the strong adsorption capacity of CH_4 and CO_2 on the coal surface hinders the spontaneous combustion of coal due to the limited adsorption sites on the coal surface. Especially, CH_4 adsorbed by residual coal will affect the chemical reaction between coal and O_2, while the reaction between CH_4 and O_2 on the surface of high-temperature coal will accelerate the spontaneous combustion of coal and increase the risk of coal spontaneous combustion. Zuo et al. [80] used a self-built experimental platform to determine the effect of different air leakage conditions on the spontaneous combustion of residual coal and obtained an exponential relationship between air supply to the working face and the spontaneous combustion of broken coal in the gob. Wang

et al. [81] used the particle flow numerical simulation software PFC3D to simulate the collapse of the overlying rock layer in the void area, extracted the quantitative porosity data of the void area, imported it into FLUENT software, simulated the leakage flow field in the void area, and obtained the main leakage area of the working face. Lu and Qin [82] used numerical simulation to study the plastic deformation process of the coal column and deduced the distribution law of porosity of the coal column. On this basis, the mathematical model of oxygen consumption and seepage in the coal pillar was established using ANSYS-FLUENT software, the distribution of oxygen concentration in the coal pillar was obtained, and the potential spontaneous combustion area in the coal pillar in the gob was determined according to the oxygen concentration index.

Not only does the research on the prevention of natural fires stop at prediction and analysis, but also researchers at home and abroad have studied the effect of measures to change the flow field in the gob (such as inert gas injection, slurry injection, fracture filling, or pressure equalization) on the prevention of spontaneous combustion fires. Wang and Tang [83] used the beam tube monitoring system to study that a comprehensive method combining pressure equalization, grouting, and crack filling has a significant effect on preventing spontaneous combustion of coal and complex air leakage in longwall gob. Qin et al. [84] established a theoretical and geometric model to quickly determine the high-temperature zone of fire by simulating the oxygen concentration and temperature distribution in the gob and evaluated the effect of liquid nitrogen infusion by comparing field measurements and numerical simulations. Zhang et al. [85] established a three-dimensional transient nonequilibrium thermal CFD model based on the actual situation of the long wall gob and studied the thermal evolution and active inserting scheme of the long wall gob. Wang et al. [86] used FLUENT software to numerically simulate the spontaneous combustion of residual coal in the air leakage area of the gob and studied that the slurry injection method can prevent the spontaneous combustion of residual coal by reducing the area of porosity in the gob and the area of oxidation zone behind the working face, which is a cost-effective method.

5.2. Study on the Prevention and Control of Explosion Risk in the Gob. With the advancement of the working face, the increase of the gob area, and the influence of the change of airflow in the roadway on the gas composition of the gob in the production process, it indirectly affects the change of the gas explosion risk area in the gob. Studying the law of gas migration in gob plays an important role in preventing gas explosion in the gob. The spontaneous combustion of coal remains in the gob fire, rock friction initiation of electricity, and other sources of spontaneous combustion as a source of ignition is the cause of ignition detonation gob gas-air mixture [87–95].

Yang et al. [93, 96, 97] and Li [98] combined the theoretical analysis of coal spontaneous combustion in the gob, mine pressure, gas flow field in the gob, and gas explosion to analyze the causes of the coupled disaster of spontaneous combustion and explosion in the gob and analyzed the possible range of gas occurrence in the gob with numerical simulation, as shown in Figure 19.

Li [99] realized the experimental environment of coal spontaneous combustion buoyancy effect in the gob and established the corresponding numerical model, systematically studied the gas movement accumulation law of coal spontaneous combustion environment in the gob, and revealed the disaster formation process of gas explosion induced by coal spontaneous combustion in the gob. Qin et al. [100] through theoretical and experimental analysis pointed out that the main product of spontaneous combustion in the gob CO greatly increases the explosive concentration limit range of gas-air mixture, and under the action of fire and wind pressure, the full mixture of CH_4, CO, and fresh air and convective exchange of heat are constantly formed between the firing and nonfiring areas, which easily lead to gas explosion accidents.

The closed gas in the extraction area experiences a critical period when the gas concentration fluctuates between the upper explosive limit and the lower explosive limit [101, 102]. Since gas influx from the extraction zone cannot be detected, some scholars have analyzed gas transport patterns by scaling down experimental devices or numerical simulations [103–107]. These methods mainly focus on the changes of oxygen or methane concentration distribution in the extraction zone.

By making a good estimation of the porosity and permeability of the mined area, the airflow characteristics of the mined area can be accurately assessed, and the distribution of the coal mine gas flow field can be predicted more accurately, which can provide a theoretical basis for the prevention of heavy gas explosions in the mined area [82, 104, 108]. Bell [109] considered the seepage pattern of the mined area as anisotropic three-dimensional according to the porous media theory. Gao et al. [110, 111] established an ideal physical model with spatial characteristics of the gob for the spatial characteristics of the gob and studied the effect of different rock diameters and arrangements on the gas explosion in the gob. The effect of different rock diameters and arrangements on the gas explosion characteristics of the extraction zone was studied.

In Vlasin et al.'s study [112], computational simulations of the explosion of a stoichiometric air-methane mixture in an enclosed space containing obstacles were implemented by changing parameters in the ANSYS-FLUENT application model to customize these data results for a specific gas explosion domain in the form of spatial maps of flame front development and graphs representing the time evolution of characteristic parameters. Li et al. [104] investigated the effect of airflow and gas outflow on the three-dimensional distribution of oxygen and gas concentrations in longwall gobs and mapped the methane-oxygen coupled explosion hazard zone based on modified Coward's triangle and linear coupling zone formulations. Che [1] determined the concentration distribution,

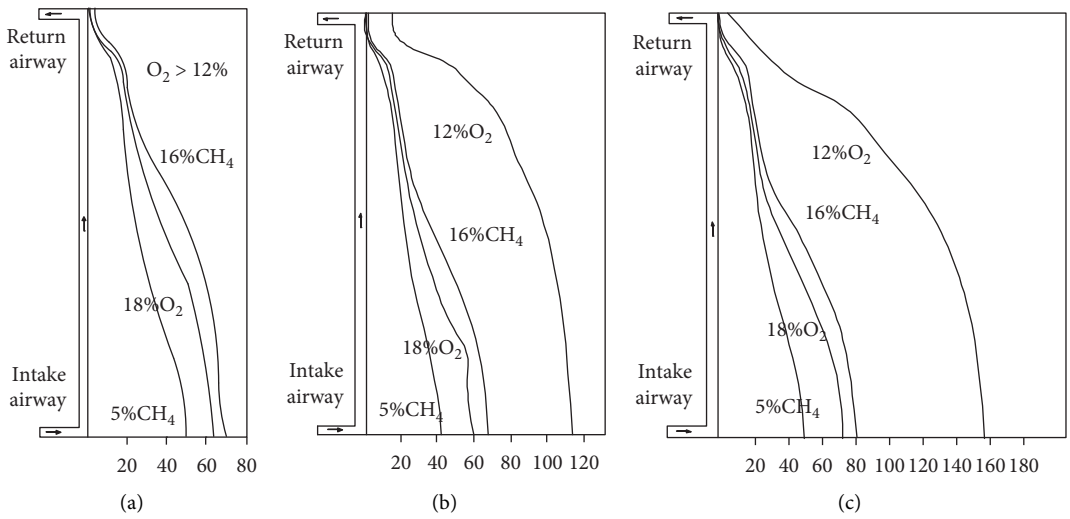

Figure 19: Distribution of gas explosion area in the gob under different advancing distances. (a) $L = 80$ m. (b) $L = 130$ m. (c) $L = 180$ m.

pressure distribution, and temperature distribution of gas in the extraction zone through large-size experiments on gas seepage and heat transfer in the extraction zone. The spatial distribution equations of porosity and permeability of the porous media in the gob were established, and the physical model of the gob and the CFD simulation mathematical model of the gas flow in the gob were improved, and the multifield coupled change law of the three-dimensional seepage field, concentration field, and temperature field of the gas components in the gob before and after the spontaneous combustion of coal relics was derived by the solution. Once the air-gob is closed, the gas components in the closed mine area will change with time. Cheng et al. [113] developed a personal computer-based software package CCMER (Comprehensive Consulting Model for Mine Air Explosion Risk), through which CCEMR can well understand and control the flow field and its change trend in the underground air-gob, and also use the mathematical model of explosion risk assessment to estimate the change from "nonexplosive" state to "explosive" state or from "explosive" state to "nonexplosive" state change time span of the explosion trend analysis model. He [114] and Yi [115] and others analyzed the combustible gas explosion characteristics in the gob from different perspectives. He established a mathematical model of gas explosion in the gob through theoretical analysis and reasonable simplification, simulated the explosion temperature and explosion pressure distribution at different gas concentrations, and derived the effect of gas concentration on multicomponent gas explosion, in which the gas concentration of 10% of the explosion pressure and explosion temperature at 10% gas concentration. Yi used a comprehensive research method combining theoretical analysis and experimental simulation to analyze the combustible gas release law at different temperature bands; finally, according to the explosion ignition source, combined with the gas explosion rheology-sudden change theory, the combustible gas explosion characteristics and influencing factors were qualitatively studied and quantitatively determined, and the control countermeasures of gas explosion accident were proposed.

6. Conclusion and Prospect

After nearly 40 years of development, Chinese scholars have been made with breakthrough progress in the field of flow field in the gob. The understanding of the geomechanical characteristics of the overlying rock layer, the principle of rock destruction, the law of fracture development, and the distribution of porosity and permeability in the gob has been deepened; the research methods have realized the leap from graphical method, filtered flow field, and similar simulation to CFD numerical simulation, and the solution means has transformed to computer independent operation from solely on manual metal relying on the advance of modern computer technology, which not only greatly shortens the calculation time but also improves the accuracy of the resolving results; numerical model equations are also gradually enriched with scholars' exploration, the emergence of linear gas seepage theory, nonlinear gas seepage theory, and ground effect flow-solid coupling gas flow theory which make the model description more closely match the real situation of gas flow in the gob; in terms of research objects, the study has extended from simple U-type to various ventilation systems, and the influence of different ventilation parameters, which are wind speed, negative pressure of extraction, etc., and geological conditions of coal mines, which is coal seam inclination angle on the flow field in the gob, also be considered, and the scope of study is gradually comprehensive. At the same time, the research and development of the flow field in the gob has a pivotal role in the prevention and control of fire and explosion in the gob. China has formed a flow field research and control system with Chinese characteristics, which has significantly improved the effect and safety of gas concentration control at the working face and laid a solid foundation for the safe and efficient production of coal mines.

Nevertheless, there are still many problems in China's coal mining flow field research, which need to continue to be explored in depth:

(1) The geological conditions of the overlying rock layer in the coal gob are characterized by complexity and variability. The interior of the gob is a nonuniform porous medium, and the compaction degree of gangue and coal remains is very large in various places, and the porosity distribution is not uniform. The lithology of the overlying rock layer in the extraction area is an important factor affecting the distribution of pore size inside the extraction area. At present, there is a lack of in-depth research on the mechanical parameters of the overlying rock and the influence of different sizes and directions of the ground stress on the destructive movement of the rock layer, etc. The traditional means of measuring the ground stress destroys the original rock stress, and the measurement results have large errors, so it is necessary to develop rapid and accurate measurement technology for the ground stress. The mining stress has the characteristics of constant movement and change in space and time, and there is a lack of technology and instruments that can monitor the mining stress in a long-term, stably and effectively, and the spatial and temporal evolution of the three-dimensional mining stress has not been completely clarified; the overlying rock structure formed after the mining of working faces with different coal mining methods and parameters, and the stability study under coal mining is not sufficient; it needs to be studied from stress testing, monitoring, and simulation, and it is necessary to systematically carry out research on mining dynamics from stress testing, monitoring, simulation, theoretical modeling, and other aspects to truly reflect the process of rock-breakage movement.

(2) The study of the flow field in the gob is a flow field problem and must be based on fluid theory. The wind flow movement in the extraction area, gas transportation, etc. is the process of evolution with the participation of fluid movement, which cannot be simply simplified as the addition of gas components into and extraction out, but it should focus on its internal connection. The gas outflow and natural fire in the quarry is in the same space, and the two affect each other; however, most scholars will study the two separately, or only the gas outflow considered as a qualitative factor affecting the natural fire. Obviously, Due to the deviation between the actual situations and simulation ones, the field flow study should be integrated to consider and further clarify the internal mechanism and coupling relationship between influence factors.

(3) The numerical simulation method is the mainstream method to study the flow field, the actual gob can provide very limited field test conditions, and with the help of numerical simulation, we can understand the inner mechanism of gas gushing out of the gob; however, the model in the process of application requires a large number of field parameters, and some of which cannot be measured directly and must be determined by fitting with the field observation results to have practical significance, and how to use experimental means and simple measurement work to obtain more accurate and complete parameters of the initial value is also the focus of future research.

Data Availability

The data used to support the findings of this study are included within the article.

Conflicts of Interest

The authors declare that they have no conflicts of interest.

Acknowledgments

This project was supported by the National Natural Science Foundation of China (Grant no. 51904292) and the Natural Science Foundation of Jiangsu Province (Grant no. BK20180655).

References

[1] Q. Che, *Study of Three-Dimensional Multi-Field Coupled Compliance Law of Gas in gob*, China University of Mining and Technology, Beijing, China, 2010.

[2] S. Li, M. Qian, and P. Shi, "Methane migration and accumulation state after seam mining," *Coal Geology & Exploration*, vol. 28, no. 5, pp. 31–34, 2000.

[3] S. Liu, B. Lin, Q. Li, F. Meng, and X. Li, "A research on comprehensive gas control technology for use in gob areas in "three-soft" unstable coal seams with poor permeability," *China Coal*, vol. 2, pp. 91–94, 2010.

[4] G. Wang, "Research progress and prospect of mine pressure appearance theory," *Inner Mongolia Coal Economy*, vol. 11, pp. 29–31, 2016.

[5] M. Qian, X. Miao, and J. Xu, "Theoretical study of key stratum in ground control," *Journal of China Coal Society*, vol. 3, pp. 2–7, 1996.

[6] M. Qian, D. Zhang, and L Li, ""S.-R" Stability for the voussoir beam and ItsApplication," *Ground pressure and strata control*, vol. 11, no. 3, pp. 6–11, 1994.

[7] M. Qian and J. Xu, "Study on the "O Shape" circle distribution characteristics of mining induced fractures in the overlaying strata," *Journal of China Coal Society*, vol. 5, pp. 20–23, 1998.

[8] S. Li, P. Shi, and M. Qian, "Study on dynamic distribution characteristics of elliptical paraboloid zone in overburden mining fracture," *Ground Pressure and Strata Control*, vol. 1, pp. 44–47, 1999.

[9] J. Xu and M. Qian, "Application research and practice of key strata theory of strata control," *China mining magazine*, vol. 6, pp. 54–57, 2001.

[10] S. Li and M. Qian, "The caving characteristics and gas flow pattern of fully mechanized caving goaf," *Ground Pressure and Strata Control*, vol. 3, pp. 76–78, 1997.

[11] M. Qian, *Key Layer Theory of Rock control*, China University of Mining and Technology Press, Xuzhou, China, 2000.
[12] M. Karmis, T. Triplett, C. Haycocks, and G. Goodman, "Mining subsidence and its prediction in the Appalachian coalfield," *International Journal of Rock Mechanics and Mining Science & Geomechanics Abstracts*, vol. 21, no. 2, p. 64, 1984.
[13] Y. Gao, "Four-zone model of rockmass movement and back anlysis of dynamic displacement," *Journal of China Coal Society*, vol. 1, pp. 51–56, 1996.
[14] M. M. Singh and F. S. Kendorski, "Strata Disturbance Prediction for Mining beneath Surface Water and Waste Impoundments," in *Proceedings of the 1st Conference on Ground Control in Mining*, Publ Morgantown: West Virginia University, Morgantown, WV, USA, July 1981.
[15] M. Qian, *Mine Pressure and its Control*, China Coal Industry Publishing House, Beijing, China, 1991.
[16] L. Li, C. Tang, and Z. Liang, "Investigation on overburden strata collapse around coal face considering effect of broken expansion of rock," *Rock and Soil Mechanics*, vol. 11, pp. 3537–3541, 2010.
[17] M. Qian, *Mine Pressure and Rock Control*, China University of Mining and Technology Press, Xuzhou, China, 2010.
[18] G. He, *Mining Subsidence*, China University of Mining and Technology Press, Xuzhou, China, 1991.
[19] V. Palchik, "Bulking factors and extents of caved zones in weathered overburden of shallow abandoned underground workings," *International Journal of Rock Mechanics and Mining Sciences*, vol. 79, pp. 227–240, 2015.
[20] C. Su, M. Gu, X. Tang, and W. Guo, "Experiment study of compaction characteristics of crushed stones from coal seam roof[J]," *Chinese Journal of Rock Mechanics and Engineering*, vol. 31, no. 1, pp. 18–26, 2012.
[21] X. Miao, X. Mao, G. Hu, and Z. Ma, "Research on broken expand and press solid characteristics of rocks and coals," *Journal of Experimental Mechanics*, vol. 3, pp. 64–70, 1997.
[22] J. Zhang, "Study of the mining-induced dynamic expansion of fractured rock mass through physical simulation," *Coal Processing Technology*, vol. 91, pp. 69–72, 2006.
[23] Z. Li, *Study of Coupling of Gas and Spontaneous Combustion in Highly Gassy and Spontaneous Combustion Goafs*, Liaoning Technical University, Fuxin, China, 2007.
[24] Y. Li, *Study on the Nonlinear Gas Seepage Pattern in the Gob Based on the Continuity Fragmentation Coefficient model*, Taiyuan University of Technology, Taiyuan, China, 2018.
[25] C. J. Neate, *Effects of Mining Subsidence on the Permeability of Coal Measures rocks*, University of Nottingham, Nottingham, England, 1980.
[26] T. R. C. Aston, R. N. Singh, and B. N. Whittaker, "The effect of test cavity geology on the in situ permeability of coal measures strata associated with longwall mining," *International Journal of Mine Water*, vol. 2, no. 4, pp. 19–34, 1983.
[27] G. Li, *Fractal and Rock Fragmentation characteristics*, Seismological Press, Beijing, China, 1997.
[28] X. Xia and Q. Huang, "Study of dynamic height of fallout zone based on void ratio," *Journal of Mining and Safety Engineering*, vol. 17, pp. 102–107, 2014.
[29] Y. Wang and X. Yu, "Void rate distribution model in gob," *Safety in Coal Mines*, vol. 44, no. 8, pp. 11–13, 2013.
[30] J. Gao and H. Wang, "Influence of permeability distribution on flow field in mining void areas," *China Safety Science Journal*, vol. 20, no. 3, pp. 81–85, 2010.
[31] C. Zhang, Z. Ti, and Z. Li, "Study on spatial three-dimensional analysis of porosity in the extraction zone," *Journal of Yangtze River Scientific Research Institute*, vol. 29, no. 6, pp. 52–57, 2012.
[32] J. Deng, J. Xu, and H. Wen, "Mathematical modeling of natural fire dynamics in a gob," *Journal of Hunan University of Science & Technology (Natural Science Edition)*, vol. 13, no. 1, pp. 11–16, 1998.
[33] S. Tu, C. Zhang, G. Yang, Q. Bai, and R. Yan, "Research on permeability evolution law of goaf and pressure-relief mining effect," *Journal of Mining and Safety Engineering*, vol. 33, no. 4, pp. 571–577, 2016.
[34] W. Wang, Y. Cheng, H. Liu, C. Fang, X. Li, and R. Zhao, "Permeability model of gob based on sigmoid function and application in the airflow field simulation," *Journal of Mining and Safety Engineering*, vol. 34, no. 6, pp. 1232–1239, 2017.
[35] T. X. Ren and J. S. Edwards, "Three-dimensional computational fluid dynamics modelling of methane flow through permeable strata around a longwall face," *Mining Technology*, vol. 109, no. 1, pp. 41–48, 2000.
[36] Y. Wang, "Three-dimensional spatial dynamic distribution model on porosity and permeability characteristics of porous media in goaf," *Journal of Safety Science and Technology*, vol. 16, no. 10, pp. 42–48, 2020.
[37] X. Kong, *Higher Seepage mechanics*, University of Science and Technology of China Press, Hefei, China, 2010.
[38] S. Lei, L. Wang, L. Jia, and C. Xia, "Relationship between porosity and permeability of granular beds," *Journal of Tsinghua University*, vol. 5, pp. 78–81, 1998.
[39] B. Huang and B. Wang, "Air flow conditions in quarries and harmful gas emergence from gobs," *Coal Science and Technology*, vol. 12, pp. 46–53, 1978.
[40] S. Shi, H. Tang, Y. Liu, and S. Zou, "Computer simulation study on the amount and distribution of air leakage in the gob," *Journal of China Coal Society*, vol. 1, pp. 69–72, 1998.
[41] W. Ding, X. Shi, and G. Zhang, "Computer simulation of "Three-zone" division in gob of fully mechanized caving face," *Mining Safety and Environmental Protection*, vol. 5, pp. 12–14, 2003.
[42] H. Zhu and X. Hui, "Electrical simulation study of ventilation in 1312 coal-free column gob of Changcun Mine," *Henan Coal*, vol. 63, pp. 2–6, 1985.
[43] R. Xu, C. Ge, Y. Liu, and F. Huang, "Physical simulation of wind flow state in a coal-less column mining field," *Coal Engineer*, vol. 81, pp. 11–14, 1990.
[44] H. Yang, Z. Liu, D. Zhu, W. Yang, D. Zhao, and W. Wang, "Study on the fractal characteristics of coal body fissure development and the law of coalbed methane migration of around the stope," *Geofluids*, vol. 2020, Article ID 9856904, 15 pages, 2020.
[45] X. Zhou, J. Wang, G. Lu, Y. Shan, and D. Liang, "Numerical simulation of the temperature field distribution law at the back mining face," *Journal of China Coal Society*, vol. 27, no. 1, pp. 59–63, 2002.
[46] S. Zhou and Z. Sun, "Theory of coal seam gas flow and its application," *Journal of China Coal Society*, vol. 31, pp. 24–37, 1965.
[47] X. Tan and J. Yuan, "Study of real gas seepage equation in coal seam of mine," *Journal of Chongqing Jianzhu University*, vol. 91, pp. 106–112, 1986.
[48] C. Yu, X. Xian, and X. Tan, "Study on the theory of coal seam gas flow and seepage control equations," *Journal of Chongqing University*, vol. 65, pp. 1–10, 1989.

[49] N. Yang and H. Li, "Study of gas flow law around penetration borehole," *Coal Technology*, vol. 29, no. 12, pp. 93-94, 2010.
[50] P. Sun, "Study on the flow law of coal seam gas flow field," *Journal of China Coal Society*, vol. 4, pp. 74–82, 1987.
[51] M. Liu, "Coal seam gas flow model on power law," *Journal of Jiaozuo Mining Institute*, vol. 19, pp. 36–42, 1994.
[52] Y. Deng, H. Xie, R. Huang, and C. Liu, "Law of gas nonlinear flow in low permeability pore-fissure media," *Advanced Engineering Sciences*, vol. 38, no. 4, pp. 1–4, 2006.
[53] Z. Zhang and B. Cheng, "Non-linear seepage in gas-bearing coal bodies. Nonlinear seepage model for gas-bearing coal bodies," *Journal of China University of Mining and Technology*, vol. 44, no. 3, pp. 453–459, 2015.
[54] B. Cheng, "Research status and development direction of seepage model for gas-bearing coal," *Mining Safety and Environmental Protection*, vol. 44, no. 5, pp. 93–97, 2017.
[55] J. Liu, D. Wang, L. Wang, and J. Gao, "A coupled flow-solid model for gas extraction considering Klinkenberg effect and its application," *China Safety Science Journal*, vol. 26, no. 12, pp. 92–97, 2016.
[56] H. Wang, Y. Du, X. Xian, and P. Luo, "Influence of geo-electric field on gas seepage characteristics in coal," *Journal of Chongqing University*, vol. 51, pp. 22–24, 2000.
[57] P. Sun, *The Solid-Gas Coupling Theory of Coalbed Methane Cross-Flow and its Computer simulation*, Chongqing University, Chongqing, China, 1998.
[58] Z. Yu, S. Yang, Y. Qin, X. Hu, and J. Cheng, "Experimental study on the goaf flow field of the "U + I" type ventilation system for a comprehensive mechanized mining face," *International Journal of Mining Science and Technology*, vol. 25, no. 6, pp. 1003–1010, 2015.
[59] Y. Tao, R. Qin, and W. Pang, "Numerical simulation of goaf flow field for U-type fully mechanized working face," *Safety in Coal Mines*, vol. 45, no. 1, pp. 186–188, 2014.
[60] Y. Tian, C. Yang, Q. Sun, C. Chang, and Z. Guo, "Air leakage law in goaf of the working face using U-type ventilation," *Coal Engineering*, vol. 52, no. 12, pp. 132–136, 2020.
[61] Q. Ma, W. Li, Y. Liu, L. Zhang, C. Sang, and E. Wang, "Contrastive analysis of gas emission of residual coal in goaf under U shape and U + I shape ventilation based on moving coordinate," *Safety In Coal Mines*, vol. 48, no. 1, pp. 164–167, 2017.
[62] X. Wu, G. Rui, and H. Zhang, "Numerical simulation of flow field in gob with U-type and U+L type ventilation modes," *Mining Safety and Environmental Protection*, vol. 42, no. 3, pp. 24–27, 2015.
[63] Y. Yu, R. Qin, and Y. Cui, "Numerical simulation of gas field and air leakage field in gob with Y-type ventilation," *Safety In Coal Mines*, vol. 44, no. 2, pp. 25–28, 2013.
[64] M. Yang, J. Gao, and P. Feng, "Numerical simulation of the gas distribution in the gobs of U-type and Y-type ventilation mining working faces," *Journal of Safety and Environment*, vol. 5, pp. 227–230, 2012.
[65] C. Zhao, L. Zhang, and Y. Liu, "Research on gas gushing pattern and over-limit management in the gob under partial Y ventilation," *Coal Science and Technology*, vol. 47, no. 4, pp. 127–133, 2019.
[66] Z. Li and J. Li, "Numerical simulation calculation of flow field in W-type ventilation fallout gob," *Journal of Liaoning Technical University*, vol. 6, pp. 816–818, 2007.
[67] C. Cheng and C. Xin, "Simulation study of gas transport law in U- and W-type ventilation fallout areas[J]," *Mining Research and Development*, vol. 36, no. 12, pp. 80–83, 2016.
[68] K. Wang and W. Wu, "Numerical simulation of flow field and gas transport in J-type ventilated general release gob[J]," *Journal of China University of Mining and Technology*, vol. 36, no. 3, pp. 277–282, 2007.
[69] J. Gao and W. Sun, "Study on the distribution law of air leakage and gas concentration in the mining void area of J-type ventilation working face," *Coal Engineering*, vol. 50, no. 1, pp. 132–136, 2018.
[70] F. Lu and X. Zhang, "Research on porosity distribution laws of goaf in inclined extra-thick coal seam," *Journal of Safety Science and Technology*, vol. 16, no. 8, pp. 119–124, 2020.
[71] M. Yang and F. Zhang, "Study on influence of coal seam dip angle to the air flow field and gas distribution in goaf," *Journal of Safety Science and Technology*, vol. 11, pp. 34–40, 2014.
[72] P. Zhou, *Study on the Spatial and Temporal Evolution Mechanism of Oxidation Warming of Coal Relics in the gob*, University of Science and Technology Beijing, Beijing. China, 2017.
[73] Q. Chen, "Research on indexes for division of "three zones" in gobs," *Mining safety and environmental protection*, vol. 3, pp. 12–15, 1997.
[74] S. Liu, S. Jiang, D. Wang, W. Zhang, and Y. Li, "Study on variation law of spontaneous combustion "three zones" in goaf[," *Coal Science and Technology*, vol. 49, pp. 74–78, 2011.
[75] J. Huang, S. Yang, T. Chu, Q. Xu, and J. Huang, "Numerical simulation on air leakage flow field in spontaneous combustion three zone of goaf," *Coal Science and Technology*, vol. 37, no. 6, pp. 60–63, 2009.
[76] M. Yu, Z. Huang, and C. Yue, "Experimental study on the classification of "three zones" of spontaneous combustion in the gob by oxygen index," *Journal of Xi'an Mining Institute*, vol. 18, no. 1, pp. 40–44, 1998.
[77] K. Deng, *Research on the Method of Dividing the Three Belts in the Gob of Header Mining Face*, Anhui University of Science and Technology, Huainan, China, 2012.
[78] Y. Zhang, K. Niu, W. Du, J. Zhang, H. Wang, and J. Zhang, "A method to identify coal spontaneous combustion-prone regions based on goaf flow field under dynamic porosity," *Fuel*, vol. 288, Article ID 119690, 2020.
[79] Y. Zheng, Q. Li, G. Zhang et al., "Effect of multi-component gases competitive adsorption on coal spontaneous combustion characteristics under goaf conditions," *Fuel Processing Technology*, vol. 208, Article ID 106510, 2020.
[80] Q. Zuo, Y. Wang, and J. Li, "Study on the oxidation and heating characteristics of residual coal in goafs under different air-leakage conditions," *Thermal Science*, vol. 314, 2020.
[81] G. Wang, H. Xu, M. Wu, Y. Wang, R. Wang, and X. Zhang, "Porosity model and air leakage flow field simulation of goaf based on DEM-CFD," *Arabian Journal of Geoences*, vol. 11, no. 7, pp. 1–17, 2018.
[82] Y. Lu and B. Qin, "Identification and control of spontaneous combustion of coal pillars: a case study in the Qianyingzi Mine, China," *Natural Hazards*, vol. 75, no. 3, pp. 2683–2697, 2015.
[83] K. Wang, H. Tang, F. Wang, Y. Miao, and D. Liu, "Research on complex air leakage method to prevent coal spontaneous combustion in longwall goaf," *PLoS One*, vol. 14, no. 3, Article ID e0213101, 2019.
[84] B. Qin, H. Wang, J. Yang, and L. Liu, "Large-area goaf fires: a numerical method for locating high-temperature zones and assessing the effect of liquid nitrogen fire control," *Environmental Earth Sciences*, vol. 75, no. 21, pp. 1–14, 2016.

[85] J. Zhang, H. Zhang, T. Ren, J. Wei, and Y. Liang, "Proactive inertisation in longwall goaf for coal spontaneous combustion control-A CFD approach," *Safety Science*, vol. 113, no. 1, pp. 445–460, 2019.

[86] Y. Wang, X. Zhang, Y. Sugai, and K. Sasaki, "A study on preventing spontaneous combustion of residual coal in a coal mine goaf," *Journal of Geological Research*, vol. 2015, Article ID 712349, 8 pages, 2015.

[87] X. Chang, *Research on the Law of Gas Combustion (Explosion) Induced by Spontaneous Combustion of Coal in a Gob and Prevention*, China University of Mining and Technology, Xuzhou, China, 2013.

[88] Z. Liu, C. Hou, J. Zhang, and J. Zhu, "Analysis of the causes of gas explosion in gobs," *Zhongzhou Coal*, vol. 6, pp. 60-61, 2005.

[89] S. Cheng, C. Zhu, and J. Cheng, "Research on gas explosion in gob and protection technology," *Shanxi Coal*, vol. 4, pp. 49-50, 2003.

[90] S. Cheng and C. Zhu, "Exploration on the causes of gas explosion in gobs," *Shanxi Coal*, vol. 74, pp. 47–50, 1998.

[91] T. Yu, *Research on the Mechanism and Technology of Combined Gas and Coal Spontaneous Combustion Disaster Prevention and Control in Gob*, University of Science and Technology of China, Hefei, China, 2014.

[92] Y. Wu, J. Wang, Y. He, and J. Wu, "Analysis of the causes of spontaneous combustion and explosion in gobs and comprehensive treatment technology," *Mining and Processing Equipment*, vol. 35, no. 8, pp. 40-41, 2007.

[93] Y. Yang, J. Meng, T. Wang, and Y. Gao, "Analysis of the causes of large gas explosion accidents in coal mining workings," *Journal of China Coal Society*, vol. 7, pp. 734–736, 2007.

[94] Z. Ren, *Study on Combustion and Explosion Coupled Hazards in Gob of High Gas Prone Coal Seam*, Xi'an University of Science and Technology, Xi'an, China, 2017.

[95] J. Cheng, C. Qi, and S. Li, "Modelling mine gas explosive pattern in underground mine gob and overlying strata," *International Journal of Oil, Gas and Coal Technology*, vol. 22, no. 4, pp. 554–577, 2019.

[96] Y. Yang, J. Meng, T. Wang, and Y. Gao, "Analysis of the causes of mega gas explosion in coal mining workings," *Journal of China Coal Society*, vol. 47, pp. 734–736, 2007.

[97] Y. Yang and H. Zhao, "Classification of gas explosion areas in coal gobs," *Coal Mine Safety*, vol. 45, no. 5, pp. 167–169, 2014.

[98] Y. Li, *Study on Gas Explosion hazard Area in Mining Void Area of High Gas Working face*, Shandong University of Science and Technology, Qingdao, China, 2018.

[99] L. Li, *Study on Gas Transport Accumulation Law of Coal Spontaneous Combustion Environment in Mining Hollow Area*, China University of Mining and Technology, Xuzhou, China, 2020.

[100] B. Qin, L. Zhang, D. Wang, and Y. Yao, "Mechanism and control technology of gas detonation by spontaneous combustion of coal in gob," *Journal of China Coal Society*, vol. 34, no. 2, pp. 1655–1659, 2009.

[101] W. Song, J. Cheng, W. Wang et al., "Underground mine gas explosion accidents and prevention techniques-an overview," *Archives of Mining Sciences*, vol. 66, no. 2, pp. 297–312, 2021.

[102] J. Cheng, W. Luo, Z. Zhao et al., "Controlling coal spontaneous combustion fire in longwall gob using comprehensive methods-a case study," *Mining, Metallurgy & Exploration*, vol. 38, no. 3, 2021.

[103] G. Wang, Y. Xu, and H. Ren, "Intelligent and ecological coal mining as well as clean utilization technology in China: r," *International Journal of Mining Science and Technology*, vol. 29, no. 2, pp. 161–169, 2019.

[104] Y. Li, H. Su, H. Ji, and W. Cheng, "Numerical simulation to determine the gas explosion risk in longwall goaf areas: a case study of Xutuan Colliery," *International Journal of Mining Science and Technology*, vol. 30, no. 6, pp. 875–882, 2020.

[105] X. Zhai, B. Wang, S. Jiang, and W. Zhang, "Oxygen distribution and air leakage law in gob of working face of U+L ventilation system," *Mathematical Problems in Engineering*, vol. 2019, Article ID 8356701, 10 pages, 2019.

[106] T. Fan, G. Zhou, and J. Wang, "Preparation and characterization of a wetting-agglomeration-based hybrid coal dust suppressant," *Process Safety and Environmental Protection*, vol. 113, pp. 282–291, 2018.

[107] C. Wang, S. Yang, and X. Li, "Simulation of the hazard arising from the coupling of gas explosions and spontaneously combustible coal due to the gas drainage of a gob," *Process Safety and Environmental Protection*, vol. 118, pp. 296–306, 2018.

[108] S. Li and Z. An, "Mechanism and prevention technology of gas explosion caused by coal spontaneous combustion in goaf," *Safety in Coal Mines*, vol. 31, no. 12, pp. 24–27, 2014.

[109] J. Bell, "Fluid dynamics in porous media," 1983.

[110] K. Gao, S. Li, Y. Liu, J. Jia, and X. Wang, "Effect of flexible obstacles on gas explosion characteristic in underground coal mine," *Process Safety and Environmental Protection*, vol. 149, pp. 362–369, 2021.

[111] K. Gao, S.-n. Li, R. Han et al., "Study on the propagation law of gas explosion in the space based on the goaf characteristic of coal mine," *Safety Science*, vol. 127, Article ID 104693, 2020.

[112] N. Vlasin, V. Pasculescu, M. C. Suvar, D. Florea, and E. Chiuzan, "First romanian computational simulation of air-methane mixture explosion," in *Proceedings of the International Multidisciplinary Scientific GeoConference SGEM*, Albena, Bulgaria, June 2017.

[113] J. Cheng, J. Mei, S. Peng, C. Qi, and Y. Shi, "Comprehensive consultation model for explosion risk in mine atmosphere-CCMER," *Safety Science*, vol. 120, pp. 798–812, 2019.

[114] J. He, *Study on the Explosive Characteristics and its Numerical Simulation of Multi-Component Gas in Goaf*, Liaoning Technical University, Fuxin, China, 2008.

[115] X. Yi, *Characteristic Research and Control Method on the Gas Explosion*, Xi'an University of Science and Technology, Xi'an, China, 2006.

Hindawi
Shock and Vibration
Volume 2021, Article ID 9985774, 16 pages
https://doi.org/10.1155/2021/9985774

Research Article

Damage Evolution and Circumferential Strain Distribution Characteristics of the Bolt-Supported Cavern under Multiple Explosion Sources

Taotao Wang,[1] Ansheng Cao,[2] Weiliang Gao,[1] Guangyong Wang,[1,2] and Xiaowang Sun[3]

[1]*Huanghe Jiaotong University, Jiaozuo 454950, China*
[2]*School of Civil Engineering, Henan Polytechnic University, Jiaozuo 454000, China*
[3]*School of Mechanical Engineering, Nanjing University of Science and Technology, Nanjing 210094, China*

Correspondence should be addressed to Guangyong Wang; wgy2003@mail.ustc.edu.cn

Received 30 March 2021; Accepted 11 June 2021; Published 21 June 2021

Academic Editor: Jianwei Cheng

The impact of multiple explosion sources on the safety of the underground cavern is enormous. Based on a similarity model test, the finite element software LS-DYNA3D was utilized to analyze the damage evolution and circumferential strain distribution characteristics of the bolt-supported cavern under the seven combinations of concentrated charge explosion sources in three places, including the side of the vault, side arch, and sidewall. The accuracy of the simulation results is verified by comparing them with test results. The research results indicate that the damage of the surrounding rock is mainly caused by the tensile stress wave reflected from the free surfaces and the superposition of the tensile stress wave. The damage of the surrounding rock in the cases of multiple explosion sources is not a simple superposition of that in the cases of a single explosion source. The peak circumferential stress and damage of the surrounding rock in the middle of two explosion sources are significantly greater than that of the cases of the corresponding single explosion source. In the seven cases, the peak circumferential strain of the cavern wall changes from tensile to compressive from the vault to the spandrel. When the explosion occurs on the sidewall, the peak circumferential strain of the floor is tensile.

1. Introduction

Underground engineering has been widely used in civil and military fields in recent years because of its advantages such as large storage space, little impact on the environment, and good concealment. However, underground engineerings are vulnerable to explosions, such as blasting excavation and demolition, terrorist attacks by bombs, and there are usually multiple explosion sources when such explosions occur. The surrounding rock is disturbed during the explosion, and the stability of the underground cavern is significantly reduced [1]. Therefore, it is of great practical significance to study the damage and strain distribution characteristics of underground caverns under multiple explosion sources.

The explosion may occur inside or outside the underground cavern. During the construction period, underground projects are prone to internal explosions, but in the operation period, due to strict inspection and monitoring, the possibility of internal explosions in underground projects is very small. Many scholars have studied the effects of internal explosions on underground caverns. Zhu et al. [2] studied the influence of internal explosions with different charge densities on the dynamic response and stress wave propagation of the surrounding rock caused by the explosion in the tunnel, and found that the charge density has a great influence on the dynamic response of the surrounding rock in an uncoupled underground explosion. Employing test and numerical methods, many scholars [3–6] have studied the dynamic response of the cavern under the internal gas explosion. On the other hand, the explosion outside the cavern cannot be predicted in advance, which is more likely to happen and cause greater damage to the

cavern. In this research field, due to the large demand for explosives, high test risk, and high cost, there are few records of the field test. The U.S. Army Corps of Engineers conducted a large-scale explosion test in sandstone to study the damage of unlined tunnels, and Hendron [7] derived the classic peak particle velocity (PPV) damage criterion for tunnels based on this. In seven coal mines, Singh [8] studied the influence of large-scale blasting in open-pit coal mines on the stability of underground working faces in adjacent coal mines, and proposed the vibration threshold to ensure the safety of underground working faces. Through field tests, Xia et al. [9] studied the influence of blasting excavation on the surrounding rock and lining system of the adjacent existing tunnel, and found that the damage degree of the surrounding rock increases linearly with the PPV. Xu et al. [10] studied the dynamic response of deep rock mass under blasting load on-site and found that deep rock mass is more vulnerable to damage than shallow rock mass under blast load. Rajmeny et al. [11] studied the phenomenon of spalling and collapse of the surrounding rock of cavern through the field blasting test.

The reduced centrifugal model technology can use fewer explosives to simulate large-scale explosions under high gravitational acceleration [12, 13]. De et al. [14, 15] used geotechnical centrifuges to study the influence of surface explosion on underground tunnels through physical models. The similarity model test can be optimized in the early stage, and has the characteristics of saving time and energy. Using the geotechnical engineering anti-blast structure model [16], Gu et al. [17–20] studied the anti-blast performance of underground caverns with different charging and anchoring methods through similarity model tests.

In recent years, with the enhancement of computer computing power, numerical simulation has been widely used in this field. Using finite element software ABAQUS, Chang et al. [21] studied the failure mode of the cement mortar cavern reinforced with aluminum bars under top explosion. Mussa et al. [22] studied the damage behavior of the underground box tunnel caused by a vehicle bomb by using ANSYS/LS-DYNA. Through discrete element software UDEC, many scholars [23–25] studied the propagation of stress waves generated by the explosion in the jointed rock mass and found that the buried depth of underground cavern and joint properties including stiffness, spacing, and dip angle have significant effects on the propagation of stress waves. Deng et al. [26] used UDEC to simulate the damage of an existing circular tunnel under an external explosion, and analyzed the damage of the tunnel through the PPV of the tunnel surface. It was found that the bolt can improve the stability of the tunnel by changing the vibration form of particle velocity instead of reducing the PPV. Many scholars [27–29] used numerical simulation methods to analyze the damage of underground caverns under the explosions by analyzing the PPV, displacement, and acceleration of the surrounding rock.

The research on the influence of external explosions on the cavern has been very comprehensive. Unfortunately, such research excessively focuses on the single explosion source, and the case of multiple explosion sources is very rare. However, the case of multiple explosion sources is more common in practice. Therefore, based on a similarity model test, the finite-element software LS-DYNA is used to build an underground cavern model that encounters multiple explosion sources. The research results can provide references for the anti-explosion design of underground caverns.

2. Overview of the Test Model

The numerical calculation model is taken from the similarity test model, and the test device has been recorded by Wang et al. [30], so only a brief overview is given here. The model test simulates the situation where a cavern with a buried depth of 15 m and a span of 7 m encounters an explosion above the vault. The density, length, and stress similarity coefficient are determined to be $K_\rho = 0.67$, $K_l = 0.09$, and $K_\sigma = 0.06$ according to the Froude scale method. After similarity conversion, the width, height, and thickness of the model are 2.4 m, 2.3 m, and 1.5 m, respectively, and the span of the cavern is 0.6 m. The cavern is reinforced by a single row of full-length bonded rock bolts with spacing and row spacing of 4 cm and a length of 24 cm. The surrounding rock is considered as class III rock mass, and the proportion of sand, cement, water, and accelerator is 15 : 1 : 1.6 : 0.0166. The cavern model is fixed by four rigid lateral limiting devices that can move forward and backward. To eliminate the reflection of the stress wave on the side, aluminum wave elimination plates with a hole ratio of up to 50% are set on the anti-explosion surface of each device. The rock bolts are simulated by aluminum rods. In the model test, a 100 g TNT explosion occurs at 0.83 m above the vault of the cavern, as shown in Figure 1.

3. Numerical Model

3.1. Finite Element Model. To improve the calculation efficiency, considering the symmetry of the test model, the numerical calculation simplified it to a geometric model with a length of 2.4 m, a width of 0.4 m, a height of 2.3 m, and a span of 0.6 m. According to the distance from the explosion source to the vault in the test model, TNT explosion sources, each with a mass of 50 g, are positioned at the side of the vault, side arch, and sidewall in the numerical calculation model, i.e., top explosion, side arch explosion, and sidewall explosion, as shown in Figure 2. The seven calculation cases include a single explosion source, double explosion sources, and three explosion sources, as shown in Table 1.

3.2. Material Model and Parameters. The left, right, and lower boundaries of the model are set as nonreflective boundary conditions to meet the infinite boundary conditions in the actual situation. Due to the shallow burial depth of the cavern, the self-weight of the rock mass is ignored. The rock mass and explosives are set as 3D Solid164, and the rock bolt is set as Beam161. The model is divided by a grid of 1 cm in size.

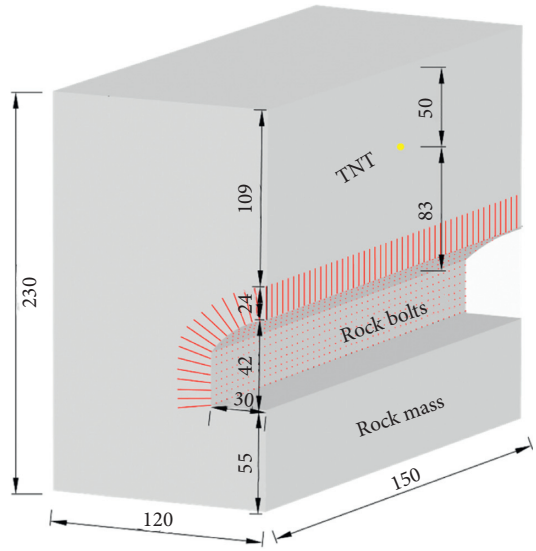

Figure 1: Dimensions for the test model (unit: cm).

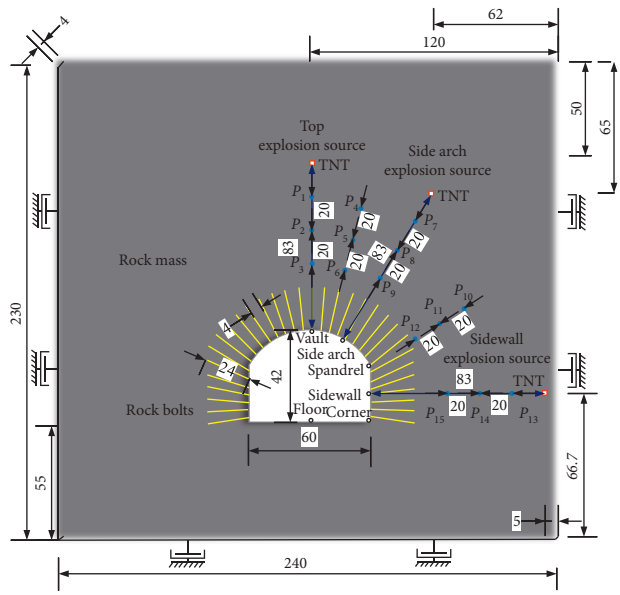

Figure 2: Model of numerical analysis (unit: cm).

Table 1: Seven cases.

Number of explosion sources	One			Two			Three
Case	1	2	3	4	5	6	7
Explosion Source location	Top	Side arch	Sidewall	Top Side arch	Top Sidewall	Side arch Sidewall	Top Side arch Sidewall

3.2.1. Surrounding Rock. To date, scholars have developed many constitutive models that can represent the surrounding rock damage, such as the HJC model, TCK model, CSCM model, RHT material model, and so on. After consulting the literature, it is found that the HJC model fails to fully consider the tensile damage P of the material when describing the material damage [31]. The TCK model can well describe the tensile damage of the material, but it cannot indicate the compression damage [32]. The CSCM model can only describe the tensile and compressive damage of concrete under low confining pressures [33]. The RHT model improves the above shortcomings and can comprehensively reflect the compression and tensile damage, strain rate effect, strain hardening, softening, and failure

phenomena of the surrounding rock [34, 35]. Because the surrounding rock in this paper needs to consider the tensile and compressive damage at the same time, after a lot of attempts and comparative analysis, the RHT model is finally selected to simulate the rock mass.

The RHT model is divided into three stages: elastic stage, linear strengthening stage, and damage softening stage, as shown in Figure 3(a). When the equivalent stress $\overline{\sigma} \le \sigma_{\text{elastic}}$, the model is in the elastic stage, and the elastic limit surface is the starting point of material plastic deformation. When $\sigma_{\text{elastic}} \le \overline{\sigma} \le \sigma_{\text{fail}}$, the material is in the linear strengthening stage, which is used to characterize the strain hardening effect of the material. In this stage, the material produces plastic deformation and transitions from the elastic limit surface to the failure surface. When $\overline{\sigma} \ge \sigma_{\text{fail}}$, the material is in the damage softening stage, and the failure stress of the material decreases to the residual stress with the accumulation of damage. The above three stages involve the equations of elastic limit surface, failure surface, and residual strength surface, which are related to pressure and are used to describe the variation law of material strength under impact loading, as shown in Figure 3(b).

The equivalent force strength of failure surface σ_{fail} is the equation of normalized pressure P, Lode angle θ, and strain rate $\dot{\varepsilon}$.

$$\sigma_{\text{fail}} = Y^*_{TXC}(P) R_3(\theta) F_{\text{rate}}(\dot{\varepsilon}), \tag{1}$$

where Y^* TXC(P) is the compressive meridian strength, $R_3(\theta)$ is the Lode angle factor, and $F_{\text{rate}}(\dot{\varepsilon})$is the dynamic enhancement factor of strain rate.

$$Y^*_{TXC}(P) = A\left[P^* - P^*_{\text{spall}} F_{\text{rate}}(\dot{e})\right]^N. \tag{2}$$

$$F_{\text{rate}}(\dot{\varepsilon}) = \begin{cases} \left(\dfrac{\dot{\varepsilon}}{\dot{\varepsilon}_0}\right)^{\alpha} > \dfrac{f_c}{3}, \ \dot{\varepsilon}_0 = 30 \times 10^{-6} s^{-1}, \\ \left(\dfrac{\dot{\varepsilon}}{\dot{\varepsilon}_0}\right)^{\delta} > \dfrac{f_c}{3}, \ \dot{\varepsilon}_0 = 3 \times 10^{-6} s^{-1}, \end{cases} \tag{3}$$

$$\begin{aligned} R_3(\theta) = {} & 2\left(1 - Q_2^2\right)\cos\theta + (2Q_2 - 1) \times \left[4\left(1 - Q_2^2\right)\cos^2\theta + 5Q_2^2 - 4Q_2\right]^{1/2} g \\ & \times \left[4\left(1 - Q_2^2\right)\cos^2\theta + (1 - 2Q_2)^2\right]^{-1}. \end{aligned} \tag{4}$$

$$\theta = \frac{\cos^{-1}\left(3\sqrt{3}\, J_3 / 2 J_2\right)}{3}, \theta \in \left[0, \frac{\pi}{3}\right]. \tag{5}$$

$$Q_2 = \frac{r_t}{r_c} = Q_{2,0} + B_Q P^*, \tag{6}$$

where P^*_{spall} is the fracture strength of the normalized layer; r_t,r_c are, respectively, the deviator stress at the meridian; B_Q is the pressure influence parameter; J_2 is the second invariant, and J_3 is the third invariant; A, N, α, δ, $Q_{2,0}$are material constants.

The elastic limit surface is derived from the failure stress of the failure surface, shown as follows:

$$\sigma^*_{\text{el}} = \sigma^*_{\text{eq}} F_{\text{el}} F_{\text{cap}}. \tag{7}$$

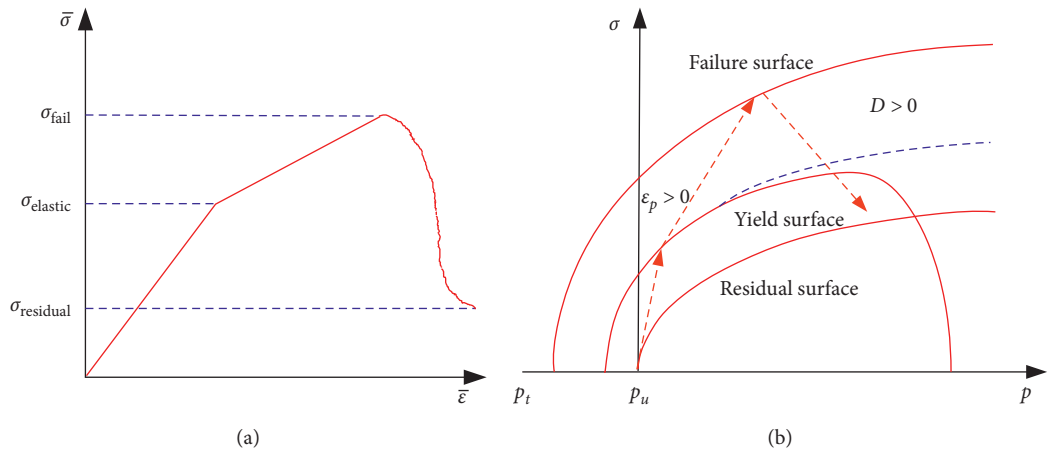

FIGURE 3: The RHT model. (a) Three phases of the RHT constitutive. (b) Stress limit surfaces and loading scenarios.

Among them, F_{elastic} is the elastic scaling function, and F_{cap} is the "cap" function.

$$F_{el} = \begin{cases} R_c, & P \geq \dfrac{f_{c,\text{el}}}{3}, \\ \dfrac{\left(P + f_{t,\text{el}}/3\right)}{\left(\left(f_{c,\text{el}}/3\right) + \left(f_{t,\text{el}}/3\right)\right)} R_c + \dfrac{\left(P - f_{c,\text{el}}/3\right)}{\left(\left(-f_{t,\text{el}}/3\right) + \left(f_{c,\text{el}}/3\right)\right)} R_t, & \dfrac{-f_{t,\text{el}}}{3} < P < \dfrac{f_{c,\text{el}}}{3}, \\ R_t, & P \leq \dfrac{-f_{t,\text{el}}}{3}, \end{cases} \tag{8}$$

$$F_{\text{cap}} = \begin{cases} 1, & P \leq P_u = \dfrac{f_c}{3}, \\ \sqrt{1 - \left[\dfrac{(P - P_u)}{(P_0 - P_u)}\right]^2}, & P_u < P < P_0, \\ 0, & P \leq P_u = \dfrac{f_c}{3}, \end{cases} \tag{9}$$

where R_t and R_c are material parameters; $f_{t,\text{el}}$ is the elastic limit of uniaxial tensile; $f_{c,\text{el}}$ is the elastic limit of uniaxial compression; $P_0$is the pressure when the pore begins to compress; andf_c is the uniaxial compressive strength.

The material does not cumulative damage in either the elastic stage or the linear strengthening stage. Only when the stress exceeds the failure stress and enters the damage softening stage, the damage starts to accumulate. The damage index D is the ratio of cumulative equivalent plastic strain increment to ultimate failure equivalent plastic strain.

$$0 \leq D = \sum \frac{\Delta\varepsilon_P}{\varepsilon_P^{\text{failure}}} \leq 1, \tag{10}$$

$$\varepsilon_P^{\text{failure}} = D_1\left(P* - P_{\text{spall}}^*\right)^{D_2} \geq \varepsilon_p^m, \tag{11}$$

where $\Delta\varepsilon_P$ is equivalent plastic strain increment, D_1 and D_2 are material parameters, and ε_p^m is the minimum equivalent plastic strain when the material fails.

When the stress exceeds the failure stress, the material is completely destroyed without deflection stress. However, due to the effect of confining pressure, there is friction between the broken parts, and the material can continue to bear the shear stress. The RHT model introduces the phenomenon of residual stress surface expression, and its equivalent stress intensity is

$$\sigma_{\text{residual}} = A_f\left(P^*\right)^{n_f}, \tag{12}$$

where A_f is the residual stress intensity parameter and n_f is the residual stress intensity index.

In this paper, several parameters of the RHT model are obtained by tests [30], and the test parameters are referenced from the literature [36] and adjusted appropriately, as shown in Table 2.

3.2.2. TNT. In this paper, the highly explosive material model ∗MAT_HIGH_EXPLOSIVE_BURN [37] is used to describe TNT explosives whose detonation is defined by the Jones-Wilkins-Lee (JWL) equation of state [38].

The relationship between pressure and specific volume is as follows:

$$P = A\left(1 - \frac{\omega}{R_1 V}\right)e^{-R_1 V} + B\left(1 - \frac{\omega}{R_2 V}\right)e^{-R_2 V} + \frac{\omega E_0}{V}, \tag{13}$$

where A, B, R_1, R_2, and ω are material constants; P is the pressure; V is the relative volume; and E_0 is the initial specific internal energy.

3.2.3. Rock Bolts. In the test, aluminum bars are employed to simulate the rock bolts. Considering the elastic-plastic properties of aluminum bars, the isotropic elastic-plastic model ∗MAT_PLASTIC_KINEMATIC [37] is used to describe the rock bolts in the calculation model. Table 3 lists the input parameters for explosives and rock bolts in LS-DYNA. The parameters of the rock bolts are obtained from the test [30], and the explosive parameters are referenced from the literature [38].

4. Results and Discussion

4.1. Comparative Analysis of Test and Numerical Results. To verify the accuracy of the simulation results, the stress time curves of the simulated and test models in the same position in case 1 are compared. Figure 4 shows the stress time curves of P_1, P_2, and P_3 measuring points (as shown in Figure 2) at 0.2 m, 0.4 m, and 0.6 m directly below the explosion source, where the positive value is the compressive stress and the negative value is the tensile stress. It can be seen from Figure 4 that several stress time curves first rise rapidly to the peak value, then gradually decrease and tend to be stable. The peak pressure of three measuring points in the numerical simulation is slightly larger than the peak of measuring points at the same positions in the test, but it is still within the same order of magnitude. However, the stress curves in the test rise later than those in the simulation, indicating that the stress in the test reaches the measuring point later than it does in the simulation.

The stress wave attenuation formula in *Fundamentals of protective design for conventional weapons* [39] is widely used in the study of stress wave propagation characteristics. The formula is as follows:

$$P_{\max} = c\left(\frac{R}{W^{1/3}}\right)^{-n}, \tag{14}$$

where $P_{\max}$ is the peak pressure; $R/W^{1/3}$ is the scaled distance; R is the distance from the explosion source; W is the charge masses; c is a typical value, which depends on the properties of explosives and materials; and n is the attenuation factor, which mainly depends on the properties of materials.

Table 2: The parameters for the RHT model of the rock mass.

Parameter	Value
Mass density RO (kg/m^3)	1700
Initial porosity ALPHA	0.0
Crush pressure PEL (GPa)	0.0
Compaction pressure PCO (GPa)	0.36
Hugoniot polynomial coefficient $A1$ (GPa)	2.1162
Hugoniot polynomial coefficient $A2$ (GPa)	2.3748
Hugoniot polynomial coefficient $A3$ (GPa)	0.5424
Parameter for polynomial EOS $B0$	1.22
Parameter for polynomial EOS $B1$	1.22
Parameter for polynomial EOS $T1$ (GPa)	2.1162
Parameter for polynomial EOS $T2$ (GPa)	0.0
Elastic shear modulus SHEAR (GPa)	1.002
Compressive strength FC (MPa)	2.1
Relative tensile strength FT*	0.1
Relative shear strength FS*	0.18
Failure surface parameter A	1.6
Failure surface parameter N	0.61
Lode angle dependence factor $Q0$	0.6805
Lode angle dependence factor B	0.0105
Porosity exponent NP	0.0
Reference compressive strain-rate EOC	$3.0E-11$
Reference tensile strain rate EOT	$3.0E-12$
Break compressive strain rate EC	$3.0E+19$
Break tensile strain rate ET	$3.0E+19$
Compressive strain rate dependence exponent BETAC	0.032
Tensile strain rate dependence exponent BETAT	0.036
Volumetric plastic strain fraction in tension PTF	0.001
Compressive yield surface parameter GC*	0.53
Tensile yield surface parameter GT*	0.7
Erosion plastic strain EPSF	2.0
Shear modulus reduction factor XI	0.5
Damage parameter $D1$	0.04
Damage parameter $D2$	1.0
Minimum damaged residual strain EPM	0.01
Residual surface parameter AF	1.6
Residual surface parameter NF	0.61
Gruneisen gamma GAMMA	0.0

Figure 5 shows the fitting curve of the peak pressure and the scaled distance of each measuring point. It can be seen from Figure 5 that the shape of the fitting curve in the test and the simulation is relatively similar. The curve is relatively steep at first, and then becomes slower. This indicates that the attenuation speed of the peak pressure of the surrounding rock is relatively large when the scaled distance is small. With the increasing of the scaled distance, the attenuation speed of the peak pressure decreases gradually. Meanwhile, it can be observed that the attenuation factor of the fitting curve in the simulation is 1.2712, which is slightly smaller than the 1.3283 in the test, indicating that the attenuation speed of the stress wave in the test is greater than that in the simulation.

The analysis believes that the above phenomenon is related to the geological conditions of the surrounding rock. In the numerical simulation, the surrounding rock is

Table 3: LS-DYNA material type, properties, and EOS input data.

Material	LS-DYNA material type, properties, and EOS input data (units: cm, g, μs)						
Rock bolt	*MAT_PLASTIC_KINEMATIC						
	RO	E	PR	SIGY	ETAN		
	2.72	0.76	0.34	0.00145	$2.50000E-4$		
TNT	*MAT_HIGH_EXPLOSIVE_BURN						
	RO	D	PCJ				
	1.63	0.693	0.27				
	*EOS_JWL						
	A	B	R_1	R_2	OMEG	$E0$	V
	3.71	0.0743	4.15	0.95	0.3	0.07	1.0

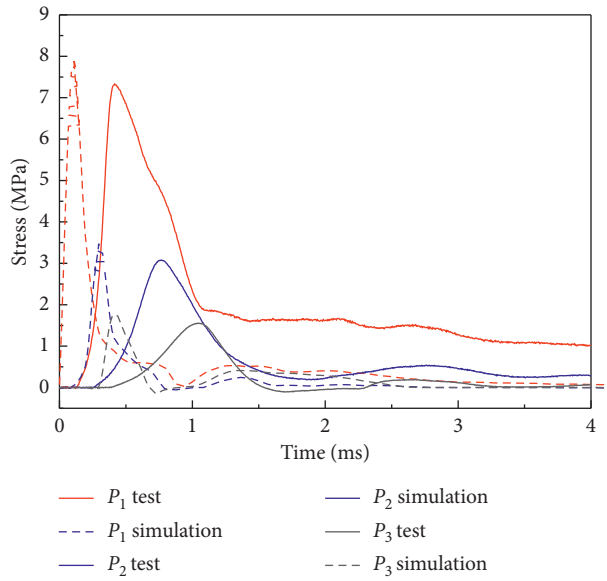

Figure 4: Comparison of stress time curves of rock elements between analysis and test.

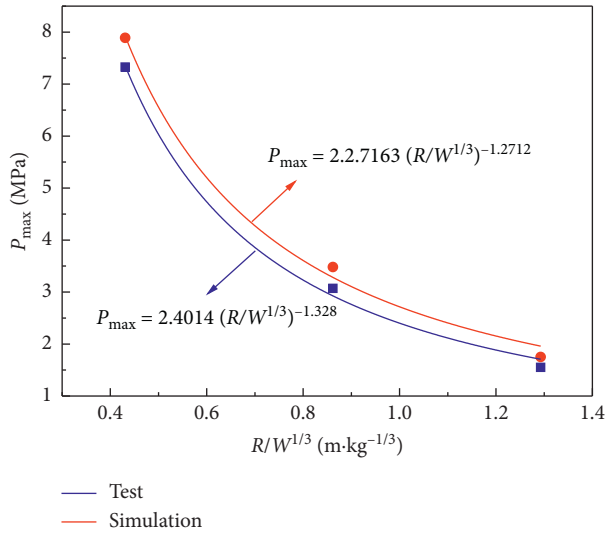

Figure 5: Relation between the peak compression stress and scaled distance.

regarded as an isotropic medium, and the model in the test is made of cement mortar. During the test construction process, the compaction of the surrounding rock is carried out in layers, leaving many layers, which increases the energy consumed during the propagation of the stress wave, accelerates the attenuation speed of the stress wave, and also slows down the propagation rate of the stress wave. Therefore, the peak pressure at the test measuring point is smaller than that at the same measuring position in the simulation, and the attenuation speed of the stress wave in the test is larger than that in the simulation. And, the reason why the stress wave curve rises first in the simulation is also explained. In summary, the numerical simulation results have high credibility.

4.2. Analysis of Peak Stress. To reveal the propagation law of the stress wave in the surrounding rock under multiple explosion sources, a measuring point is arranged every 20 cm on the line connecting the explosion source and the arch center. In addition, the measuring points are arranged in the middle of the two adjacent measuring points, as shown in Figure 2. In each case, 15 measuring points numbered P_1–P_{15} are arranged. The peak pressure of each measurement point in the seven cases is shown in Table 4. It can be seen from the three measuring points in the same direction that the peak pressure decreases with the increasing distance from the explosion source. Comparing case 1, case 2, and case 4, it can be found that there is not much difference in the peak pressure of the measuring points on the line connecting the explosion source and the arch center in the cases of two explosion sources and a single explosion source. The main difference is in the middle of the two explosion sources. For example, the peak pressure of P_4, P_5, and P_6 measuring points in case 4 is 2.52, 2.14, and 2.88 times of the same measuring point in case 1. Similarly, the peak pressure of P_4, P_5, and P_6 measuring points in case 4 is 2.61, 2.05, and 2.83 times of that of case 2, respectively. Compared with case 2, case 3, and case 6, it can also be found that the peak pressure of the measuring points in the direction of the connection between the explosion source and the arch center is not much different. The peak pressure of P_{10}, P_{11}, and P_{12} in case 6 is increased by 76.8%, 74.5%, and 114.2%, respectively, compared with that at the same position in case 2, and increased by 86.9%, 69.7%, and 118.3%, respectively, compared with that at the same position in case 3. By comparing

Table 4: Peak compressive stress of the measuring points.

Case	Peak compressive stress (MPa)														
	P_1	P_2	P_3	P_4	P_5	P_6	P_7	P_8	P_9	P_{10}	P_{11}	P_{12}	P_{13}	P_{14}	P_{15}
Case 1	7.89	3.84	1.75	5.75	3.21	1.52	2.64	2.25	1.38	1.24	1.27	1.29	1.04	1.17	1.32
Case 2	2.74	2.32	1.01	5.55	3.34	1.55	7.55	3.62	1.83	3.71	3.21	2.12	1.33	1.35	1.34
Case 3	0.92	1.11	1.17	1.08	1.13	1.68	1.29	1.31	2.01	3.51	3.33	2.08	7.63	4.61	2.85
Case 4	7.65	3.50	2.57	14.5	6.88	4.39	7.66	3.45	2.74	4.10	4.21	3.58	1.31	1.71	1.87
Case 5	7.65	3.57	2.51	5.86	3.18	1.79	2.63	2.19	1.92	4.58	3.72	2.36	7.75	4.69	2.92
Case 6	2.68	2.37	1.20	5.88	3.54	1.86	7.75	3.80	2.18	6.56	5.60	4.54	7.85	4.19	3.02
Case 7	7.55	3.66	2.59	14.7	6.80	4.49	7.70	3.52	2.63	7.75	6.55	5.55	7.65	4.62	3.10

case 1, case 2, case 3, and case 7, it can be found that the peak pressure of the measuring points on the line connecting the explosion source and the arch center in case 7 is close to the peak pressure of the measuring points at the same position in the case of single explosion source. In case 4, case 6, and case 7, the peak pressure difference between the two explosion sources is very small. In general, the increasing explosion source number has little effect on the peak pressure on the line connecting the explosion source and the arch center. Due to the loading wave formed by the interaction of the stress wave, the influence of the increasing explosion source number on the peak pressure is mainly in the middle of the two explosion sources.

4.3. Analysis of Damage Evolution of the Surrounding Rock. From the damage evolution process of the surrounding rock, the specific reasons for the damage of the cavern can be seen, which has guiding significance for the antiexplosion design of the cavern. Representative case 1, case 4, and case 7 are selected from the seven cases to analyze the damage evolution process of the surrounding rock under a single explosion source, double explosion sources, and triple explosion sources.

4.3.1. Damage Evolution Process of the Surrounding Rock in Case 1. Figure 6 shows the damage evolution process of the underground cavern under the top explosion. Different colors in the figure correspond to different damage indexes. The closer the damage index is to 1, the greater the damage, and 1 represents complete damage. Figure 6(a) shows the damage of the cavern at 0.3 ms after the explosion, from which it can be seen that the high temperature and high pressure of the explosion cause circular damage around the explosion source. At 0.4 ms, a damaged strip is formed near the ground. This is because the compressive stress waves generated by the explosion propagate to the ground and reflect to form tensile stress waves. The tensile strength of the surrounding rock is relatively weak and tensile damage will occur. Similarly, when the compressive stress wave propagates to the free surface of the vault at 0.6 ms, the surrounding rock around the vault also begins to produce tensile damage. The damage of the surrounding rock accumulates with the increasing repeated impact times and the subsequent stress wave will increase the damage degree of the damaged surrounding rock [40]. When the stress wave transmitted from the ground and the free surface of the vault meets the blast cavity formed by the explosion, it will reflect again. Due to the accumulation of damage, the radius of the damage circle around the explosion source becomes larger and larger, as shown in Figures 6(c) and 6(d). Besides, as time goes on, the damage zone near the surface expands to both sides of the model and explosion source, and the closer to the explosion source, the narrower the width of the damage zone becomes. With the increasing range of the stress wave propagating to the vault, the damage zone near the vault becomes larger and larger. At 0.8 ms, horizontal and vertical damage zones are generated below the detonation source in Figure 6(e). Analysis believes that the tensile stress waves reflected from the ground and the vault meet and overlap here, increasing the tensile stress wave strength. With the propagation of the stress wave, the superimposed position of the tensile stress wave gradually moves to the sides and the vault, and the damage zone also gradually extends in these two directions, as shown in Figures 6(f) and 6(g). Due to the decrease of the subsequent stress wave intensity, the damage of the surrounding rock of the cavern does not change after 2.2 ms. It can be seen from Figure 6(h) that the surrounding rock near the ground is a serious damage zone and has been connected with the damage circle around the explosion source. The damage zone near the vault is distributed in an arched shape, and the damage of the surrounding rock in the reinforced area shows the characteristics of the distribution along the bolt direction. As the tensile strength of the rock mass in the nonreinforced area is weaker than that in the reinforced area, the damage degree of the rock mass at the junction of the reinforced and nonreinforced area increases significantly. Due to the diffraction and reflection of the stress wave, a slight vertical damage zone is formed in the middle of the cavern floor. The compressive stress wave caused by the explosion source diffracts through the cavern and reflects on the cavern floor, and a slight vertical damage zone is formed in the middle of the cavern floor.

4.3.2. Damage Evolution Process of the Surrounding Rock in Case 4. Figure 7 shows the damage evolution process of the underground cavern under the simultaneous top explosion and side arch explosion. In Figure 7(a), there is an obvious damage circle around the explosion source. At 0.4 ms and 0.5 ms, the compressive stress caused by the explosion source on the side of the vault and side arch reflects on the ground to produce tensile damage zones. In Figure 7(d), a

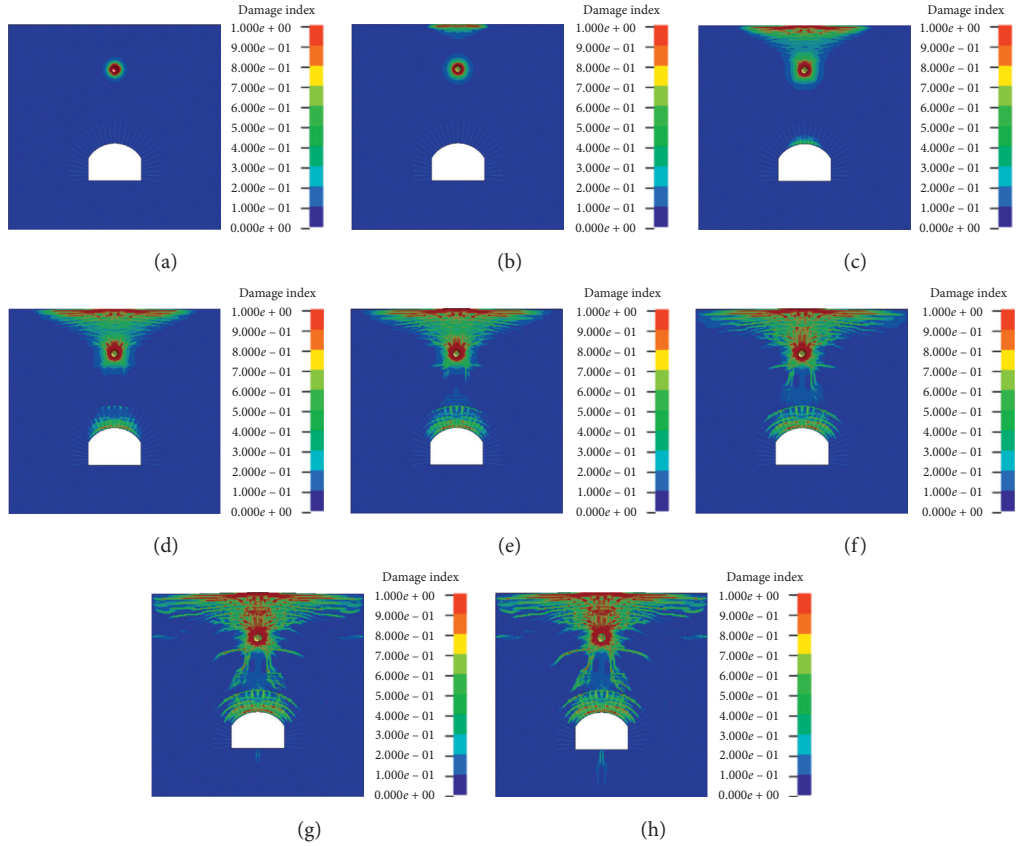

Figure 6: The damage evolution process of the underground cavern under the top explosion. (a) (t) = 0.3 ms. (b) (t) = 0.4 ms. (c) (t) = 0.6 ms. (d) (t) = 0.7 ms. (e) (t) = 0.8 ms. (f) (t) = 1.0 ms. (g) (t) = 1.6 ms. (h) (t) = 2.2 ms.

damage zone is generated between the vault and the side arch, and the damage degree of the middle part of the damage zone is obviously greater than that of other parts. This is because the compressive stress waves caused by the two explosion sources are superimposed here, and the strength of the stress wave increases obviously, so the damage to the surrounding rock is increased. Meanwhile, it can be observed that there is obvious damage in the connection direction of the two explosion sources, which is caused by the tensile stress reflected by the free surface of the blast cavity formed by the explosion. In the middle of the line connecting the two explosion sources, the damage degree is slightly higher due to the superposition of tensile stress waves reflected from the two blast cavities. With time, the damage of the surrounding rock caused by the stress wave generated by the two explosion sources is accumulating. In Figures 7(e) and 7(f), the damage around the arch has extended beyond the reinforced zone, and the damage near the ground has further extended downward. Besides, the damage of the surrounding rock on the line connecting the midpoint of the two explosion sources and the arch center is greater than that of other places. This is caused by the superposition of the tensile stress formed by the reflection of the compressive stress waves generated by the two explosion sources on the ground. At 1.5 ms, the tensile stress wave formed by the reflection from the ground and cavern meets about 60 cm at the upper left of the cavern, resulting in a damage zone extending to the boundary of the model. In Figure 7(h), a damage zone inclined to the left is formed in the middle of the cavern floor.

4.3.3. Damage Evolution Process of the Surrounding Rock in Case 7. Figure 8 shows the damage evolution process of the underground cavern under the simultaneous top explosion, side arch explosion, and sidewall explosion. In Figures 8(b) and 8(c), the shape and cause of the damage zone near the ground are the same as the damage here in case 4. At 0.6 ms, the compressive stress waves generated by the three blasting sources all propagate to the free surface of the cavern, and the tensile damage zone is formed at the arch and sidewall. With the propagation of the stress wave, at 1.0 ms, the damage zone near the ground expands downward, and the damage zone around the arch and sidewall has exceeded the reinforced area, reaching the nonreinforced area. The damage at the middle position of the top and side arch explosion sources increases significantly. In addition, when the stress waves reflected from the surface pass through the explosion sources, the damage around the blast cavities will be further expanded due to the accumulation of damage. A slight vertical damage zone is formed between the side arch explosion source and the sidewall explosion source due to the superposition of the tensile wave reflected by the ground and the sidewall. At the right foot of the sidewall, there is a

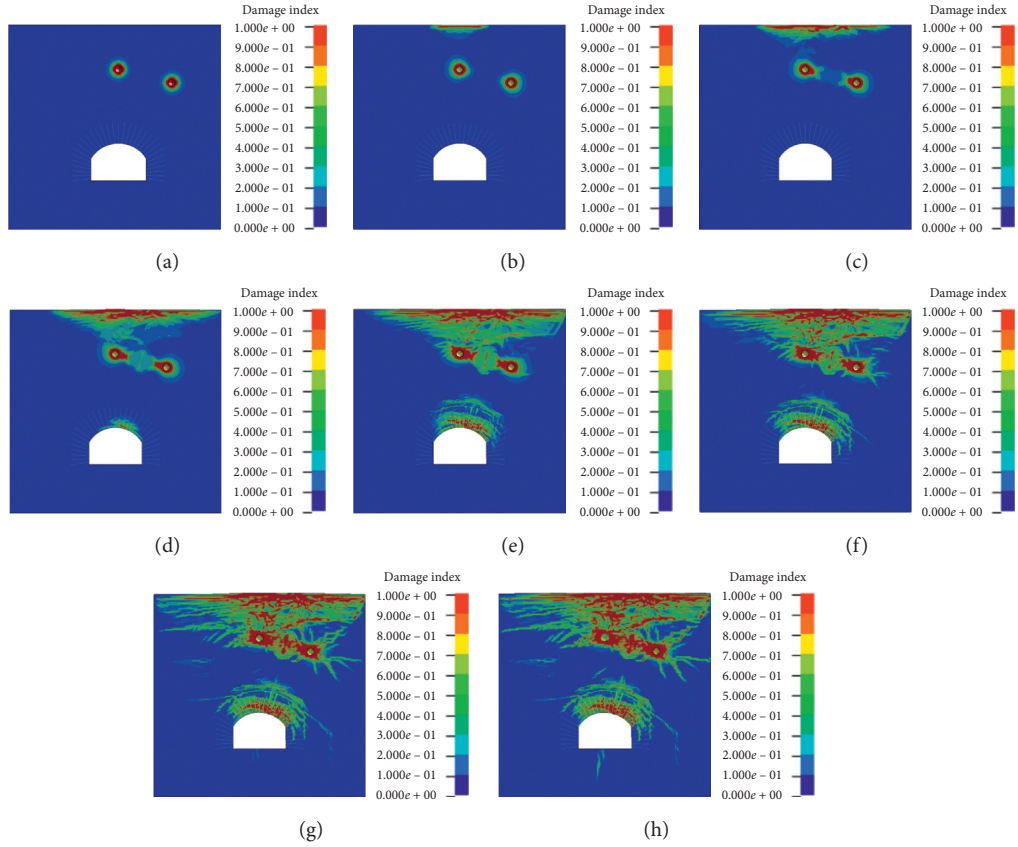

Figure 7: The damage evolution process of the underground cavern under the simultaneous top explosion and side arch explosion. (a) $t = 0.3$ ms. (b) $t = 0.4$ ms. (c) $t = 0.5$ ms. (d) $t = 0.6$ ms. (e) $t = 0.8$ ms. (f) $t = 1.0$ ms. (g) $t = 1.5$ ms. (h) $t = 2.2$ ms.

damage zone extending to the left, which is caused by the compressive stress wave generated by the sidewall explosion reflecting on the floor. In Figure 8(f), the stress wave reflected from the side arch and the sidewall blast cavity meets, which further increases the damage zone between the two explosion sources. Besides, the superposition of the tensile stress wave from the ground and the stress wave reflected from the blast cavity on the sidewall further increases the damage range between the side arch and the sidewall explosion sources. At about 60 cm on the upper left of the vault, a superposition of tensile stress waves reflected from the ground and the free surface of the cavern forms a damage zone. After 2.2 ms, the damage of the surrounding rock tends to be stable.

4.3.4. Comparative Analysis of the Surrounding Rock Damage in Seven Cases. To study the damage distribution characteristics of the surrounding rock under explosions, Figure 9 shows the damage distribution of the surrounding rock in seven cases. According to the causes of the surrounding rock damage, the damage is divided into seven zones. Zone 1 is the surrounding rock damage caused by high temperature and high pressure caused by explosion source; zone 2 represents the damage formed by tensile waves reflected by the ground surface; zone 3 represents the damage formed by tensile waves reflected by the free surface of the cavern; the damage in zone 4 is caused by the reflection of stress waves from the ground and the free surface when they meet the blast cavity; zone 5 is the damage zone formed by the superposition of tensile stress waves reflected from the ground and the free surface of the cavern; the damage in zone 6 is formed by the superposition of the stress waves reflected by the two blasting cavities; The damage in zone 7 is formed by the encounter of the tensile stress waves reflected from the ground and the sidewall blast cavity.

By comparing Figures 9(a)–9(g), it can be seen that the damage distribution range is the widest in the case of three explosion sources, followed by the case of two explosion sources, and the single detonation source case is the smallest. The damage range of zone 1 is basically the same in the seven cases, and the radius of the damage circle is roughly three times the charging radius. The distribution range and damage degree of zone 2 near the ground surface decrease with the increasing distance between the explosion source and the ground and increase with the increasing explosion source numbers. In the single explosion source cases, most of the damage in zone 3 is distributed toward the direction of the explosion source, and the damage degree is the largest on the line connecting the explosion source and arch center. Due to the stress wave diffraction and the tensile stress wave generated by the reflection of the floor, damage zone 3 also exists near the floor. When the explosion source increases to two or three, the damage is the most serious on the line connecting the middle

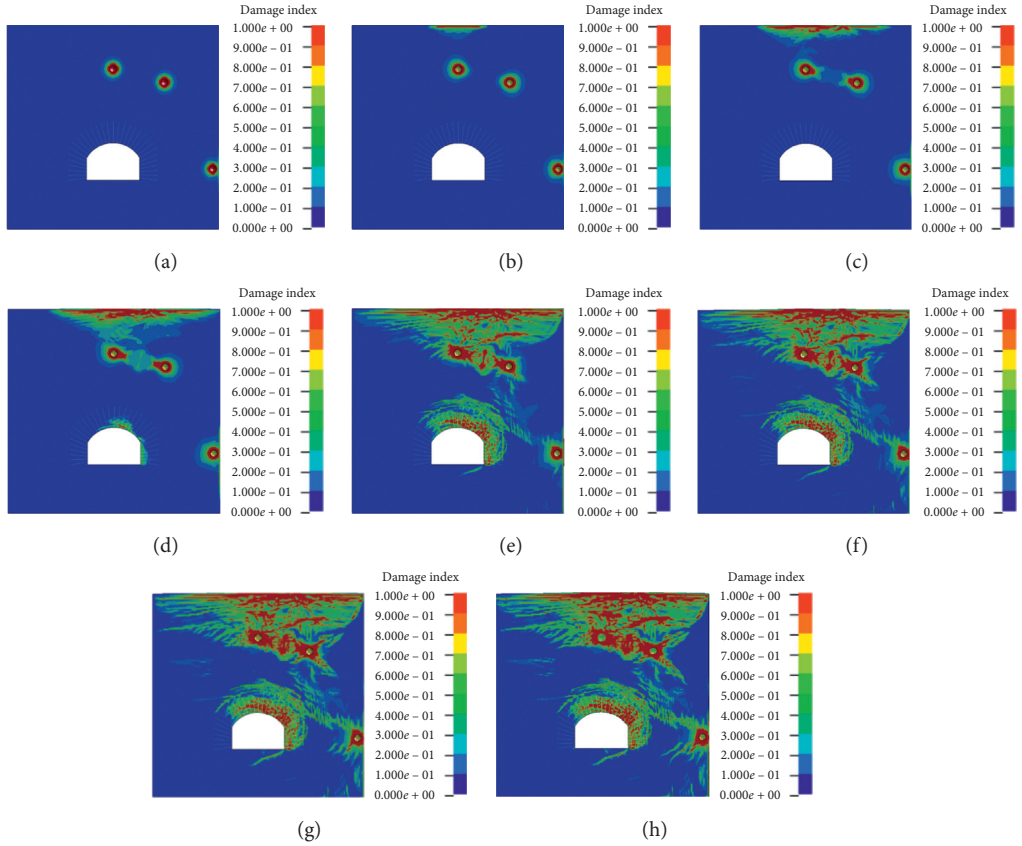

Figure 8: The damage evolution process of the underground cavern under the simultaneous top explosion, side arch explosion, and sidewall explosion. (a) $t = 0.3$ ms. (b) $t = 0.4$ ms. (c) $t = 0.5$ ms. (d) $t = 0.6$ ms. (e) $t = 1.0$ ms. (f) $t = 1.2$ ms. (g) $t = 1.5$ ms. (h) $t = 2.2$ ms.

position of two explosion sources and the arch center. This is caused by the superposition of tensile stress formed by the two explosion sources. In all cases, the distribution range and degree of damage in zone 4 near the same explosion source are similar, which indicates that damage in zone 4 is less affected by the number of explosion sources. It can be seen from Figures 9(a)–9(c) that the position of damage zone 5 gradually moves upward as the explosion source position moves downward. The distribution of damage in zone 5 in multiple explosion sources is different from that in the corresponding single explosion source, and this situation is more obvious in case 4 and case 7. Analysis indicates that the distance between the vault and the side arch explosion source in case 4 and case 7 is relatively close. When the stress wave reflected from the ground passes through damage zone 1, the stress wave energy attenuation increases and the superposition of tensile stress waves is also difficult to cause serious damage to the surrounding rock. In case 5 and case 6, the distance between the vault and the sidewall explosion source is far, and the attenuation of the stress wave propagation process is similar to the corresponding single explosion source. Damage in zone 6 only appears in the case of two explosion sources and three explosion sources and does not exist in the single explosion source case and is mainly distributed in the middle area of the two explosion sources. Damage zone 7 only exists in the presence of the sidewall explosion source, mainly distributed near the right arch of the cavern, and its damage degree is low. It can be seen from Figure 9 that the damage zones 2–7 occupy most of the surrounding rock damage, and the damage zones 2–7 are caused by the tensile stress wave and superposition of the tensile stress wave. Therefore, the damage of the surrounding rock is mainly caused by the tensile stress wave reflected from the free surfaces and the superposition of the tensile stress wave.

In general, the damage of the surrounding rock in the case of multiple explosion sources is not a simple addition of the damage to the surrounding rock of the corresponding single explosion source. The main difference is that in the single explosion source case, there is no damage zone formed by the superposition of stress waves reflected from blasting cavities. The damage zone formed by the superposition of the stress waves reflected from the ground and the free surface of the cavern is also obviously different from that of the single explosion source due to the increase of the explosion source number. Besides, when the buried depth of the cavern increases, the tensile stress intensity generated by the ground reflection will gradually decrease, and zones 2, 4, 5, and 7 will gradually disappear. It can be seen that the increase in the buried depth of the cavern can reduce the damage of the ground reflected stress wave to the surrounding rock.

4.4. Analysis of Circumferential Peak Stress of the Cavern Wall.

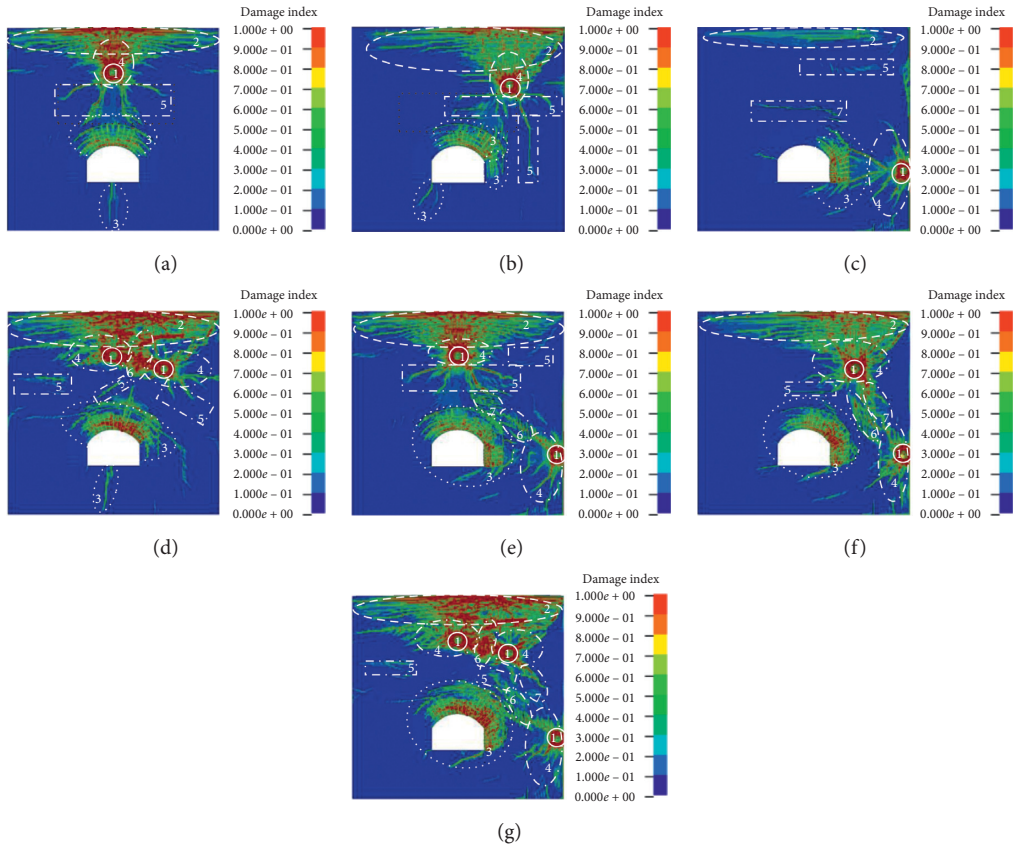

Figure 9: Damage distribution in seven cases. (a) Case 1. (b) Case 2. (c) Case 3. (d) Case 4. (e) Case 5. (f) Case 6. (g) Case 7.

The circumferential strain of the cavern wall can reflect the circumferential stress of the cavern wall, which has important reference significance for analyzing the anti-blast performance of the cavern. Twenty-four circumferential strain measuring points (ε_1–ε_{24}) are arranged on the cavern wall, as shown in Figure 10.

Figure 11 shows the peak circumferential strain at each measuring point of the cavern wall in the seven cases. The absolute value at each measuring point represents the magnitude of the strain. A positive value represents tensile strain, and a negative value represents compressive strain. It can be seen from Figure 11 that the peak circumferential strain from the vault to the side arch is all tensile. The reason is that the vault will produce downward displacement under explosion, and the surrounding rock around the vault is transversely tensioned, so there is tensile strain near the vault. When the explosion source near the sidewall exists, the sidewall will also produce tensile circumferential strain. This phenomenon is caused by the stress wave generated by the sidewall explosion that propagates to the sidewall, The surrounding rock near the sidewall will produce displacement to the interior of the cavern. The surrounding rock here is vertically tensioned, so the surrounding rock produces tensile strain. Meanwhile, it can be found that in case 3, case 5, case 6, and case 7, where the sidewall explosion source exists, the circumferential strain at the floor is tensile. The main reason is that the floor will be squeezed by the right sidewall under the sidewall explosion, and the floor will

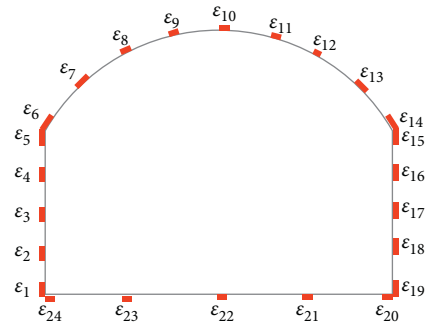

Figure 10: Arrangement of circumferential strain measuring points.

bulge upward and be stretched laterally, resulting in tensile strain. Consider that the tensile strength of the surrounding rock is far less than the compressive strength. Moreover, important instruments and equipment are often located on the floor. Therefore, it is necessary to avoid the sidewall explosion. When the explosion occurs only above the cavern, the sidewall and floor produce compressive circumferential strain. This is because the arch moves downward under the explosion above the cavern, squeezing the sidewall, and the sidewall compresses longitudinally, producing compressive circumferential strain. In the seven cases, from the vault to the spandrel, the strain changes from tension to compression, because the surrounding rock at the spandrel can be

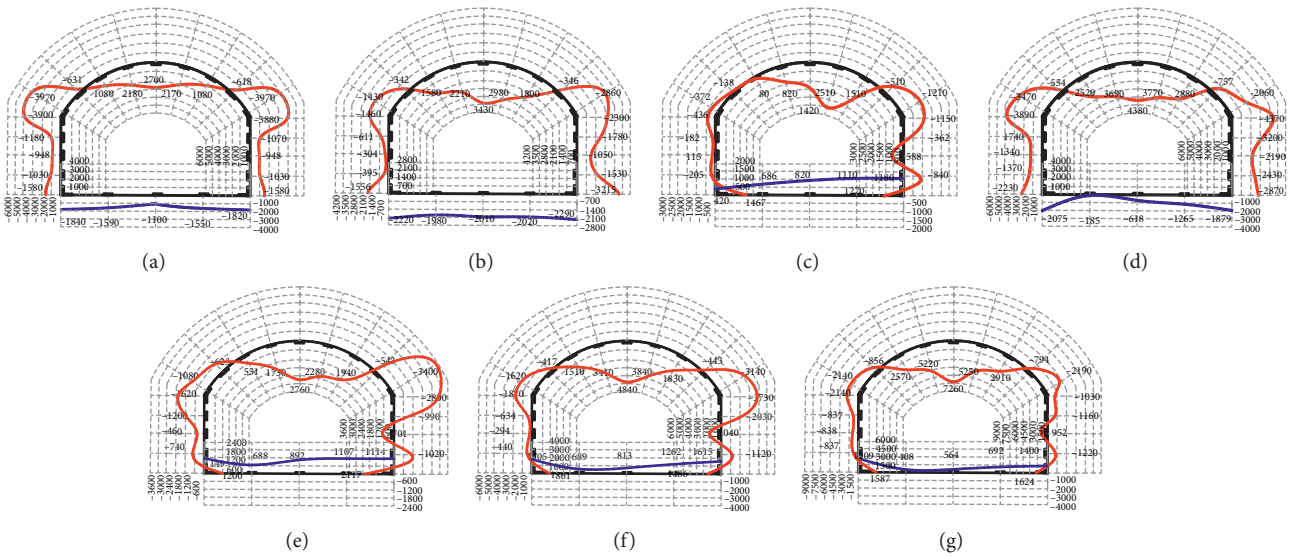

FIGURE 11: The peak circumferential strain distribution of the cavern wall (unit:10^{-6}). (a) Case 1. (b) Case 2. (c) Case 3. (d) Case 4. (e) Case 5. (f) Case 6. (g) Case 7.

supported by the lower surrounding rock, which makes it difficult to produce tensile circumferential strain here. In the seven cases, the absolute value of the peak circumferential strain from the vault to the spandrel first decreases and then increases. This is because the lack of effective support at the vault leads to greater circumferential strain in the surrounding rock, and the spandrel is at the junction of the two parts, which is prone to stress concentration. However, the circumferential strain of the spandrel is compressive, while the circumferential strain of the vault is tensile, so the vault is prone to damage under explosion. When the explosion source is presented at the sidewall, the tensile circumferential strain will be generated in the lower right corner of the sidewall, and the compressive circumferential strain is generated on the nonblasting cavern wall.

Comparing the case of multiple explosion sources and the corresponding single explosion source, it can be found that the absolute value of the peak circumferential strain at the measuring point on the line connecting the explosion source and arch center is larger than that of the corresponding single explosion source. For example, the peak circumferential strain of the measuring point ε_{10} in case 4 is 62.22% larger than that of the measuring point ε_{10} in case 1, and the peak circumferential strain of the measuring point ε_{12} in case 4 is 60% larger than that of the measuring point ε_{12} in case 2. The peak circumferential strains of measuring poinst ε_{10}, ε_{12}, and ε_{17} are 168.8%, 58.11%, and 27.8% larger than the corresponding single explosion source measuring points, respectively.

From the circumferential strain-time curve of the surrounding rock, the specific process of the circumferential strain of the surrounding rock can be seen. As there are many cases in numerical calculations, the most representative case 7 is selected here to analyze the circumferential strain-time curve of its measuring points. Figure 12 shows the circumferential strain-time curve of the measuring point (ε_1–ε_{24}) in case 7. The positive value in the figure is the tensile circumferential strain and the negative value is the compressive circumferential strain.

It can be seen from Figure 12 that when the stress wave propagates to the measuring point, the circumferential strain-time curve will rapidly rise or drop to the peak, then there will be a fall or increase, and finally, gradually stabilize. The circumferential strain-time curve of the surrounding rock is not smooth. There is a period of falling in the rising process, and then it continues to rise, and there will also be a rising stage in the descending process. This is because the stress waves produced by the three explosions arrive at the measuring point at different times. It can be seen from Figure 12(a) that the circumferential strain of ε_1 changes from compressive to tensile, and the other four measuring points produce compressive circumferential strain. It can be seen from Figure 12(b) that from ε_6 to ε_9, the circumferential strain of the cavern wall changes from compressive to tensile, and with the decreasing distance from the measuring point to the vault, the compressive circumferential strain becomes smaller and the tensile circumferential strain becomes larger and larger. From the circumferential strain-time curves of several measuring points in Figure 12(c), it can be found that the values of the circumferential strain at measuring points ε_{10}, ε_{11}, and ε_{12} are always positive. Therefore, the circumferential strain of the vault is tensile throughout the explosion process. In addition, the residual circumferential strain at measuring points ε_{10}, ε_{11}, and ε_{12} is relatively large, indicating that the surrounding rock near the vault is in a state of large deformation. The measurement point ε_{13} is in a state of alternating tension and compression, where the surrounding rock first produces tensile circumferential strain and then becomes compressive circumferential strain. Comparing Figures 12(c) and 12(d), it can be seen that the absolute value of the circumferential strain of the sidewall is significantly smaller than that of the arch. The circumferential strain-time curve of

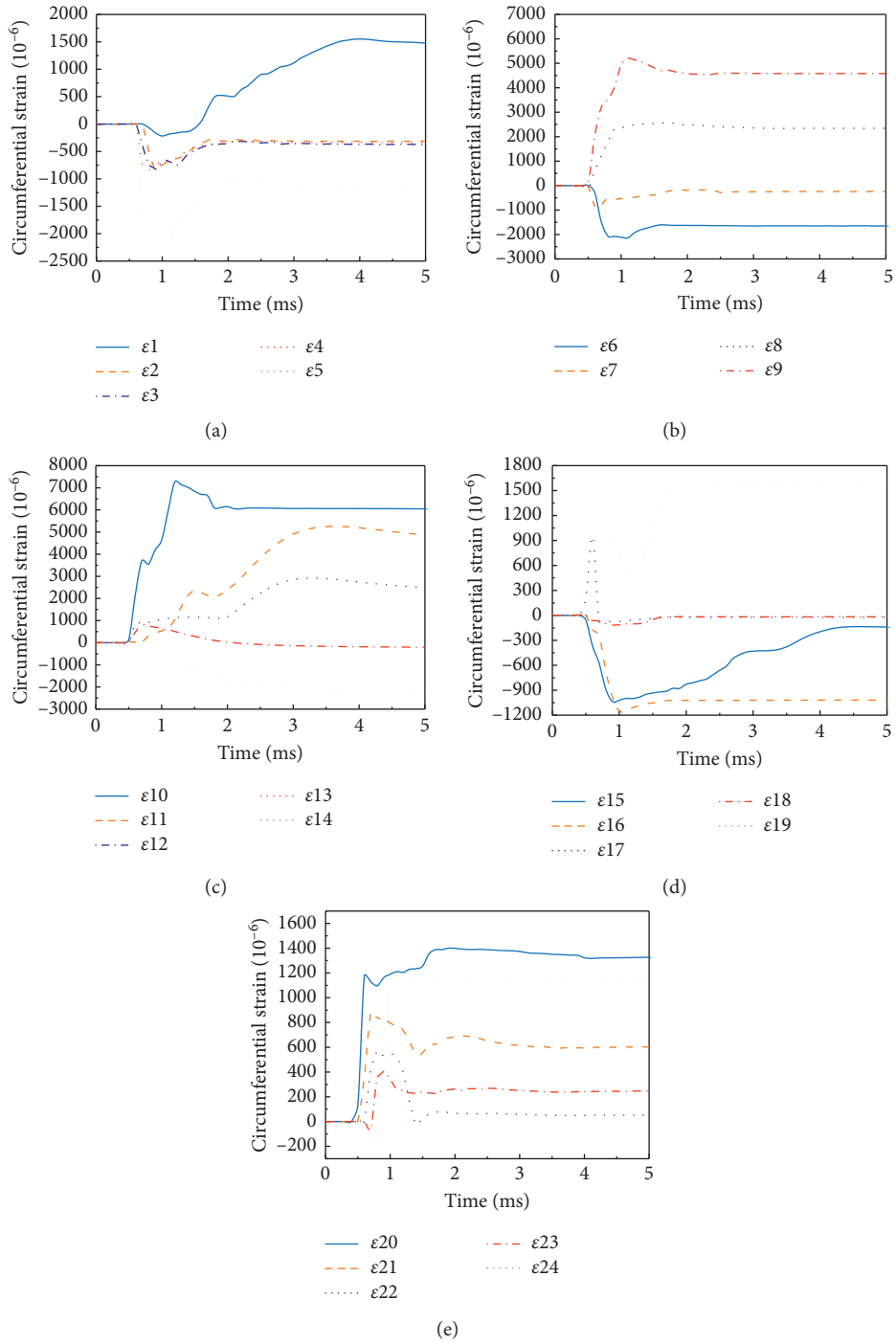

Figure 12: The circumferential strain-time curves of the measuring points. (a) Measuring points ε_1–ε_5. (b) Measuring points ε_6–ε_9. (c) Measuring points ε_{10}–ε_{14}. (d) Measuring points ε_{15}–ε_{19}. (e) Measuring points ε_{20}–ε_{24}.

measuring point ε_{17} rapidly rises to the peak tensile strain, and then rapidly drops and changes into a compressive strain, while measuring point ε_{19} changes from a compressive strain state to a tensile strain state. Figure 12(e) shows that the circumferential strain of the measuring point at the right floor is always tensile, while the left floor generates compressive circumferential strain first and then turns to tensile circumferential strain, and the final residual circumferential strain is tensile.

5. Conclusions

To evaluate the influence of multiple explosion sources on the underground cavern, based on a similarity model test, the damage evolution and circumferential strain distribution law of underground cavern in the seven cases are analyzed by using the numerical analysis method, and the following main conclusions are obtained:

(1) In the cases of multiple explosion sources, the stress of the surrounding rock in the middle part of the two explosion sources is greater than that of the corresponding single explosion source.

(2) The damage of the underground cavern is mainly concentrated around the explosion source, the ground, and the free surface of the cavern. The damage of the surrounding rock in the cases of multiple explosion sources is not a simple cumulative superposition of the damage of the surrounding rock in the corresponding single explosion source cases. The difference lies in the middle part of the two detonation sources, where the damage degree and range of multiple detonation sources are larger.

(3) The damage of the surrounding rock at the junction of the reinforced area and nonreinforced area increases obviously, and high-strength concrete can be used to improve the performance of the surrounding rock during the construction process.

(4) The peak circumferential strain from the vault to the side arch is all tensile, and from the vault to the spandrel, it changes from tensile to compressive. The vault can easily be damaged when encountering explosions, and the support should be strengthened.

(5) When explosions occur near the sidewall, the floor will produce tensile circumferential strain, and such explosions should be avoided.

Data Availability

The data used to support the findings of this study are available from the corresponding author upon request.

Conflicts of Interest

The authors declare that there are no conflicts of interest regarding the publication of this paper.

Acknowledgments

This research was supported by the State Key Project of National Natural Science Foundation of China (Grant No. U1810203).

References

[1] H. Xie, J. Zhu, T. Zhou, K. Zhang, and C. Zhou, "Conceptualization and preliminary study of engineering disturbed rock dynamics," *Geomechanics and Geophysics for Geo-Energy and Geo-Resources*, vol. 6, no. 2, pp. 1–14, 2020.

[2] J. B. Zhu, Y. S. Li, S. Y. Wu, R. Zhang, and L. Ren, "Decoupled explosion in an underground opening and dynamic responses of surrounding rock masses and structures and induced ground motions: a FEM-DEM numerical study," *Tunnelling and Underground Space Technology*, vol. 82, pp. 442–454, 2018.

[3] C. Wu, M. Lukaszewicz, K. Schebella, and L. Antanovskii, "Experimental and numerical investigation of confined explosion in a blast chamber," *Journal of Loss Prevention in the Process Industries*, vol. 26, no. 4, pp. 737–750, 2013.

[4] I. C. Tolias, J. R. Stewart, A. Newton et al., "Numerical simulations of vented hydrogen deflagration in a medium-scale enclosure," *Journal of Loss Prevention in the Process Industries*, vol. 52, pp. 125–139, 2018.

[5] W. Xu, W. Wu, and Y. Lin, "Numerical method and simplified analytical model for predicting the blast load in a partially confined chamber," *Computers & Mathematics with Applications*, vol. 76, no. 2, pp. 284–314, 2018.

[6] R. K. Singh, "Composite wall test-chamber assessment for hydrogen blast loads," *Thin-Walled Structures*, vol. 126, pp. 220–237, 2018.

[7] A. J. Hendron, "Engineering of rock blasting on civil projects," in *Structural and Geotechnical Echanics, A Volume Honoring NM Newmark*, W. J. Hall, Ed., Prentice-Hall, Hoboken, NY, USA, 1977.

[8] P. K. Singh, "Blast vibration damage to underground coal mines from adjacent open-pit blasting," *International Journal of Rock Mechanics and Mining Sciences*, vol. 39, no. 8, pp. 959–973, 2002.

[9] X. Xia, H. B. Li, J. C. Li, B. Liu, and C. Yu, "A case study on rock damage prediction and control method for underground tunnels subjected to adjacent excavation blasting," *Tunnelling and Underground Space Technology*, vol. 35, pp. 1–7, 2013.

[10] J. Xu, Y. Kang, X. Wang, G. Feng, and Z. Wang, "Dynamic characteristics and safety criterion of deep rock mine opening under blast loading," *International Journal of Rock Mechanics and Mining Sciences*, vol. 119, pp. 156–167, 2019.

[11] P. K. Rajmeny, U. K. Singh, and B. K. P. Sinha, "Predicting rock failure around boreholes and drives adjacent to stopes in Indian mines in high stress regions," *International Journal of Rock Mechanics and Mining Sciences*, vol. 39, no. 2, pp. 151–164, 2002.

[12] B. L. Kutter, L. M. O'Leary, P. Y. Thompson, and R. Lather, "Gravity-scaled tests on blast-induced soil-structure interaction," *Journal of Geotechnical Engineering*, vol. 114, no. 4, pp. 431–447, 1988.

[13] M. C. R. Davies, "Buried structures subjected to dynamic loading," in *Structures Subjected to Dynamic Loading*, R. Naryanan and T. M. Roberts, Eds., pp. 271–302, Elsevier, Amsterdam, Netherland, 1991.

[14] A. De and R. Conry, "Modeling of surface blast effects on underground structures," in *Proceedings of the 2011 American Society of Civil Engineers Geo-Frontiers Congress*, pp. 1534–1543, Dallas, TX, USA, March 2011.

[15] A. De, A. N. Morgante, and T. F. Zimmie, "Numerical and physical modeling of geofoam barriers as protection against effects of surface blast on underground tunnels," *Geotextiles and Geomembranes*, vol. 44, no. 1, pp. 1–12, 2016.

[16] J. Shen, J. C. Gu, A. M. Chen, J. M. Xu, Z. Q. Ming, and X. Y. Zhang, "Development and applications of the model test apparatus on anti-explosion structures in geotechnical engineering," *Chinese Journal of Underground Space and Engineering*, vol. 6, pp. 1077–1080, 2007.

[17] J. C. Gu, A. M. Chen, J. M. Xu et al., "Model test study of failure patterns of anchored tunnel subjected to explosion load," *Chinese Journal of Rock Mechanics and Engineering*, vol. 27, no. 7, pp. 1315–1320, 2008.

[18] G. Y. Wang, J. C. Gu, A. M. Chen, J. M. Xu, and X. Y. Zhang, "Model test research on anti-explosion capacity of underground openings with end wave-decay by holes and reinforced by dense rock bolts," *Chinese Journal of Rock Mechanics and Engineering*, vol. 29, no. 1, pp. 51–58, 2010.

[19] J. M. Xu and J. C. Gu, "Model test study of anti-explosion capacity of anchored tunnel with local lengthening anchors in

arch springing," *Chinese Journal of Rock Mechanics and Engineering*, vol. 31, no. 11, pp. 2182–2186, 2012.

[20] G. C. Xu, W. Z. Yuan, and J. C. Gu, "Explosive resistivity of anchored cavern surface rock," *Chinese Journal of Rock Mechanics and Engineering*, vol. 34, no. 09, pp. 1767–1776, 2015.

[21] X. Chang, G. Wang, C. Tang, and Z. Ru, "Dynamic behavior of cement-mortar cavern reinforced by bars," *Engineering Failure Analysis*, vol. 55, pp. 343–354, 2015.

[22] M. H. Mussa, A. A. Mutalib, R. Hamid, S. R. Naidu, N. A. M. Radzi, and M. Abedini, "Assessment of damage to an underground box tunnel by a surface explosion," *Tunnelling and Underground Space Technology*, vol. 66, pp. 64–76, 2017.

[23] J. Zhu, Y. li, Q. Peng, X. Deng, M. Gao, and J. Zhang, "Stress wave propagation across jointed rock mass under dynamic extension and its effect on dynamic response and supporting of underground opening," *Tunnelling and Underground Space Technology*, vol. 108, Article ID 103648, 2021.

[24] X. F. Deng, S. G. Chen, J. B. Zhu, Y. X. Zhou, Z. Y. Zhao, and J. Zhao, "UDEC-AUTODYN hybrid modeling of a large-scale underground explosion test," *Rock Mechanics and Rock Engineering*, vol. 48, no. 2, pp. 737–747, 2014.

[25] S. Kuili and V. R. Sastry, "A numerical modelling approach to assess the behaviour of underground cavern subjected to blast loads," *International Journal of Mining Science and Technology*, vol. 28, no. 6, pp. 975–983, 2018.

[26] X. F. Deng, J. B. Zhu, S. G. Chen, Z. Y. Zhao, Y. X. Zhou, and J. Zhao, "Numerical study on tunnel damage subject to blast-induced shock wave in jointed rock masses," *Tunnelling and Underground Space Technology*, vol. 43, no. 6, pp. 88–100, 2014.

[27] G. Ma, H. Hao, and Y. Zhou, "Assessment of structure damage to blasting induced ground motions," *Engineering Structures*, vol. 22, no. 10, pp. 1378–1389, 2000.

[28] C. Gao, Z. Zhou, Z. Li, L. Li, and S. Cheng, "Peridynamics simulation of surrounding rock damage characteristics during tunnel excavation," *Tunnelling and Underground Space Technology*, vol. 97, Article ID 103289, 2020 pages, 2020.

[29] Y. B. Yang, X. Y. Xie, and R. L. Wang, "Numerical simulation of dynamic response of operating metro tunnel induced by ground explosion," *Journal of Rock Mechanics & Geotechnical Engineering*, vol. 2, no. 4, pp. 373–384, 2010.

[30] G. Y. Wang, J. C. Gu, A. M. Chen, J. M. Xu, and X. Y. Zhang, "Model tests on anti explosion anchoring effect of tunnels reinforced by dense bolts at arch top," *Chinese Journal of Geotechnical Engineering*, vol. 31, no. 3, pp. 378–383, 2009.

[31] T. J. Holmquist and G. R. Johnson, "A computational constitutive model for glass subjected to large strains, high strain rates and high pressures," *Journal of Applied Mechanics*, vol. 78, no. 5, Article ID 051003, 2011.

[32] L. M. Taylor, E. P. Chen, and J. S. Kuszmaul, "Microcrack-induced damage accumulation in brittle rock under dynamic loading," *Computer Methods in Applied Mechanics and Engineering*, vol. 55, no. 3, pp. 301–320, 1986.

[33] Y. D. Murray, A. Abu-odeh, and R. Bligh, *Evaluation Of LS-DYNA Concrete Material Model 159; FHWA-HRT-05-062*, US Department of Transportation, Federal Highway Administration National Transportation Systems Center, Mclean, VA, USA, 2007.

[34] W. Riedel, K. Thoma, and S. Hiermaier, "Penetration of reinforced concrete by BETA-B-500 numerical analysis using a new macroscopic concrete model for hydrocodes," in *Proceedings of the 9th International Symposium on the Effects of Munitions with Structures*, pp. 315–322, Berlin-Strausberg, Berlin, Germany, May 1999.

[35] W. Riedel, N. Kawai, and K.-i. Kondo, "Numerical assessment for impact strength measurements in concrete materials," *International Journal of Impact Engineering*, vol. 36, no. 2, pp. 283–293, 2009.

[36] T. Borrvall and W. Riedel, "The RHT concrete model in LS-DYNA," in *Proceedings of the 8th European LS-DYNA Users Conference*, pp. 23-24, Strasbourg, France, May 2011.

[37] J. O. Hallquist, *LS-DYNA Keyword User's Manual*, Livermore Software Technology Corporation: California, Livermore, CA, USA, 2007.

[38] R. Meyer, J. Kohler, and A. Homburg, *Explosives*pp. 339–341, Wiley VCH, Weinheim, Germany, 5nd edition, 2002.

[39] TM 5-855-1, *Fundamental of Protective Design for Conventional Weapons*, US Army Engineers Waterways Experimental Station, Vicksburg, Mississippi, USA, 1986.

[40] T. Zhou, S. L. Dong, G. F. Zhao, R. Zhang, S. Y. Wu, and J. B. Zhu, "An experimental study of fatigue behavior of granite under low-cycle repetitive compressive impacts," *Rock Mechanics and Rock Engineering*, vol. 51, no. 10, pp. 3157–3166, 2018.

Hindawi
Shock and Vibration
Volume 2021, Article ID 7975005, 11 pages
https://doi.org/10.1155/2021/7975005

Research Article

The Airflow Reversal Law in Ventilation System after Coal and Gas Outburst in Tunneling Roadway

Junhong Si, Yiqiao Wang, Genyin Cheng, Lin Li, Yitian Shao, Tan Li, and Wei Hu

School of Emergency Technology and Management, North China Institute of Science and Technology, Beijing 101601, China

Correspondence should be addressed to Yiqiao Wang; 201908522442wyq@ncist.edu.cn

Received 11 April 2021; Accepted 4 June 2021; Published 17 June 2021

Academic Editor: Jianwei Cheng

Considering the coal and gas outburst phenomenon in the mining space, this paper analyzes the main characteristics of coal and gas outburst accidents, defines the outburst airflow reversal degree, and constructs a simplified topology graph of tunneling ventilation system, while the air door is not destroyed. Using the numerical simulation method, this paper elaborates on the relationship between the outburst pressure and airflow reversal degree. The results indicate that the inlet pressure increases to 264 hPa and the outlet pressure increases to 289 hPa when the outburst pressure increases from 1 hPa to 1 MPa, and the relative variation coefficient of pressure decreases from 1501.5 to 1.62 in the inlet of return airway and decreases from 2002 to 1.65 in the outlet of return airway. Furthermore, the air velocity decreases from −1.38 to −284.44 m/s in the inlet and increases from 3.10 to 297.38 m/s in the outlet. Moreover, the gas concentration of the inlet and outlet in return airway increases rapidly with the increase of outburst pressure. When the outburst pressure is greater than 0.15 MPa, the gas concentration will be over 98% in tunneling ventilation system. This paper also finds out a cubic polynomial relationship existing between the reversal degree and the outburst pressure. It provides the prediction of coal and gas outburst and serves as a guidance in case mine ventilation disturbances occur.

1. Introduction

The coal and gas outburst is a phenomenon where a large amount of coal and gas is ejected into the mining space almost immediately [1, 2]. In an outburst accident, the high pressure often injures people in underground roadway [3]. Furthermore, coal and gas outburst destroys equipment, such as the ventilation facilities, making airflow disorder in mine ventilation system easier to occur. More seriously, it causes secondary disasters, such as the gas explosion accident [4, 5] and the coal dust explosion accident. Generally speaking, there are two ways of transmission after an outburst accident—one is the shock wave and the other is gas pressure [6, 7]. The pressure of outburst gas is the main reason in mine airflow disorder after the outburst power fades away.

After a disaster happens, an effective ventilation system can help avoid secondary disasters caused by airflow reversal and, at the same time, safeguard the disaster relief work. Currently, some researchers have studied the reverse flow and turbulence of airflow in the overall mine tunnel ventilation system during the disaster period. Firstly, the underground roadway space is regarded as the flow field. When the flow field after gas outburst is disturbed by the shock waves, the huge energy and pressure involved in the process of the gas outburst as well as the influence the operating parameters of the ventilation system pose on roadway airflow are studied [8]. Then, the model of outburst source was established to study the unsteady flow and distribution of gas after gas outburst. By using the outburst disaster simulation software, the outburst danger area is determined. Combining with the automatic control system of the air door, the gas in the return airway is controlled [9]. At the same time, the gas migration model of the mine ventilation system was established, and it was concluded that the mine ventilation system would experience the gas reversal states, the natural flow states, and the gas flow states after the occurrence of gas outburst accident [10]. Finally, through the case of the gas outburst accident, the main influencing factors of airflow reversal in the upwind roadway are studied; that is, the

airflow is easily reserved if the height difference of the roadway is large, and the impact scope of gas outburst accident expanded if the gas reversal time was short [11].

The safety and stability of mine ventilation system usually referring to the airflow direction are stable and the air velocity does not exceed the limit when the ventilation system is disturbed. They reflect the antidisturbance capability of the ventilation system. Through establishing a mathematical model of unsteady gas flow and studying the flow variation law induced by the gas outburst, it was found that ventilation pressure is the main factor affecting airflow reversal [7]. Then FLUENT software was used to study the influence of the direction of gas flow in inclined roadway on gas distribution and accumulation [12]. The results show that the downward ventilation is beneficial to the combination of gas and air. The greater the air speed is or the smaller the roadway angle is, the smaller the possibility of gas accumulation is; the transient model of airflow stability induced by gas accumulation was established, and it was found that the main reason for airflow disorder is the air pressure of gas accumulation [13]. Furthermore, methane buoyancy [14], shock wave, and main fan pressure [15] could cause the flow to stall or reverse. The dynamic simulation of gas migration in coal and gas outburst can be realized with the help of the mine ventilation network software during the disaster period [16]. Combined with laws between outburst gas and max impact power of ventilation structures, as well as the reasonable location of air door [17], the destructiveness of gas outburst to the damper [18] provides a theoretical basis for the stable operation of ventilation system.

In summary, the outburst gas is prone to air disorder and airflow reverse. However, the transmission law of outburst gas is a complex problem in ventilation system, which has many influence factors of ventilation parameters, such as the length of underground roadway, the air resistance, and the air pressure, as well as the complexity of ventilation network [19, 20]. There is little research on the process of outburst air disorder and airflow reversal law, as well as its quantitative analysis and evaluation.

This paper uses the numerical simulation method to study the airflow variation law of the tunneling ventilation system under different outburst pressure conditions. It provides the basis for monitoring and early warning before the disaster, ventilation decision-making during the disaster, and ventilation management during the disaster relief, which is of great significance for the prediction and prevention of coal and gas outburst accidents.

2. Gas Outburst and Airflow Reversal

2.1. Principle of Outburst Gas Flow. The airflow is an unstable state after the coal and gas outburst accident. The air pressure and air velocity changes were accompanied with plenty of the outburst gas, which obeys the energy conservation equation, the mass conservation equation, and the momentum conservation equation.

In a gas outburst, the gas concentration is suddenly rising with a large amount of gas entering into the roadway in a short time, and the air pressure of roadway is redistributed in ventilation system. Furthermore, the air pressure of the upwind and leeward side increases; in particular, the airflow would be reversed when the air pressure at the upwind side is lower than the outburst pressure.

2.2. Main Factors of Gas Outburst. The outburst intensity, the outburst position, and the physical conditions of roadway are main factors in a gas outburst.

Outburst intensity represents the scale of an outburst accident, which refers to the amount of coal and rock thrown into the roadway and the amount of ejected gas. According to the amount of outburst coal and rock, the outburst accident is divided into small outburst accident (<100 t), medium outburst accident (<500 t), large outburst accident (<1000 t), and extra-large outburst accident (≥1000 t).

Outburst position refers to the place where the outburst accident occurs. The outburst gas can be faster exhausted to the ground if the outburst position is closer to the air exhausted shaft. So reducing the air resistance of the return airway and increasing the intake airway are two main methods to decrease the impact of outburst accident on ventilation system.

The characteristics of roadway are determined by the physical conditions, such as the section and length of the roadway. Specifically, the outburst gas is easy to exhaust in the large section or the shorter length of roadway.

2.3. Airflow Reversal Degree. The outburst airflow reversal degree is defined as the ratio of the air quantity variation of the roadway after gas outburst and the original air quantity, which represents the airflow variation of a roadway affected by the gas outburst accident. It can be calculated by the following equation:

$$\varphi = \frac{Q_i - Q_0}{Q_0}, \tag{1}$$

where φ is the outburst airflow reversal degree; Q_i is the air quantity of the roadway after gas outburst, m^3/s; Q_0 is the original air quantity.

A positive value means that the outburst airflow is consistent with the original airflow, and a negative one means that the airflow is reversed.

3. Ventilation System of Tunneling Roadway

3.1. Composition of Tunneling Ventilation System. The ventilation system in tunneling roadway is composed of tunneling roadway, heading face, auxiliary fan, and air duct, as shown in Figure 1. Most of the gas outburst accident occurs in the heading face [21].

The forced ventilation style is adopted in tunneling roadway ventilation, which has the advantages of small air leakage and large air supply. The fresh air is transported from the intake airway to the heading face through the auxiliary fan and air duct, and the polluted air enters the return airway through the tunneling roadway. The air door obstructs the air, and the air duct needs to pass through the

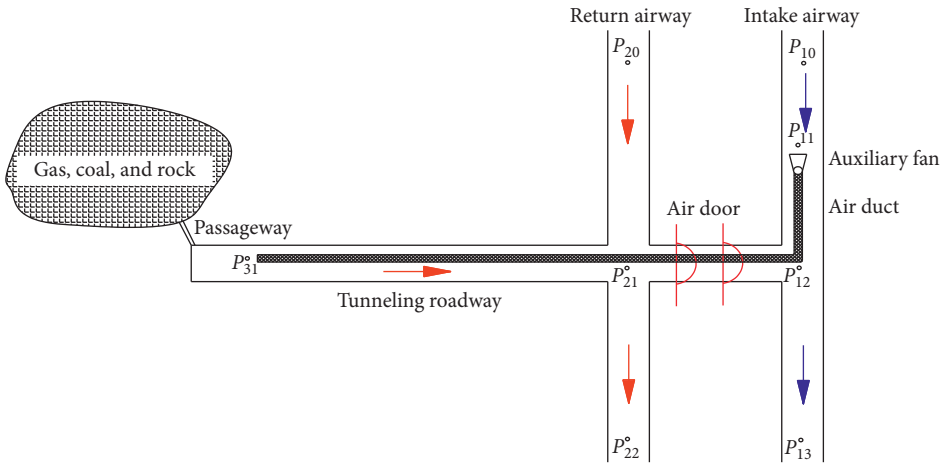

Figure 1: Sketch map of ventilation system in tunneling roadway.

air door. The blue arrow in Figure 1 indicates the airflow direction of the fresh air, and the red one indicates the polluted air.

3.2. Airflow Reversal of Tunneling Ventilation System. Suppose that P_i represents the gauge total pressure in position i, the magnitude of air pressure is $P_{20} > P_{21} > P_{22}$, $P_{10} > P_{11} > P_{12} > P_{13}$, and $P_{11} > P_{31} > P_{21}$ in the tunneling ventilation system shown in Figure 1.

In a gas outburst, P_{12} rises rapidly with the high pressure released by the outburst gas. When it reaches Point 21, one part of the gas attacks the air door, and the other part directly flows into the return airway. If $P_{21} > P_{20}$, the gas will flow in the opposite direction from Point 21 to Point 20. If the air door is destroyed, the gas reaches the intake airway. The flow direction depends on the magnitude of air pressure of Points 10, 12, and 13. With the exhaustion of outburst energy, the mine ventilation system reaches a new equilibrium state.

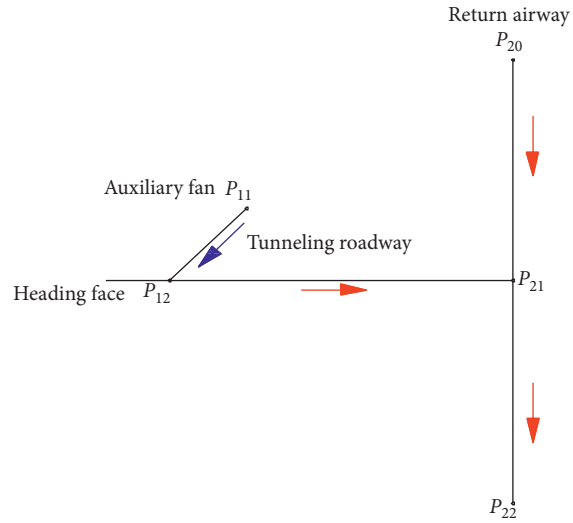

Figure 2: Simplified ventilation network of tunneling roadway.

3.3. Simplification of Tunneling Ventilation System. A ventilation facility usually has two states, a destroyed state and a normal state, in a gas outburst. The air door plays an important role in the accident, especially the safety of air door, which directly affects the scope of gas outburst. At present, it is particularly difficult to destroy the antioutburst air door in a gas outburst accident as a better shock-resistant capability. So, the air migration is more significant in the return airway after gas outburst.

The tunneling ventilation system can be simplified in Figure 2 in a normal state. There are 4 branches, the return airways (P_{20}–P_{21} and P_{21}–P_{22}), the tunneling roadway (P_{12}–P_{21}), and the auxiliary fan (P_{11}–P_{12}).

3.4. Calculation of Ventilation Parameters of Tunneling Ventilation System. Suppose that both sectional areas of the return airway and tunneling roadway are 15 m^2, the friction resistance coefficient is 100×10^{-4}, the inlet air quantity of return airway Q_{20} is 40 m^3/s, and the air quantity of auxiliary fan Q_{fan} is 9 m^3/s. Then the outlet of return airway Q_{21} is 49 m^3/s. According to the relationship between the air resistance and the friction resistance coefficient of the roadway,

$$R = \frac{LU\alpha}{S^3}, \tag{2}$$

where R represents the air resistance, kg/m^7; L represents the length of roadway, m; α represents the friction resistance coefficient, kg/m^3; U represents the perimeter of roadway section, m; S represents the sectional area of the roadway, m^2.

In equation (2), the air resistance of return airway $R_{20} = R_{21} = 0.0032\ kg/m^7$, and the tunneling roadway from the air duct outlet to the return airway $R_{12} = 0.00576\ kg/m^7$. Assuming that the operation pressure is the standard atmospheric pressure (101.35 hPa), the gauge total pressure at the inlet of return airway $P_{20} = 6$ Pa, and the node pressure $P_{22} = -14$ Pa.

4. Modeling of Gas Outburst in Tunneling Roadway

4.1. Model Assumptions

(1) Assuming that there is no heat transfer and no chemical reaction in the airflow, the gas flow process in the roadway is isothermal; then the gas compression factor and friction coefficient are constants.

(2) The airflow expansion coefficient of wall and the local resistance loss of equipment and pipeline are 0.

(3) The gas outburst source, the gas emission, and external sources in the pipeline network are not considered temporarily.

(4) The error of uneven distribution of flow field in tunnel caused by transient is ignored.

4.2. Physical Model and Meshing. The intersection of the tunneling roadway and return airway is the key position of this model. The airflow direction is determined by calculating the ventilation parameters. The physical model and its physical parameters are shown in Figure 3.

In Figure 3, the length of tunneling roadway is 500 m, and the length of return airway is 500 m, including 250 m at the upwind side of the intersection and 250 m at the downward side. The section area is 15 m^2, the width is 5 m, and the height is 3 m. The length of the air duct is 450 m, the radius is 0.5 m, its outlet is 50 m from the heading face, and the center of air duct is 1 m from the roof and 1 m from the roadway.

The physical model is divided with Tet/Hybrid elements and TGrid type, the spacing is 0.5 m, and the mesh quantity is 608110. The meshing is shown in Figure 3.

4.3. Mathematical Model. The boundary conditions of the model are shown in Table 1.

In Table 1, the physical model area is fluid type, and the pressure of operation condition is 101.35 hPa. The inlet boundary condition of return airway and outburst position is pressure inlet, the initial gauge total pressure is calculated by equation (2), and the result is shown in Table 1. The species of inlet of return airway is 20% oxygen and 80% nitrogen, and the outburst position is 100% CH_4.

The inlet boundary condition of the air duct is velocity inlet, and the species is 20% oxygen and 80% nitrogen. The outlet of return airway is pressure outlet.

Turbulent flow is a common flow phenomenon in most engineering problems. FLUENT software provides standard k–ε, RNG k–ε, and realizable k–ε models. The realizable k–ε model has good performance for solving the adverse pressure gradient and vortex problems.

The pressure-based type, the absolute velocity formulation, and pressure-velocity coupling algorithm are used to solve the problem. Further, adopting SIMPLE scheme to calculate the mathematical model, it computes the mass conservation and obtains the pressure field by the mutual correction of pressure and velocity.

A reasonable accuracy is an important parameter to ensure the convergence of the model. The convergence residual is 10^{-6} in this model and the number of iterations is 1000, so the calculation will be finished when the residuals of each variable were less than 10^{-6} or when the iterations reach 1000. Furthermore, the convergence of the calculation results can be dynamically monitored by checking the iterative residuals of each variable.

5. Results and Discussion

5.1. Distribution Laws of Ventilation Parameters. Using Fluent software, the flow field distributions of outburst gas in tunneling ventilation when the outburst pressure is 0.1001 MPa, 0.1005 MPa, 0.101 MPa, 0.105 MPa, 0.11 MPa, 0.15 MPa, 0.2 MPa, 0.5 MPa, 0.74 MPa, 1 MPa, and 5 MPa are obtained, respectively. Data from the simulation results are extracted and the cloud charts of air pressure, air velocity, and gas concentration under different outburst pressure conditions are drawn, as shown in Figures 4(a)~4(k). The cloud chart of air pressure is the plane where the height equals 1 m ($z = 1$). The two contour maps of velocity and gas concentration above are the outlet of return air roadway, and the two contour maps below are the inlet of the return airway.

The outburst gas is the external energy source into the tunneling ventilation system after the gas outburst accident. From Figure 4, with the increase of outburst pressure, the air pressure is rapidly rising in the heading face. Then, a high-pressure zone instantly formed; it makes all of the inlet and outlet in return airway into relative low pressure areas. As the outburst pressure is higher than the inlet of return airway, the outburst gas can overcome the air resistance loss of the return airway, and then the airflow will be reversed.

The data of velocity magnitude, CH_4 concentration, and total pressure of inlet and outlet of the return airway extracted from simulation results are shown in Table 2. All parameters are taken as the maximum value on the plane.

As shown in Table 2, the inlet velocity and CH_4 concentration are less than the outlet velocity and CH_4 concentration with the increase of outburst pressure. Before the outburst pressure is 0.1001 MPa, the absolute pressure at the inlet is less than the absolute pressure at the outlet, and the other states are opposite.

Defining the relative variation coefficient is the quotient of the relative change rate of air pressure and the relative change rate of the outburst gas pressure, which is calculated as shown in Figure 5. Moreover, the variation law of inlet and outlet pressure in return airway with outburst pressure is also shown in Figure 5.

From Figure 5, there is a gradually decreasing relationship between inlet and outlet of return airway and the outburst pressure. With the increase of the outburst pressure (from 1 hPa to 1 MPa), the inlet pressure increases to 264 hPa and the outlet pressure increases to 289 hPa. The relative variation coefficient of pressure in the inlet of return airway decreases from 1501.5 to 1.62, and the outlet decreases from 2002 to 1.65. Then, the gas emission rates of inlet and outlet in return airway are calculated. The variation

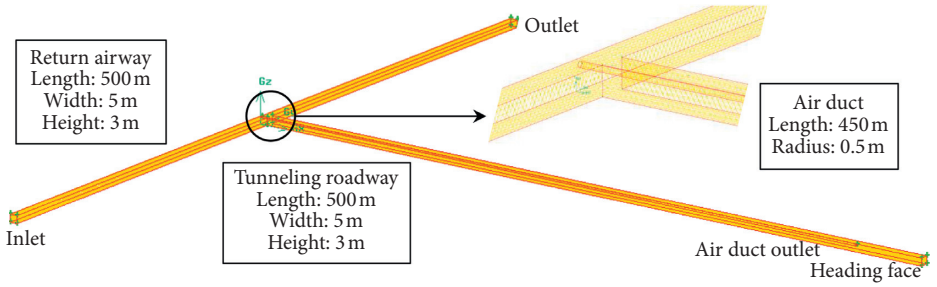

Figure 3: Physical model and its meshing.

Table 1: Boundary conditions.

Boundary category	Location	Boundary type	Species	Gauge total pressure
Inlet boundary	Inlet of return airway	Pressure inlet	$O_2 = 20\%$, $N_2 = 80\%$	6 Pa
	Outburst	Pressure inlet	$CH_4 = 100\%$	(1, 5, 10, 50,100, 500) hPa; (0.1, 0.4, 0.64, 0.9, 4.9) MPa
Outlet boundary	Air duct outlet	Velocity inlet	$O_2 = 20\%$, $N_2 = 80\%$	−14 Pa
	Outlet of return airway	Pressure outlet		

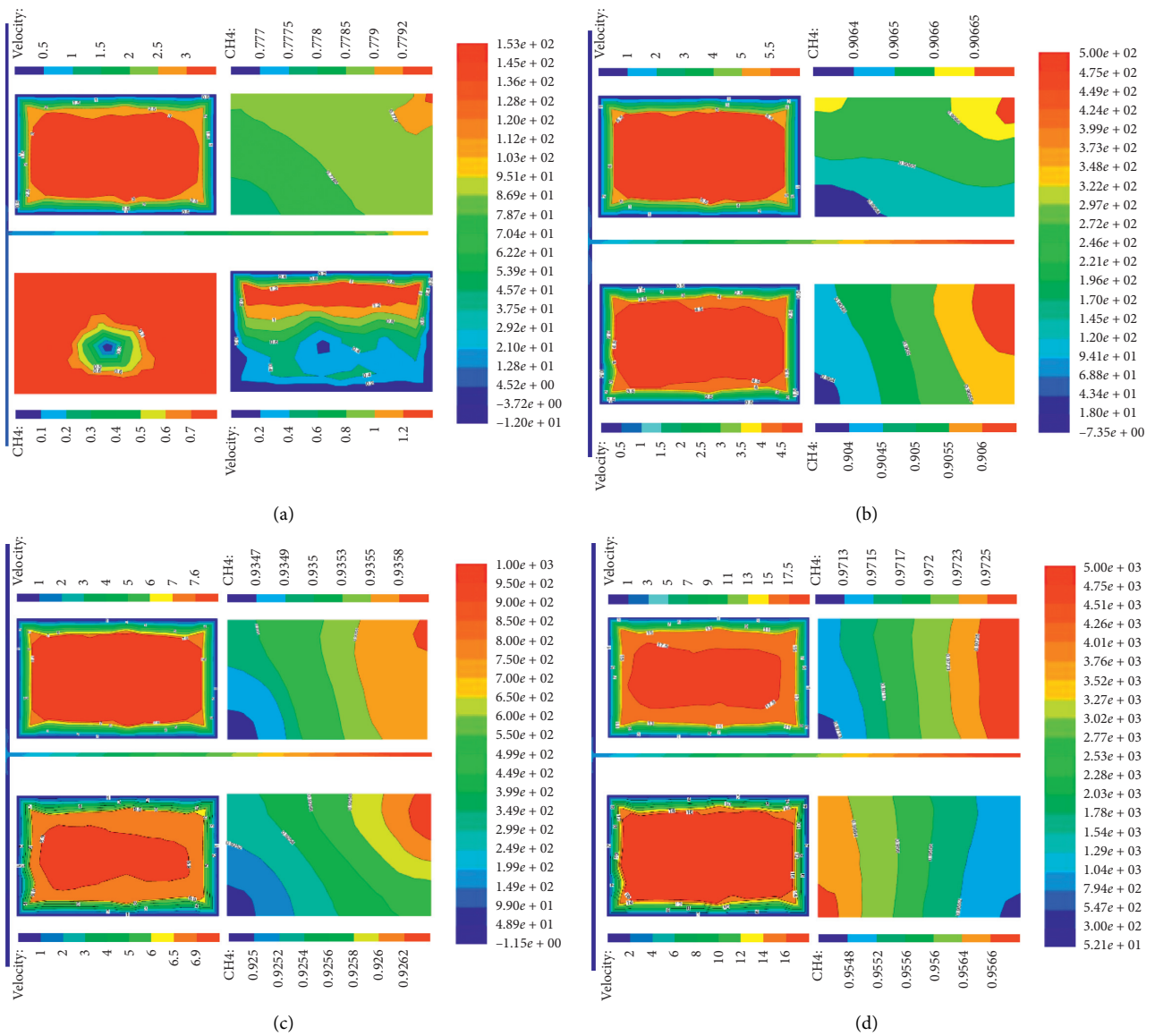

Figure 4: Continued.

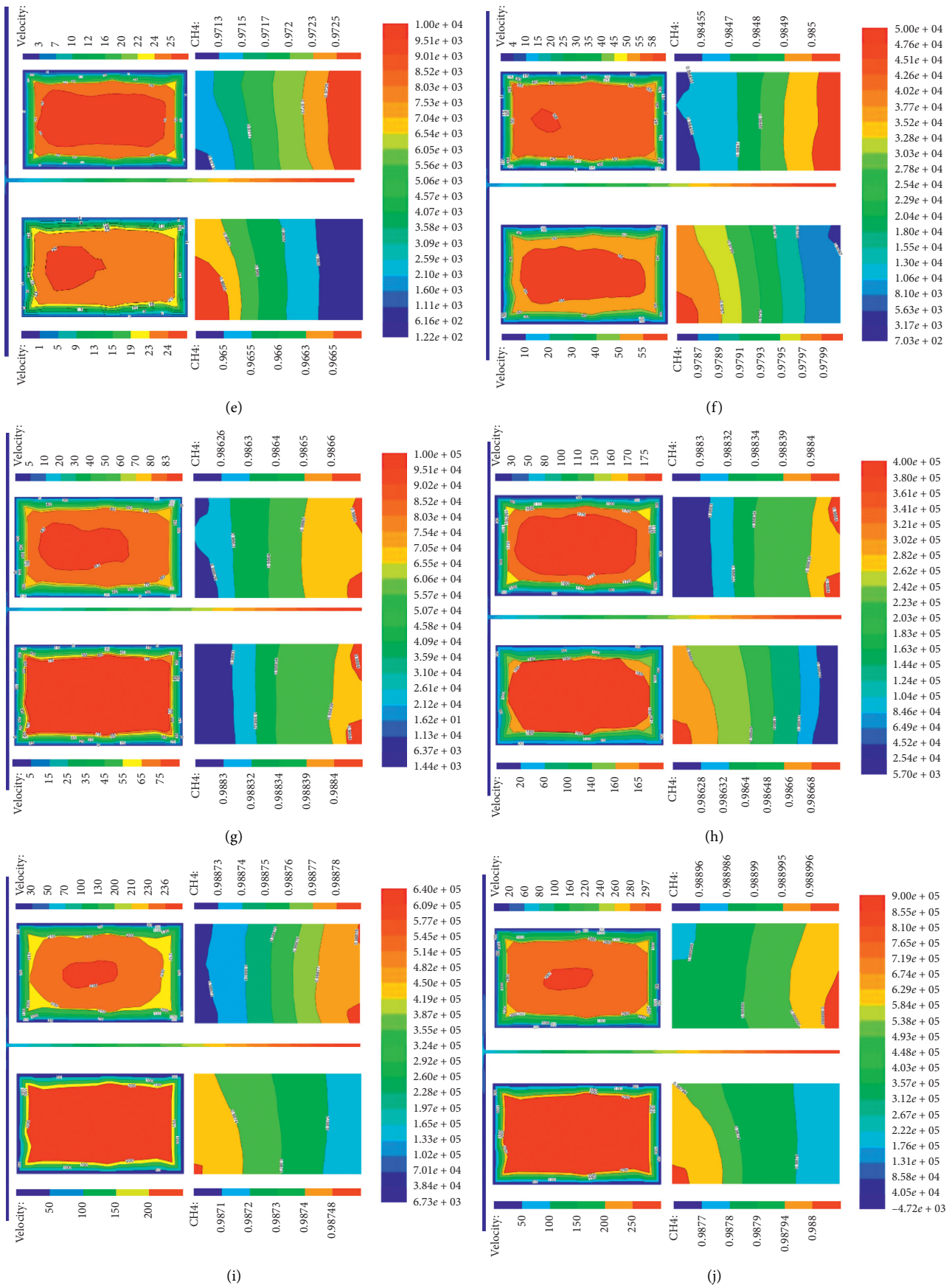

Figure 4: Continued.

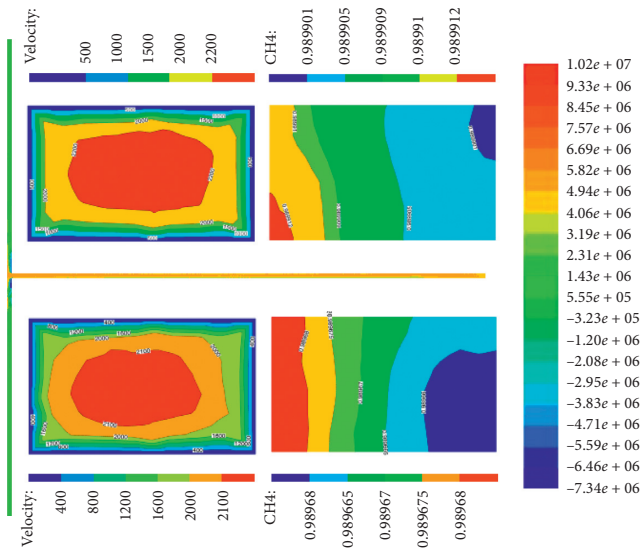

(k)

Figure 4: Cloud charts of ventilation parameters under different outburst pressures in heading roadway. (a) 0.1001 MPa. (b) 0.1005 MPa. (c) 0.101 MPa. (d) 0.105 MPa. (e) 0.11 MPa. (f) 0.15 MPa. (g) 0.2 MPa. (h) 0.5 MPa. (i) 0.74 MPa. (j) 1 MPa. (k) 5 MPa.

of gas concentration and gas emission rate with outburst pressure are shown in Figure 6.

As shown in Figure 6, the gas concentration of the inlet and outlet in return airway increases rapidly with the increase of outburst pressure. When the outburst pressure is greater than 0.15 MPa, the gas concentration exceeds 98% in tunneling ventilation system. Furthermore, the gas emission also increases due to the high concentration of outburst gas. It can reach 2.5×10^5 m^3/min, while the outburst pressure was 1 MPa of inlet and outlet of return airway. Because the air velocity of the outlet of return airway is greater than the inlet and the pressure is lower than inlet, the gas concentration and gas emission of the outlet are greater than those of the inlet.

5.2. Airflow Disturbance Law of Roadway Intersection. The intersection of tunneling roadway and return airway is the confluence point of airflow, and it is the key position of tunneling ventilation system. The pathline of air velocity at 1 m ($z = 1$ m) is drawn in Figure 7. Figure 7(a) shows the conditions of no outburst, and Figures 7(b) to 7(l) are the different outburst pressures from 0.1001 MPa to 5 MPa.

Figure 7 shows that, before the occurrence of gas outburst accident, the pathline of windward return airway and the intersection are relatively gentle. There is merely a small vortex in the upwind return airway. After the occurrence of gas outburst accident, the pathline vortex appears in both the windward and the upwind sides of the return airway. In addition, the range and intensity of vortex are larger with the increase of outburst gas pressure. Because the leeward return airway cannot exhaust the outburst gas in time, the gas migrated in reverse direction along the windward return airway. Then the airflow reversal phenomenon emerges.

5.3. Airflow Reversal Law of Return Airway. According to the air velocity of the inlet and outlet of return airway, the variation curve of inlet and outlet air velocity of return airway with outburst pressure is shown in Figure 8.

Airflow reversion will seriously affect the safety and stability of ventilation system, especially in the intake airway. Figure 8 shows that when the outburst pressure increases from 1 hPa to 1 MPa, the air velocity of the inlet decreases from −1.38 to −284.44 m/s, and the air velocity of the outlet increases from 3.10 to 297.38 m/s. A negative sign indicates the opposite direction of airflow. The airflow reversal quantity has an important impact on the ventilation system. Calculating the airflow reversal degree in each state, the relationship between outburst airflow pressure and airflow reversal degree is drawn in Figure 9.

Form Figure 9, the airflow reversal degree of the inlet of return airway decreases from −1.29 to −265.8 when the outburst pressure increases from 1 hPa to 1 MPa. It is a cubic

Table 2: Ventilation parameters of inlet and outlet in return airway.

Outburst pressure (MPa)	Inlet			Outlet		
	Velocity magnitude (ms^{-1})	CH_4 (%)	Pressure (Pa)	Velocity magnitude (ms^{-1})	CH_4 (%)	Pressure (Pa)
0	1.07	0	6	1.62	0	−12
0.1001	−1.38	78.89	7	3.10	77.93	−11
0.1005	−4.65	90.64	13	5.72	90.67	−3
0.101	−7.00	92.63	22	7.91	93.58	7
0.105	−16.72	95.67	99	17.72	97.27	90
0.11	−24.15	96.68	198	25.36	97.82	198
0.15	−55.75	97.99	1025	58.07	98.5	1092
0.2	−80.07	98.29	2104	83.49	98.66	2271
0.5	−170.00	98.67	9450	177.54	98.84	10305
0.74	−226.95	98.75	16829	236.41	98.88	18275
1	−284.44	98.80	26422	297.38	98.99	28914
5	−2142.67	98.97	1496880	2255.34	98.99	1659410

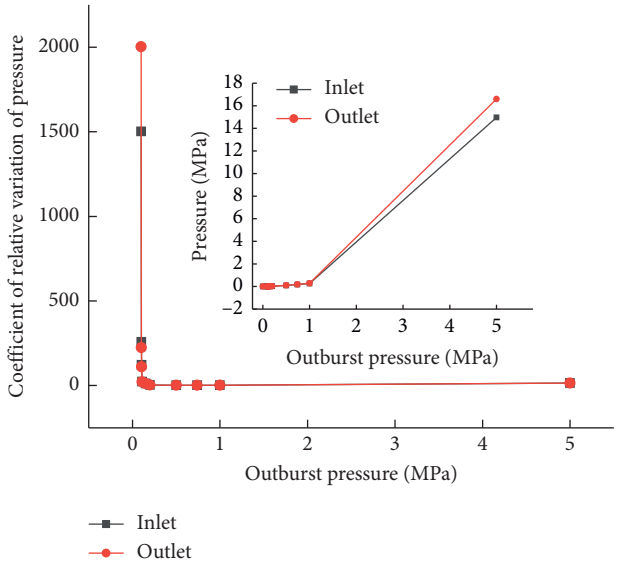

Figure 5: Variation law of inlet and outlet pressure in return airway.

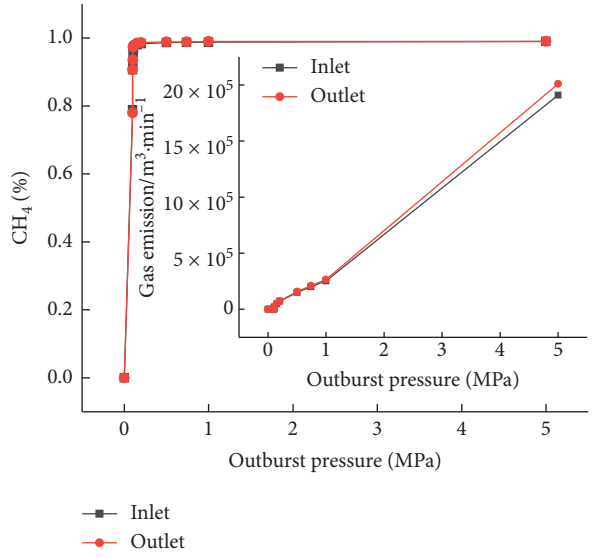

Figure 6: Variation of gas concentration and gas emission rate with outburst pressure.

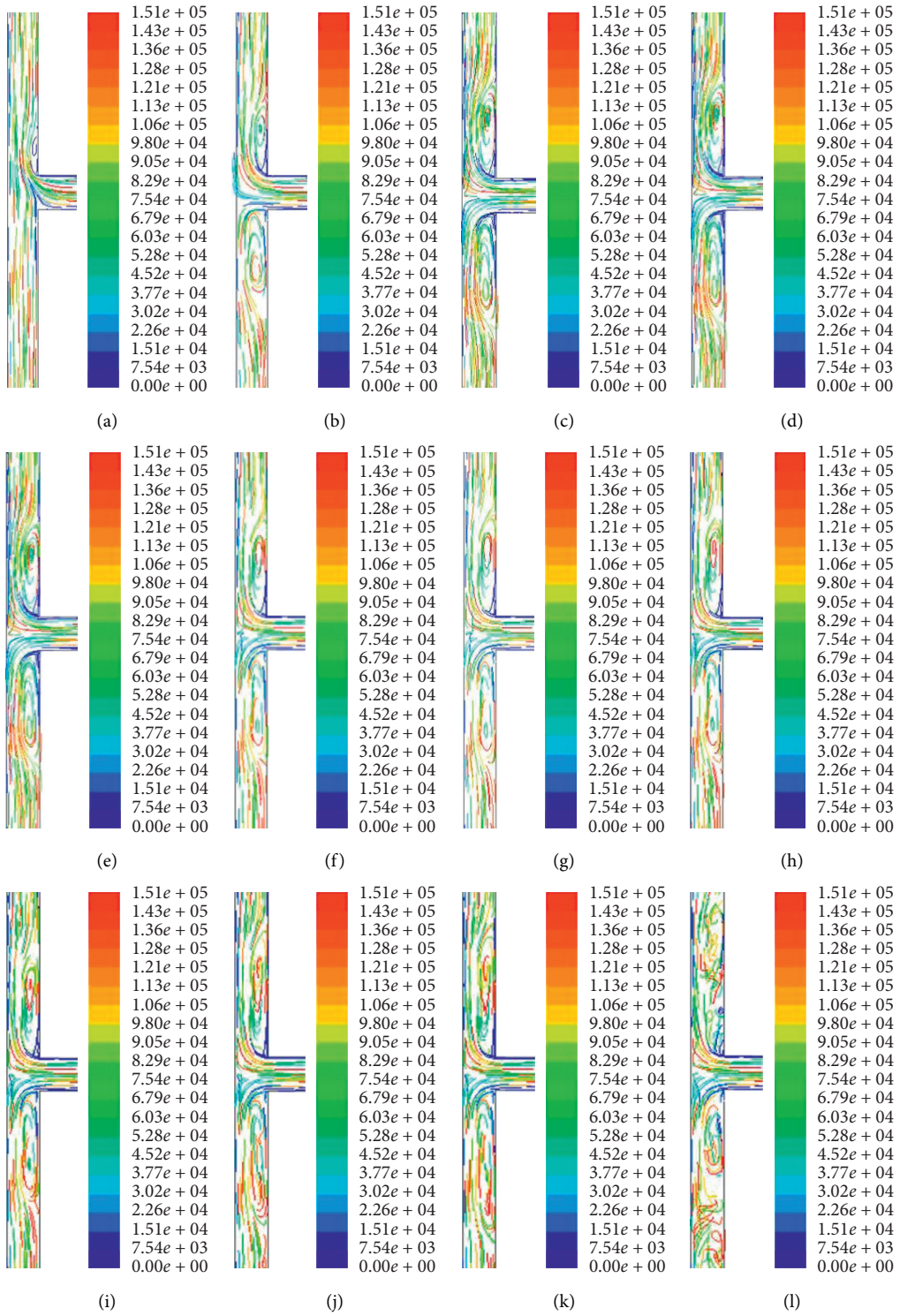

Figure 7: Ventilation pathline of tunneling roadway intersection.

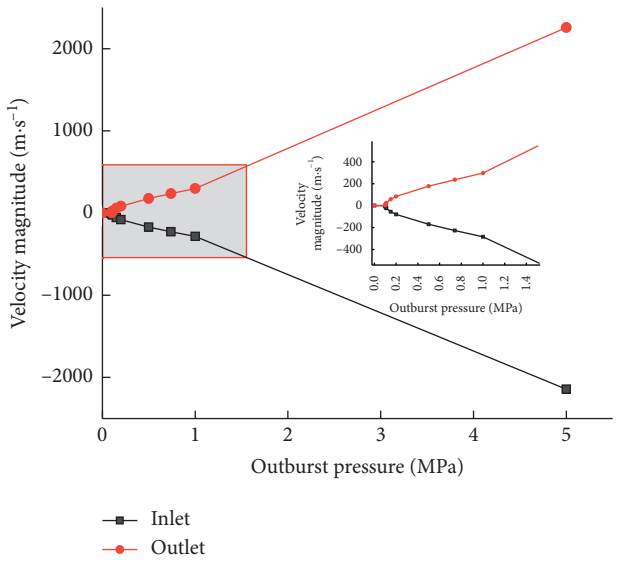

Figure 8: Variation curve of inlet and outlet air velocity with outburst pressure.

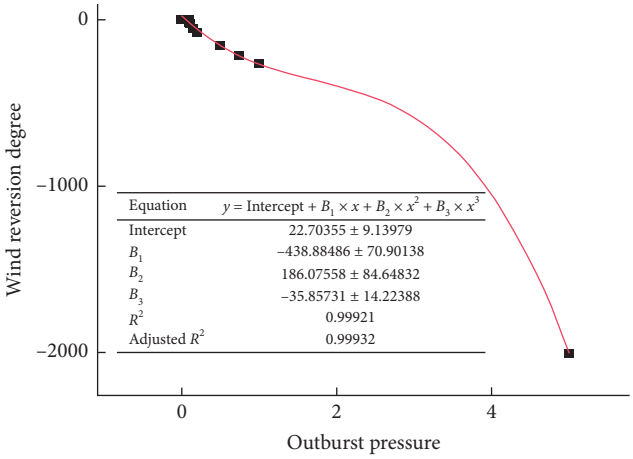

Figure 9: Relationship between airflow reversal degree and outburst airflow pressure.

polynomial relationship between airflow reversal degree and outburst airflow pressure. The correlation coefficient is 0.99932.

6. Conclusions

This paper analyzes the main characteristics of coal and gas outburst accidents, proposes the degree of outburst airflow reversal, and studies the principle of airflow reversal in the tunneling ventilation system. Then, ventilation parameters are calculated by the simplified topology diagram of the tunneling ventilation system, and the airflow reversal model of tunneling ventilation system under different conditions is established. The main results are as follows.

The inlet pressure increases to 264 hPa and the outlet pressure increases to 289 hPa, while the outburst pressure increases from 1 hPa to 1 MPa. Furthermore, the relative variation coefficient of pressure in the inlet of return airway decreases from 1501.5 to 1.62, and the outlet decreases from 2002 to 1.65. The air velocity of the inlet decreases from −1.38 to −284.44 m/s, and the air velocity of the outlet increases from 3.10 to 297.38 m/s.

The gas concentration of the inlet and outlet increases rapidly in return airway with the increase of outburst pressure. When the outburst pressure is greater than 0.15 MPa, the gas concentration exceeds 98% in tunneling ventilation system; and there is a cubic polynomial relationship between airflow reversal degree and outburst pressure.

Data Availability

The data used to support the findings of this study are included within the article.

Conflicts of Interest

The authors declare that they have no conflicts of interest.

Acknowledgments

This work was supported by "the Fundamental Research Funds for the National Natural Science Foundation of China" (51804120 and 52074122), "the Fundamental Research Funds for the Central Universities" (3142018003), and Science and Technology Research Project of Higher Education in Hebei Province (Z2018004).

References

[1] Z. H. Li, E. Y. Wang, J. C. Ou, and Z. T. Liu, "Hazard evaluation of coal and gas outbursts in a coal-mine roadway based on logistic regression model," *International Journal of Rock Mechanics and Mining Sciences*, vol. 80, 2015.

[2] K. P. Chen, "A new mechanistic model for prediction of instantaneous coal outbursts- Dedicated to the memory of Prof. Daniel D. Joseph," *International Journal of Coal Geology*, vol. 87, no. 2, 2011.

[3] N. Kursunoglu and M. Onder, "Application of structural equation modeling to evaluate coal and gas outbursts," *Tunnelling and Underground Space Technology Incorporating Trenchless Technology Research*, vol. 88, 2019.

[4] Q. Ye, G. G. X. Wang, Z. Z. Jia, and C. S. Zheng, "Experimental study on the influence of wall heat effect on gas explosion and its propagation," *Applied Thermal Engineering*, vol. 118, 2017.

[5] S. Zhu, J. Cheng, Z. Wang, and M. Borowski, "Physical simulation experiment of factors affecting temperature field of heat adjustment circle in rock surrounding mine roadway," *Energy Sources, Part A: Recovery, Utilization, and Environmental Effects*, vol. 30, 2020.

[6] K. Wang, S G. Jiang, X. P. Ma, Z. G. Wu, W. Zhang, and H. Shao, "Study of the destruction of ventilation systems in coal mines due to gas explosions," *Powder Technology*, vol. 286, 2015.

[7] A. T. Zhou and K. Wang, "Airflow stabilization in airways induced by gas flows following an outburst," *Journal of Natural Gas Science and Engineering*, vol. 35, 2016.

[8] D. M. Ma, Z. H. Li, and Y. L. Yang, "Research on coal and gas outburst accident of Xinxing coal mine based on shock wave

theory," *Journal of Safety Science and Technology*, vol. 8, no. 8, pp. 69–73, 2012, in Chinese.

[9] Y. D. Wang, *Research on disaster evolution of ventilation system during coal and gas outburst*, Ph.D. dissertation, Liaoning Technical University, Fuxin, China, 2017.

[10] Z. X. Li, Yu Liu, and X. J. Yu, "Dynamic superposition and simulation research on flowing of gas outburst and mine ventilation network," *Journal of Chongqing University*, vol. 35, no. 11, pp. 111–116, 2012, in Chinese.

[11] Y. F. Feng, Y. Liu, and J. L. Yu, "Discussion on airflow reversal of parallel branch of upper roadway after coal and gas outburst," *Coal*, vol. 38, no. 12, 2012, in Chinese.

[12] J. L. Gao and D. Luo, "Numerical simulation of backward flow of methane roof layer in an airway," *Journal of Chongqing University*, vol. 32, no. 3, pp. 319–323, 2009, in Chinese.

[13] A. Zhou and K. Wang, "A transient model for airflow stabilization induced by gas accumulations in a mine ventilation network," *Journal of Loss Prevention in the Process Industries*, vol. 47, pp. 104–109, 2017.

[14] A. Zhou, K. Wang, J. Wang, and T. Feng, "The role of methane buoyancy on the stability of airway airflow in underground coal mine ventilation," *Journal of Loss Prevention in the Process Industries*, vol. 54, pp. 346–351, 2018.

[15] A. T. Zhou, M. Zhang, K. Wang, D. Elsworth, J. Wang, and L. P. Fan, "Airflow disturbance induced by coal mine outburst shock waves: a case study of a gas outburst disaster in China," *International Journal of Rock Mechanics and Mining Sciences*, vol. 128, Article ID 104262, 2020.

[16] Y. X. Chen, T. X. Chu, X. X. Chen, P. Chen, J. H. Si, and R. Peng, "Numerical simulation study of influencing factors for 3D coal seam gas drainage efficiency," *Arabian Journal of Geosciences*, vol. 8, no. 14, p. 678, 2021.

[17] S. J. Huang, X. X. Ma, and Y. Cai, "Calculation of influence of gas outburst on ventilation system," *Journal of Mining Safety & Environmental Protection*, vol. 2, pp. 16–18, 2000, in Chinese.

[18] G. Wang, "Catastrophic damage and failure characteristics of coal and gas outburst," Master Dissertation, Shandong University of Science and Technology, Qingdao, China, 2008.

[19] H. R. Zhang, S. Q. P. Lluis, Y. J. Zhao, and C. V. Sancheza, "Researches and applications on geostatistical simulation and laboratory modeling of mine ventilation network and gas drainage zone," *Process Safety and Environmental Protection*, vol. 94, pp. 55–64, 2015.

[20] K. A. El-Nagdy, "Stability of multiple fans in mine ventilation networks," *International Journal of Mining Science and Technology*, vol. 23, no. 4, pp. 569–571, 2013.

[21] Z. M. Qu, X. Q. Zhou, and H. Y. Wang, "The law of attenuation of ultimate gas explosion overpressure," *Journal of Coal Science and Engineering (China)*, vol. 4, pp. 410–414, 2008, in Chinese.